

Durham E-Theses

Computation of ground waves from pile driving and their effects on structures

Ramshaw, Christine Lesley

How to cite:

Ramshaw, Christine Lesley (2002) *Computation of ground waves from pile driving and their effects on structures*, Durham theses, Durham University. Available at Durham E-Theses Online:
<http://etheses.dur.ac.uk/3762/>

Use policy

The full-text may be used and/or reproduced, and given to third parties in any format or medium, without prior permission or charge, for personal research or study, educational, or not-for-profit purposes provided that:

- a full bibliographic reference is made to the original source
- a [link](#) is made to the metadata record in Durham E-Theses
- the full-text is not changed in any way

The full-text must not be sold in any format or medium without the formal permission of the copyright holders.

Please consult the [full Durham E-Theses policy](#) for further details.

COMPUTATION OF GROUND WAVES FROM PILE DRIVING AND THEIR EFFECTS ON STRUCTURES

by

Christine Lesley Ramshaw MEng CEng MICE

The copyright of this thesis rests with the author. No quotation from it should be published in any form, including Electronic and the Internet, without the author's prior written consent. All information derived from this thesis must be acknowledged appropriately.

A thesis submitted for the degree of
Doctor of Philosophy

School of Engineering
University of Durham

March 2002



31 MAY 2002

ABSTRACT

Present guidance on levels of vibration generated by pile driving is primarily empirical, conservative and often contradictory. The objective of this research was to model the ground waves generated by pile driving using the ABAQUS finite element program in order to predict the free ground surface response resulting from installation by both impact and vibratory hammers.

New procedures including infinite element and quiet boundary formulations have been developed for the computation of ground surface vibrations caused by impact and vibratory driving of pre-formed piles. The procedures do not require a detailed knowledge of site conditions and are therefore particularly useful as a preliminary design tool and for modelling the large amount of site data that currently exists in order to assist in the development of more rational guidance. The work has brought together research from several areas of study in order to produce computational procedures for modelling vibrations from pile driving.

The new models have been validated by comparisons with measurements from various piling sites. The new methods now need to be applied to a large number of varied sites in order to develop site specific guidance. It is envisaged that this guidance could be in the form of design charts or simple formulae for incorporation into the relevant British Standards or Eurocodes.

A range of common building forms has been incorporated into the models. The results indicate that slender frames can be analysed by transient displacements imposed on the foundations; however, a full three-dimensional analysis with soil-structure interaction is required for walls and infilled panels so that the reduced foundation displacements are modelled correctly. The techniques developed during this project could be usefully extended to model the effects of pile driving on various geotechnical structures and pipelines and also other forms of excitation, such as vibrocompaction.

ACKNOWLEDGEMENTS

I would like to express my grateful thanks to my academic supervisors Dr A R Selby and Professor P Bettess for their help and guidance during this work. Thanks are also due to Dr J A Bettess and Dr K Brazier of the Information Technology Service for their assistance in the installation and maintenance of the ABAQUS program on the University network.

The funding of this work by EPSRC through Grant No GR/L18679 and by British Steel is gratefully acknowledged.

Thanks are also due to Dr D M Hiller & Mr G I Crabb of the Transport Research Laboratory for allowing me access to their vibration database and to Mr M Heaton of Mouchel Consulting for the provision of the M66 data.

Thanks are extended to my colleagues in Arup (Newcastle), particularly Mrs C Matthews and Mr D W Brown for covering for me during several periods of unpaid leave. The assistance of the graphics team in the preparation of some of the figures is gratefully acknowledged.

Apologies to all of my family and friends for the lack of contact over the last couple of years – thank you for your patience. Particular thanks go to my parents, Helen and Tony Gammage, for their encouragement and support.

Special thanks are extended to my husband, Martin, without whose support, particularly the many hours of child-care, this thesis would not have been completed. Thanks also go to my daughter Frances for being so good and loving despite my absences.

STATEMENT OF COPYRIGHT

The copyright of this thesis rests with the author. No quotations from it shall be published without the author's prior written consent and information derived from it should be acknowledged.

DECLARATION

No material from this thesis has been previously submitted for a degree at this or any other university.

TABLE OF CONTENTS

Abstract	i
Acknowledgements.....	ii
Statement of copyright.....	ii
Declaration.....	ii
Table of Contents.....	iii
List of Tables	viii
List of Figures.....	ix

CHAPTER 1: INTRODUCTION

1.1 General Background.....	1
1.2 Current Guidelines	1
1.2.1 Thresholds for damage.....	2
1.2.2 Thresholds for perception and disturbance.....	3
1.3 Aims and Objectives	3
1.4 General Approach to the Problem.....	4
1.5 Thesis Structure.....	5

CHAPTER 2: GROUND VIBRATIONS FROM PILING

2.1 Introduction.....	7
2.2 Vibration Terms and Definitions	7
2.3 Measures of Vibration	8
2.4 Factors affecting the energy transmitted from pile driving	10
2.4.1 Types of pile and hammer	10
2.4.2 Driving energy	13
2.4.3 The properties of the pile	14
2.4.4 Ground conditions	14
2.5 Wave Propagation.....	15
2.5.1 Compressional waves (P waves).....	16
2.5.2 Shear waves (S waves)	16
2.5.3 Surface waves (R waves).....	17
2.5.4 Propagation of ground waves from pile driving	17
2.6 Attenuation of ground vibrations generated by piling.....	17
2.6.1 Geometrical damping.....	17
2.6.2 Material damping.....	18
2.7 Factors affecting the transmission of groundborne vibrations into structures.....	19
2.8 Prediction of vibrations generated by piling.....	19
2.9 Vibration databases.....	20
2.10 Summary	20

CHAPTER 3: NUMERICAL MODELLING OF GROUND WAVES IN ABAQUS

3.1 Introduction.....	29
3.2 The ABAQUS finite element program	29
3.3 Verification of the infinite elements available in ABAQUS	30
3.3.1 Infinite elements	30

3.3.2	Static response: The Boussinesq and Flamant problems	31
3.3.3	Dynamic response: Wave propagation in an infinite medium....	32
3.4	Verification of FE/IE model to transmit P, S and R waves	33
3.4.1	General	
3.4.2	Compressional waves (P waves).....	33
3.4.3	Shear waves (S waves)	35
3.4.4	Rayleigh waves (R waves).....	35
3.5	Verification of wave attenuation in ABAQUS	36
3.6	Conclusions.....	37

CHAPTER 4: DEVELOPMENT OF A QUIET BOUNDARY FOR THE EFFECTIVE ABSORPTION OF GROUND WAVES GENERATED BY PILE DRIVING

4.1	Introduction	64
4.2	Literature review	65
4.2.1	Viscous boundaries	65
4.2.2	Para-axial boundaries.....	66
4.2.3	Time-dependent problems	66
4.2.4	Multi-directional boundaries.....	67
4.2.5	Extrapolation boundaries	67
4.2.6	Boundary for a layered medium – Love or Rayleigh waves	67
4.2.7	Smith technique	68
4.2.8	Damping techniques	68
4.2.9	Substructuring.....	69
4.2.10	Large finite element meshes	69
4.2.11	Periodic infinite elements	69
4.2.12	Transient infinite elements.....	72
4.3	Assessment of the various quiet boundary techniques for the simulation of ground waves from pile driving.....	72
4.4	Derivation and insertion of viscous boundary formulations into ABAQUS	73
4.4.1	Description of the ABAQUS user element interface.....	73
4.4.2	Standard viscous boundary	73
4.4.3	Rayleigh viscous boundary.....	77
4.5	Application of viscous boundary formulations to the pile driving model	79
4.6	Proposed technique for inserting periodic infinite elements into ABAQUS	80
4.7	Conclusions and recommendations for further work	81

CHAPTER 5: DEVELOPMENT OF A NUMERICAL MODEL FOR VIBRATORY PILING

5.1	Introduction.....	99
5.2	Chronological development of the model.....	102
5.3	A finite element model for vibratory piling.....	107
5.3.1	General.....	107
5.3.2	Mesh design	108
5.3.3	Representation of the pile	109
5.3.4	Material properties (soil behaviour under vibratory loading)...	109
5.3.5	Simulation of pile-soil interaction	110

5.3.6	One-dimensional model for pile toe response	111
5.3.7	Simulation of vibratory hammer motion	112
5.3.8	Analysis procedure	112
5.4	The 'Standing Wave' phenomenon	114
5.4.1	Identification of the phenomenon	114
5.4.2	Frequency effects	115
5.4.3	Influence of the depth of pile penetration/distribution of shaft friction	115
5.4.4	Summary	116
5.5	Application of new quiet boundary to model	116
5.6	Modelling vibratory extraction at the Second Severn Crossing	119
5.6.1	Site conditions	119
5.6.2	Parameters used in the pile/soil interaction model	120
5.6.3	Parameters used in the wave propagation model	122
5.6.4	Parametric studies of vibratory pile extraction	123
5.6.5	Conclusions resulting from vibratory extraction simulation	127
5.7	Modelling vibratory pile installation at the Second Severn Crossing ..	128
5.7.1	General	128
5.7.2	Parametric studies of vibratory pile installation	128
5.7.3	Conclusions resulting from vibratory pile installation simulation	131
5.8	Validation of vibratory piling model	131
5.8.1	General	131
5.8.2	Site conditions at Flitwick, Bedfordshire	132
5.8.3	Parameters used in the pile/soil interaction model	132
5.8.4	Parameters used in the wave propagation model	134
5.8.5	Comparison of measured and predicted ground response at Flitwick	135
5.9	Conclusions and recommendations for further work	136

CHAPTER 6: DEVELOPMENT OF A NUMERICAL MODEL FOR IMPACT PILING

6.1	General background	235
6.2	Chronological development of the model	237
6.3	A finite element model for impact piling	242
6.3.1	Hammer impact model	242
6.3.2	Pile/soil model	242
6.3.3	Wave propagation model	244
6.4	Modelling impact piling at Greengate Railbridge, M66, Manchester ..	247
6.4.1	Site conditions	247
6.4.2	Initial parameters and assumptions	248
6.4.3	Parametric study of hammer impact model	249
6.4.4	Parametric study of pile/soil model	249
6.4.5	Derivation of input functions for pile 18 and application to the wave propagation model	250
6.4.6	Determination of small strain stiffness parameters from measured vibration traces	250
6.4.7	The ground response predicted by the wave propagation model	253
6.4.8	Conclusions resulting from impact piling simulation	254

6.5	Validation of impact piling model	255
6.5.1	General.....	255
6.5.2	Site conditions	255
6.5.3	Hammer impact model.....	256
6.5.4	Pile./soil model	256
6.5.5	Determination of small strain stiffness parameters from measured vibration traces.....	258
6.5.6	Wave propagation model.....	259
6.6	Conclusions and recommendations for further work.....	260

CHAPTER 7: INCORPORATION OF STRUCTURES INTO THE NUMERICAL MODELS FOR VIBRATORY AND IMPACT PILING

7.1	Introduction	311
7.2	Chronological development of model.....	311
7.3	A finite element model for pile-soil-structure interaction.....	313
7.3.1	General.....	313
7.3.2	Mesh design	313
7.3.3	Application of the computed piling induced ground excitation to the three-dimensional model	314
7.3.4	Representation of a steel portal frame	314
7.3.5	Representation of a brick wall	315
7.4	Vibratory waves on soil and structure.....	315
7.4.1	General.....	315
7.4.2	Comparison of ground response predicted by axisymmetric mesh and 3D mesh	315
7.4.3	Effect on a portal frame structure	316
7.4.4	Effects on an in-plane wall	317
7.5	Impact waves on soil and structure	317
7.5.1	General.....	317
7.5.2	Comparison of ground response predicted by axisymmetric mesh and 3D mesh	318
7.5.3	Effect on a portal frame structure	318
7.5.4	Effects on an in-plane wall	318
7.6	Conclusions and recommendations for further work.....	319

CHAPTER 8: CONCLUSIONS

8.1	Introduction	355
8.2	Quiet boundaries for the effective absorption of ground waves from pile driving	355
8.3	A numerical model for vibratory piling	356
8.4	A numerical model for impact piling	357
8.5	The incorporation of structures into the wave propagation models.....	358

REFERENCES	359
-------------------------	-----

APPENDICES

Appendix A: Publications resulting from this research

Appendix B: Calculation of Fourier constants for P, S and R waves

Appendix C: Listings of ABAQUS input files and *UEL subroutines for user-defined standard viscous boundaries in plane strain and axisymmetric conditions

Appendix D: Listings of ABAQUS input files and *UEL subroutines for user-defined Rayleigh viscous boundaries in plane strain and axisymmetric conditions

Appendix E: Velocity/time traces recorded during vibratory piling

Appendix F: FORTRAN program disp2vib.f

Appendix G: Parametric study of the effect of soil stiffness parameters on the ground response resulting from extraction of a casing from 13.8m depth at the Second Severn Crossing site

Appendix H: Borehole records and laboratory test data for the Flitwick site

Appendix I: Penetration Records for 10 piles subjected to dynamic load testing by the SIMBAT Method at the M66 site in Manchester/Borehole records and laboratory test results for the M66 site.

LIST OF TABLES

		Page
Table 2.1	Suggested <i>C</i> values given by Draft Eurocode 3	13
Table 5.1	Soil parameters used in pile/soil interaction model (SSC site)	120
Table 5.2	Measured arrival times of S wavefront from the pile shaft (SSC site)	122
Table 5.3	Measured vertical peak particle velocities during extraction: toe of casing at 13.8m below GL (SSC site)	124
Table 5.4	Vertical particle velocities (mm/s) at 8.9m, 16.9m and 33m geophones for various values of <i>E</i> for the alluvium and marl (SSC site)	124
Table 5.5	Measured radial peak particle velocities during extraction: toe of casing at 13.8m below GL (SSC site)	124
Table 5.6	Radial particle velocities at 8.9m, 16.9m and 33m geophones for various values of <i>E</i> for the alluvium and marl (SSC site)	125
Table 5.7	Effect of the soil stiffness under the toe on the amount of pile movement for various coefficients of friction (SSC site)	129
Table 5.8	Soil parameters used in the pile/soil interaction model (Flitwick)	133
Table 5.9	Mohr-Coulomb parameters used in the pile/soil interaction model (Flitwick)	134
Table 5.10	Soil parameters used in the wave propagation model (Flitwick)	134
Table 6.1	Calculation of pile impedance	248
Table 6.2	Soil parameters at the M66 site	249
Table 6.3	Arrival times of the P wave from the pile shaft (M66 site)	251
Table 6.4	Arrival times of the S wave from the pile shaft (M66 site)	252
Table 6.5	Arrival times of the P wave from the pile toe (M66 site)	253
Table 6.6	Soil and shaft resistance parameters for impact piling at Flitwick	257
Table 6.7	Pile toe parameters for impact piling at Flitwick	257
Table 6.8	Arrival times of the P wave from the pile toe (Flitwick)	258
Table 7.1	Dimensions of the ABAQUS beam elements representing the Universal Columns and Beams in the portal frame	316

LIST OF FIGURES

	Page
Figure 1.1	Comparison of transient vibration damage thresholds for domestic buildings given in national standards
	6
Figure 2.1	Example of periodic vibration generated by vibratory piling
	22
Figure 2.2	Example of transient vibration generated by impact piling
	23
Figure 2.3	The relationships between displacement, velocity and acceleration for sinusoidal vibration (after Das, 1983)
	24
Figure 2.4	Summary of the variables associated with groundborne vibration and piling (after CIRIA Technical Note 142, Head & Jardine, 1992)
	25
Figure 2.5	Propagation of P and S waves (after Uromeihy, 1990)
	26
Figure 2.6	Propagation of a Rayleigh wave (after Uromeihy, 1990)
	27
Figure 2.7	Attenuation of waves from a pile driving operation (after Attewell & Farmer, 1973)
	28
Figure 3.1	FE/IE mesh used in the Boussinesq and Flamant problems
	38
Figure 3.2	FE mesh used in the Boussinesq and Flamant problems
	39
Figure 3.3	The Boussinesq problem: displacement results
	40
Figure 3.4	The Flamant problem: displacement results
	41
Figure 3.5	Small FE/IE mesh used in wave propagation problem
	42
Figure 3.6	Small FE mesh used in wave propagation problem
	43
Figure 3.7	Extended FE mesh used in wave propagation problem
	44
Figure 3.8	Vertical displacement responses at node 7
	45
Figure 3.9	Vertical displacement responses at node 27
	46
Figure 3.10	Vertical displacement responses at node 151
	47
Figure 3.11	Axisymmetric wavefronts from a pulse load on a small radial disc
	48
Figure 3.12	FE/IE mesh used for P wave verification
	49
Figure 3.13	'Snapshots' of P wave in an FE/IE mesh
	50
Figure 3.14	Horizontal displacement of nodes at 3.6 seconds: Analytical vs ABAQUS solution
	51
Figure 3.15	FE/IE mesh used for S wave verification
	52
Figure 3.16	'Snapshots' of S wave in an FE/IE mesh
	53
Figure 3.17	Vertical displacement of nodes at 3.6 seconds: Analytical vs ABAQUS solution
	54
Figure 3.18	FE/IE mesh used for R wave verification
	55
Figure 3.19	'Snapshots' of R wave in an FE/IE mesh
	56
Figure 3.20	Displacement of nodes at 2.1 seconds: Analytical solution vs ABAQUS
	57
	(a) Horizontal displacements
	(b) Vertical displacements

Figure 3.21	Displacement of nodes at 4.2 seconds: Analytical solution vs ABAQUS (a) Horizontal displacements (b) Vertical displacements	58
Figure 3.22	Displacement of nodes at 8.4 seconds: Analytical solution vs ABAQUS (a) Horizontal displacements (b) Vertical displacements	59
Figure 3.23	Displacement of nodes at 16.8 seconds: Analytical solution vs ABAQUS (a) Horizontal displacements (b) Vertical displacements	60
Figure 3.24	Normalised plots of the horizontal and vertical components of an R wave with depth at a time of 3.6 seconds	61
Figure 3.25	FE/IE mesh used for uniaxial and axisymmetric conditions	62
Figure 3.26	FE/IE mesh used for spherical conditions	62
Figure 3.27	Attenuation of energy densities for a P wave in uniaxial, axisymmetric and spherical conditions	63
Figure 3.28	Attenuation of vertical amplitude for an R wave in uniaxial and axisymmetric conditions	63
Figure 4.1	Distribution of the standard and Rayleigh viscous boundaries around a finite element mesh proposed by Chow & Smith (1981)	82
Figure 4.2(a)	FE/IE plane strain mesh used to test the effectiveness of a user-defined standard viscous boundary in absorbing P waves	83
Figure 4.2(b)	FE/IE plane strain mesh used to test the effectiveness of ABAQUS infinite elements in absorbing P waves	83
Figure 4.2 (c)	Comparison of the effectiveness of the boundaries in absorbing P waves in a plane strain FE/IE mesh	84
Figure 4.3(a)	FE/IE plane strain mesh used to test the effectiveness of a user-defined standard viscous boundary in absorbing S waves	85
Figure 4.3(b)	FE/IE plane strain mesh used to test the effectiveness of ABAQUS infinite elements in absorbing S waves	85
Figure 4.3(c)	Comparison of the effectiveness of the boundaries in absorbing S waves in a plane strain FE/IE mesh	86
Figure 4.4(a)	FE/IE axisymmetric mesh used to test the effectiveness of a user-defined standard viscous boundary in absorbing P waves	87
Figure 4.4(b)	FE/IE axisymmetric mesh used to test the effectiveness of ABAQUS infinite elements in absorbing P waves	87
Figure 4.4(c)	Comparison of the effectiveness of the boundaries in absorbing P waves in an axisymmetric FE/IE mesh	88
Figure 4.5(a)	FE/IE axisymmetric mesh used to test the effectiveness of a user-defined standard viscous boundary in absorbing S waves	89

Figure 4.5(b)	FE/IE axisymmetric mesh used to test the effectiveness of ABAQUS infinite elements in absorbing S waves	89
Figure 4.5(c)	Comparison of the effectiveness of the boundaries in absorbing S waves in an axisymmetric FE/IE mesh	90
Figure 4.6	Rayleigh wave absorption	91
Figure 4.7	Variation of functions f and g in a homogenous half-space	92
Figure 4.8	Variation of parameters a and b in a homogenous half-space	93
Figure 4.9(a)	FE/IE plane strain mesh used to test the effectiveness of a user-defined standard viscous boundary in absorbing R waves	94
Figure 4.9(b)	FE/IE plane strain mesh used to test the effectiveness of ABAQUS infinite elements in absorbing R waves	94
Figure 4.9(c)	Comparison of the effectiveness of the boundaries in absorbing R waves in a plane strain FE/IE mesh: horizontal displacements across mesh	95
Figure 4.9(d)	Comparison of the effectiveness of the boundaries in absorbing R waves in a plane strain FE/IE mesh: vertical displacements across mesh	95
Figure 4.10(a)	'Snapshot' of R wave in mesh with ABAQUS infinite elements modelling far-field domain at 16.8 secs (Displacement magnification factor = 100)	96
Figure 4.10(b)	'Snapshot' of R wave in mesh with user-defined Rayleigh viscous boundary modelling far-field domain at 16.8 secs (Displacement magnification factor = 100)	96
Figure 4.11(a)	FE/IE axisymmetric mesh used to test the effectiveness of a user-defined standard viscous boundary in absorbing R waves	97
Figure 4.11(b)	FE/IE axisymmetric mesh used to test the effectiveness of ABAQUS infinite elements in absorbing R waves	97
Figure 4.11(c)	Comparison of the effectiveness of the boundaries in absorbing R waves in an axisymmetric FE/IE mesh: horizontal displacements across mesh	98
Figure 4.11(d)	Comparison of the effectiveness of the boundaries in absorbing R waves in an axisymmetric FE/IE mesh: vertical displacements across mesh	98
Figure 5.1(a)	Vertical particle velocity/time traces recorded during first 12 seconds of extraction of casing from a depth of 15.5m (Second Severn Crossing) (a) 0-3 secs	139
Figure 5.1(b)	Vertical particle velocity/time traces recorded during first 12 seconds of extraction of casing from a depth of 15.5m (Second Severn Crossing) (b) 3-6 secs	140
Figure 5.1(c)	Vertical particle velocity/time traces recorded during first 12 seconds of extraction of casing from a depth of 15.5m (Second Severn Crossing) (c) 6-9 secs	141
Figure 5.1(d)	Vertical particle velocity/time traces recorded during first 12 seconds of extraction of casing from a depth of 15.5m (Second Severn Crossing) (d) 9-12 secs	142

Figure 5.2(a)	Radial particle velocity/time traces recorded during first 12 seconds of extraction of casing from a depth of 15.5m (Second Severn Crossing) (a) 0-3 secs	143
Figure 5.2(b)	Radial particle velocity/time traces recorded during first 12 seconds of extraction of casing from a depth of 15.5m (Second Severn Crossing) (b) 3-6 secs	144
Figure 5.2(c)	Radial particle velocity/time traces recorded during first 12 seconds of extraction of casing from a depth of 15.5m (Second Severn Crossing) (c) 6-9 secs	145
Figure 5.2(d)	Radial particle velocity/time traces recorded during first 12 seconds of extraction of casing from a depth of 15.5m (Second Severn Crossing) (d) 9-12 secs	146
Figure 5.3	The ABAQUS friction model	147
Figure 5.4	Displaced mesh for a plane strain model of a pile resting on the ground surface subjected to a downward vertical displacement of 1 unit	148
Figure 5.5	Vertical stresses for a plane strain model of a pile resting on the ground surface subjected to a downward vertical displacement of 1 unit	149
Figure 5.6	Displaced mesh for an axisymmetric model of a pile resting on the ground surface subjected to a downward vertical displacement of 1 unit	150
Figure 5.7	Vertical stresses for an axisymmetric model of a pile resting on the ground surface subjected to a downward vertical displacement of 1 unit	151
Figure 5.8	Displaced mesh for an axisymmetric model of a pile resting on the ground surface subjected to a downward vertical displacement of 1 unit: Pointed toe	152
Figure 5.9	Vertical stresses for an axisymmetric model of a pile resting on the ground surface subjected to a downward vertical displacement of 1 unit: Pointed toe	153
Figure 5.10	Displaced mesh for an axisymmetric model of a pile resting on the ground surface subjected to a downward vertical displacement of 1 unit: Rounded toe	154
Figure 5.11	Vertical stresses for an axisymmetric model of a pile resting on the ground surface subjected to a downward vertical displacement of 1 unit: Rounded toe	155
Figure 5.12	Displaced mesh for an axisymmetric model of a pile sliding vertically against a soil surface	156
Figure 5.13	Vertical and horizontal stresses for an axisymmetric model of a pile sliding vertically against a soil surface (a) Step 0: initial geostatic stresses (b) Step 1: following pile displacement	157
Figure 5.14	Displaced mesh for an axisymmetric model of a pile with a rounded toe at a depth of 1m subjected to a downward vertical displacement of 0.9 units	158
Figure 5.15	Vertical stresses for an axisymmetric model of a pile with a rounded toe at a depth of 1m subjected to a downward vertical displacement of 0.9 units	159

Figure 5.16	Verification of ABAQUS friction model: Case 1 – no contact pressure between plane strain elements	160
Figure 5.17	Verification of ABAQUS friction model: Case 2 - contact pressure between plane strain elements, coefficient of friction of 0.3	161
Figure 5.18	Verification of ABAQUS friction model: Case 3a – pressure applied to top of element	162
Figure 5.19	Verification of ABAQUS friction model: Case 3b – equivalent force applied to rigid surface via the reference node	163
Figure 5.20	Verification of ABAQUS friction model: Case 4 – axisymmetric case	164
Figure 5.21	Rigid body motion	165
Figure 5.22	Limited axisymmetric FE/IE mesh used for pile/soil interaction analysis (mesh used for Flitwick data)	166
Figure 5.23	One-dimensional model for pile toe response (Lysmer & Richart, 1966)	167
Figure 5.24	Large axisymmetric FE/IE mesh used for wave propagation analysis (mesh used for Flitwick data)	168
Figure 5.25	Vertical velocity/time traces for surface nodes at various horizontal distances from the pile	169
Figure 5.26	80m wide FE/IE mesh used to investigate ‘standing wave’ phenomenon (Second Severn Crossing site)	170
Figure 5.27	Standing wave generated by vibratory extraction: Vertical velocity/time traces for all surface nodes between 0.75m and 40m	171
Figure 5.28	Standing wave generated by vibratory extraction: Radial velocity/time traces for all surface nodes between 0.75m and 40m	172
Figure 5.29	Comparison of the response induced by uniform displacement of all soil/pile interface nodes and that induced by non-uniform displacement of the interface nodes: Vertical velocity/time traces (0.75m and 40m)	173
Figure 5.30	Comparison of the response induced by uniform displacement of all soil/pile interface nodes and that induced by non-uniform displacement of the interface nodes: Radial velocity/time traces (0.75m and 40m)	174
Figure 5.31	Comparison of the response induced by an excitation frequency of 15.2Hz and that induced by a frequency of 20.9Hz: Vertical velocity/time traces (0.75m and 40m)	175
Figure 5.32	Comparison of the response induced by an excitation frequency of 15.2Hz and that induced by a frequency of 20.9Hz: Radial velocity/time traces (0.75m and 40m)	176
Figure 5.33	Comparison of the response induced by extraction of a pile from a depth of 11m with that from 13.8m (excitation frequency of 22.3 Hz for both): Vertical velocity/time traces	177

Figure 5.34	Comparison of the response induced by extraction of a pile from a depth of 11m with that from 13.8m (excitation frequency of 22.3 Hz for both): Radial velocity/time traces	178
Figure 5.35	80m wide FE mesh with ABAQUS infinite elements on right hand and bottom boundaries	179
Figure 5.36	40m wide FE mesh with ABAQUS infinite elements on bottom boundary	180
Figure 5.37	40m wide FE mesh with ABAQUS infinite elements on right hand and bottom boundaries	181
Figure 5.38	Comparison of the response from a 40m wide FE mesh with ABAQUS infinite elements and an 80m wide FE mesh with ABAQUS infinite elements (time period of 0.8-1.0 second): Vertical velocity/time traces	182
Figure 5.39	Comparison of the response from a 40m wide FE mesh with ABAQUS infinite elements and an 80m wide FE mesh with ABAQUS infinite elements (time period of 0.8-1.0 second): Radial velocity/time traces	183
Figure 5.40	Comparison of the response from a 40m wide FE mesh with ABAQUS infinite elements and an 80m wide FE mesh with ABAQUS infinite elements (time period of 0.0-1.0 second): Vertical velocity/time traces	184
Figure 5.41	(a) 40m wide FE mesh (ABAQUS IE on RH boundary) (b) 80m wide FE mesh (ABAQUS IE on RH boundary) Comparison of the response from a 40m wide FE mesh with a Rayleigh viscous boundary and an 80m wide FE mesh with ABAQUS infinite elements (time period of 0.8-1.0 second): Vertical velocity/time traces	185
Figure 5.42	(a) 40m wide FE mesh with Rayleigh viscous boundary applied over full depth of RH boundary (b) 80m wide FE mesh with ABAQUS IE on RH boundary Comparison of the response from a 40m wide FE mesh with a Rayleigh viscous boundary and an 80m wide FE mesh with ABAQUS infinite elements (time period of 0.8-1.0 second): Radial velocity/time traces	186
Figure 5.43	a) 40m wide FE mesh with Rayleigh viscous boundary applied over full depth of RH boundary b) 80m wide FE mesh with ABAQUS IE on RH boundary Vertical displacements of nodes between GL and 15.5m depth at various horizontal distances from pile at time of 0.35 seconds	187
Figure 5.44	Horizontal displacements of nodes between GL and 15.5m depth at various horizontal distances from pile at time of 0.35 seconds	188
Figure 5.45	40m wide FE mesh with Rayleigh viscous boundary over the top 3m (0.5 x R wavelength) and ABAQUS infinite elements below	189

Figure 5.46	Comparison of the response from a 40m wide FE mesh with a Rayleigh viscous boundary over the top 3m and an 80m wide FE mesh with ABAQUS IE (time period of 0.8-1.0 second): Vertical velocity/time traces	190
	a) 40m wide FE mesh with combined Rayleigh/ABAQUS IE boundary	
	b) 80m wide FE mesh (ABAQUS IE on RH boundary)	
Figure 5.47	Comparison of the response from a 40m wide FE mesh with a Rayleigh viscous boundary over the top 3m and an 80m wide FE mesh with ABAQUS IE (time period of 0.8-1.0 second): Radial velocity/time traces	191
Figure 5.48	Geological Profile of Second Severn Crossing site	192
Figure 5.49	Limited FE/IE mesh used in pile/soil interaction model for Second Severn Crossing site	193
Figure 5.50	Sensitivity of pile/soil interaction model to Mohr Coulomb parameters: Vertical displacements of all soil nodes on pile/soil interface (SSC site)	194
Figure 5.51	Large axisymmetric FE/IE mesh used for wave propagation analysis (Second Severn Crossing site)	195
Figure 5.52	Arrival times of wavefronts in FE/IE model assuming Eoverall = 50MPa (SSC site)	196
Figure 5.53	Vertical velocity/time traces recorded during extraction. Toe of casing at 13.8m below GL (SSC site)	197
Figure 5.54	Radial velocity/time traces recorded during extraction. Toe of casing at 13.8m below GL (SSC site)	198
Figure 5.55	Comparison of predicted and measured vertical velocity/time traces during vibratory extraction. Toe of casing at 13.8m below GL. Assuming Ealluvium of 42MPa and Emarl of 200MPa. (SSC site)	199
	a) Predicted (assuming $\mu = 0.15$ and 5% damping)	
	b) Measured	
Figure 5.56	Comparison of predicted and measured radial velocity/time traces during vibratory extraction. Toe of casing at 13.8m below GL. Assuming Ealluvium of 42MPa and Emarl of 200MPa. (SSC site)	200
	a) Predicted (assuming $\mu = 0.15$ and 5% damping)	
	b) Measured	
Figure 5.57	Typical forcing function from impact piling	201
Figure 5.58	Predicted arrival times of wavefronts generated by typical impact assuming Eoverall = 50MPa (SSC site)	202
Figure 5.59	Comparison of predicted vertical velocity/time traces assuming an overall coefficient of friction of 0.1 and an overall coefficient of friction of 0.15 (SSC site)	203
Figure 5.60	Comparison of predicted radial velocity/time traces assuming an overall coefficient of friction of 0.1 and an overall coefficient of friction of 0.15 (SSC site)	204

Figure 5.61	Comparison of predicted vertical velocity/time traces for two different distributions of friction along the shaft of the casing (SSC site) a) Three average values (stepped) of friction assumed between 6m – 13.8m depth b) One average value of friction assumed between 6m – 13.8m depth	205
Figure 5.62	Comparison of predicted radial velocity/time traces for two different distributions of friction along the shaft of the casing (SSC site) a) Three average values (stepped) of friction assumed between 6m – 13.8m depth b) One average value of friction assumed between 6m – 13.8m depth	206
Figure 5.63	Comparison of predicted vertical velocity/time traces for material damping ratios of 0%, 3% and 5%. (All surface nodes between 0.75m and 20m) (SSC site)	207
Figure 5.64	Comparison of predicted vertical velocity/time traces for material damping ratios of 0%, 3% and 5%. (All surface nodes between 20.25m and 40m) (SSC site)	208
Figure 5.65	Comparison of predicted vertical velocity/time traces assuming overall coefficients of friction of 0.1 and 0.15 and the measured radial velocity/time traces. Toe of casing at 11m below GL. (SSC site)	209
Figure 5.66	Comparison of predicted radial velocity/time traces assuming overall coefficients of friction of 0.1 and 0.15 and the measured radial velocity/time traces. Toe of casing at 11m below GL. (SSC site)	210
Figure 5.67	Vertical velocity/time traces recorded during installation of casing as the toe moves from alluvium into marl at 13.8m depth (SSC site)	211
Figure 5.68	Radial velocity/time traces recorded during installation of casing as the toe moves from alluvium into marl at 13.8m depth (SSC site)	212
Figure 5.69	Comparison of predicted vertical velocity/time traces for $E_{toe} = 15\text{MPa}$ and $E_{toe} = 200\text{MPa}$. Overall coefficient of friction of 0.15 assumed in both cases. (SSC site)	213
Figure 5.70	Comparison of predicted radial velocity/time traces for $E_{toe} = 15\text{MPa}$ and $E_{toe} = 200\text{MPa}$. Overall coefficient of friction of 0.15 assumed in both cases. (SSC site)	214
Figure 5.71	The effect of the magnitude of the soil displacement under the toe on the predicted vertical velocity/time traces. Toe in alluvium (assuming $E_{toe} = 15\text{MPa}$ and $\mu=0.15$). (SSC site) (a) 100% of the pile displacement (b) 50% of the pile displacement (c) 10% of the pile displacement	215

Figure 5.72	The effect of the magnitude of the soil displacement under the toe on the predicted radial velocity/time traces. Toe in alluvium (assuming $E_{toe} = 15\text{MPa}$ and $\mu=0.15$). (SSC site) (a) 100% of the pile displacement (b) 50% of the pile displacement (c) 10% of the pile displacement	216
Figure 5.73	The effect of the magnitude of the soil displacement under the toe on the predicted vertical velocity/time traces. Toe in marl (assuming $E_{toe} = 200\text{MPa}$ and $\mu=0.15$). (SSC site) (a) 100% of the pile displacement (b) 50% of the pile displacement (c) 10% of the pile displacement	217
Figure 5.74	The effect of the magnitude of the soil displacement under the toe on the predicted radial velocity/time traces. Toe in marl (assuming $E_{toe} = 200\text{MPa}$ and $\mu=0.15$). (SSC site) (a) 100% of the pile displacement (b) 50% of the pile displacement (c) 10% of the pile displacement	218
Figure 5.75	Comparison of predicted and measured vertical velocity/time traces. Toe in alluvium. (SSC site) (a) Predicted (assuming $E_{toe} = 15\text{MPa}$, toe displacement = 10% of pile displacement and $\mu=0.15$). (b) Measured	219
Figure 5.76	Comparison of predicted and measured radial velocity/time traces. Toe in alluvium. (SSC site) (a) Predicted (assuming $E_{toe} = 15\text{MPa}$, toe displacement = 10% of pile displacement and $\mu=0.15$). (b) Measured	220
Figure 5.77	Comparison of predicted and measured vertical velocity/time traces. Toe in marl. (SSC site) (a) Predicted (assuming $E_{toe} = 200\text{MPa}$, toe displacement = 10% of pile displacement and $\mu=0.1$). (b) Measured	221
Figure 5.78	Comparison of predicted and measured radial velocity/time traces. Toe in marl. (SSC site) (a) Predicted (assuming $E_{toe} = 200\text{MPa}$, toe displacement = 10% of pile displacement and $\mu=0.1$). (b) Measured	222
Figure 5.79	Plan of the site at Flitwick showing borehole locations	223
Figure 5.80	Ground conditions at Flitwick	224
Figure 5.81	Sensitivity of pile/soil interaction model to Mohr Coulomb parameters: Vertical displacements of all soil nodes on pile/soil interface (Flitwick site)	225
Figure 5.82	FE/IE mesh used for wave propagation analysis at Flitwick site	226
Figure 5.83	Comparison of the predicted vertical velocity/time traces from a 35m wide FE mesh with ABAQUS IE and a 35m wide FE mesh with a Rayleigh viscous boundary (time period of 0.8-1.0 second). (Flitwick site).	227

Figure 5.84	Comparison of the predicted radial velocity/time traces from a 35m wide FE mesh with ABAQUS IE and a 35m wide FE mesh with a Rayleigh viscous boundary (time period of 0.8-1.0 second). (Flitwick site).	228
Figure 5.85	Comparison of the predicted vertical velocity/time traces assuming material damping ratios of 0% and 5% (time period of 0.8-1.0 second). (Flitwick site).	229
Figure 5.86	Comparison of the predicted radial velocity/time traces assuming material damping ratios of 0% and 5% (time period of 0.8-1.0 second). (Flitwick site).	230
Figure 5.87	The effect of the magnitude of the soil displacement under the toe on the predicted vertical velocity/time traces. (Flitwick site) (a) 100% of the pile displacement (b) 50% of the pile displacement (c) 10% of the pile displacement	231
Figure 5.88	The effect of the magnitude of the soil displacement under the toe on the predicted radial velocity/time traces. (Flitwick site) (a) 100% of the pile displacement (b) 50% of the pile displacement (c) 10% of the pile displacement	232
Figure 5.89	Comparison of the predicted and measured radial velocity/time traces at geophone locations (Flitwick site)	233
Figure 5.90	Predicted vertical velocity/time traces at geophone locations (Flitwick site)	234
Figure 6.1	Modelling of pile by discrete springs and dashpots (after Smith, 1960)	261
Figure 6.2	Vertical velocity of pile head: Simple hammer/pile model	262
Figure 6.3	Analytical pile hammer models (after Deeks, 1992)	263
Figure 6.4	FE model of the pile with new base model and new shaft model. Typical forcing function applied to pile head.	264
Figure 6.5	Vertical stresses in the pile at various intervals during the first 0.02 seconds.	265
Figure 6.6	Contour plots of the vertical stresses in the pile at intervals of 0.001 seconds	266
Figure 6.7	The 'dummy' pile	267
Figure 6.8	Hammer impact model	268
Figure 6.9	Large FE/IE mesh used for wave propagation analysis	269
Figure 6.10a	Force/time functions at the pile head (pile 23) for $k_c=1e^{10}$ N/m and various values of c_c^*	270
Figure 6.10b	Force/time functions at the pile head (pile 23) for $k_c=1e^9$ N/m and various values of c_c^*	271
Figure 6.10c	Force/time functions at the pile head (pile 23) for $k_c=1e^8$ N/m and various values of c_c^*	272

Figure 6.10d	Force/time functions at the pile head (pile 23) for $k_c=1e^7$ N/m and various values of c_c^*	273
Figure 6.11	Comparison of measured and computed force/time functions at the pile head (pile 23) assuming $k_c=1e^7$ N/m and $c_c^*=0.15$	274
Figure 6.12	Effect of increasing dashpot constants on pile head displacement (pile 23)	275
Figure 6.13	Effect of soil stiffness on pile head displacement (pile 23)	276
Figure 6.14	Comparison of the measured and computed force/time functions at the pile head (pile 23) assuming $k_c=1e^7$ N/m and $c_c^*=0.15$ ($E_{clay}=13e^6$ MPa and $E_{sand}=50e^6$ MPa)	277
Figure 6.15	Comparison of the measured and computed pile head displacements (pile 23) assuming $k_c=1e^7$ N/m and $c_c^*=0.15$ ($E_{clay}=13e^6$ MPa and $E_{sand}=50e^6$ MPa)	278
Figure 6.16	Computed force/time function for pile 18 assuming $k_c=1e^7$ N/m and $c_c^*=0.15$	279
Figure 6.17a	Computed pile head displacement for pile 18	280
Figure 6.17b	Computed vertical displacement of all pile interface nodes for pile 18	281
Figure 6.18	Wave propagation model for pile 18 (M66 site)	282
Figure 6.19	Vertical velocity/time traces recorded at the M66 site at horizontal distances of 5.5m, 10m and 16.5m from pile.	283
Figure 6.20	Radial velocity/time traces recorded at the M66 site at horizontal distances of 5.5m, 10m and 16.5m from pile.	284
Figure 6.21(a)	Comparison of predicted and measured vertical velocity/time traces for geophone at 5.5m (M66 site)	285
Figure 6.21(b)	Comparison of predicted and measured vertical velocity/time traces for geophone at 10m (M66 site)	286
Figure 6.21(c)	Comparison of predicted and measured vertical velocity/time traces for geophone at 16.5m (M66 site)	287
Figure 6.22(a)	Comparison of predicted and measured radial velocity/time traces for geophone at 5.5m (M66 site)	288
Figure 6.22(b)	Comparison of predicted and measured radial velocity/time traces for geophone at 10m (M66 site)	289
Figure 6.22(c)	Comparison of predicted and measured radial velocity/time traces for geophone at 16.5m (M66 site)	290
Figure 6.23(a)	Computed vertical velocity/time traces for geophones at 5.5m, 10m and 16.5m assuming an overall stiffness for the soil of 150MPa. (M66 site)	291
Figure 6.23(b)	Computed radial velocity/time traces for geophones at 5.5m, 10m and 16.5m assuming an overall stiffness for the soil of 150MPa. (M66 site)	292
Figure 6.24(a)	Computed vertical velocity/time traces for geophones at 5.5m, 10m and 16.5m assuming values of $k_c = 1e^8$ N/m and $c_c^* = 0.1$. (M66 site)	293
Figure 6.24(b)	Computed radial velocity/time traces for geophones at 5.5m, 10m and 16.5m assuming values of $k_c = 1e^8$ N/m and $c_c^* = 0.1$. (M66 site)	294

Figure 6.25	Computed force/time function at the pile head (Flitwick site)	295
Figure 6.26	Computed vertical displacement/time functions for all of the nodes on the pile/soil interface (Flitwick site)	296
Figure 6.27	Radial velocity/time traces recorded by geophones at 2m, 7m, 12m, 15m, and 16.5m (Flitwick site)	297
Figure 6.28	Vertical, radial and transverse velocity/time traces recorded by a geophone at 7m from the pile (Flitwick site)	298
Figure 6.29	FE/IE mesh used for the wave propagation analysis (Flitwick site)	299
Figure 6.30	Comparison of the predicted and measured radial velocity/time traces at 7m and 16.5m (Flitwick site)	300
Figure 6.31	Comparison of the predicted and measured vertical velocity/time traces at 7m and 16.5m (Flitwick site) ($E_{\text{overall}} = 66\text{MPa}$)	301
Figure 6.32	Computed velocity/time traces at 7m and 16.5m assuming $E_{\text{clay}} = 20\text{MPa}$ and $E_{\text{sand}} = 200\text{MPa}$ (Flitwick site) ($E_{\text{overall}} = 66\text{MPa}$)	302
Figure 6.33	Computed velocity/time traces at 7m and 16.5m assuming $E_{\text{clay}} = 27\text{MPa}$ and $E_{\text{sand}} = 267\text{MPa}$ (Flitwick site)	303
Figure 6.34	Computed velocity/time traces at 7m and 16.5m assuming $E_{\text{clay}} = 30\text{MPa}$ and $E_{\text{sand}} = 300\text{MPa}$ (Flitwick site)	304
Figure 6.35	Cross-section showing computed travel times of P waves generated at pile toe (Flitwick site)	305
Figure 6.36	Comparison of the predicted and measured radial velocity/time traces for geophones at 7m and 16.5m assuming $E_{\text{clay}} = 15\text{MPa}$ and $E_{\text{sand}} = 349\text{MPa}$ (Flitwick site)	306
Figure 6.37	Comparison of the predicted and measured vertical velocity/time traces for geophones at 7m and 16.5m assuming $E_{\text{clay}} = 15\text{MPa}$ and $E_{\text{sand}} = 349\text{MPa}$ (Flitwick site)	307
Figure 6.38	Computed velocity/time traces for geophones at 7m and 16.5m assuming an overall coefficient of friction of 0.2 ($E_{\text{clay}} = 20\text{MPa}$ and $E_{\text{sand}} = 200\text{MPa}$) (Flitwick site)	308
Figure 6.39	Computed velocity/time traces for geophones at 7m and 16.5m assuming an overall coefficient of friction of 0.4 ($E_{\text{clay}} = 20\text{MPa}$ and $E_{\text{sand}} = 200\text{MPa}$) (Flitwick site)	309
Figure 6.40	Computed velocity/time traces for geophones at 7m and 16.5m assuming an overall coefficient of friction of 0.7 ($E_{\text{clay}} = 20\text{MPa}$ and $E_{\text{sand}} = 200\text{MPa}$) (Flitwick site)	310
Figure 7.1	FE/IE mesh used in axisymmetric analysis	321
Figure 7.2	FE/IE mesh used in 3D analysis	321
Figure 7.3	Simplified view of 3D model of ground around the pile	322
Figure 7.4	Boundary conditions applied to 3D FE/IE mesh	323
Figure 7.5	Definition of a beam in ABAQUS	324
Figure 7.6	Radial velocity/time traces predicted by the axisymmetric and 3D models at horizontal distances of 2m, 7m, 10m and 16.5m	325

Figure 7.7	Vertical velocity/time traces predicted by the axisymmetric and 3D models at horizontal distances of 2m, 7m, 10m and 16.5m	326
Figure 7.8	Steel portal frame on 3D mesh	327
Figure 7.9(a)	Typical deformation of the ground and the portal frame as the vibratory waves pass through. Time = 0.15 seconds. (Magnification x 3000)	328
Figure 7.9(b)	Typical deformation of the ground and the portal frame as the vibratory waves pass through. Time = 0.3 seconds. (Magnification x 3000)	328
Figure 7.9(c)	Typical deformation of the ground and the portal frame as the vibratory waves pass through. Time = 0.45 seconds. (Magnification x 3000)	329
Figure 7.9(d)	Typical deformation of the ground and the portal frame as the vibratory waves pass through. Time = 0.6 seconds. (Magnification x 3000)	329
Figure 7.9(e)	Typical deformation of the ground and the portal frame as the vibratory waves pass through. Time = 0.75 seconds. (Magnification x 3000)	330
Figure 7.9(f)	Typical deformation of the ground and the portal frame as the vibratory waves pass through. Time = 0.9 seconds. (Magnification x 3000)	330
Figure 7.10(a)	Locations of nodes 223 and 505	331
Figure 7.10(b)	Comparison of the vibratory displacements of the free ground surface with no structure against those with the portal frame in place: vertical displacements	332
Figure 7.10(c)	Comparison of the vibratory displacements of the free ground surface with no structure against those with the portal frame in place: horizontal displacements	333
Figure 7.11	In-plane wall on 3D mesh	334
Figure 7.12(a)	Typical deformation of the ground and the wall as the vibratory waves pass through. Time = 0.05 seconds. (Magnification x 5000)	335
Figure 7.12(b)	Typical deformation of the ground and the wall as the vibratory waves pass through. Time = 0.10 seconds. (Magnification x 5000)	335
Figure 7.12(c)	Typical deformation of the ground and the wall as the vibratory waves pass through. Time = 0.15 seconds. (Magnification x 5000)	336
Figure 7.12(d)	Typical deformation of the ground and the wall as the vibratory waves pass through. Time = 0.20 seconds. (Magnification x 5000)	336
Figure 7.13(a)	Contour plot of the vertical stresses in the wall during vibratory piling	337
Figure 7.13(b)	Contour plot of the horizontal stresses in the wall during vibratory piling	338
Figure 7.14(a)	Location of nodes 223, 325 and 475	339

Figure 7.14(b)	Comparison of the vibratory displacements of the free ground surface with no structure against those with the brick wall in place: vertical displacements	340
Figure 7.14(c)	Comparison of the vibratory displacements of the free ground surface with no structure against those with the brick wall in place: horizontal displacements	341
Figure 7.15	Comparison of the radial velocity/time traces computed by the axisymmetric and 3D models at horizontal distances of 7m and 16.5m	342
Figure 7.16	Comparison of the vertical velocity/time traces computed by the axisymmetric and 3D models at horizontal distances of 7m and 16.5m	343
Figure 7.17(a)	Typical deformation of the ground and the portal frame as the impact waves pass through. Time = 0.10 seconds. (Magnification x 5000)	344
Figure 7.17(b)	Typical deformation of the ground and the portal frame as the impact waves pass through. Time = 0.15 seconds. (Magnification x 5000)	344
Figure 7.17(c)	Typical deformation of the ground and the portal frame as the impact waves pass through. Time = 0.20 seconds. (Magnification x 5000)	345
Figure 7.17(d)	Typical deformation of the ground and the portal frame as the impact waves pass through. Time = 0.25 seconds. (Magnification x 5000)	345
Figure 7.17(e)	Typical deformation of the ground and the portal frame as the impact waves pass through. Time = 0.30 seconds. (Magnification x 5000)	346
Figure 7.17(f)	Typical deformation of the ground and the portal frame as the impact waves pass through. Time = 0.45 seconds. (Magnification x 5000)	346
Figure 7.17(g)	Typical deformation of the ground and the portal frame as the impact waves pass through. Time = 0.60 seconds. (Magnification x 5000)	347
Figure 7.17(h)	Typical deformation of the ground and the portal frame as the impact waves pass through. Time = 0.75 seconds. (Magnification x 5000)	347
Figure 7.18(a)	Locations of nodes 223 and 505	348
Figure 7.18(b)	Comparison of the transient displacements of the free ground surface with no structure against those with the portal frame in place: vertical displacements	349
Figure 7.18(c)	Comparison of the transient displacements of the free ground surface with no structure against those with the portal frame in place: horizontal displacements	350
Figure 7.19(a)	Typical deformation of the ground and the wall as the impact waves pass through. Time = 0.05 seconds. (Magnification x 10000)	351
Figure 7.19(b)	Typical deformation of the ground and the wall as the impact waves pass through. Time = 0.10 seconds. (Magnification x 10000)	351

Figure 7.19(c)	Typical deformation of the ground and the wall as the impact waves pass through. Time = 0.15 seconds. (Magnification x 10000)	352
Figure 7.19(d)	Typical deformation of the ground and the wall as the impact waves pass through. Time = 0.20 seconds. (Magnification x 10000)	352
Figure 7.20(a)	Contour plot of the vertical stresses in the wall during impact piling	353
Figure 7.20(b)	Contour plot of the horizontal stresses in the wall during impact piling	354

CHAPTER 1

INTRODUCTION

1.1 GENERAL BACKGROUND

Piles are widely used for transmitting building loads from ground surface through weak soils to more competent soil or rock strata, while interlocking sheet piles are used for temporary or permanent retaining walls. The process of pile installation using high energy impact or vibratory hammers causes outgoing ground waves which can have a significant influence on the surrounding ground, on adjacent buildings and on their occupants. In severe cases, adjacent structures are at risk of damage. Although the issue of vibration from piling is addressed in codes and regulatory standards, little is understood about how the various aspects of the pile installation process influence the generation of ground waves. Assessment of risk is conventionally by reference to threshold limits of vibration, primarily based on empirical rules, often with no consideration given to the interactive effects between ground and structure nor to frequency and duration. It is not therefore surprising that the prediction of vibration is, in many cases, unreliable.

Within this framework of empiricism, it would be of considerable reference value to the piling industry to clarify the risk of direct vibration damage, and to classify combinations of piling and structure systems which offer higher or lower risk of damage.

Although several workers have developed finite element and analytical models for the simulation of pile driving in the context of pile drivability, the ground waves generated by pile driving have not been modelled computationally.

Recent developments within finite element computational methods, including infinite elements and quiet boundaries (Bettess 1992, Noorzai et al 1994), allow the generation of a suitable two-dimensional axisymmetric representation of appropriate ground vibration systems of vertical and radial wave components, and then the incorporation of a range of structural forms and dimensions. The latter must include dynamic soil-structure interaction.

The main objective of the work described in this thesis was to develop computational models based on finite element techniques that satisfactorily simulate the piling-induced vibrations that have been recorded on many sites and held in databases at Durham University (Uromeihy 1990) and the Transport Research Laboratory (Hiller 1999 and Hiller & Crabb, 2000). Techniques were then devised to extend the computational models to include common structural forms.

1.2 CURRENT GUIDELINES

The environmental consequences of groundborne vibration generally take one of three forms. The most severe cases of vibration may cause direct cosmetic or structural damage to existing structures or buried services, although this is uncommon during construction works (Siskind et al 1980). However damage may occur indirectly due to



compaction settlement of loose granular soils by the action of the groundborne vibration. The third effect comprises the disturbance of occupiers of neighbouring properties. The latter is the most common problem because the magnitudes of vibration which are perceptible to humans are at least an order of magnitude smaller than those which might cause damage.

Current UK and overseas standards generally provide two sets of threshold limits for vibration. The first relates to the prevention of damage to adjacent structures and the second to the perception and disturbance of occupiers in adjacent structures. No standards address the specific issue of structural damage due to vibration-induced compaction settlement.

1.2.1 Thresholds for damage

Two British Standards, BS 5228 Part 4 (1992) and BS 7385 Part 2 (1993) address the specific issue of threshold limits of vibration on nearby structures so as to provide an acceptably low risk of cosmetic and structural damage. BS 7385 is based on a survey of UK damage data and experience from overseas (Malam 1993) and relates to vibration generated by a variety of sources.

BS 7385 consists of two parts. Part 1 (BSI 1990a) describes the principles for carrying out vibration measurements and processing the data. Part 2 (BSI 1993) suggests vibration magnitudes at which cosmetic, minor and major damage might occur in terms of the peak particle velocity (ppv). At frequencies below 4Hz the damage threshold is specified in terms of the peak particle displacement. The threshold limits in BS 7385 relate to transient vibrations but the Standard states that these values may need to be reduced by up to 50 per cent for continuous vibration because of the potential for dynamic magnification of continuous vibrations by elements of structures.

BS 5228 Part 4 (BSI 1992b) gives guidance on thresholds for damage to structures by groundborne vibration from piling. A conservative threshold for minor or cosmetic damage to residential property of 10mm/s for intermittent vibration and 5mm/s for continuous vibration is recommended. The threshold magnitudes from BS 5228 are generally lower than those from BS 7385.

Hiller (1999) has undertaken a detailed review of vibration standards in use outside the UK. He concludes that there is considerable difference between the magnitudes of vibration that are acceptable in different countries (see Figure 1.1). New (1986) reported that, in general, the more recent the standard the more conservative were the specified vibration limits. The British Standard BS 7385 : Part 2 (BSI 1993) reversed this trend but the most recent European guidance (CEN 1998) has reverted to a greater degree of conservatism.

The basis for the recommendations given in the British Standards, and various other overseas standards, is primarily empirical and they sometimes offer conflicting advice. There is a general recognition that continuous vibration is more damaging than intermittent, and that high frequency vibration poses a smaller risk than low frequency vibration.

1.2.2 Thresholds for perception and disturbance

BS 6472 (BSI 1992a) specifies threshold values which take account of the different sensitivity of humans to x- y- and z-axis vibration when standing, sitting and lying down. Base curves are presented for the most sensitive environments such as hospital operating theatres and precision laboratories. Multiplying factors are given to specify acceptable magnitudes of vibration for other environments and for different times of day.

Hiller (1999) has reviewed and compared the threshold limits for human perception given by various national standards and concludes the threshold of perceptible vibration is considered to be the same in all countries. However, the levels of vibration which are considered to be acceptable within residential properties vary between different countries. Adopted European Prestandard Eurocode 3, Chapter 5 (CEN 1998) is concerned specifically with the appraisal of vibration arising from pile driving. Eurocode 3 adopts a different approach to intrusion assessment to that given by other standards, recognising that human tolerance is dependent upon the duration as well as the magnitude of the vibration. For a thorough assessment of the potential for groundborne vibration to cause disturbance it is necessary to consider not only the magnitude of vibration, but also its duration, direction, time of day and the particular environment which is affected.

1.3 AIMS AND OBJECTIVES

The various UK and overseas national standards have been shown to offer conflicting advice as to threshold limits for vibration on nearby structures. This is perhaps not surprising, since the basis for the recommendations is primarily empirical, sometimes taking into account the condition of the building. However, the global approach adopted by these standards considers neither the interactive effects of foundation and structure, nor detailed frequency and duration.

The mechanisms involved in the generation of vibration from piling are extremely complex and are not presently well understood. There are many parameters involved and the selection of parameters is likely to vary with the particular set of circumstances at each site and the method of pile installation. It would be therefore particularly valuable to be able to simulate the generation, propagation and interaction of ground waves from pile driving by numerical modelling techniques. This approach potentially offers a means of understanding the complex processes of vibration generation during piling.

Improved prediction of vibration from pile driving at an early stage in the design process has many benefits. The correct choice of piling method and pile type to minimise vibration for the particular site conditions avoids delays to construction works which may be caused if excessive vibrations cause annoyance to occupants of nearby buildings or, in severe cases, result in damage to adjacent structures. One of the particular benefits of numerical modelling is that it allows the rapid assessment of the effectiveness of various types of vibration reduction measures, such as cut-off walls and barriers.

The main beneficiaries of improved vibration prediction are likely to be consultants, local authority officers implementing the Control of Pollution Act, and specialist piling contractors.

The main objectives of the work contained in this thesis are:

- To develop finite element/infinite element models which simulate the transmission of ground waves correctly
- To investigate the effectiveness of various quiet boundaries in the absorption of ground waves generated by piling
- To generate realistic input force functions for both impact and vibratory hammers
- To calibrate the methods against site data
- To use the models in limited parametric studies of hammer, pile and soil variables
- To include structures in the models, so as to identify damaging wave types
- To devise a computationally efficient method to overcome the difficulties of modelling structures without the need for a time-consuming and expensive full three-dimensional analysis.

The FE/IE models developed in this work have been designed to be computationally efficient so that they can be analysed using a reasonably powerful computer likely to be available to engineers in the design office.

1.4 GENERAL APPROACH TO THE PROBLEM

Although several substantial databases of site records of “green-field” vibrations exist, including one held at Durham University (Uromeihy 1990) the data tend to be confined to ground surface vibrations at various stand-off distances, together with a description of the hammer and pile type and a brief description of ground conditions usually in the form of borehole records. The databases do not contain detailed records of pile excitation such as pile head strain, acceleration and transient displacement and they certainly do not provide information about suitable plastic and dynamic soil parameters.

Following an extensive literature search and discussions with various engineering companies and research organisations, it became evident that high quality and simultaneous measurement of most of these parameters does not presently exist. However, it is likely that valuable comprehensive data sets will become available when the ‘SIPDIS’ programme of monitored pile installation tests are analysed (partly by BRE) and published. The SIPDIS programme is described in more detail in Section 2.8.

Given the lack of comprehensive data, it was decided that a pragmatic approach to the problem was required. The computational models that have been developed to simulate the ground waves generated by piling are designed to use a minimum of site data but are versatile enough to be refined as comprehensive data sets become available and the complex dynamic behaviour of soils subjected to piling becomes better understood.

The models provide a preliminary framework for the computation of ground waves generated by pile driving by finite element techniques. It is hoped that future workers will adopt and refine them in order to develop a robust computational model for the confident prediction of vibrations from pile driving. The ultimate aim might be the

publication of design charts for various piling methods, site conditions and common structural forms for incorporation into the relevant British standards.

1.5 THESIS STRUCTURE

The structure of the remainder of this thesis is as follows. Chapter 2 presents a general overview of the mechanisms involved in the generation of vibration from piling. It reviews the common methods of pile installation and the empirical techniques available in the literature for vibration prediction. As the work in this thesis encompasses a number of different areas of research, literature reviews on more specific areas are contained in the relevant chapters.

The work described in this thesis was undertaken using the ABAQUS finite element program. Chapter 3 describes the work that was undertaken to validate the ability of the program to simulate the ground waves satisfactorily.

Chapter 4 describes the development of a new quiet boundary to effectively absorb the complex ground waves generated by piling, thus providing an accurate representation of the far field and preventing reflection back into the finite element mesh.

The development of a new finite element model for the computation of ground waves from vibratory piling is described in Chapter 5. The ground response predicted by the model is compared with vibration measurements taken during vibratory extraction and installation of different pile types at two sites with contrasting ground conditions. The effectiveness of the new quiet boundary developed in Chapter 4 is investigated by applying it to the model developed in Chapter 5.

A new finite element model for impact piling is described in Chapter 6 and the predicted ground response is compared to measurements of vibration at two very different sites.

The models developed in Chapters 5 and 6 are then extended in Chapter 7 to incorporate some common structural forms. A computationally efficient technique is developed to overcome the difficulties of modelling soil-structure interaction without the need for a full three-dimensional analysis.

Chapter 8 gives a brief review of the major observations of the work, and includes recommendations for further work.

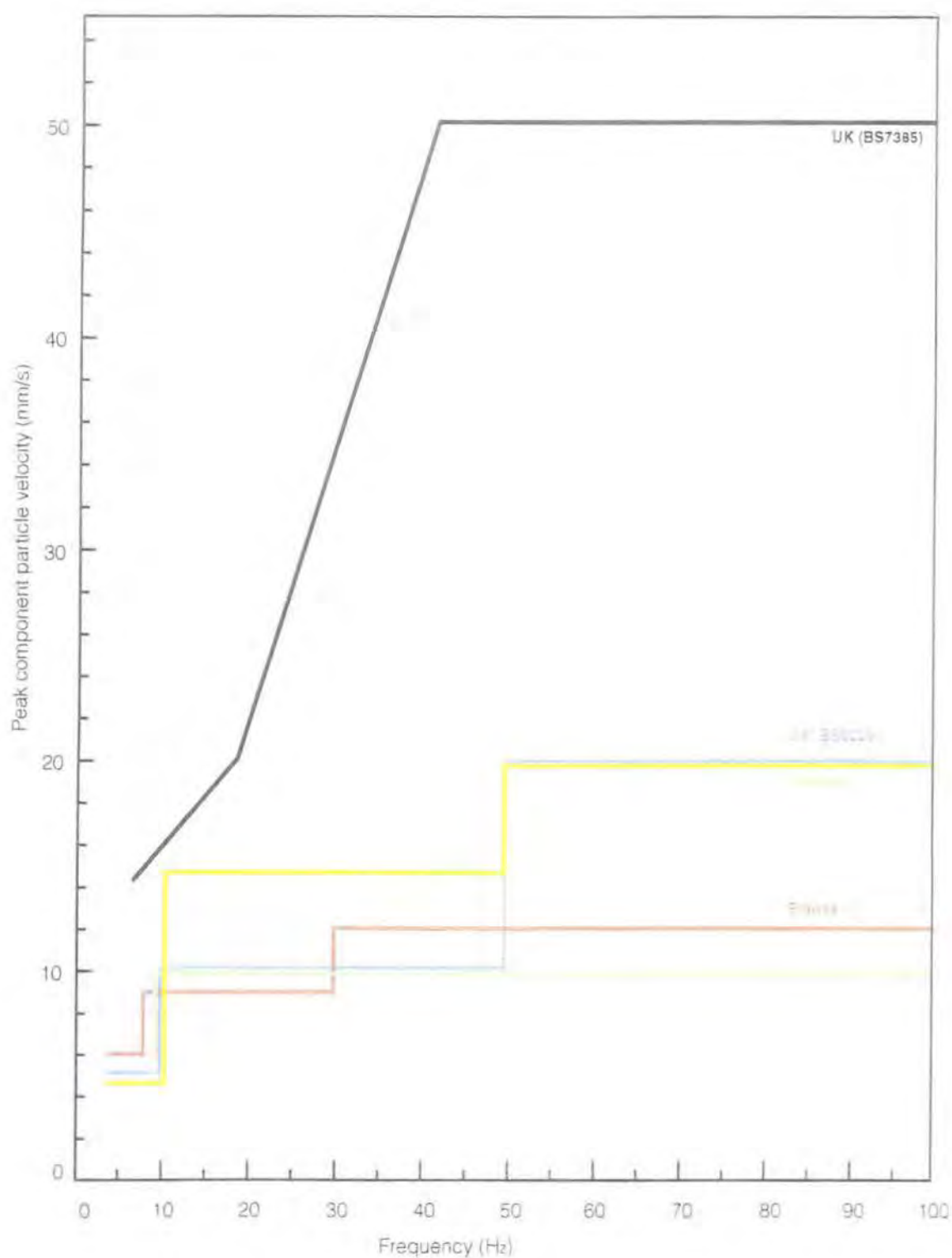


Figure 1.1 Comparison of transient vibration damage thresholds for domestic buildings given in national standards

CHAPTER 2 GROUND VIBRATIONS FROM PILING

2.1 INTRODUCTION

This Chapter provides basic background information on the mechanisms involved in the generation of ground waves from piling operations and their propagation through the ground and into adjacent structures. It defines the terms and measures used to describe vibration and provides a summary of the factors affecting the transmission of energy from pile driving into the ground wave. This includes a description of pile types and installation methods. The mechanisms of the propagation and attenuation of ground waves from pile driving and the transmission of vibrations into structures are then described. The Chapter concludes with a review of the (mainly empirical) techniques available in the literature for vibration prediction.

As the work contained in this thesis encompasses and brings together a number of several different areas of research, literature reviews on more specific areas are contained in the relevant Chapters.

2.2 VIBRATION TERMS AND DEFINITIONS

Vibration is usually defined by the following terms:

Amplitude (A) – Single amplitude is defined as the maximum displacement of a body from its equilibrium position. Peak-to-peak amplitude is described as the double amplitude. Amplitude is also used to loosely describe the magnitude of particle velocity and acceleration. (mm, mm/s, mm/s²)

Period (T) – The duration of one complete vibration cycle. (s)

Wavelength (λ) – This is the distance between any two identical parts of adjacent vibration cycles. The wavelength is proportional to wave velocity and inversely proportional to frequency (ie $\lambda = c/f$). (m)

Frequency (f) – The number of vibrations occurring in a given period of time, in cycles per second. (Hz)

Wave velocity (c) – The ratio of change in distance position (Δx) to the time change (Δt) ie $c = \Delta x / \Delta t$. (m/s)

Particle velocity (v) – Temporal velocity of a particle as a wave passes through. (mm/s)

Free vibration – The vibration of a system under the action of its internal forces (ie natural frequency)

Forced vibration – The vibration of a system due to excitation of external forces, occurring at the frequency of the exciting force.

Resonance – This state occurs when an exciting frequency coincides with a system's natural frequency. At resonance, a system's amplitude may dramatically increase.

Degrees of freedom – The number of independent co-ordinates necessary to describe the motion of a system. A free particle may have three degrees of freedom in three orthogonal positions (longitudinal, vertical and transverse). A rigid block may have six degrees of freedom; three describing its displacements along the x, y and z axes which are known as lateral, longitudinal and vertical, and three describing the rotations of the block about x, y and z axes which are known as pitching, rocking/rolling and yawing.

Damping – When the motion of a particle is affected by frictional or viscous resistance, the amplitude of vibration decreases with time and with distance. The degree of damping depends on the presence of friction forces. The vibrating system is said to be weakly damped where the friction forces have little effect, over-damped where the effect of friction is greater and critically damped where the system returns to its equilibrium position in the shortest possible time. Damping has a great influence in limiting the amplitude of vibration at resonance.

Periodic vibration – The same form of vibration motion occurs repeatedly. Sinusoidal vibration is the basic form of periodic motion generated by vibratory hammers. An example of sinusoidal vibration is illustrated in Figure 2.1.

Transient vibration – This is characterised by the occurrence of an impulsive force, causing a vibratory motion of relatively short duration. Impact piling generates transient vibrations similar to that illustrated in Figure 2.2.

2.3 MEASURES OF VIBRATION

The amplitude of vibration may be expressed in terms of particle displacement, velocity or acceleration. For sinusoidal vibration, these quantities are related to each other. Referring to Figure 2.3, the particle displacement and its amplitude is given by:

$$x = A \sin \omega t \quad (2.1)$$

Particle velocity can be obtained by differentiating equation (2.1) with respect to time:

$$v = \omega A \cos \omega t \quad (2.2)$$

or

$$v = \omega A \sin(\omega t + \pi/2) \quad (2.3)$$

Differentiation of equation (2.2) with respect to time gives the particle acceleration:

$$a = -\omega^2 A \sin \omega t \quad (2.4)$$

or

$$a = \omega^2 A \sin(\omega t + \pi) \quad (2.5)$$

The phase relationships between displacement, velocity and acceleration are illustrated in Figure 2.3.

Transient vibrations do not have a similar simple relationship. If any one parameter is known as a function of time, then the signal may be differentiated or integrated digitally to obtain the other two.

Exposure of the human body to vibration is often quoted in terms of acceleration (Griffin 1998). Human response to vibration is frequency dependent when specified in terms of acceleration but, in the range of frequencies typically generated by piling operations, human perception is independent of frequency when quantified in terms of velocity (British Standards Institution 1992a).

The assessment of the susceptibility of structures to damage is commonly measured in velocity terms, except at frequencies below 4Hz, where the British Standards Institution specifies damage thresholds in terms of displacement (BSI 1993). The particle velocity is used in most cases because this is the parameter which has been found to correlate best with the onset of damage (Siskind et al 1980). Furthermore, the dynamic strain induced during the passage of a wave is proportional to the particle velocity; it is strain which causes damage (New 1986).

Field measurement of vibrations from piling is commonly made using geophones which give output proportional to velocity. Geophones have a low output impedance which enables their use with long cable lengths (Crabb et al 1991). They are also ruggedly designed making them well suited to use on construction sites (New 1982). The parameter most often used for the quantification of groundborne vibration is therefore the peak particle velocity (Maguire & Wyatt 1999), abbreviated to ppv. The prefix “peak” refers to the maximum magnitude achieved during a specified period of time.

The motion of the ground during vibration can be resolved into three orthogonal components namely the vertical, radial and transverse. In the literature, the term “ppv” has been defined in various ways which can present difficulties when attempting to compare data from different sources (Hiller & Bowers 1997). The four main definitions of ppv are as follows:

- (i) The peak value attained by any one of the three mutually perpendicular components (v_{Vmax} , v_{Rmax} , v_{Tmax}).
- (ii) The peak value attained by the vertical component (v_{Vmax}).
- (iii) The vector sum of the maximum of each component regardless of whether these individual component maxima occurred simultaneously:

$$v'_{res} = \sqrt{[(v_{Vmax})^2 + (v_{Rmax})^2 + (v_{Tmax})^2]} \quad (2.6)$$

- (iv) The true resultant, which is the maximum value of the instantaneous vector summation of the three components.

$$v_{res} = \left| \sqrt{v_V^2 + v_R^2 + v_T^2} \right|_{\max} \quad (2.7)$$

2.4 FACTORS AFFECTING THE ENERGY TRANSMITTED FROM PILE DRIVING INTO THE GROUND

The magnitude of vibration at any point in the ground, arising from any activity, is dependent on the amount of energy transmitted into the ground by the source, the rate of attenuation of the energy as it propagates through the ground and the distance of the observation point from the location at which the energy enters the ground. The factors affecting the transmission of energy generated by piling through the surrounding ground and adjacent structures are summarised in Figure 2.4.

Vibrations generated by piling operations differ from many other sources of groundborne vibration in several respects. Firstly, the actual energy source used for piling, the hammer or driver, does not, in most cases, come into direct contact with the ground; the energy is transmitted to the ground via the pile. The amount of energy transmitted from the hammer to the pile may be affected by the size, shape and material of the pile, the piling hammer or driver, and any packing between the pile and driver. Secondly, the depth of the pile toe increases as driving progresses and the length of the pile shaft also increases. The source therefore changes throughout the drive, whether the source is the toe of the pile, the pile shaft or a combination of the toe and shaft. The nature of the ground into which the pile is driven and the distance from the pile to the measurement location also change continuously during the driving of a pile.

2.4.1 Types of pile and hammer

Piles are relatively long and slender structural members used to transmit foundation loads through soil strata of low bearing capacity to deeper soil or rock strata having a high bearing capacity thereby reducing the potential for excessive settlement of the structure. They are also used in normal ground conditions to resist heavy uplift forces or in poor soil conditions to resist horizontal loads. Piles are a convenient method of foundation construction for works over water, such as jetties or bridge piers. Piles may be classified by their function either as load bearing piles (jacked, driven or bored piles) or retaining piles (sheet piles, contiguous or secant bored pile retaining walls), BS 8004 (1986).

In general, piles may be classified with respect to the way in which load is transferred to the soil either as friction piles or end bearing piles. In friction piles, the applied load is transmitted to the surrounding soil primarily through friction at the pile/soil interface, although some of the load may be carried by the pile toe. End bearing piles are driven into a layer having a high bearing capacity and the applied load is transferred from the pile to the ground mainly through the pile toe, although some of the load may be carried by skin friction. In settling ground, end bearing piles may attract negative skin friction, which imposes additional loads.

The main types of pile in general use are as follows:

Driven piles. Preformed units, usually in timber, concrete or steel, driven into the soil by vibratory motion or the blows of a hammer.

Driven and cast-in-place piles. Formed by driving a tube with a closed end into the soil, and filling the tube with concrete. The tube may or may not be withdrawn.

Jacked piles. Steel or concrete units jacked into the soil.

Bored and cast-in-place piles. Piles formed by boring a hole into the soil and filling it with concrete.

Continuous-flight augered (CFA) piles. Piles are constructed by screwing the continuous-flight auger into the ground to the required depth, then injecting grout down the hollow auger stem to the head of the auger. The auger is lifted out of the ground as the grout continues to be injected.

Composite piles. Combinations of two or more of the preceding types, or combinations of different materials in the same type of pile.

The driven and jacked piles are sometimes called displacement piles because the soil is disturbed and laterally displaced during pile driving. The properties of the surrounding soil are changed, and demonstrate local compaction in cohesionless soils and reduction of the shear strength in cohesive soils. Small displacement piles such as H-section and steel sheet piles cause small changes in the strength and properties of the surrounding soil provided that such piling activity does not induce plugging at the pile toe. In the case of non-displacement piles (augered, bored piles and drilled casings), the soil is first removed by boring a hole, into which concrete is placed.

Driven piles are installed into the ground by means of a hammer. There are many types of hammers available to suit driving different types of piles in varied ground conditions. The selection of the most effective type of hammer for a given situation involves consideration of the length and weight of the pile and the ground conditions. The choice of hammer and pile type may also be restricted by environmental considerations such as restrictions on the levels of noise and vibration.

Hammers may be classified into two main types: impact hammers, which include drop hammers, air hammers, diesel hammers and hydraulic hammers; and vibratory hammers for granular soils. Detailed descriptions of the operation and specification of such hammers can be found in standard textbooks, such as Harris (1983) and Tomlinson (1994), and manufacturers' handbooks. Air hammers and diesel hammers are no longer used in the UK because of environmental considerations.

The mechanism of an impact or percussive piling hammer simply comprises a solid mass usually made of cast steel and known as a ram falling through a certain height on to the pile head or a mandrel to cause an impact which drives the pile into the ground. The simplest type is the winch operated drop hammer but modern impact hammers are powered by hydraulics to speed up the number of strikes per minute and to enhance the efficiency of the blow. The driving assembly of an impact hammer basically consists of a leader which has the function of holding and guiding the pile and hammer at its correct alignment. A cap, usually made of cast steel, is attached to the top of the pile to protect the pile head from potential damage from the hammer during driving. A wooden or plastic cushion (or dolly) may be used between the pile head and the cap to reduce damage from the hammer impact. The notional input energy of most impact hammers can be obtained by multiplying the ram weight by the drop height as follows:

$$\text{Notional input energy (J)} = \text{ram mass (kg)} \times g \text{ (m.s}^{-2}\text{)} \times \text{drop height (m)}$$

For effective pile driving, the weight of the hammer should normally be between 0.5 to 2 times the weight of the pile. The overall efficiency of the hammer may be affected by a number of factors including the presence of friction between the hammer and the guide, misalignment of the hammer and pile, and the amount of packing material between the hammer and pile.

Hydraulic drop hammers are now widely used. They are more efficient than simple drop weights and are both controllable and energy-efficient.

During percussive driving, the hammer impact initiates a stress wave in the pile which travels down the pile until it reaches the pile toe, where the energy which is not dissipated in advancing the pile is partly reflected and partly transmitted into the ground. The relative proportions of the energy transmitted and reflected are governed by the contrast in acoustic impedances of the pile and ground (Attewell & Farmer 1973). Although the stress pulse does not transmit energy into the ground whilst propagating along the shaft, Attewell & Farmer (1973), Martin (1980), Selby (1991) and Massarsch (1992) considered that energy may be transmitted to the ground along the pile shaft through friction as the pile moves through the soil. This would generate a vertically polarised shear wave, with a conical or cylindrical wavefront. Mallard & Bastow (1979), Selby (1989) and Massarsch (1992) suggested that flexure of the pile shaft may also occur during driving, which may initiate vibration from the shaft.

Vibratory hammers, or vibrodrivers, introduce continuous sinusoidal vibration into the pile and the surrounding ground during its operation. The soil particles are forced to vibrate at the operating frequency of the vibrodriver, irrespective of the natural frequency of the ground. The forced vibration may be made up of a number of component frequencies, but the dominant frequency will be that of the vibrodriver. This method is used to reduce the pile/soil interface friction and toe resistance during driving (the granular soil immediately adjacent to the pile is effectively fluidised), allowing pile penetration under the self-weight of the pile, the vibrodriver and its reaction block. The vibrodriver is suitable for driving most types of pile in granular soil deposits. In cohesive soils, fluidisation will not occur, and vibratory pile driving methods are not generally as effective.

Vibrodrivers may be classified into two main groups, namely standard frequency (up to about 30 Hz) and high frequency or 'City' vibrators (over about 35Hz). Non-resonant vibrodrivers, where the counter-rotating eccentric masses are not applied during start-up and shut-down until the operating frequency has been reached, are used in some cases to minimise vibration levels. Vibrodrivers are also sometimes classified as sub-sonic (6-50Hz), and sonic (140-150Hz). At frequencies of operation above about 100Hz, the pile will resonant longitudinally, and penetration rates can approach 20m per minute in loose to moderately dense granular soils. However, noise and vibration propagation can be high, leading to settlement in nearby structures.

Many makes of vibrodriver are currently available which encompass a wide range of input energies and operation frequencies. Recently the vibrodriver has become a popular choice with pile driving contractors, especially when piling is undertaken in residential areas where stringent noise and vibration restrictions apply. Vibrodrivers

have several advantages over impact hammers in that they can be used for both driving and extraction, they generally produce low levels of noise and vibration, driving is very rapid in granular soils, there is a low risk of damage to the pile head and they are relatively lightweight. However, they are generally unsuitable for use in cohesive soils, they are not very efficient in medium dense to dense granular materials, they can generate substantial ground vibrations when the operating frequency matches the resonant frequency of the ground and the load-carrying capacity of the pile can not be estimated during pile driving.

2.4.2 Driving energy

The concept of scaled energy (the quotient of the square root of the nominal energy rating of the hammer divided by the distance from the pile toe) for the presentation of vibration data from percussive pile driving was first introduced by Wiss (1967). A similar approach, with the distance term specified in various ways, has since been adopted by many other workers for data presentation (Attewell & Farmer 1973, Mallard & Bastow 1979, Martin 1980, Uromeihy 1990, Whyley & Sarsby 1992) and is used in many documents as a basis for vibration prediction (Head & Jardine 1982, BSI 1992b, CEN 1998). Such predictors are provided in the form:

$$v = \frac{C\sqrt{W}}{r} \tag{2.8}$$

where

- v is the ppv, which may be measured in a number of ways (Section 2.3);
- W is an estimate of the nominal energy input;
- r is the distance from the source;
- C is a factor for driving conditions, see Table 2.1 below.

Driving Method	Ground conditions	C
Impact	Very stiff cohesive soils, dense granular, obstructions	1.0
	Stiff cohesive soils, medium dense granular, compact fill	0.75
	Soft cohesive soils, loose granular media, loose fill	0.5
Vibratory	All soil conditions	0.7

Table 2.1: Suggested C values given by Draft Eurocode 3

Relating the groundborne vibration to the energy of the driver has a theoretical basis, since the particle velocity is proportional to the square root of the energy propagated by a surface wave. However the use of the nominal energy of the pile driver takes no account of the variability which may exist in the inefficiencies of different hammer and pile systems. Svinkin (1992) reported that the measured energy transferred to the pile is typically only 20 to 60 per cent of the rated hammer energy, and in most cases between 30 and 40 per cent.

The use of the nominal energy of the hammer for estimating the energy input during percussive piling has been adapted for vibrodriving of piles. For vibrodriving, the

energy per cycle of the vibratory mechanism is used, calculated from the output of the power supply divided by the operating frequency (Head & Jardine 1992). This method has been used by many authors (Uromeihy 1990, Attewell *et al* 1992a & 1992b, Head & Jardine 1992) and has been adopted by the British and European standardising authorities (BSI 1992b, CEN 1998) for vibration prediction.

2.4.3 The properties of the pile

The energy transmitted from the pile to the soil depends mainly on the type and efficiency of the hammer, the nature of the impulse (transient or steady-state) and the impedance of the pile, which can vary significantly with pile type. For example, the impedance of a steel pile is almost 10 times higher than that of a timber pile. The impedance, I , is a measure of the capability of the pile to transmit the longitudinal force generated by the impact of the hammer, and is given by

$$I = \rho c A \quad (2.9)$$

where

ρ is the mass density of the pile;

c is the velocity of longitudinal wave propagation in the pile;

A is the cross-sectional area of the pile

Heckman and Hagerty (1978) considered that the magnitude of groundborne vibration arising from percussive piling was dependent upon the cross-sectional area of the pile and upon the acoustic impedance of the pile material. They presented a summary of field data in which the maximum vibration magnitude arising from piling was plotted against the impedance. Heckman and Hagerty reported that, as the pile impedance increased, the maximum magnitude of ground vibration decreased. Head & Jardine (1992), however, concluded that, because of the wide range of ground conditions and the difficulties in accurately defining the energy levels of the drivers and the impedance of the piles, it was impossible to draw any general conclusions on the validity of Heckman and Hagerty's work. Conversely, Massarsch (1992) considered Heckman and Hagerty's observations to be important and commented that a reduction in pile impedance of 30 per cent could increase the ground vibration amplitude by a factor of ten. Massarsch added further case history data which supported Heckman and Hagerty's conclusions.

2.4.4 Ground conditions

Interaction between the pile and the soil may affect the transmission of energy into the ground from the pile. The dynamic behaviour of the soil subjected to transient loading from percussive piling is likely to be very different to the behaviour of soil subjected to continuous cyclic loading from vibratory piling. The behaviour of the soil and the pile/soil interaction under each of these loading conditions is therefore considered separately in the following sub-section.

The energy transferred from an impact hammer to a pile remains approximately constant throughout driving (Rempe & Davisson, 1977). For a constant energy input to the pile, D'Appolonia (1971) considered that the vibration magnitude was dependent upon the relative amounts of energy used in advancing the pile through the ground and in causing elastic deformation of the soil. It is the elastic deformations which give rise

to groundborne vibrations. D'Appolonia therefore concluded that, in stiff or dense soils, a high magnitude of vibration would arise because the rate of penetration is small so more energy is dissipated as elastic deformation of the soil than occurs when driving in weaker soils. In easily penetrated soils, most of the energy is expended in advancing the pile, resulting in relatively low magnitudes of groundborne vibration.

Increasing ground vibration magnitudes with increasing penetration resistance have been observed by many other workers (for example, Wiss 1967, Martin 1980 and Whyley & Sarsby 1992).

The apparent relationship between penetration resistance and the magnitude of groundborne vibration has led to attempts to correlate the ppv with field data from penetration tests. The cone penetration test enables toe resistance and skin friction to be measured separately and is therefore used to interpret stratification, soil type and engineering soil properties. The cone penetration test is the basis of the TNOWAVE program developed by Van Staadlduinen & Waarts (1992) who used data from the cone penetrometer to predict vibration magnitudes from percussive piling.

Following a review of vibratory driving analysis, Holeyman (2000) concluded that the soil resistance to vibratory driving was the most critical parameter affecting vibro-drivability and argued that a proper understanding of soil behaviour was the key to dealing with the issues related to vibratory driving, including vibration prediction. Hiller (1999) concluded that the source of ground borne vibration during vibratory piling is the interaction between the pile shaft and the ground, with little contribution being made by the pile toe. He also concluded that the magnitude of vibration increases as the rate of penetration decreases. However, measurements of the rate of driving were not undertaken to verify this.

Clough & Chameau (1980) reported a case history of vibration arising from vibratory piling which showed that higher magnitudes of vibration arose when the penetration rate was low than when driving was relatively easy. The threshold values and empirical relationships for the prediction of vibration from vibratory piling in the British Standards and Eurocodes (BSI 1992b; CEN 1998) do not make any allowance for different ground conditions.

Following a review of published data, Massarsch (1992) concluded that in spite of the great significance of dynamic soil properties (wave propagation velocity and material damping) for almost all aspects of ground vibration problems, most empirical estimates of vibration ignore them.

2.5 WAVE PROPAGATION

In order to drive a pile into the ground, sufficient force must be transmitted to the pile head to overcome the shaft and toe resistance provided by the soil. Part of the energy, transmitted through the pile is transferred to the soil along the pile shaft and part to the toe. The displacement of the soil by the penetrating pile generates both plastic and elastic deformation. Beyond a short distance from the pile (about one pile radius) most of the energy is propagated in the form of elastic waves (Massarsch (1992)). These elastic waves comprise body waves, which radiate energy in all directions in the ground and surface waves, which transmit the energy close to the ground surface.

Body waves are classified according to the propagation direction as compressional (P) waves or shear (S) waves.

2.5.1 Compressional waves (P waves)

These waves (also known as dilational, longitudinal and primary waves) cause particles to vibrate parallel to the direction of the wave propagation as shown in Figure 2.5. Volume change occurs in the propagation medium as the particles vibrate back and forth causing compression and expansion. The degree of soil saturation directly affects P wave propagation velocity. As water is relatively incompressible compared to the soil skeleton, the measurement of P wave velocity in a saturated soil does not represent the velocity in the soil alone. Das (1983) suggested that a P wave propagates in a saturated soil via the pore water and the soil skeleton as two components, a “fluid” and a “frame” wave.

The propagation velocity of a P wave, (c_p), in a medium with a Young's Modulus, E , a Poisson's ratio, ν , and a density, ρ , is given by:

$$c_p = \sqrt{\frac{\lambda + 2G}{\rho}} \quad (2.10)$$

where

$$G = \frac{E}{2(1+\nu)} \quad (2.11)$$

$$\lambda = \frac{E\nu}{(1+\nu)(1-2\nu)} \quad (2.12)$$

2.5.2 Shear waves (S waves)

Shear waves (also known as transverse, distortional and secondary waves) cause particles to vibrate normal to the direction of the wave propagation, as shown in Figure 2.5. S waves may be polarised into a single plane such as a vertical plane as an S_v wave or a horizontal plane as a S_h wave. A propagating S wave causes distortion of an element in the medium, but no volume change.

Propagation of a shear wave depends on the degree of saturation of the medium. As pore water has no shear strength, the S wave velocity in a saturated soil represents the wave velocity in the soil only if the particles remain in direct contact i.e. in effective stress terms. The propagation velocity of a shear wave, (c_s), is related to the elastic properties of the medium through which it passes and is given by:

$$c_s = \sqrt{\frac{G}{\rho}} \quad (2.13)$$

2.5.3 Surface waves (R waves)

Surface waves are generated at boundaries between media that have different acoustic impedances. Surface waves include Rayleigh waves (R waves) which are a combination of refracted and reflected P and S waves, with no horizontal shear component, and Love waves which are horizontally polarised (S_h) waves transmitted through a surface layer. The propagation velocity of a Rayleigh wave (c_r), assuming a Poisson's ratio of 0.25, is given by:

$$c_r = 0.9194 \sqrt{\frac{G}{\rho}} \quad (2.14)$$

The motion of a Rayleigh wave is illustrated in Figure 2.6.

2.5.4 Propagation of ground waves from pile driving

The propagation of ground waves from pile driving is complex as the source of vibration varies both in location and excitation mechanism. Attewell & Farmer (1973) proposed two sources of energy transfer during driven piling (Figure 2.7): the pile toe, from which a quasi-spherical wavefront emanates, and the pile shaft from which a quasi-cylindrical wavefront propagates as a result of shaft friction.

2.6 ATTENUATION OF GROUND VIBRATIONS GENERATED BY PILING

Wave attenuation is caused by two types of damping. Geometrical damping is due to enlargement of the wave front as the distance from the source increases. Material damping is caused by internal absorption of wave energy by the soil.

2.6.1 Geometrical damping

If an impulse of short duration is created at a point on the surface of an elastic half space, the body waves travel into the medium with a hemispherical wavefront (Das, 1983). The Rayleigh waves will propagate outwards along a cylindrical wavefront. When body waves spread out around a hemispherical wave front, the energy is distributed over an area that increases with the square of the radius:

$$E' \propto \frac{1}{r^2} \quad (2.15)$$

where E' is the energy per unit area and r is the radius. However, the amplitude is proportional to the square root of the energy per unit area:

$$Amplitude \propto \sqrt{E'} \propto \sqrt{\frac{1}{r^2}} \quad (2.16)$$

or

$$Amplitude \propto \frac{1}{r} \quad (2.17)$$

The Rayleigh waves expand on a cylindrical wavefront, so E' is proportional to $1/r$. Hence, the amplitude of the Rayleigh waves, which spread out in a cylindrical wave

front, is proportional to $1/\sqrt{r}$. Thus the attenuation of the amplitude of the Rayleigh waves is slower than for the body waves.

The relationships for wave attenuation given above are for waves propagating from a point source on the surface of an elastic half space. However, in the case of piling, the source of vibration is not a discrete point, but is complex with P waves generated at the toe, S waves generated down the entire length of the pile shaft and R waves generated on the ground surface and at material boundaries. As illustrated in Figure 2.7, the S waves will tend to propagate on a cylindrical or conical wavefront rather than a hemispherical wavefront. The attenuation of S waves generated from a pile shaft is therefore much slower than the attenuation of S waves generated by a vibrating point source on the surface of a half space.

2.6.2 Material damping

As waves pass through the soil, part of the energy is absorbed by friction and cohesion, and this reduction in the vibration amplitude is due to material damping. Mintrop (1911, cited by Bornitz 1931) proposed an equation for the attenuation of surface waves in terms of geometric attenuation, dependent upon the square root of distance measured along the ground surface (d), and an exponential material damping component:

$$v = v_1 \sqrt{\frac{d_1}{d}} e^{-\alpha(d-d_1)} \quad (2.18)$$

where

v is the ppv at a distance d measured along the ground surface from the source
 v_1 is the ppv at a reference distance d_1
 α is the material damping coefficient.

The value of α is dependent upon the properties of the soil (Barkan, 1962, Woods & Jedele 1985) and is also proportional to the vibration frequency (Richart et al 1970). Massarsch (1992) states that the assessment of the material damping coefficient is of great importance for a reliable prediction of wave attenuation and suggests the following relationship after Haupt (1986):

$$\alpha = \frac{(2\pi Df)}{c} \quad (2.19)$$

where D is the material damping (%), f the vibration frequency and c the wave propagation velocity.

A further consideration which may affect the attenuation of vibration and which may disturb the relationship between frequency and material damping is that soils behave as bandpass filters, possessing a limited range of frequencies within which vibration energy propagates with least attenuation (Attewell 1995).

2.7 FACTORS AFFECTING THE TRANSMISSION OF GROUNDBORNE VIBRATIONS INTO STRUCTURES

Damage to structures from ground vibrations are usually attributed to “dynamic effects” such as vibration amplification and soil resonance. Massarsch and Broms (1991) demonstrated both theoretically and by a review of the available literature that ground distortion caused by pseudo-dynamic ground movements (resulting from the passage of waves below a building) is the single most important factor controlling building damage. While during static deformations, the soil supporting the structure can either settle or heave, both upward and downward deformations of structural supports can occur at the same time during the passage of waves travelling below a building. Generally a ‘rigid’ floor slab shows reduced vibrations, while a slender suspended floor may amplify vibrations (BS5228, 1992).

Massarsch (1992) concluded that the most critical situation arises when the building length corresponds to about half of the length of the propagating wave. Massarsch emphasised that other factors can cause vibration problems or damage to structures, especially at high frequencies and in the vicinity of the vibration source, or when resonance occurs between the induced vibrations and various components of a building.

2.8 PREDICTION OF VIBRATIONS GENERATED BY PILING

The intrusive nature of piling and the perceived risk of vibration-induced damage on adjacent structures have led to many attempts to predict the magnitude of vibration generated by piling. Many case histories have been reported in the literature but in a fairly inconsistent manner. Head & Jardine (1992) attempted to compile a database on piling vibrations with the objective of assessing the potential for piling to cause annoyance or damage. They commented that many records lacked important information.

The most common form of relationship for the prediction of ground vibration from piling is based on that proposed by Attewell & Farmer (1973) as

$$v_v = k \left[\frac{\sqrt{W}}{d} \right]^y \quad (2.20)$$

where

v_v is the vertical component ppv (mm/s)

W is the nominal energy per blow (or per cycle) (J)

d is the radial distance between source and receiver (m)

k and y are empirically determined constants

This relationship has been the basis of many empirical methods which consider the nominal energy at the source and attempt to fit curves to field data. This has resulted in a series of different scaling factors which can be applied within essentially the same equation. This approach has been developed for percussive piling and adapted for vibratory piling by use of the energy per cycle of the vibrodriver. Attewell et al (1992),

Whyley & Sarsby (1992) and CEN (1998) proposed different scaling factors for the prediction of vibration from percussive piling which were dependent on the ground conditions. Van Staalduinen and Waarts (1992) and Jongmans (1996) attempted to quantify the effects of vibration magnitude on parameters other than the driver energy so that site specific predictions could be developed.

More recently, the use of numerical modelling techniques has been considered as a possible tool for the prediction of vibration from piling (Mabsout 1995; Ramshaw et al 1998). Such techniques potentially offer a means to understanding the complex processes of vibration generated by piling but they can not be used in isolation: they require high quality field data for validation (Ramshaw et al 1998).

2.9 VIBRATION DATABASES

Various workers (Uromeihy 1990; Head & Jardine 1992; Hiller 1999) have attempted to quantify the magnitude of vibrations by compiling large databases of vibration measurements recorded during piling operations at many sites. The data from these measurements have generally been used to refine the empirical relationships suggested in the literature. However, the data sets are often not very comprehensive and do not include sufficient data for detailed numerical modelling.

The 'SIPDIS' program, initiated by Massarsch in the early 1990's, was an extensive suite of controlled pile driving with comprehensive in situ measurements. Steel piles of various sizes were driven at one site in Germany and at one site in the UK (Immingham) using both impact and vibratory hammers. Water-flush was used occasionally.

Instrumentation was designed by Loster, GmbH, and was based on a digital acquisition system linked to a range of sensors. These included pile head strain gauges and accelerometers, ground surface and sub-surface velocity transducers, and pore pressure transducers.

A massive data set has been recorded but, as yet, it has not been released into the public domain.

2.10 SUMMARY

Ground waves from piling mainly comprise P (compressional), S (shear) and R (Rayleigh or surface) waves. The source of vibration is not a discrete point, but is complex with P and S wavefronts generated from various parts of the pile. The transmission of vibration from the pile to the soil is also dependent on the method of installation, whether impact or vibratory, as the dynamic response of the soil is likely to be very different in each case. The wavefronts propagate outwards from the pile at differing velocities depending on the properties of the soil through which they travel. The wavefronts may be reflected or refracted at changes in strata and may interact with each other.

The attenuation of vibration from piling is complex and prediction relies on many site-specific parameters. The usefulness of empirical relationships based on case history data are therefore limited for confident prediction of piling vibration at any particular site. The use of numerical modelling techniques to simulate the ground waves

generated by pile driving therefore appears to be an attractive alternative, as these techniques potentially offer a means of understanding the complex processes of vibration generation during piling. However, numerical modelling requires high quality and comprehensive field data for validation.

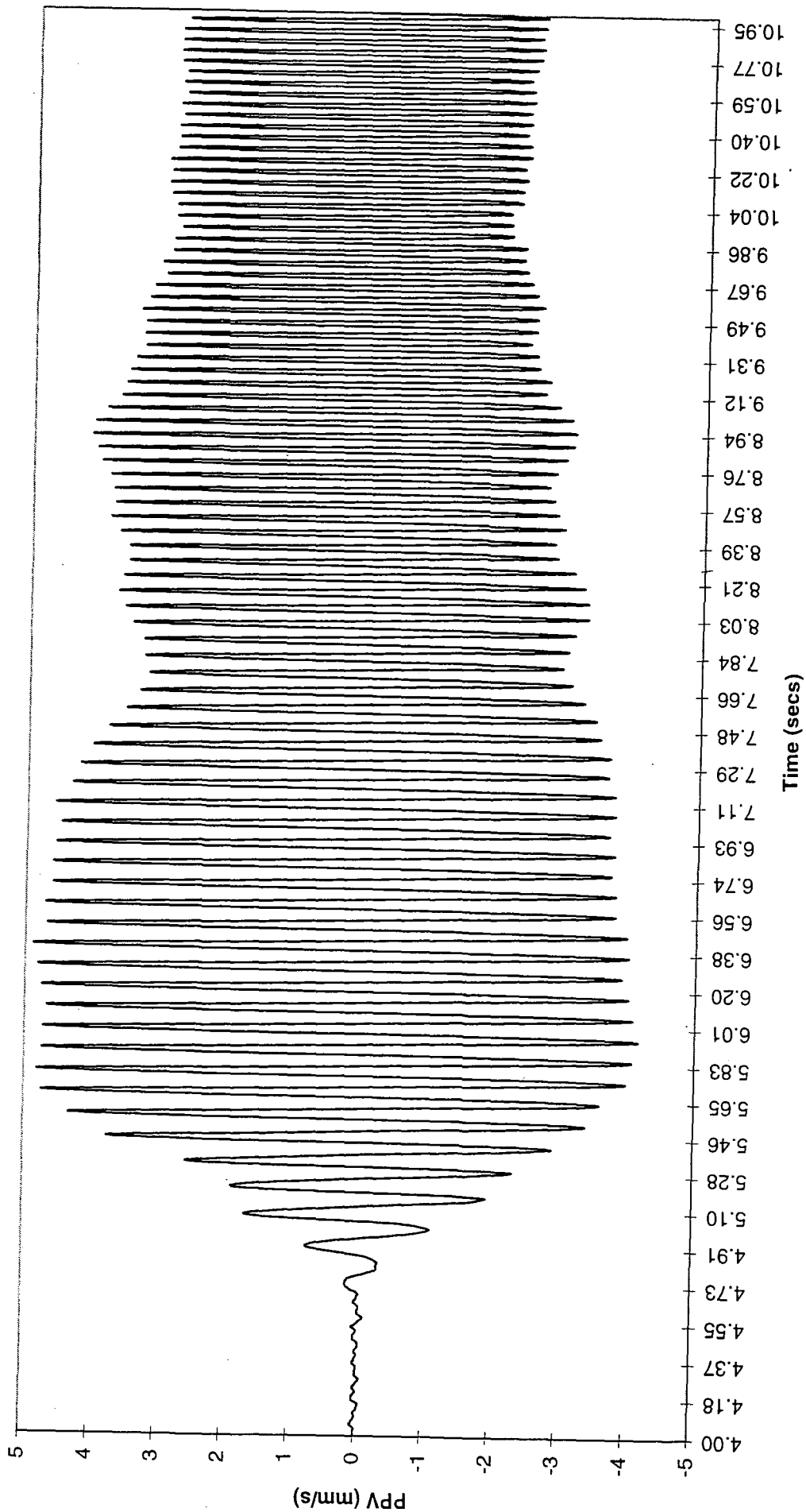


Figure 2.1 Example of periodic vibration generated by vibratory piling

ABAQUS

— 10M

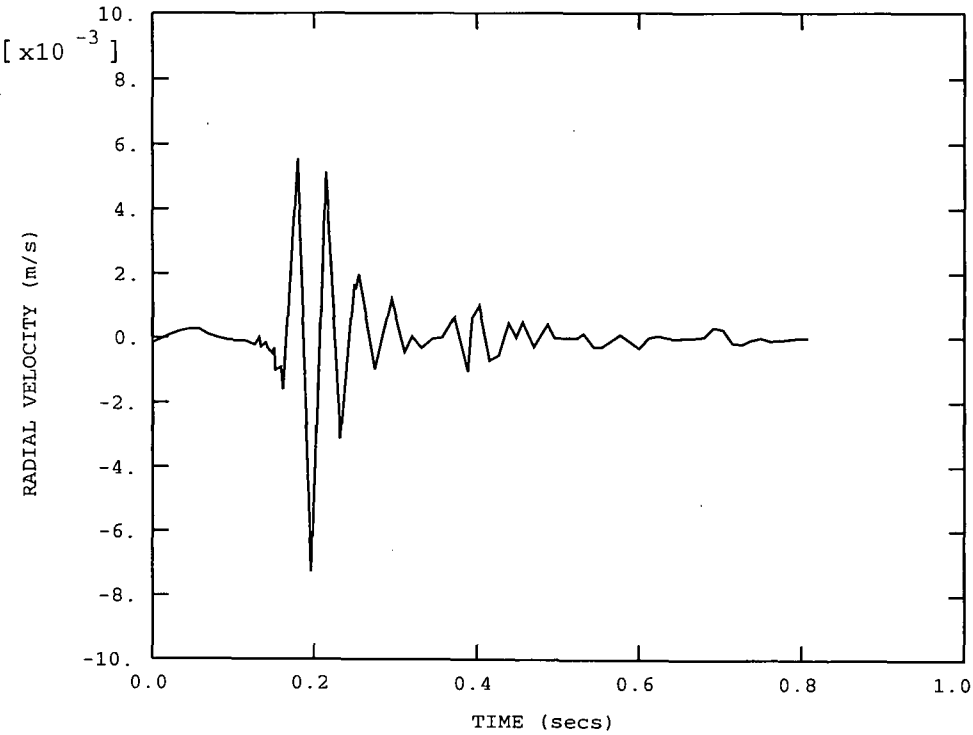


Figure 2.2 Example of transient vibration generated by impact piling

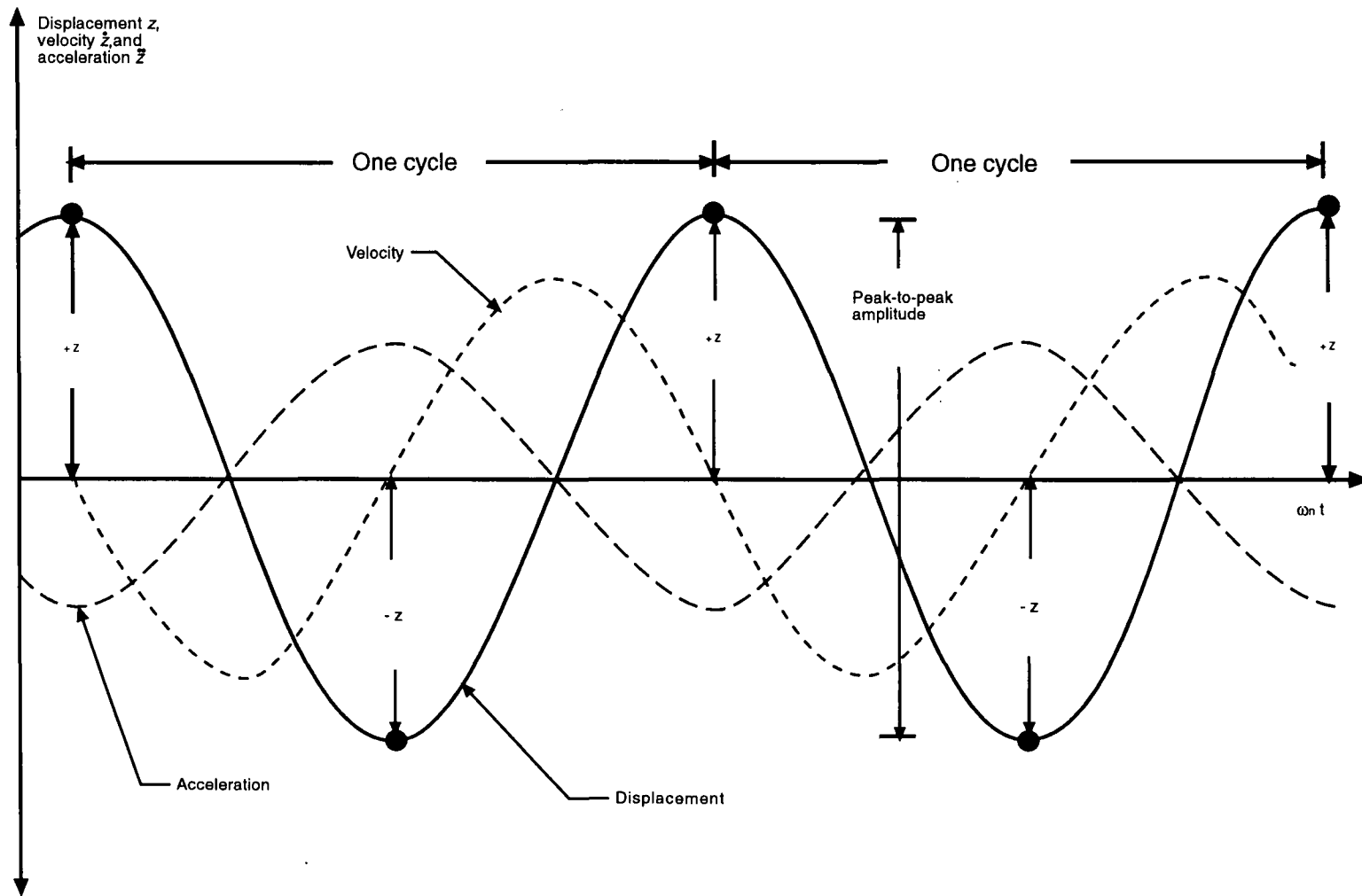


Figure 2.3

The relationships between displacement, velocity and acceleration for sinusoidal vibration (after Das, 1983)

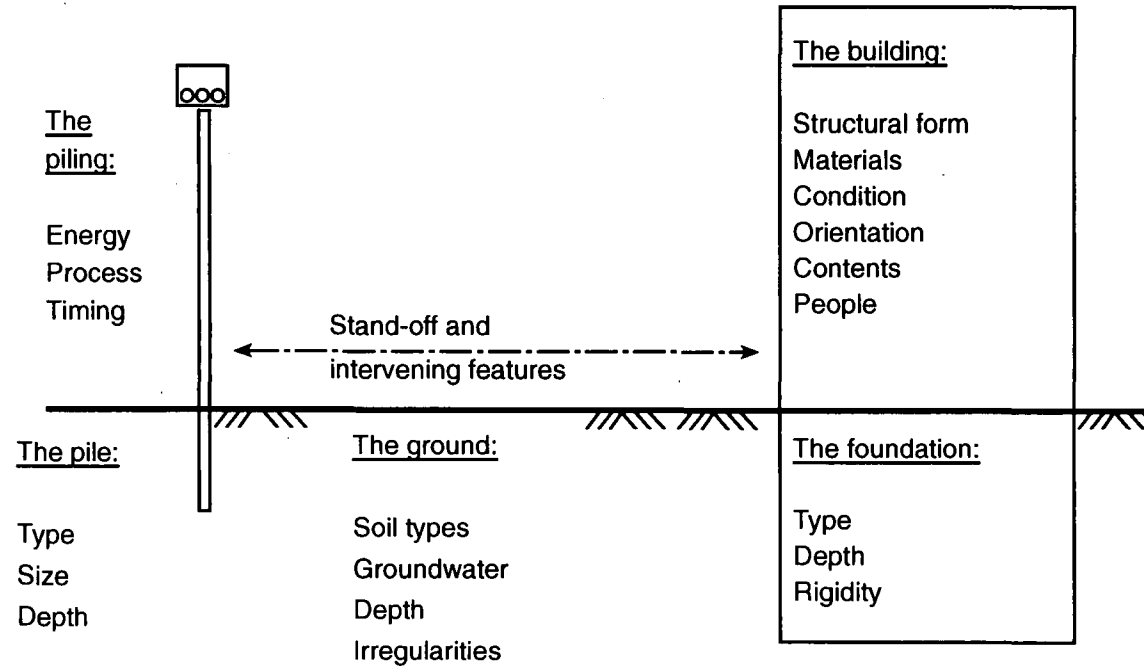


Figure 2.4

Summary of the variables associated with groundborne vibration and piling (after CIRIA Technical Note 142, Head & Jardine, 1992)

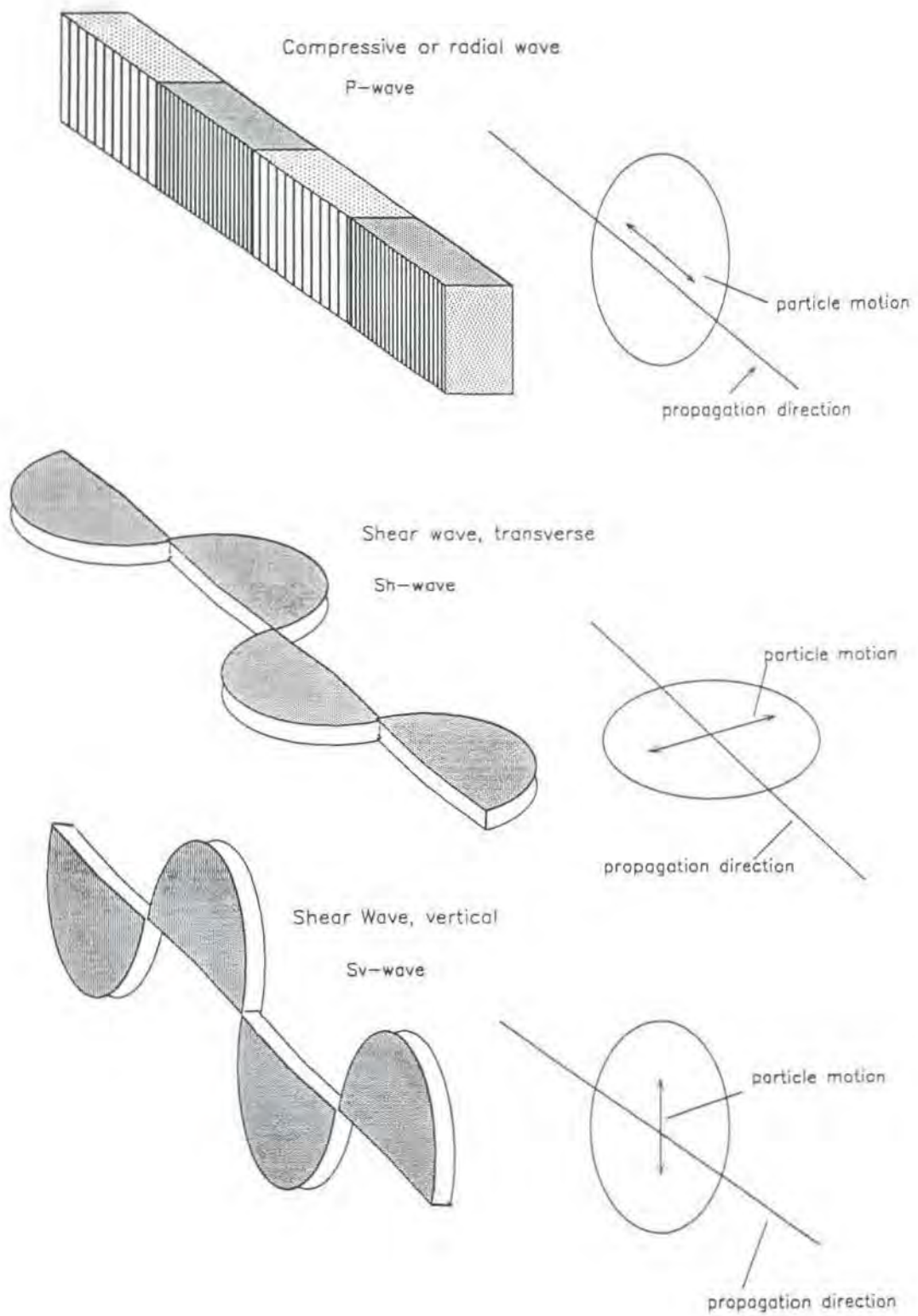


Figure 2.5

Propagation of P and S waves (after Uromeihy, 1990)

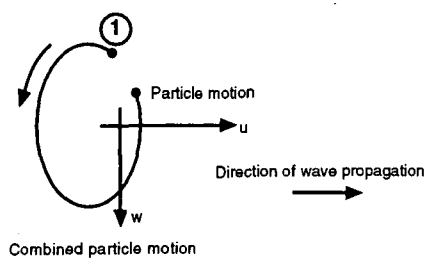
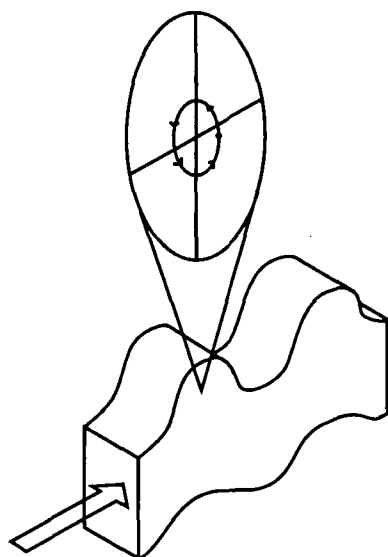


Figure 2.6

Propagation of a Rayleigh wave (after Uromeihy, 1990)

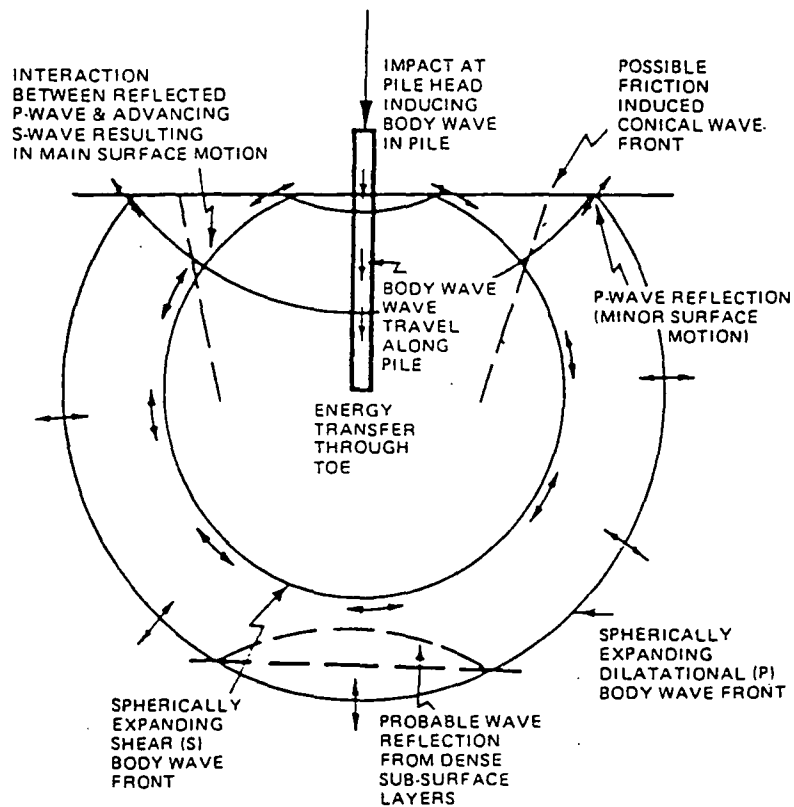


Figure 2.7

Attenuation of waves from a pile driving operation (after Attewell & Farmer, 1973)

CHAPTER 3

NUMERICAL MODELLING OF GROUND WAVES IN ABAQUS

3.1 INTRODUCTION

The work detailed in this thesis was undertaken using the ABAQUS finite element program, developed and distributed by Hibbitt, Karlsson & Sorensen, Inc. It is one of the most powerful and versatile finite element programs on the market. Of particular value to this work is the availability of infinite elements within the program together with an interface which allows the user to define additional element types in FORTRAN code.

This Chapter details the preliminary work that was undertaken to validate the ability of ABAQUS to simulate ground waves satisfactorily. The first section describes the ABAQUS finite element program and the system that it was run on at the University of Durham. The performance of the infinite elements provided by ABAQUS in modelling the far field domain is then verified in Section 3.3 using some of the examples given in the ABAQUS Example Manual (HKS, 1998). The ability of the program to simulate ground waves with sufficient accuracy is demonstrated in Section 3.4 by transmitting pure P, S and R waves in turn along a channelled wave guide of finite elements with infinite elements at the far end (Ramshaw *et al* 1998). Various finite element/infinite element (FE/IE) meshes were then used to verify the geometrical attenuation of P, S and R waves against analytical solutions (section 3.5).

3.2 THE ABAQUS FINITE ELEMENT PROGRAM

ABAQUS is a suite of powerful engineering simulation programs, based on the finite element method, which can solve problems ranging from relatively simple linear analyses to highly complex non-linear simulations. ABAQUS contains an extensive library of elements that can model virtually any geometry. It has an equally extensive list of material models that can simulate the behaviour of most engineering materials.

The ABAQUS system comprises three main modules, namely ABAQUS/Pre, ABAQUS/Standard and ABAQUS/Post.

ABAQUS/Pre is an interactive, graphical pre-processor that allows models to be created quickly and easily by producing or importing the geometry of the structure to be analysed and decomposing the geometry into meshable regions. Physical and material properties can be assigned to the geometry, together with loads and boundary conditions. ABAQUS/Pre contains powerful options to mesh the geometry and verify the resulting analysis model. Once the model is complete, it produces an ABAQUS input file.

ABAQUS/Standard is a general-purpose analysis module that can solve a wide range of linear and non-linear problems involving the static, dynamic, thermal and electrical response of components. General transient dynamic analysis in ABAQUS/Standard uses implicit integration of the entire model to calculate the transient dynamic response

of the system. An implicit integration method is one where the equations are solved at each time increment and therefore requires an inversion of the system equations.

ABAQUS/Post is an interactive, graphical post-processor that supports all of the capabilities in the ABAQUS analysis modules and provides a wide range of options for interpreting the results.

The ABAQUS suite of programs was installed onto two UNIX systems at the University of Durham. The first was a general time sharing server called deneb comprising a Sparc E450 with four 250 MHz processors with 1GB of memory plus 13GB of swap space (4GB + 9GB disks). The Solaris 2.6 operating system was installed on deneb. The larger analyses were run on a computer called marvin which comprised a Silicon Graphics Power Challenge with 16 x R10000 processors and 1Gb of memory. Its operating system was IRIX 6.5.

The data for the ABAQUS analyses were prepared and the results were viewed on a SUN Ultra 1 workstation. Versions 5.5 through to 5.8 of ABAQUS were used in this work.

The analyses were run and the results output to a temporary file space which was automatically deleted about once a week. The size of the various types of output files generated by ABAQUS were generally too large to be saved routinely so post-processing of the results usually took place immediately. Selected results files, usually those suffixed *.fil* in binary format containing the data for x-y plots or printed tabular output, were saved onto 'Zip' disks.

3.3 VERIFICATION OF THE INFINITE ELEMENTS AVAILABLE IN ABAQUS

3.3.1 Infinite Elements

One of the limitations of finite element methods arises when they are employed for the modelling of an infinite domain, in which energy radiates from a source outwardly towards infinity. In numerical calculations, only a finite region of the medium is analysed. Unless something is done to prevent outwardly radiating waves from reflecting from the region's boundaries, errors are introduced into the results.

The use of infinite elements in conjunction with finite elements has been demonstrated to be a very effective means for simulating interaction problems with unbounded domains. Following the conceptual works of Ungless (1973) and Zienkiewicz & Bettess (1975), infinite elements have been widely applied to the solution of various wave propagation problems, and are particularly applicable to geotechnical problems where the engineering medium, the soil/rock, is effectively modelled as a semi-infinite half-space.

ABAQUS provides first- and second-order infinite elements that are based on the work of Zienkiewicz *et al* (1983) for static response, and of Lysmer & Kuhlemeyer (1969) for dynamic response. The elements are used in conjunction with standard finite elements, which model the area of interest, with the infinite elements modelling the far field domain.

3.3.2 Static Response: The Boussinesq and Flamant Problems

These examples, which are included in the ABAQUS Example Manual (HKS, 1998), verify the performance of infinite elements in modelling the far field domain. The results from the problem of a point load on a half-space and a line load on a half-space are compared with the analytical solutions due to Boussinesq and Flamant (Timoshenko & Goodier, 1970), respectively. For comparison purposes, results obtained using only finite elements are also given.

Two axisymmetric mesh configurations are used for the Boussinesq problem of a point load on a half-space. The finite element/infinite element (FE/IE) mesh, Figure 3.1, is composed of twelve finite elements extending to a radius of 4.0, with four infinite elements modelling the far field domain. The finite element (FE) mesh, Figure 3.2, is made up of sixteen finite elements, truncated at a radius of 5.0, where fully fixed boundary conditions are applied.

The material is chosen to be linear elastic, with a Young's modulus, E , of 1.0 and a Poisson's ratio, ν , of 0.1. A unit load is applied in both problems.

Boussinesq's analytical solution for the problem of a point load on a half-space gives the vertical displacement as:

$$w = \frac{P}{2\pi E} \left[(1+\nu)z^2(r^2+z^2)^{-\frac{3}{2}} + 2(1-\nu^2)(r^2+z^2)^{-\frac{1}{2}} \right] \quad (3.1)$$

where r and z are the radial and vertical distance from the point load, respectively. This equation clearly shows the $1/r$ singularity at the point of application of the load ($r=0$).

The displacement variation along a vertical line beneath the point load obtained from the finite and infinite element models is shown together with a plot of the analytical solution in Figure 3.3.

It is clear that the results obtained with the infinite element meshes show a significant improvement over the finite element meshes with the same number of elements, and that the infinite elements provide reasonable accuracy even with a relatively coarse mesh.

The same mesh configurations are used for the Flamant problem of a line load on a half-space. This case is a plane strain problem and a vertical plane of symmetry is used.

Flamant's analytical solution for the problem of a line load on a half-space gives the displacement along a vertical line beneath the line load as:

$$w = \frac{2P}{\pi E} \ln\left(\frac{d}{z}\right) \quad (3.2)$$

where d is an arbitrary large distance at which the displacement is assumed to be zero. In this example, the far field nodes on the infinite elements are chosen to be fixed so that the value of d is 8.0. The results obtained from the finite and infinite element

models are shown in Figure 3.4 together with a plot of the analytical solution. This graph shows that even though the infinite elements contain displacement interpolations in the infinite direction with terms of order $1/z$, $1/z^2$ while the analytical solution is of a $\ln(z)$ nature, they provide a significant improvement over the solution obtained with finite elements only.

3.3.3 Dynamic Response: Wave Propagation in an Infinite Medium

This example, which is included in the ABAQUS Example Manual (HKS, 1998), tests the effectiveness of the infinite element (quiet boundary) formulation in dynamic applications. The problem is similar to that analysed by Cohen & Jennings (1983). The purpose of this example is to compare the results obtained using a small mesh including infinite element quiet boundaries with an extended mesh of finite elements only. Results obtained using the small mesh without the infinite element quiet boundaries are also given to show how the solution is affected by the reflection of the propagating waves.

The problem is an infinite half-space (plane strain is assumed) subjected to a vertical pulse line load. A vertical plane of symmetry is used so that only half the configuration is meshed. Three meshes are used: a small FE/IE (quiet boundary) mesh of 8 x 8 first order (4 noded) finite elements plus sixteen first order infinite elements as shown in Figure 3.5; a small FE mesh of 8 x 8 first order elements as shown in Figure 3.6; and an extended FE mesh of 24 x 24 first order elements as shown in Figure 3.7. The FE meshes are assumed to have free boundaries at the far field and will reflect the propagating waves, whereas the FE/IE mesh models the infinite domain and provides quiet boundaries that minimise reflection of propagating waves back into the mesh.

The material is assumed to be elastic with Young's Modulus, E , of 1.0, a Poisson's ratio, ν , of 0.1 and a density, ρ , of 0.01. Material damping is not included in the analyses. Based on these material properties, the speed of propagation of compression waves (P-waves) in the material is approximately 10.0 and the speed of propagation of shear waves (S-waves) is approximately 6.7. Therefore the compression waves, which are predominant with the vertical pulse excitation, should reach the boundary of the extended mesh in about 2.4 time units. The analyses are run for 4.0 time units so that the waves are allowed to reflect significantly into the finite element meshes that do not have quiet boundaries. The applied vertical pulse is in the form of unit impulse function, or Dirac delta function, with an amplitude of 1.0.

The results of the analyses for the meshes are shown in the form of time histories of vertical displacements at nodes 7, 27 and 151 (Figures 3.8, 3.9 and 3.10 respectively). The wave reflection caused by the free boundaries in the small FE mesh is evident, while the small FE/IE quiet boundary mesh largely succeeds in eliminating this reflection.

The next test of the computational method was to apply a pulse load to a small circular disc on the surface of an axisymmetric elastic half-space. A 'snapshot' of displacements is presented in Figure 3.11. Outgoing wavefronts can be clearly observed, in which the first is a P wave expanding over a hemispherical surface. The displacements are normal to the polar source; they are largest directly below the origin, and reduce towards zero as the ground surface is approached, with values being negligible after some 40° from the axis of symmetry. Following behind the P wavefront

is an S wave, also mapped around an expanding hemisphere, but this time with larger values nearer ground surface; there is a sharp reduction close to the axis of symmetry; close to ground surface the S wave regresses into a Rayleigh wave. Intermingled with the S wave is a second P wavefront.

Other features emerge: firstly, the ratio of the two wave speeds is close to 0.577, which is the theoretical ratio (calculated as $c_s/c_p = \sqrt{[(1-2\nu)/2(1-\nu)]}$), for the chosen Poisson's ratio of 0.25. The estimated ratio of half-wavelengths of the two waves is about 0.6, slightly higher than the 0.577 value for pure sine waves. The ratio of energies between the P and S wavefronts is difficult to compute, but a rough estimate suggests a value very close to the ratio of 0.21:0.79 derived by Miller & Pursey (1955).

VERIFICATION OF FE/IE MODEL TO TRANSMIT P, S, AND R WAVES

3.4.1 General

This section of work was undertaken to verify that ABAQUS models P, S, and R waves sufficiently accurately. Pure P, S and R waves were modelled in ABAQUS and were compared with analytical solutions. These analyses also provided a check of the efficiency of the ABAQUS infinite elements in absorbing outgoing waves.

3.4.2 Compressional Waves (P waves)

For examination of P waves, a plane strain mesh of finite elements, 10 elements wide and 10 elements high, with infinite elements applied to the right-hand vertical boundary was used with upper and lower boundaries restrained in the y-direction, Figure 3.12.

A pure sinusoidal P wave was applied to the left-hand vertical boundary of the mesh. The analytical form of a P wave is given by

$$u(x,t) = a \cos(kx - \omega t) \quad (3.3)$$

where ω is a chosen angular frequency, k is the wave number and a is the amplitude

For a pure P-wave, the displacements u_x and u_y are given by

$$u_x = \frac{\partial \phi}{\partial x}, \quad u_y = 0 \quad (3.4)$$

Hence, assuming $a=1$,

$$u_x = \frac{\partial \phi}{\partial x} = -k \sin(kx - \omega t) \quad (3.5)$$

The P wave was applied to the FE mesh by specifying the horizontal displacements on the vertical boundaries as a function of time using the following technique.

1. Choose elastic constants E , ν and ρ .
2. Calculate the Lamé constants from the following equations,

$$\lambda = \frac{Ev}{(1+\nu)(1-2\nu)} \quad (3.6)$$

$$G = \frac{E}{2(1+\nu)} \quad (3.7)$$

3. Choose an angular frequency, ω
4. Calculate the propagation velocity of the P wave, c_p ,

$$c_p = \sqrt{\frac{\lambda + 2G}{\rho}} \quad (3.8)$$

5. Calculate the wave number, k ,

$$k = \frac{\omega}{c_p} \quad (3.9)$$

6. Calculate the wavelength, Λ ,

$$\Lambda = \frac{2\pi}{k} \quad (3.10)$$

7. In ABAQUS, the periodic displacement of nodes is specified by the use of the *AMPLITUDE and *BOUNDARY commands. Periodic variation of amplitude is defined as a Fourier series as follows:

$$a = A_0 + \sum_{n=1}^N [A_n \cos n\omega(t-t_0) + B_n \sin n\omega(t-t_0)] \quad \text{for } t \geq t_0 \quad (3.11)$$

$$a = A_0 \quad \text{for } t < 0 \quad (3.12)$$

where the constants, t_0 , ω , A_0 , A_n , B_n , $n = 1, 2 \dots N$ are defined on the datalines following the *AMPLITUDE command in ABAQUS.

The calculation of the Fourier constant for a P wave is given in Appendix B.

The P wave was applied to the left-hand vertical boundary of the FE mesh shown in Figure 3.12 using the technique described above.

The displacements produced by a pure P wave are plotted at intervals of 0.18 seconds in Figures 3.13. The P wave plotted spatially was found to reproduce the analytical sine wave as shown in Figure 3.14. These plots demonstrate that ABAQUS models the P-wave almost exactly and that the infinite elements absorb the P waves very effectively.

3.4.3 Shear Waves (S waves)

The capability of ABAQUS to model pure shear waves was verified using a similar technique to that described above for P waves except that the upper and lower boundaries of the mesh were restrained against movement in the x-direction and the prescribed disturbances were tangential to the left- and right-hand sides (Figure 3.15). The displacements u_x and u_y for a pure shear wave are given by:

$$u_y = \frac{\partial \phi}{\partial x} = -k \sin(kx - \omega t), \quad u_x = 0 \quad (3.13)$$

These equations were used to specify the displacements on the vertical boundaries of the mesh as a function of time. The wave number, k , was based on the propagation velocity of an S wave, c_s , which is given by

$$c_s = \sqrt{\frac{G}{\rho}} \quad (3.14)$$

The calculation of the Fourier constant for an S wave is given in Appendix B.

The displacements produced by a pure S wave in an FE/IE mesh are plotted at intervals of 0.18 seconds in Figures 3.16. The S wave plotted spatially was found to reproduce the analytical sine wave as shown in Figure 3.17. These plots demonstrate that ABAQUS models the S wave almost exactly and that the infinite elements absorb the S waves very effectively. The displacement of the infinite elements is representative rather than realistic.

3.4.4 Rayleigh Waves (R waves)

The capability of ABAQUS to model pure Rayleigh surface waves was undertaken using a similar technique to that described above for P and S waves. A 20 x 20 mesh was used (Figure 3.18). However, the specification of R waves is more complex because they are defined by a combination of horizontal and vertical displacements as a function of depth (y is negative down). As shown by Ewing, Jardetzky & Press (1957), and substituting $-y$ for depth z , the analytical form of an R wave is given by

$$u = D[e^{0.8475ky} - 0.5773e^{0.3933ky}] \sin(kx - \omega t) \quad (3.15)$$

and,

$$v = D[-0.8475e^{0.8475ky} + 1.4679e^{0.3933ky}] \cos(kx - \omega t) \quad (3.16)$$

where k is the wave number, ω is the frequency, and D is a constant. (D is taken as 1.0 in this theoretical case; the actual magnitude of the R wave depends on how it is generated.) The other constants in the equations correspond to a Poisson's ratio of 0.25, for which the propagation velocity, c_r , is given by

$$c_r = 0.9194 \sqrt{\frac{G}{\rho}} \quad (3.17)$$

These equations were used to specify the displacements on the left-hand vertical boundary and the bottom boundary of the mesh as a function of time. In this case, the top boundary of the FE mesh was unrestrained.

The calculations of the Fourier constants for an R wave are given in Appendix B.

The displacements produced by a pure R wave are plotted at intervals of 0.18 seconds in Figures 3.19. The horizontal and vertical displacements along a horizontal line 55.19m below the top of the mesh at times of 2.1, 4.2, 8.4 and 16.8 seconds are compared with the analytical solutions in Figures 3.20 – 3.23. Reflection from the boundary is evident and the predicted displacements diverge from the analytical solution with time as the amount of reflection increases. This indicates that the ABAQUS infinite elements do not absorb the complex Rayleigh wave very effectively.

The variation of the amplitude of the horizontal and vertical components of the R wave with depth at a time of 3.6 seconds, before significant reflection has taken place, match the analytical solution closely as shown in Figure 3.24.

3.5 VERIFICATION OF WAVE ATTENUATION IN ABAQUS

The performance of the finite element meshes in representing each of the three wave types, P, S and R, was tested by setting up a wave channel with appropriate boundary conditions, including infinite elements to model the far field, in both plane strain and axisymmetric conditions. A pure P wave was imposed, and the difference between the uniform waves of the plane strain condition and the attenuating waves in the axisymmetric condition was observed. The peaks of amplitude were found to attenuate with $r^{-0.5}$, while energy density attenuated with r^{-1} ; these values correspond with geometric attenuation around a *cylindrical* wavefront (Figure 3.25). The P-wave system was next applied to a spherical cavity in an elastic continuum (Figure 3.26); this time the geometric attenuations were in proportion to r^{-1} for amplitude, and r^{-2} for energy density, correlating with standard theory, Figure 3.27.

Shear wave attenuation could be tested only in the cylindrical configuration, in which it showed behaviour similar to the P-wave test. Finally, the R-waves were tested for attenuation of vertical and horizontal components of amplitude and for energy density. Again, the attenuations correlated with the theoretical values of $r^{-0.5}$ and r^{-1} respectively (Figure 3.28).

3.6 CONCLUSIONS

This Chapter verifies the ability of the ABAQUS finite element program to model ground waves accurately. The performance of the FE/IE model has been verified by applying pure P, S and R waves in turn along a channelled wave guide of finite elements with infinite elements at the far end. The model reproduced the analytical wave patterns very closely within the finite element zone and the ABAQUS infinite elements were shown to absorb the P and S waves almost exactly. However inaccuracies were observed for the more complex Rayleigh waveform where some reflection from the boundary of ABAQUS infinite elements was evident. Improvement of this boundary is the subject of Chapter 4.

Methods were also devised to test the performance of ABAQUS to simulate geometrical attenuation of the three wave types. Comparisons with analytical solutions demonstrated the ability of the program to simulate the attenuation of elastic waves accurately.

Further detailed verification of the performance of various elements, materials and analysis types can be found in the ABAQUS Verification manual.

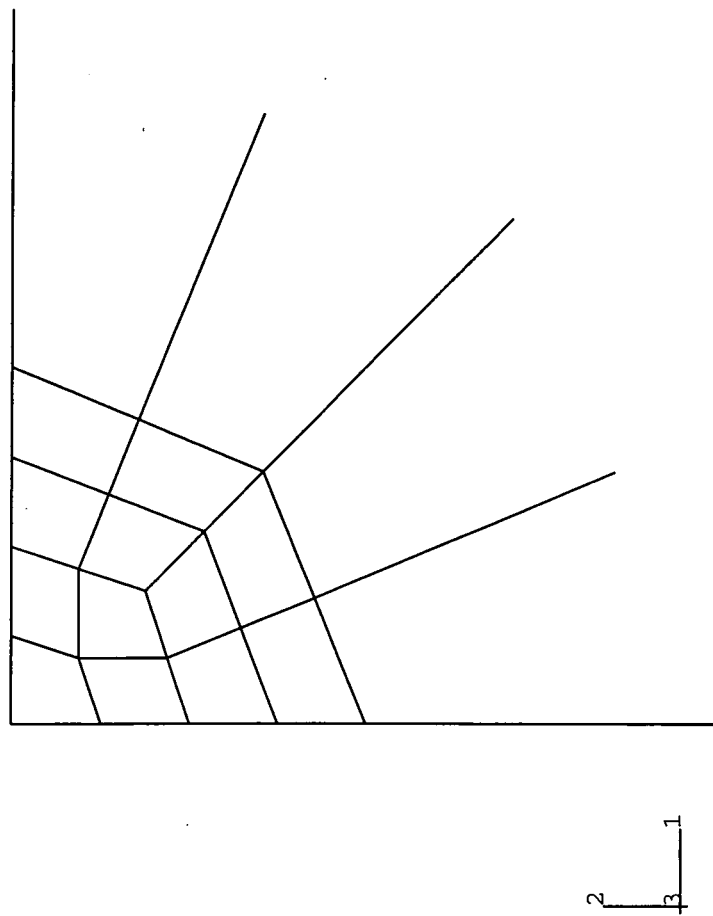


Figure 3.1 FE/IE mesh used in the Boussinesq and Flamant problems

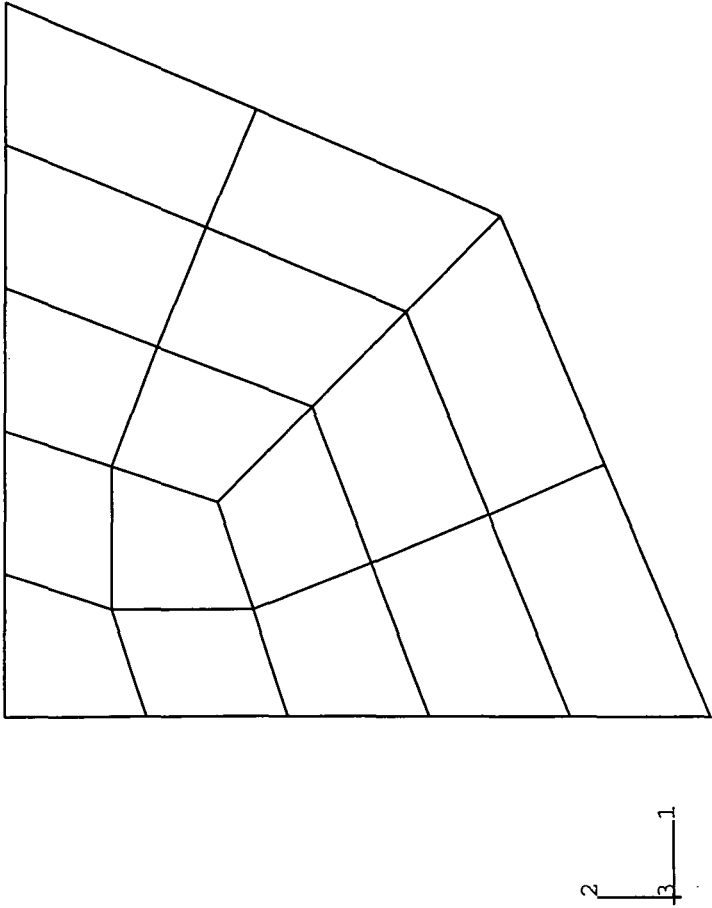
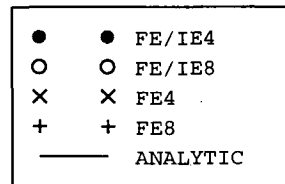


Figure 3.2 FE mesh used in the Boussinesq and Flamant problems

ABAQUS



XMIN 0.000E+00
XMAX 8.000E+00
YMIN -5.933E-39
YMAX 4.902E+00

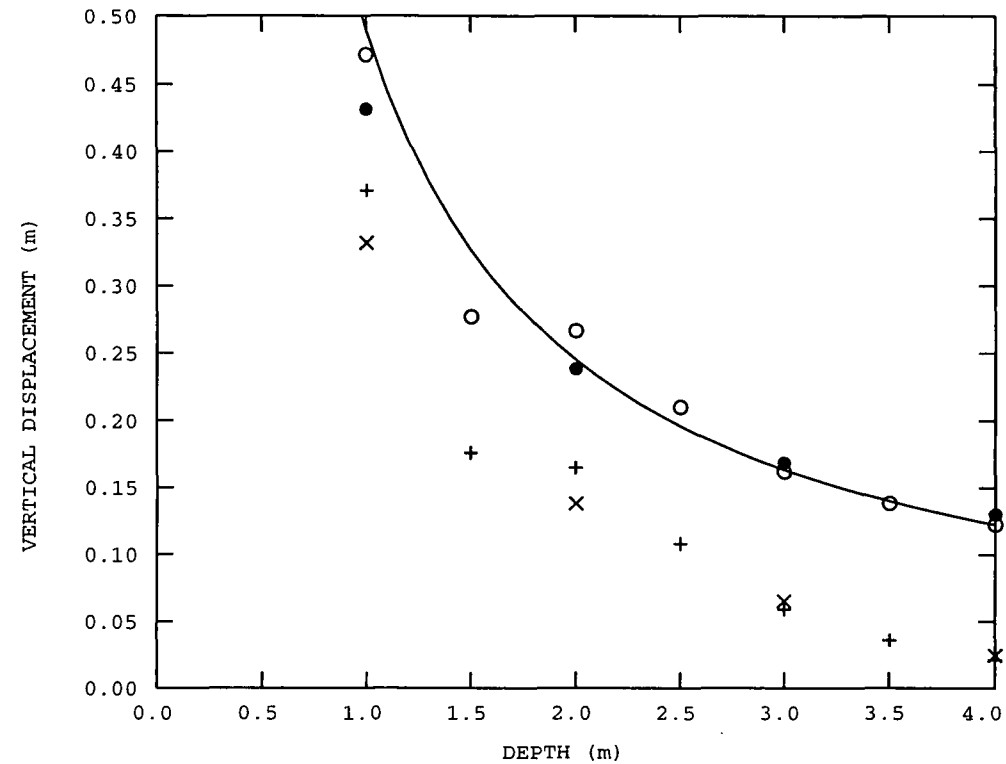
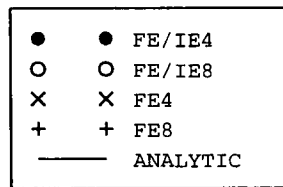


Figure 3.3 The Boussinesq problem: displacement results

ABAQUS



XMIN 0.000E+00
XMAX 8.000E+00
YMIN 3.116E-38
YMAX 2.790E+00

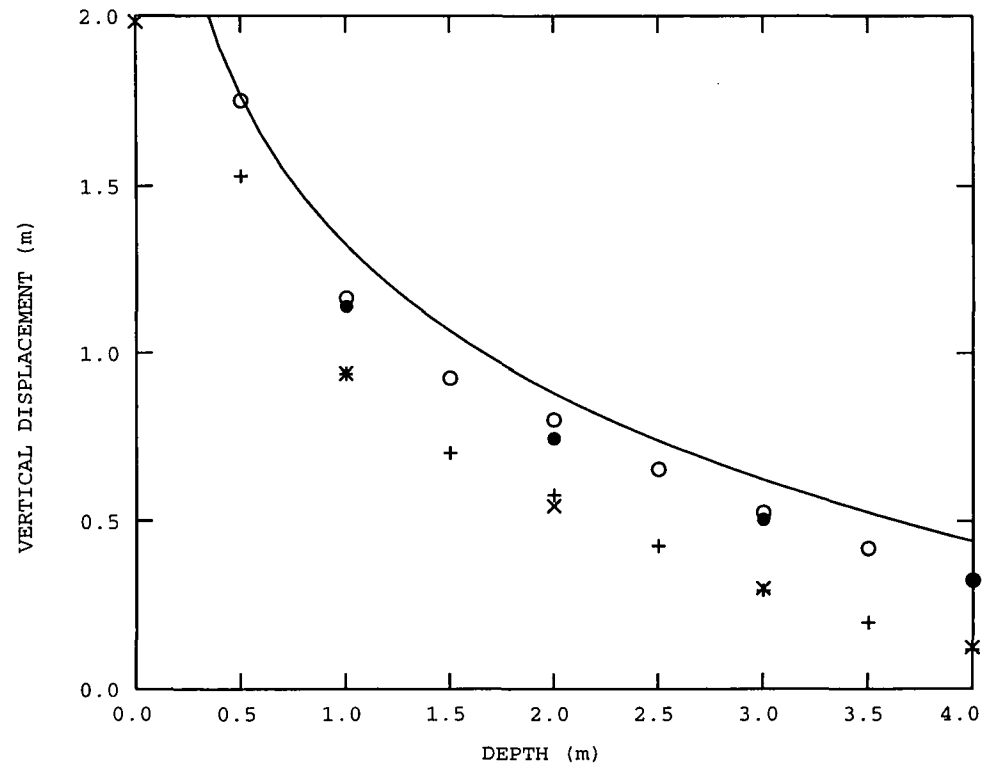


Figure 3.4

The Flamant problem: displacement results

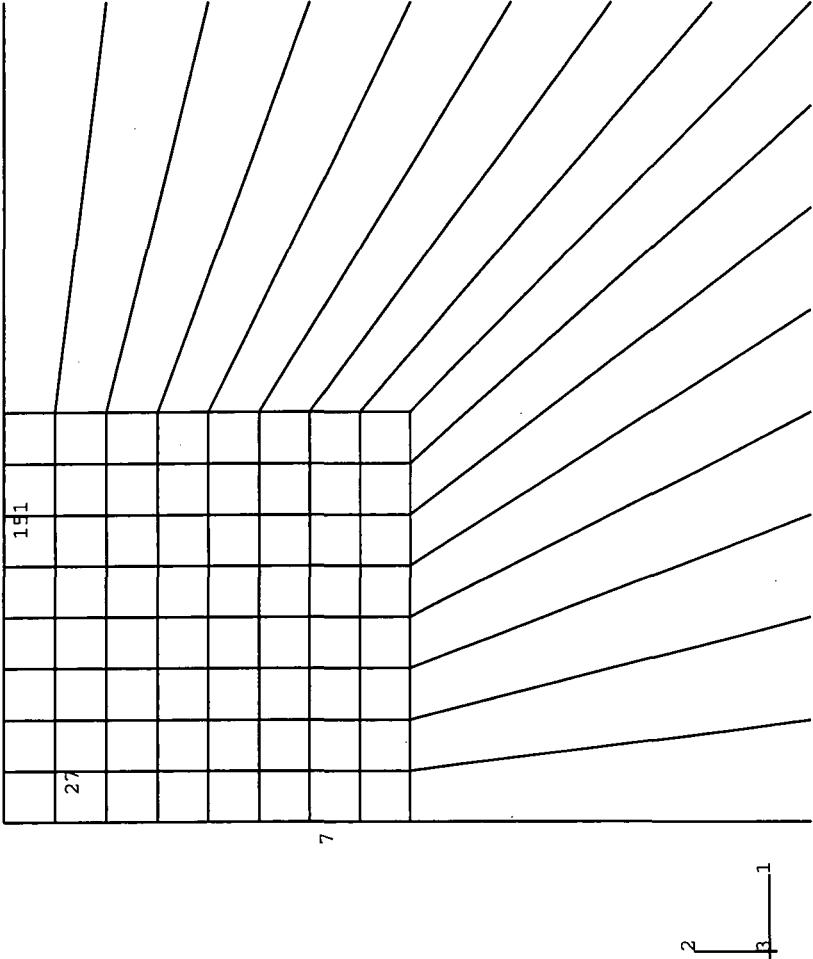


Figure 3.5 Small FE/IE mesh used in wave propagation problem

ABAQUS

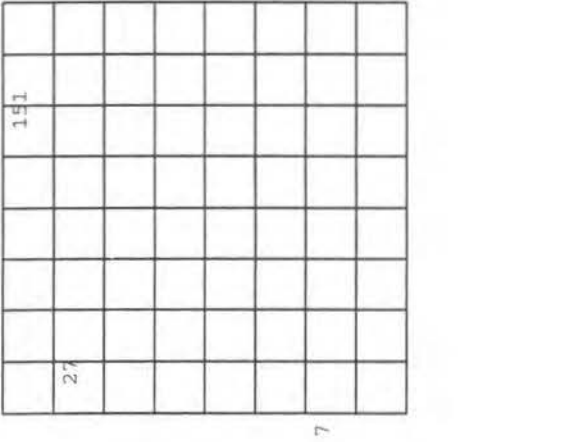


Figure 3.6 Small FE mesh used in wave propagation problem

ABAQUS

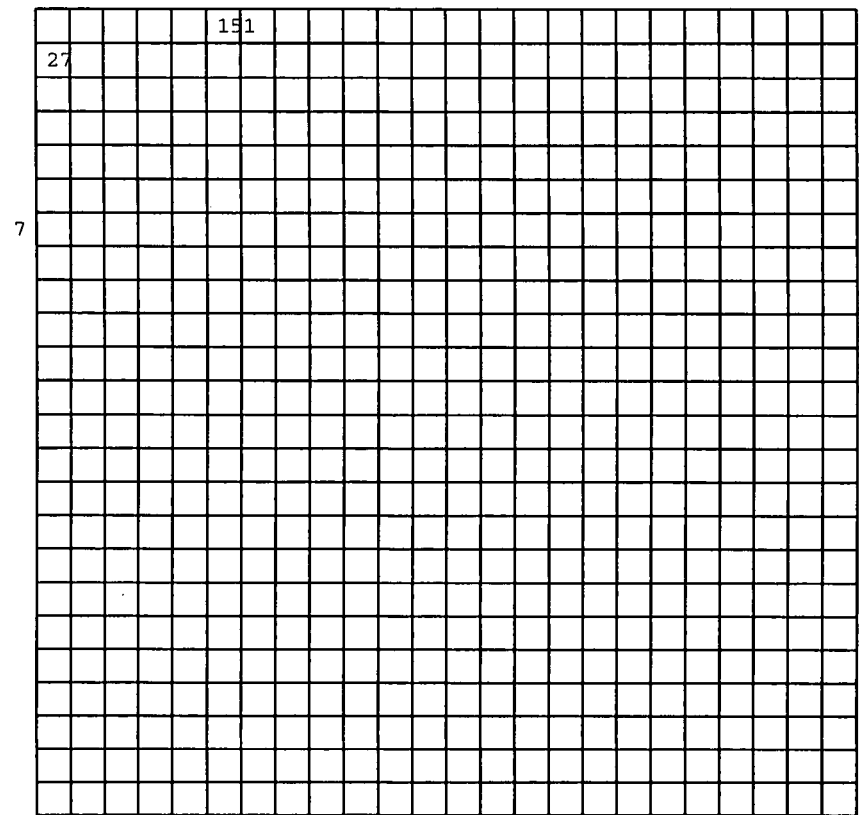


Figure 3.7

Extended FE mesh used in wave propagation problem

ABAQUS

1 — quiet boundary
2 — small mesh
3 — extended mesh

XMIN 1.000E-01
XMAX 4.000E+00
YMIN -3.268E-01
YMAX 2.919E-02

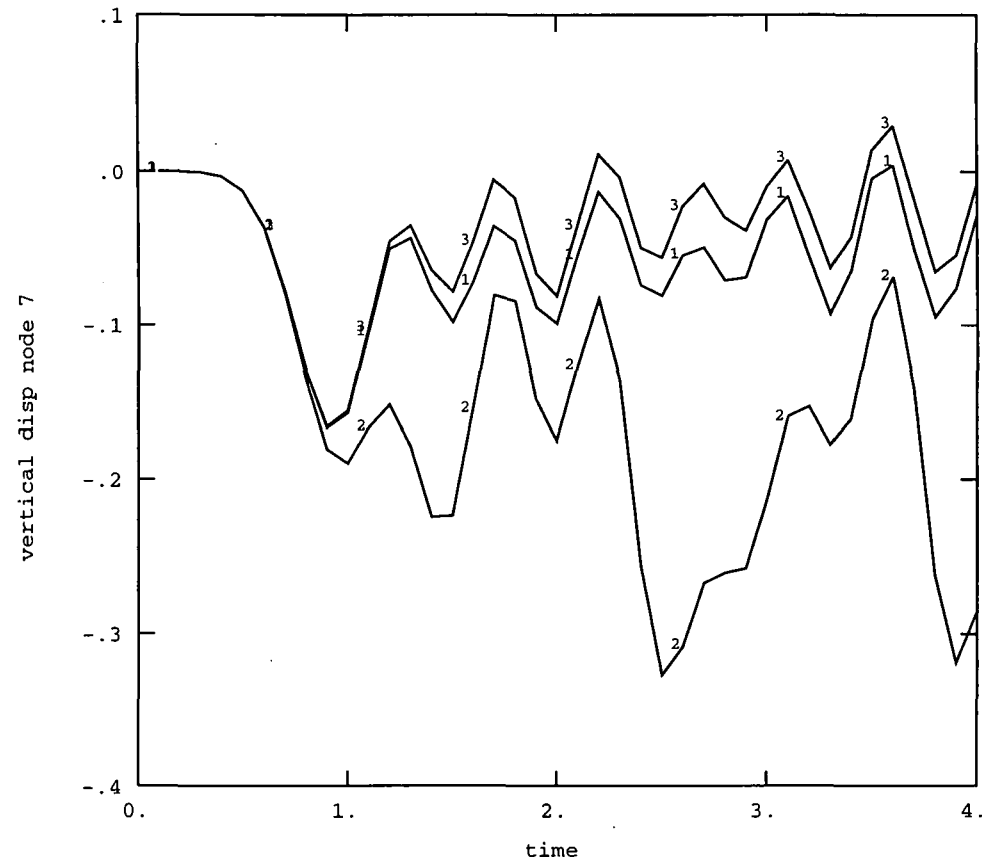


Figure 3.8 Vertical displacement responses at node 7

ABAQUS

1 quiet boundary
2 small mesh
3 extended mesh

XMIN 1.000E-01
XMAX 4.000E+00
YMIN -3.776E-01
YMAX 5.937E-02

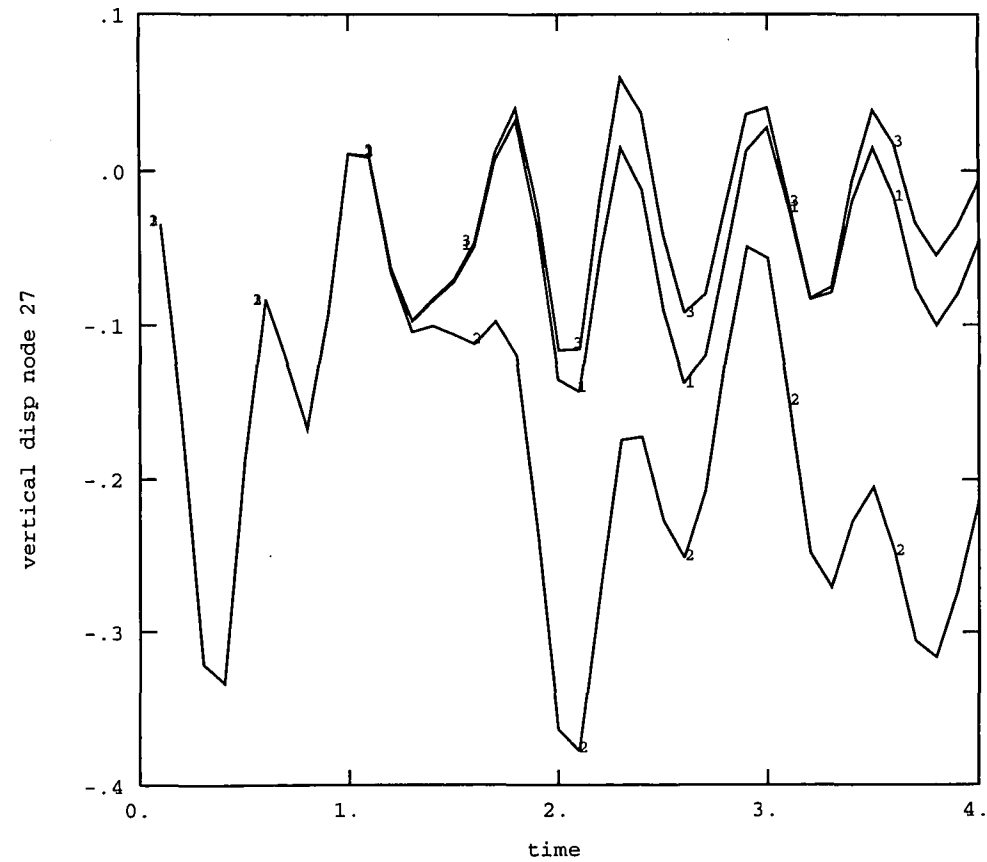


Figure 3.9 Vertical displacement responses at node 27

ABAQUS

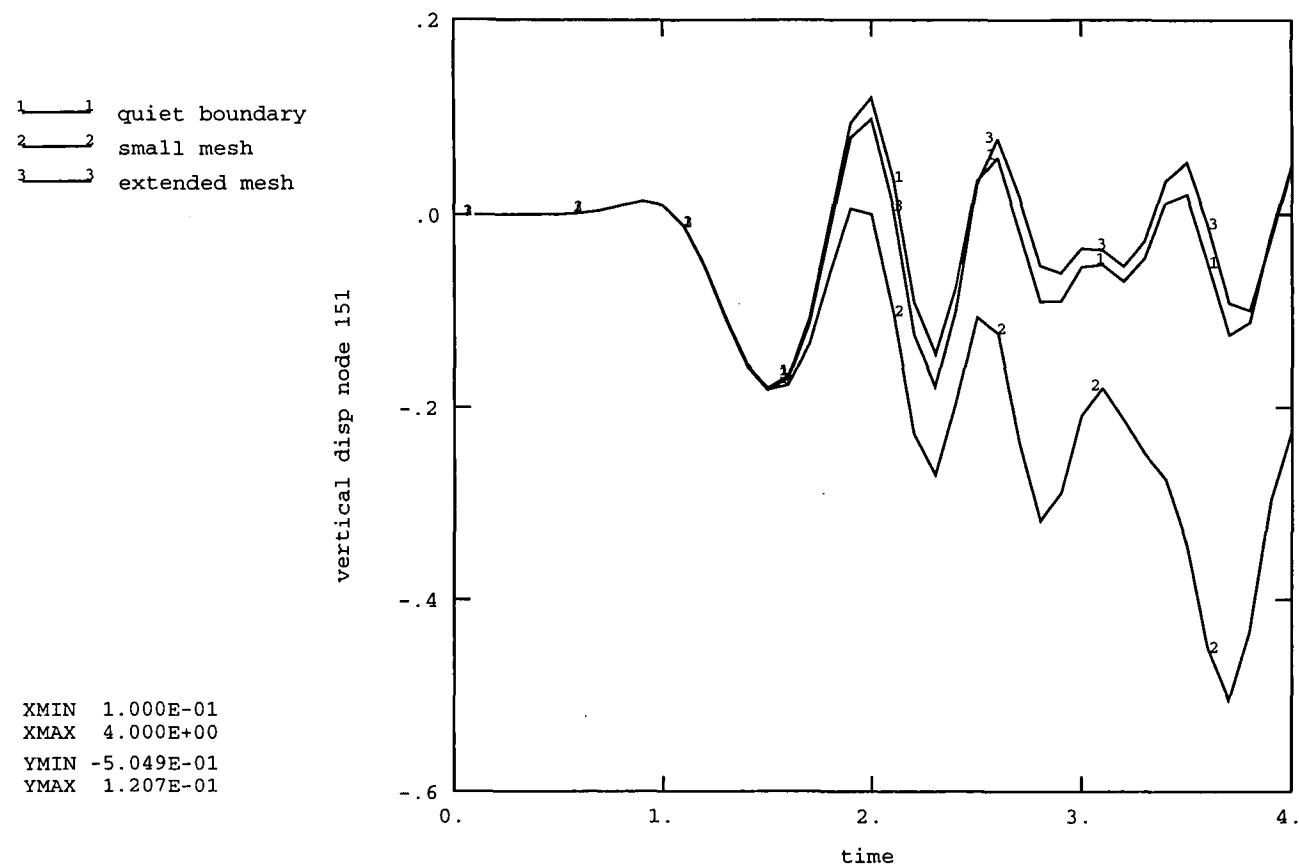


Figure 3.10 Vertical displacement responses at node 151

ABAQUS

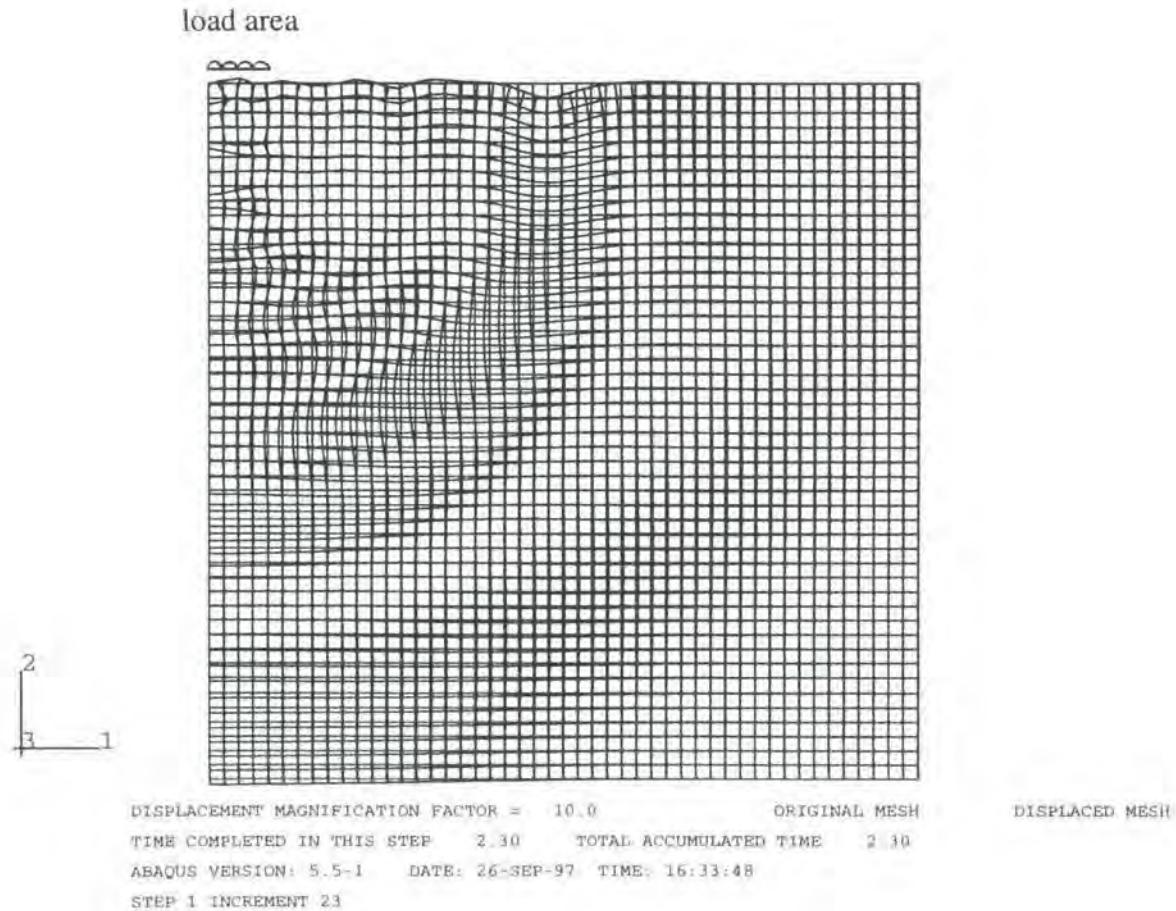


Figure 3.11 Axisymmetric wavefronts from a pulse load on a small radial disc

ABAQUS

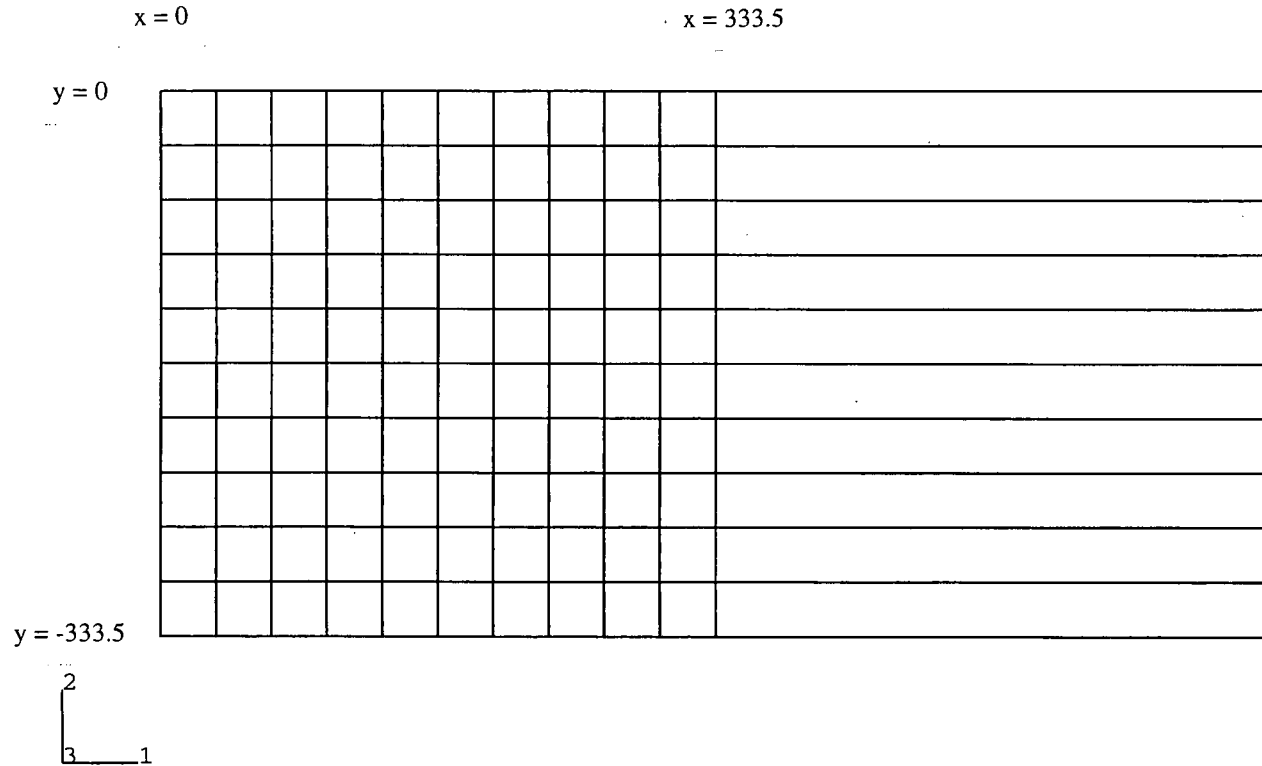


Figure 3.12 FE/IE mesh used for P wave verification

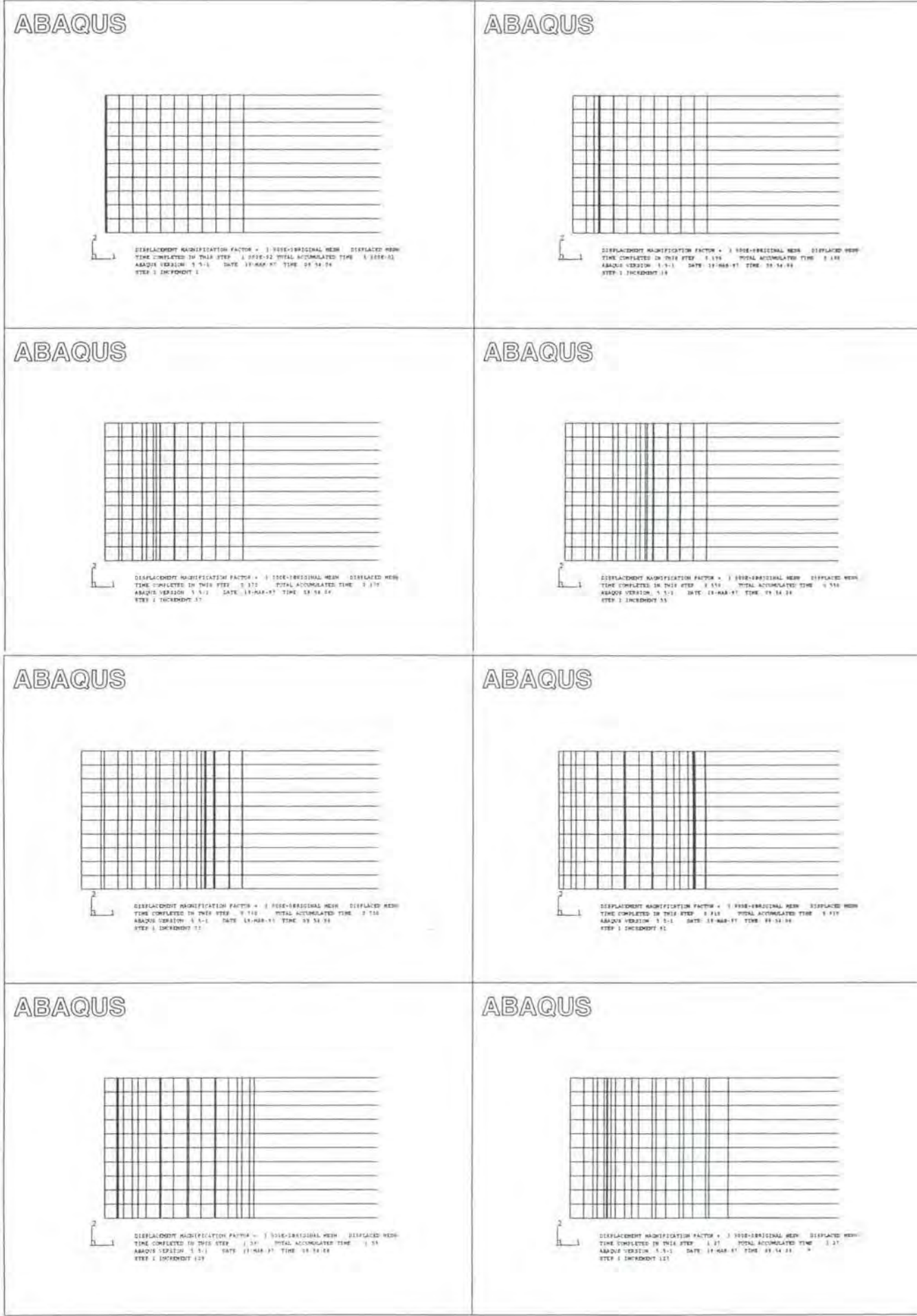


Figure 3.13 ‘Snapshots’ of P wave in an FE/IE mesh

ABAQUS

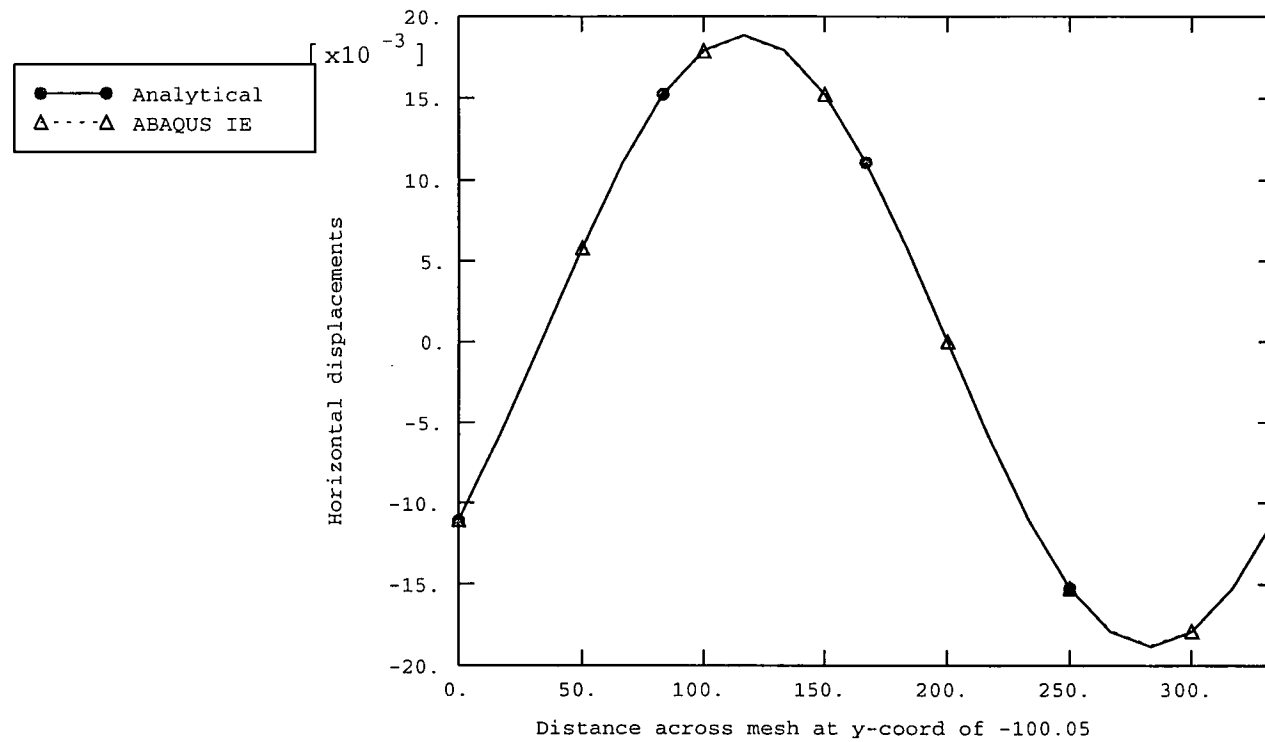


Figure 3.14 Horizontal displacement of nodes at 3.6 seconds: Analytical vs ABAQUS solution

ABAQUS

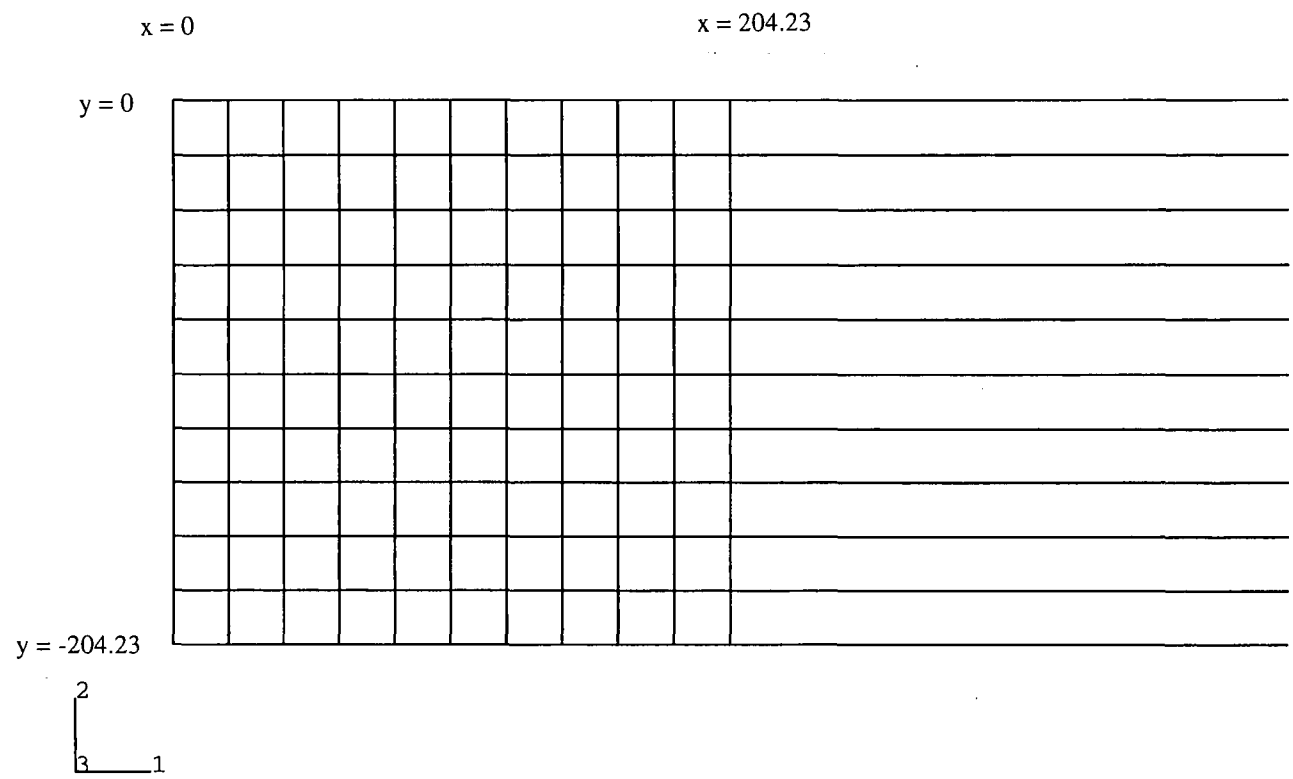


Figure 3.15 FE/IE mesh used for S wave verification

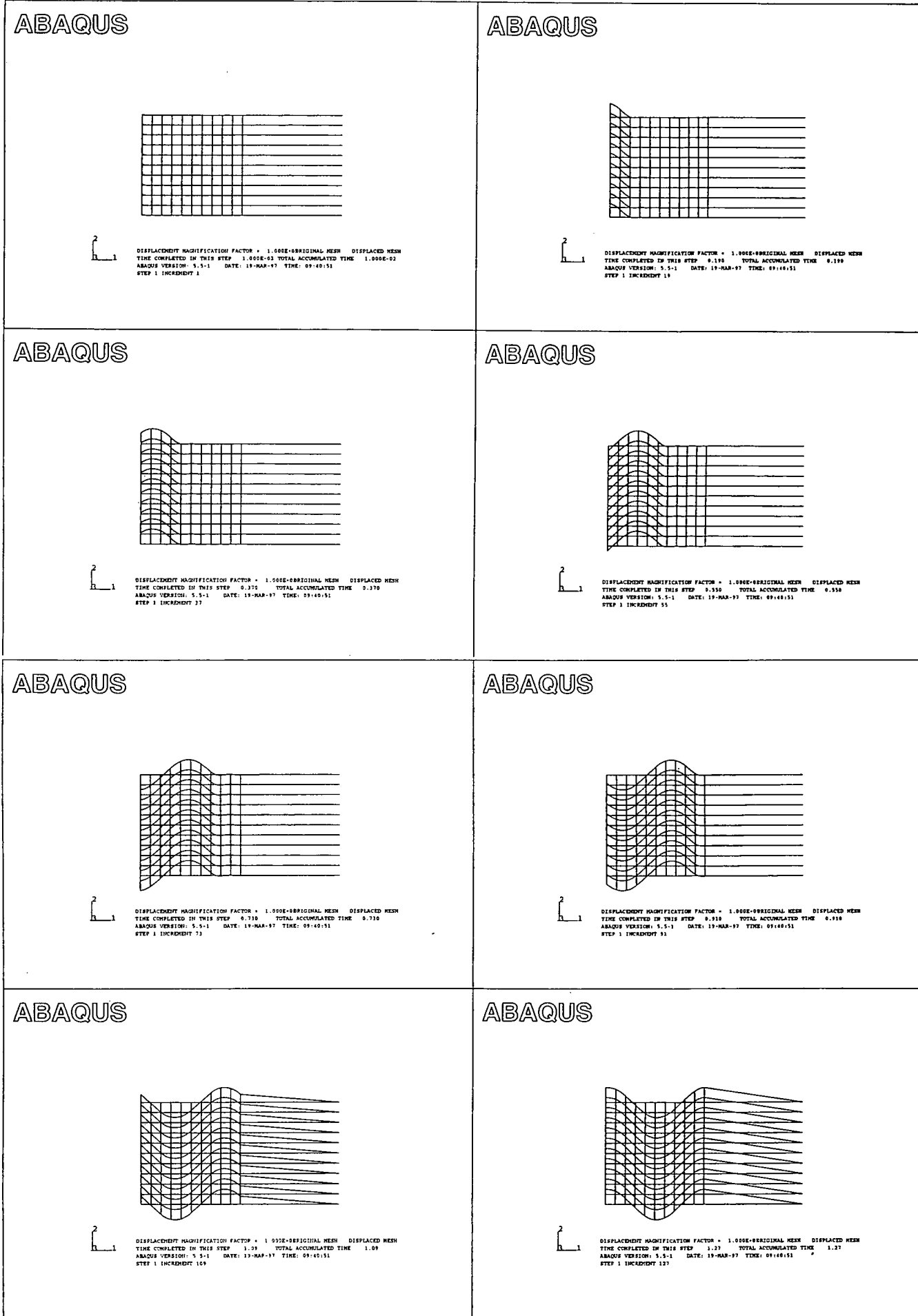


Figure 3.16 'Snapshots' of S wave in an FE/IE mesh

ABAQUS

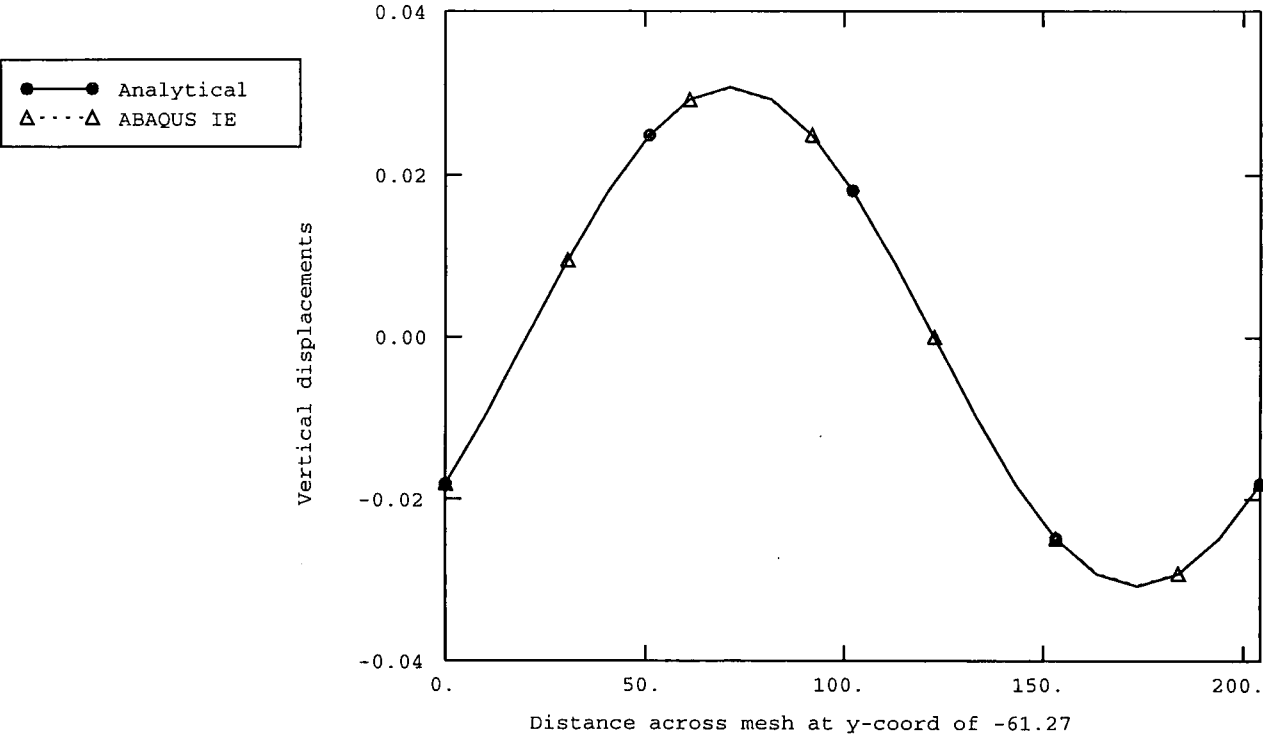


Figure 3.17 Vertical displacement of nodes at 3.6 seconds: Analytical vs ABAQUS solution

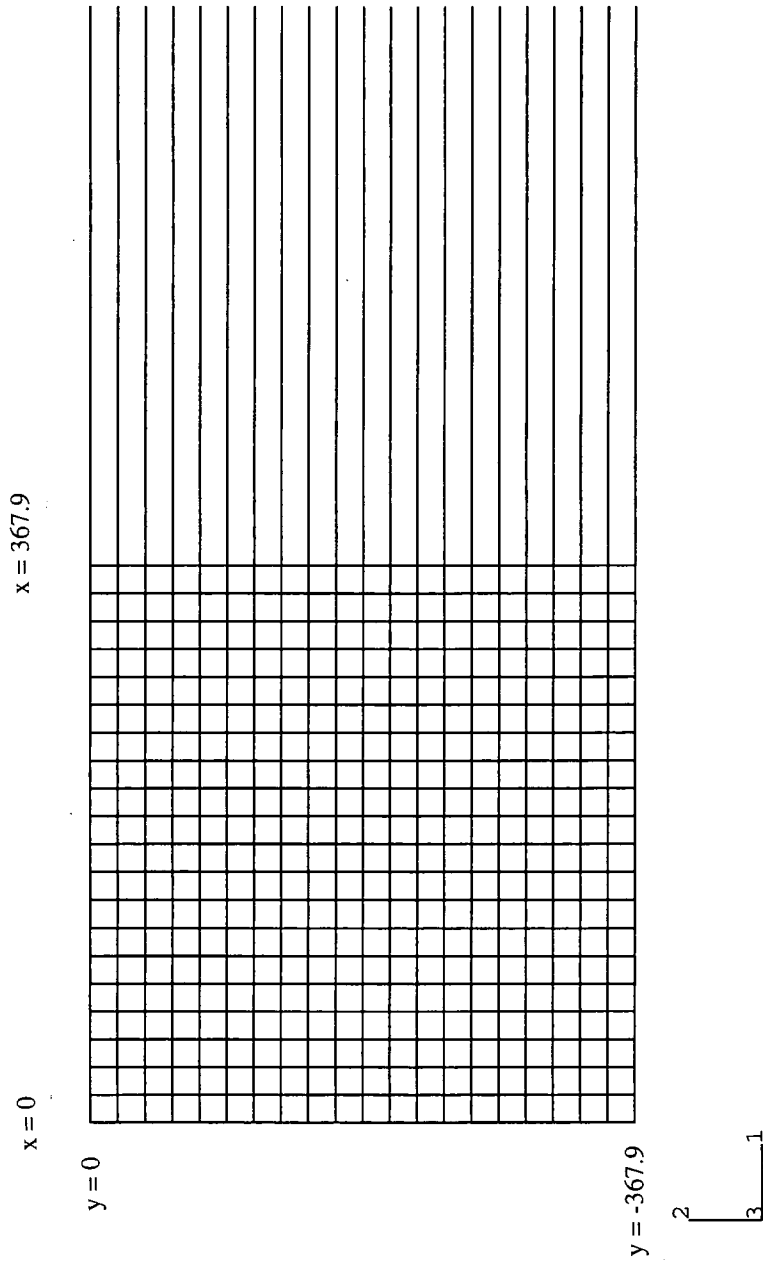
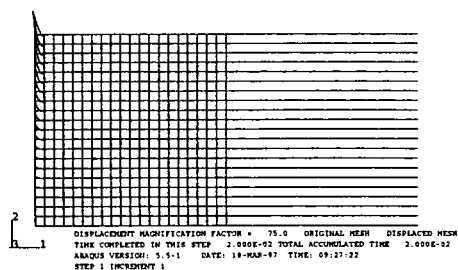
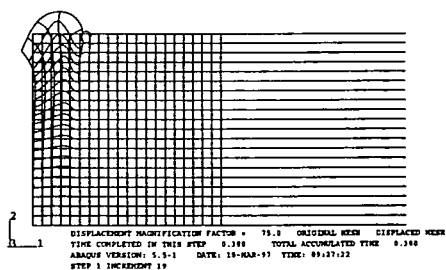


Figure 3.18 FE/IE mesh used for R wave verification

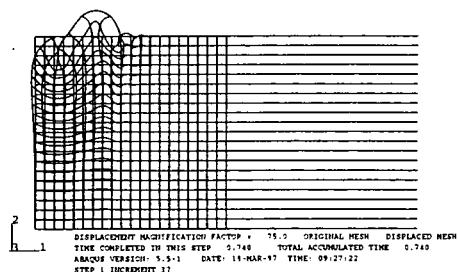
ABAQUS



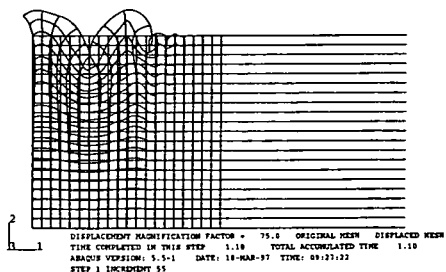
ABAQUS



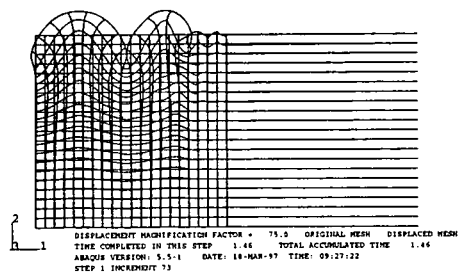
ABAQUS



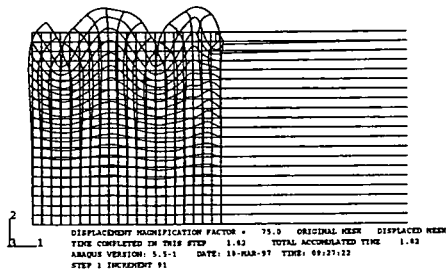
ABAQUS



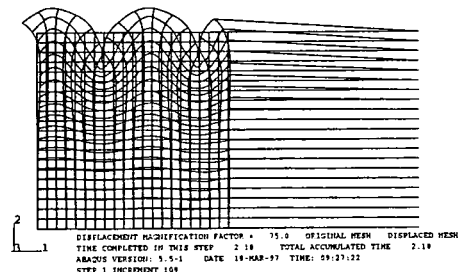
ABAQUS



ABAQUS



ABAQUS



ABAQUS

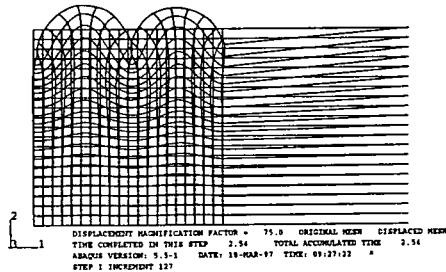
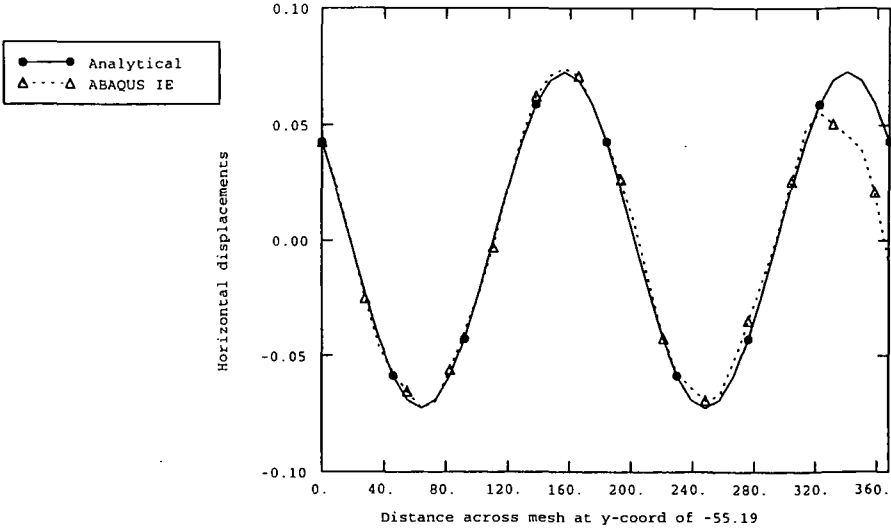
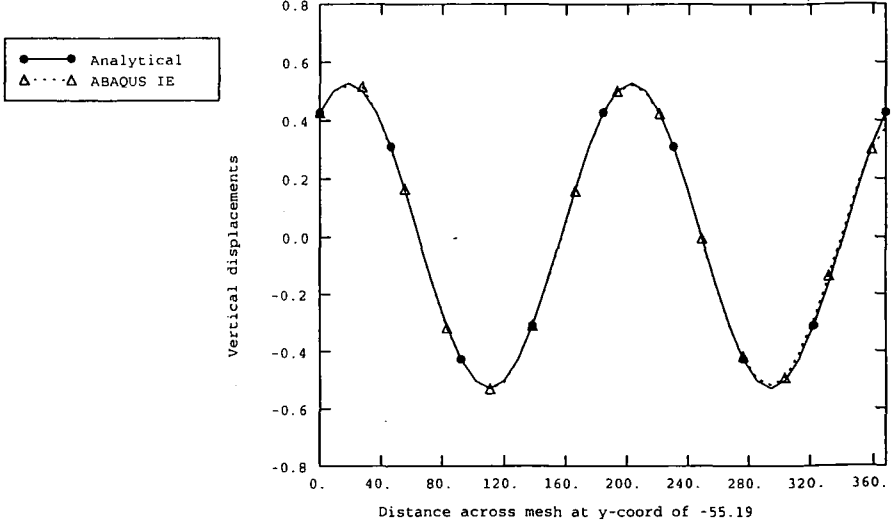


Figure 3.19 'Snapshots' of R wave in an FE/IE mesh

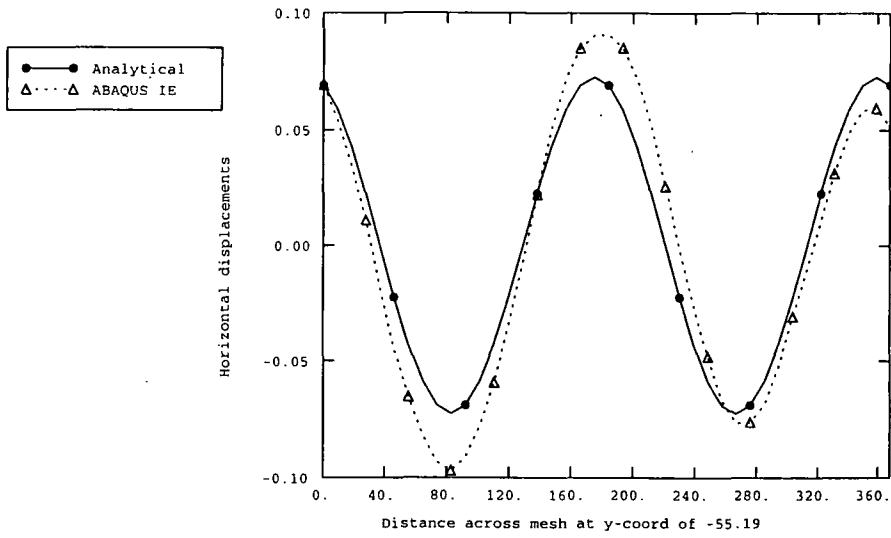


(a) Horizontal displacements

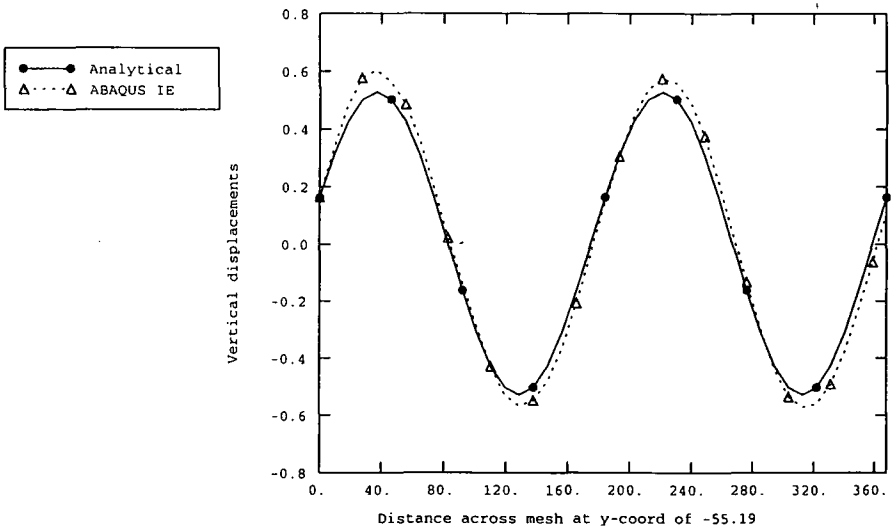


(b) Vertical displacements

Figure 3.20 Displacement of nodes at 2.1 seconds: Analytical solution vs ABAQUS



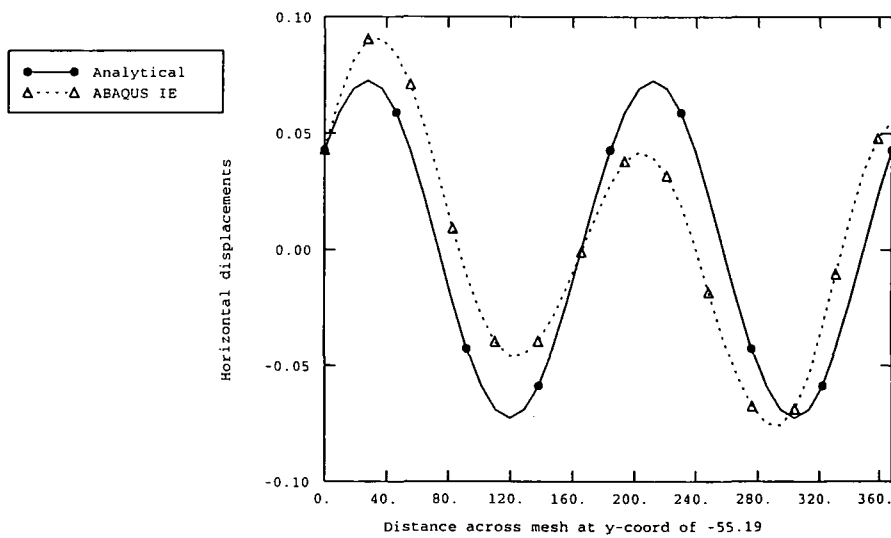
(a) Horizontal displacements



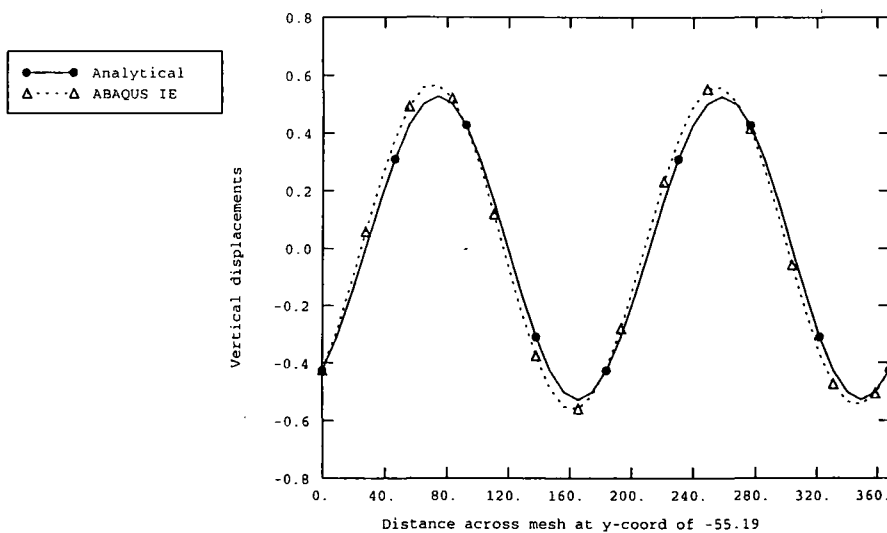
(b) Vertical displacements

Figure 3.21

Displacement of nodes at 4.2 seconds: Analytical solution vs ABAQUS



(a) Horizontal displacements

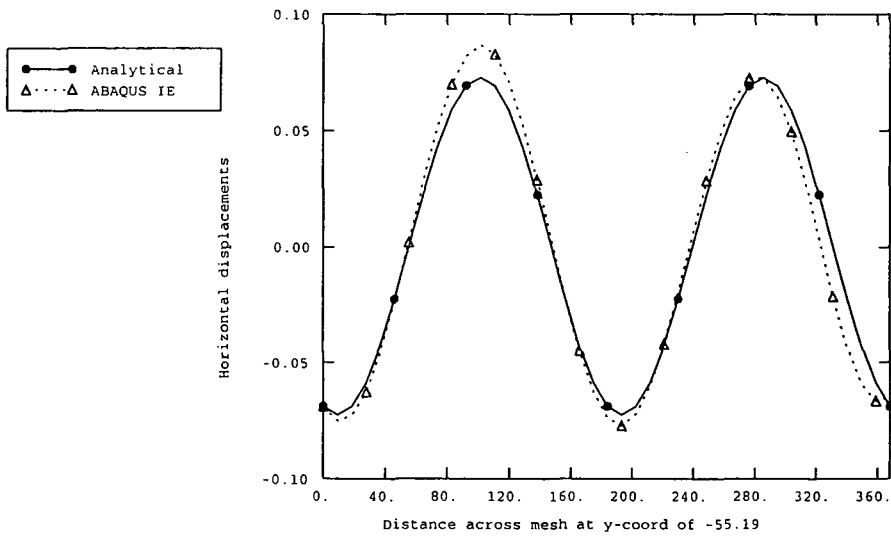


(b) Vertical displacements

Figure 3.22

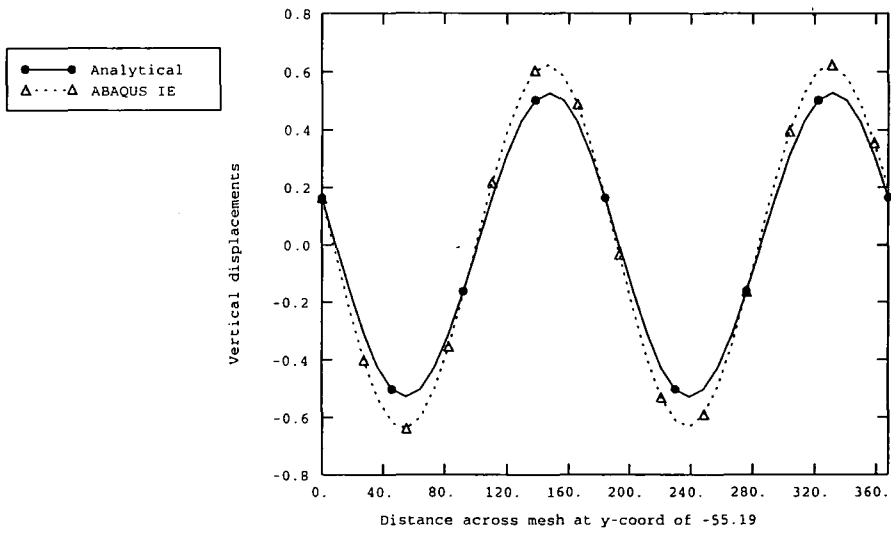
Displacement of nodes at 8.4 seconds: Analytical solution vs ABAQUS

ABAQUS



(a) Horizontal displacements

ABAQUS



(b) Vertical displacements

Figure 3.23

Displacement of nodes at 16.8 seconds: Analytical solution vs ABAQUS

ABAQUS

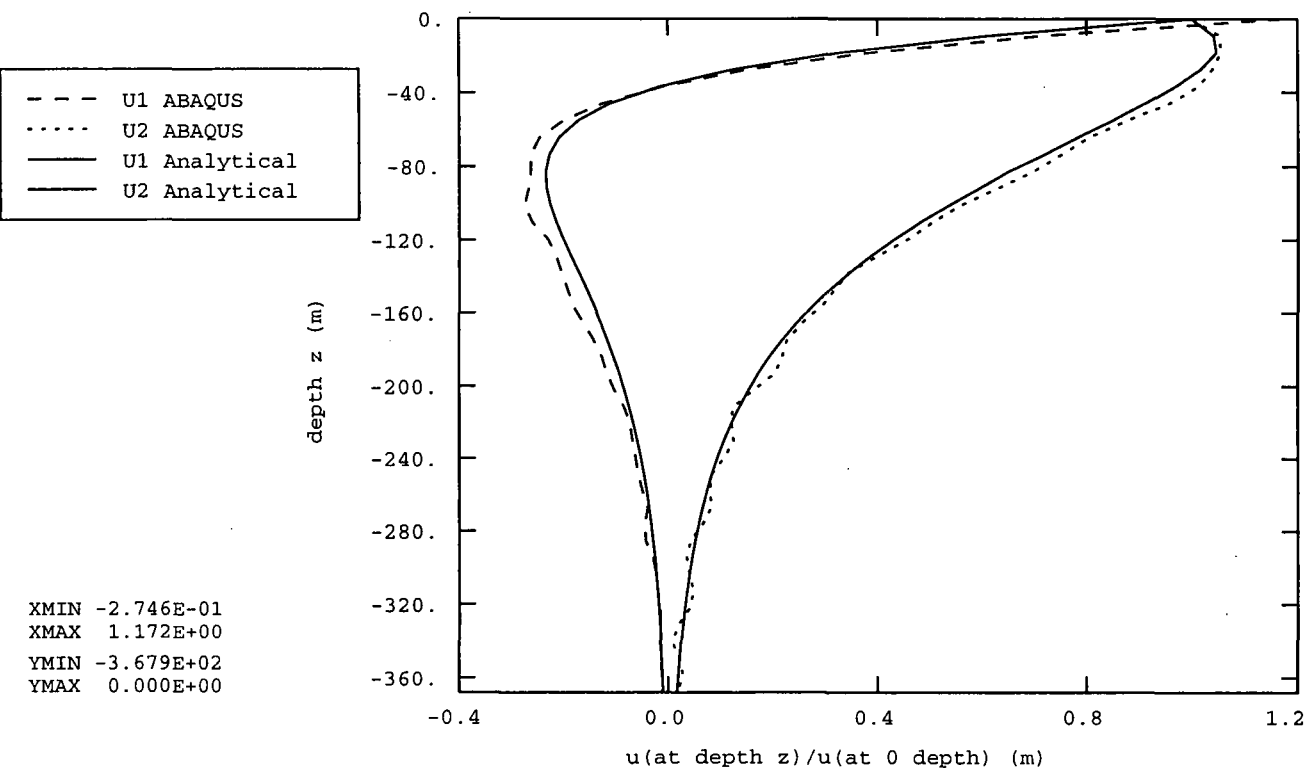


Figure 3.24

Normalised plots of the horizontal and vertical components of an R wave with depth at a time of 3.6 seconds

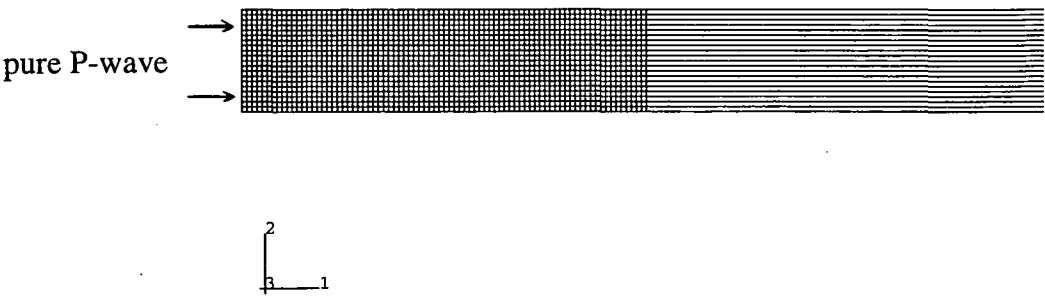


Figure 3.25 FE/IE mesh used for uniaxial and axisymmetric conditions

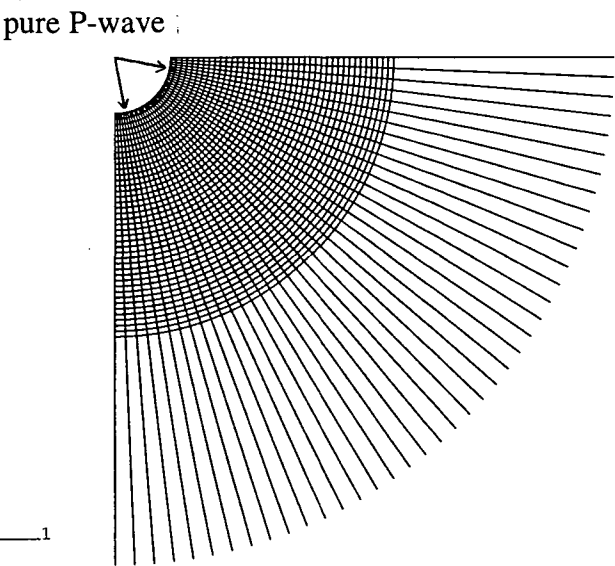


Figure 3.26 FE/IE mesh used for spherical conditions

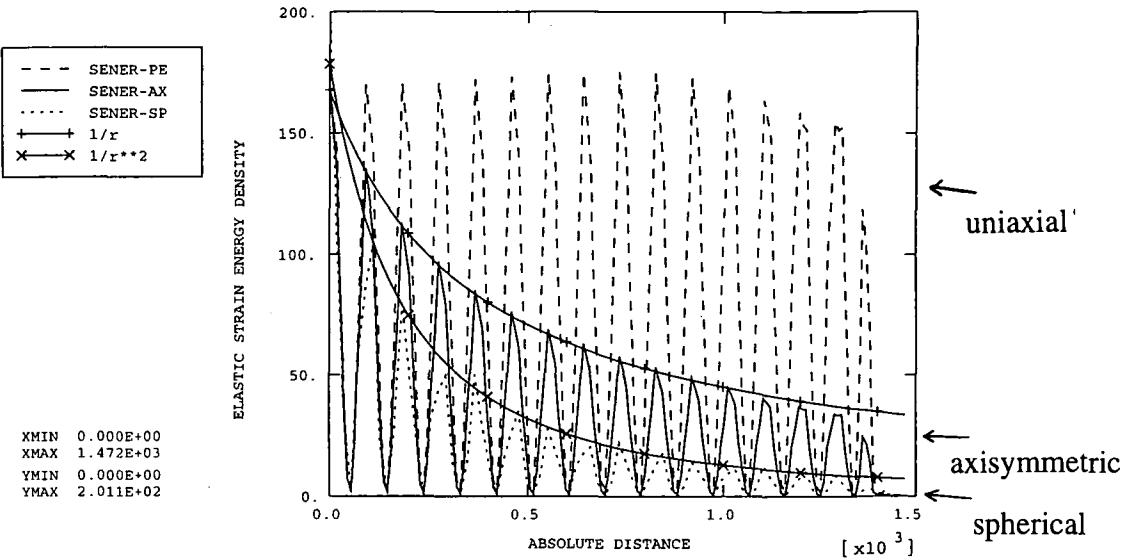


Figure 3.27 Attenuation of energy densities for a P wave in uniaxial, axisymmetric and spherical conditions

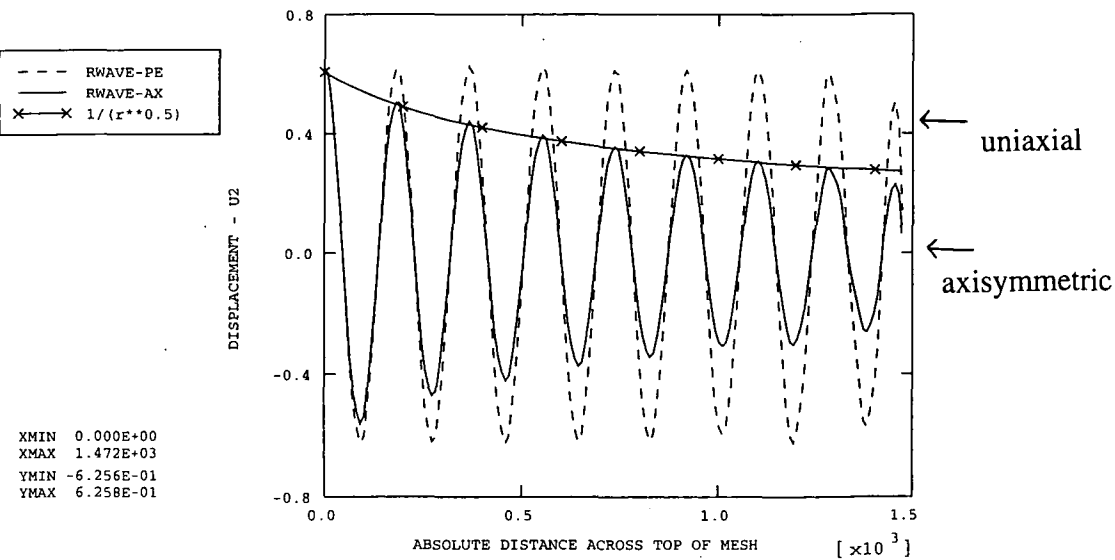


Figure 3.28 Attenuation of vertical amplitude for an R wave in uniaxial and axisymmetric conditions

CHAPTER 4

DEVELOPMENT OF A QUIET BOUNDARY FOR THE EFFECTIVE ABSORPTION OF GROUND WAVES GENERATED BY PILE DRIVING

4.1 INTRODUCTION

One of the limitations of finite element methods arises when they are employed as a discrete mesh for the modelling of an infinite domain, in which energy radiates from a source outwardly towards infinity. Unless something is done to prevent outwardly radiating waves from reflecting from the region's boundaries, errors are introduced into the results. In the past, several different methods for the treatment of absorbing boundaries have been proposed and employed with varying success. In all cases, the object of the work has been to make the artificial boundary behave, as nearly as possible, as if the mesh extended to infinity. The resulting techniques are variously known as silent, radiating, absorbing, non-reflecting, transmitting, open, free-space, and one-way boundary conditions. Some of the absorbing boundaries developed in this Chapter (the standard viscous boundary, for example) transmit all normally impinging plane body waves exactly (provided that the material behaviour close to the boundary is linear elastic). General problems involve body waves that do not impinge on the boundary from an orthogonal direction and may also involve Rayleigh surface waves. Nevertheless these 'quiet boundaries' work quite well even for such general cases, provided that they are arranged so that the dominant direction of wave propagation is orthogonal to the surface. As the boundaries are 'quiet' rather than silent (perfect transmitters of all waveforms), and because the boundaries rely on the solution adjacent to them being linear elastic, they should be placed some reasonable distance from the region of main interest.

Application of the various silent boundaries to wave propagation problems in an elastic medium has, to date, been limited to wave propagation problems originating from a point source, usually a vibrating plate or disc on the surface of an elastic half-space. Some workers (eg Gutowski and Dym, 1976) have also considered a point source vibrating at depth in the elastic medium. However, in the case of pile driving, the source of vibration is very complex, with P waves generated at the pile toe, S waves generated down the entire length of the pile shaft, and R waves generated both as the P and S waves are reflected at the free ground surface (see Chapter 2). The attenuations of the various waves also differ from the classical case of a vibrating disc on the surface of an elastic half-space (Miller & Pursey, 1955), because the S waves propagate on a near-cylindrical wavefront instead of a hemispherical wavefront. The attenuation of S waves generated from a pile shaft is therefore much slower than for those generated from a vibrating disc. The S waves tend to combine with the R waves which also propagate on a cylindrical wavefront at a slightly slower velocity. (In the case of a vibrating disc, the R waves are the dominant waves at distance from the source because the energy from the P and S waves rapidly attenuates over their respective hemispherical wavefronts.)

The ABAQUS finite element program currently provides first- and second-order infinite elements which can be used for dynamic response in the form of a simple tuned damper giving silent boundary behaviour. The performance of the finite/infinite element model has been verified by applying pure P, S and R waves in turn along a channelled wave

guide of finite elements with the ABAQUS infinite elements at the far end as described in Chapter 3. The model reproduced the analytical wave patterns very closely within the finite element zone and the ABAQUS infinite elements were shown to absorb the P and S waves almost exactly (see Figures 3.14 and 3.17). However inaccuracies were observed for the more complex Rayleigh waveform where some reflection from the boundary was evident (Figures 3.20-3.23). It is particularly important to address these inaccuracies as the model needs to be calibrated against measurements of vertical and horizontal particle velocities from geophones on the ground surface and, as stated above, R waves tend to be the dominant waveform at distance from the source.

The main objective of the work described in this Chapter is to develop a quiet boundary which will absorb effectively the complex ground waves generated by pile driving and allow the size of the finite element mesh and thus the computation time to be minimised.

This Chapter firstly presents a literature review (Section 4.2) of the various types of absorbing boundaries which have been developed to date, followed by an assessment of their suitability for this problem (Section 4.3). Derivations of two viscous boundary formulations are presented in Section 4.4. These boundaries are then attached to the far end of a simple channelled wave guide of finite elements for comparison with analytical solutions for pure P S and R waves. Proposals for the application of the viscous boundary formulations to the pile driving model are given in Section 4.5 for maximum effectiveness. These proposals are developed further in Chapter 5 where the viscous boundary formulations are applied to a model for the computation of ground waves generated by vibratory piling. Section 4.6 contains some proposals for the insertion of periodic infinite elements into an ABAQUS time domain analysis using a transformation technique developed by Astley (1995). Conclusions and recommendations for further work are given in Section 4.7.

4.2 LITERATURE REVIEW

4.2.1 Viscous boundaries

The first local silent boundary was proposed by Lysmer and Kuhlemeyer (1969) and later improved by White *et al* (1977). The method uses viscous damping forces, which act along the boundary, as a means of absorbing, rather than reflecting, the radiated energy. The method, being directly analogous to the use of viscous dashpots, is relatively easy to implement, and it appears to absorb both dilatational and shear waves with acceptable accuracy in many applications. The viscous forces, or dashpots, have another advantage in that they do not depend upon the frequencies of the transmitted waves. This technique is therefore suitable for transient analysis.

One drawback of the standard viscous boundary described above, is its inability to transmit Rayleigh waves as effectively as it transmits body waves. In addition to the standard viscous boundary, Lysmer and Kuhlemeyer (1969) also developed a special viscous boundary for Rayleigh waves, the Rayleigh viscous boundary, in which the dashpots have coefficients that depend upon the frequency of the transmitted waves. The accuracy of the Rayleigh viscous boundary is not well established. The computational mesh has to be refined especially near the ground surface because at one point a parameter of the dashpot goes to infinity. In addition, there have been few

comparisons between the standard viscous and Rayleigh viscous boundaries, except for the axisymmetric problem discussed in Lysmer and Kuhlemeyer. The use of standard viscous boundaries for problems that involve Rayleigh waves should not necessarily be ruled out. Unlike the Rayleigh viscous boundary, it is independent of frequency and is much easier to implement. For example Haupt (1977) used the standard viscous boundary along with some of his own boundary innovations to achieve a good, steady state, Rayleigh wave solution. Cohen and Jennings presented a further Rayleigh wave example in 1983.

White, Valliappan and Lee (1977) attempted to improve upon Lysmer and Kuhlemeyer's technique, and also tried to broaden the theory to include anisotropic materials. However, the authors did not demonstrate the effectiveness of this technique for anisotropic materials. For the isotropic case, the method offered virtually no improvement on the Lysmer-Kuhlemeyer boundary and was more complicated to implement.

4.2.2 Para-axial Boundaries

Claerbout (1976) devised the idea of creating equations that transmit waves in only one direction. He derived these equations, termed para-axial approximations, for the two-dimensional, scalar-wave case. Clayton and Engquist (1977) later expanded Claerbout's method to include elastic waves and conceived the notion of applying it as an energy-absorbing boundary.

The method is based on differential operators that satisfy the condition of only outgoing waves. While these differential operators may be of a high order, the para-axial boundary of the first order is identical to the viscous boundary. The technique has several disadvantages. The first is that the technique was originally implemented using a finite difference technique and it does not directly lend itself to finite element utilisation. Hughes (1978) and Cohen & Jennings (1983) adapted this technique for finite element applications. However, in numerical tests, their boundary condition performed only slightly better than those of Lysmer and Kuhlemeyer and White *et al.*

Another major problem with the para-axial technique is that when Poisson's ratio is greater than 1/3, a negative stiffness term is introduced into the para-axial equations. This term leads to instabilities; the boundary erroneously causes the displacements and stresses to increase with time.

4.2.3 Time-dependent problems

Bamberger et al (1988) considered time-dependent elastodynamics. They proposed to modify the first-order boundary condition of Cohen and Jennings in order to absorb Rayleigh surface waves as well. Their modified boundary condition involves the operator $(\partial/\partial t - c_R \partial/\partial x_1)$ similar to the Clayton-Engquist condition, where c_R is the Rayleigh wave speed. The authors proved that the proposed boundary condition is perfectly absorbing for P and S waves at normal incidence, as well as for Rayleigh waves. They used finite elements in the spatial domain together with a time-stepping scheme.

Robinson (1976) considered time-harmonic elastic waves in two dimensions and proposed a non-reflecting boundary condition that involved the elastic potentials

associated with the Helmholtz decomposition. Both plane waves and cylindrical waves were considered.

4.2.4 Multi-directional boundaries

Higdon (1990 & 1992) developed a silent boundary condition based on a series of first-order differential operators. This boundary is a generalisation of the higher-order differential operators used in the para-axial boundary. Higdon's boundary gives perfect absorption at certain angles of incidence and is therefore called a multi-directional boundary. It also has the advantage of avoiding tangential derivatives at the boundary so that the implementation near a corner is straightforward. Surface waves were not treated.

Higdon (1992) demonstrated how to generalise the silent boundaries for the case of stratified media. He also showed that his silent boundaries were effective in absorbing Rayleigh surface waves.

Gajo *et al* (1996) developed the first-order form of the multi-directional boundary, i.e. the viscous boundary, to extend to saturated porous media for time-dependent problems. This was achieved by first developing a set of first-order differential equations which allowed the propagation of elastic waves travelling only in a single direction; higher order multi-directional boundaries were thus obtained by using the same generalisations proposed by Higdon (1990 & 1992) for one-phase media. Gajo *et al* demonstrated the use of this boundary for wave propagation along a pile shaft to simulate a non-destructive dynamic pile test.

4.2.5 Extrapolation Boundaries

A silent boundary method related to the para-axial technique but which avoids the numerical difficulties of the latter is the scheme proposed by Liao and Wong (1984). This method is also related to the space-time extrapolation scheme proposed by Higdon (1986). These methods are well suited to finite element applications and are based on predicting the motion at the boundary by extrapolating the motion at points in the neighbourhood of the boundary. An analysis of the numerical stability of this method can be found in Liao and Liu (1992). An improvement to this method has been proposed by Peng and Toksoz (1994).

4.2.6 Boundary for a layered medium - Love or Rayleigh waves

In a series of papers (Lysmer (1970), Lysmer and Waas (1972) and Lysmer and Drake (1972)), a boundary was developed in order to transmit either Love waves or Rayleigh waves. In particular, the boundary was designed for a layered medium.

The method initially assumes that a wave of a certain frequency is propagating in a certain layer. The displacements of a finite element of width h beyond the boundary are then calculated by multiplying the displacements of the last element at the boundary by e^{-ikh} (where k is the wave number). The stiffness of the elements beyond the boundary are then calculated and inserted into the equations of motion for the lumped masses at the boundary. This reduces to an eigenvalue problem for each layer. The impinging wave (shear or Rayleigh) causes stresses at the boundary. The idea is to apply oppositional forces to effectively nullify them. In the case of a shear wave, these stresses are proportional to both the displacements at the boundary and the eigenvalues.

A matrix can therefore be assembled which relates the nullifying forces to be applied at the boundary to the displacements at the boundary.

Although this method is suitable for transmitting periodic surface waves, it is highly restrictive. First, the boundary terms are frequency dependent and are therefore unsuitable for transient analyses in the time domain. Also, the method can not be used if the interior equations are non-linear. Only shear or Rayleigh waves can be transmitted and this transmitting boundary is more difficult to implement than most other boundary schemes.

4.2.7 Smith technique - adding wave solutions for fixed and free boundary conditions

A completely different silent boundary method is the scheme originally proposed by Smith (1974) and modified by Cundall *et al* (1978). This method is based on averaging the solutions of two complementary problems, one involving a fixed and the other a free boundary condition. The efficiency of the method, as modified by Cundall *et al* (1978) is comparable with that of the viscous method.

Smith demonstrated that this boundary method eliminates all reflections, regardless of frequency or angle of incidence. It also absorbs all types of waves, including body, Rayleigh or Love waves. The only drawback of this method is that two solutions are required for each possible wave reflection. For example, a two-dimensional corner requires two solutions for each boundary side meaning that the problem must be solved four times to cancel the reflections. Similarly, if there is enough time for a wave to reflect from one boundary, strike another and return then the number of calculations must be doubled. Therefore, the number of complete solutions required is equal to $2n$, where n is the number of possible reflections. If the calculations are performed over a long period of time, the number of required solutions increases very rapidly. This method does not therefore appear to be as attractive as other approaches, except for one-dimensional problems and problems with very short characteristic times.

Cundall *et al* (1978) introduced a cost-saving scheme that attempts to retain the advantages of the Smith method. This scheme sets up a small boundary region in which equations are formed and solved for each boundary condition. The two solutions are added together at every fourth time step. Thus, the boundary area that is four elements deep requires two solutions at each step while the interior region only requires one solution. The efficiency of the modified Smith method is comparable with that of viscous boundary techniques.

4.2.8 Damping techniques

Luco *et al* (1975) attempted to simulate the effects of wave radiation by incorporating material damping into the model. Alternatively, Hilber *et al* (1977) employed numerical damping to account for the transmitted energy. While these techniques are easily implemented it is not clear how they could be practically employed. For example, questions remain as to how much damping should be put into the system, where it should be applied and how the damping can discriminate between the effects of wave radiation and the actual physical dissipation within the model.

A systematic approach to the use of damping in various systems is not available. Luco *et al* (1975) demonstrated some of the problems that can occur. They compared

analytical solutions for wave propagation to calculations from a finite element model that used 'plausible' damping estimates. In general, the material damping did not duplicate the radiation effect satisfactorily.

4.2.9 Substructuring

A relatively simple idea proposed by Haupt (1977) can be applied for repetitive analyses of certain systems that can be split into interior and exterior parts. The interior is altered for each analysis (for example, the geometry or load history) but the exterior region remains constant. Initially an extensive mesh of the whole system is set up, but then the degrees of freedom in the outlying region are condensed. Each successive problem can then be solved by utilising just the small interior mesh and the force contribution from the condensed equations. This method reduces the computational expense for these special cases.

4.2.10 Large finite element meshes

Several investigators, namely Anderson (1972), Day (1977) and Isenberg *et al* (1978), experimented with extensive meshes to determine where the boundary should be placed in order to produce acceptably small reflections. Day (1977) found that undesirable reflections could be prevented by successively increasing the size of outlying elements by a factor of 1.1. This growth factor of 1.1 helps to reduce the number of required elements, but the computational costs still remain high, and prohibitively so for three-dimensional elements.

4.2.11 Periodic infinite elements

A simple numerical method for treating infinite domains in the context of the finite element method is the use of 'infinite elements'. An infinite element is a semi-infinite interval (in one dimension) or a semi-infinite strip (in two dimensions) or a semi-infinite prism (in three dimensions), associated with shape functions that attempt to represent the far-field behaviour of the solution. Sometimes the semi-infinite domain is replaced by a finite but very large domain (see below). In both cases, the numerical solution contains errors due to the fact that the infinite domain is not accounted for exactly. In general, some integrals over infinite domains must be calculated numerically.

The construction of one-dimensional infinite elements and of two- and three-dimensional parallel-edged elements, (e.g. semi-infinite rectangles) can be performed directly in the 'physical' system. Special shape functions are used: they are defined over the infinite domain of the elements, and try to mimic the asymptotic behaviour of the exact solution at infinity.

For elements with a more general geometry (e.g. a general semi-infinite quadrilateral element) two approaches have been employed. In the first approach, special shape functions, expressed in the 'physical' co-ordinate system and having the appropriate behaviour at infinity, are used. Usually in this case, the semi-infinite element domain is replaced by a very large finite element. In the second approach, which has become more popular, a semi-infinite element is obtained by *mapping* the domain of a parent parallel-edged finite element. The usual Lagrangian or serendipity shape functions are used in the local co-ordinates of the parent element, and transformed via the mapping.

Bettess (1977 & 1980) devised the first version of the general one-dimensional and two-dimensional infinite element. For non-rectangular geometry he proposed the first

approach mentioned above, namely that of constructing the shape functions in the 'physical' co-ordinates of a large finite element domain. This infinite element was developed in the context of static problems, such as problems of steady-state heat conduction.

Bettess and Zienkiewicz (1977 & 1981) developed an analogous infinite element for time-harmonic wave problems. Their second-order element has 9 nodes, including 3 that are very far away towards infinity. The shape functions are chosen so that they have the correct behaviour at infinity, namely that they satisfy the Sommerfeld radiation condition there. Numerical integration must be performed over a semi-infinite domain to compute the stiffness matrix and load vector. To this end, a special Newton-Cotes integration rule was devised and used in the infinite direction.

Following the increasing popularity of the serendipity-type finite elements at the beginning of the 1980's, Chow and Smith (1981) proposed to use an infinite element similar to that of Bettess and Zienkiewicz, but with serendipity shape functions rather than the Lagrangian type. Serendipity elements do not contain interior nodes; they have nodes only on their boundaries. Chow and Smith's second-order element has 8 nodes. Serendipity elements up to third order are more efficient than their Lagrangian counterparts, while maintaining the same rate of convergence.

Chow and Smith (1981) then examined the problem of developing a suitable quiet boundary to absorb the waves generated by a vibrating disc on the surface of a layered and anisotropic elastic half-space (as is common in geotechnical models). For each wave speed there is a separate wavelength, since the problem has a fixed period, T , and thus a separate wave number, k . Since the wave number forms part of the element shape function in the original concept of an infinite element for surface waves, the formulation rapidly becomes extremely complicated.

Chow and Smith (1981) developed a simple and pragmatic solution to reduce the complexity of the problem. They considered two-dimensional problems and reasoned that the vertical displacement, u_y , is related to shear waves and the horizontal displacement, u_x , is related to dilatation waves. Thus the appropriate wave number could be used in the shape function for u_x or u_y . This is clearly only an approximation. In addition they reasoned that near to the free surface, the Rayleigh waves would be more important and so the Rayleigh wave number could be used in that region. They interpreted 'close to the surface' as $0.1L_s$ where L_s is the wavelength of the shear wave, see Figure 4.1. They then developed suitable infinite element models with the infinite elements extending both horizontally and vertically. Although this approach was based on approximations and assumptions, the results obtained in comparison with classical solutions were excellent.

Beer and Meek (1981) devised a five-noded serendipity infinite element based on the mapping of a parent element. Both two- and three-dimensional problems in elasticity were considered. Results were compared with exact solutions and with solutions obtained by the boundary element method.

Medina (1981) proposed a similar axisymmetric frequency-dependent infinite element, capable of propagating multi-component waves, using a Gauss-Laguerre integration rule. The shape functions are formulated by using approximate expressions for the

analytical far-field solutions. Although acceptable results are obtained using the method, the accuracy of the results deteriorates due to the non-conforming conditions between the finite and infinite elements and also between adjacent infinite elements. Furthermore the method can not easily be extended to more complex problems such as those with layered media, since it is very difficult to obtain the analytical far-field solutions and also to formulate the shape functions based on analytical results. Medina and Taylor (1983) applied this infinite element to problems in elasto-dynamics.

Yang and Yun (1992) further developed the dynamic infinite element proposed by Medina (1981) by formulating the shape functions using more general expressions for the wave components. They are in terms of complex exponential functions of the corresponding wave numbers, and satisfy the Sommerfeld radiation condition. Hence, this infinite element may be easily extended to problems for which analytical far-field solutions can not easily be computed.

Zhao and Valliappan (1993) developed a three-dimensional dynamic infinite element that can absorb P, S and R waves simultaneously. The infinite element demonstrates displacement compatibility on the finite/infinite element boundary, and between adjacent infinite elements in the case of multiple material layers or multiple wave numbers within the foundation. Wave propagation functions are used to define the wave propagation and amplitude attenuation behaviours in the infinite element. The seismic response of an arch-dam foundation system can be economically calculated using this infinite element coupled with finite elements. This case demonstrates the computational advantage of the infinite element over the boundary element method for simulating wave scattering problems in non-homogeneous media due to the banded and symmetrical nature of the global and stiffness matrices. This infinite element can, in principle, be used to simulate any non-homogeneous foundation provided that each of the infinite elements has constant material properties. However it is only suitable for the absorption of waves generated by a point source, such as a vibrating plate on the surface of an elastic half-space. It is not designed for a multi-source excitation such as pile driving.

Laghrouche (1996) developed a two-dimensional form of Zhao & Valliappan's three-dimensional periodic infinite element. He developed a coupled finite/infinite element model to simulate wave propagation in soils and then extended the model to investigate the effectiveness of various forms of vibration isolation. However, Laghrouche only considered wave propagation from a point source on the surface of the elastic half-space.

Yang, Kuo and Hung (1996) developed a method of dynamic condensation whereby the far-field impedance matrices for waves of lower frequencies can be obtained repetitively from the one for waves of the highest frequency, using exactly the same finite/infinite mesh. Such an approach ensures that accuracy of the same degree can be maintained for waves of all frequencies within the range of consideration. For the case of an elastic half-space subjected to a line load on the free surface, the amplitude decay parameter, α , should be selected as $\alpha=1/(2R)$ for modelling the regions where the body waves are dominant, with R denoting the distance between the source and the boundary of the far-field. Since the Rayleigh waves do not decay on the free surface under the same loading condition, it is suggested that $\alpha=0$ be used for regions near the free surface.

4.2.12 Transient infinite elements

Hägglad and Nordgren (1987) applied infinite elements to transient problems of non-linear soil interaction. Their infinite elements were based on the standard viscous boundary proposed by Lysmer and Kuhlemeyer (1969) with the improvement suggested by White *et al* (1977).

Astley (1995) developed a technique for the solution of transient wave problems in unbounded domains. He proposed a family of infinite 'wave envelope' elements that are formed by applying an inverse Fourier transformation to a discrete wave envelope model in the frequency domain. The infinite elements formed in this way can be applied quite generally to two-dimensional and three-dimensional problems and are fully compatible with conventional finite elements.

4.3 ASSESSMENT OF THE VARIOUS QUIET BOUNDARY TECHNIQUES FOR THE SIMULATION OF GROUND WAVES FROM PILE DRIVING

The literature review has revealed that many different silent boundary formulations are available. However only a few of them are suitable for elasto-dynamic problems, some can not absorb Rayleigh waves effectively, and some are frequency dependent and are not therefore suitable for transient analyses. A further complication arises in that the current version of ABAQUS does not allow the insertion of user-defined elements into a frequency domain analysis. The periodic infinite elements developed by various workers can not therefore be inserted into ABAQUS unless they are transformed in some way for use in a time domain analysis.

The literature review has also revealed that, although silent boundary formulations have been developed to absorb the waves generated by a relatively simple excitation point source (such as a vibrating disc on the surface of an elastic half-space), they have not been extended to deal with more complex excitation sources such as pile driving.

For the purposes of this research, it was decided that a good starting point would be to use a combination of standard and Rayleigh viscous boundaries around the sides of a large finite element mesh in a similar manner to that described by Chow and Smith (1981), see Figure 4.1. As the infinite elements in ABAQUS are based on the standard viscous boundary developed by Lysmer and Kuhlemeyer (1969), this approach had the particular advantage that the performance of the user-defined standard viscous boundaries could be checked against that of the ABAQUS infinite elements as well as the analytical solutions. The method of applying a user-defined boundary within ABAQUS could then be extended to the insertion of a Rayleigh viscous boundary.

Once these viscous boundary formulations were performing satisfactorily in ABAQUS, it was then possible to investigate the optimum arrangement of standard and Rayleigh viscous boundaries around the finite element mesh for the effective absorption of ground waves generated by pile driving.

Some speculative work was also undertaken to look at the possibility of using Astley's (1995) transformation technique in order to insert periodic infinite elements into an ABAQUS time domain analysis. This is described in Section 4.5.

4.4 DERIVATION AND INSERTION OF VISCOUS BOUNDARY FORMULATIONS INTO ABAQUS

4.4.1 Description of the ABAQUS user element interface

ABAQUS allows the user to introduce 'user-defined element' types into a model in a very general way. The element may be a finite element in the usual sense of representing a geometric part of the model, or it may be a feedback link such as silent boundary, supplying forces at some points as functions of values of displacement, velocity, etc at other points in the model. For a general user element, user subroutine UEL must be coded to define the contribution of the element to the model. ABAQUS calls this subroutine each time any information about a user-defined element is needed. At each such call, ABAQUS provides the values of the nodal co-ordinates and of all solution dependent nodal variables at all degrees of freedoms associated with the element, as well as values, at the beginning of the current increment, of the solution dependent state variables associated with the element. ABAQUS also provides the values of all element parameters associated with this element which have been defined in the *UEL PROPERTY option, and a control flag array indicating what functions the user subroutine must perform. Depending on this set of control flags, the subroutine must: define the contribution of the element to the residual vector; define the contribution of the element to the Jacobian (stiffness) matrix; update the solution dependent state variables associated with the element; and so on. Often several of these functions must be performed in a single call to the subroutine.

4.4.2 Standard viscous boundary

In order to test the interface for user-defined infinite elements, the standard viscous boundary proposed by Lysmer and Kuhlemeyer (1969) has been programmed into ABAQUS and its behaviour compared with that of the corresponding infinite elements available in ABAQUS. The derivation of the standard viscous boundary is given below:

Commencing with the one-dimensional wave equation

$$\frac{\partial^2 \phi}{\partial t^2} = c^2 \frac{\partial^2 \phi}{\partial x^2} \quad (4.1)$$

where ϕ is the variable of interest, t is the time and x is the single co-ordinate.

The general solution to equation (4.1) was first given by d'Alembert as

$$\phi = f_1(x - ct) + f_2(x + ct) \quad (4.2)$$

where f_1 represents any disturbance travelling in the positive x direction, f_2 represents any disturbance travelling in the negative x direction and c is the wave celerity. The exact form of f_1 and f_2 will depend upon the initial conditions for the problem.

Consider plane waves travelling along the x -axis. There are two body wave solutions of equation (4.2). One describes plane, longitudinal P waves that have the form

$$u_x = f(x \pm c_p t), \quad u_y = u_z = 0 \quad (4.3)$$

where the wave speed, c_p , is given by

$$c_p = \sqrt{\frac{\lambda + 2G}{\rho}} \quad (4.4)$$

The other solution of this form is the shear or S wave solution

$$u_y = f(x \pm c_s t), \quad u_x = u_z = 0 \quad (4.5)$$

or

$$u_z = f(x \pm c_s t), \quad u_x = u_y = 0 \quad (4.6)$$

where the wave speed, c_s , is given by

$$c_s = \sqrt{\frac{G}{\rho}} \quad (4.7)$$

Now consider a boundary at $x=L$ of a medium modelled by finite elements in $x < L$. In order to eliminate the incoming disturbance we introduce damping on this boundary so that

$$\sigma_{xx} = -d_p \dot{u}_x \quad (4.8)$$

and

$$\sigma_{xy} = -d_s \dot{u}_y \quad (4.9)$$

$$\sigma_{xz} = -d_s \dot{u}_z \quad (4.10)$$

where we choose the damping constants d_p and d_s to avoid reflection of longitudinal and shear wave energy back into the medium where $x < L$, (ie. no incoming waves or the 'radiation condition').

Plane longitudinal P waves approaching the boundary have the form

$$u_x = f_1(x - c_p t), \quad u_y = u_z = 0 \quad (4.11)$$

If they are reflected back at all as plane longitudinal waves, their reflection will travel away from the boundary in some form

$$u_x = f_2(x + c_p t), \quad u_y = u_z = 0 \quad (4.12)$$

As the problem is linear, the total displacement is calculated by superposition

$$u_x = f_1 + f_2 \quad (4.13)$$

with corresponding stresses

$$\sigma_{xx} = (\lambda + 2G)(f_1' + f_2'), \quad \text{all other } \sigma_{ij} = 0 \quad (4.14)$$

and velocity

$$\dot{u}_x = -c_p(f_1' - f_2') \quad (4.15)$$

For this solution to satisfy the damping behaviour, $\sigma_{xx} = -d_p \dot{u}_x$ introduced on the boundary at $x=L$ requires

$$(\lambda + 2G)(f_1' + f_2') = -d_p(-c_p(f_1' - f_2')) \quad (4.16)$$

Rearranging

$$(\lambda + 2G - d_p c_p)f_1' + (\lambda + 2G + d_p c_p)f_2' = 0 \quad (4.17)$$

To ensure that $f_2 = 0$ (so that $f_2' = 0$) for any f_1 , choose

$$d_p c_p = \lambda + 2G \quad (4.18)$$

Therefore

$$d_p = \frac{\lambda + 2G}{c_p} = c_p \rho \quad (4.19)$$

A similar argument for shear waves gives

$$d_s = c_s \rho \quad (4.20)$$

The normal and shear stresses, σ and τ , on the boundary can therefore be expressed as

$$\sigma = a d_p \dot{u}_x \quad (4.21)$$

and

$$\tau = b d_s \dot{u}_y \quad (4.22)$$

where a and b are dimensionless parameters. This boundary condition corresponds to a situation where the boundary is supported on infinitesimal dashpots oriented normal and tangential to the boundary.

Lysmer and Kuhlemeyer (1969) demonstrated that maximum absorption of P and S waves occurs when $a=b=1$ (98.5% effective for P waves and 95% effective for S waves).

To summarise, the viscous boundary defined by equations (4.21) and (4.22) is an almost perfect absorber of harmonic elastic waves. Because the absorption characteristics are independent of frequency, the boundary can absorb both harmonic and non-harmonic waves and is known as the standard viscous boundary.

The subroutine is reproduced in full in Appendix C together with the ABAQUS/Standard input file that calls the subroutine. The horizontal displacements across the mesh resulting from applying a pure P wave to the left-hand side of the finite element mesh and a user-defined standard viscous boundary to the right-hand side (Figure 4.2a) are compared to those obtained using the ABAQUS infinite elements (Figure 4.2b) in Figure 4.2(c). A similar comparison of the vertical displacements resulting from an S wave is shown in Figures 4.3(a-c). These graphs show that the user-defined standard viscous boundary performs as well as the ABAQUS infinite element in absorbing body waves.

The derivations given above are for plane body waves travelling through a mesh of plane strain finite elements. However, the computational models for pile driving will need to be assembled with axisymmetric finite elements to simulate the radial propagation of the waves through the ground. It is therefore necessary to convert the viscous boundary formulations from plane strain to axisymmetric conditions.

This simply involves calculating the cross-sectional area of the element at the FE/IE boundary. This is equal to the circumference of the circle swept out by the axisymmetric mesh at the FE/IE boundary ($2\pi r$). (In the plane strain case the cross-sectional area is taken as equal to 1.0.)

The analytical solution is determined as follows:

$$A_{ax} = \left(\frac{1/\sqrt{r}}{1/\sqrt{r_0}} \right) * A_{pe} \quad (4.23)$$

where A_{ax} is the amplitude of the body wave component (u_x or u_y) in the axisymmetric case at any radius r , r_0 is the radius at the point of application of the body wave and A_{pe} is the amplitude of the body wave component (u_x or u_y) for the plane strain case at any radius r .

The subroutine for the axisymmetric standard viscous boundary is also reproduced in full in Appendix C together with the ABAQUS/Standard input file that calls the subroutine. The horizontal displacements resulting from a P wave travelling across the axisymmetric mesh (Figure 4.4a) with a user-defined standard viscous boundary are compared with the analytical solutions and the ABAQUS infinite elements in Figures 4.4(b) and 4.4(c) respectively. The corresponding plots for an S wave in an axisymmetric mesh are given in Figures 4.5(a-c). These graphs show that the user-

defined standard viscous boundary performs as well as the ABAQUS infinite elements in absorbing body waves in an axisymmetric mesh.

4.4.3 Rayleigh viscous boundary

As stated earlier, one drawback of the standard viscous boundary is its inability to transmit Rayleigh waves as effectively as it transmits body waves. In order to overcome this problem, Lysmer and Kuhlemeyer (1969) also developed a special viscous boundary for Rayleigh waves in which the dashpots have coefficients that depend upon the frequency of the transmitted waves. The derivation of the Rayleigh viscous boundary is given below:

Consider a Rayleigh wave travelling with velocity c_r in the positive x direction (Figure 4.6). As shown by Ewing, Jardetzky and Press (1957), the displacements are given by

$$u_x = f(ky)\sin(kx - \omega t) \quad (4.24)$$

and

$$u_y = g(ky)\cos(kx - \omega t) \quad (4.25)$$

in which the wave number, k , is defined as

$$k = \frac{\omega}{c_r} \quad (4.26)$$

For the special case of a homogeneous half space, the functions $f(ky)$ and $g(ky)$ vary as shown in Figure 4.7. The velocity of the Rayleigh wave may be expressed as a fraction of the shear wave velocity by

$$c_r = \frac{c_s}{\eta} \quad (4.27)$$

The value of η and the functions $f(ky)$ and $g(ky)$ vary with Poisson's ratio. For $\nu=0.25$,

$$\eta = 1.08766,$$

$$f(ky) = D[e^{0.8475ky} - 0.5773e^{0.3933ky}] \quad (4.28)$$

and

$$g(ky) = D[-0.8475e^{0.8475ky} + 1.4679e^{0.3933ky}] \quad (4.29)$$

in which D is a constant. (D is taken as 1.0 in this theoretical case: the actual magnitude of R wave depends on how it is generated).

The compressive stress on a vertical plane is

$$\sigma = -(\lambda + 2G)\frac{\partial u_x}{\partial x} - \lambda\frac{\partial u_y}{\partial y} \quad (4.30)$$

Substitution of equations (4.24) and (4.25) into equation (4.30) gives

$$\sigma = k[(\lambda + 2G)f(ky) - \lambda g'(ky)]\cos(kx - \omega t) \quad (4.31)$$

where $g'(ky)$ indicates the differentiation $d(g)/d(ky)$ so that

$$g'(ky) = D[-0.7183e^{0.8475ky} + 0.5773e^{0.3933ky}] \quad (4.32)$$

Similarly, the shear stress on a vertical plane is given by

$$\tau = -kG[f'(ky) + g(ky)]\sin(kx - \omega t) \quad (4.33)$$

where

$$f'(ky) = D[0.8475e^{0.8475ky} - 0.2271e^{0.3933ky}] \quad (4.34)$$

The particle velocities are found by simple differentiation of equations (4.24) and (4.25) to give

$$\dot{u}_x = -\omega f(ky)\cos(kx - \omega t) \quad (4.35)$$

and

$$\dot{u}_y = \omega g(ky)\sin(kx - \omega t) \quad (4.36)$$

Perfect energy absorption will be obtained if equations (4.21) and (4.22) are satisfied identically. The values of a and b are therefore found by simple substitution of equations (4.31) and (4.33) into equations (4.21) and (4.22) as follows

$$a(ky) = \frac{1}{c_p \rho} \cdot \frac{\sigma}{\dot{u}_x} = \frac{\eta}{s} \left[1 - (1 - 2s^2) \frac{g'(ky)}{f(ky)} \right] \quad (4.37)$$

$$b(ky) = \frac{1}{c_s \rho} \cdot \frac{\tau}{\dot{u}_y} = \eta \left[1 + \frac{f'(ky)}{g(ky)} \right] \quad (4.38)$$

where s is an elastic constant defined by

$$s^2 = \frac{1 - 2\nu}{2(1 - \nu)} \quad (4.39)$$

The variation of a and b with ky is shown in Figure 4.8. Recognising that the physical meaning of the variable ky is $2\pi \times \text{depth/wavelength}$, it can be seen that at depths greater than one half-wavelength, the parameters a and b approach constant values. At the depth where the horizontal displacement vanishes, the parameter a goes to infinity which agrees with the physical fact that an infinitely viscous dashpot is required to fix a point. The computational finite element mesh has to be refined near the ground surface so that the asymptote falls at a mid-node position. The horizontal displacement at this node is then set to zero in the code (see Appendix D).

The subroutine for the Rayleigh viscous boundary is reproduced in full in Appendix D together with the ABAQUS/Standard input file that calls the subroutine. The horizontal and vertical displacements across the mesh resulting from the application of a user-defined Rayleigh viscous boundary are compared with the analytical solutions and the ABAQUS infinite elements in Figures 4.9(c) and 4.9(d) respectively. The user-defined Rayleigh viscous boundary demonstrates a marked improvement over the ABAQUS infinite element in absorbing Rayleigh waves (Figures 4.10a and 4.10b).

The derivations given above are for plane body waves travelling through a mesh of plane strain finite elements. However, the computational models for pile driving will need to be assembled with axisymmetric finite elements to simulate the radial propagation of the waves through the ground. It is therefore necessary to convert the viscous boundary formulations from plane strain to axisymmetric conditions.

This simply involves calculating the cross-sectional area of the element at the FE/IE boundary. This is equal to the circumference of the circle swept out by the axisymmetric mesh at the FE/IE boundary ($2\pi r$). (In the plane strain case the cross-sectional area is taken as equal to 1.0.)

The analytical solution is determined as follows:

$$A_{ax} = \left(\frac{1/\sqrt{r}}{1/\sqrt{r_0}} \right) * A_{pe} \quad (4.40)$$

where A_{ax} is the amplitude of the Rayleigh wave component (u_x or u_y) in the axisymmetric case at any radius r , r_0 is the radius at the point of application of the R wave and A_{pe} is the amplitude of the Rayleigh wave component (u_x or u_y) for the plane strain case at any radius r .

The subroutine for the axisymmetric Rayleigh viscous boundary is also reproduced in full in Appendix D together with the ABAQUS/Standard input file that calls the subroutine. The horizontal and vertical displacements a P wave travelling across the axisymmetric mesh with a user-defined standard viscous boundary (Figure 4.11a) are compared with the analytical solutions and the ABAQUS infinite elements (Figure 4.11b) in Figures 4.11(c) and 4.11(d) respectively. The axisymmetric user-defined Rayleigh viscous boundary demonstrates a marked improvement over the ABAQUS infinite elements in absorbing Rayleigh waves.

4.5 APPLICATION OF VISCOUS BOUNDARY FORMULATIONS TO THE PILE DRIVING MODEL

The standard and Rayleigh viscous boundaries can now be applied to boundaries of an axisymmetric finite element mesh within ABAQUS. As mentioned in Section 4.2 above, Chow and Smith (1981) developed a “quiet boundary” for the absorption of waves generated by a vertically vibrating disc on the surface of an elastic half-space, see Figure 4.1. The results compared extremely well with classical solutions. However, the

waves generated by pile driving are much more complex than those generated by a single excitation source, and classical solutions or experimental data do not exist.

The only method available for determining the effectiveness of a quiet boundary for such a complex case is to compare the response of the FE/IE mesh with that of a very large finite element mesh, of sufficient size to prevent any boundary reflection into the area (time period) of interest. This is the approach used in Chapter 5 to investigate the effectiveness of the combined standard/Rayleigh viscous boundaries in the absorption of ground waves generated by vibratory pile driving, see Section 5.5. The approach is further verified by comparison with actual field measurements of surface vibrations (Section 5.5).

A disadvantage of the Rayleigh viscous boundary is that it is frequency-dependent and therefore can not be used for transient problems. The boundary is therefore suitable for use in a vibratory piling model where there is a known frequency of excitation but it can not be used to absorb waves generated by impact piling, which contain many different frequencies. This limitation, however, is not particularly troublesome as impact piling comprises discrete “events” (when the hammer hits the pile) rather than the continuous excitation of vibratory piling. The standard viscous boundary (or ABAQUS infinite elements) in conjunction with a large finite element mesh therefore provides an adequate model for impact piling because the boundary only needs to absorb the faster moving P and S waves. Once the R waves (the slowest waves) have reached the furthest point of interest, the analysis can be stopped (before the R waves reach and reflect off the standard viscous boundary).

4.6 PROPOSED TECHNIQUE FOR INSERTING PERIODIC INFINITE ELEMENTS INTO ABAQUS

Unfortunately, the current version of ABAQUS does not allow the insertion of user-defined elements into a frequency domain analysis. The periodic infinite elements developed by various workers can not therefore be inserted into ABAQUS unless they are transformed in some way for use in a time domain analysis. Such a technique has been developed by Astley (1995). He developed a family of infinite ‘wave envelope’ elements which are formed by applying an inverse Fourier transform to a discrete wave envelope model in the frequency domain. This gives a coupled system of second-order ordinary differential equations which are readily integrated in time to yield transient pressure histories at nodal points on the surface of the radiating body, and, in retarded form, at discrete points within the infinite domain.

Some preliminary work was undertaken as part of this research project to test the suitability of Astley’s technique for the insertion of periodic infinite elements into an ABAQUS time domain analysis. Unfortunately, time constraints prevented completion of this work. The proposed technique is outlined below for the benefit of others who may wish to develop it further.

- Modify the two-dimensional infinite element code developed by Laghrouche (1996), which is based on the work of Zhao and Valliappan (1993), to incorporate the values of α suggested by Yang and Hung (1997).

- Transform Laghrouche's periodic infinite element code for use in a time domain analysis using Astley's technique.
- Insert the transformed infinite elements into an equivalent model in ABAQUS as user-defined elements. (The method for inserting a user-defined quadrilateral element into an ABAQUS time domain analysis was determined and verified as part of this preliminary work.)
- Compare the performance of the infinite element within Laghrouche's finite element program with its performance within ABAQUS for a range of frequencies.
- Following validation of this technique, other types of periodic infinite elements could be incorporated into ABAQUS using this technique. The efficiency of the various types of infinite elements in eliminating wave reflection could then be compared.

4.7 CONCLUSIONS AND RECOMMENDATIONS FOR FURTHER WORK

A number of quiet boundary methods have been reviewed, but none offer a total solution for the case of pile driving. Standard and Rayleigh viscous boundaries have therefore been developed for use in an ABAQUS axisymmetric FE mesh. The Rayleigh viscous boundary has demonstrated a marked improvement over the ABAQUS infinite elements in absorbing R waves.

It was therefore decided to apply a combination of standard and Rayleigh viscous boundaries to the sides of the axisymmetric finite element mesh in similar manner to technique developed by Chow & Smith (1981). The effectiveness of the combined standard/Rayleigh viscous boundary in the absorption of ground waves generated by vibratory piling is investigated in Chapter 5.

The boundary proposed by Chow & Smith (1981) is only an approximation and was developed for a single excitation source. Further work is required to develop a boundary that can absorb P, S and R waves simultaneously for a multi-source excitation such as piling. Some preliminary work has been undertaken to test the suitability of the transformation technique developed by Astley (1995) for the insertion of periodic infinite elements into an ABAQUS time domain analysis.

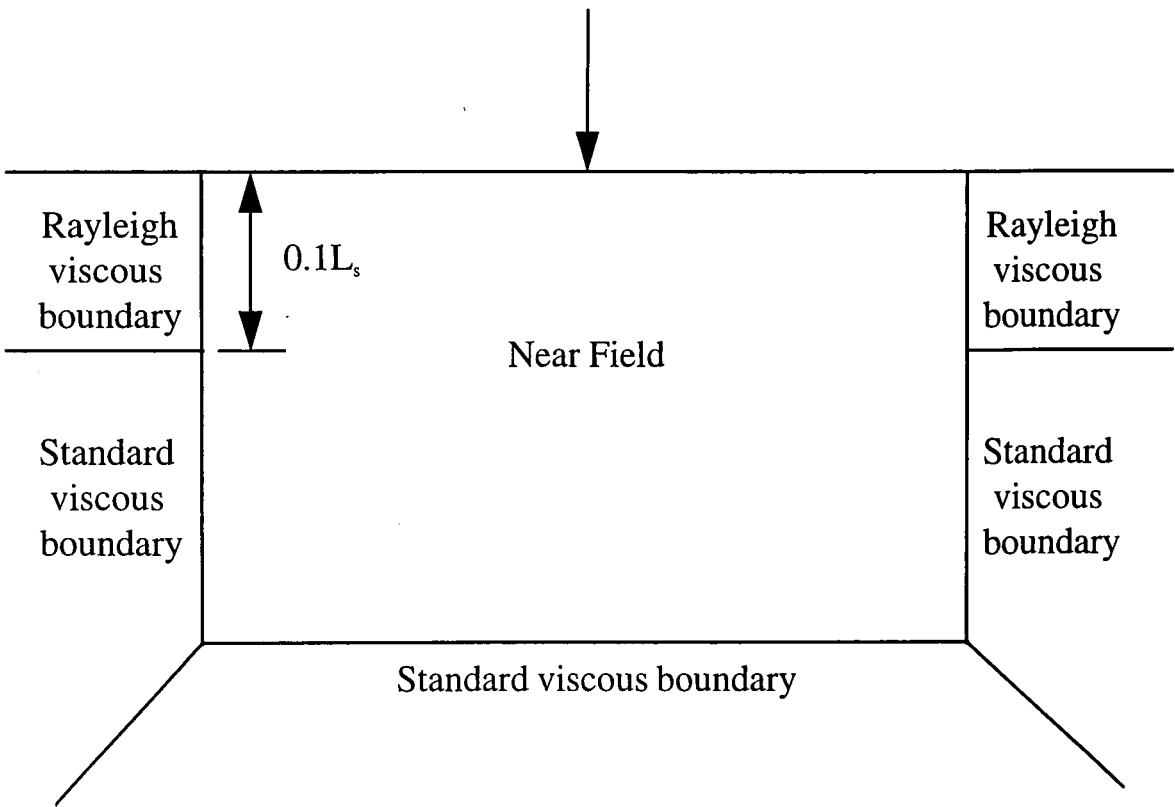


Figure 4.1

Distribution of the standard and Rayleigh viscous boundaries around a finite element mesh proposed by Chow & Smith (1981)

ABAQUS

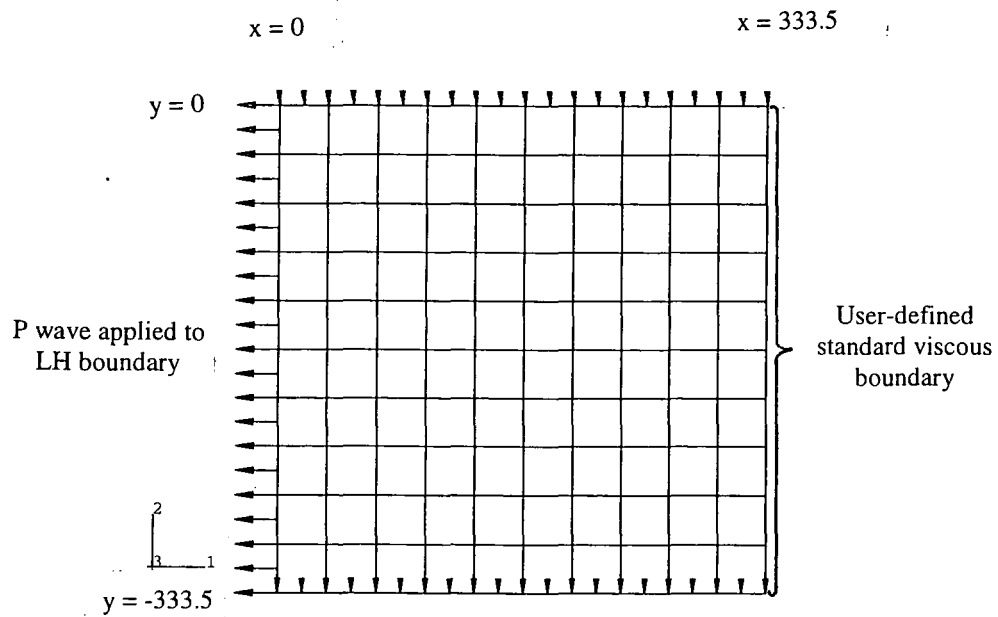


Figure 4.2(a) FE/IE plane strain mesh used to test the effectiveness of a user-defined standard viscous boundary in absorbing P waves

ABAQUS

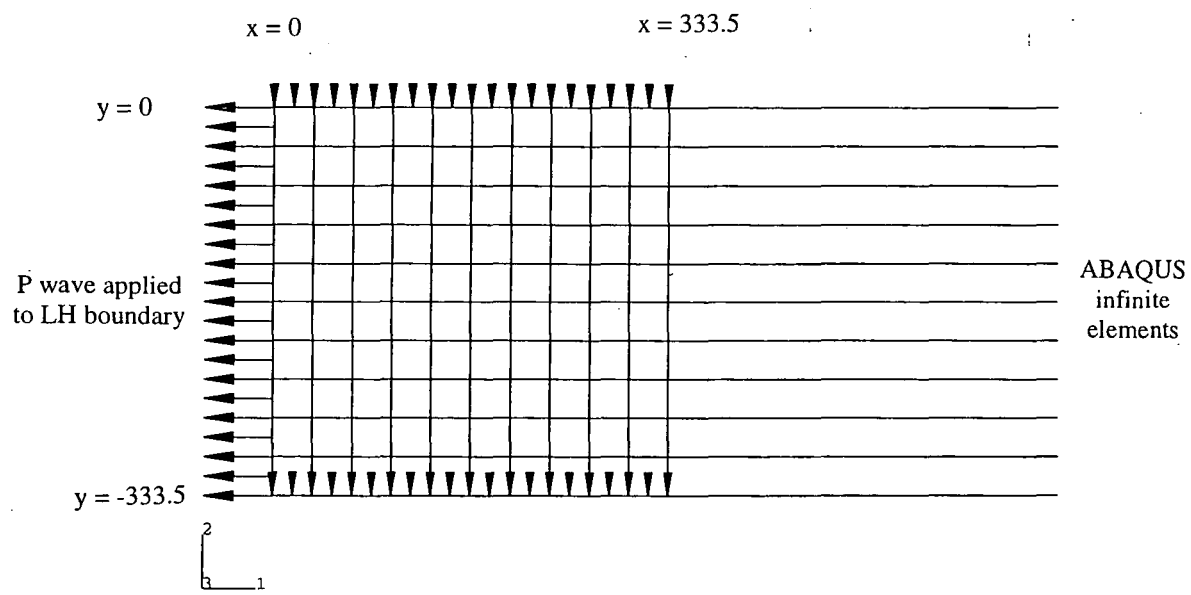


Figure 4.2(b) FE/IE plane strain mesh used to test the effectiveness of ABAQUS infinite elements in absorbing P waves

ABAQUS

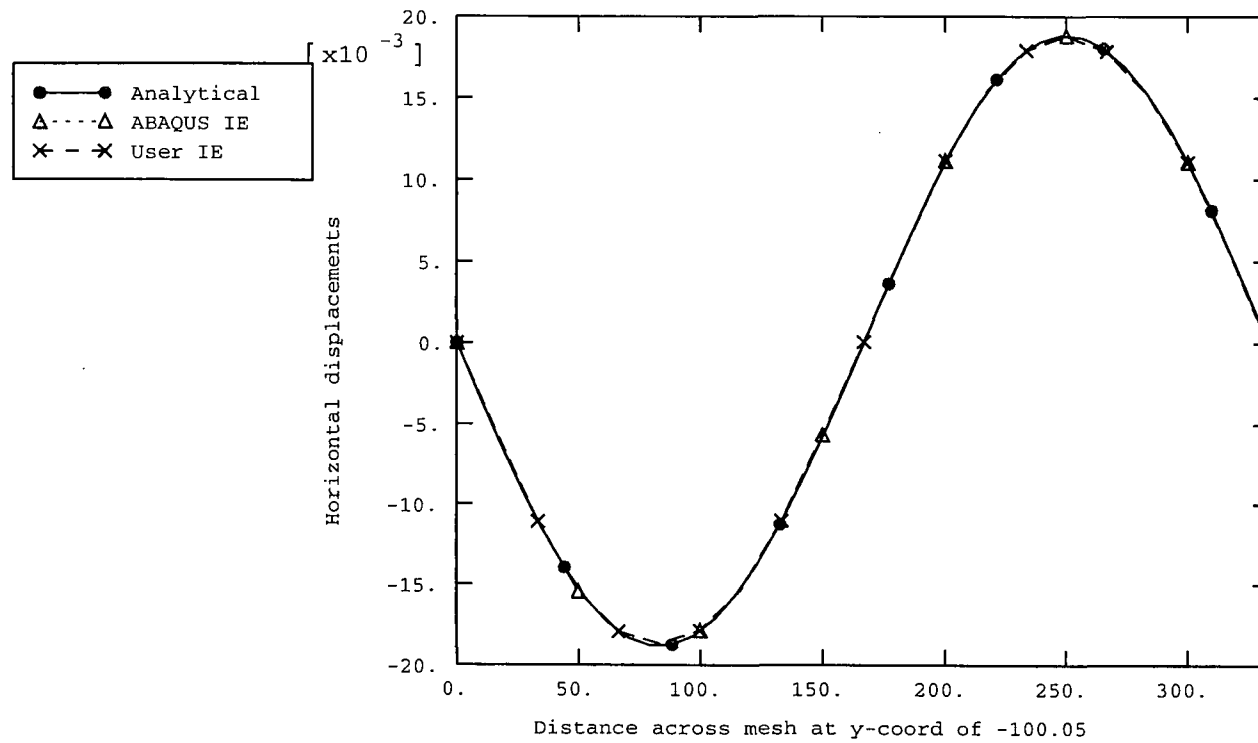


Figure 4.2 (c) Comparison of the effectiveness of the boundaries in absorbing P waves in a plane strain FE/IE mesh

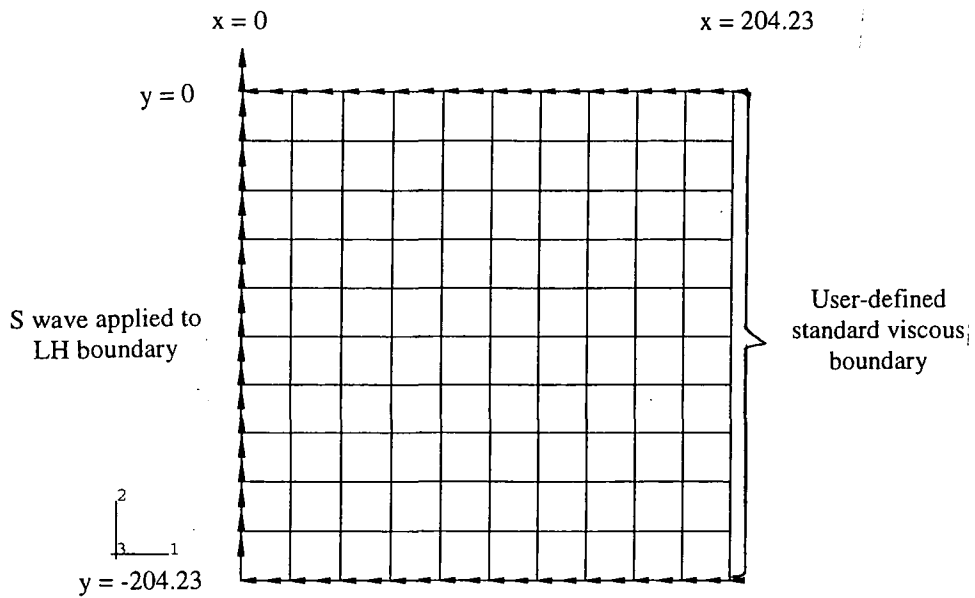


Figure 4.3(a) FE/IE plane strain mesh used to test the effectiveness of a user-defined standard viscous boundary in absorbing S waves

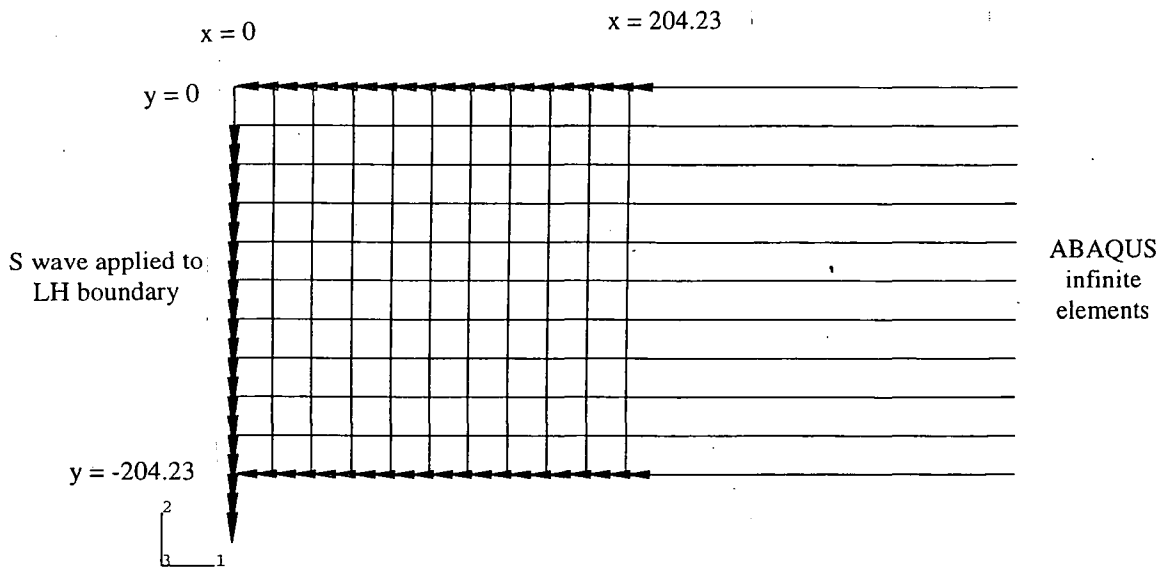


Figure 4.3(b) FE/IE plane strain mesh used to test the effectiveness of ABAQUS infinite elements in absorbing S waves

ABAQUS

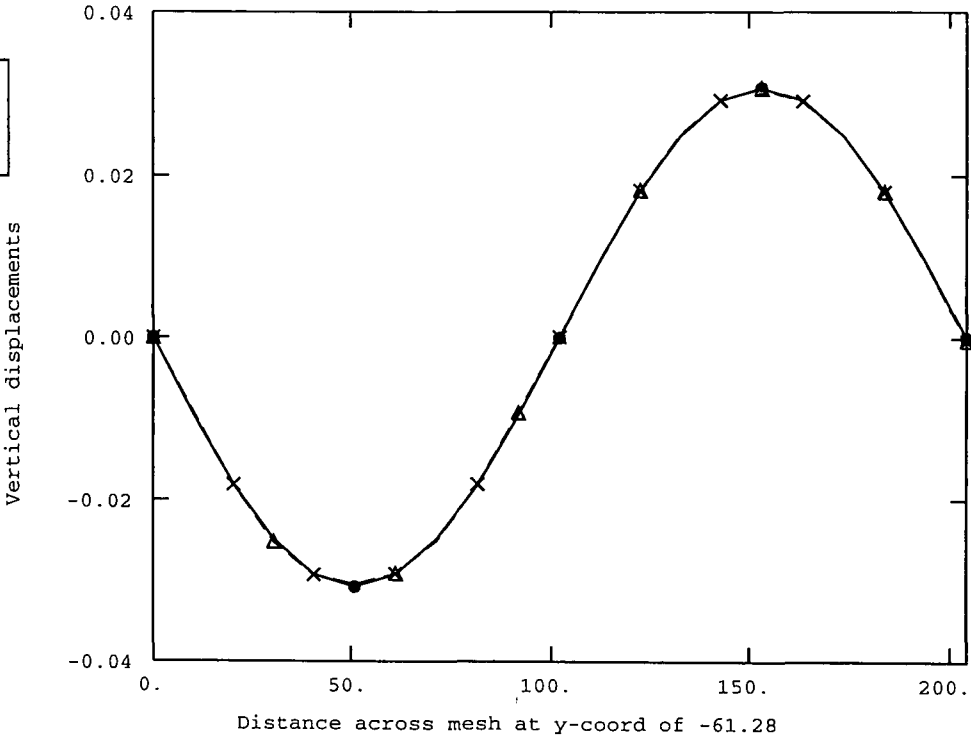
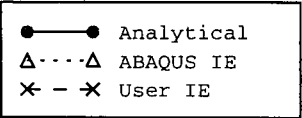


Figure 4.3(c) Comparison of the effectiveness of the boundaries in absorbing S waves in a plane strain FE/IE mesh

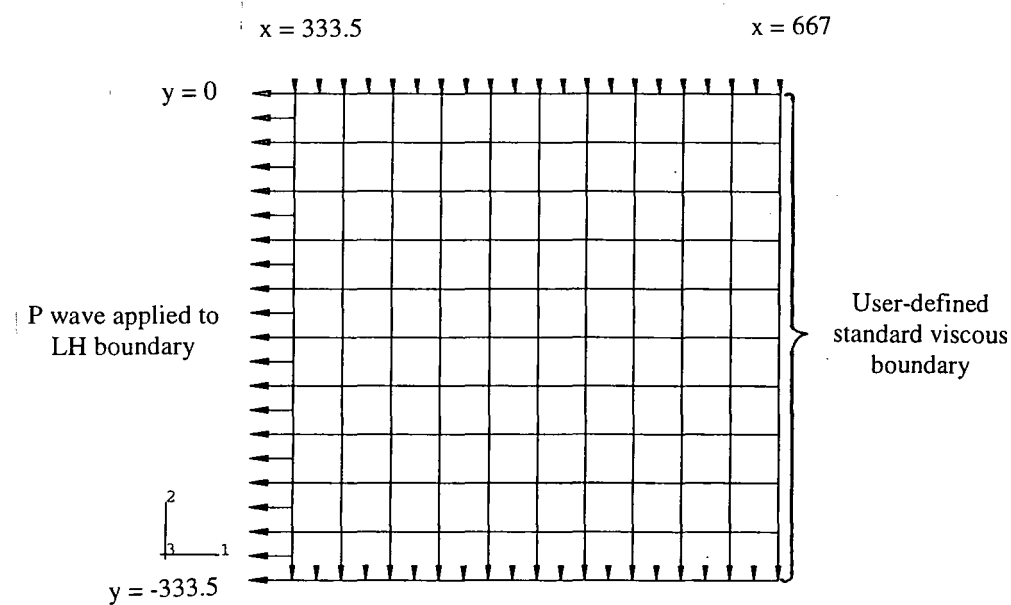


Figure 4.4(a) FE/IE axisymmetric mesh used to test the effectiveness of a user-defined standard viscous boundary in absorbing P waves

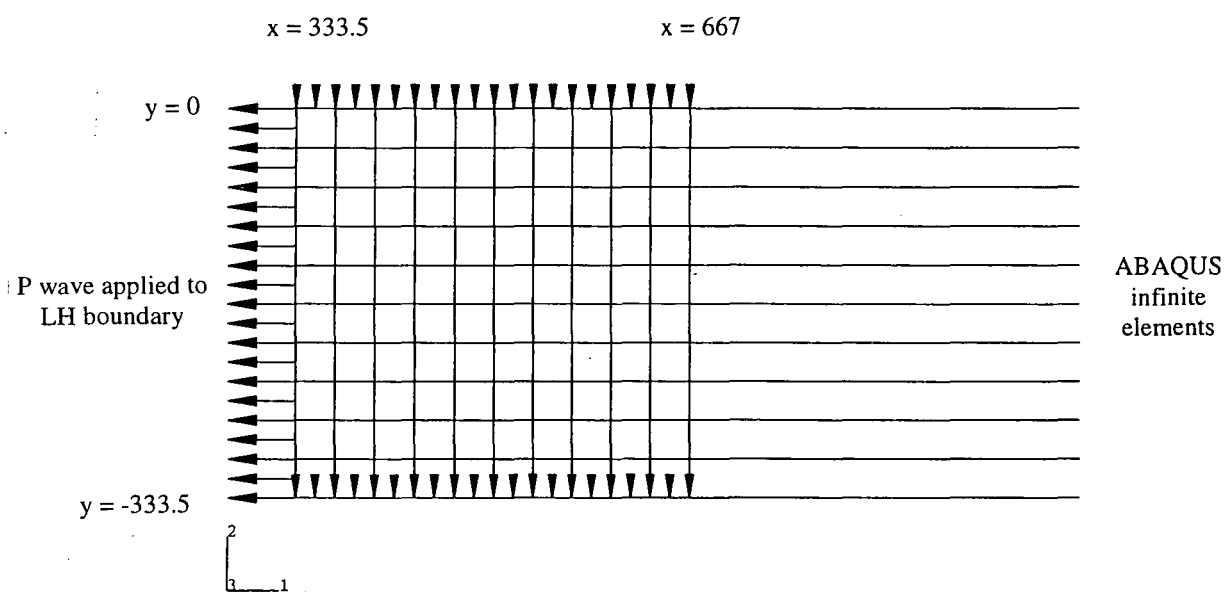


Figure 4.4(b) FE/IE axisymmetric mesh used to test the effectiveness of ABAQUS infinite elements in absorbing P waves

ABAQUS

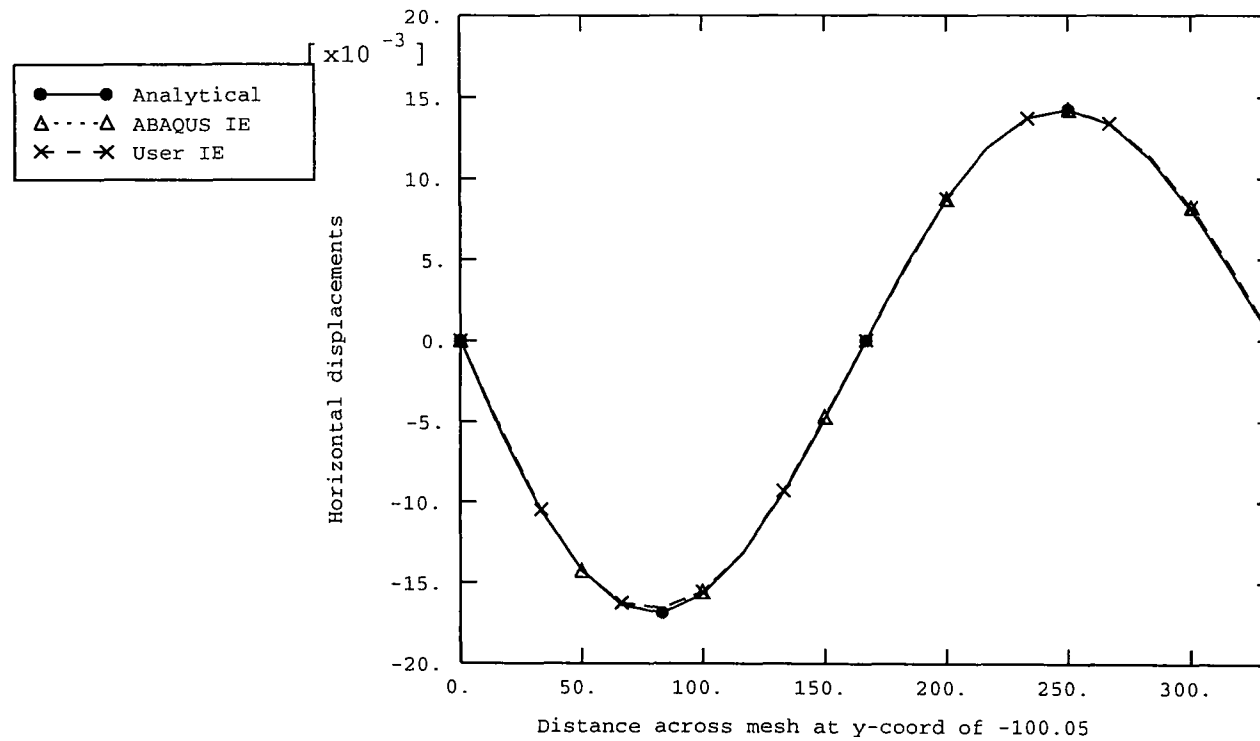


Figure 4.4(c) Comparison of the effectiveness of the boundaries in absorbing P waves in an axisymmetric FE/IE mesh

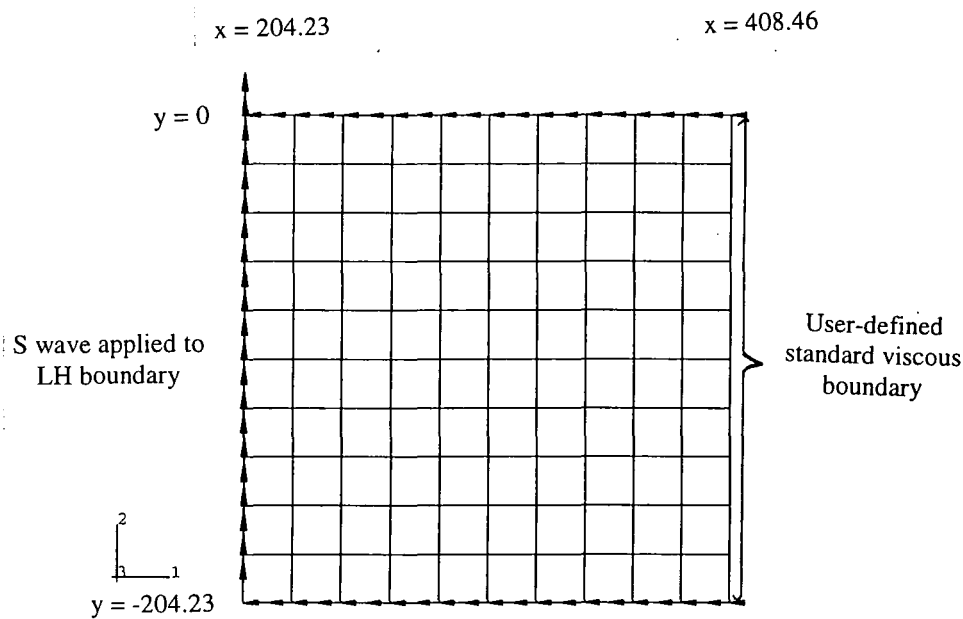


Figure 4.5(a) FE/IE axisymmetric mesh used to test the effectiveness of a user-defined standard viscous boundary in absorbing S waves

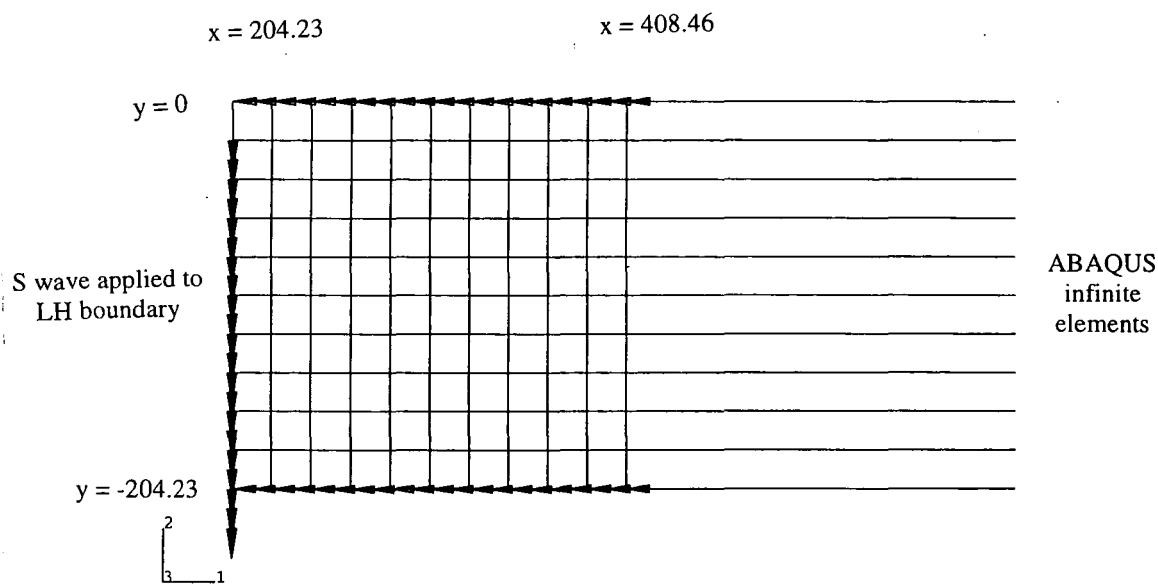


Figure 4.5(b) FE/IE axisymmetric mesh used to test the effectiveness of ABAQUS infinite elements in absorbing S waves

ABAQUS

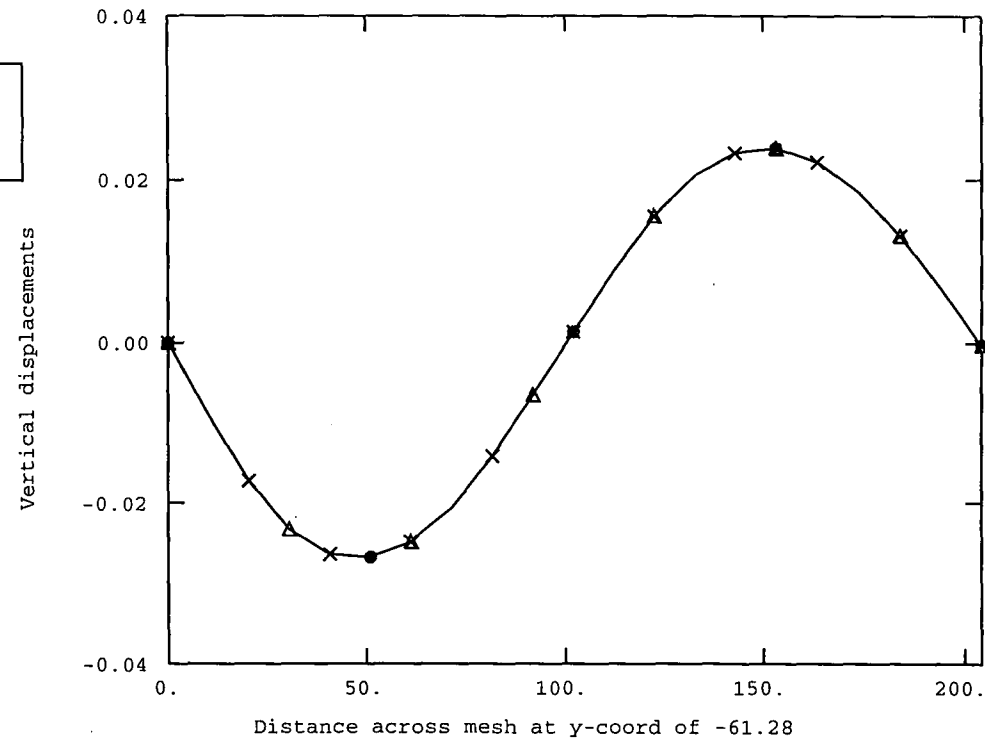
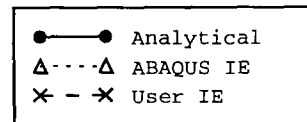


Figure 4.5(c) Comparison of the effectiveness of the boundaries in absorbing S waves in an axisymmetric FE/IE mesh

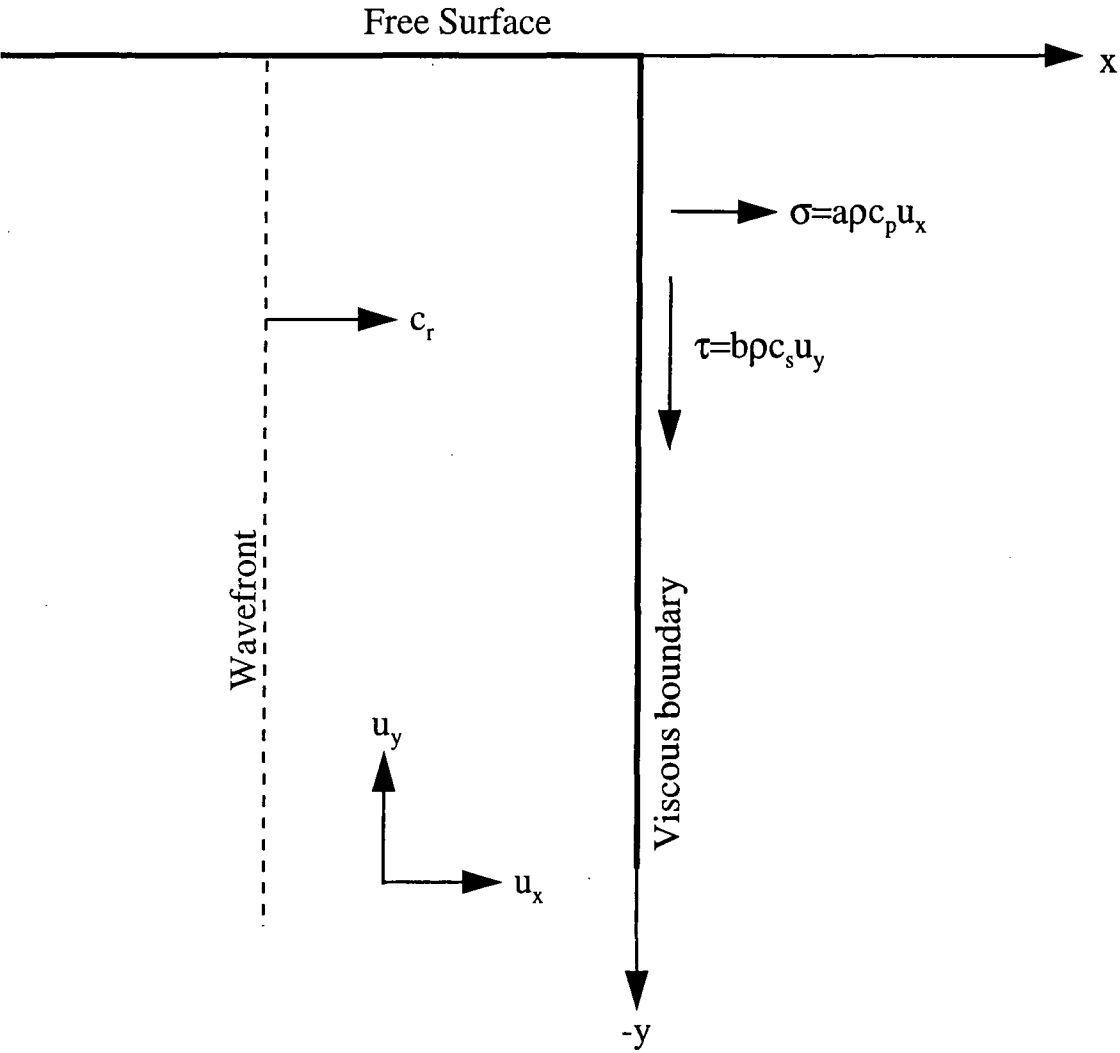


Figure 4.6 Rayleigh wave absorption

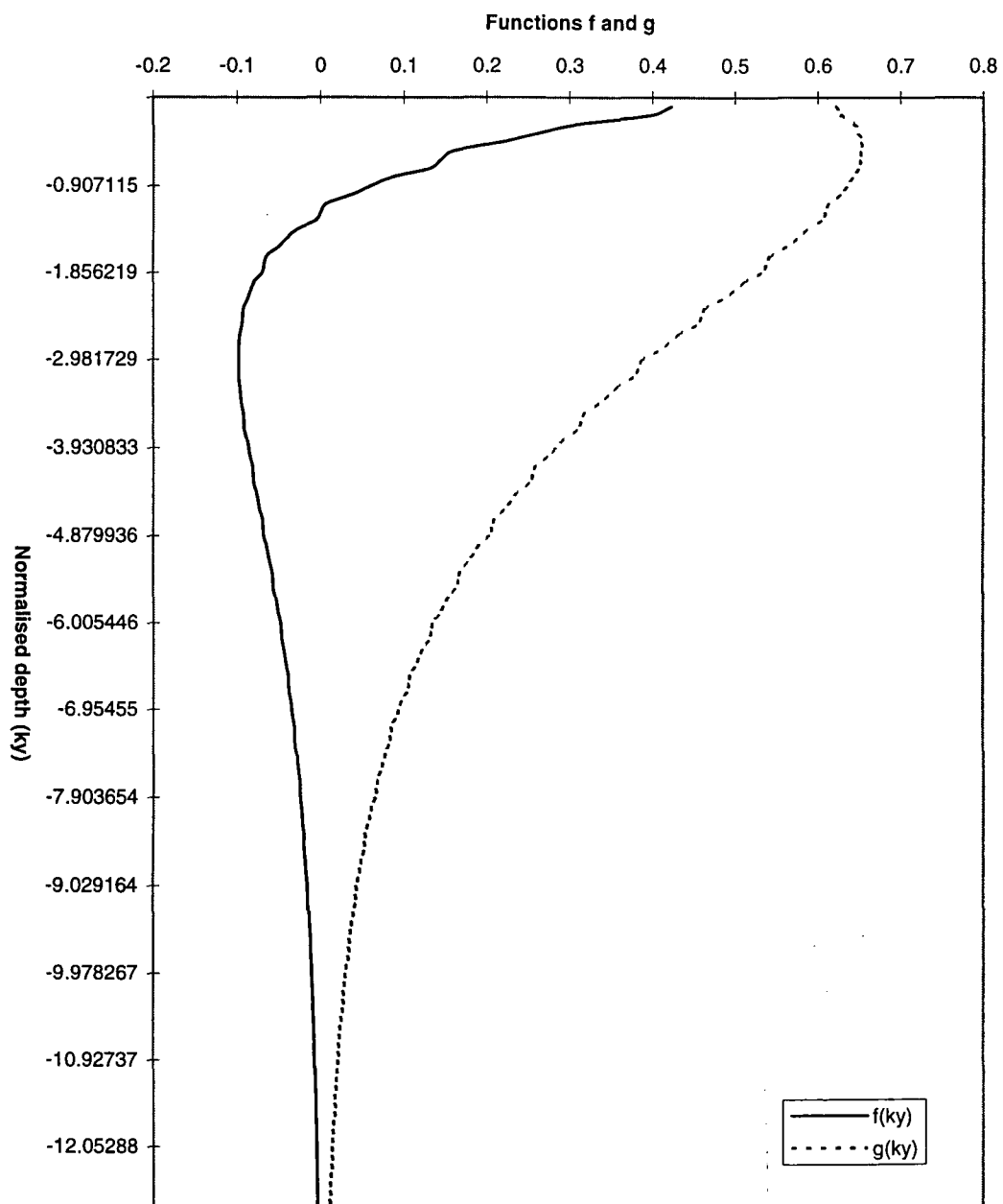


Figure 4.7

Variation of functions f and g in a homogenous half-space

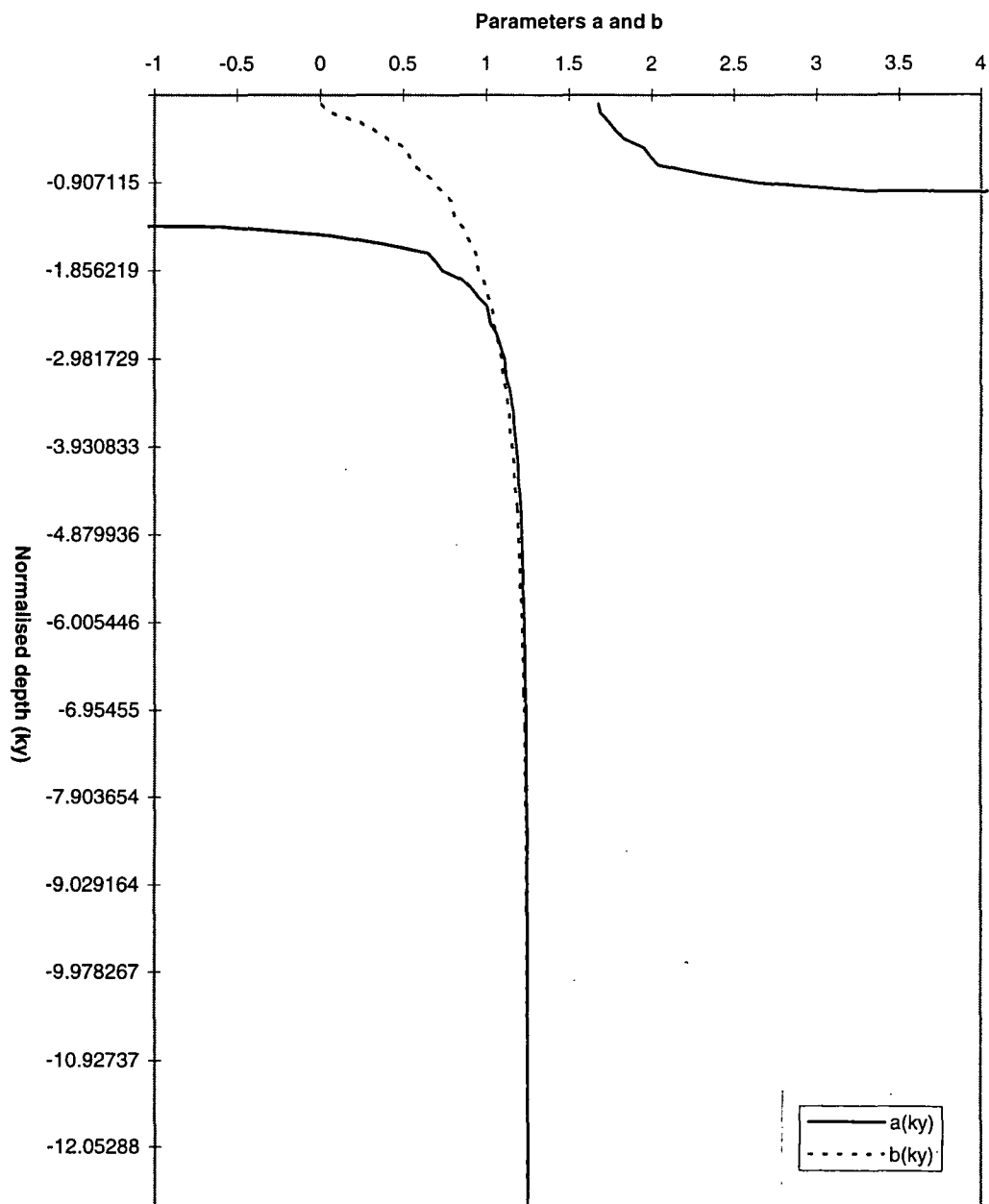


Figure 4.8

Variation of parameters a and b in a homogenous half-space

ABAQUS

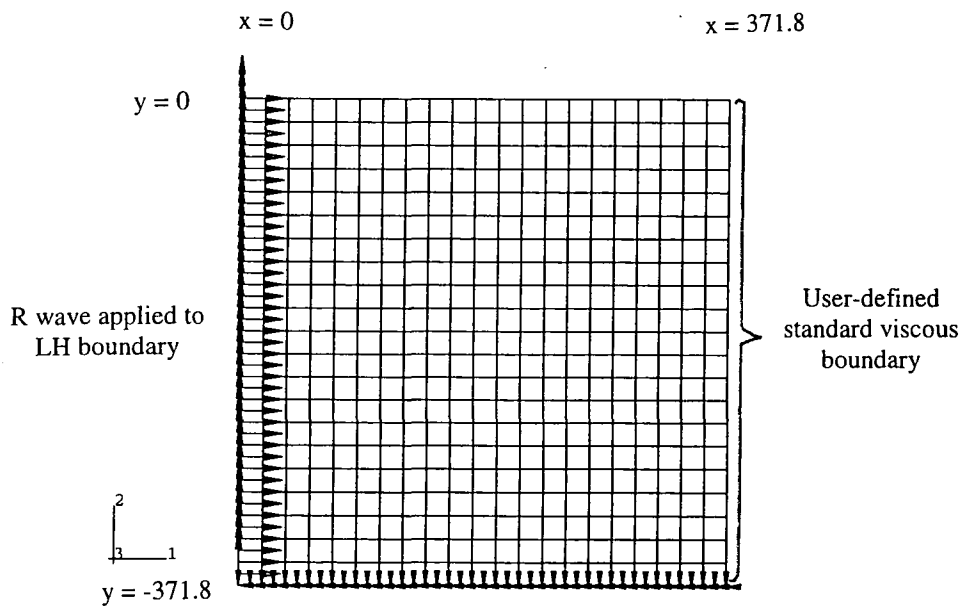


Figure 4.9(a) FE/IE plane strain mesh used to test the effectiveness of a user-defined standard viscous boundary in absorbing R waves

ABAQUS

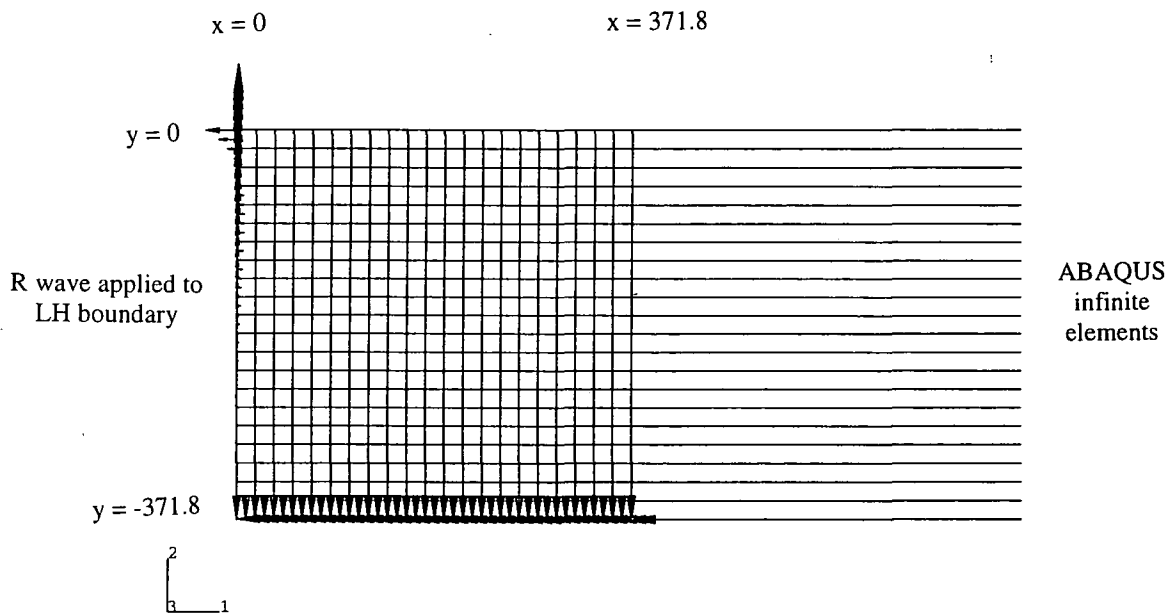


Figure 4.9(b) FE/IE plane strain mesh used to test the effectiveness of ABAQUS infinite elements in absorbing R waves

ABAQUS

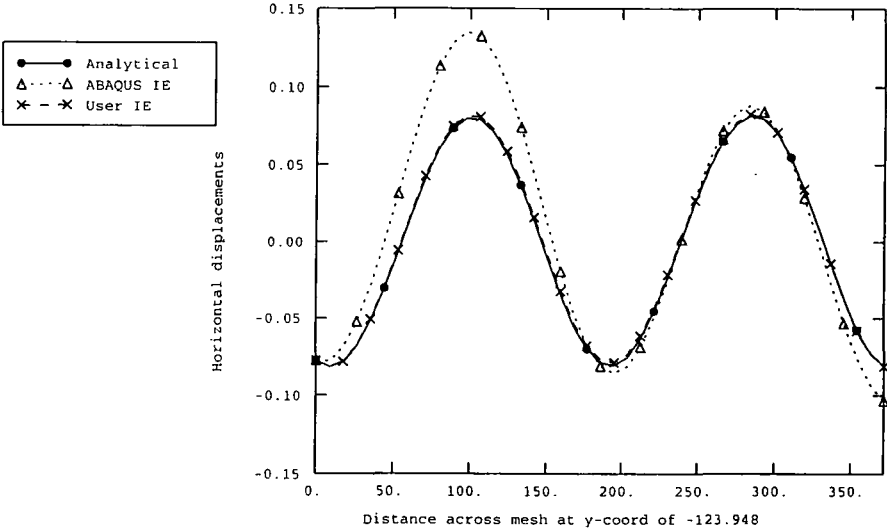


Figure 4.9(c) Comparison of the effectiveness of the boundaries in absorbing R waves in a plane strain FE/IE mesh: horizontal displacements across mesh

ABAQUS

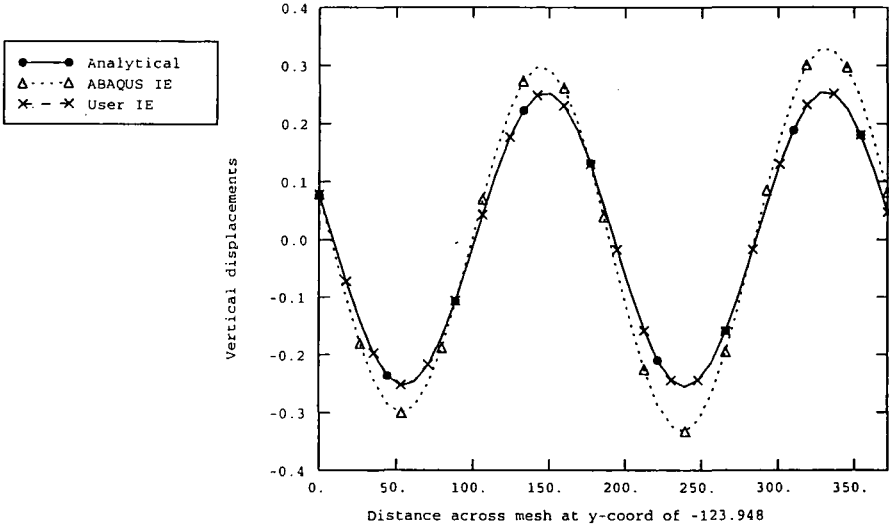


Figure 4.9(d) Comparison of the effectiveness of the boundaries in absorbing R waves in a plane strain FE/IE mesh: vertical displacements across mesh

ABAQUS

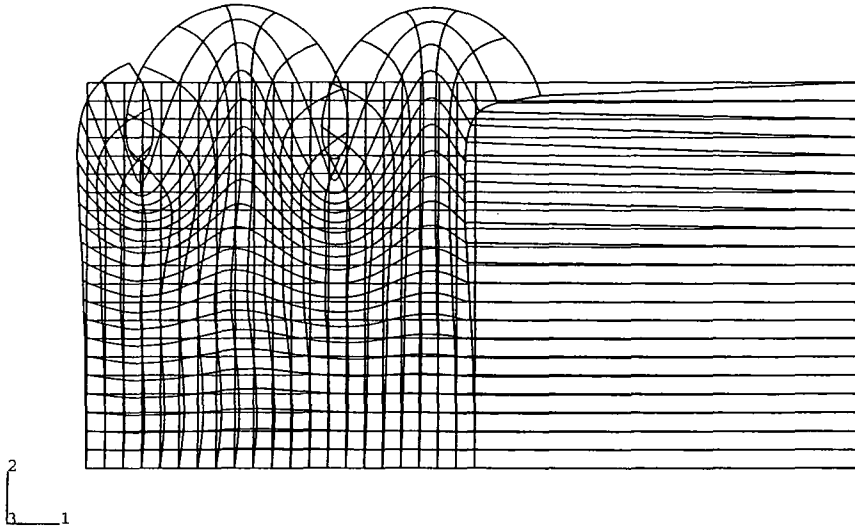


Figure 4.10(a) 'Snapshot' of R wave in mesh with ABAQUS infinite elements modelling far-field domain at 16.8 secs (Displacement magnification factor = 100)

ABAQUS

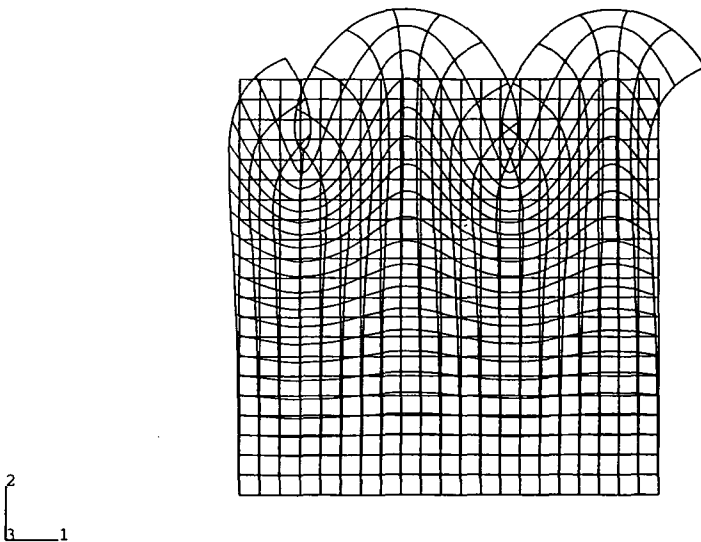


Figure 4.10(b) 'Snapshot' of R wave in mesh with user-defined Rayleigh viscous boundary modelling far-field domain at 16.8 secs (Displacement magnification factor = 100)

ABAQUS

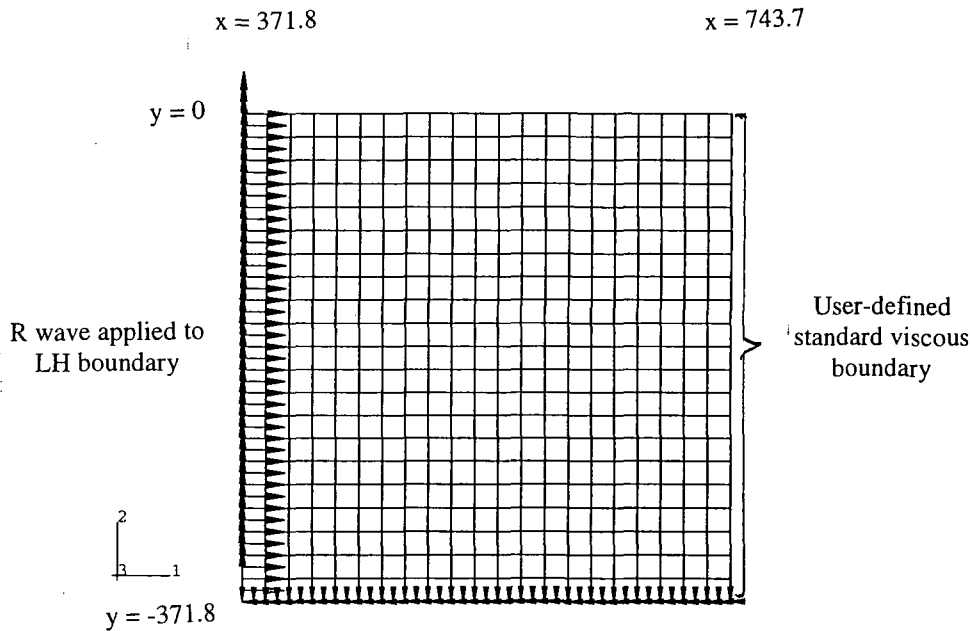


Figure 4.11(a) FE/IE axisymmetric mesh used to test the effectiveness of a user-defined standard viscous boundary in absorbing R waves

ABAQUS

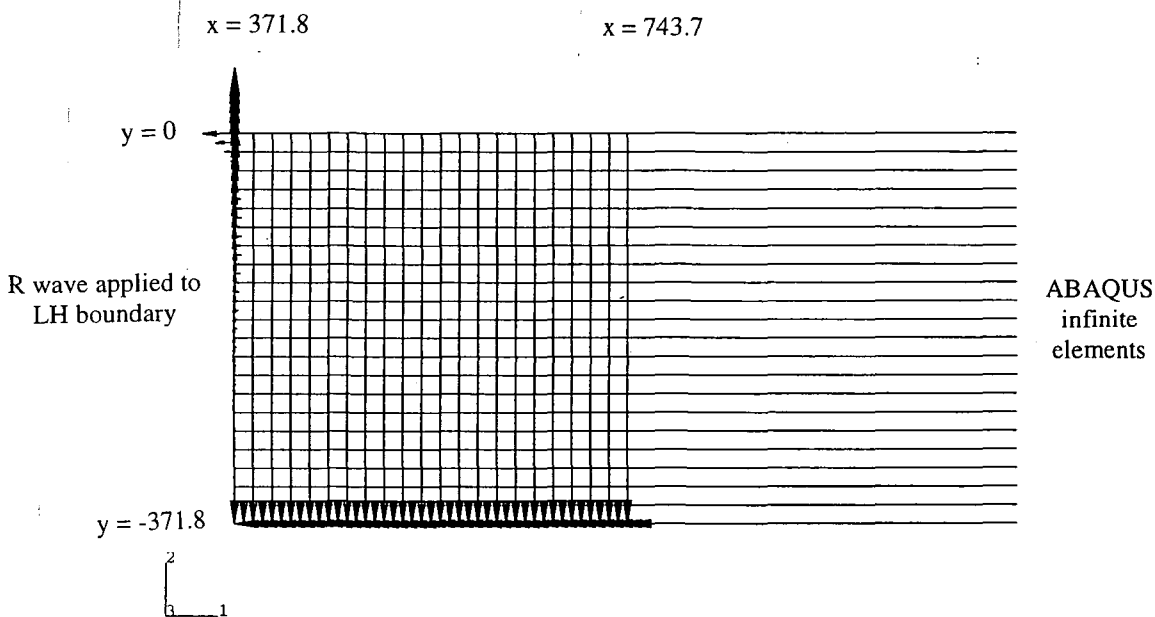


Figure 4.11(b) FE/IE axisymmetric mesh used to test the effectiveness of ABAQUS infinite elements in absorbing R waves

ABAQUS

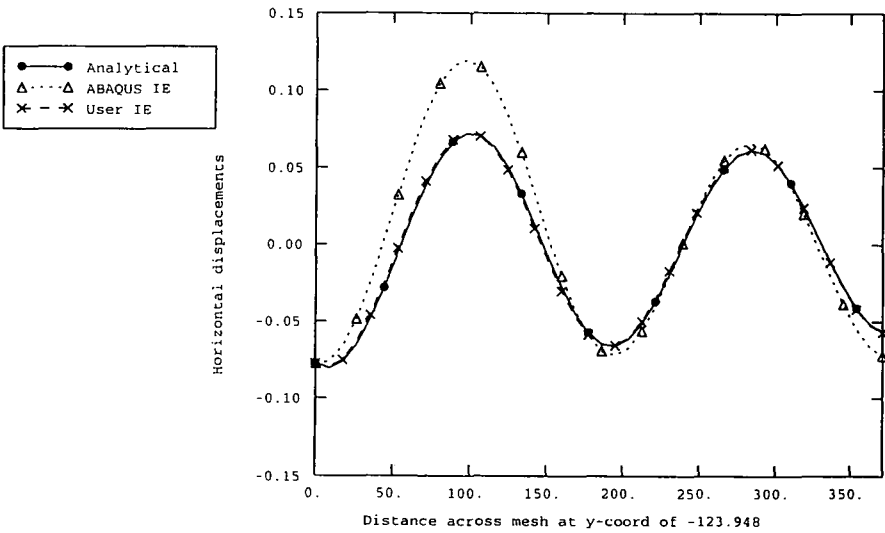


Figure 4.11(c) Comparison of the effectiveness of the boundaries in absorbing R waves in an axisymmetric FE/IE mesh: horizontal displacements across mesh

ABAQUS

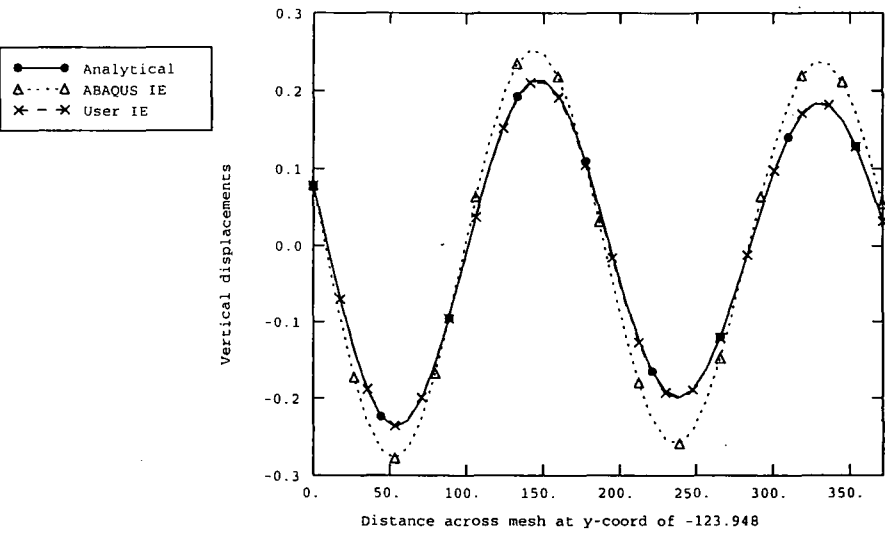


Figure 4.11(d) Comparison of the effectiveness of the boundaries in absorbing R waves in an axisymmetric FE/IE mesh: vertical displacements across mesh

CHAPTER 5

DEVELOPMENT OF A NUMERICAL MODEL FOR VIBRATORY PILING

5.1 INTRODUCTION

The prediction of ground vibrations generated by vibratory piling has, to date, been based on similar empirical techniques to those developed for percussive driving. Both the British Standard (BSI 1992b) and Eurocode (CEN 1998) relate the peak particle velocity at a given distance from the source to the square root of the energy per cycle of the vibrodriver. None of the methods for predicting vibration generated by vibratory piling consider the influence of any other variables, see Chapter 2.

Hiller (1999) has examined the validity of the methods presented in the literature for the prediction of vibration generated by vibrodriving on the basis of continuous vibration records for complete vibratory piling drives acquired during his research. Hiller suggests that the magnitude of vibration from vibrodriving is not related to the vibrodriver energy rating. Instead, he suggests that the magnitude of vibration at any instant in the drive is related to the resistance to driving, mainly on the pile shaft, which is a function of the soil type. This is also the opinion of Holeyman (2000), who concluded that the most critical parameter to be assessed in order to produce a reasonable prediction of vibro-drivability is the soil resistance to vibratory driving.

Further examination of the vibratory pile driving data obtained from the Transport Research Laboratory (Hiller, 1999) and by Uromeihy (1990) reveals some interesting phenomena. For example, the vertical particle velocities recorded during the first 12 seconds of the extraction of a pile from 15.5m depth by geophones at 8.9m, 16.9m, 33m and 61m on the Second Severn Crossing site are plotted in Figure 5.1. This shows that although the largest particle velocities are generally recorded by the geophones closest to the pile, as would be expected, there are occasions where the particle velocities recorded by the more distant exceed those of the nearer geophones. Similar non-monotonical decay of vibration with distance from source was observed during the extraction and installation of other piles on the Second Severn Crossing, as shown in Appendix E, and at other sites (Hiller, 1999).

Detailed inspection of Figure 5.1 indicates that the vibratory extraction commenced at an operating frequency of about 6.5 Hz increasing gradually to about 17.5 Hz in the first 5 seconds. During this time, the magnitudes of vibration recorded by the four geophones were highly variable, and the more distant geophones often recorded higher levels of vibration than the nearer geophones. For example, although the largest vertical particle velocities during the first 12 seconds were always recorded by the geophone at 8.9m, the geophone at 33m recorded significantly larger vibrations than the geophone at 16.9m for most of the first 3 seconds. On a few occasions, the geophone at 61m recorded higher vertical particle velocities than that at 33m. Similar effects were recorded by the geophones in the radial (longitudinal) direction (Figure 5.2), but it should be noted that increases in vertical particle velocity recorded by a particular geophone were not necessarily reflected by similar increases in the radial direction. This demonstrates the importance of recording and reporting the velocity/time traces in all three orthogonal directions, especially when the data are to be used to validate

computational models. These records indicate that the magnitude of vibration at any point on the ground surface appears to be a function of the operating frequency. However, the relative magnitudes of vibration at the geophones also appeared to vary when there was no apparent change in frequency, only a change in the depth of penetration of the pile into the ground. Of particular interest is the way in which amplification of vibration occurred discretely at certain horizontal distances from the source at various times during the extraction process. This phenomenon does not appear to have been previously identified or commented on in the literature.

The non-monotonical decay of ground surface vibrations has been observed on other sites for various types of pile driving (Uromehy 1990, Hiller 1999, Attewell et al 1991) and various attempts have been made to explain it. O'Neill (1971) and Massarsch (1992) suggested that the significant amplification that can occur during start-up and shut-down of a vibratory hammer is due to soil layer resonance. This occurs when the dominating frequency of the propagating wave coincides with the natural frequency of one or several soil layers. However, Holeyman (2000) suggested that this apparent resonance of soil vibration may be no more than the transient combination of increased rotation speed and soil degradation. He suggested that vibratory pile/soil interaction occurs in two modes; a coupled mode, where the soil remains in contact with the slowly vibrating pile and so the transfer of energy from pile to soil is nearly perfect, and an uncoupled mode, where as the vibratory motion accelerates, the soil degrades and liquefies, and the soil effectively uncouples itself from the motion of the pile. Hiller (1999) also suggested that the greater magnitudes of vibration that are often observed during start-up of the vibratory hammer may be because the energy transferred to the soil is dependent upon the resistance to movement. As the soil resistance will be greatest when the pile first starts to move, the greatest amount of energy will be transferred to the ground during the start-up process.

Attewell et al (1991) also identified that vibration amplitude at ground surface resulting from pile driving does not decay progressively as distance from the pile increases. They attributed this effect to the superposition of body waves from the pile toe and shear waves generated by pile/soil interaction on the pile shaft. This does not appear to be the explanation for the non-monotonical decay recorded during the extraction of piles at the Second Severn Crossing site because body waves are not generated at the toe during extraction of a pile.

There is clearly a case here for a new approach to the prediction of vibration generated by vibratory piling. The process is obviously extremely complex – Hiller suggests that the location of the vibration source is centred on the location of greatest soil resistance on the pile shaft and this will obviously move during the installation or extraction of the pile. The simple straight-line empirical relationships presented in the literature offer reasonable upper bounds to ground vibration. However they do not account for, or explain, the non-monotonical decay of ground surface vibrations shown in Figures 5.1 and 5.2 which has also been identified by Uromehy (1990), Attewell et al (1991) and Hiller (1999).

Computation and simulation of the ground waves generated by pile driving by finite element methods is now becoming feasible with the increasing power of computers (Ramshaw et al, 1998a,b, 2000, 2001). Analysis of the reasonably large finite element meshes required to model the ground waves generated by vibrodriving to distances of

about 50m can now be undertaken within a reasonable time frame (within 12 hours). Simulation of the generation and propagation of the ground waves may provide a scientific explanation for the variability of ground vibrations measured by geophones at various locations.

Extensive literature searches have revealed that full computational modelling of the ground waves generated by vibratory pile driving and extraction has not been attempted to date. Various workers have developed computational models to investigate vibro-drivability, (Holeyman, 2000 and Wong *et al*, 1992) and some of these modelling techniques have been adapted for this study. The only attempt to model the ground waves generated by piling is the work by van Staalduinen & Waarts (1992) who have developed a technique which uses data from cone penetration tests to characterise the ground conditions which are then used in a finite element program to predict ground vibrations. However, the proposed model had only been developed on one site for impact piling at the time of publication and required further validation. Waarts & Bielefeld (1994) report the modelling of another case history of impact piling using the same technique, and Bielefeld (1994) describes a technique for modelling vibratory stress waves in piles. However this was not extended to the modelling of ground vibrations from vibratory piling.

This Chapter presents new techniques using finite element methods for modelling the ground waves resulting from vibratory pile driving and extraction. The main objective in the development of the pile driving simulation is to design a model that can use, and be calibrated against, the large amount of vibration data available. Although several large databases of site records of "green-field" vibrations exist, including those held at Durham University (Uromeihy, 1990) and the Transport Research Laboratory (Hiller & Crabb, 2000), the data tend to be confined to ground surface vibrations at a few discrete stand-off distances, a description of the hammer and pile type and a brief description of ground conditions usually in the form of borehole records. The databases generally do not contain detailed records of pile excitation, such as amplitude of pile displacement and they certainly do not contain information about plastic and dynamic soil behaviour. Extensive literature searches have revealed that high quality measurements of all these parameters do not presently exist, although the data set from the 'SIPDIS' programme, referred to in Chapter 2, should become available in the next few years.

This thesis therefore presents a pragmatic approach to the problem. The lack of excitation data in conjunction with vibration measurements necessitated the modelling of the entire pile driving process including the hammer vibratory motion. This was achieved by combining, adapting and extending analytical models and finite element techniques developed by other workers. Various assumptions and simplifications were adopted in the absence of detailed information on soil parameters and the degradation and liquefaction of soils under vibratory loading. Soil response at the pile toe was modelled by simple mass-spring-dashpot systems based on typical soil parameters and pile/soil interaction was simulated using the friction model available in ABAQUS. Propagation of the ground waves was simulated with the soil assumed to be an elastic medium. Parametric studies based on the arrival times of ground waves at various distances from the vibration source were used to estimate values for the small strain stiffness of various soil types.



The resulting procedures are therefore not intended to be rigorous geotechnical analyses as the complex large-strain, dynamic and cyclic shear stress-strain strength behaviour of the soils surrounding the vibrating pile is not included. The models are designed so that they can be calibrated against the large databases of vibration data that exist and then used to improve the current empirical and conservative guidelines. The particular advantage of the models over empirical equations is that they offer an aid to understanding the complex patterns of ground waves that are generated by vibratory piling. The simplicity of the models also means that they could be used as a preliminary design tool for the prediction of ground surface vibrations where site data are sparse.

Development of the vibratory piling model has been undertaken in a number of stages and these are reflected in the structure of the remainder of this chapter. The chronological development of the model including the difficulties encountered and how they were resolved is described in Section 5.2. A detailed description of the resulting computational model for vibratory piling is given in Section 5.3. Preliminary use of this model to simulate case history data revealed that the vibratory motion induced by the piling process can cause a standing wave to be set up on the ground surface at certain frequencies. This is the first time that this phenomenon has been identified in the context of vibrations from vibratory piling and it is described in detail in Section 5.4. The effectiveness of the quiet boundary developed in Chapter 4 is investigated in Section 5.5. Calibration of the model against vibration data recorded during the extraction of casings at a site at the Second Severn Crossing is described in Section 5.6. Simulation of vibratory extraction as a first stage in the validation process allows calibration of the simulation of pile shaft/soil interaction without the complication of pile toe effects. Extension of the model to simulate the vibratory installation of casings at the Second Severn Crossing is described and compared with measured data in Section 5.7. The vibratory piling model is validated in Section 5.8 by simulating and comparing the results with the vibrations measured during the installation of an H pile into dense sand at a site in Flitwick, Bedfordshire. Conclusions and recommendations for further work are given in Section 5.9.

5.2 CHRONOLOGICAL DEVELOPMENT OF THE MODEL

Finite element modelling of the interaction between hammer, pile and soil does in itself present a number of difficulties. The model was developed in stages as a series of smaller pilot runs to determine the most effective method of simulating each part of the model, and several parametric studies were carried out before the main analysis. For example, many runs were undertaken to determine the most effective method of modelling the contact between pile and soil. This section describes the chronological development of the model, the difficulties encountered and how they were overcome, and the thought processes behind the design of the model presented in Section 5.3.

Work on the model began with the simulation of the pile driving process. Pile driving involves contact between the pile and the soil. Contact conditions in a finite element analysis are a special class of discontinuous restraint, allowing forces to be transmitted from one part of the model to another. The constraint is discontinuous because it is applied only when the two surfaces are in contact. When the two surfaces separate, no constraint is applied. The analysis has to be able to detect when the two surfaces are in

contact and apply the contact constraints accordingly. Similarly, the analysis must be able to detect when the two surfaces separate and remove the contact restraints.

To model contact conditions in ABAQUS, contact surfaces must be created on the various components of the model. The pairs of surfaces that may contact each other, known as contact pairs, must be identified. Finally, the constitutive models governing the interactions between the various surfaces, such as friction, must be defined.

ABAQUS provides several mechanical interaction models to describe the interaction of contacting surfaces, including a friction model. The ABAQUS friction model characterises the frictional behaviour between the surfaces using a coefficient of friction, μ . The product μp , where p is the contact pressure between the two surfaces, gives the limiting frictional shear stress for the contacting surfaces. The contacting surfaces will not slip until the shear stress across their interface equals the limiting frictional shear stress, μp . The solid line in Figure 5.3 summarises the ideal behaviour of the ABAQUS friction model: there is zero relative motion, or slip, of the surfaces when the shear stresses are less than μp . Modelling the ideal friction behaviour can be very difficult; therefore ABAQUS uses a penalty friction formulation with an allowable 'elastic slip', shown by the dotted line in Figure 5.3. The 'elastic slip' is the small amount of relative motion between the surfaces that occurs when the surfaces should be sticking. ABAQUS automatically chooses the penalty stiffness (the gradient of the dotted line) so that this allowable 'elastic slip' is a very small fraction of the characteristic element length.

Simulation of pile-soil contact was modelled in a number of stages to investigate and verify the contact capabilities of ABAQUS. In all cases, the pile was modelled as a number of connecting rigid elements. The first stage comprised a plane strain model of a pile resting on the ground surface subjected to a downward vertical displacement of 1 unit. The displaced mesh is shown in Figure 5.4 and shows that the pile has deformed the surface layers of the soil in the expected manner. The vertical stresses in the soil are plotted as contours in Figure 5.5. The displaced mesh and the contour plot of vertical stresses for the axisymmetric case are shown in Figures 5.6 and 5.7 respectively. These examples highlight a problem at the pile-soil interface: a gap appears because the nodes of the master surface (the pile) are coincident with those of the slave surface (the soil). In order to overcome this problem, the same axisymmetric case was modelled for a pile with a pointed toe, as shown in Figures 5.8 and 5.9, and for a pile with a rounded toe, as shown in Figures 5.10 and 5.11. These latter examples model the pile-soil interface very effectively with no gaps appearing between the contact surfaces.

The next stage of the simulation comprised an axisymmetric model of a pile sliding vertically against a soil surface in order to model the interaction between the pile shaft and the soil. The ABAQUS friction model was used to model the interaction between the pile shaft and the soil with a value for the coefficient of friction, μ , of 0.1. The soil elements beneath the pile toe were omitted for simplicity. The displaced mesh is shown in Figure 5.12 and the vertical and horizontal stresses in the soil at step 0 (initial geostatic stress) and step 1 (following pile displacement) are shown in Figure 5.13.

The final stage of the simulation comprised the combination of the pile toe and pile shaft models described above in order to model a pile being driven into the soil at depth. This simulation comprised an axisymmetric model of a pile with a rounded toe at a

depth of 1 unit. The pile was subjected to a vertical displacement of 0.9 units assuming a coefficient of friction, μ , of 0.1. The displaced mesh is shown in Figure 5.14 and the vertical stresses are plotted in Figure 5.15. This example appears to model pile-soil interaction fairly realistically but the plots do indicate some separation of the pile and soil elements at the corner between the pile toe and the pile shaft. The plot of vertical stress indicates a tensile stress concentration at this corner. This is probably caused by the soil elements at the corner being pulled down by the pile toe as the pile is displaced downwards and, at the same time, remaining connected to the rest of the finite element mesh. In reality, the soil particles at the corner of the pile would rearrange themselves and separate as the pile moved downwards.

This problem was largely overcome by the development of the two-stage model described in Section 5.3. In the first stage, the soil response at the toe is simulated by a spring and dashpot in parallel and a contact analysis is performed to model the interaction of the pile shaft with the surrounding soil. This effectively isolates the interaction of the pile shaft with the soil from the pile/soil interaction at the toe and the tensile stress concentration in the soil elements at the corner does not occur.

The simple finite element models described above were all constructed with a fixed boundary along the bottom of the mesh and a free boundary on the right hand side. An initial geostatic stress condition was applied prior to the contact analysis in order to model typical geotechnical conditions of a vertical stress increasing linearly with depth, equilibrated by the weight of the soil, and horizontal stresses caused by tectonic effects. These horizontal stresses provide the contact pressure, p , between the two contact surfaces (the pile and the soil) which is required to define the limiting frictional shear stress, μp , in the ABAQUS friction model. The soil was assumed to be unsaturated.

Some work was undertaken to validate the ABAQUS contact model by adapting some of the verification examples provided as part of the ABAQUS package. The units of the parameters used in these examples are not defined and appear to be fairly arbitrary (ABAQUS has no units built into it. The units chosen by the user must therefore be self-consistent.). A simple case of a 1.75 x 1.75 8-noded plane strain element coming into contact with a line of three 8-noded plane strain elements, sitting on a rigid surface, was set up in ABAQUS as shown in Figure 5.16. The single element was moved down so that its bottom surface coincided with the top surface of the line of three elements. A spring with a stiffness of 100 was attached to one side of the single element and a force of 100 was applied to the other side. The single element moved by 1 unit in the direction of the applied force and was independent of the value of the coefficient of friction applied. This demonstrates that a normal pressure must exist between contact surfaces in order for the ABAQUS friction model to work. (The application of a lateral force of 10 resulted in a horizontal displacement of 0.1.)

The case was repeated but this time a vertical pressure of 10 was applied to the top of the single element in the first step of the analysis as shown in Figure 5.17. A horizontal force of 100 was applied to the single element in the second stage of the analysis and resulted in a lateral displacement of 0.9475 for a coefficient of friction of 0.3 which agreed with hand calculations.

The methods of applying a contact pressure between a deformable element ($E=30e^6$, $\nu=0.3$) and a rigid surface were then investigated. (Again, the units of the parameters in

these examples were not defined.) A vertical pressure of 250 was applied to the top surface of an 8-noded plane strain element (5 wide and 5 high) in contact with a rigid surface as shown in Figure 5.18. This resulted in a contact pressure of 250 between the bottom of the element and the rigid surface and the top nodes of the element displaced downwards by $3.7917e^{-5}$. The analysis was then repeated but this time the top nodes of the deformable elements were fixed in the vertical direction and an upward force of 1250 (250×5) was applied to the rigid surface (Figure 5.19). Again, this resulted in a contact pressure of 250 between the bottom of the element and the rigid surface and the top nodes of the element displaced downwards by $3.7917e^{-5}$.

A similar case was then analysed for the axisymmetric condition as shown in Figure 5.20. A lateral pressure of 250 was applied to the right-hand side of the deformable element ($\nu=0.3$) resulting in a contact pressure of about 367 between the deformable element and the rigid surface. Hand calculations for this case indicate a contact pressure of about 379.

These simple test cases verified the contact surface mechanisms and behaviour.

Although the method of modelling pile-soil interaction appeared to be satisfactory at first, difficulties arose when infinite elements were added to the boundaries of the finite element mesh. Infinite elements were required to prevent the outwardly radiating ground waves generated by pile driving from reflecting from the boundaries of the finite element mesh and introducing errors into the results.

A significant problem encountered was that of rigid body motion. During dynamic response analysis following static preload, as is common in geotechnical applications, the traction provided by the infinite elements to the boundary of the finite element mesh consists of the constant stress obtained from the static response, with the quiet boundary damping stress added. Since the infinite elements have no stiffness during dynamic analysis, they allow a net rigid body motion to occur, as illustrated in Figure 5.21. The magnitude of this effect appears to be independent of the magnitude of the load: in this case the net displacement at the point of application of load is equal to 0.51 units for loads of 1 unit and 300 units.

Before the contact model could be implemented, it was necessary to develop a technique for applying the horizontal (normal) stresses on the pile from the soil in the FE/IE model in such a way as to avoid rigid body motion. The first problem was to determine the magnitude and distribution of the normal stress on the pile shaft during vibratory pile driving. The vertical harmonic motion of the pile induces shear stresses and strains in the soils in contact with the pile shaft. The pile also forces normal and potentially convective movement of soil below the pile toe. The behaviour of soil under loading from vibratory piling is therefore highly complex and the main elements that affect the complex large-strain, dynamic and cyclic stress-strain behaviour of the soil are summarised by Holeyman (2000).

Wong et al (1992) proposed a model for vibratory pile driving in sand which was verified with large-scale laboratory tests. In particular, they demonstrated the importance of the soil parameters (relative density and particle size) and in situ stress conditions on pile drivability in the determination of the non-linear soil resistance.

Holeyman's opinion (2000) is that the most critical factor determining vibro-drivability is the soil resistance to vibratory driving. Holeyman (1996) suggested a more involved assessment of the degradation parameters adopted to assess the vibratory penetration resistance based on CPT results. In this method, the soil driving resistance is obtained by interpolation between a static value and an ultimately degraded value. The driving base and shaft unit resistances are derived from the static and the liquefied soil resistances depending on the vibration amplitude

From the literature it appears that horizontal in situ stress is an important factor in the determination of the non-linear soil resistance to vibratory pile driving. It is likely that the in situ stress is a major factor in the initial resistance to motion provided by the shear strength of the soil during first few cycles (coupled behaviour), before soil degrades and liquefies (uncoupled behaviour). Degradation of soil can be modelled by reduction in the coefficient of friction used in the contact model.

The values of skin friction, τ_s , for piles in non-cohesive soils can be calculated from the expression

$$\tau_s = \sigma'_n \tan \delta = K \sigma'_v \tan \delta \quad (5.1)$$

where σ'_n is the normal effective stress acting around the pile shaft after installation, and δ is the angle of friction between the pile and the soil. The normal stress may be represented by some ratio K of the vertical effective stress σ'_v , as shown. The appropriate values of K will depend on the in-situ earth pressure coefficient, K_0 , the method of installation of the pile and the initial density of the non-cohesive soil.

In the past, the skin friction around a pile shaft in a cohesive soil was usually estimated in terms of the undrained shear strength of the soil, by means of an empirical factor, α , (Tomlinson, 1957) giving

$$\tau_s = \alpha \cdot c_u \quad (5.2)$$

The value of α deduced from pile load tests appears to reduce from unity or more for piles in clay of low strength, down to 0.5 or below for clay above about 100kN/m². However, plots of measured values of skin friction from driven piles against the shear strength of the soil generally demonstrate a large amount of scatter and this has led to the development of alternative, more scientific approaches.

Chandler (1968) considered the bond between pile and soil as purely frictional in nature, with the resulting skin friction a function of the normal effective stress, σ'_n , and an interface friction angle, δ , in much the same way as for piles in free-draining soils. The normal stress was related to the effective overburden stress, σ'_v , by a factor, K , to give

$$\tau_s = \sigma'_n \tan \delta = K \sigma'_v \tan \delta = \beta \sigma'_v \quad (5.3)$$

where $\beta = K \tan \delta$. The value of K will vary depending on the type of pile (driven or bored) and the past stress history of the soil.

The skin friction on the pile in both non-cohesive and cohesive soils has been shown to be dependent on the effective overburden pressure (equations 5.1 and 5.3) and this is likely to be the case during, as well as after, installation. It was therefore decided to simulate the normal stresses on the pile by applying a lateral force, equivalent to the sum of all of the horizontal forces on the pile from the soil, to the rigid pile elements. In ABAQUS, forces and displacements are applied to rigid bodies (rigid elements or rigid surfaces) through a reference node at some convenient position in the mesh. The application of this lateral force to the reference node for the rigid pile elements simulated a radial expansion of the pile into the surrounding soil, thereby generating a normal pressure on the pile/soil interface equivalent to the average lateral pressure on the pile. Mabsout & Tassoulas (1994) used a similar approach by inserting special “pressure elements” down the length of the pile shaft in order to apply the lateral soil pressure on the pile.

Variation in the lateral soil pressure with depth was simulated by factoring the relevant coefficient of friction with respect to the average horizontal stress for the whole depth of penetration of the pile. A series of rigid surfaces was used to model the contact surfaces of the pile as opposed to rigid elements because the latter resulted in convergence problems when a number of varying friction coefficients were applied. Several analyses were undertaken to check that both analyses gave similar results for simple cases.

When the main modelling difficulties had been resolved, the model was used to simulate some case history data from the Second Severn Crossing. An extensive parametric study was undertaken to determine the sensitivity of the model to various parameters. Once reasonable matches were obtained with measured data, the techniques developed for choosing parameters were tested by modelling a completely different case history from Flitwick, Bedfordshire.

The finite element model that has been developed for vibratory piling is presented in the following section.

5.3 A FINITE ELEMENT MODEL FOR VIBRATORY PILING

5.3.1 General

The model for simulating pile response to cyclic excitation and the generation and propagation of ground waves has been developed as a two-stage procedure as follows.

In stage one, the objective is to establish a model for rigid body vertical oscillation of the pile in response to the cyclic excitation of the vibro-driver. This is done by the use of rigid axisymmetric elements for the pile shaft, limited slip contact elements at the interface nodes, a limited axisymmetric finite element/infinite (FE/IE) mesh representing the soil around the pile shaft (Figure 5.22), and a mechanical model for toe reaction based on a spring and dashpot in parallel (Figure 5.23), proposed by Lysmer & Richart (1966). The pile/soil interface comprises a two-surface contact and the interaction between the surfaces is modelled using the friction model available in ABAQUS. A static computation is made to simulate the normal stresses on the pile/soil interface from the soil. A dynamic analysis is then conducted to set up a steady state response of the rigid pile to the cyclic excitation from the hammer using the technique developed to avoid rigid body motion of the entire FE mesh as described previously.

In the second stage, a large FE/IE mesh is established (Figure 5.24) and the sinusoidal displacements of the soil nodes on the pile/soil interface and under the pile toe, computed in stage one, are imposed in the form of Fourier series. Spurious wave reflections from artificial boundaries are prevented by the use of infinite elements around the periphery of the model. Material damping is applied in the form of Rayleigh damping.

There are several advantages of breaking down the computations in this way. Complex inelastic soil properties and contact conditions can be modelled in the first stage using a relatively small finite element mesh, thus reducing the number of computations required. Once the displacements on the pile/soil interface have been determined, these can be applied directly to the soil interface nodes in the second stage of analysis where a simpler linear-elastic model of the soil is used to model the propagation of ground waves over large distances. In addition, this staged approach allows each parameter or group of parameters to be isolated, and rapid parametric studies can be used to ascribe values. This approach is particularly useful for modelling vibratory pile installation because the first stage allows the interaction of pile shaft with the soil to be isolated from the pile/soil interaction at the toe.

5.3.2 Mesh Design (Representation of the Ground)

A two-dimensional axisymmetric finite element/infinite element (FE/IE) mesh is used to represent the ground in all cases. This obviously assumes axial symmetry but is much less computationally expensive than a full three-dimensional analysis. An axisymmetric mesh gives the best two-dimensional representation of the geometric damping of ground waves from a central source such as a pile.

Eight-noded (second order) quadrilateral elements are used to represent the soil as these have the advantage of being computationally efficient and allow curved geometries to be modelled more accurately.

A given element can only propagate waves accurately up to a cut off frequency defined by the size of the element and its shape functions. The element acts as a low pass filter and will filter out the high frequency components of the signal. The elements are therefore chosen so that there are 10 nodes per wavelength of the shortest wavelength to be propagated (usually the P-wave at the highest frequency of the vibrodriver).

Since the mesh will be used in dynamic analyses, it is designed to be as uniform as possible in order to prevent spurious wave reflection within the finite element mesh itself. As the wavefronts will travel through all parts of the model given sufficient time, all points within the mesh are equally important at different times in the response and therefore a uniform mesh is required. If a non-uniform mesh is used, the finer part of the mesh will propagate higher frequencies than the coarser part. There will then be reflections of the high frequency components and the wave will not propagate correctly. The mesh must therefore be fine enough in its coarsest region for it to propagate the highest frequency in the input.

In terms of the practicalities of mesh design, it is necessary to ensure that nodes occur at geophone locations for comparison with measured vibration records. The elements are defined in groups to simplify the definition of the various soil strata and water table.

The meshes are also created for the maximum depth of pile so that the same mesh can be used to model the pile at various shallower depths.

For simplicity, the finite element mesh for the first stage of analysis is taken to be a truncated version of the main mesh, usually terminating at a convenient point about 10-12m from the pile. Check analyses have been performed to ensure that the closer boundary does not affect the pile-soil interaction.

Infinite elements are placed around the boundaries of both the truncated and main finite element meshes to model the far-field and minimise the reflection of outgoing waves back into the finite element mesh. As the first stage of the analysis is primarily concerned with pile/soil interaction rather than wave propagation, the ABAQUS infinite elements are considered to provide an adequate quiet boundary. The most effective boundary for the second stage of analysis, which simulates the propagation of ground waves, is the new quiet boundary developed in Chapter 4. The application of the new boundary to the vibratory piling model and its performance is discussed in more detail in Section 5.5.

5.3.3 Representation of the pile

As the model is defined in an axisymmetric plane, it is necessary to model the pile as an equivalent circular section. The diameter of the pile is assumed to be the maximum dimension of the pile section. This is accurate for a cylindrical or tubular pile, closely similar for a square section, and an adequate representation for 'H' sections and sheet piles. Makris and Gazetas (1993) have shown that during longitudinal oscillation, every point along a pile can be assumed to be in phase, or very nearly in phase. The pile is therefore modelled as a rigid axisymmetric body in the finite element analysis oscillating about a fixed point or reference node. The inertial properties of the pile are incorporated in ABAQUS by attaching a mass element to the reference node associated with the rigid pile elements.

5.3.4 Material Properties (Soil behaviour under vibratory loading)

A staged approach to the analysis is helpful because it allows the insertion of large-deformation, high strain parameters for the near-field (stage one) model and very small strain parameters for the far-field modelling of the propagation of the ground waves (stage two).

The behaviour of soil under loading from vibratory piling is highly complex. The vertical harmonic motion of the pile induces shear stresses and strains in the soils in contact with the pile shaft. The pile also forces normal and potentially convective movement of soil below the pile toe. The understanding of the shear stress/shear strain relationship is therefore of paramount importance and has been extensively studied within the field of earthquake engineering. Laboratory testing of soil samples (mainly triaxial and simple shear testing) has led to the development of constitutive relationships representing the complex large-strain, dynamic and cyclic shear stress-strain strength behaviour of the soils surrounding the vibrating pile. Holeyman (2000) summarises the elements that require characterisation for these constitutive relationships as follows:

- Static stress-strain law expressing non-linear behaviour under monotonic loading and hysteresis upon strain reversal,
- Shear modulus at small strains and ultimate shear strength,
- Softening and increase of hysteretic damping with increasing strain,
- Effect of strain rate on initial shear modulus and ultimate shear strength,
- Degradation of properties resulting from the application of numerous cycles, and
- Generation of excess pore pressure leading to substantial loss of resistance and possibly to liquefaction.

Holeyman (2000) reviews the current state of knowledge on the above mainly in the context of vibro-drivability.

The problem for this study, however, is that detailed data about soil parameters are currently not available for the sites where vibration data have been acquired. The characterisation of the relationships described above is therefore not possible, although the staged approach would allow such relationships to be modelled if the data became available.

As the soil data from pile installation sites are often confined to a description, a range of typical values for shear stiffness and density have been used for the first stage of analysis where the strains local to the pile are very large and liquefaction commonly occurs. Typical Mohr-Coulomb parameters have been derived from the soil descriptions, standard penetration test data and laboratory test results using the guidance given in BS5930 (1981).

In the second stage of analysis the soil is modelled as a linear-elastic medium as it has been shown that beyond a short distance from the pile (about one pile radius) most of the energy is propagated in the form of elastic waves (Massarsch 1992). Parametric studies based on the arrival times of ground waves at various distances from the vibration source indicate that the small strain stiffness of the ground in the far-field is much greater than the large-strain stiffness in the vicinity of the pile. The non-linear stress-strain behaviour of soils which demonstrate very high stiffness at very small strains has often been observed (eg. Matthews et al, 1996). The small-strain stiffness of the soils in the cases presented in this thesis have therefore been back-analysed from the observed arrival times of various wavefronts at the geophones, see Section 5.6.3.

Material damping is applied in the form of a Rayleigh damping ratio given by

$$\xi = \frac{\alpha}{2\omega_u} + \beta \frac{\omega_u}{2} \quad (5.4)$$

where $\omega_u = \sqrt{k/m}$ = undamped frequency of vibration. A typical damping ratio of 5% has been suggested by Massarsch (1992) for the elastic range of soil deformations.

5.3.5 Simulation of pile-soil interaction

For the purposes of this study, the interface between the pile shaft and the soil is modelled using a surface-based contact simulation, with slip controlled by the friction

model available in ABAQUS. It is possible to apply a maximum allowable equivalent shear stress limit, τ_{\max} , across the interface so that regardless of the magnitude of the contact pressure stress, sliding will occur if the magnitude of the equivalent shear stress reaches this value.

In order to generate the horizontal stresses on the pile from the soil, a lateral force equivalent to the sum of the horizontal forces on the pile shaft is applied to the reference node associated with the rigid pile elements. This avoids the problem of rigid body motion described in Section 5.2. The application of this lateral force to the reference node for the rigid pile elements simulates a radial expansion of the pile into the surrounding soil, thereby generating a normal pressure on the pile/soil interface equivalent to the average lateral pressure on the pile.

Variation in the lateral soil pressure with depth was simulated by factoring the relevant coefficients of friction with respect to the average horizontal stress for the whole depth of penetration of the pile.

5.3.6 One-dimensional model for pile toe response

The dynamic response of the soil under the pile toe is simulated using the one-dimensional model proposed by Lysmer and Richart (1966) to simplify the analysis of the dynamic response of rigid footings. This model comprises a spring and dashpot in parallel as shown in Figure 5.23

Lysmer and Richart used the complex compliance of a half-space model with a Poisson's ratio of 1/3 to compute equivalent spring and dashpot constants. Although these parameters are dependent on dimensionless frequency, constant values were selected which gave reasonable agreement with the half-space model. Because the variation of complex compliance with Poisson's ratio is quite small, Lysmer and Richart suggested that the model be used for all values of Poisson's ratio. This suggestion has largely been followed, and all rational models of pile-driving dynamics have employed base models derived from the elastic response of Lysmer's analogue (eg. Deeks and Randolph, 1995, Wong et al, 1992)

The values for spring constant (k), and damping constant (c) are calculated from the following equations:

$$k = \frac{4GR}{1-\nu} \quad (5.5)$$

$$c = 0.85K \frac{R}{c_s} \quad (5.6)$$

where G is the soil shear modulus, R is the radius of the footing, ρ is the soil bulk density and c_s is the shear wave velocity,

$$c_s = \sqrt{\frac{G}{\rho}} \quad \text{bis (2.13)}$$

In ABAQUS all of the springs and dashpots in the model have to be defined and inserted before the first step of the analysis. They can not be defined and inserted within the analysis steps themselves. As the first step of the analysis is a static computation to generate the normal stresses on the pile from the soil, the springs and dashpots attached to the rigid pile have to be removed using the *MODEL CHANGE command in ABAQUS. The spring and dashpots can then be reapplied using the same command in the second dynamic step of the analysis.

5.3.7 Simulation of vibratory hammer motion

The cyclic excitation of the hammer in the dynamic analysis is given by

$$F(t) = m.e.\omega^2 \quad (5.7)$$

where m is the total mass at eccentricity e , rotating at ω rad/s.

The range of operating frequencies and the eccentric moment ($m.e$) of any particular piling hammer are generally given in the manufacturer's hammer specification.

Care must be taken to ensure that the analysis does not allow the motion of the pile to exceed the maximum amplitude rating of the specified vibratory hammer. This is a possibility where the friction on the pile-soil interface is very low, thus allowing large oscillation of the pile. In this case, the sinusoidal displacement of the pile should be specified directly in the analysis and should be equal to the maximum amplitude rating of the hammer.

5.3.8 Analysis Procedure

Excitation of the ground by vibratory piling is primarily sinusoidal and continuous (a periodic forcing function). The most efficient solution methods for periodic forcing functions are those which calculate the steady state response directly. This is usually done in terms of the harmonic response in the frequency domain for each frequency in the Fourier series rather than in the time domain where the computation has to continue long enough for the transient response to have decayed away. This is typically fifty to one hundred cycles of oscillation for light damping.

ABAQUS provides a direct harmonic response analysis but unfortunately ABAQUS does not allow the insertion of user-defined elements into any of its frequency domain analyses. As one of the main objectives of this work was to develop a new quiet boundary for the absorption of ground waves from piling, this was a serious restriction and dictated the use of the general dynamic analysis in the time domain for the vibratory model. This type of analysis is more computationally expensive in that the computation has to continue until a steady state response is achieved – usually after 1.0-1.5 seconds. Although the method did not appear to be ideal, several advantages became apparent with the use of a time domain analysis. Firstly, the initial start up transient response could be used to determine suitable parameters for the dynamic stiffness of the soils from the measured arrival times of the various wavefronts at the geophones. Secondly, the output from the time domain analyses could be directly compared to the velocity/time traces recorded by geophones. A limitation of frequency domain analyses in ABAQUS is that the program only allows the user to plot variables against frequency

and not time. Finally, the use of time domain analyses indirectly led to the discovery of the 'standing wave' phenomenon described in Section 5.4.

This work was primarily concerned with developing a model to simulate the measured ground response from vibratory piling. Validation of the model has been achieved by matching the predicted ground response with the measured response for the single operating frequency recorded at each discrete depth of pile penetration. Frequency analyses are particularly valuable in the prediction of ground response for a range of operating frequencies, and can be used to specify and control the range of operating frequencies used during vibratory piling so as to control excessive vibration.

It was decided to split the problem into two stages of analysis for the reasons given in Section 5.3.1 above. The analysis procedures for each stage are described in detail below.

Stage One: Pile/soil interaction model

The pile/soil interaction model requires an initial static analysis where the lateral stresses on the pile from the soil are simulated by applying an average lateral force to the reference node associated with the rigid pile elements. In effect, this expands the pile into the soil to create contact pressures between the pile shaft and the soil. After static equilibrium has been achieved, a periodic forcing function representing the vibrating hammer (see Section 5.3.7) is applied in a vertical direction to the reference node of the rigid pile and a dynamic analysis is undertaken. Where preliminary analyses indicate that the pile displacement exceeds the maximum amplitude rating of the hammer, the maximum amplitude is applied to the reference node directly at the frequency of the vibrodriver.

The purpose of the stage one analysis is to undertake a contact analysis to compute the vertical displacement functions of the soil nodes on the pile-soil interface for input into the stage two analysis. Extraction of these functions from the output generated by an ABAQUS time domain analyses involves a lengthy procedure as follows. The vertical displacement functions are extracted during post-processing and saved in a separate file. The maximum and minimum displacements, together with the times at which the maximum displacements occur, are then manually extracted from this file for each node on the pile-soil interface and inserted into three separate files (max.dat, min.dat and tmax.dat respectively). These data are then read into a short fortran program (disp2vib.f) which was written to calculate the Fourier constants which describe the sinusoidal displacement of each node. The program then puts them into the correct format for input into ABAQUS. The fortran program is presented in Appendix F.

Stage Two: Wave propagation model

The sinusoidal displacements of the nodes on the pile-soil interface calculated by the stage one analysis are imposed on the equivalent soil interface nodes on the edge of the stage two FE/IE mesh in the form of Fourier series. A dynamic analysis is undertaken to simulate the ground waves generated by the oscillating pile and to calculate the vertical and radial particle velocities at various distances from the pile at the surface for comparison with measured vibration traces at geophone locations.

5.4 THE 'STANDING WAVE' PHENOMENON

5.4.1 Identification of the phenomenon

Following development of the model for vibratory piling, work commenced on using the model to simulate some case history data of vibratory piling at the Second Severn Crossing. A parametric study was commenced to investigate, in the first instance, the sensitivity of the ground response to the magnitude and distribution of the shaft friction, the effects of material damping and the stiffness of the soil. However, as the work proceeded, it became apparent that the ground response did not attenuate uniformly with distance from the source, as shown in Figure 5.25 which plots the velocity/time traces for nodes on the surface of the mesh at various distances from the pile. This shows that the maximum amplitude of vibration (the ppv) does not decay uniformly with distance from the pile, indeed, at distances of 6.3m to 10.35m from the pile the ppv increases from about 4.5mm/s to almost 9mm/s. In order to investigate this further, the vertical and radial particle velocities for all of the nodes along the top edge of the finite element mesh (Figure 5.26), representing the ground surface, were plotted against time (Figures 5.27 and 5.28). Although these figures appear to be quite complex, they are simply the velocity/time traces for each surface node on the surface of the mesh superimposed onto one graph. The data have been separated into four sets, namely the nodes between 0.75m to 10m, 10.25m to 20m, 20.25m to 30m and 30.25m to 40m, for clarity.

Unfortunately, ABAQUS/Post did not allow the generation of plots of maximum particle velocity at each node on the surface of the mesh against horizontal distance from the pile. However, as the nodes were equally spaced at 0.25m centres, portions of the envelopes of these plots are the same as the corresponding graphs of maximum particle velocity versus horizontal distance from the pile, as shown in Figures 5.27 and 5.28. These plots revealed that the vibratory motion induced by the piling process may generate a component of a standing wave on the ground surface at certain frequencies. The non-travelling wave generated on the ground surface by vibratory piling does not contain nodal points (points of zero amplitude) and is not therefore a true standing wave. However, for convenience, the term 'standing wave' will be used to describe the phenomenon in this thesis. This is the first time that this 'standing wave' phenomenon has been identified in the context of vibrations from vibratory piling.

The 'standing wave' phenomenon was first identified for a simulation of vibratory piling extraction in a uniform soil. It was therefore concluded that the 'standing wave' was not caused by a particularly complex pattern of ground waves, and therefore may be a common occurrence where the frequency range of the vibratory hammer falls within the range of natural frequencies of the soils.

Checks were then undertaken to ensure that the 'standing wave' was not due to reflection from boundaries or some other function of the size of the finite element mesh. Identical analyses were run using finite element meshes of varying size and nodal spacing. The 'standing wave' patterns obtained for the same input into various mesh configurations were the same apart from some minor reflection depending on the position of the boundary.

The 'standing wave' appears to be caused by the differing soil displacements that are generated as a result of the pile/soil interaction analysis. If a uniform displacement is

applied to all of the pile/soil interface nodes, the maximum particle velocities of the surface nodes decrease uniformly with distance from the source as shown in Figures 5.29 and 5.30. However, when the differing sinusoidal displacement functions of the nodes on the pile-soil interface calculated by the stage one contact analysis are imposed on the equivalent pile-soil interface nodes on the edge of the FE/IE mesh, the maximum particle velocities of the surface nodes do not decay uniformly with distance, and may actually increase with distance from the source, as shown in Figure 5.29 and 5.30. This indicates that the interaction of the vibrating pile with the soil around the pile shaft which varies down the pile shaft may generate a complex pattern of ground waves which interact to form a 'standing wave' on the ground surface. (It should be noted that Figures 5.29 and 5.30 are only illustrative as the input functions are not directly comparable).

5.4.2 Frequency effects

As expected, the shape of the 'standing wave' alters with change in frequency, particularly in the vicinity of the pile, as shown in Figures 5.31 and 5.32 which show the velocity/time traces obtained for the same input parameters but for frequencies of 15.2 Hz and 20.9 Hz respectively. This is because the 'standing wave' is generated when the frequency of the vibratory hammer matches a natural frequency of the ground. In particular, the magnitude of particle velocity at any point on the ground surface may change markedly in relation to other points in response to changes in frequency. For example, referring to Figure 5.31, the peak vertical particle velocity for the node at 10m changes from about 2.4mm/s at an operating frequency of 15.2 Hz to 1.6mm/s at a frequency of 20.9Hz.

It should be noted that the operating frequency of the hammer affects the value of the maximum vertical force applied to the pile ($F=m_0e\omega^2$) and therefore the effect on the vertical force on the pile of any change of frequency is squared. A change in the vertical force on the pile will result in a change in the amplitude of the vibratory motion of the pile and hence an increase or reduction in the motion transmitted to the ground.

5.4.3 Influence of the depth of pile penetration/distribution of shaft friction

Several analyses were undertaken to study the effect of depth of pile penetration on the shape of the 'standing wave'. This was achieved by analysing parallel runs with the same operating frequency, but with differing depths of penetration. The resulting velocity/time traces for an example of a pile at depths of 11m and 13.8m, vibrating at a frequency of 22.3 Hz in both cases, are shown in Figures 5.33 and 5.34. The magnitude of vibration at each of the nodes changes very significantly, particularly in relation to each other, indicating that the shape of the 'standing wave' is also dependent on the depth of penetration of the pile. It is suggested that the shape of the 'standing wave' is primarily influenced by the nature of soil displacement around the pile shaft and so the depth of pile penetration has a major influence. However, it should be noted that the resistance of the soil to vibratory motion is dependent upon many factors, not least the frequency of the motion.

It is very difficult to determine whether the discrete increases in vibration amplitude that were observed at particular geophones during pile extraction at the Second Severn Crossing site were caused principally by changes in frequency or by changes in the depth of penetration. This is because, during vibratory pile extraction or installation, the operating frequency tends to change with the depth of penetration of the pile into the

soil. However, it has been shown above that changes in the depth of pile penetration at a constant operating frequency can significantly change the shape of the 'standing wave' and thus the relative magnitudes of the vibrations at geophone positions. This supports the view of Holeyman (2000) and Hiller (1999) that the magnitude of vibrations generated by vibratory piling primarily depends on the pile/soil interaction. Changes of operating frequency also appear to affect the shape of the 'standing wave'. These effects are likely to be more obvious during start-up simply because this is usually the time of greatest change in frequency, but also because as the frequency increases it may pass through some of the natural frequencies of the soil leading to resonance.

5.4.4 Summary

The generation of a 'standing wave' on the ground surface at certain combinations of hammer frequency, depth of pile penetration and ground conditions has several implications for the monitoring and modelling of ground waves generated by vibratory piling, as follows:

- The presence of a standing wave on the ground surface means that attenuation of the surface vibrations may be highly non-linear and can not be interpolated from measurement of particle velocities at discrete, widely spaced, geophone locations.
- The particle velocities recorded at discrete locations on the ground surface will not necessarily record the maximum amplitudes of vibration generated by the vibratory piling.
- When hammer operating frequencies and ground conditions are such that generation of a standing wave is likely, it is recommended that geophones are placed at closely spaced intervals in order to determine the shape of the resulting standing wave.
- In order to validate fully the vibratory piling model presented in this chapter, a full set of data recorded by closely spaced geophones is required to check that the standing wave predicted by the model is correct. Unfortunately, such a data set is currently not available.
- The vertical and radial particle velocities resulting from vibratory piling simulations should be plotted for all of the surface nodes to check for the presence of a standing wave.

5.5 APPLICATION OF NEW QUIET BOUNDARY TO MODEL

This section investigates the effectiveness of the new quiet boundary developed in Chapter 4 in absorbing ground waves produced by vibratory piling. The vibratory piling model used in this study was based on typical parameters from the Second Severn Crossing data.

It was decided to model a vibratory extraction case first because the excitation is limited to the interaction between the pile shaft and the soil and is not complicated by additional P wave generation at the pile toe.

The extraction of a 15.5m long, 1050mm diameter, casing from a depth of 13.8m was modelled. The PTC50H3 vibratory hammer was assumed to vibrate at its maximum amplitude of $\pm 22\text{mm}$ in order to model the worst case scenario. The coefficient of friction between the pile and soil was assumed to be 0.1 for simplicity.

Uniform ground conditions were assumed and the parameters used in the wave propagation model were as follows:

$$E=50e^6N/m^2$$

$$\nu=0.25$$

$$\rho= 1750kg/m^3$$

The size of the axisymmetric finite element mesh was then chosen on the basis of the propagation velocities of the P, S and R waves calculated for this material, as follows.

The propagation velocity of a P wave is given by

$$c_p = \sqrt{\frac{\lambda + 2G}{\rho}} \quad \text{bis (2.10)}$$

The propagation velocity of an S wave is given by

$$c_s = \sqrt{\frac{G}{\rho}} \quad \text{bis (2.13)}$$

and the propagation velocity of an R wave for a Poisson's ratio of 0.25 is given by

$$c_r = 0.9194 \sqrt{\frac{G}{\rho}} \quad \text{bis (2.14)}$$

Inserting the soil parameters into equations (2.10) - (2.14) gives the following wave propagation velocities:

$$c_p=185m/s$$

$$c_s =107m/s$$

$$c_r =98m/s$$

To investigate the effectiveness of the various boundaries, it was decided to compare the responses with a finite element (FE) mesh large enough to prevent any reflections from reaching the area of interest. With the particular set of soil parameters chosen above, the most appropriate mesh appeared to be an 80m wide, 40m deep FE mesh with ABAQUS infinite elements attached to the right-hand vertical boundary and the bottom horizontal boundary as shown in Figure 5.35.

This mesh size allowed the study of the first 1.0 second of response without any significant reflection back into a 40m radius of the pile. With the particular set of parameters chosen, any S wave reflection would only have travelled to within 53m of the pile ($80-[107-80]=53$) and any R wave reflection would have only travelled to within 62m of the pile ($80-[98-80]=62$). Only any P wave reflection would be travelling fast enough to reach the vicinity of the pile. However in this case P wave reflection

could be considered to be negligible as the choice of vibratory extraction minimised P wave generation, P waves attenuate on a hemispherical wavefront and the ABAQUS infinite elements on boundaries should totally absorb any plane P waves impinging orthogonally on the boundary. The 80m wide FE mesh can therefore be considered to give a realistic response within a 40m radius of the pile for the first 1.0 second.

The FE mesh comprised 8-noded quadrilateral elements of equal size throughout to prevent reflection within the mesh. The size of the elements (0.5m x 0.5m) was chosen to be small enough to model all of the waves accurately for a typical frequency of vibratory hammer operation of 15.2 Hz.

The various boundary conditions were then applied to the right-hand vertical boundary of a 40m x 40m FE mesh with ABAQUS infinite elements along the bottom horizontal boundary as shown in Figure 5.36. The particle velocities of all of the surface nodes between 0.75m and 40m could then be compared to those for the 80m x 40m FE/IE mesh (Figure 5.35).

The performance of the ABAQUS infinite elements was determined first. The ABAQUS infinite elements were applied to the vertical boundary of the 40m wide FE mesh as shown in Figure 5.37. The vertical particle velocity/time traces for all of the surface nodes between 0.75m and 10m, 10m and 20m, 20m and 30m, and 30m and 40m are compared with those for the 80m wide FE/IE mesh in Figure 5.38. The corresponding radial particle velocity/time traces are given in Figures 5.39.

These figures demonstrate that the ABAQUS infinite elements do not provide a perfect boundary. The reflection from the boundary is immediately obvious.

If the same vertical particle velocity/time traces are produced for the whole time period of 0.0 to 1.0 second, the propagation of the reflecting waves can be clearly seen (Figure 5.40). The first indication of reflection within a 10m radius of the pile occurs at about 0.74 seconds. This means that the reflected wave must have travelled 40m to the boundary and then at least 30m back in order for the effect to be visible within this part of the mesh. This means that the wave must have travelled with a velocity of between 95m/s and 108m/s and must therefore be an S or R wave. No reflection from the faster moving P waves is evident in these graphs, as expected.

The Rayleigh viscous boundary, developed in Chapter 4, was then applied to the vertical boundary of the 40m wide FE mesh, from the ground surface to a depth of 40m, as shown in Figure 5.36. The vertical and radial particle velocity/time traces of all of the surface nodes are compared with those for the 80m wide FE/IE mesh in Figures 5.41 and 5.41. These figures demonstrate the superiority of the Rayleigh viscous boundary over the ABAQUS infinite elements in absorbing ground waves from vibratory piling. Some reflection is still evident which is likely to be due to the reflection of S waves which are not perfectly absorbed by the Rayleigh viscous boundary.

In order to try and improve the performance of the boundary, it was decided to adopt a similar approach to that used by Chow & Smith (1981) who applied infinite elements derived using the Rayleigh wave number near to the free surface. They interpreted 'close to the surface' as 0.1 times the wavelength of the shear wave. Below this, they applied infinite elements derived using the P wave number in the shape function for

horizontal displacement and the S wave number in the shape function for vertical displacement. Chow & Smith developed this boundary for a vibrating disc on the surface of an elastic half-space where the S wave is propagated on a hemispherical wavefront rather than a cylindrical wavefront as is the case with a vibrating pile. In order to modify this approach for the latter, the vertical and horizontal particle displacements were plotted for various vertical sections between 25m and 40m from the pile from the ground surface to a depth of 15m (Figures 5.43 and 5.44). These plots show that the wavefront approximates to an R wave over the top 3.2m which is equivalent to half of the R wavelength. The wavefront appears to be a combination of the R and S waves below this.

It was therefore decided to apply a Rayleigh viscous boundary to the top 3m of the vertical boundary of the 40m wide FE mesh. ABAQUS infinite elements (equivalent to a standard viscous boundary) were applied to the remainder of the vertical boundary as shown in Figure 5.45. The vertical and radial particle velocity time traces of all of the surface nodes are compared with those for the 80m wide FE/IE mesh in Figures 5.46 and 5.47.

These plots show that the Rayleigh viscous boundary over the whole depth of the vertical boundary gives better results than the combined Rayleigh/standard viscous boundary. This suggests that the R wave is the dominant wave at 40m from the pile. The insertion of a standard viscous boundary below the R viscous boundary may reduce the amount of S wave reflection but the benefit of this does not outweigh the benefit derived by full absorption of the R wave. On balance the most effective boundary for the absorption of ground waves from piling appears to be a Rayleigh viscous boundary over the whole depth of influence of the Rayleigh wave. It is suggested the insertion of the Rayleigh viscous boundary over the top 12.9m ($2.0 \times R$ wavelength) with the standard viscous boundary below might give slightly better results. Further work is required to determine the optimum depth of the Rayleigh viscous boundary, but it is questionable whether the minimal improvement that might be achieved is worth the extra effort.

The Rayleigh viscous boundary has been shown to be very effective and could be used to reduce the size of FE meshes used to model ground waves and thus the computing time required. Unfortunately the interface for inserting user-defined elements into ABAQUS is very inefficient and it was found that analyses of large FE meshes coupled with ABAQUS infinite elements took less time than smaller FE meshes with the new boundary applied. If the Rayleigh boundary was programmed directly into ABAQUS, the size of the FE mesh could be limited to the area of interest and thus would be considerably smaller and quicker to analyse.

5.6 MODELLING VIBRATORY EXTRACTION AT THE SECOND SEVERN CROSSING

5.6.1 Site Conditions

The model for vibratory extraction simulation has been developed using case history data collected and reported by the Transport Research Laboratory (Hiller, 2000 & TRL Report 429). Vibration data were collected during the extraction of 1050mm diameter casings for one of the M49 southern approach bridges to the Second Severn Crossing

where cast in situ piles were being installed to provide bridge pier foundations. All of the geophones were installed in flat and level natural ground alongside a haul road. The geological profile of this site is illustrated in Figure 5.48. The closest geophone array was at a distance of 5.7m from the piles and data were acquired at distances extending to 107m. The pile was sleeved to a depth of 6m, so all the vibration data are for pile extraction out of the firm to stiff marl in which the piles were founded and then up through the overlying soft to very soft alluvial clay.

The vibratory hammer used to extract the casings was a PTC 50H3 which is one of the larger hydraulic vibratory hammers. It operates at a maximum frequency of 27.5Hz with a maximum amplitude of $\pm 22\text{mm}$. The power of the vibrator is equal to 290kW and it has an equivalent energy per cycle of 10.5kJ

5.6.2 Parameters used in the pile/soil interaction model

The FE/IE mesh used in the pile/soil interaction model is shown in Figure 5.49. The 1050mm diameter casings were modelled in ABAQUS as a line of rigid axisymmetric elements at a radius of 0.525m from the central axis of symmetry. The vibratory motion of the pile was then simulated by defining a sinusoidal motion of these rigid elements about a fixed reference node. The inertial properties of the casing were incorporated by attaching a mass element, equivalent to the casing mass, to the reference node. The casing mass was taken to be the sum of the mass of the casing (98kg, ignoring the mass of any soil inside the casing), the clamp (1600kg) and the mass of the dynamic section of the PTC 50H3 vibratory hammer (4650kg).

The vibratory hammer motion was simulated by imposing the cyclic forcing function given in equation (5.7) onto the reference node. The operation frequency of the hammer was assumed to be equal to the frequency of the resulting vibration traces measured by the geophones at any particular pile penetration. The eccentric moment of a PTC50H3 vibrating hammer was assumed to be 50m.kg as given in the manufacturer's hammer specification.

Unfortunately the soil data for this case study were limited to soil descriptions from drillers' logs recorded during installation of the casings and installation of an inclinometer. No data about water levels or laboratory test data were available. In the absence of any detailed information on soil parameters, typical values for the various soil types based on the soil descriptions were used in the analyses as follows.

Depth	Soil Description	E (N/m ²)	ν	ρ (kg/m ³)
0.0m-1.0m	Fill	$15e^6$	0.3	1750
1.0m-4.0m	Alluvium (firm clay)	$15e^6$	0.4	1900
4.0-5.5m	Peat	$15e^6$	0.45	1750
5.5-13.8m	Alluvium (soft to very soft clay)	$15e^6$	0.4	1750
13.8m>>	Keuper Marl (firm becoming stiff marl)	$200e^6$	0.4	2070

Table 5.1: Soil parameters used in pile/soil interaction model

As discussed in Section 5.2, the skin friction on the pile in cohesive soils has been shown to be dependent on the effective overburden pressure (equation 5.3). Meyerhof (1976) deduced an empirical expression for the ratio $\beta = \tau_s/\sigma'_v$, from the results of a number of pile tests in clay of varying overconsolidation ratio. Assuming that the full angle of internal friction, ϕ' , was mobilised on the shaft of the pile, he showed that the value of K consistent with the measured shaft capacities varied between 1 and 2 times the in-situ horizontal stress, with an average ratio of 1.5. Francescon (1982) undertook a series of instrumented model pile tests, where the normal effective stress acting on the pile was measured directly, and demonstrated that this stress was close to 1.5 times the original horizontal effective stress in the soil.

The assumed total normal stress distribution on the pile from the soil was calculated using equation (5.3), assuming a value of K_0 of about 0.65 (using the formula $K_0=1-\sin\phi'$ for normally consolidated soils proposed by Jaky, 1944) multiplied by a factor of 1.5 as suggested by Meyerhof (1976) and Francescon (1982) resulting in a value of K of about 1.0. Total stresses have been used to calculate the equivalent lateral force on the pile because pore water pressures are not included in the FE model. The assumption of a value of K of unity does not take account of the stress changes which occur during and after pile installation or extraction. However, as the actual value of the coefficient of friction, μ , down the pile shaft was unknown and the ABAQUS friction model defines the limiting frictional shear stress between the contacting surfaces as the product μp , where p is the contact pressure between the two surfaces, the actual value of K is academic. If the normal stresses on the pile are calculated assuming a value of K of 1.0 on total vertical stresses, it is relatively straightforward to manipulate the value of friction to take account of stress changes during pile extraction or installation and increases in pore water pressures by factoring the friction coefficient accordingly.

An average overall friction coefficient of 0.15 was assumed for the pile. This coefficient was factored with respect to the average normal stress on the pile/soil interface over the whole depth of penetration to simulate the variation in the horizontal soil pressure with depth.

As the casings were sleeved to a depth of 6m, it was assumed that there was no contact interaction ($\mu=0$) between the soil and the casing over this depth.

Given the lack of data as to the dynamic behaviour of the alluvial soils at this site, a range of typical Mohr-Coulomb parameters, based on BS5930 guidance, was assumed for the soft clays between 6m and 13.8m below ground level. The vertical displacements of the nodes on the soil/pile interface resulting from the vibratory motion of the pile for the assumed range of Mohr-Coulomb parameters are plotted against time in Figure 5.50. These graphs indicate that the pile/soil interaction model is not particularly sensitive to the Mohr-Coulomb parameters and so typical values of the undrained shear strength, $c_u=30\text{e}^3 \text{ N/m}^2$ and $\phi_u=0^\circ$ were used in all subsequent analyses.

The typical material damping ratio of 5% which has been suggested by Massarch (1992) has been assumed for this site.

5.6.3 Parameters used in the wave propagation model

The FE/IE mesh used in the wave propagation model is shown in Figure 5.51. Uniform eight-noded square elements were used throughout to prevent reflection within the mesh.

During the transmission of ground waves generated by pile driving, it has been shown (Massarsch 1992) that the soil tends to act as an elastic medium beyond a short distance from the pile. It is therefore possible to derive small strain stiffness parameters from the measured vibration traces for any particular site.

The arrival times of wavefronts at the various geophones on the Second Severn Crossing site were used to calculate the propagation velocities of the P, S and R waves. Assuming that soils behave elastically at very small strains, an upper bound value of stiffness, G_{max} , can be calculated for the soil.

The vertical and radial particle velocities recorded at the geophones at the start of vibratory extraction (casing installed to a depth of 15.5m) are plotted against time in Figures 5.1 and 5.2 respectively. In the case of vibratory extraction, the main wavefront will be the S wave generated by the pile shaft (there is unlikely to be any P wave generation at the toe).

The interpreted arrival times of the S wave from the shaft at each geophone are summarised in Table 5.2 below together with the calculated S wave velocity (=distance travelled/time taken)

Geophone locations (horizontal distances from pile)	Arrival time of S wave from shaft	Distance travelled by S wave between geophones	Velocity (calculated) of S wave from shaft
VERTICAL TRACES			
8.9m – 16.9m	63.9ms	8m	125m/s
8.9m – 33m	267ms	24.1m	90m/s
8.9m – 61m	589ms	52.1m	88m/s
RADIAL TRACES			
8.9m – 16.9m	83.4ms	8m	96m/s
8.9m – 33m	318.5ms	24.1m	76m/s
8.9m – 61m	561.1ms	52.1m	93m/s

TABLE 5.2: Measured arrival times of S wavefront from the pile shaft

Table 5.2 indicates that the S wave from the shaft travels at about 100m/s through the upper soils. Substituting values of v of 0.4 and ρ of 1750kg/m^3 for the alluvium (see Table 5.1) into equations (2.9) and (2.11), gives an E value for the alluvium of about 50MPa.

The small strain stiffness values derived from the measured data were then inserted into the wave propagation model and an analysis was undertaken to check that the time

taken for the simulated S waves to arrive at the geophone locations corresponded to the measured arrival times (Figure 5.52). A typical sinusoidal input for vibratory extraction with a frequency of 15.2Hz was applied as displacement functions to all of the soil nodes on the pile/soil interface.

5.6.4 Parametric studies of vibratory pile extraction

Development of the model involved a step-by-step approach involving many hundreds of runs using various parametric combinations. The model was gradually improved and refined as the effects of each parameter was understood and compared to the measured vibration data. Inevitably some incorrect assumptions and over-simplifications were made during this process and then corrected and refined, but all of the analyses helped to form an understanding of the mechanism of ground wave generation and propagation from vibratory piling.

The parametric studies were very time consuming. Two finite element analyses had to be carried out for each case. First the pile/soil interaction analysis was run to determine the vertical displacements of the soil nodes on the pile/soil interface. These displacements then had to be manually extracted and manipulated into the correct format for insertion into the wave propagation model for the second stage of analysis. Each finite element analysis took between 6-10 hours to run depending on the size of the mesh and the complexity of the contact conditions.

A selection of the parametric studies undertaken is presented below to demonstrate the sensitivity of the model. The studies using the vibratory extraction model are particularly useful as they do not include any toe contribution: the generated waves are solely due to the interaction between the pile shaft and the surrounding soil. This allows examination of the pile shaft model and its parameters in isolation.

The parametric studies were undertaken on the same basic FE/IE model for the extraction of 1050mm diameter casings from a depth of 13.8m at the Second Severn Crossing site. At this depth of penetration the only soil type in contact with the shaft of the casing was the lower layer of alluvium because the casings were sleeved to a depth of 6m. The frequency of hammer operation at this depth of penetration was measured from the recorded vibration traces as 22.31Hz (140.2 radians/sec).

The parametric studies commenced by investigating the sensitivity of the ground response to the relative stiffness of the alluvium to that of the underlying marl. The arrival time data given in Table 5.2 above indicated an overall Young's Modulus, E , for the ground of about $50e^6$ based on the velocity of the S wave generated by the pile shaft in the alluvial soils. However, subsequent analyses indicated that the response at the ground surface was very sensitive to the relative stiffness of the alluvium to the marl. The results of the parametric study for an overall coefficient of friction, μ , of 0.15 are summarised in Tables 5.3 and 5.4 below. The graphs of vertical and radial particle velocities against time at the geophone locations are reproduced for all of these analyses in Appendix G.

The vertical and radial peak particle velocities measured at three of the geophones on the ground surface during the extraction of a casing from 13.8m below ground level (GL) are shown in 5.52 and 5.53 and are summarised in Tables 5.3 and 5.5 below.

Horizontal distance between pile and geophone	Peak vertical particle velocities measured at geophone
8.9m	2.00mm/s
16.9m	0.75mm/s
33m	0.80mm/s

Table 5.3: Measured vertical peak particle velocities during extraction: toe of casing at 13.8m below GL

E_{marl}			E_{alluvium}		
	30 MPa	40 MPa	42 MPa	45 MPa	50 MPa
50 MPa	2.80 (8.9m) 1.70 (16.9m) 0.40 (33m)				
70 MPa	2.88 1.77 0.30	2.00 0.87 0.46	2.17 0.70 0.58	2.60 0.75 0.46	3.54 0.44 0.73
100 MPa			2.30 0.68 0.46		
120 MPa			2.40 0.63 0.20		
150 MPa			2.46 0.62 0.50		3.78 0.47 0.57
200 MPa		2.47 0.55 0.72	2.60 0.72 0.72	3.00 0.81 0.57	

Table 5.4: Vertical particle velocities (mm/s) at 8.9m, 16.9m and 33m geophones for various values of E for the alluvium and marl

Horizontal distance between casing and geophone	Peak radial particle velocities measured at geophone
8.9m	5.50mm/s
16.9m	1.60mm/s
33m	0.70mm/s

Table 5.5: Measured radial peak particle velocities during extraction: toe of casing at 13.8m below GL

			E_{alluvium}		
E_{marl}	30 MPa	40 MPa	42 MPa	45 MPa	50 MPa
50 MPa	0.38 (8.9m) 0.93 (16.9m) 0.23 (33m)				
70 MPa	0.25 0.90 0.24	2.00 0.60 0.35	2.17 0.89 0.40	2.20 1.25 0.35	1.90 1.70 0.25
100 MPa			2.40 0.90 0.38		
120 MPa			2.55 0.85 0.37		
150 MPa			2.69 0.71 0.27		2.10 1.50 0.65
200 MPa		2.74 0.52 0.36	2.80 0.70 0.20	2.77 0.97 0.13	

Table 5.6: Radial particle velocities at 8.9m, 16.9m and 33m geophones for various values of E for the alluvium and marl

From tables 5.4 and 5.6, the optimum combination of stiffness parameters to give a ground response similar to that recorded by the geophones appears to be E values of 42MPa for the alluvium and 200MPa for the marl, see Figures 5.55 and 5.56. Examination of the predicted velocity/time traces also shows that the arrival times of the S wavefront simulated in the FE/IE model at the geophone locations compare well with the measured arrival times. A further check of the wave propagation speeds in the FE/IE model was carried out by applying a forcing function, typical of that generated during impact piling (Figure 5.57). The forcing function was applied to all of the soil nodes on the pile/soil interface. The advantage of applying a forcing function of this type is that it results in a discrete wavefront which propagates through the FE mesh. It is therefore relatively simple to identify the arrival times of the wavefront at the geophone locations, as shown in Figure 5.58. This plot demonstrates that the wave propagation velocities in the FE/IE model compare very well with those recorded by the geophones for E values of 42MPa for the alluvium and 200MPa for the marl.

The magnitude of the peak particle velocities predicted by the model assuming E values of 42MPa for the alluvium and 200MPa for the marl and an overall coefficient of friction of 0.15 were slightly larger than those recorded by the geophones (see Figures 5.55 and 5.56). The analysis was therefore rerun using an overall coefficient of friction of 0.1. The resulting velocity/time traces are compared with those for an overall coefficient of friction of 0.15 in Figures 5.59 and 5.60. This demonstrates that the magnitude of the peak particle velocities is directly proportional to the magnitude of friction coefficient. The comparison given in these figures indicates that the most appropriate overall coefficient of friction for this case is about 0.14.

The radial velocity/time traces recorded on site were significantly larger than those predicted by the model. This is likely to be due to the generation of P waves from the pile shaft due to lateral vibration of the pile during vibratory extraction. This effect is not simulated in the model.

Some analyses were then undertaken to assess the sensitivity of the model to the distribution of friction along the shaft of the casing. Instead of assuming one average friction coefficient for the alluvium between 5.5m and 13.8m, the model was refined to incorporate three average friction coefficients to simulate an increase in normal stress with depth within the lower alluvium. Comparison of the velocity/time traces predicted by the two cases (Figures 5.61 and 5.62) against the measured velocity/time traces indicates that the insertion of one average coefficient of friction for the lower alluvium actually gave a better match with the measured data than the model which simulated an increase in normal stress with depth in the lower alluvium. This would seem to indicate either that the friction between the casing and the soil decreases with depth or that the normal stresses on the shaft are fairly constant throughout the lower alluvium. The latter would seem to be more plausible and could be caused by cyclic shearing and liquefaction of the soil around the shaft.

The results indicate that the model is quite sensitive to the distribution of friction on the shaft. Further work is required to investigate how the normal stresses alter around a pile shaft during vibratory extraction and the distribution of friction on the pile/soil interface.

Further analyses were undertaken to assess the effect of the magnitude of material damping on the resulting ground response. The case described above assuming one average friction coefficient for the alluvium between 5.5m and 13.8m (equivalent to an overall coefficient of friction of 0.15) was analysed for material damping ratios of 5%, 3% and 0%. The resulting vertical particle velocity/time traces for all of the nodes along the ground surface are compared in Figure 5.63 and 5.64. These graphs show that material damping has a very significant effect on the magnitude of the particle velocities. As expected, the differences between the results of the three analyses increase with distance from the source as the damping takes effect.

Following extensive parametric studies, a selection of which are described above, the best match with the measured vibration data was achieved assuming small strain E values for the alluvium and marl of 42MPa and 200MPa respectively (for the wave propagation model), an average friction coefficient for the alluvium between 5.5m and 13.8m (equivalent to an overall coefficient of friction of 0.15), and 5% material damping (Figures 5.55 and 5.56). However, it is important to realise that these values have been selected on the basis of sparse site data and many assumptions have been necessary. In addition, the recorded data are limited to those from a few discrete geophone positions on the ground surface. The identification of the presence and form of any standing wave is impossible with such a limited data set.

One method of increasing confidence in the choice of parameters inserted into the model is to rerun the analysis for extraction from a different depth of penetration. It is recognised that this is not a completely robust method because the normal stresses on the shaft are likely to be different but it provides an indication that the model gives a reasonable prediction of the actual ground response.

The analyses were rerun for a casing extracted from a depth of 11m. The measured vibration traces indicated the hammer was operating at a frequency of 22.27Hz (139.9 radians/second) when the casing was at this depth. The same soil parameters were assumed with a damping ratio of 5%.

The resulting particle velocity/time traces, assuming overall coefficients of friction of 0.15 and 0.1, are compared to the corresponding measured velocity/time traces in Figures 5.65 and 5.66. The model assuming a friction coefficient of 0.15 predicts larger vibrations than those measured, but the proportions of the peak particle velocities at the various geophones are approximately correct. The analysis run with an overall friction coefficient of 0.1 gave a better match. This suggests a reduction in the amount of shaft resistance as the casing is extracted. This seems quite feasible as the strength of the soil around the shaft is likely to reduce as it continues to be remoulded and liquefied by the vibratory motion. Further work is required to investigate this effect in more detail.

To summarise, the parametric studies undertaken using the vibratory extraction model have demonstrated the influence of the various parameters to be as follows:

- The ground response is quite sensitive to the relative small strain stiffness parameters assumed for the various soil layers in the wave propagation model because this affects the shape of the standing wave generated on the surface of the FE mesh
- The magnitude of the particle velocities are directly proportional to the value of the coefficient of friction specified for shaft/soil interaction
- The analyses are quite sensitive to the distribution of friction specified on the shaft. The assumption of an overall average coefficient of friction for the lower alluvium actually gave a better match with the measured data than that which simulated an increase in normal stress with depth in the lower alluvium. This suggests that the normal stresses on the shaft are fairly constant throughout the lower alluvium due to cyclic shearing and liquefaction of the soil around the shaft.
- The ground response, particularly at distances greater than 20m from the source, is very sensitive to the magnitude of material damping applied.

5.6.5 Conclusions resulting from vibratory extraction simulation

Hiller (1999) and Holeyman (2000) suggested that the most critical parameter affecting vibration response is the soil resistance to the vibratory motion of the pile. This study supports this suggestion but it also demonstrates that the relative frequency of the hammer to that of the ground is critical in determining whether a standing wave is generated on the ground surface. In this case, the particle velocities recorded at discrete geophone locations are likely to display non-uniform attenuation and will not necessarily identify the maximum magnitudes of vibration generated by the vibratory extraction. It has been shown that the shape of the standing wave changes with frequency of hammer operation and with depth of pile penetration, thus explaining the observed changes in relative magnitude of particle velocities at geophone locations.

The possible generation of a standing wave on the ground surface during vibratory piling has major implications for future vibration monitoring strategy. This study has indicated that the geophones placed in the field did not always register the maximum levels of vibration due to their discrete positions within the standing wave. It is recommended that geophones are placed every few metres along the ground surface when monitoring vibrations from vibratory piling in order to define any standing wave that may be generated and also to ensure that the maximum levels of vibration are recorded. It is suggested that the FE model for vibratory piling described in this Chapter could be used to determine the likelihood of a standing wave occurring at any particular site.

Given the high dependence of the resulting vibration patterns on the operating frequency, the use of the finite element model as a predictive tool for vibratory piling is likely to be limited in its usefulness. A large number of analyses would be necessary to model the entire range of operating frequencies. Although vibration prediction for discrete points may be beyond the capabilities of the model, it could be used for predicting a range of vibration response and the area of influence. The model has already demonstrated its usefulness in the understanding of how ground waves are generated during vibratory piling and how they interact.

This study has shown that the ground response is very sensitive to the magnitude and distribution of friction down the shaft. In the model, the coefficient of friction is factored to take account of changes in the normal stresses acting on the shaft and so this parameter defines both the normal stress distribution and the shaft/soil interaction. Further work is required to determine the normal stresses acting on piles and pile/soil interaction during vibratory extraction for various soil types.

5.7 MODELLING VIBRATORY PILE INSTALLATION AT THE SECOND SEVERN CROSSING

5.7.1 General

Following development of the FE model for vibratory extraction, the model was extended to allow the simulation of vibratory pile installation. It was assumed that shaft/soil interaction during vibratory extraction is the same as that during vibratory installation. The shaft model in the vibratory extraction model was therefore used in the vibratory installation model with the addition of the one-dimensional model described in Section 5.3.6 to simulate the toe response.

The vibratory installation model was developed using vibration data collected during the installation of the casings at the Second Severn Crossing site. The data set was for the installation of a 1050mm diameter casing a few metres away from that described in Section 5.6. The same vibratory hammer was used for installation and extraction of the casings.

5.7.2 Parametric studies of vibratory pile installation

Parametric studies for the installation case concentrated on the sensitivity of the model to the parameters used to simulate the soil response at the pile toe.

Inspection of the measured ground response indicates that the magnitudes of the surface particle velocities for any depth of casing are of very similar magnitude for both vibratory extraction and vibratory installation. This suggests that most of the ground waves were generated on the interface between the casing shaft and the soil as S waves rather than at the toe of the casing as P waves.

However the soil response under the toe affects the magnitude of the pile movement and hence the magnitude of the waves generated on the shaft/soil interface. This can be seen in the vibration traces recorded as the toe of the casing encountered the firm to stiff marl at a depth of 13.8m after moving down through the overlying soft to very soft alluvium (Figures 5.67 and 5.68). As the casing entered the marl, the increased toe resistance resulted in less vertical pile movement. This led to smaller vertical particle velocities at ground surface but larger radial particle velocities. The latter were likely to be caused by lateral flexing of the casing when the toe resistance suddenly increased. It is unlikely that the soft alluvium provided much lateral restraint. The measured data presented in Figures 5.67 and 5.68 are particularly valuable for the development of the toe response model because they show the effect of increasing the resistance of the soil under the toe from virtually nothing in the alluvium to a high value in the marl.

The pile/soil interaction model was used to evaluate the effect of the soil stiffness under the toe on the amount of pile movement. The analyses assumed the same soil parameters as those given in Section 5.6.2 for the pile/soil interaction model for vibratory extraction with an overall coefficient of friction of 0.15. The frequency of hammer operation at a depth of penetration of 13.8m was measured from the recorded vibration traces as 16.7Hz (105.2 radians/sec). The toe response was modelled as a spring and dashpot in parallel with spring and dashpot constants calculated using equations (5.5 and 5.6) for various values of E. The results of varying the stiffness of the soil response under the toe are summarised in Table 5.7 below.

E_{toe} (MN/m ²)	Amplitude of pile movement				
	$\mu=0.05$	$\mu=0.075$	$\mu=0.1$	$\mu=0.15$	$\mu=0.2$
5	±13.8mm	±14.0mm	±14.2mm		
10			±15.5mm		
15			±16.3mm	±16.7mm	
100	±11.6mm	±10.8mm	±10.2mm	±8.9mm	±7.8mm
200			±3.7mm	±3.3mm	

Table 5.7: Effect of the soil stiffness under the toe on the amount of pile movement for various coefficients of friction

These results show that the magnitude of the pile movement is not particularly sensitive to the stiffness of the soil under the toe. (It should be noted that the pile response is actually frequency-dependent.)

In order to simulate the marked change in ground response which occurred when the toe of the casing encountered the marl, two similar analyses were run assuming different toe

conditions. The first assumed that the toe was still in the alluvium and the spring and dashpot constants were based on an E value of 15MPa. The second assumed that the toe had hit the marl and an E value of 200MPa was used in the toe model. The latter was used to model a lower bound value for pile displacement (an almost completely rigid response).

The resulting displacements of the soil nodes on the shaft/soil interface were applied to the corresponding nodes in the wave propagation model. Small strain E values for the alluvium and marl of 42MPa and 200MPa respectively were assumed in the wave propagation model together with 5% material damping. The resulting particle velocity/time traces for the two toe conditions (alluvium and marl) are compared in Figures 5.69 and 5.70. These plots show that the particle velocities at 14.5m and 33m predicted by the model are much too large and suggest that the model was overestimating the magnitude of the P waves generated by the toe of the casing.

The model simulates the generation of P waves by assuming that the soil immediately under the toe has the same amplitude as that of the pile. This is modelled by applying the sinusoidal displacement function for the rigid pile yielded by the pile/soil interaction analysis onto the soil nodes immediately under the pile toe in the wave propagation analysis. It seems reasonable that this assumption overestimates the magnitude of P wave generation by the toe of a casing for the following reasons:

- It is unlikely that the soft alluvium, liquefied by the vibratory motion, provided much resistance to the toe of the large diameter casing and simply 'flowed' around the inner and outer cutting edges of the casing.
- It is considered unlikely that any alluvium forced inside the casing would have acted as a 'plug' of material to make the casing behave as a closed ended pile. Any alluvium inside the casing is likely to have been in a liquefied state.
- As it is considered unlikely that the casings acted as closed ended piles, the cross-sectional area of the toe would have been very small, resulting in more of a cutting action than an impact between toe and soil.
- P wave generation may have increased when the casing hit the marl at 13.8m but it is likely that the zone of liquefied alluvium prevented the transmission of these waves back to the surface.

The effect of reducing the magnitude of P wave generation under the toe on the resulting ground response was investigated by factoring the magnitude of the displacement function applied to the soil nodes under the toe. The resulting particle velocity/time traces for application of 100%, 50% and 10% of the pile displacement function to the soil nodes under the toe are compared in Figures 5.71 to 5.74. These figures demonstrate how the levels of P wave generation at the toe affect the levels of vibration generated at the ground surface. Comparison with the measured particle velocity/time traces suggests that the toe of the casing only generated soil displacements of the order of 10% of the pile displacement in both the alluvium and the marl.

Reducing the magnitude of P wave generation under the toe seems to reduce the magnitude of vibrations at 14.5m and 33m from the source to acceptable levels. However, the magnitudes of the particle velocities within 10m of the pile appear to be largely unaffected by the large difference in the soil stiffness values used in the toe model. The vertical particle velocities predicted by the model only demonstrated a 90%

reduction when the toe of the casing hit the marl whereas the measured particle velocities demonstrated a 40% reduction. Further analyses demonstrated that even when the pile movement was increased to the maximum operating amplitude of $\pm 22\text{mm}$, the resulting particle velocities were only 10% greater than those resulting from an amplitude of $\pm 3.7\text{mm}$.

This suggests that the soil resistance around the pile shaft reduced when the casing encountered the marl. This may have been caused by liquefaction of the soil as the relatively rapid advance of the pile through the soft alluvium was suddenly reduced when the toe hit the marl. This effect was simulated by reducing the coefficient of friction in the vibratory installation model from 0.15 to 0.1.

The particle velocity/time traces assuming an E_{toe} of 15MPa and an overall coefficient of friction of 0.15 (simulating the casing in the alluvium just before the toe hits the marl) are compared with the measured vibration traces in Figures 5.75 and 5.76. The particle velocity/time traces assuming an E_{toe} of 200MPa and an overall coefficient of friction of 0.1 (simulating the casing when the toe first encounters the marl) are compared with the measured vibration traces in Figures 5.77 and 5.78. These comparisons are very encouraging.

5.7.3 Conclusions resulting from vibratory pile installation simulation

A model for vibratory pile installation has been developed assuming the shaft parameters used in the vibratory extraction model. The performance of the resulting model seems to indicate that this is a reasonable assumption.

Parametric studies have demonstrated that the Lysmer and Richart model for toe response can be used to calculate the magnitude of pile displacement for various end conditions. However difficulties arose in the determination of the magnitude of the soil displacement under the toe, especially in the case of an open-ended casing.

Further work is required to investigate the mechanisms of P wave generation during vibratory installation for various pile types in different soils. Parametric studies undertaken for the installation of 1050mm diameter casings at the Second Severn Crossing site indicated that approximately 10% of the pile displacement was transferred to the alluvium and marl under the toe.

5.8 VALIDATION OF VIBRATORY PILING MODEL

5.8.1 General

Validation of the vibratory piling model developed in this Chapter is very difficult for several reasons. Firstly, vibration data from piling sites which include detailed information on soil parameters are not available. Data on ground conditions are usually in the form of a few borehole record descriptions. There may be little data relating to the excitation of the pile such as the amplitude of pile displacement with depth. The vibration data itself tends to be confined to ground surface vibrations at a few discrete, and usually arbitrary stand-off distances. This is the main reason why the standing wave phenomenon which has been identified by this work has not been noticed previously. In addition, the dynamic behaviour of soils during vibratory piling is not

well understood and there is little documented data from which to deduce suitable parameters.

The only method of validating the model is to use it to simulate the ground waves recorded by various case histories with different ground conditions, hammer sizes and pile types. As more cases are modelled, confidence in the model to predict vibrations from vibratory piling will increase and it may be possible to develop guidance for the choice of parameters to be used in the model from limited site data.

This section describes the simulation of ground waves generated by vibratory piling at a site in Flitwick in Bedfordshire reported by Uromeihy (1990). The Flitwick data set is particularly useful because vibration data are available for both impact and vibratory piling of the same H-pile. The vibrations recorded during impact piling provide accurate data on the arrival times of wavefronts at the geophone locations which can be used to derive the small strain stiffness characteristics of the soils.

5.8.2 Site Conditions at Flitwick, Bedfordshire

The site near Flitwick in Bedfordshire was loaned to the University of Durham for pile testing by Dawson Construction Plant in July 1988. The site was chosen because of its fairly uniform ground conditions and the access to various types of pile driving equipment in the adjacent yard.

The topsoil over an area of approximately 24m by 20m was removed and the soft subsoil was trimmed level prior to the commencement of pile driving.

A site investigation was carried out in August 1988 which comprised three boreholes to a maximum depth of 9m. The locations of the boreholes are indicated in Figure 5.79. The borehole logs are included in Appendix H and are summarised in Figure 5.80.

A number of laboratory tests, including particle size distributions, undrained triaxial tests and consolidated shear box tests were undertaken on selected samples. The results of these tests are summarised in Tables H1-H4 in Appendix H.

Monitoring of pile driving was undertaken in October 1988. A 12m long steel H pile (305 x 305 x 89kg/m) was installed to a depth of 7m by a PTC 13HF1 vibratory hammer with an eccentric moment of 13m.kg. This hammer has a maximum operating frequency of 38Hz and vibrates with a maximum amplitude of ± 22 mm. The power of the vibrator is equal to 130kW and it has an equivalent energy per cycle of 3.4kJ.

The vibrations induced by pile driving were recorded by a portable digital recorder unit which stored and later processed the data. The ground vibrations were measured simultaneously by five sets of geophones which were placed at different horizontal stand-offs from the driven pile. Each set included three geophone units which were oriented orthogonally for measuring the three components of vibration along the radial, transverse and vertical axes.

5.8.3 Parameters used in the pile/soil interaction model

The H pile was modelled in ABAQUS as a line of rigid axisymmetric elements at a radius of 0.1525m from the central axis of symmetry. The FE/IE mesh used in the pile/soil interaction model is shown in Figure 5.22. The vibratory motion of the pile

was then simulated by defining a sinusoidal motion of these rigid elements about a fixed reference node. The inertial properties of the pile were incorporated by attaching a mass element, equivalent to the mass of the pile, to the reference node. The mass of the pile was taken to be the sum of the pile mass (1068kg), the clamp (1250kg) and the mass of the dynamic section of the PTC 13HF1 vibratory hammer (1200kg).

The operating frequency of the hammer was assumed to be equal to the frequency of the resulting vibration traces of 19.1Hz (120.0 radians/second) at a depth of penetration of 7m. The eccentric moment of the PTC 13HF1 vibrating hammer was assumed to be 13m.kg as given in the manufacturer’s hammer specification.

The soil data for this site were limited to three borehole records and some classification and undrained triaxial test results. The water table was encountered at an average depth of 2.8m. Typical values for the various soil types based on the descriptions, the SPT values and the laboratory test data were used in the analyses as follows:

SOIL TYPE	E (MPa)	v	ρ (kg/m ³)
Soft Clay (0.0 – 2.4m)	5	0.45	1920
Medium dense to dense Sand & Gravel	35	0.33	1750
Dense to very dense Sand (4.8m>>)	50	0.25	2000

Table 5.8: Soil parameters used in the pile/soil interaction model (Flitwick)

As discussed in Section 5.2, the skin friction on the pile in non-cohesive soils has been shown to be dependent on the effective overburden pressure (Equation 5.1). From pile test results (Vesic, 1977), the rate of increase of skin friction with depth gradually reduces and there is a tendency towards some limiting value. Fleming et al (1992) suggest that for full displacement, driven piles, K varies between about 1.5 at low stress levels, down to unity or even lower at greater depths, with an average value around 1.2.

The assumed total normal stress distribution on the pile from the soil was calculated using equation (5.1) assuming a value of K of about 1.0. Total stresses have been used to calculate the equivalent lateral force on the pile because pore pressures are not included in the FE model. The assumption of a value of K of unity does not take account of the stress changes which occur during and after pile installation.

An overall coefficient of friction of 0.1 was assumed for the pile. This coefficient was factored with respect to the average normal stress on the pile/soil interface over the whole depth of penetration to simulate the variation in the horizontal soil pressure with depth.

Given the lack of data as to the dynamic behaviour of the soils at this site, a range of typical Mohr-Coulomb parameters, based on BS5930 guidance, was assumed. The vertical displacements of the nodes on the pile/soil interface resulting from the vibratory motion of the pile for the assumed range of Mohr-Coulomb parameters are plotted

against time in Figure 5.81. It should be noted that these analyses assumed an overall coefficient of friction of 0.5 rather than 0.1. These graphs indicate that the pile/soil interaction model is not particularly sensitive to the Mohr-Coulomb parameters. As the values of the parameters change, it affects the plastic deformation of the soil. However, the magnitude of sinusoidal displacement, and thus the excitation of the soil particles, is approximately the same in all of the cases shown. It was therefore decided to assume the typical parameters given in Table 5.9 in all subsequent analyses.

SOIL TYPE	ϕ_u (degrees)	c_u (kN/m ²)
Soft Clay (0.0 – 2.4m)	5	20
Medium dense to dense Sand & Gravel	30	5
Dense to very dense Sand (4.8m>>)	40	5

Table 5.9: Mohr-Coulomb parameters used in the pile/soil interaction model (Flitwick)

5.8.4 Parameters used in wave propagation model

The small strain stiffness parameters used in the wave propagation model are those calculated from the measured arrival times of wavefronts generated by hitting the same pile with an impact hammer. In general, it is easier to determine arrival times from impact piling because the waves are propagated as discrete events as opposed to the continuous response that results from vibratory piling. The derivation of these parameters is presented in Section 6.5 in the following Chapter and are summarised in Table 5.10 below.

SOIL TYPE	E (MPa)	ν	ρ (kg/m ³)
Soft Clay (0.0 – 2.4m)	15	0.25	1998
Medium dense to very dense Sand below water table (2.4m>>)	349	0.25	1998

Table 5.10 : Soil parameters used in the wave propagation model (Flitwick)

The typical material damping ratio of 5% suggested by Massarsch (1992) has been assumed for this site.

The FE/IE mesh used in the wave propagation model is shown in Figure 5.24. The FE mesh was 35m wide and 35m deep with ABAQUS infinite elements attached to the right-hand vertical and bottom horizontal boundaries. Eight-noded 0.5m square

elements were used throughout the FE mesh to ensure that there were at least 10 nodes per wavelength for each type of wave travelling through each stratum. A time step of 0.001 seconds was used in the dynamic analyses.

Inserting the parameters in Table 5.10 into equations (2.8) – (2.12) indicates that the wave propagation velocities in the dense sand are likely to be very high and the wavefronts are likely to arrive at the 35m boundary in the following times:

- P waves will reach the boundary at 35m in about 0.08 secs
- S waves will reach the boundary at 35m in about 0.13 secs
- R waves will reach the boundary at 35m in about 0.14 secs.

Reflection from the boundary is therefore very likely. The ABAQUS infinite elements have been shown to absorb totally any P and S waves which approach the boundary orthogonally. However, they do not absorb Rayleigh waves very effectively (see Chapter 4 and Section 5.5).

In order to determine the magnitude of any reflection from the boundary of the wave propagation model for the Flitwick site, two analyses were undertaken with different boundary conditions. The first analysis used a FE mesh with ABAQUS infinite elements down the right-hand vertical boundary (Figure 5.24) and the second used an FE mesh with the new Rayleigh viscous boundary, developed in Chapter 4 and Section 5.5, over the whole depth of the vertical boundary (Figure 5.82). Both analyses assumed a material damping ratio of 5% and assumed that the soil nodes under the pile toe displaced by 10% of the pile displacement. The resulting particle velocity/time traces for all of the surface nodes are compared in Figures 5.83 and 5.84. These graphs show that there is virtually no difference in the ground response resulting from the differing boundary conditions. It is concluded that this is because the application of material damping reduces the particle velocities to very small magnitudes before they reach the boundary at 35m. Any reflection from the boundary is therefore negligible.

A further analysis was undertaken for a case with no material damping to check the performance of the ABAQUS infinite elements. The results of the analyses with no damping and 5% damping using the FE mesh with ABAQUS infinite elements are compared in Figures 5.85 and 5.86. The resulting reflection is particularly evident in the nodes near the boundary between 30m and 35m.

It is concluded that the application of material damping of 5% reduces the magnitude of ground response to levels where reflection of R waves from the boundary is negligible. The ABAQUS infinite elements have been shown to be adequate absorbers of P waves and S waves. The FE mesh with ABAQUS infinite elements therefore needs to be wide enough for the magnitude of the ground waves to have reduced to sufficiently low levels for any reflection to be considered negligible. In the case of the Flitwick model, the FE mesh was 35m wide to accommodate an area of interest within a 16.5m radius of the pile.

5.8.5 Comparison of Measured and Predicted Ground Response at Flitwick

The parameters given in Tables 5.8–5.10 for the Flitwick site were inserted into the vibratory extraction model assuming an overall coefficient of friction of 0.1 and a material damping ratio of 5%. The resulting particle velocity/time traces for application

of 100%, 50% and 10% of the pile displacement function to the soil nodes under the toe are compared in Figures 5.87 and 5.88. Comparison with the measured vibration traces (Figure 5.89 and 5.90) indicates that the application of 10% of the pile displacement function to the soil nodes under the toe gave the best match with the measured data. This is the same toe contribution as that applied in the Second Severn Crossing case for the installation of a casing. This suggests that the magnitude of P wave generation at the toe of a pile installed by vibratory installation is independent of the cross-sectional shape of the pile and is of the order of 10% of the magnitude of the pile amplitude.

The performance of the model in the simulation of the ground response at the Flitwick site is very encouraging. It should be noted that vibratory piling is much more effective in granular soils such as the dense sands at the Flitwick site than cohesive soils such as the soft clays at the Second Severn Crossing site. The good correlations achieved between the measured and predicted vibrations at the Flitwick site suggest that further testing of the model by simulating a range of case history data could lead to the development of a very useful predictive tool.

5.9 CONCLUSIONS AND RECOMMENDATIONS FOR FURTHER WORK

A new finite element model including infinite element and quiet boundary formulations has been developed for the computation of ground waves generated by vibratory piling. The model does not require a detailed knowledge of site conditions and is therefore particularly useful as a preliminary design tool and for modelling the large amount of site data that currently exists in order to assist in the development of more rational guidance. The work has brought together research from several areas of study in order to produce computational procedures for modelling ground waves from vibratory piling.

One of the main conclusions of this work has been that much more field testing with very comprehensive monitoring is required in order to construct viable computational models. The models in this Chapter have been constructed on the basis of many assumptions and simplifications but they have demonstrated that numerical modelling of this complex problem is a suitable technique and potentially very valuable. The work has shown that it is the lack of high density field data rather than computational capability which is preventing further progress.

The model has been validated by comparisons with vibration measurements taken during vibratory extraction and installation of different pile types at two sites with very different ground conditions. The performance of the model in simulating the ground response at each site is very encouraging and suggests that further testing of the model by simulating a range of case history data or very comprehensive sets, such as that which will be provided when the 'SIPDIS' results are published, could lead to the development of a very useful predictive tool.

The model requires many assumptions and simplifications, particularly about ground conditions and pile excitation, mainly because the dynamic behaviour of soils during vibratory piling is not yet well understood (Holeyman 2000) and comprehensive data sets do not presently exist. However, the model provides a framework for the computation of ground waves from vibratory piling and it is hoped that the approach will be adopted and refined as comprehensive data sets become available and as

dynamic pile/soil interaction becomes better understood. The model simulates only the ground waves generated by a pile at a discrete depth of pile penetration whereas the vibrating pile is usually a moving source during installation or extraction. The technique is also quite time-consuming to use, mainly because it comprises two stages of analysis with some manual extraction and manipulation of data between the two stages. This approach is beneficial during development of the model – it allows rapid parametric studies to be used to ascribe values and the computationally expensive contact analysis can be undertaken on a truncated FE/IE mesh. However, as the power of computers increases, there is no reason why the model could not be developed to require only a single stage of analysis.

The modelling of vibratory piling using finite element techniques has been shown to be very helpful in identifying and explaining various phenomena. The parametric studies that have been undertaken give some indication of the sensitivity of the ground response to various parameters and, in conjunction with the interpretation of measured vibration records, give some indication as to the nature of pile/soil interaction, the mechanisms whereby ground waves are formed and the interaction between the various wavefronts.

One of the main findings of this work has been the identification of a ‘standing wave’ on the ground surface which may be generated by the vibratory motion at certain frequencies and ground conditions. This phenomenon appears to explain the non-monotonical decay of ground surface vibrations with distance from the vibratory piling which has been recorded on many sites. It is suggested that the shape of the ‘standing wave’ is primarily influenced by the nature of soil displacement around the pile shaft and so the depth of pile penetration has a major influence. However, it should be noted that the resistance of the soil to vibratory motion is dependent upon many factors, not least the frequency of the motion.

The possible generation of a ‘standing wave’ on the ground surface has several important implications for the monitoring and modelling of ground waves generated by vibratory piling. Primarily it means that attenuation of surface vibrations will be highly non-linear and therefore can not be interpolated from vibrations recorded at discrete, widely spaced geophones. It is therefore recommended that, where preliminary analyses indicate that a ‘standing wave’ is likely to be generated, geophones are placed at closely spaced intervals in order to determine the shape of the resulting standing wave. The resulting measurements would provide a valuable data set for validation of the model described in this Chapter.

The application of the new quiet boundary developed in Chapter 4 to the vibratory piling model resulted in several important conclusions. Before work commenced on the vibratory piling model, it was assumed that the performance of the boundaries would be a critical factor in the performance of the model. A new quiet boundary was therefore developed and was shown to be very effective in absorbing the ground waves generated by vibratory piling. Since ABAQUS did not allow the insertion of user-defined elements into any of its frequency domain analyses, computationally expensive general dynamic analyses in the time domain analyses were necessary. These analyses revealed that the interface for inserting user-defined elements into ABAQUS was very inefficient. As a result, it was discovered that the use of large FE meshes in conjunction with ABAQUS infinite elements was found to give satisfactory results, particularly in the cases where material damping greatly reduced the magnitude of the ground waves

reaching the boundaries. In these cases, it would be possible and desirable to undertake a direct harmonic response analysis and thus allow the identification of the natural frequencies of the soils and the likelihood of resonance and amplification of ground vibrations at certain operating frequencies.

Further work is required in several areas, as follows:

- Soil mechanics research is required in the area of large cyclic deformation to better understand and assess the effects of degradation and liquefaction under those extreme conditions
- Full scale vibratory driving tests with extensive and comprehensive field monitoring are required to provide sufficient data for full refinement and validation of the computational model.
- The mechanical behaviour of vibrators needs to be better defined to allow accurate modelling
- The new procedures developed in this Chapter now need to be applied to a large number of varied sites in order to develop site specific guidance. It is envisaged that this guidance could be in the form of design charts or simple formulae for incorporation into the relevant British Standards and Eurocodes

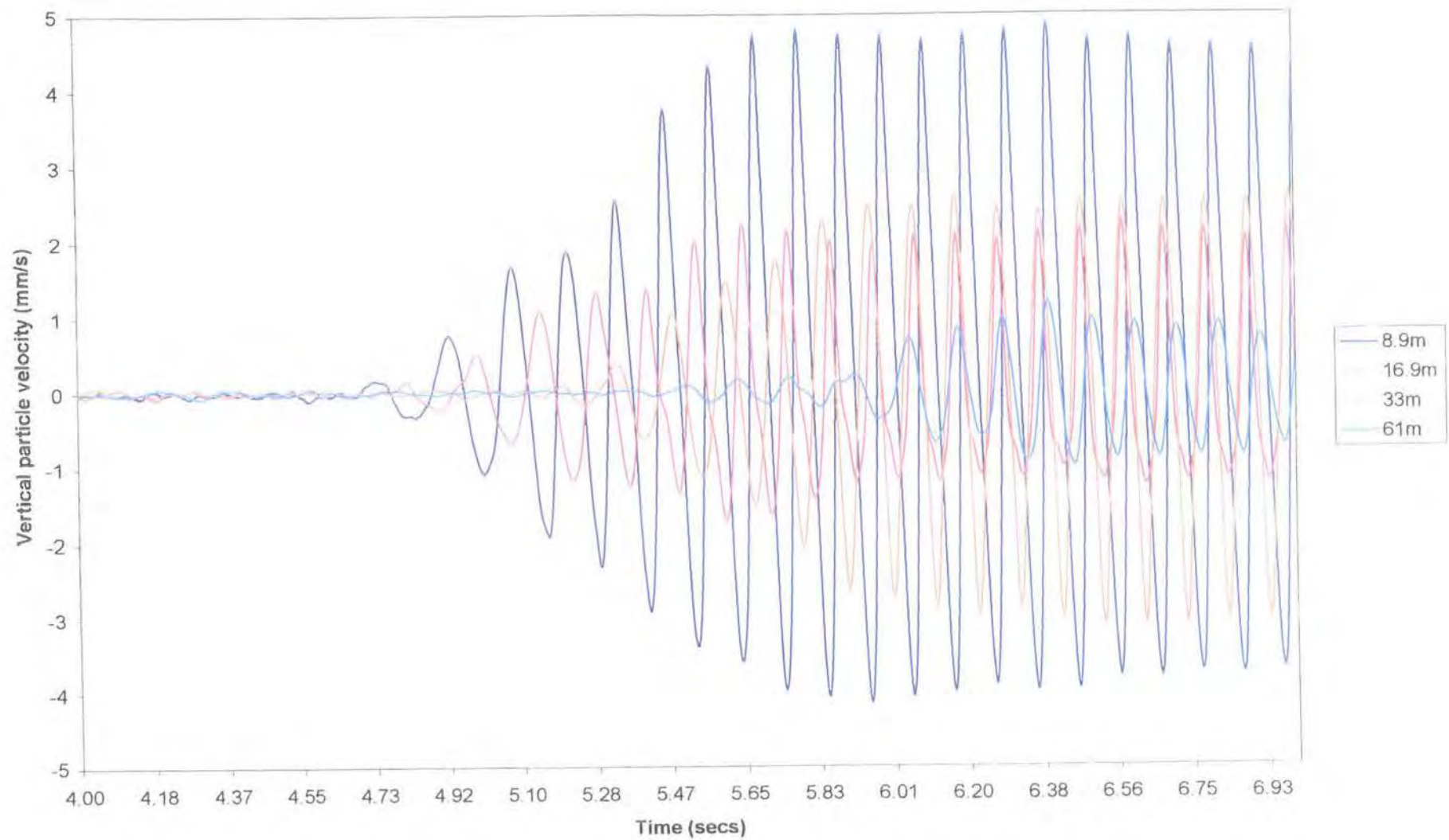


Figure 5.1(a) Vertical particle velocity/time traces recorded during first 12 seconds of extraction of casing from a depth of 15.5m (Second Severn Crossing) (a) 0-3 secs

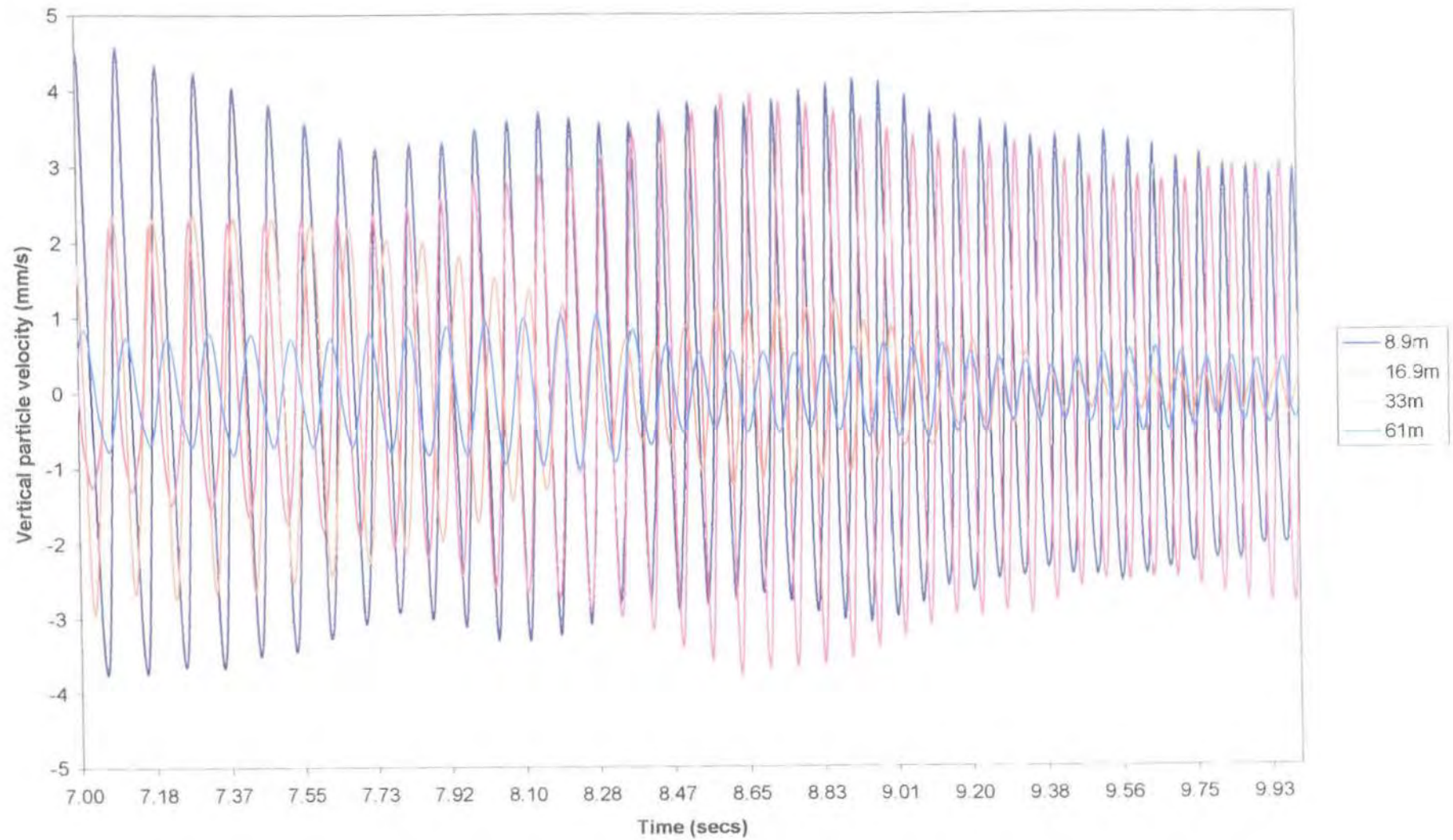


Figure 5.1(b) Vertical particle velocity/time traces recorded during first 12 seconds of extraction of casing from a depth of 15.5m (Second Severn Crossing) (b) 3-6 secs

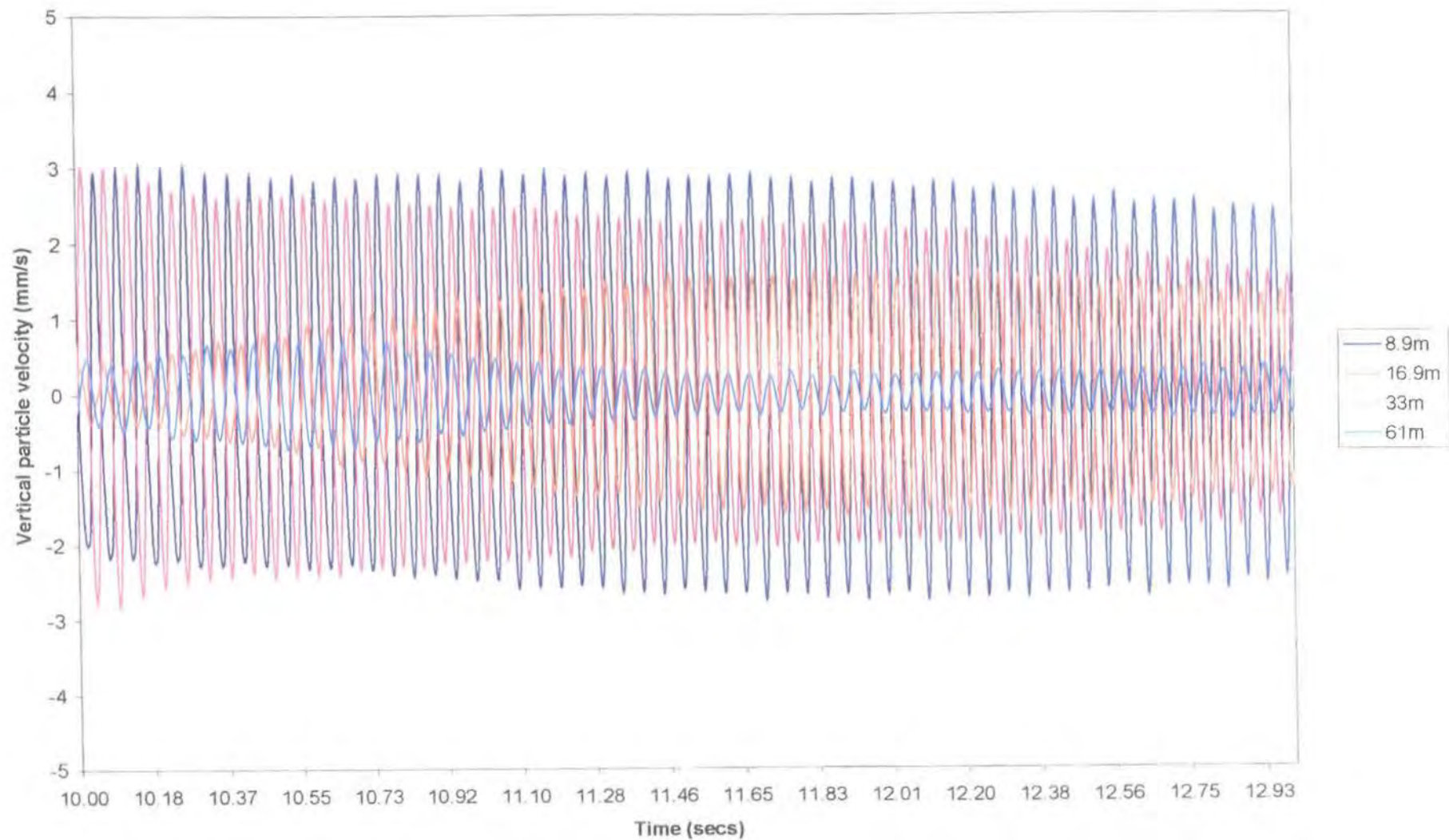


Figure 5.1(c) Vertical particle velocity/time traces recorded during first 12 seconds of extraction of casing from a depth of 15.5m (Second Severn Crossing) (c) 6-9 secs

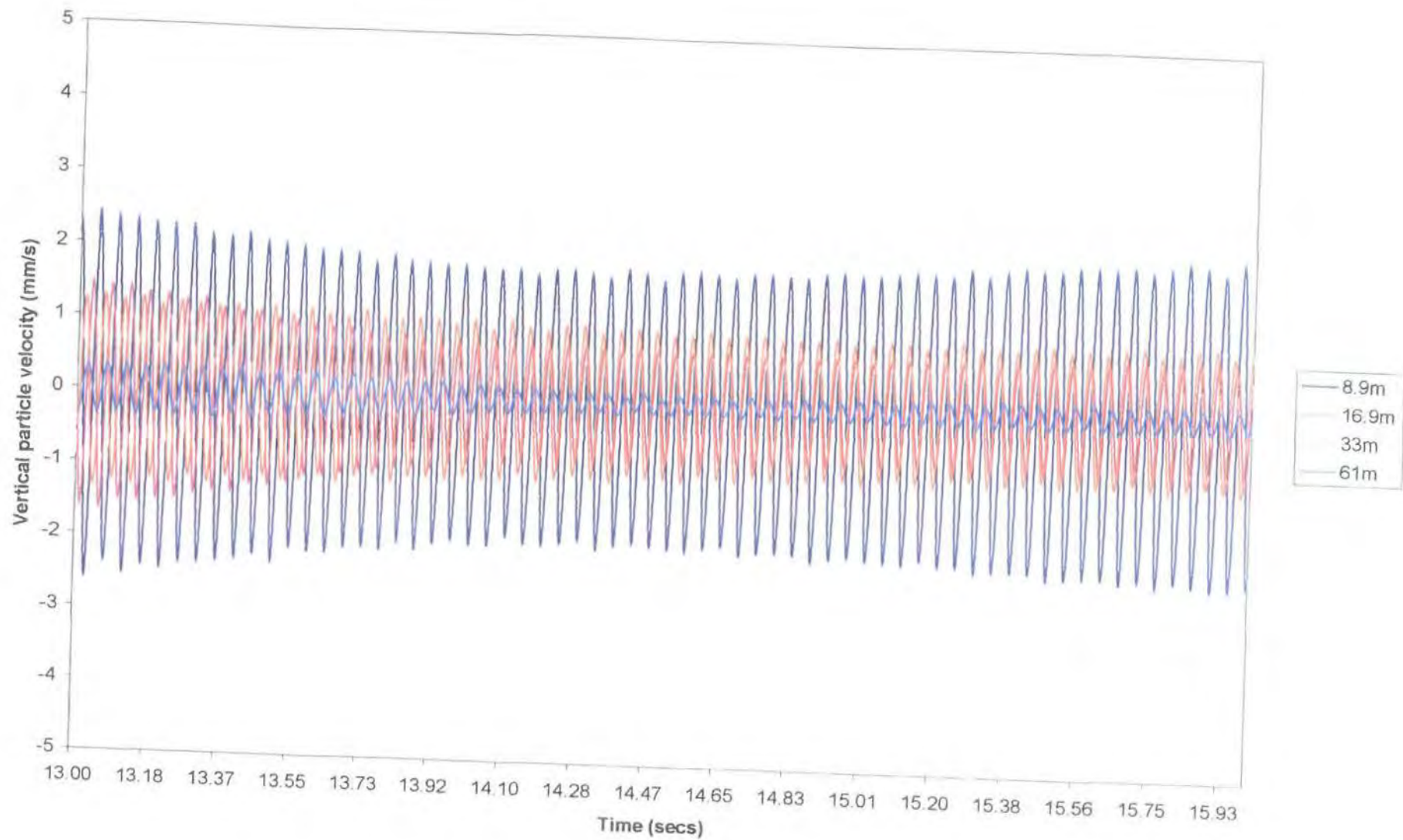


Figure 5.1(d) Vertical particle velocity/time traces recorded during first 12 seconds of extraction of casing from a depth of 15.5m (Second Severn Crossing) (d) 9-12 secs

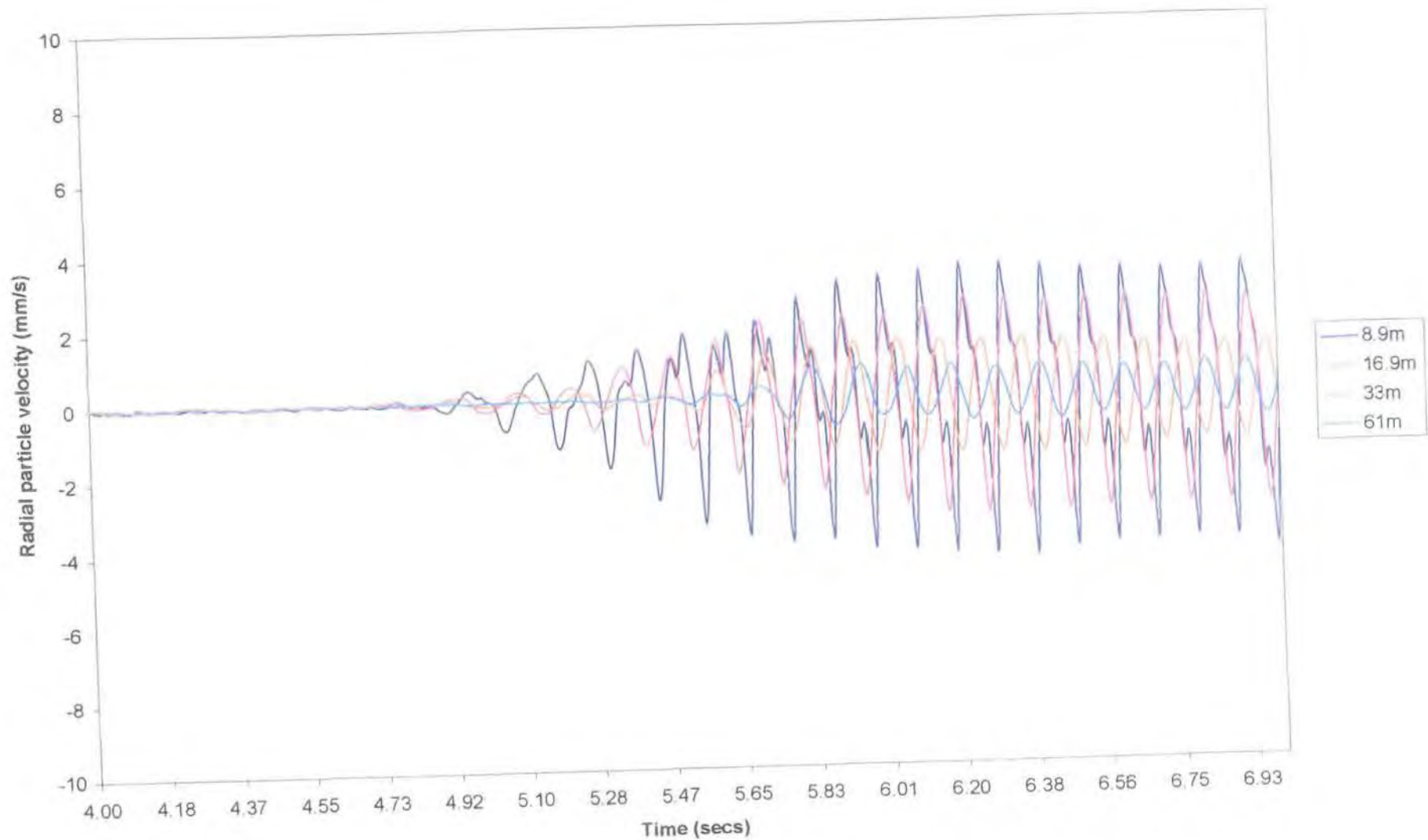


Figure 5.2(a) Radial particle velocity/time traces recorded during first 12 seconds of extraction of casing from a depth of 15.5m (Second Severn Crossing) (a) 0-3 secs

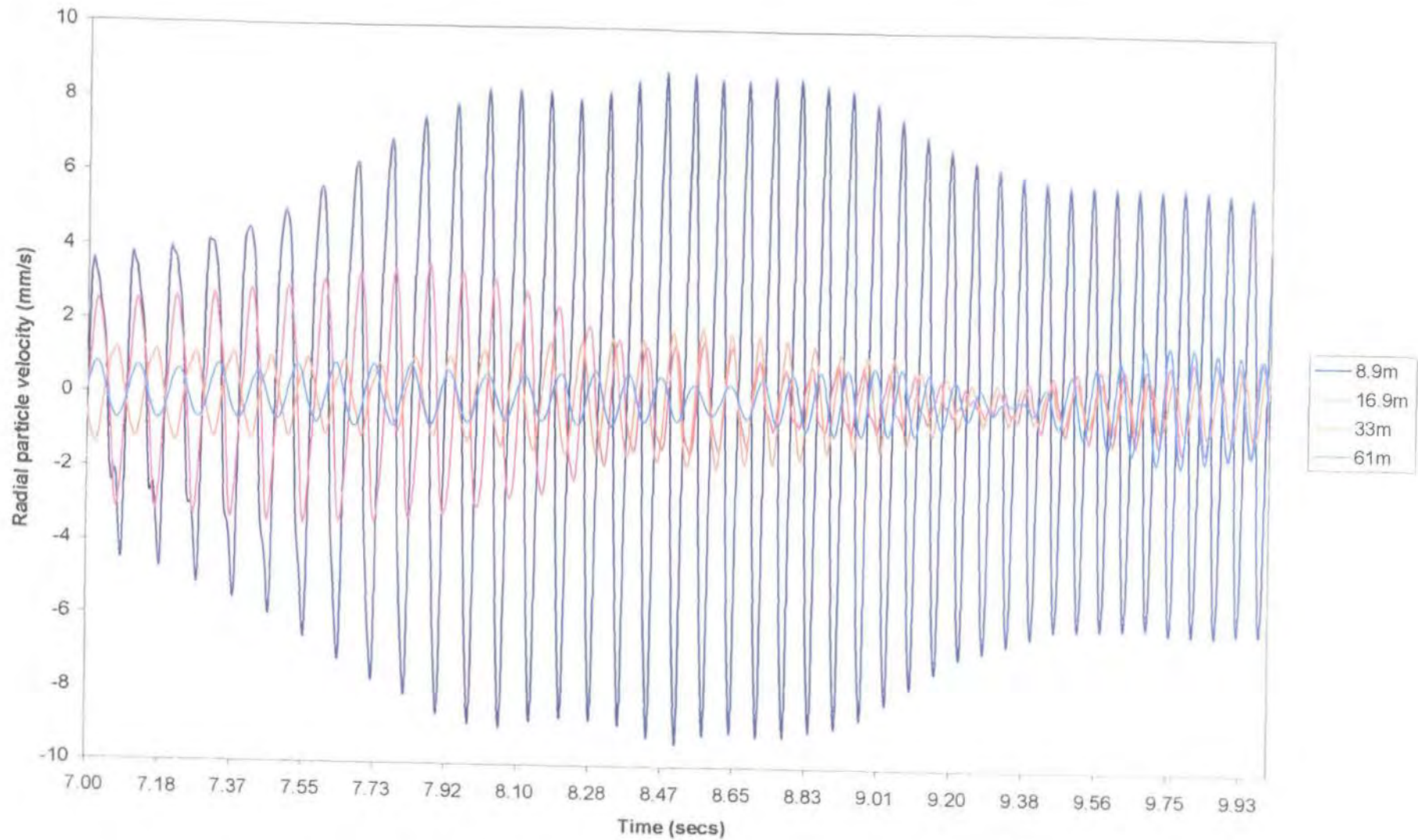


Figure 5.2(b) Radial particle velocity/time traces recorded during first 12 seconds of extraction of casing from a depth of 15.5m (Second Severn Crossing) (b) 3-6 secs

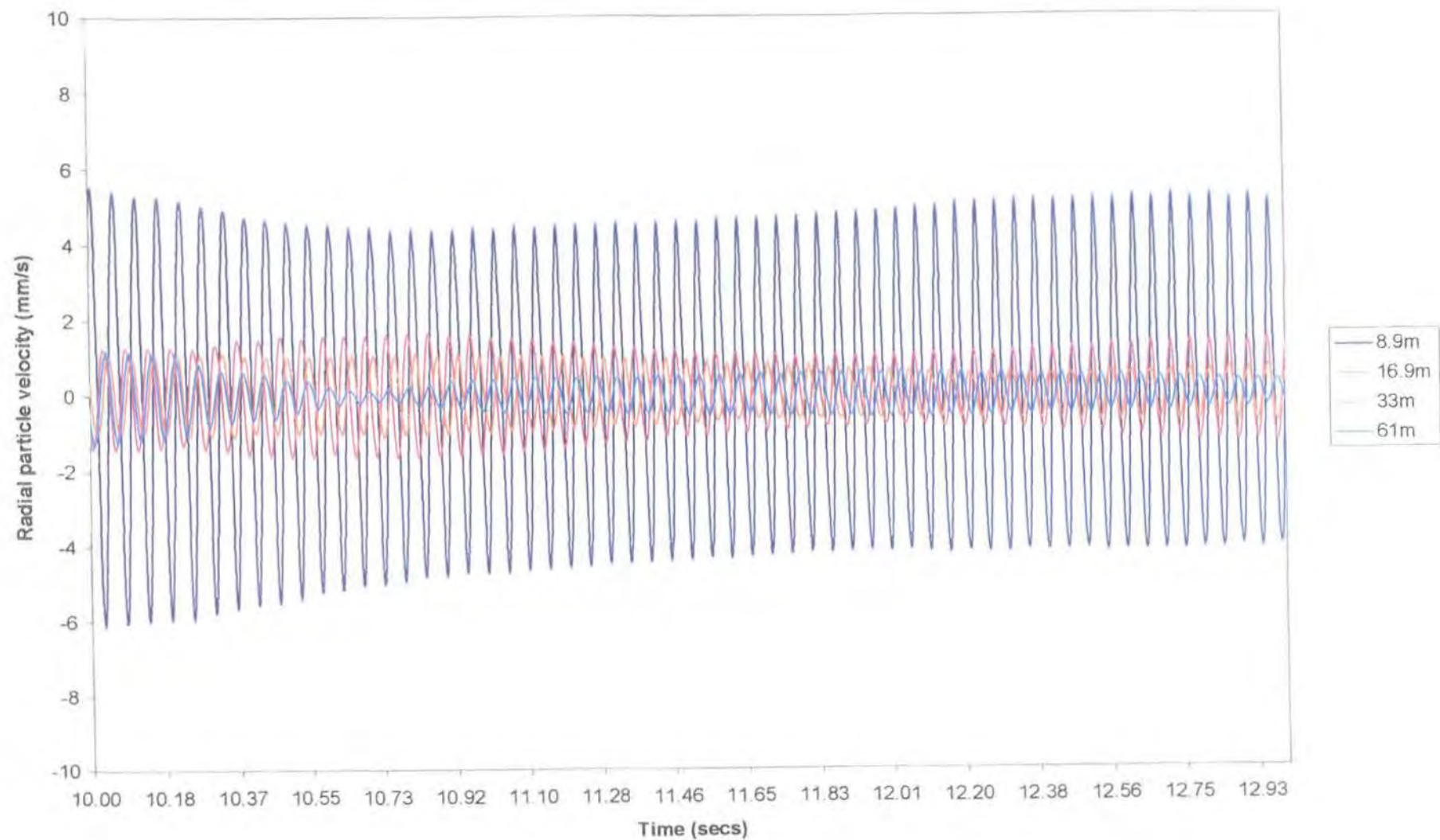


Figure 5.2(c) Radial particle velocity/time traces recorded during first 12 seconds of extraction of casing from a depth of 15.5m (Second Severn Crossing) (c) 6-9 secs

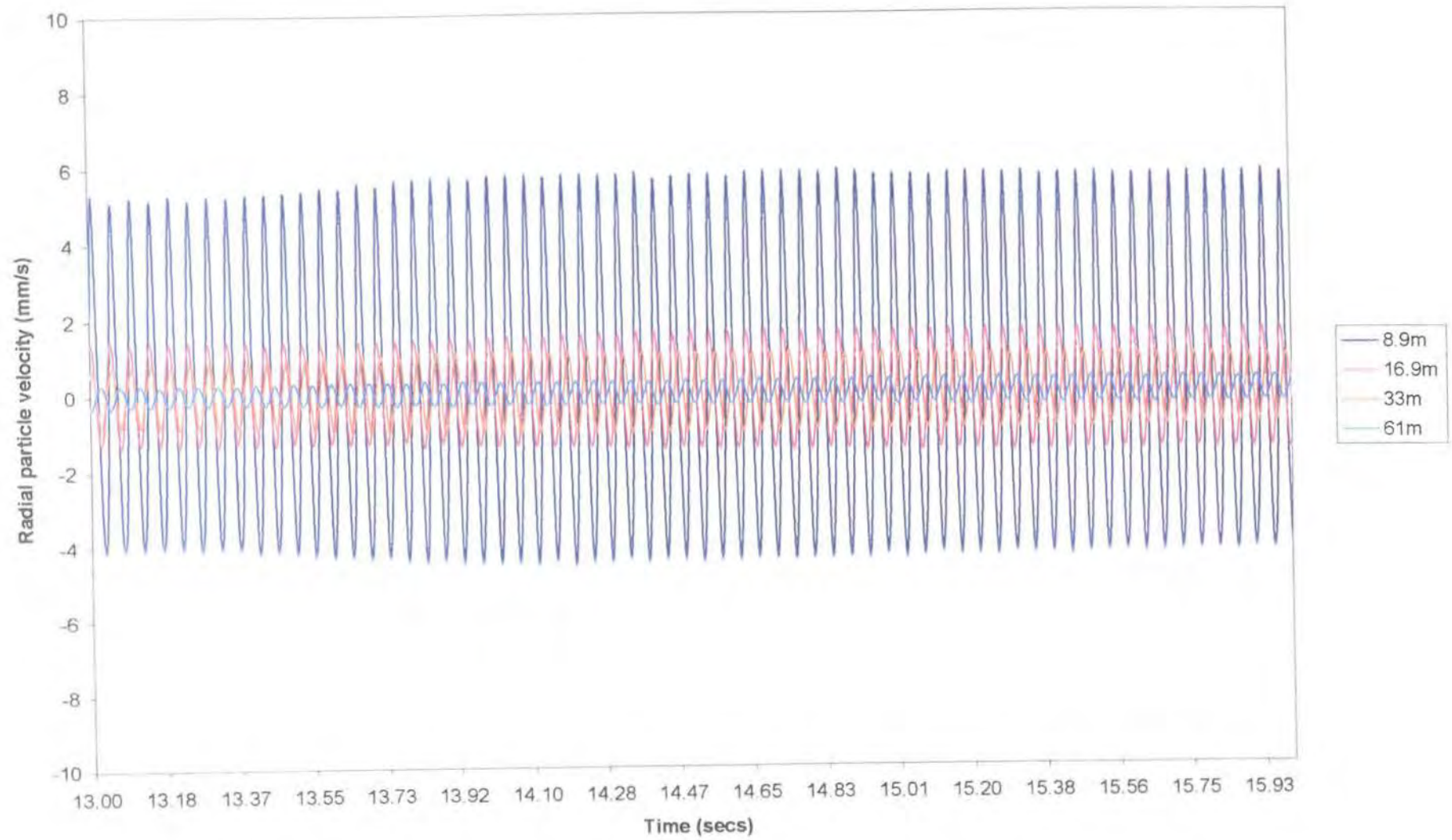


Figure 5.2(d) Radial particle velocity/time traces recorded during first 12 seconds of extraction of casing from a depth of 15.5m (Second Severn Crossing) (d) 9-12 secs

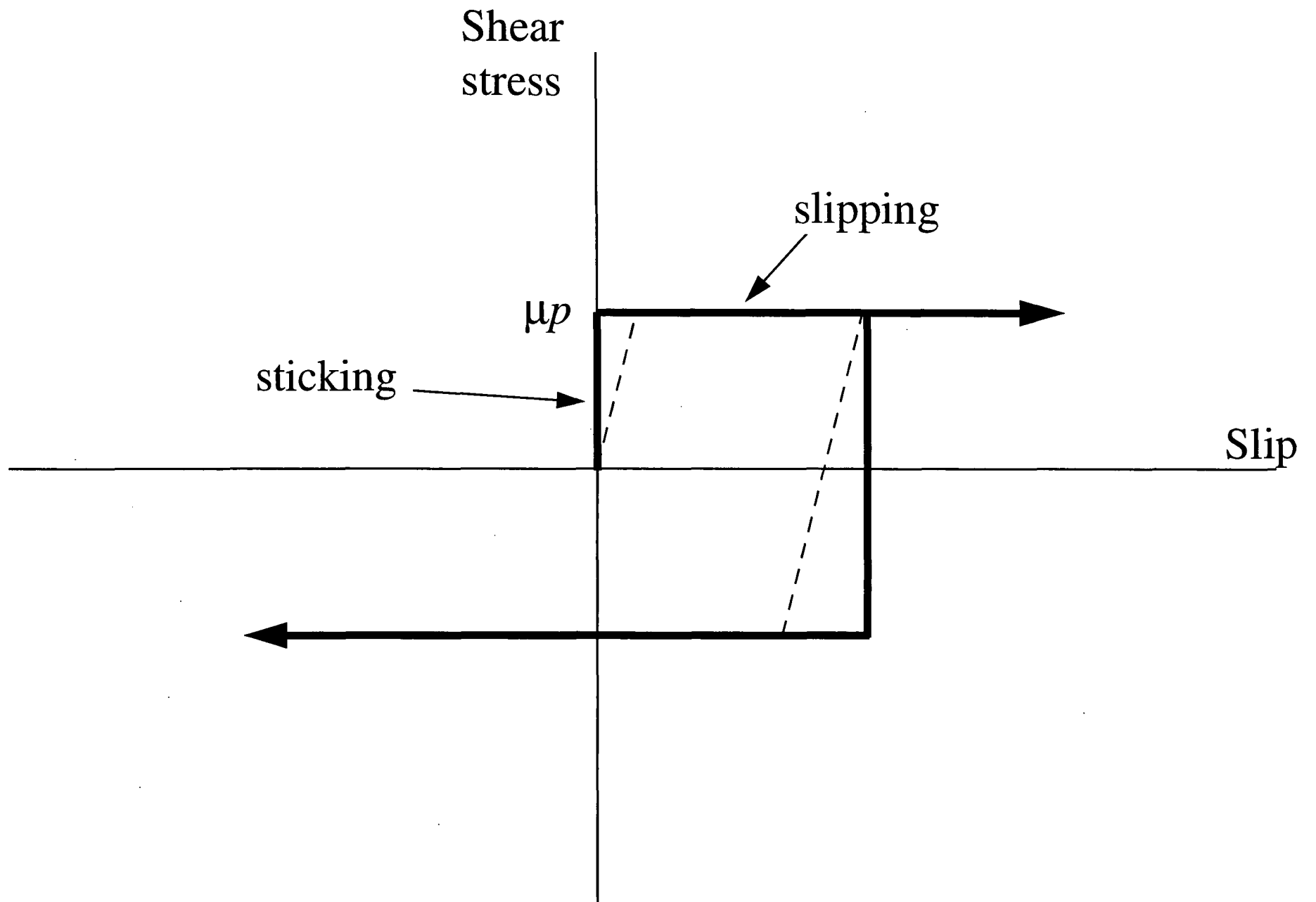


Figure 5.3

The ABAQUS friction model

ABAQUS

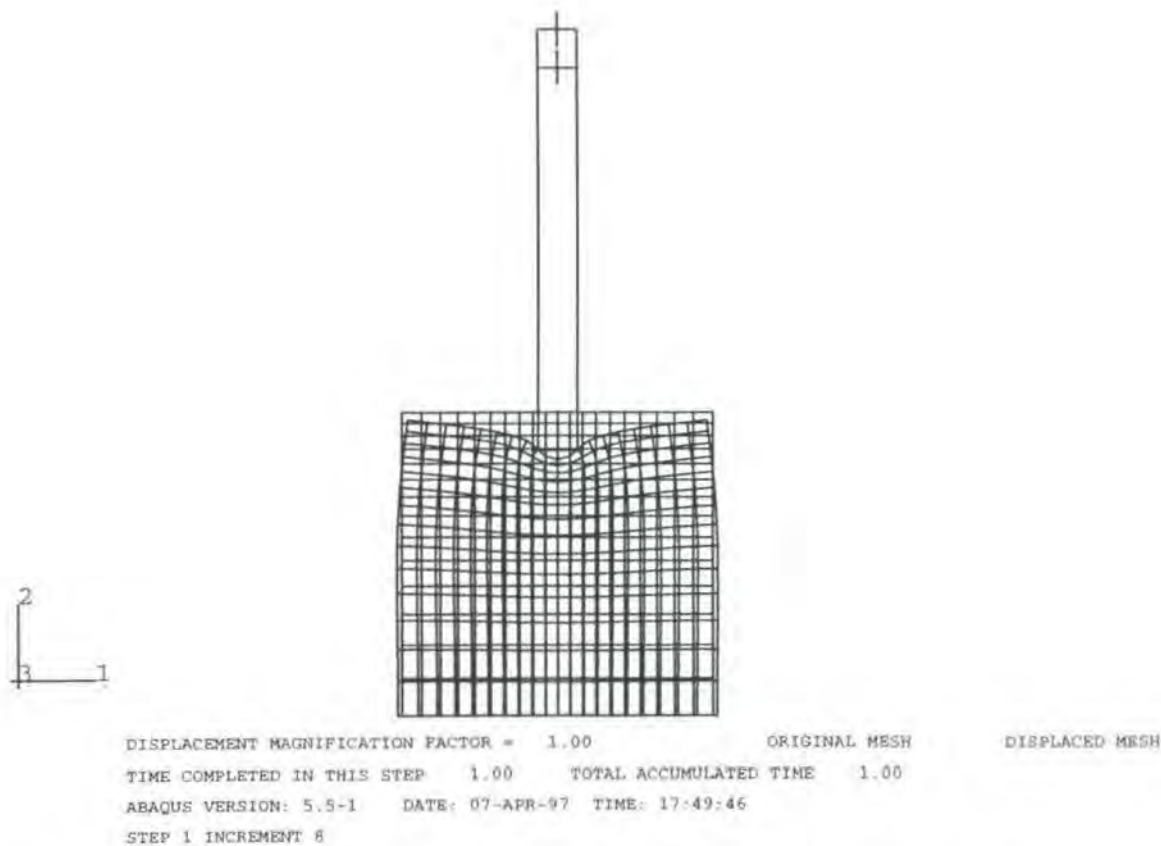


Figure 5.4

Displaced mesh for a plane strain model of a pile resting on the ground surface subjected to a downward vertical displacement of 1 unit

ABAQUS

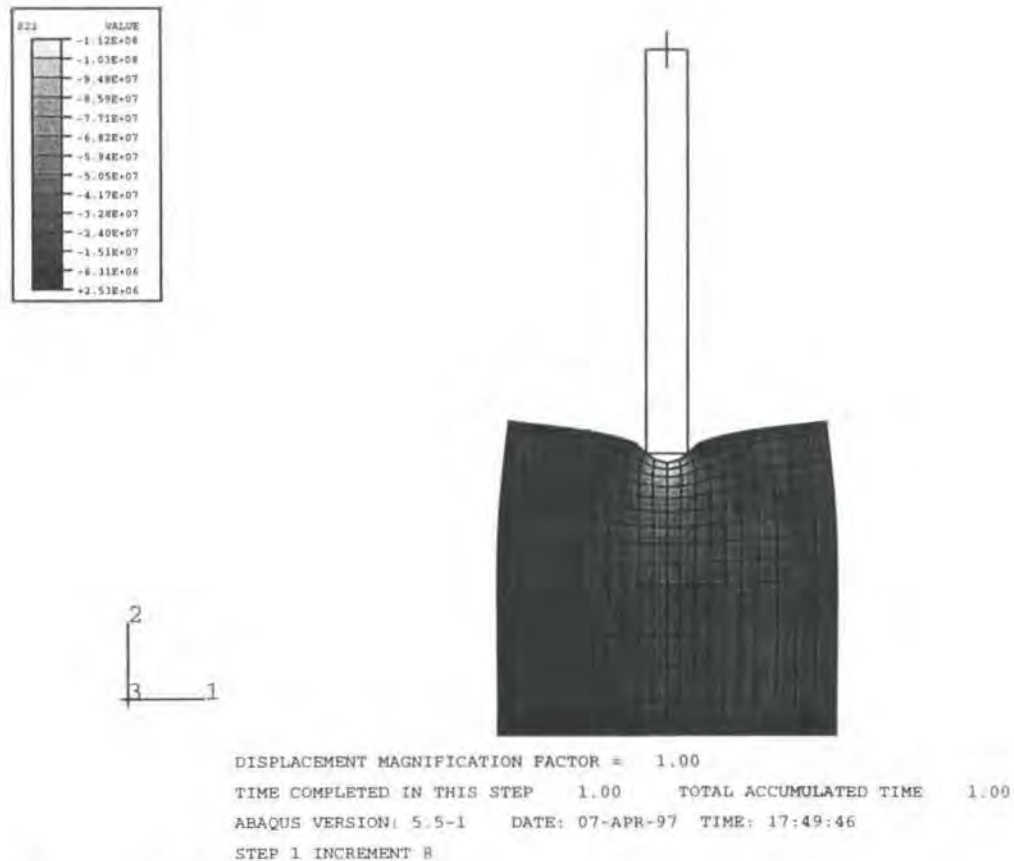


Figure 5.5

Vertical stresses for a plane strain model of a pile resting on the ground surface subjected to a downward vertical displacement of 1 unit

ABAQUS

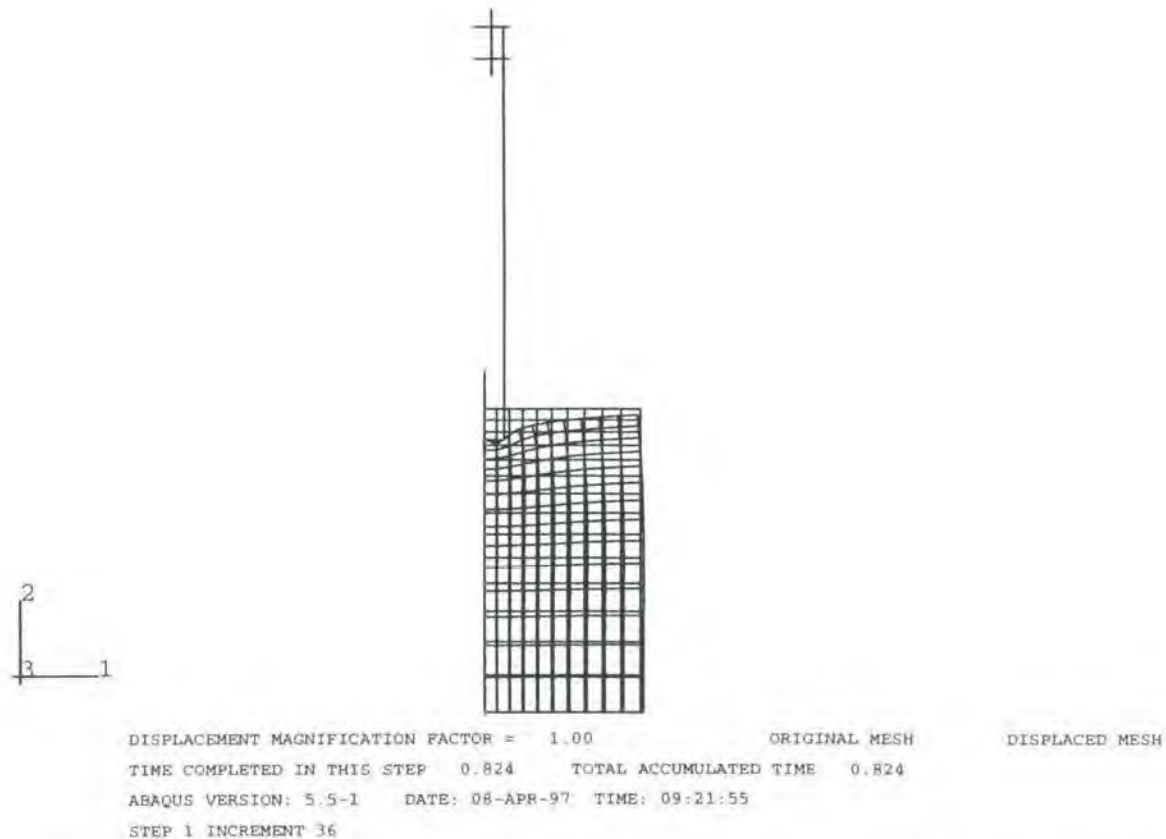


Figure 5.6

Displaced mesh for an axisymmetric model of a pile resting on the ground surface subjected to a downward vertical displacement of 1 unit

ABAQUS

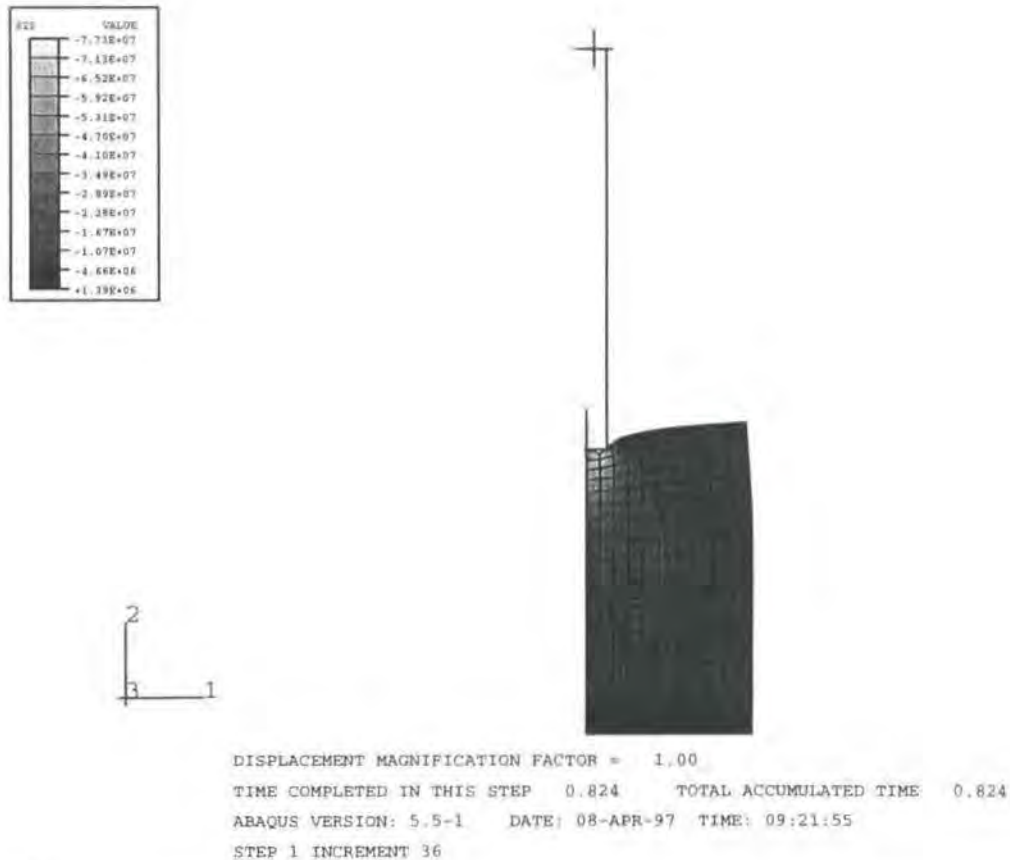


Figure 5.7

Vertical stresses for an axisymmetric model of a pile resting on the ground surface subjected to a downward vertical displacement of 1 unit

ABAQUS

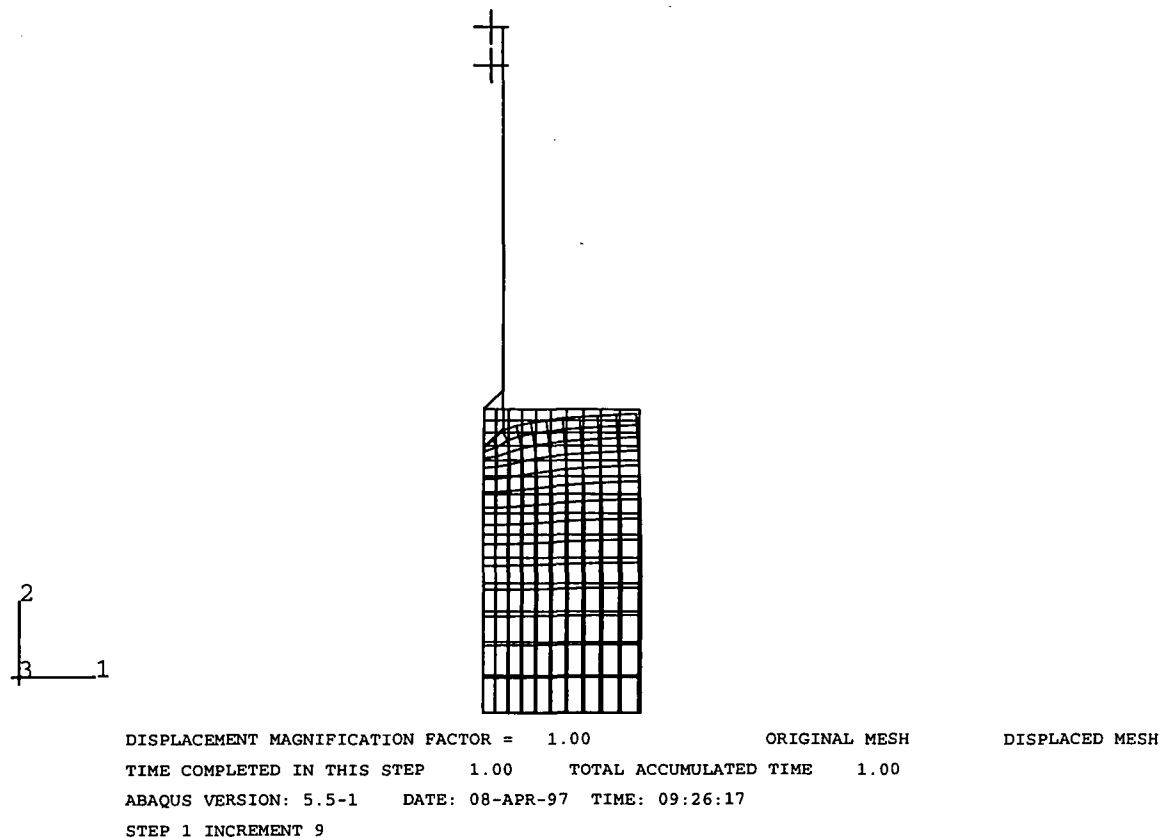


Figure 5.8

Displaced mesh for an axisymmetric model of a pile resting on the ground surface subjected to a downward vertical displacement of 1 unit: Pointed toe

ABAQUS

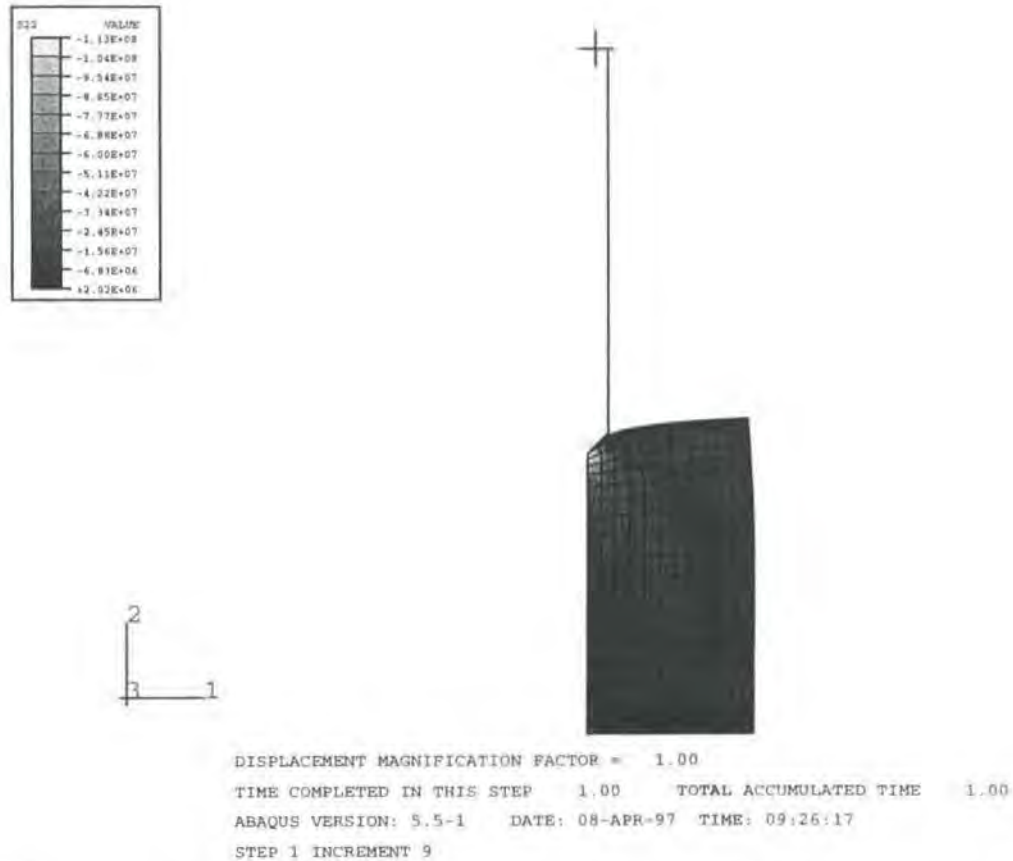


Figure 5.9

Vertical stresses for an axisymmetric model of a pile resting on the ground surface subjected to a downward vertical displacement of 1 unit: Pointed toe

ABAQUS

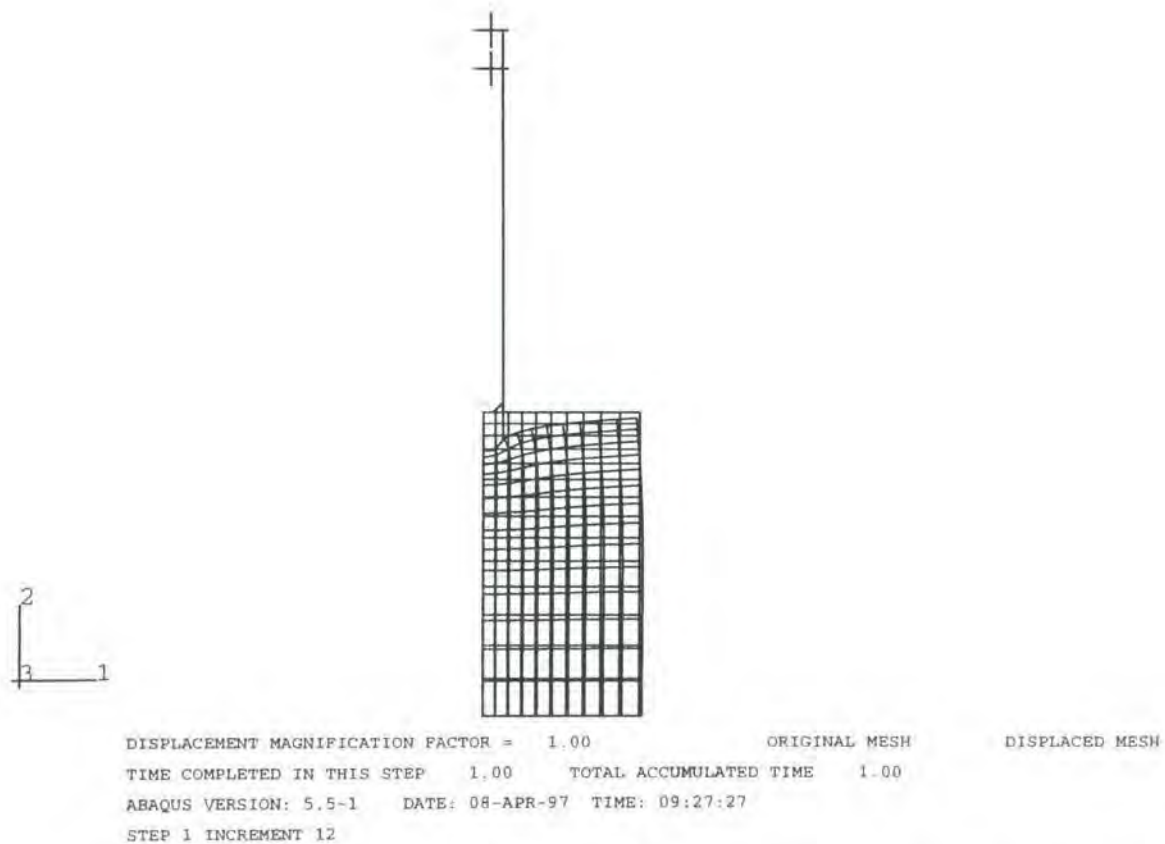


Figure 5.10

Displaced mesh for an axisymmetric model of a pile resting on the ground surface subjected to a downward vertical displacement of 1 unit: Rounded toe

ABAQUS

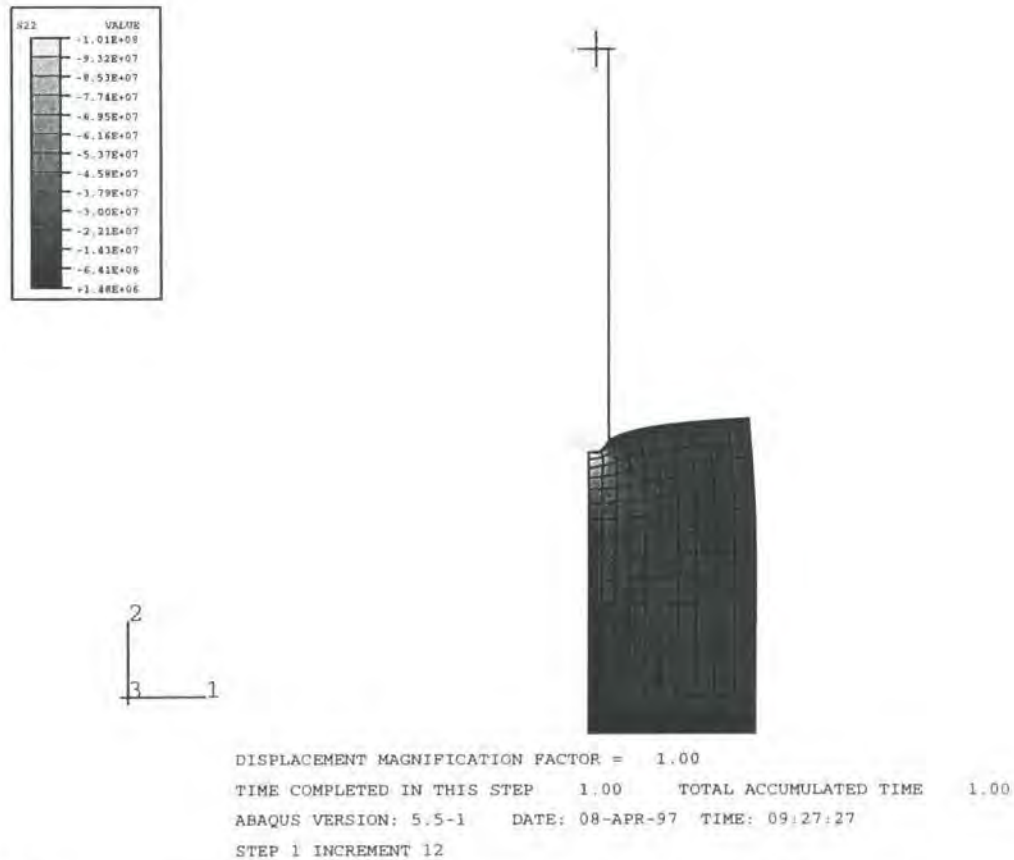


Figure 5.11

Vertical stresses for an axisymmetric model of a pile resting on the ground surface subjected to a downward vertical displacement of 1 unit: Rounded toe

ABAQUS

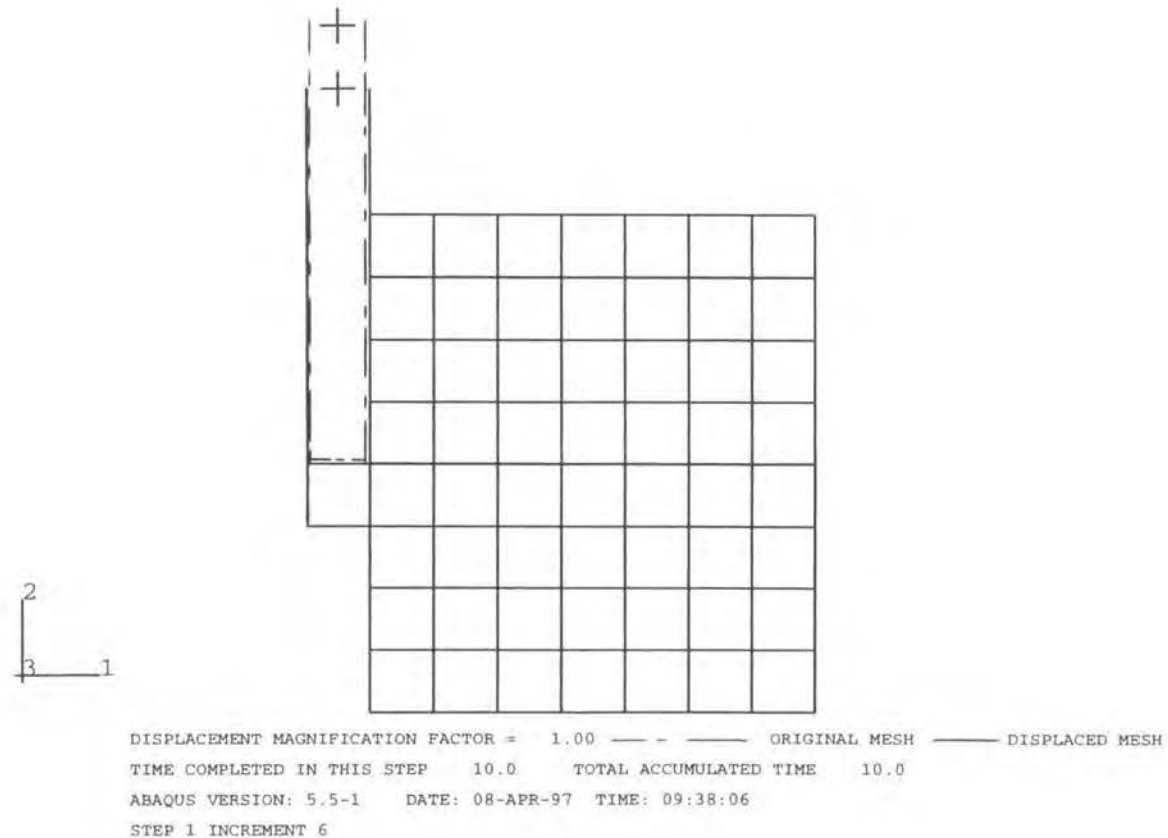
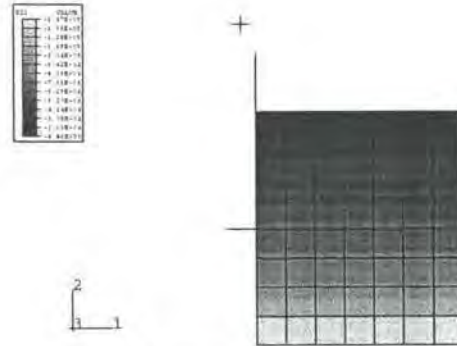


Figure 5.12

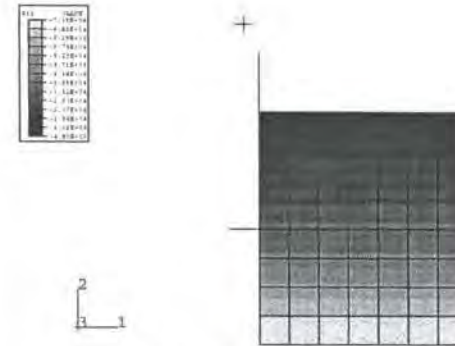
Displaced mesh for an axisymmetric model of a pile sliding vertically against a soil surface

ABAQUS



TIME COMPLETED IN THIS STEP 0. TOTAL ACCUMULATED TIME 0.
ABAQUS VERSION: 5.5-1 DATE: 08-APR-97 TIME: 09:38:06 STEP 0

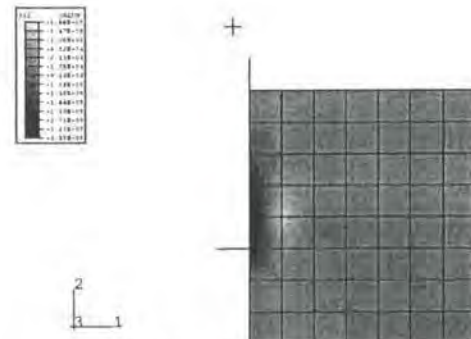
ABAQUS



TIME COMPLETED IN THIS STEP 0. TOTAL ACCUMULATED TIME 0.
ABAQUS VERSION: 5.5-1 DATE: 08-APR-97 TIME: 09:38:06 STEP 0

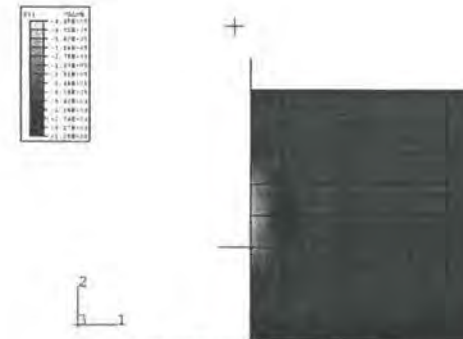
(a) Step 0: initial geostatic stresses

ABAQUS



DISPLACEMENT MAGNIFICATION FACTOR = 1.00
TIME COMPLETED IN THIS STEP 10.0 TOTAL ACCUMULATED TIME 10.0
ABAQUS VERSION: 5.5-1 DATE: 08-APR-97 TIME: 09:38:06
STEP 1 INCREMENT 6

ABAQUS



DISPLACEMENT MAGNIFICATION FACTOR = 1.00
TIME COMPLETED IN THIS STEP 10.0 TOTAL ACCUMULATED TIME 10.0
ABAQUS VERSION: 5.5-1 DATE: 08-APR-97 TIME: 09:38:06
STEP 1 INCREMENT 6

(b) Step 1: following pile displacement

Figure 5.13

Vertical and horizontal stresses for an axisymmetric model of a pile sliding vertically against a soil surface

ABAQUS

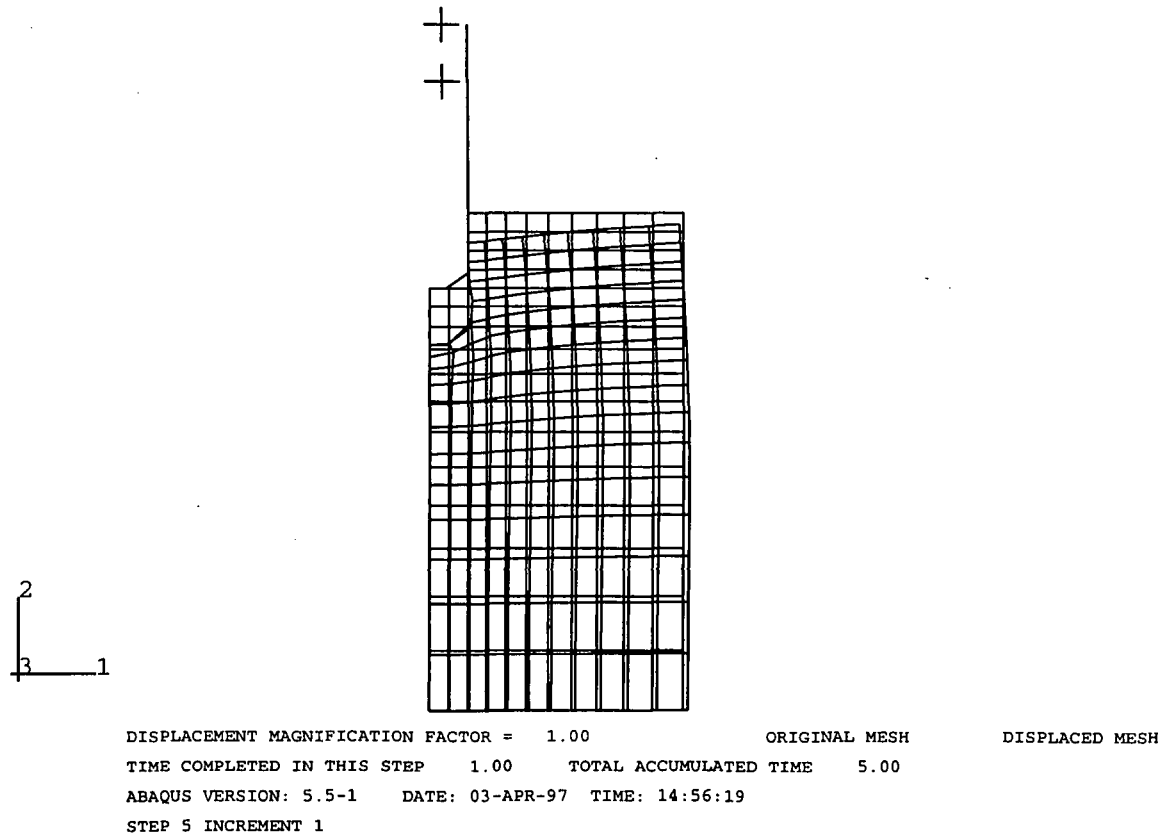


Figure 5.14

Displaced mesh for an axisymmetric model of a pile with a rounded toe at a depth of 1m subjected to a downward vertical displacement of 0.9 units

ABAQUS

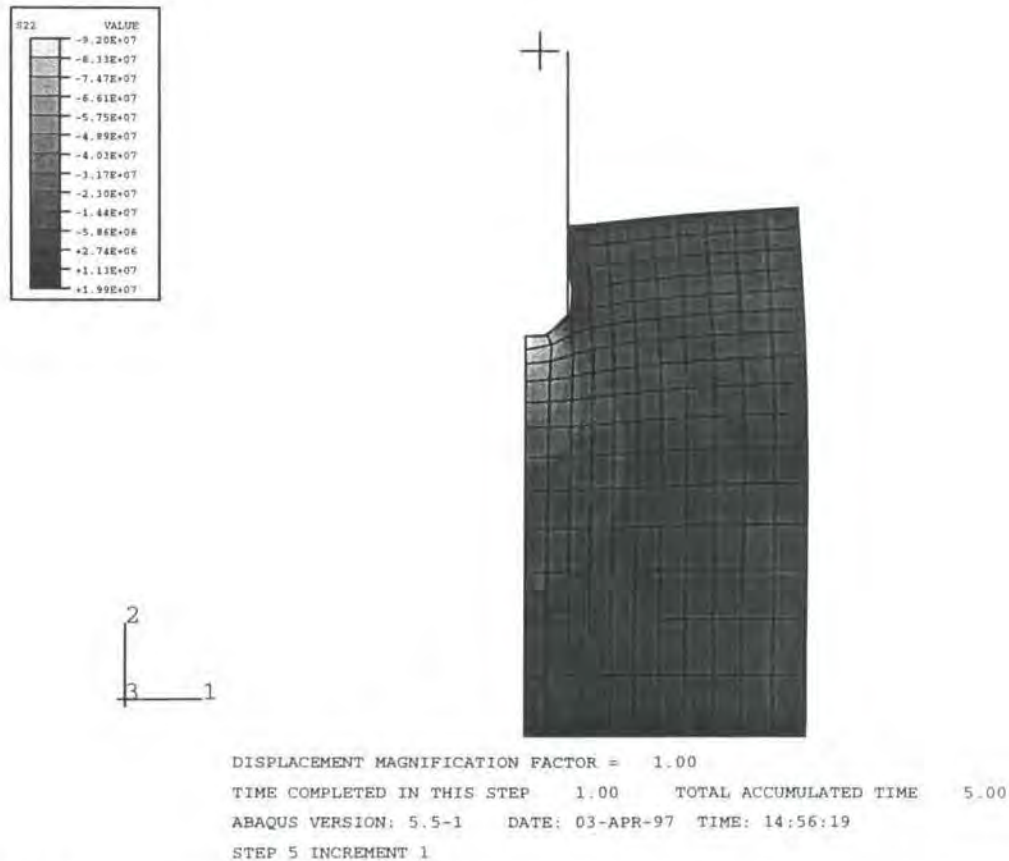


Figure 5.15

Vertical stresses for an axisymmetric model of a pile with a rounded toe at a depth of 1m subjected to a downward vertical displacement of 0.9 units

ABAQUS

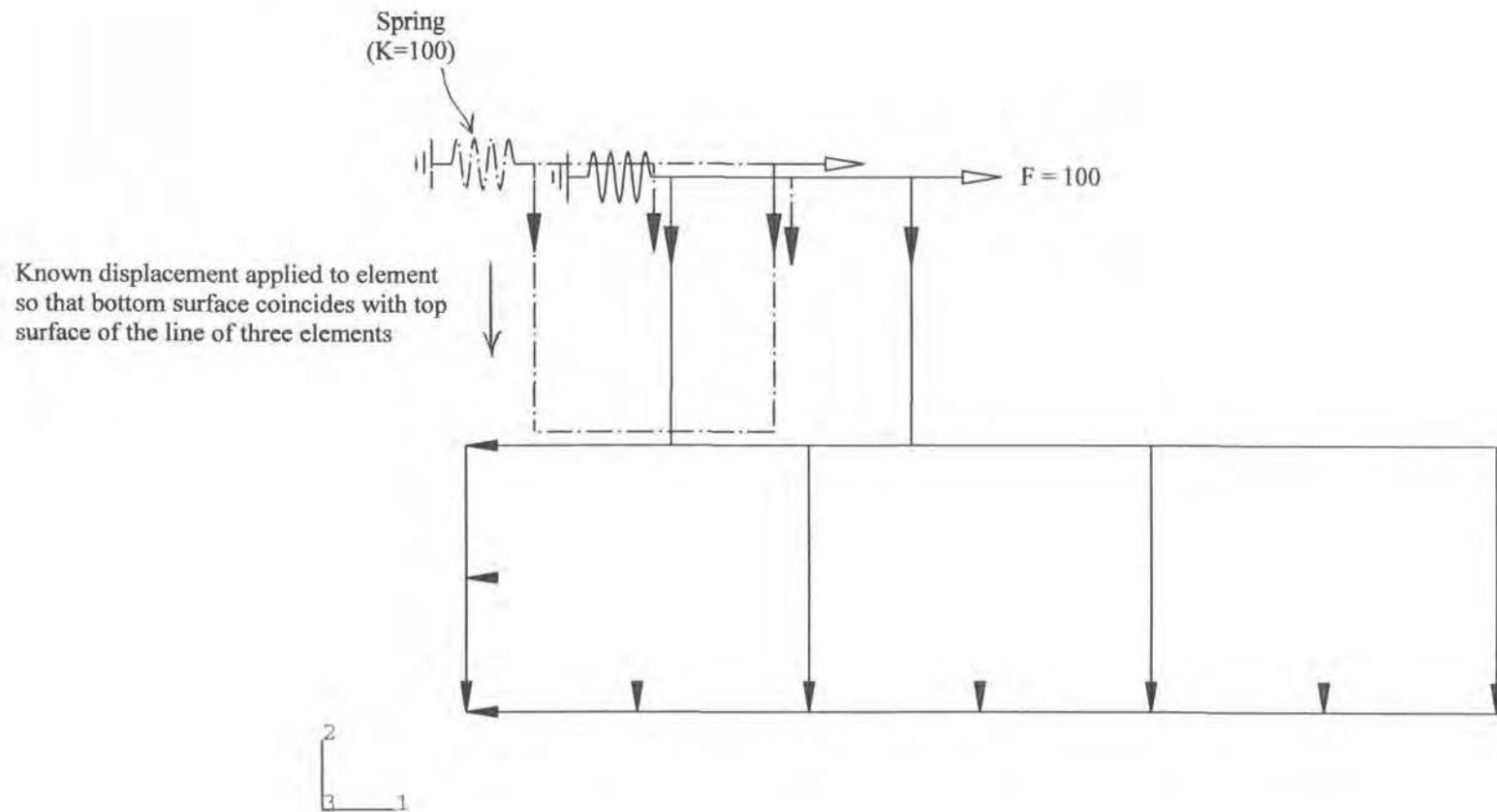


Figure 5.16 Verification of ABAQUS friction model:
Case 1 – no contact pressure between plane strain elements

ABAQUS

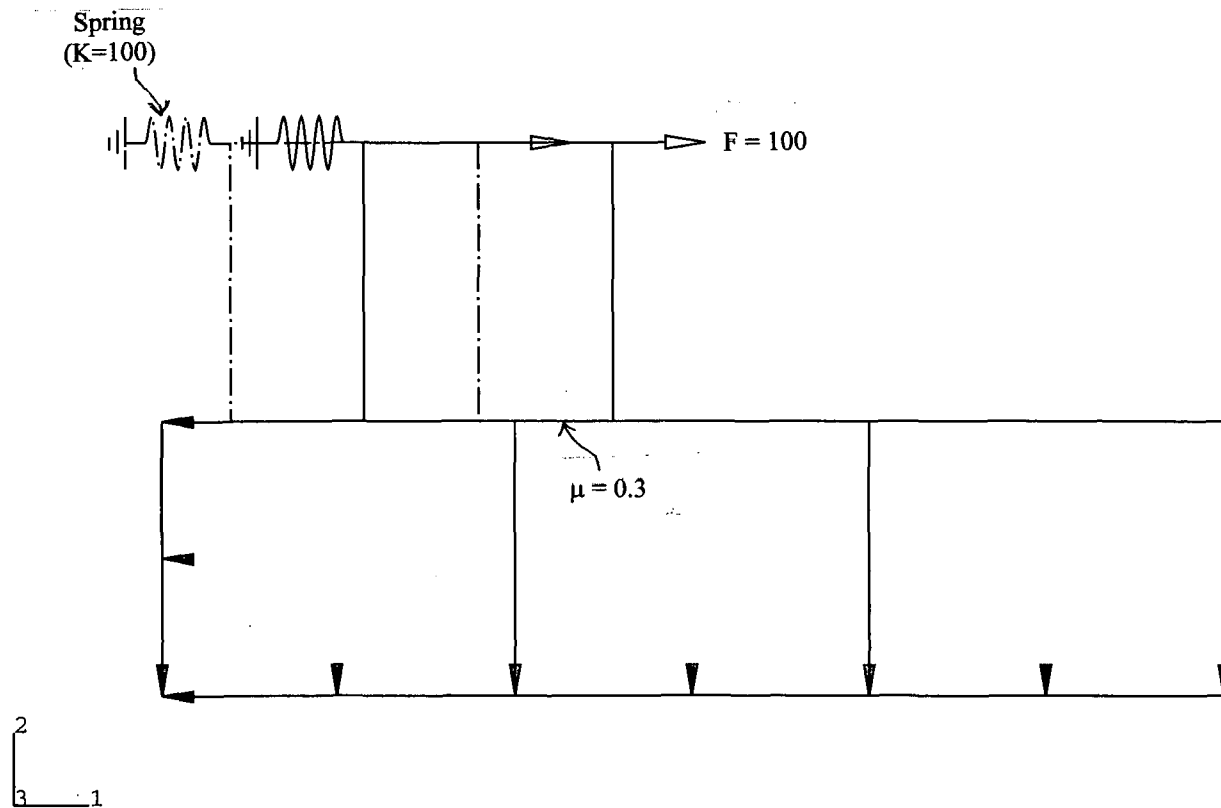


Figure 5.17

Verification of ABAQUS friction model:

Case 2 - contact pressure between plane strain elements, coefficient of friction of 0.3

ABAQUS

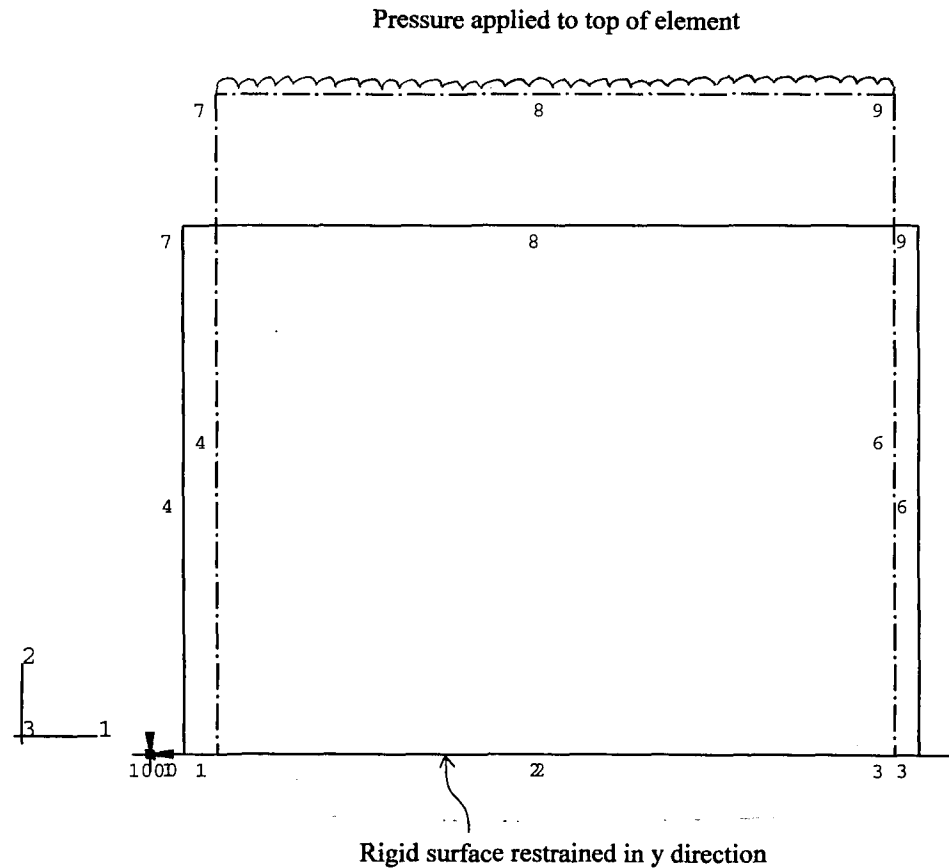


Figure 5.18

Verification of ABAQUS friction model:
Case 3a – pressure applied to top of element

ABAQUS

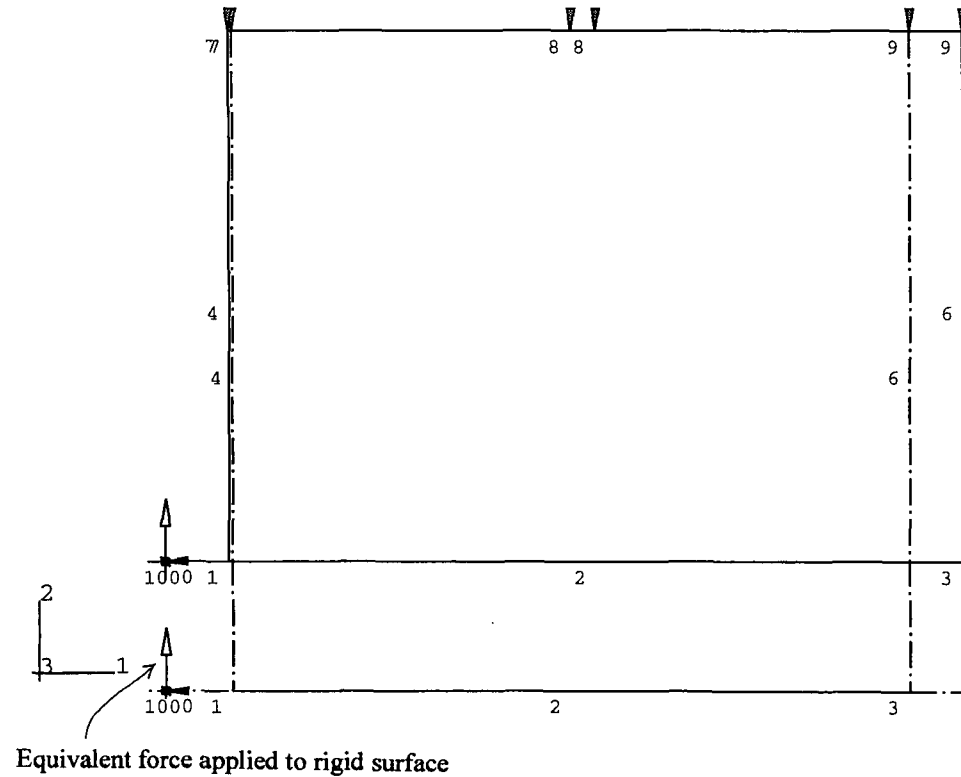


Figure 5.19

Verification of ABAQUS friction model:
Case 3b – equivalent force applied to rigid surface via the reference node

ABAQUS

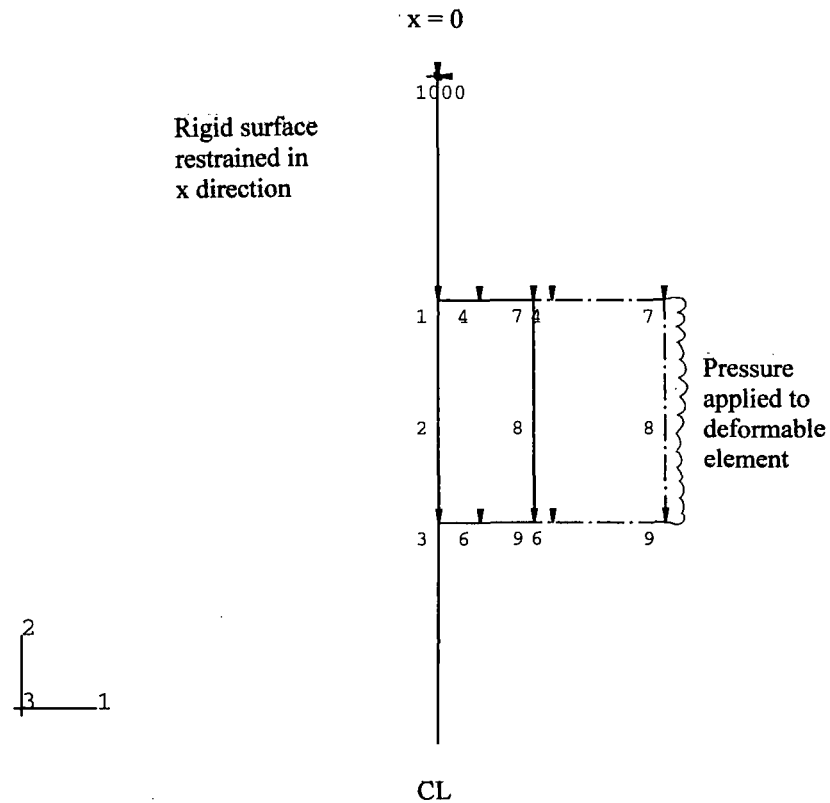


Figure 5.20

Verification of ABAQUS friction model:
Case 4 – axisymmetric case

ABAQUS

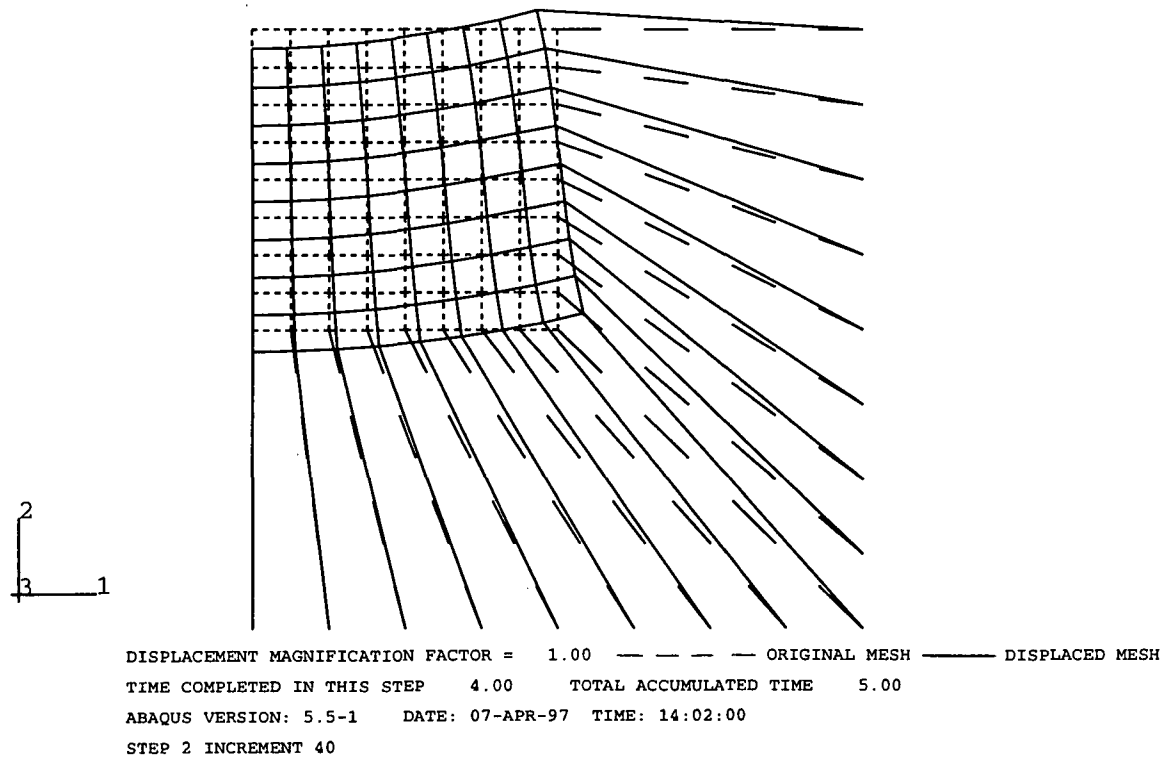


Figure 5.21 Rigid body motion

ABAQUS

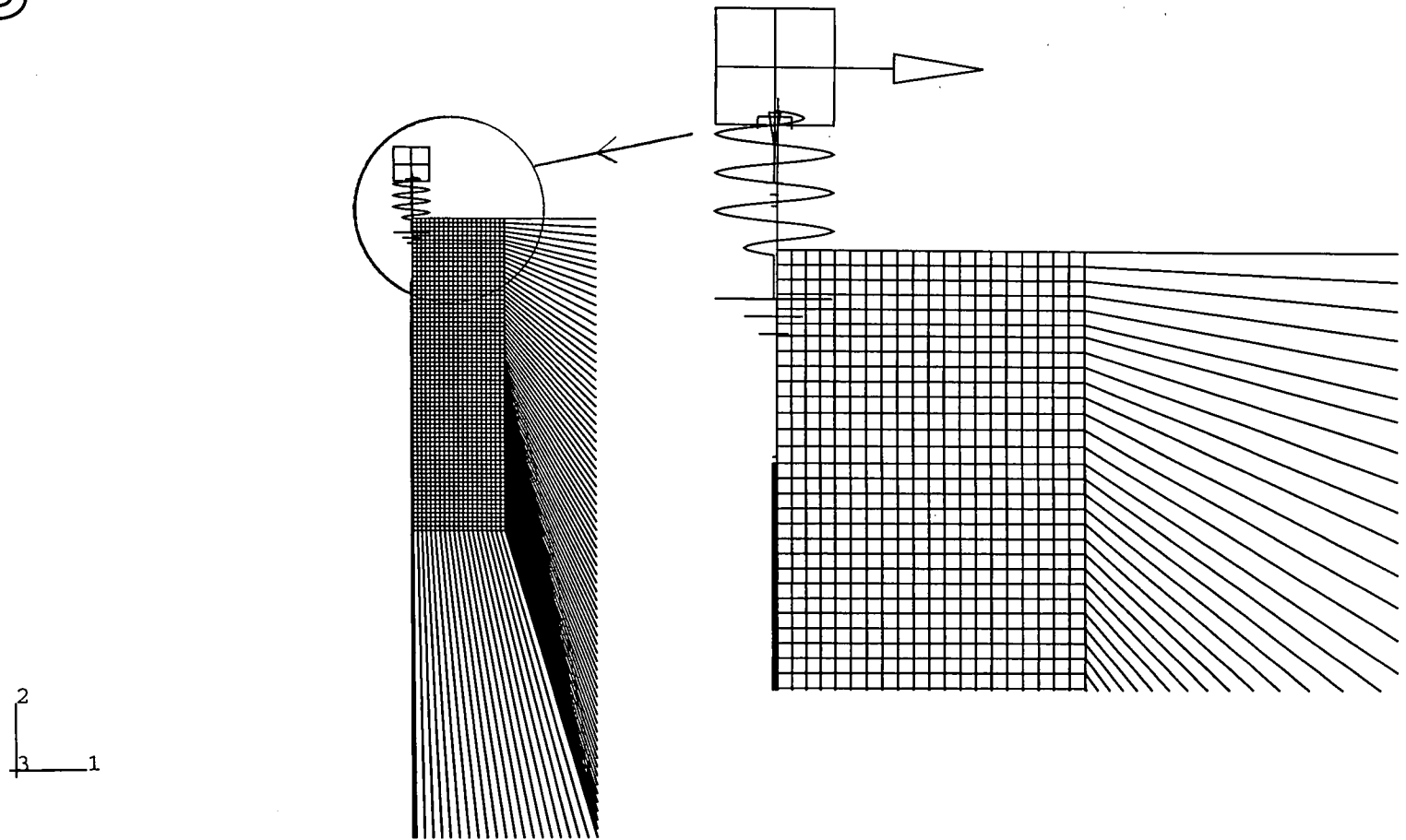


Figure 5.22

Limited axisymmetric FE/IE mesh used for pile/soil interaction analysis (mesh used for Flitwick data)

ABAQUS

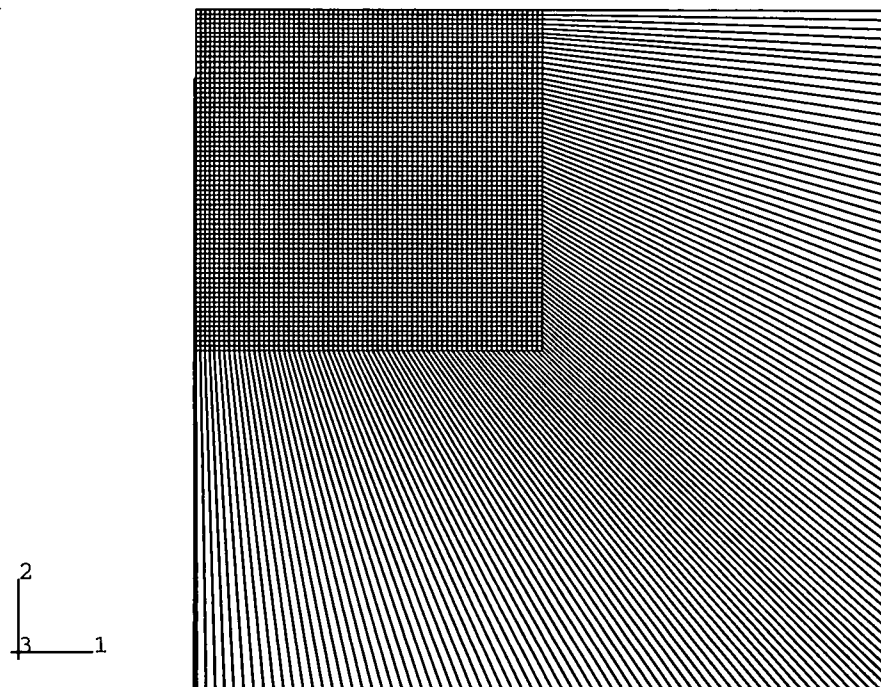


Figure 5.24

Large axisymmetric FE/IE mesh used for wave propagation analysis (mesh used for Flitwick data)

ABAQUS

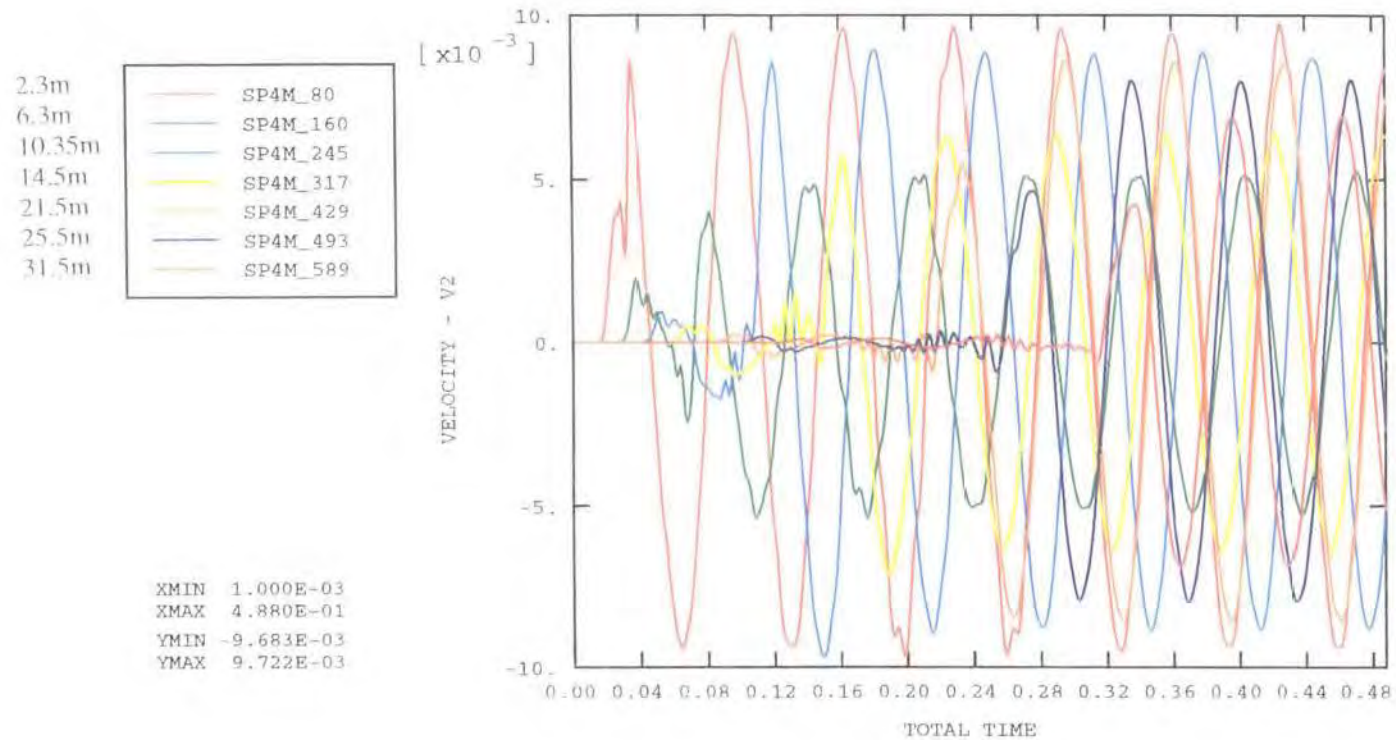
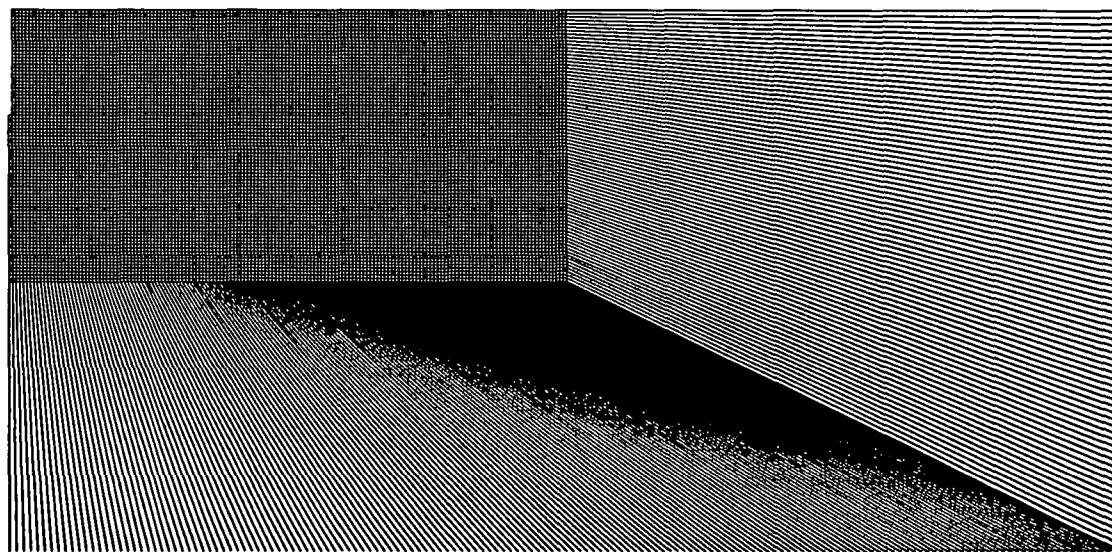


Figure 5.25

Vertical velocity/time traces for surface nodes at various horizontal distances from the pile

ABAQUS



170

Figure 5.26 80m wide FE/IE mesh used to investigate 'standing wave' phenomenon (Second Severn Crossing site)

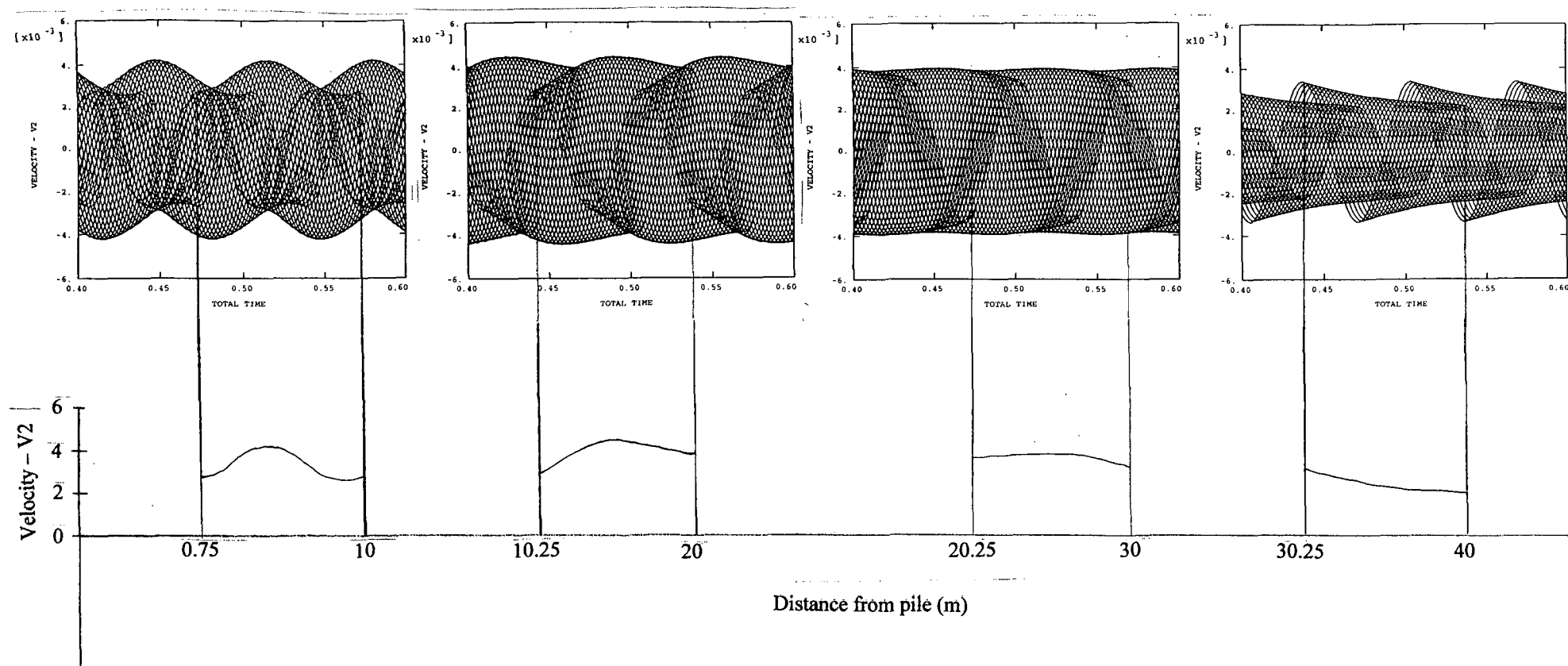


Figure 5.27

Standing wave generated by vibratory extraction:
Vertical velocity/time traces for all surface nodes between 0.75m and 40m

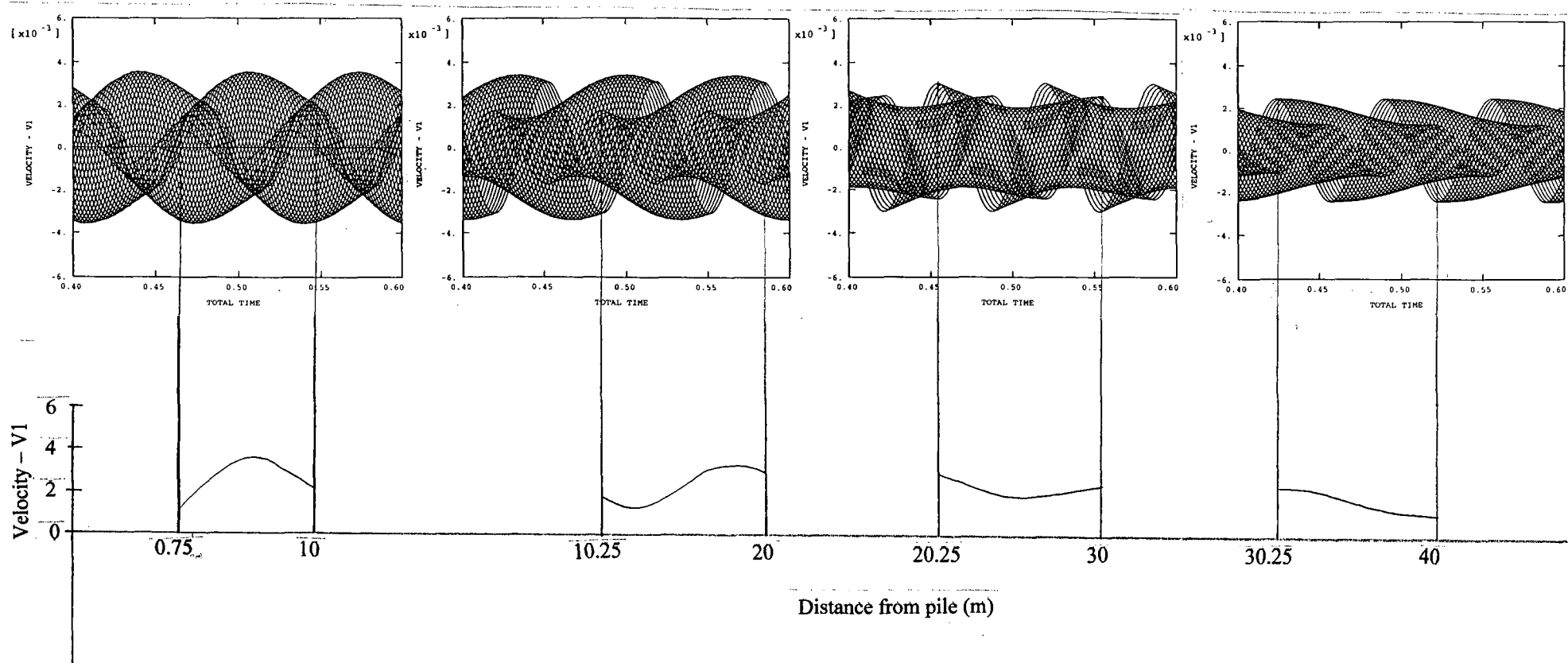
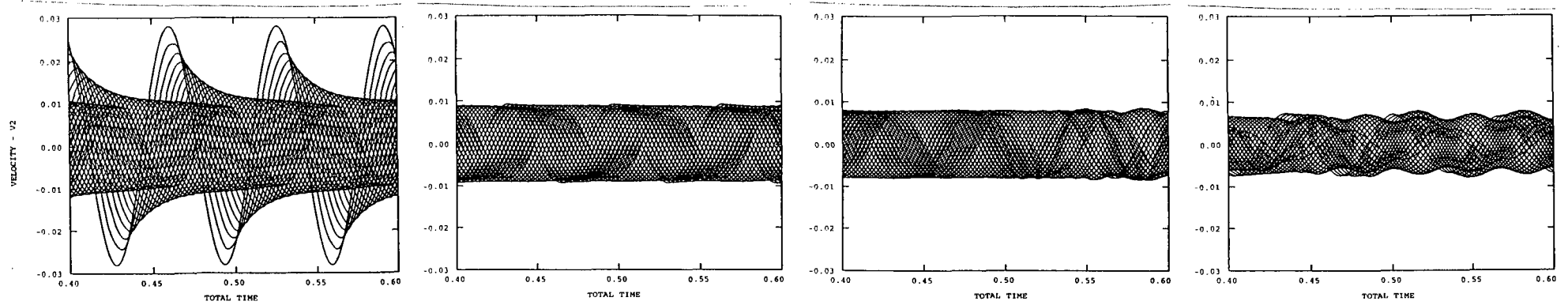
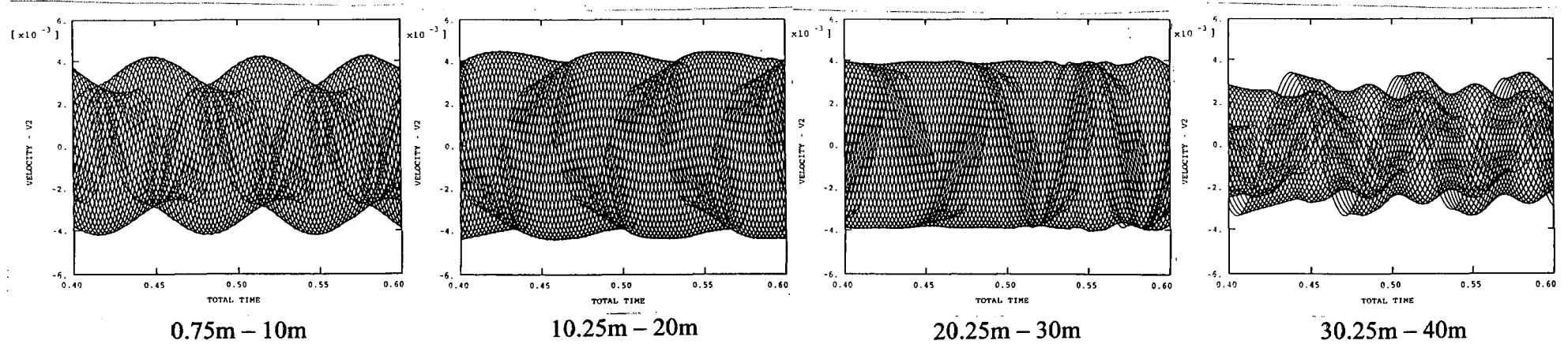


Figure 5.28

Standing wave generated by vibratory extraction:
Radial velocity/time traces for all surface nodes between 0.75m and 40m



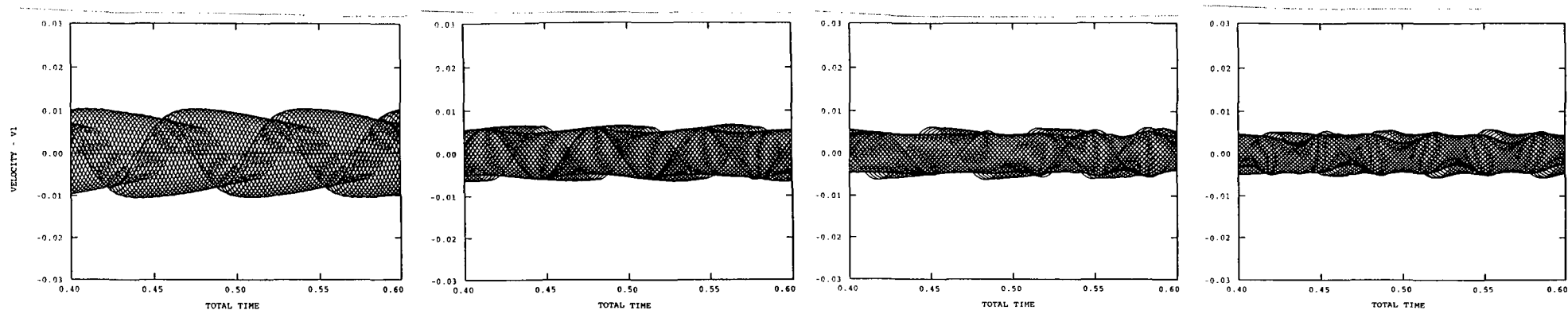
(a) Uniform displacement of all soil/pile interface nodes



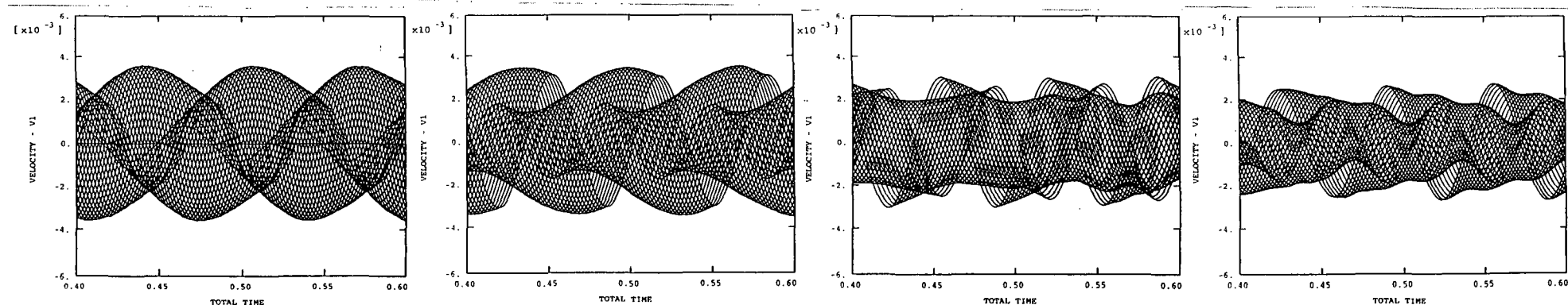
(b) Non-uniform displacement of all soil/pile interface nodes

Figure 5.29

Comparison of the response induced by uniform displacement of all soil/pile interface nodes and that induced by non-uniform displacement of the interface nodes: Vertical velocity/time traces (0.75m and 40m)



(a) Uniform displacement of all soil/pile interface nodes



0.75m – 10m

10.25m – 20m

20.25m – 30m

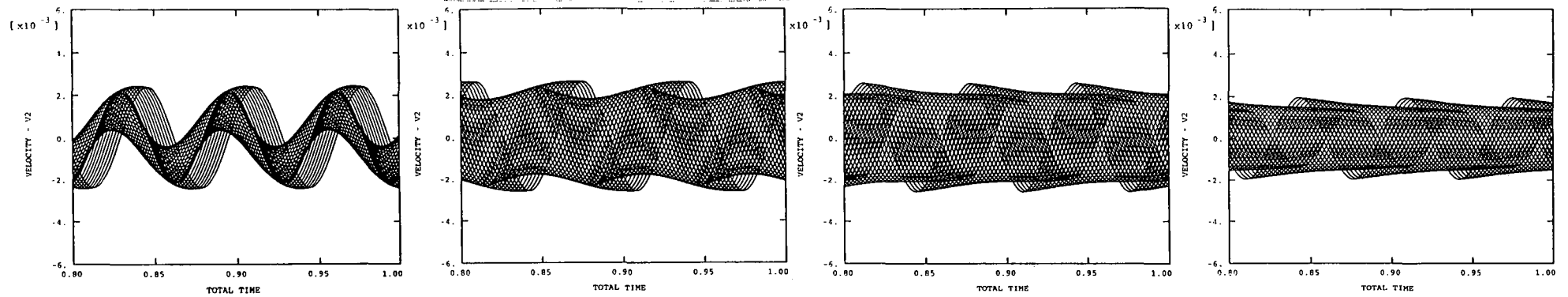
30.25m – 40m

(b) Non-uniform displacement of all soil/pile interface nodes

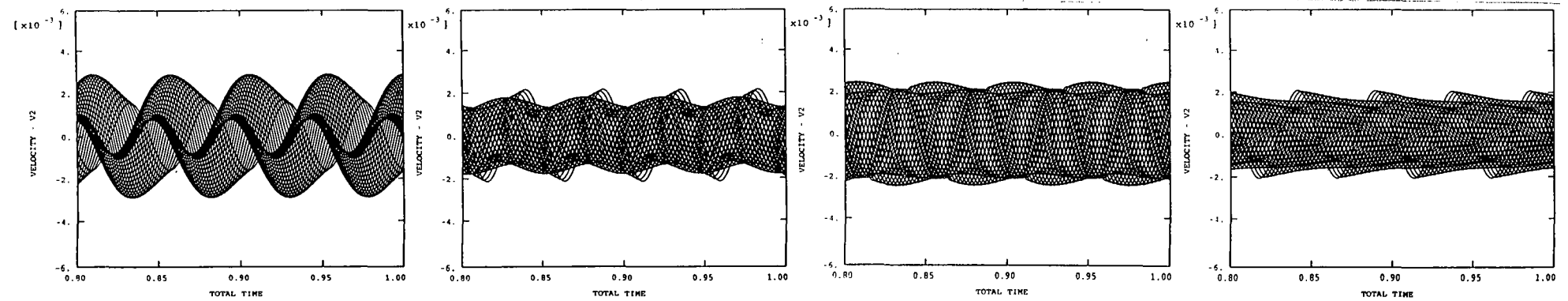
Figure 5.30

Comparison of the response induced by uniform displacement of all soil/pile interface nodes and that induced by non-uniform displacement of the interface nodes: Radial velocity/time traces (0.75m and 40m)

441



(a) Frequency = 15.2 Hz



0.75m – 10m

10.25m – 20m

20.25m – 30m

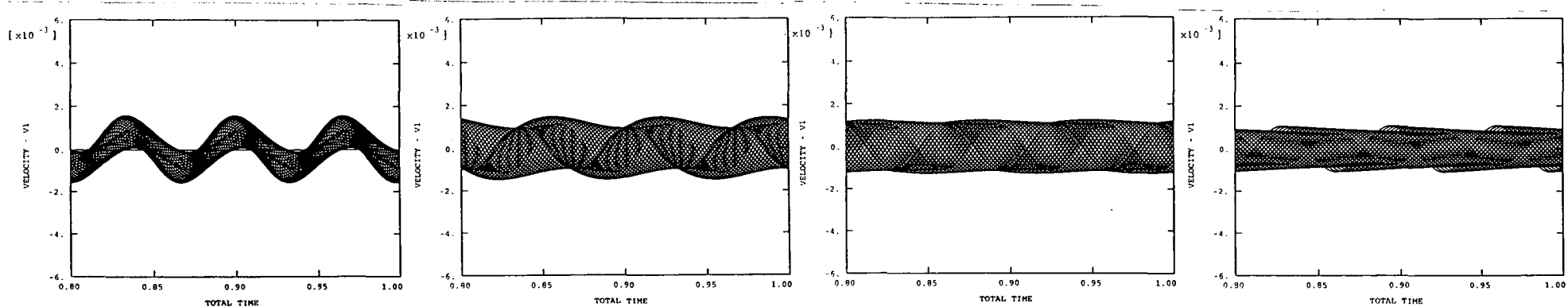
30.25m – 40m

(b) Frequency = 20.9 Hz

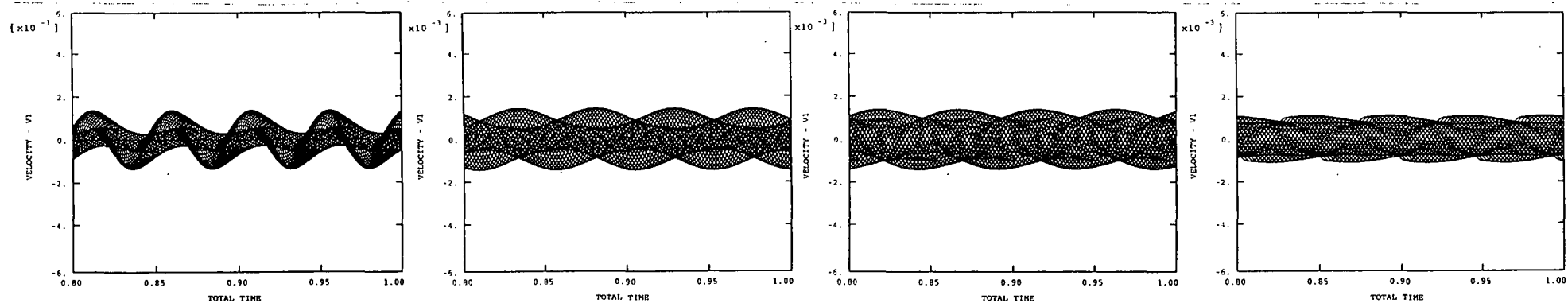
Figure 5.31

Comparison of the response induced by an excitation frequency of 15.2Hz and that induced by a frequency of 20.9Hz: Vertical velocity/time traces (0.75m and 40m)

SL



(a) Frequency = 15.2 Hz



0.75m – 10m

10.25m – 20m

20.25m – 30m

30.25m – 40m

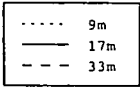
(b) Frequency = 20.9 Hz

Figure 5.32

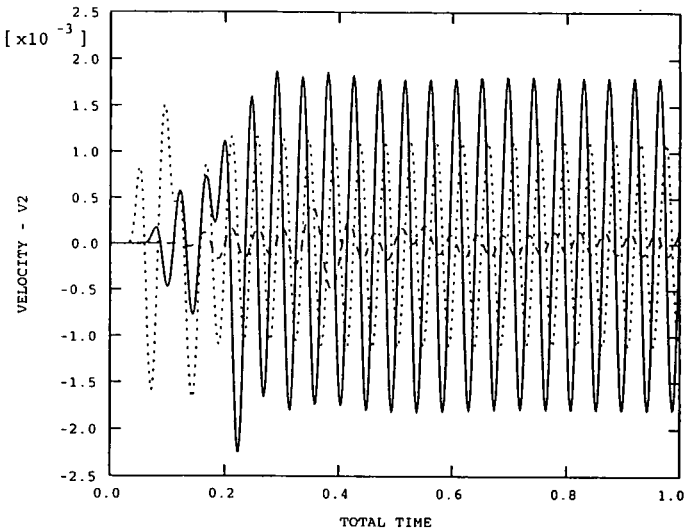
Comparison of the response induced by an excitation frequency of 15.2Hz and that induced by a frequency of 20.9Hz: Radial velocity/time traces (0.75m and 40m)

961

ABAQUS

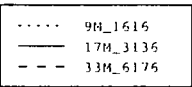


XMIN 1.000E-03
XMAX 1.000E+00
YMIN -2.245E-03
YMAX 1.858E-03

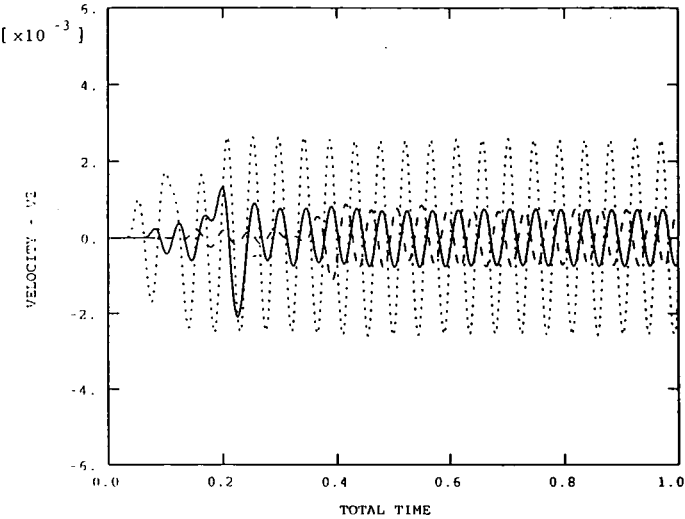


(a) Extraction from 11m

ABAQUS



XMIN 1.000E-03
XMAX 1.000E+00
YMIN -2.605E-03
YMAX 2.639E-03

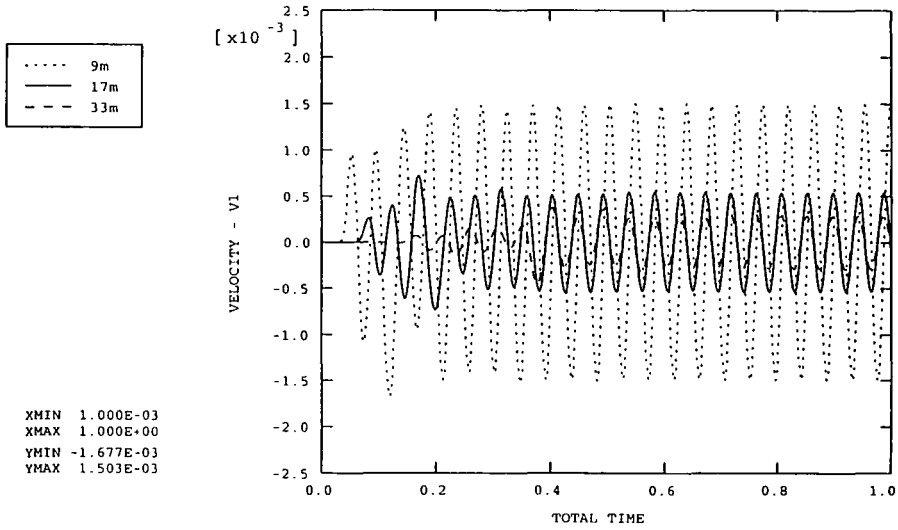


(b) Extraction from 13.8m

Figure 5.33

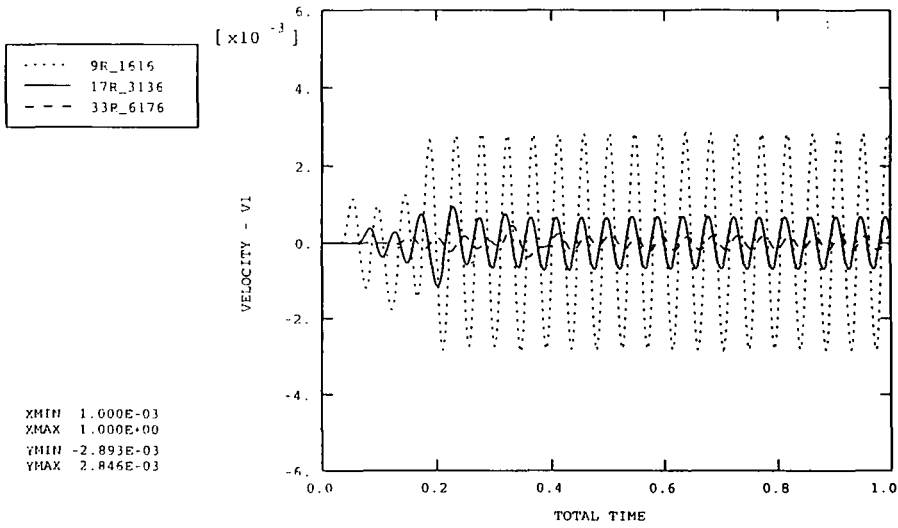
Comparison of the response induced by extraction of a pile from a depth of 11m with that from 13.8m (excitation frequency of 22.3 Hz for both): Vertical velocity/time traces

ABAQUS



(a) Extraction from 11m

ABAQUS



(b) Extraction from 13.8m

Figure 5.34

Comparison of the response induced by extraction of a pile from a depth of 11m with that from 13.8m (excitation frequency of 22.3 Hz for both): Radial velocity/time traces

ABAQUS

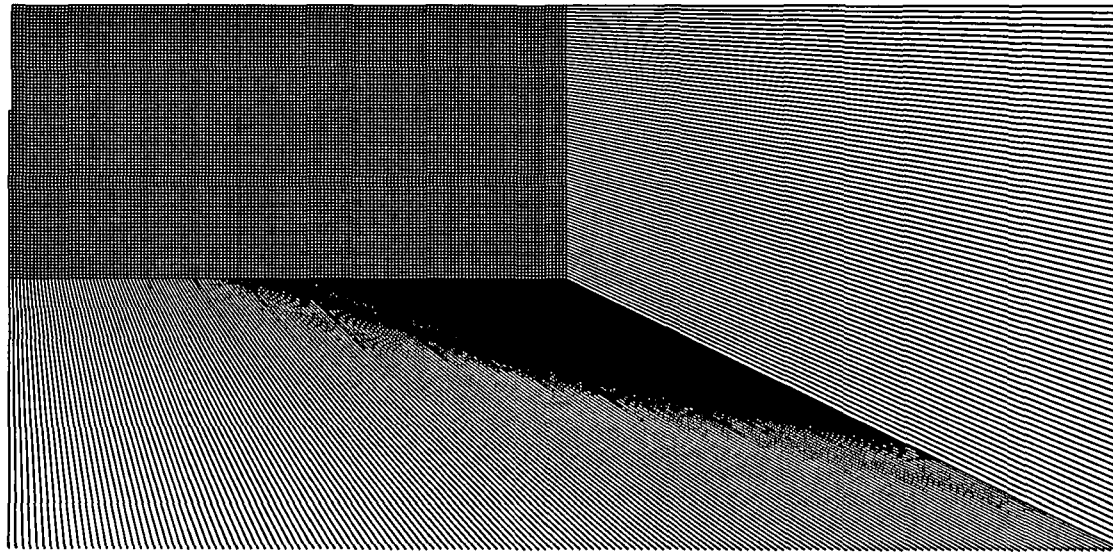


Figure 5.35 80m wide FE mesh with ABAQUS infinite elements on right hand and bottom boundaries

ABAQUS

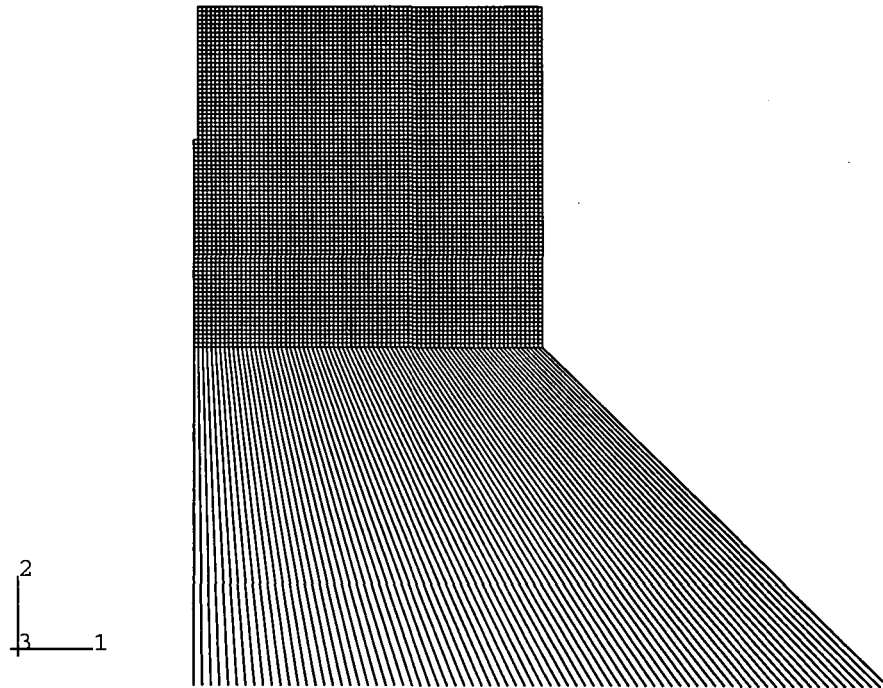


Figure 5.36

40m wide FE mesh with ABAQUS infinite elements on bottom boundary

ABAQUS

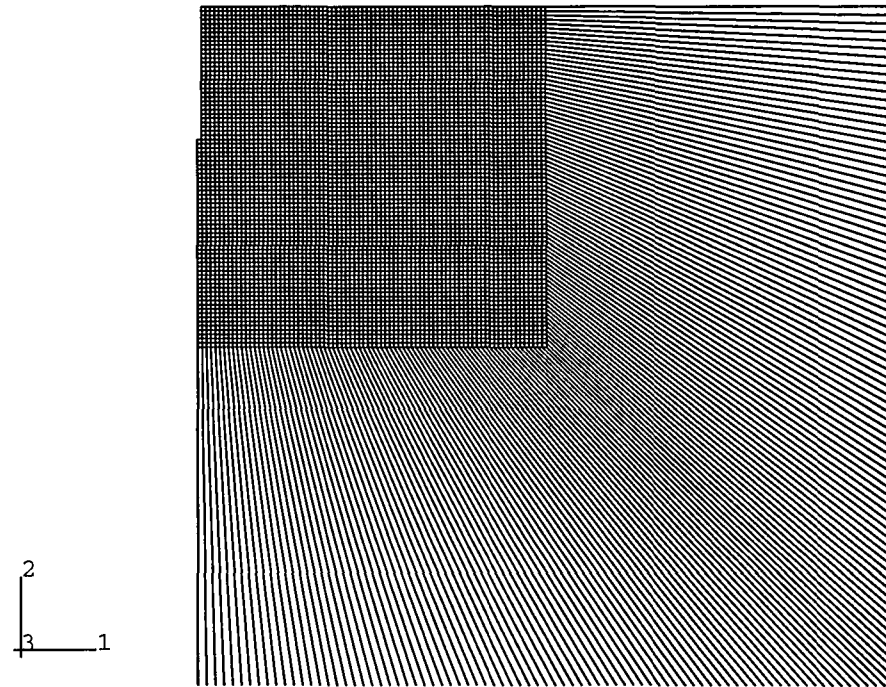
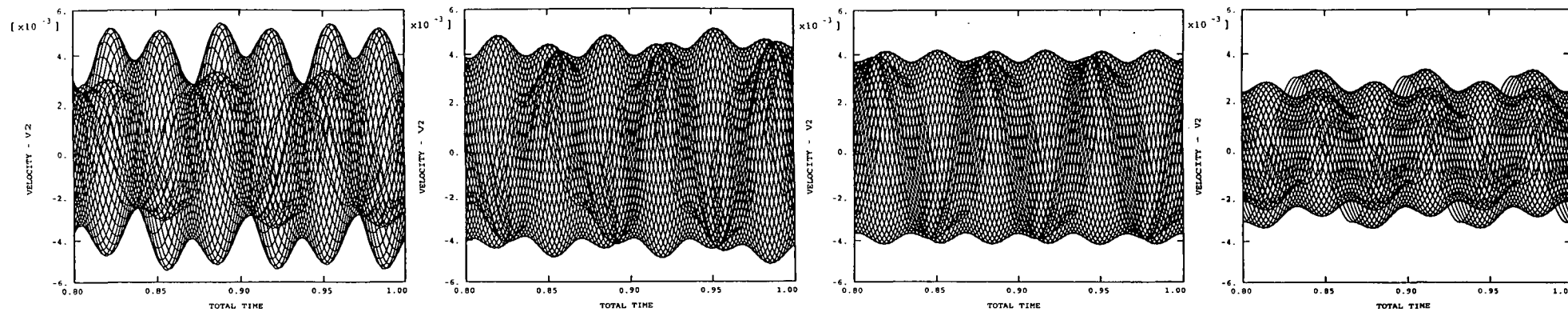
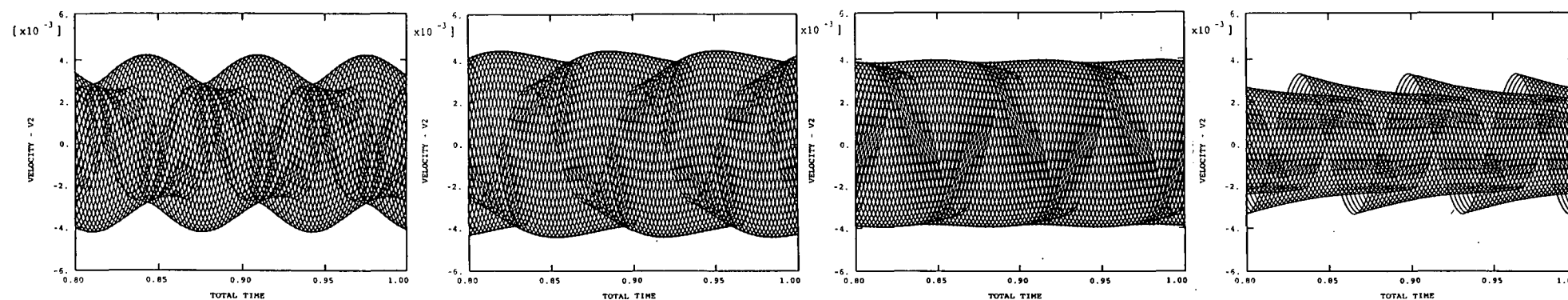


Figure 5.37 40m wide FE mesh with ABAQUS infinite elements on right hand and bottom boundaries



(a) 40m wide FE mesh (ABAQUS IE on RH boundary)



0.75m - 10m

10.25m - 20m

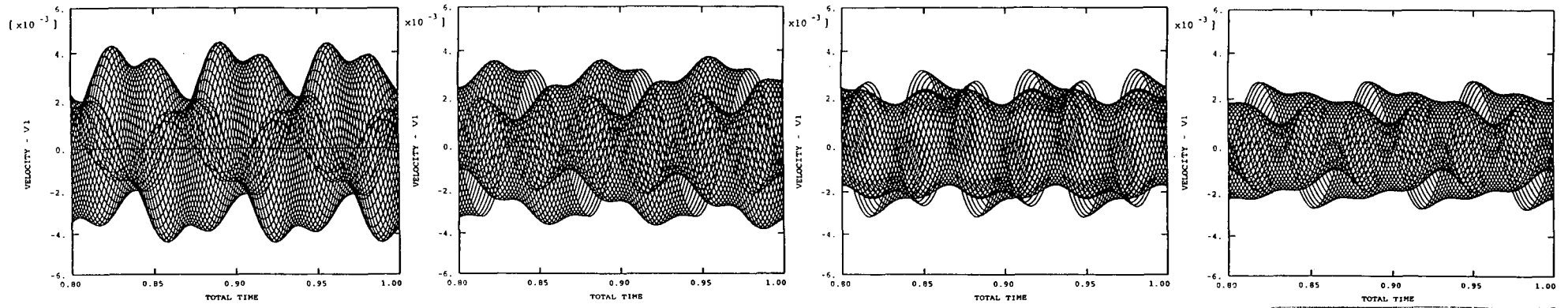
20.25m - 30m

30.25m - 40m

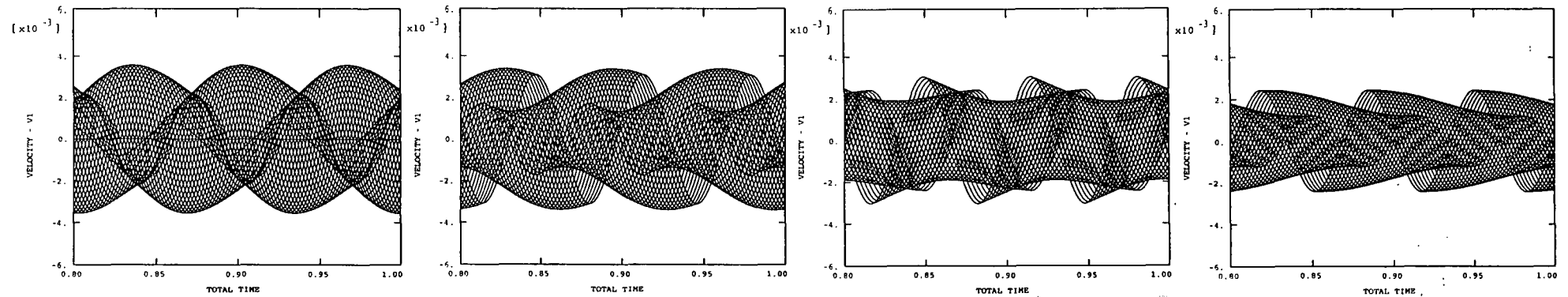
(b) 80m wide FE mesh (ABAQUS IE on RH boundary)

Figure 5.38

Comparison of the response from a 40m wide FE mesh with ABAQUS infinite elements and an 80m wide FE mesh with ABAQUS infinite elements (time period of 0.8-1.0 second): Vertical velocity/time traces



(a) 40m wide FE mesh (ABAQUS IE on RH boundary)



0.75m – 10m

10.25m – 20m

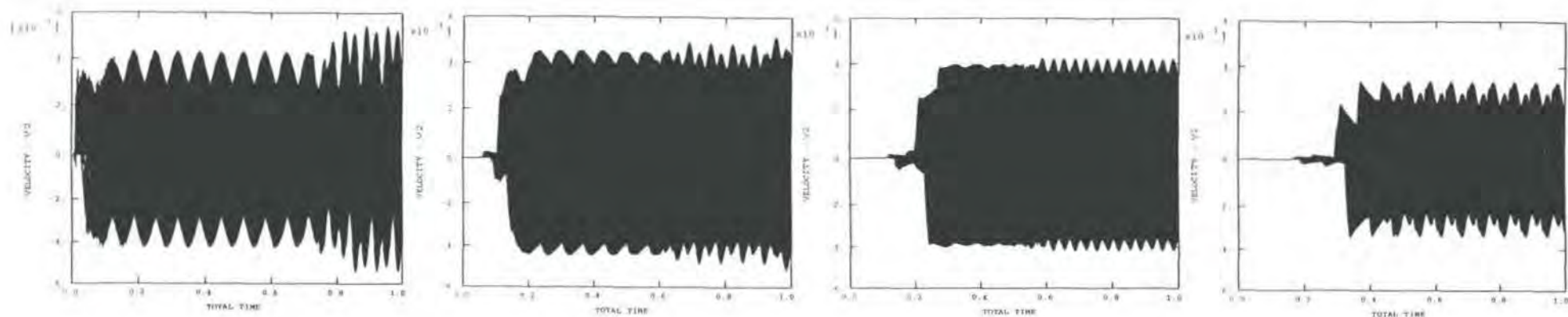
20.25m – 30m

30.25m – 40m

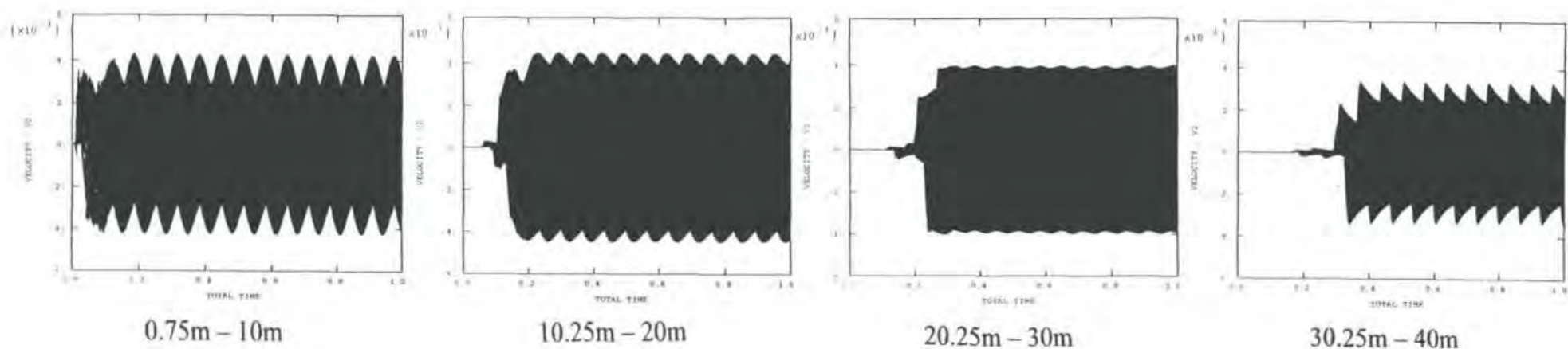
(b) 80m wide FE mesh (ABAQUS IE on RH boundary)

Figure 5.39

Comparison of the response from a 40m wide FE mesh with ABAQUS infinite elements and an 80m wide FE mesh with ABAQUS infinite elements (time period of 0.8-1.0 second): Radial velocity/time traces



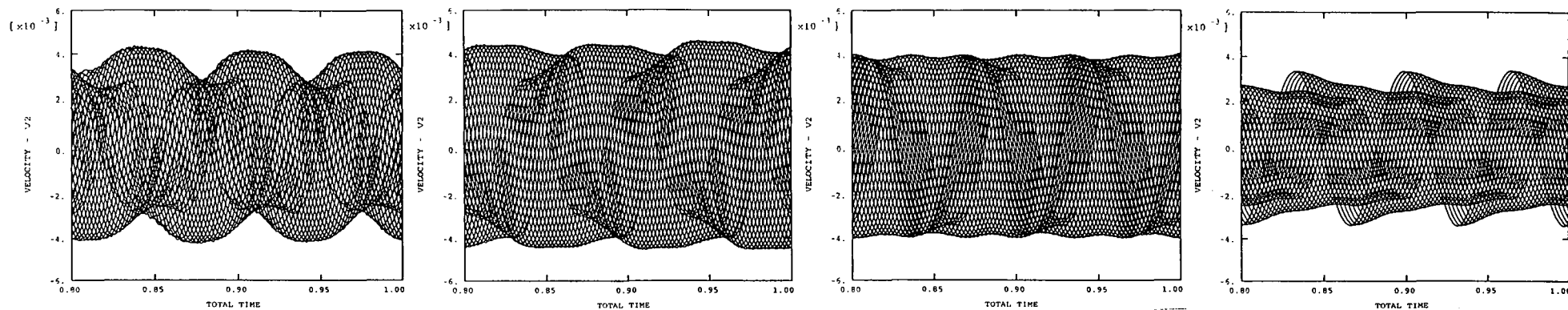
(a) 40m wide FE mesh (ABAQUS IE on RH boundary)



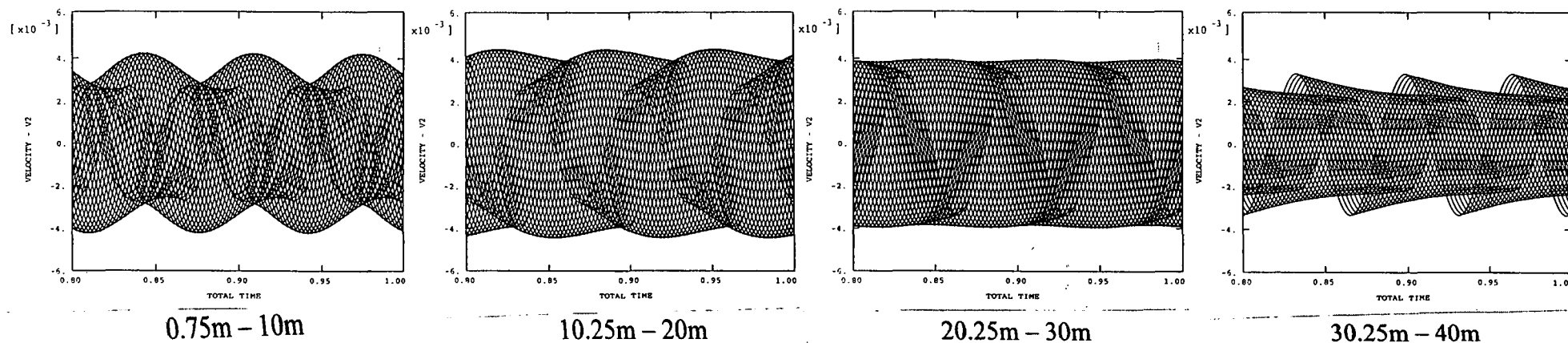
(b) 80m wide FE mesh (ABAQUS IE on RH boundary)

Figure 5.40

Comparison of the response from a 40m wide FE mesh with ABAQUS infinite elements and an 80m wide FE mesh with ABAQUS infinite elements (time period of 0.0-1.0 second): Vertical velocity/time traces



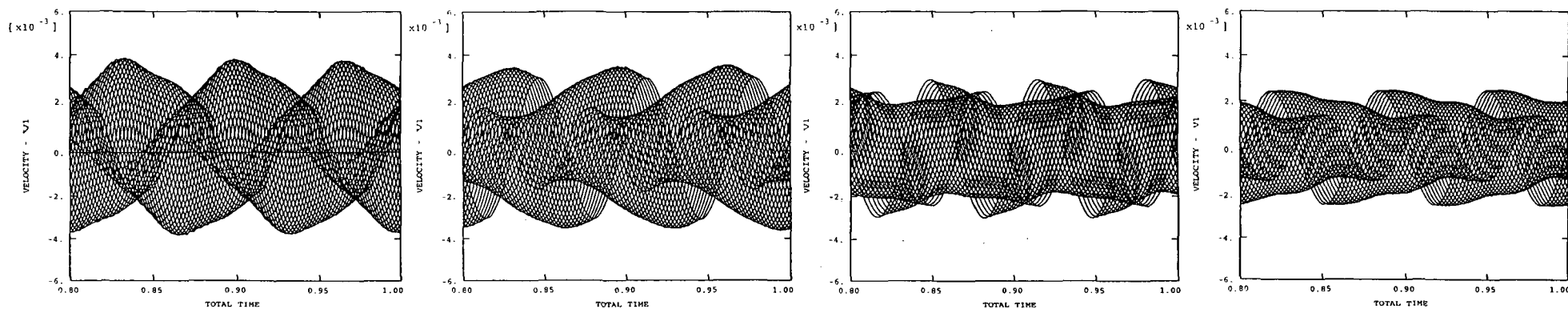
(a) 40m wide FE mesh with Rayleigh viscous boundary applied over full depth of RH boundary



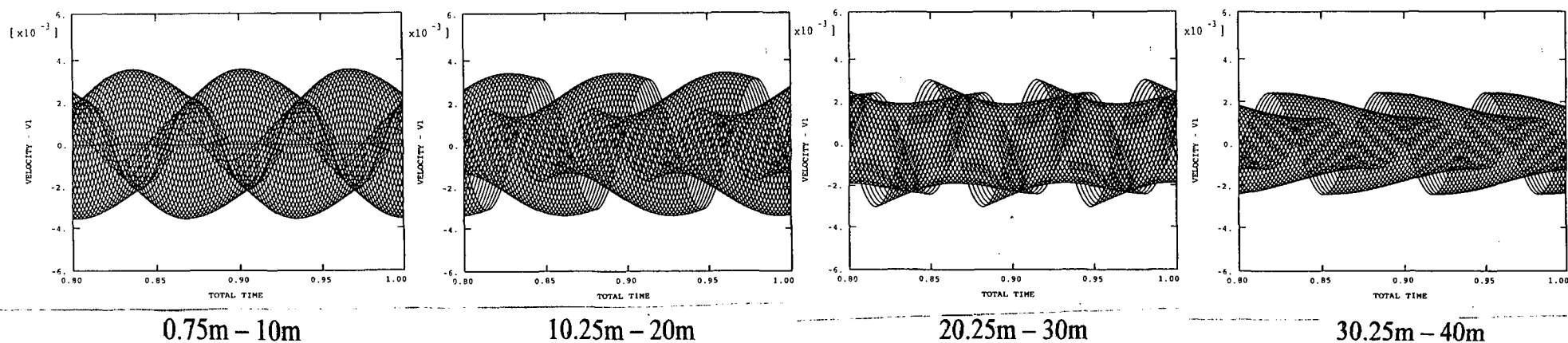
(b) 80m wide FE mesh with ABAQUS IE on RH boundary

Figure 5.41

Comparison of the response from a 40m wide FE mesh with a Rayleigh viscous boundary and an 80m wide FE mesh with ABAQUS infinite elements (time period of 0.8-1.0 second): Vertical velocity/time traces



(a) 40m wide FE mesh with Rayleigh viscous boundary applied over full depth of RH boundary



(b) 80m wide FE mesh with ABAQUS IE on RH boundary

Figure 5.42

Comparison of the response from a 40m wide FE mesh with a Rayleigh viscous boundary and an 80m wide FE mesh with ABAQUS infinite elements (time period of 0.8-1.0 second): Radial velocity/time traces

ABAQUS

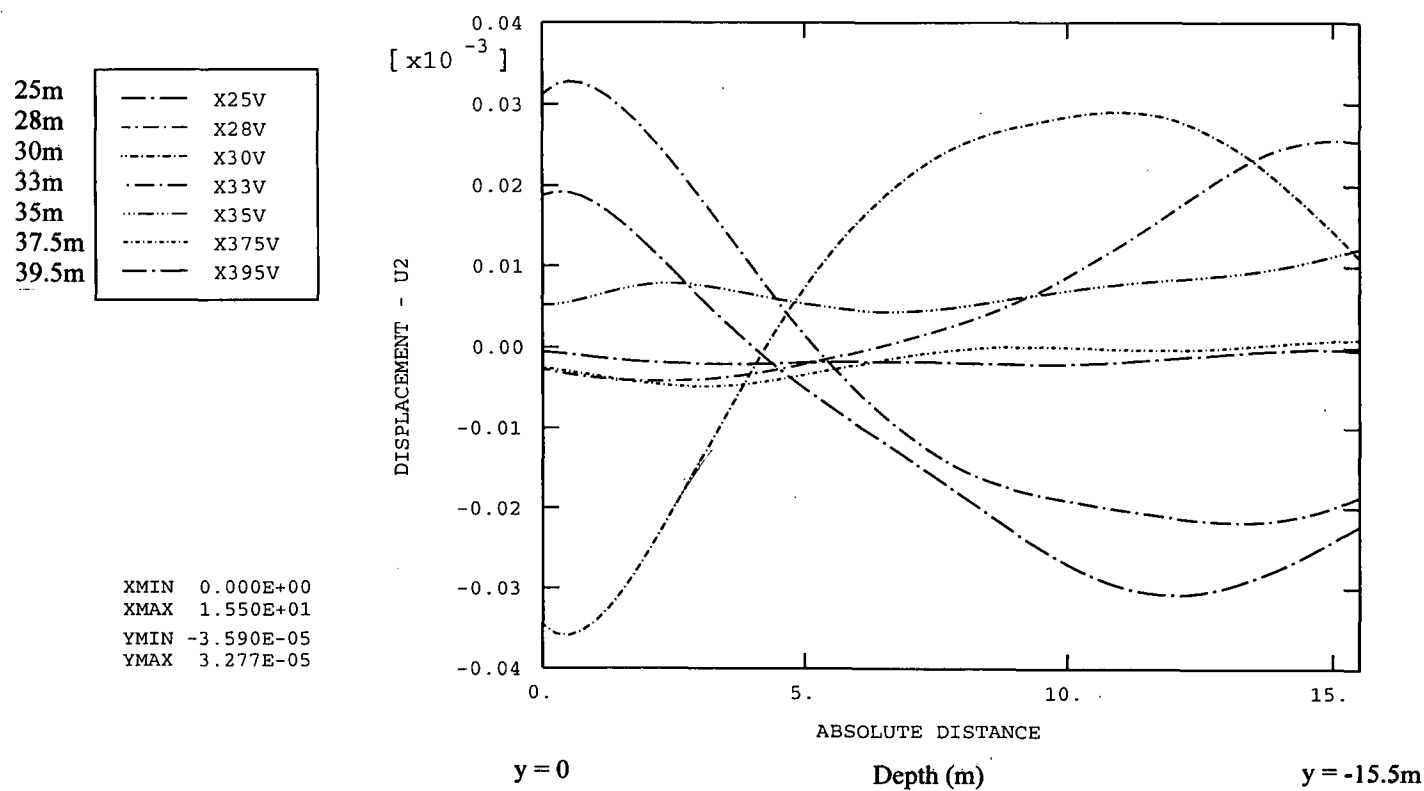


Figure 5.43

Vertical displacements of nodes between GL and 15.5m depth at various horizontal distances from pile at time of 0.35 seconds

ABAQUS

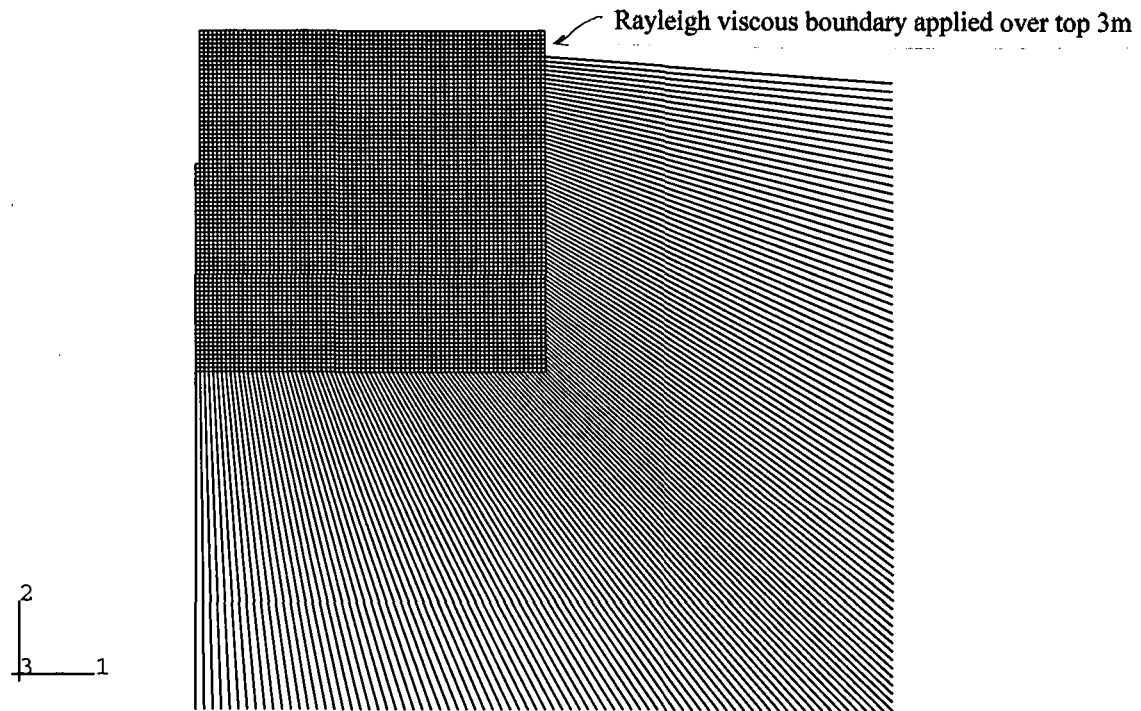
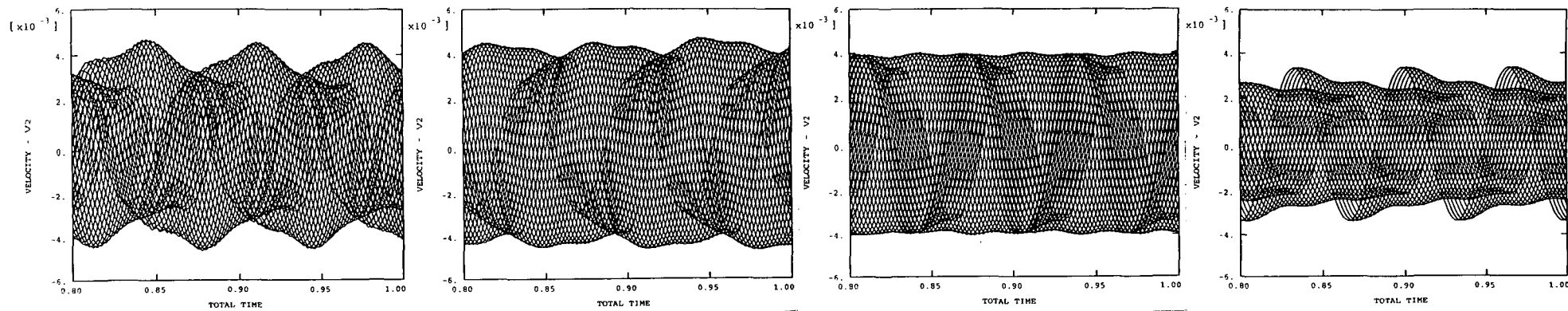
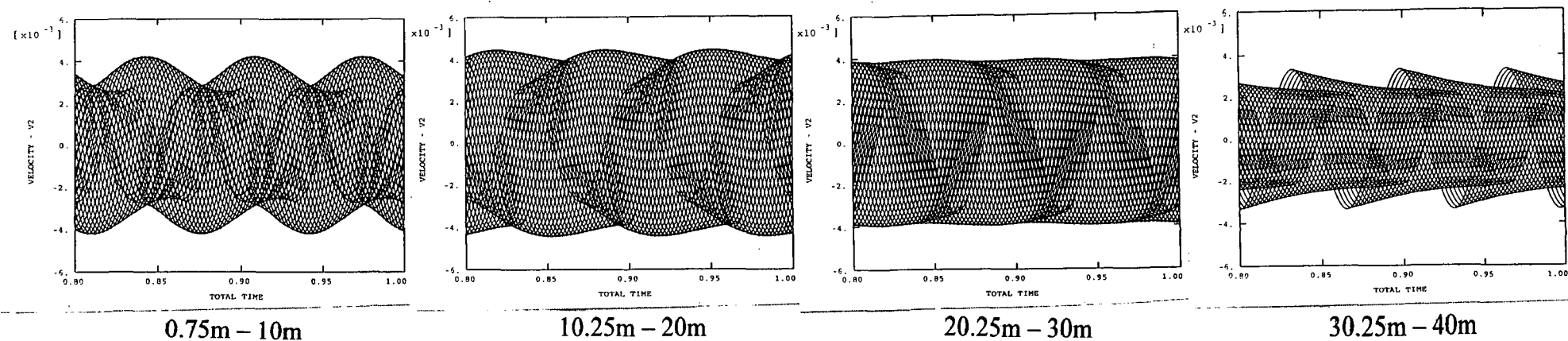


Figure 5.45

40m wide FE mesh with Rayleigh viscous boundary over the top 3m ($0.5 \times R$ wavelength) and ABAQUS infinite elements below



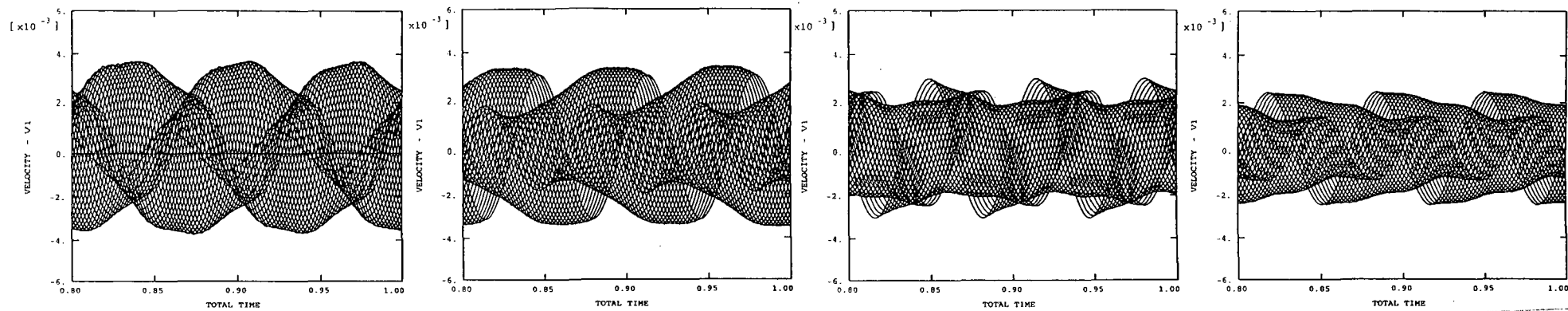
(a) 40m wide FE mesh with combined Rayleigh/ABAQUS IE boundary



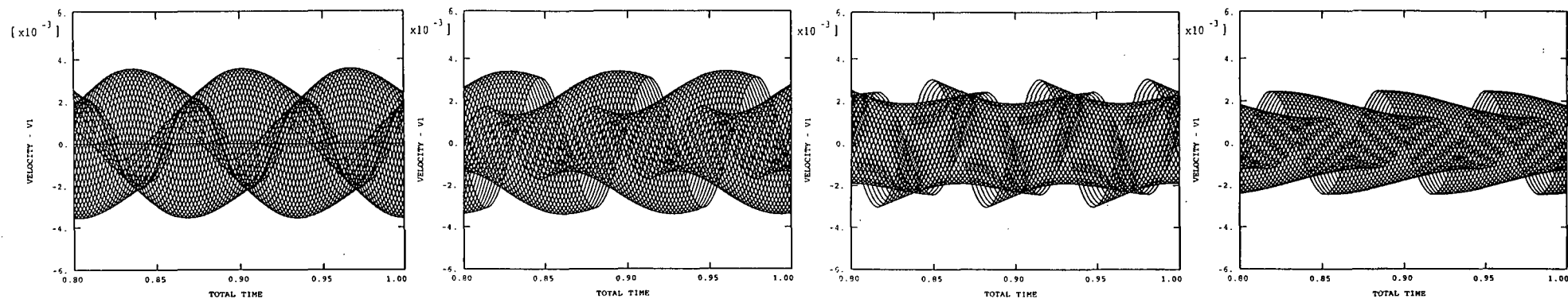
(b) 80m wide FE mesh (ABAQUS IE on RH boundary)

Figure 5.46

Comparison of the response from a 40m wide FE mesh with a Rayleigh viscous boundary over the top 3m and an 80m wide FE mesh with ABAQUS IE (time period of 0.8-1.0 second): Vertical velocity/time traces



(a) 40m wide FE mesh with combined Rayleigh/ABAQUS IE boundary



0.75m – 10m

10.25m – 20m

20.25m – 30m

30.25m – 40m

(b) 80m wide FE mesh (ABAQUS IE on RH boundary)

Figure 5.47

Comparison of the response from a 40m wide FE mesh with a Rayleigh viscous boundary over the top 3m and an 80m wide FE mesh with ABAQUS IE (time period of 0.8-1.0 second): Radial velocity/time traces

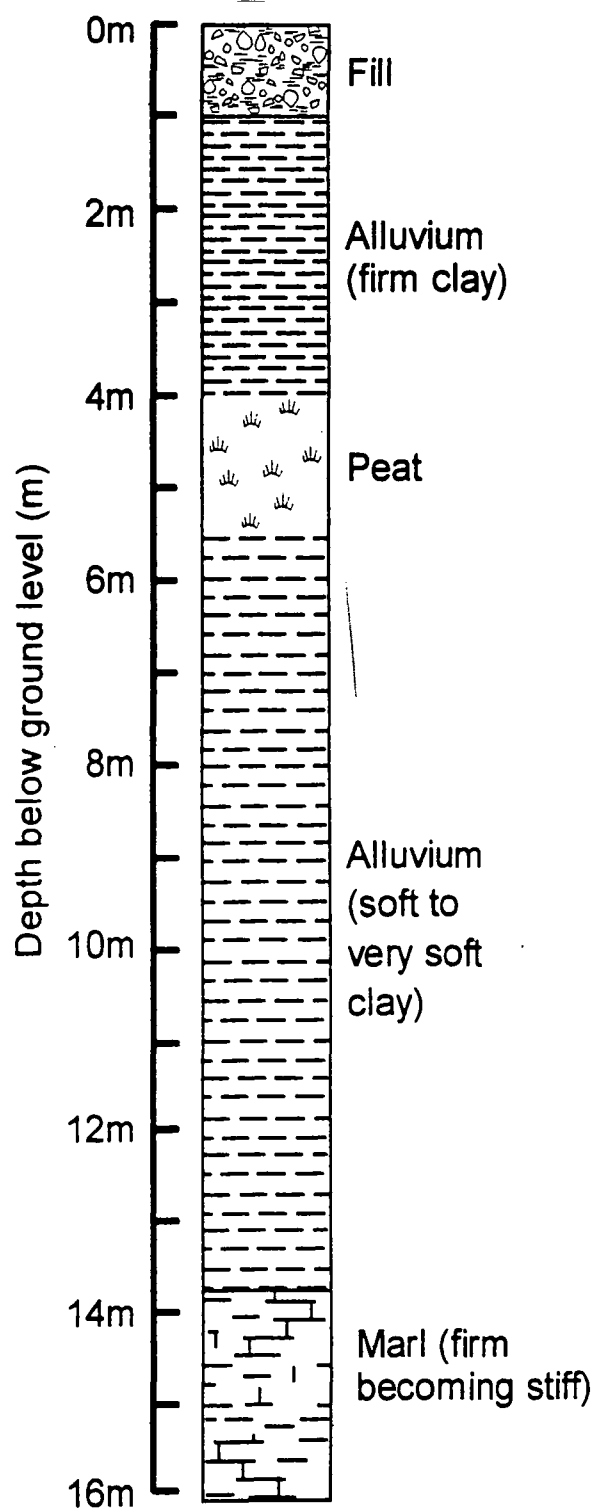


Figure 5.48

Geological Profile of Second Severn Crossing site

ABAQUS

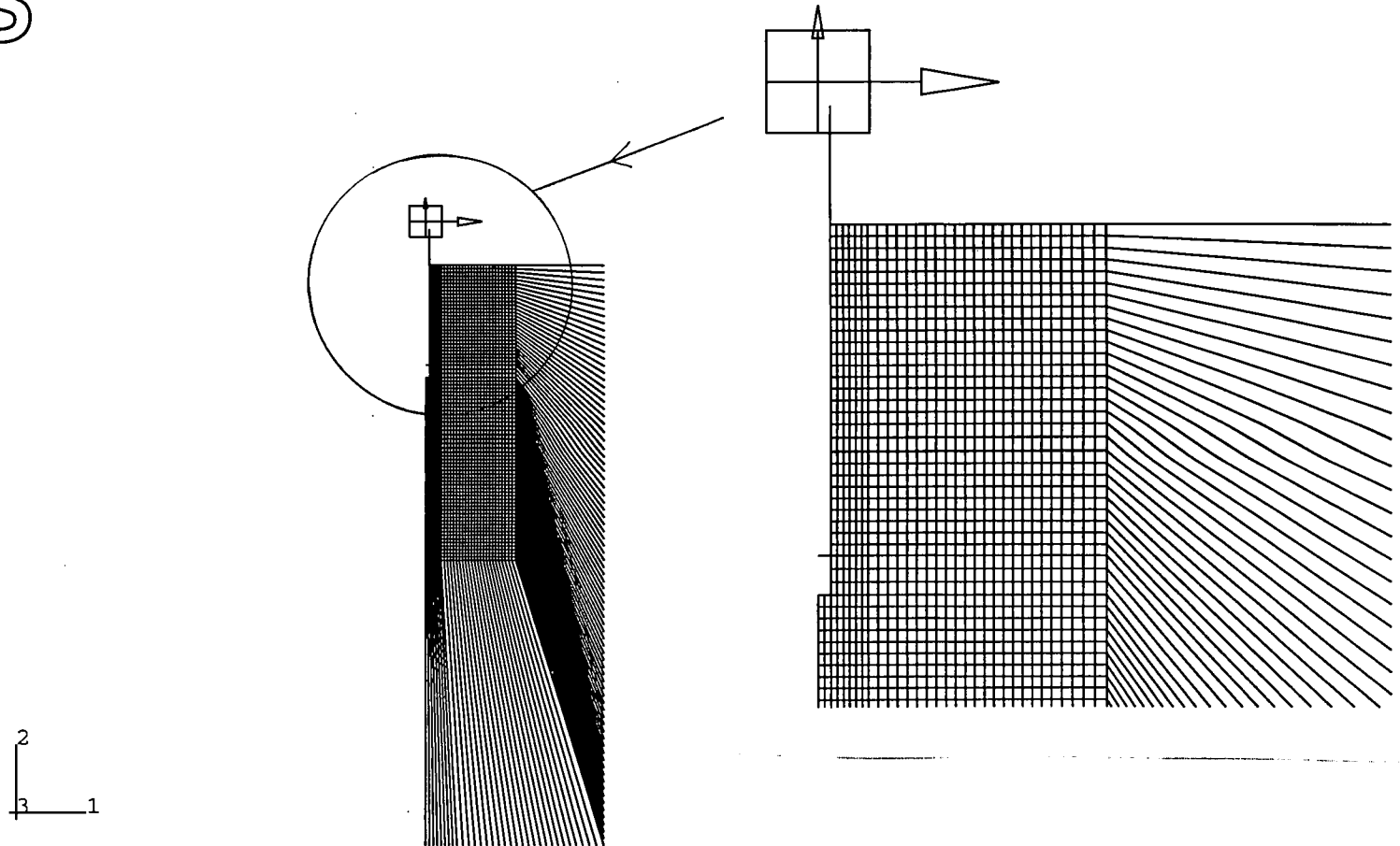


Figure 5.49

Limited FE/IE mesh used in pile/soil interaction model for Second Severn Crossing site

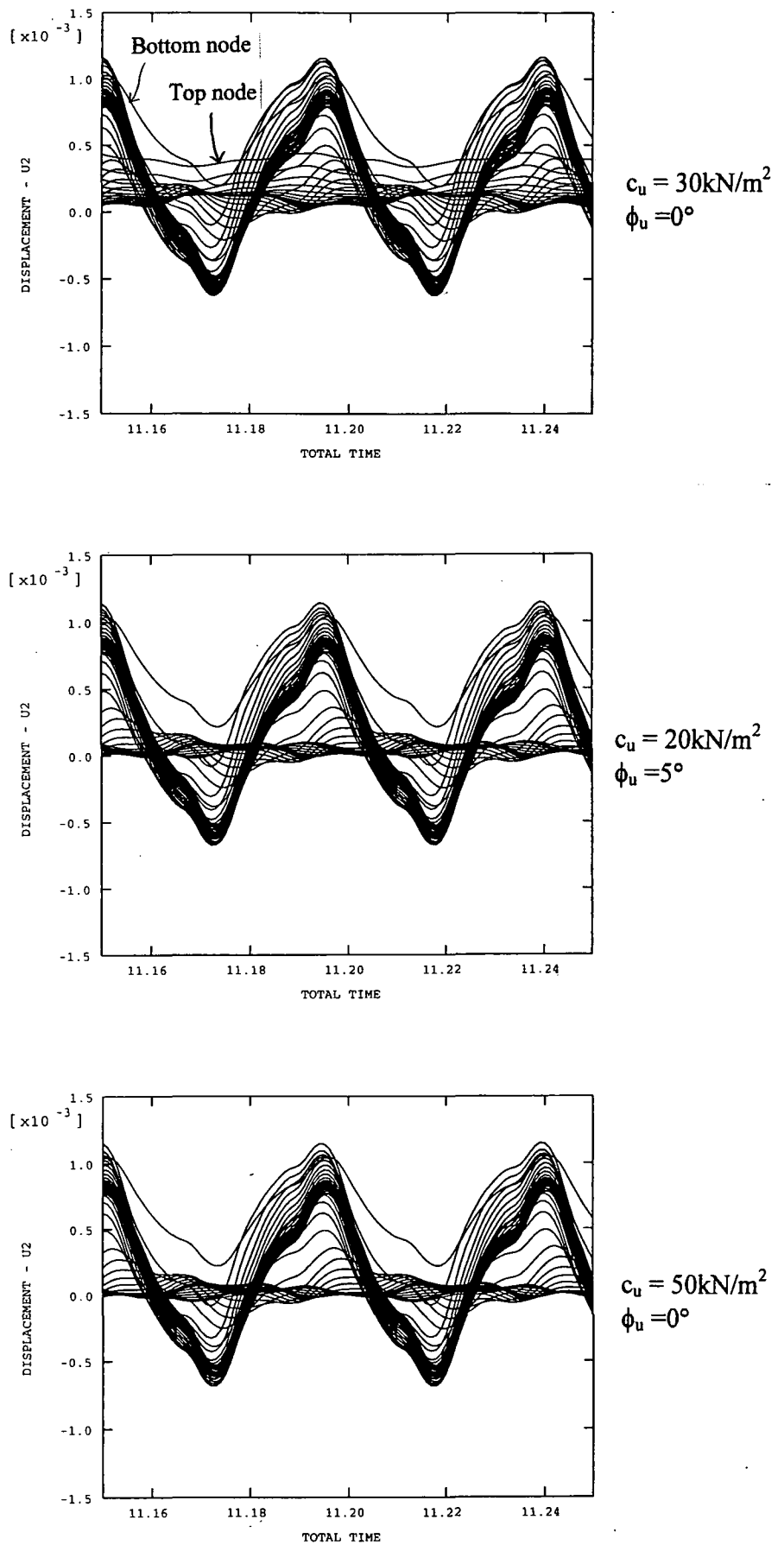


Figure 5.50

Sensitivity of pile/soil interaction model to Mohr Coulomb parameters: Vertical displacements of all soil nodes on pile/soil interface (SSC site)

ABAQUS

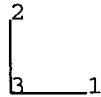
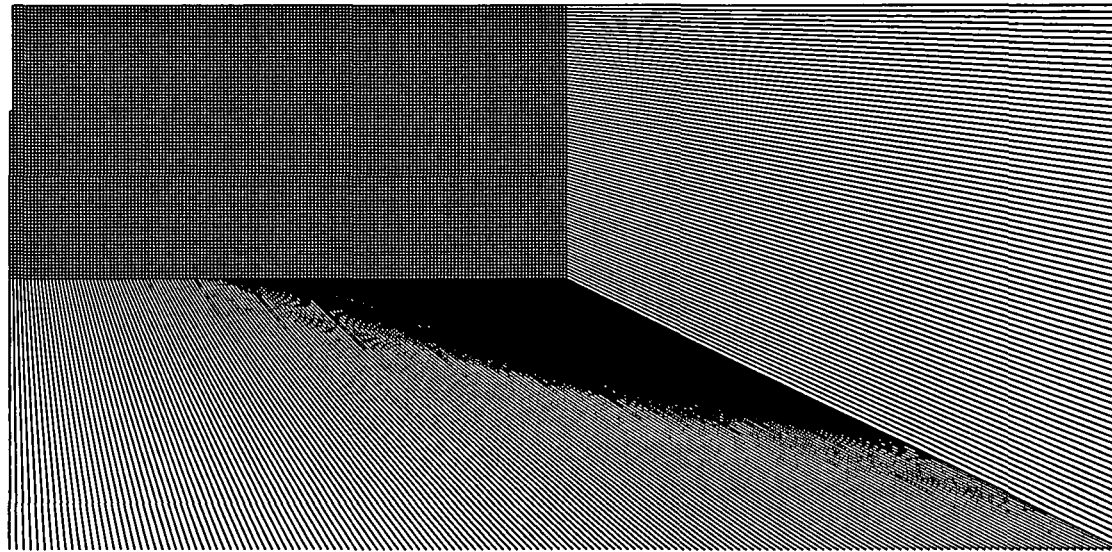


Figure 5.51

Large axisymmetric FE/IE mesh used for wave propagation analysis (Second Severn Crossing site)

ABAQUS

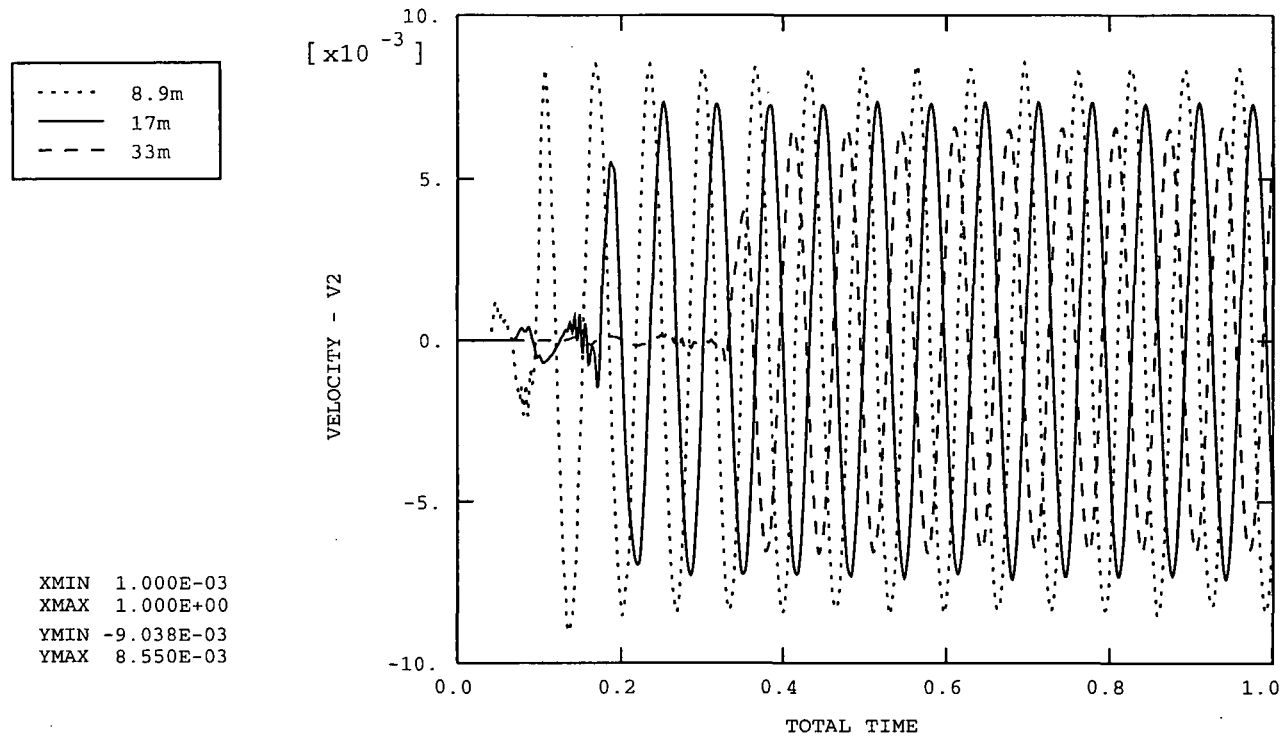


Figure 5.52

Arrival times of wavefronts in FE/IE model assuming $E_{\text{overall}} = 50\text{MPa}$ (SSC site)

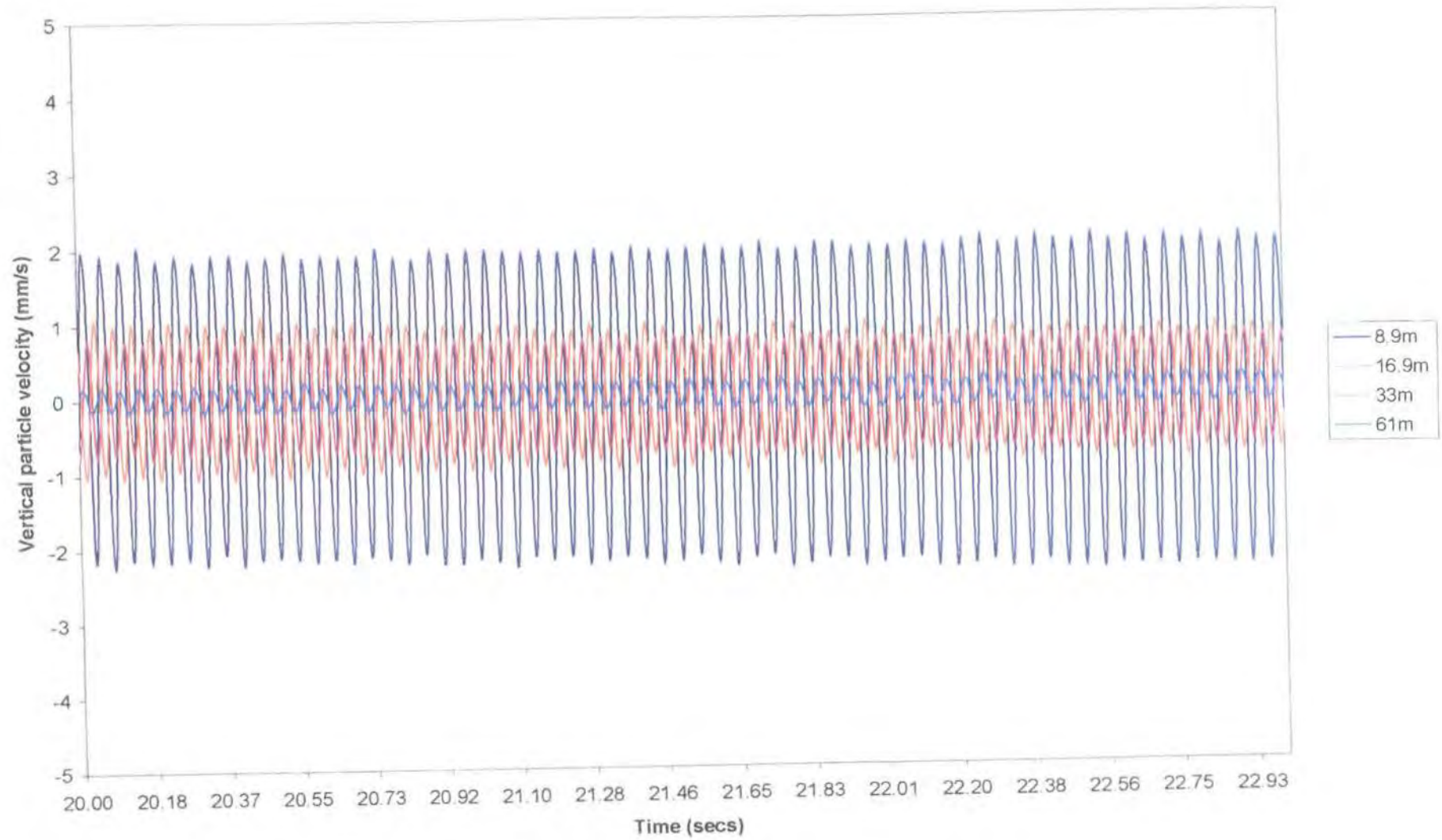


Figure 5.53 Vertical velocity/time traces recorded during extraction. Toe of casing at 13.8m below GL (SSC site)

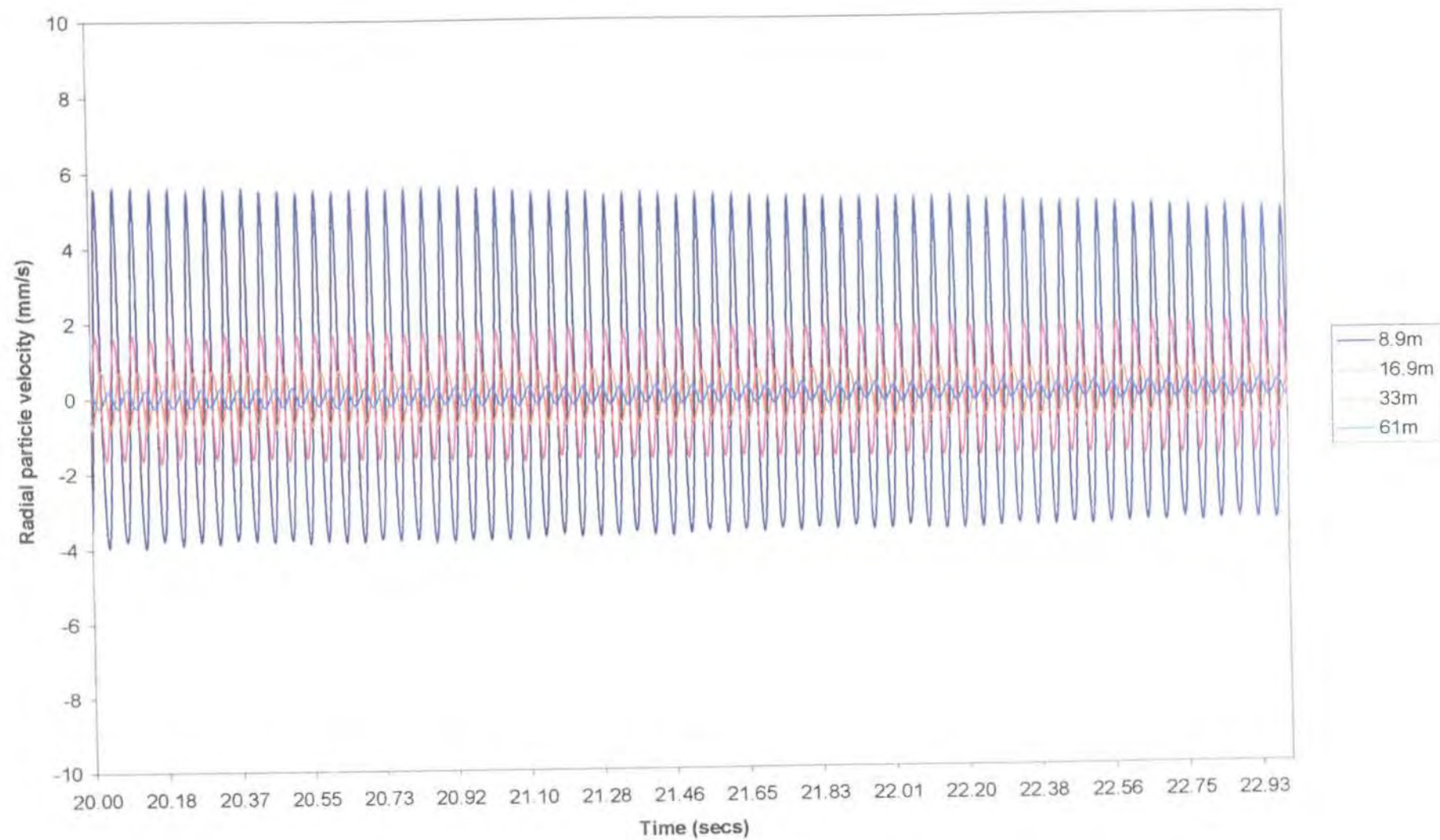
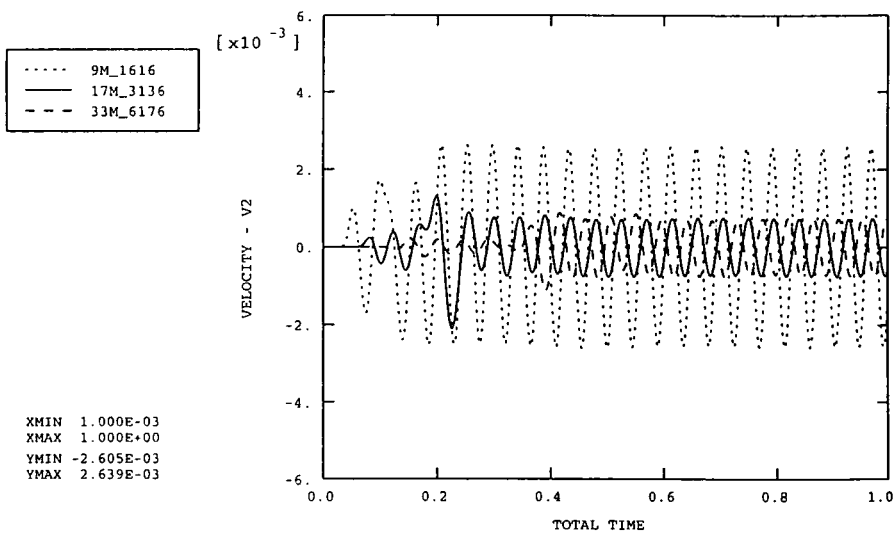
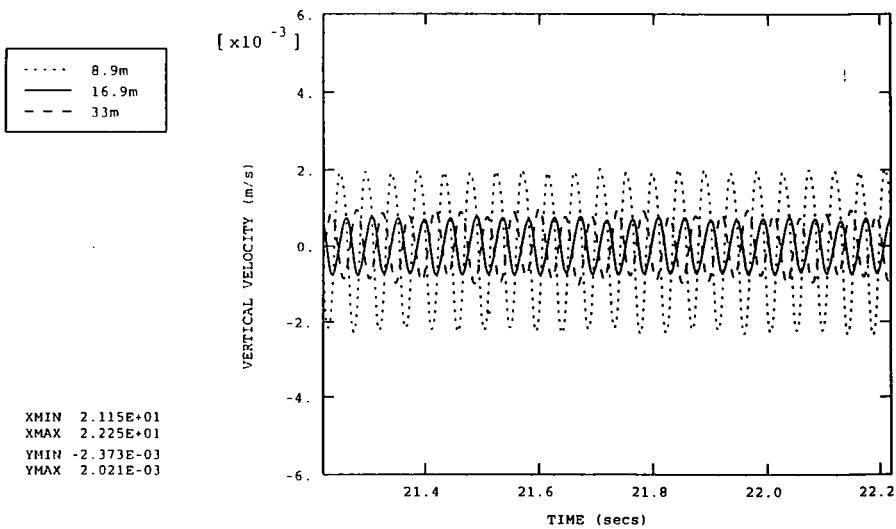


Figure 5.54 Radial velocity/time traces recorded during extraction. Toe of casing at 13.8m below GL (SSC site)

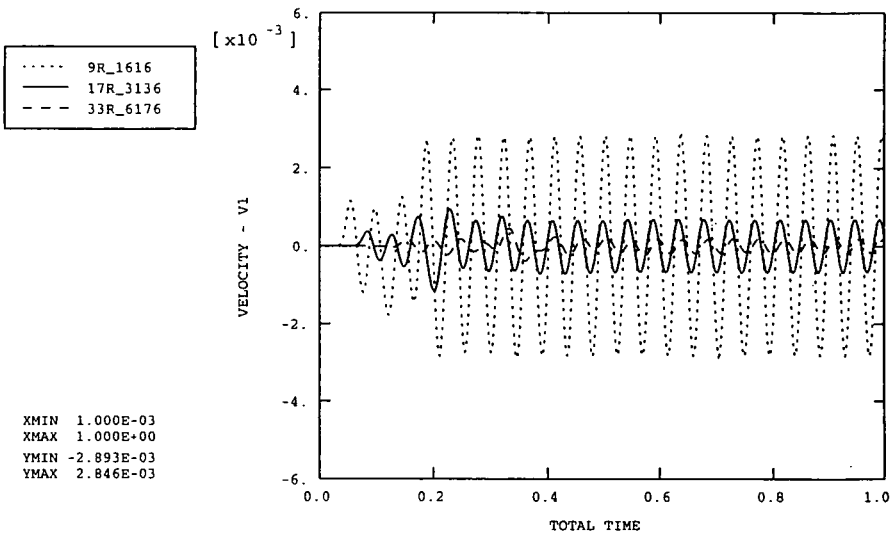


(a) Predicted (assuming $\mu = 0.15$ and 5% damping)

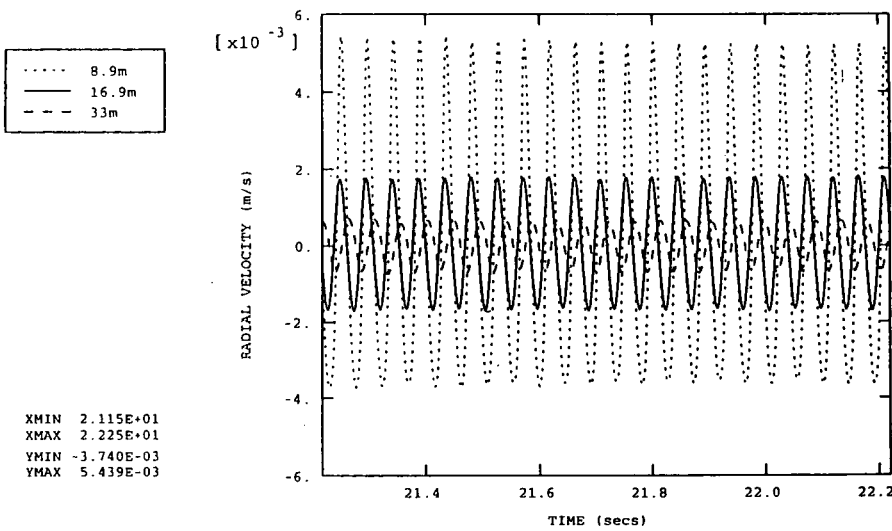


(b) Measured

Figure 5.55 Comparison of predicted and measured vertical velocity/time traces during vibratory extraction. Toe of casing at 13.8m below GL. Assuming E_{alluvium} of 42MPa and E_{marl} of 200MPa. (SSC site)



(a) Predicted (assuming $\mu = 0.15$ and 5% damping)



(b) Measured

Figure 5.56 Comparison of predicted and measured radial velocity/time traces during vibratory extraction. Toe of casing at 13.8m below GL. Assuming E_{alluvium} of 42MPa and E_{marl} of 200MPa. (SSC site)

ABAQUS

— CF2_1

XMIN 1.000E-03
XMAX 5.500E-02
YMIN -2.810E+04
YMAX 1.323E+03

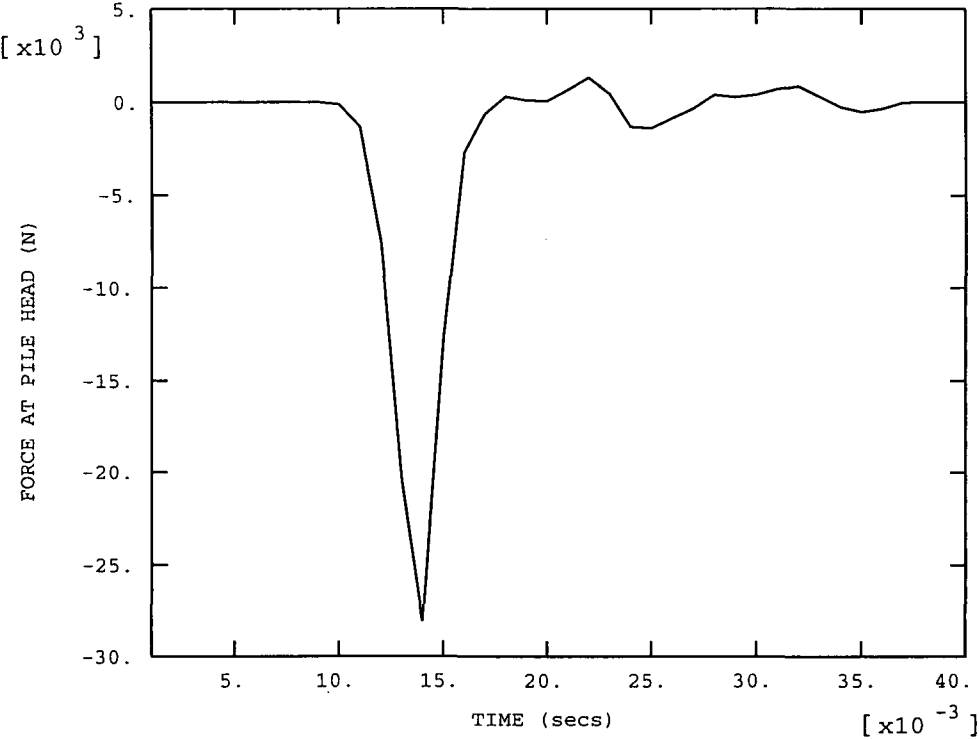
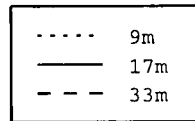


Figure 5.57 Typical forcing function from impact piling

ABAQUS



XMIN 1.000E-03
XMAX 8.000E-01
YMIN -9.860E-04
YMAX 1.049E-03

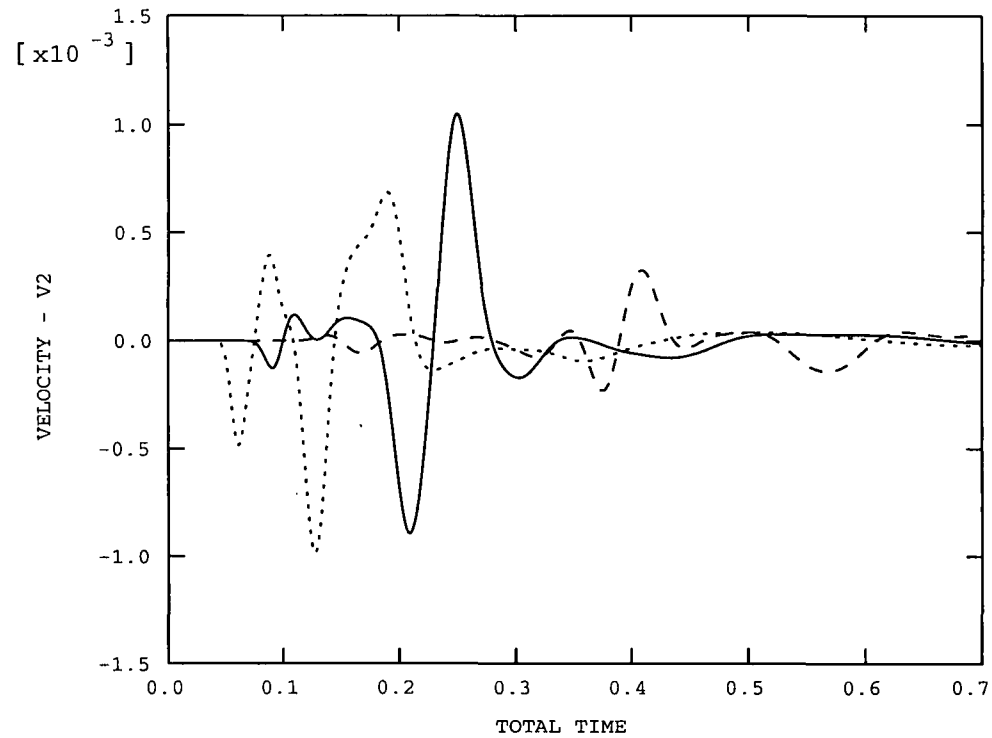
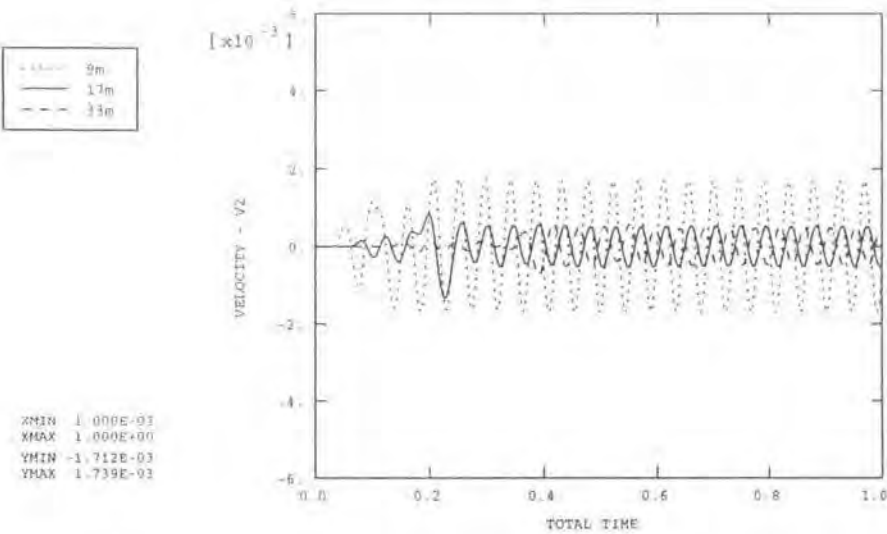
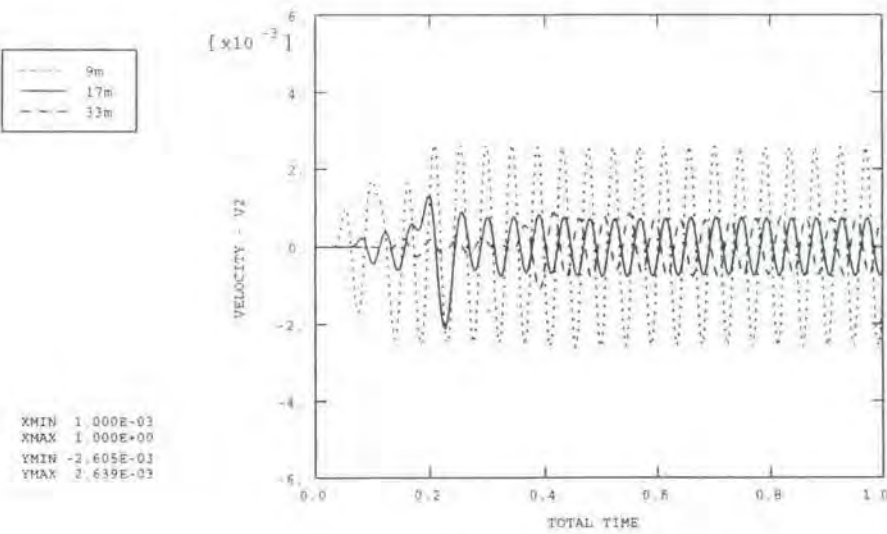


Figure 5.58

Predicted arrival times of wavefronts generated by typical impact assuming $E_{\text{overall}} = 50\text{MPa}$ (SSC site)

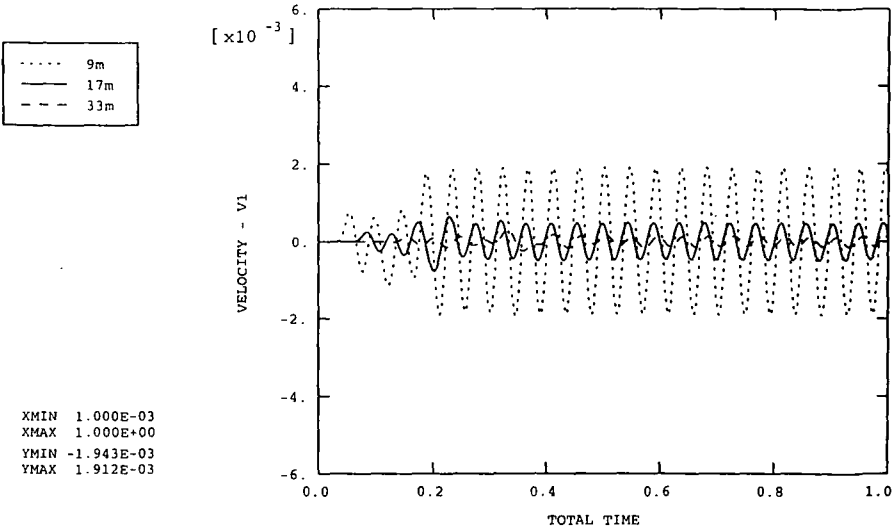


(a) Overall friction coefficient = 0.1

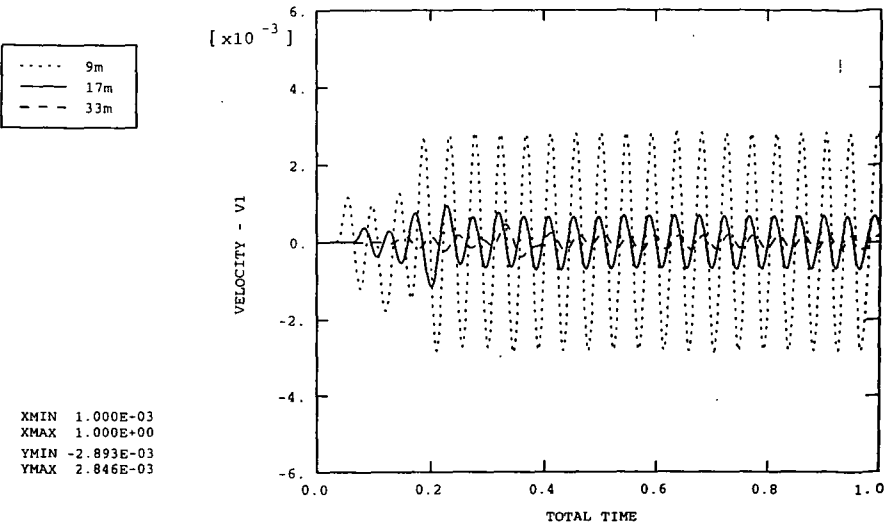


(b) Overall friction coefficient = 0.15

Figure 5.59 Comparison of predicted vertical velocity/time traces assuming an overall coefficient of friction of 0.1 and an overall coefficient of friction of 0.15 (SSC site)



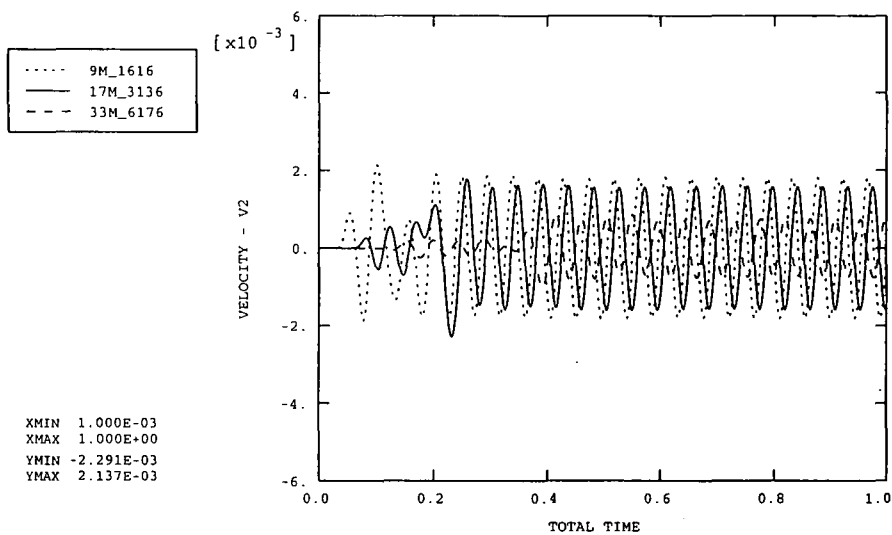
(a) Overall friction coefficient = 0.1



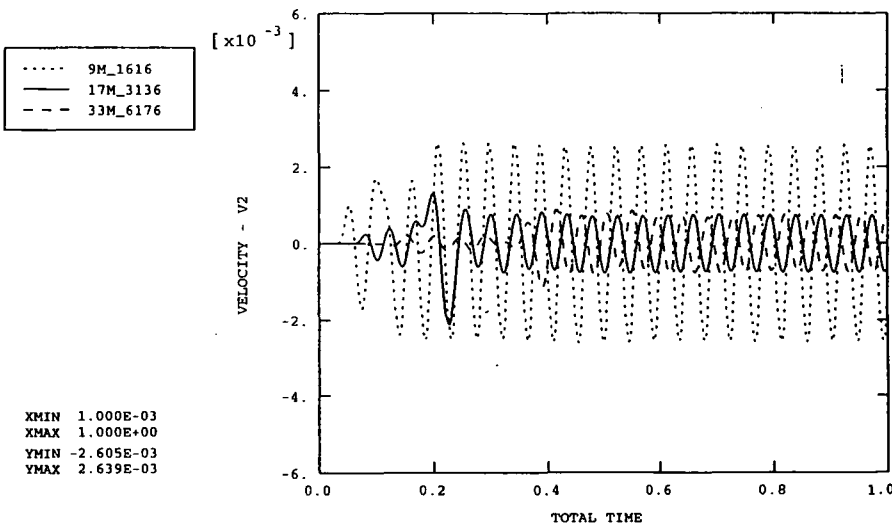
(b) Overall friction coefficient = 0.15

Figure 5.60

Comparison of predicted radial velocity/time traces assuming an overall coefficient of friction of 0.1 and an overall coefficient of friction of 0.15 (SSC site)

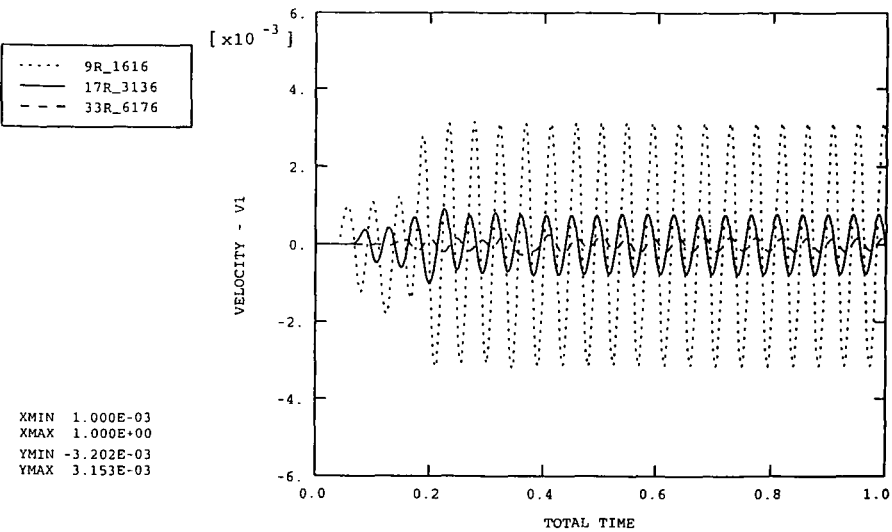


(a) Three average values (stepped) of friction assumed between 6m – 13.8m depth

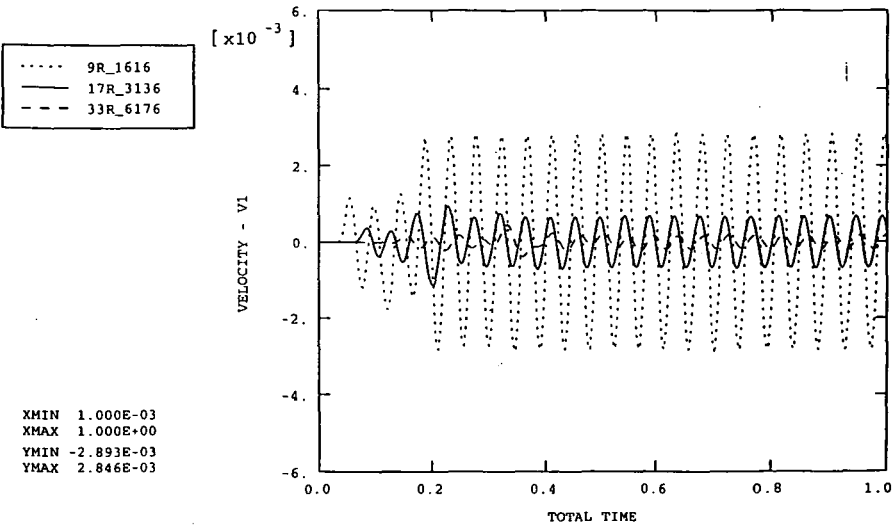


(b) One average value of friction assumed between 6m – 13.8m depth

Figure 5.61 Comparison of predicted vertical velocity/time traces for two different distributions of friction along the shaft of the casing (SSC site)



(a) Three average values (stepped) of friction assumed between 6m – 13.8m depth



(b) One average value of friction assumed between 6m – 13.8m depth

Figure 5.62 Comparison of predicted radial velocity/time traces for two different distributions of friction along the shaft of the casing (SSC site)

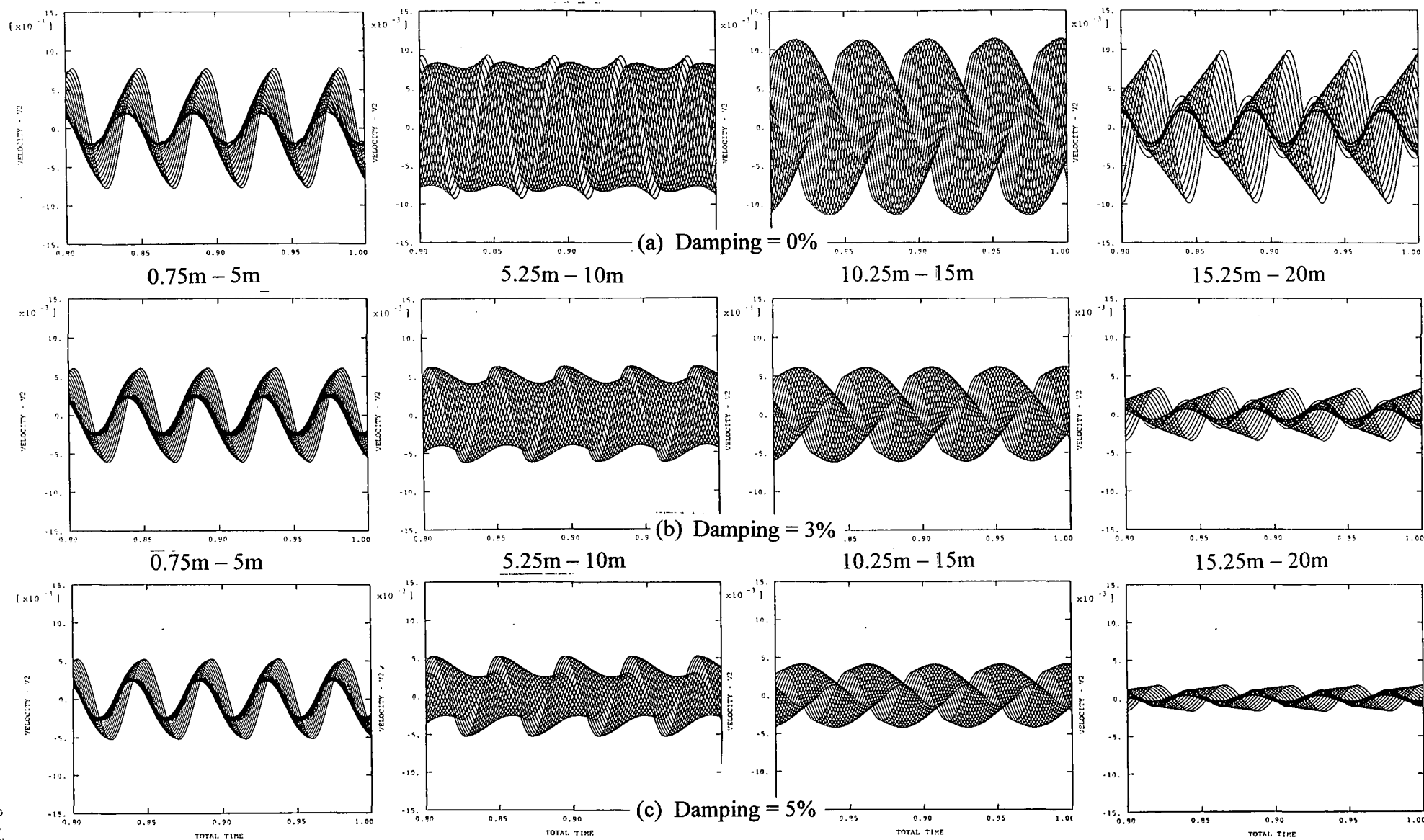


Figure 5.63

Comparison of predicted vertical velocity/time traces for material damping ratios of 0%, 3% and 5%. (All surface nodes between 0.75m and 20m) (SSC site)

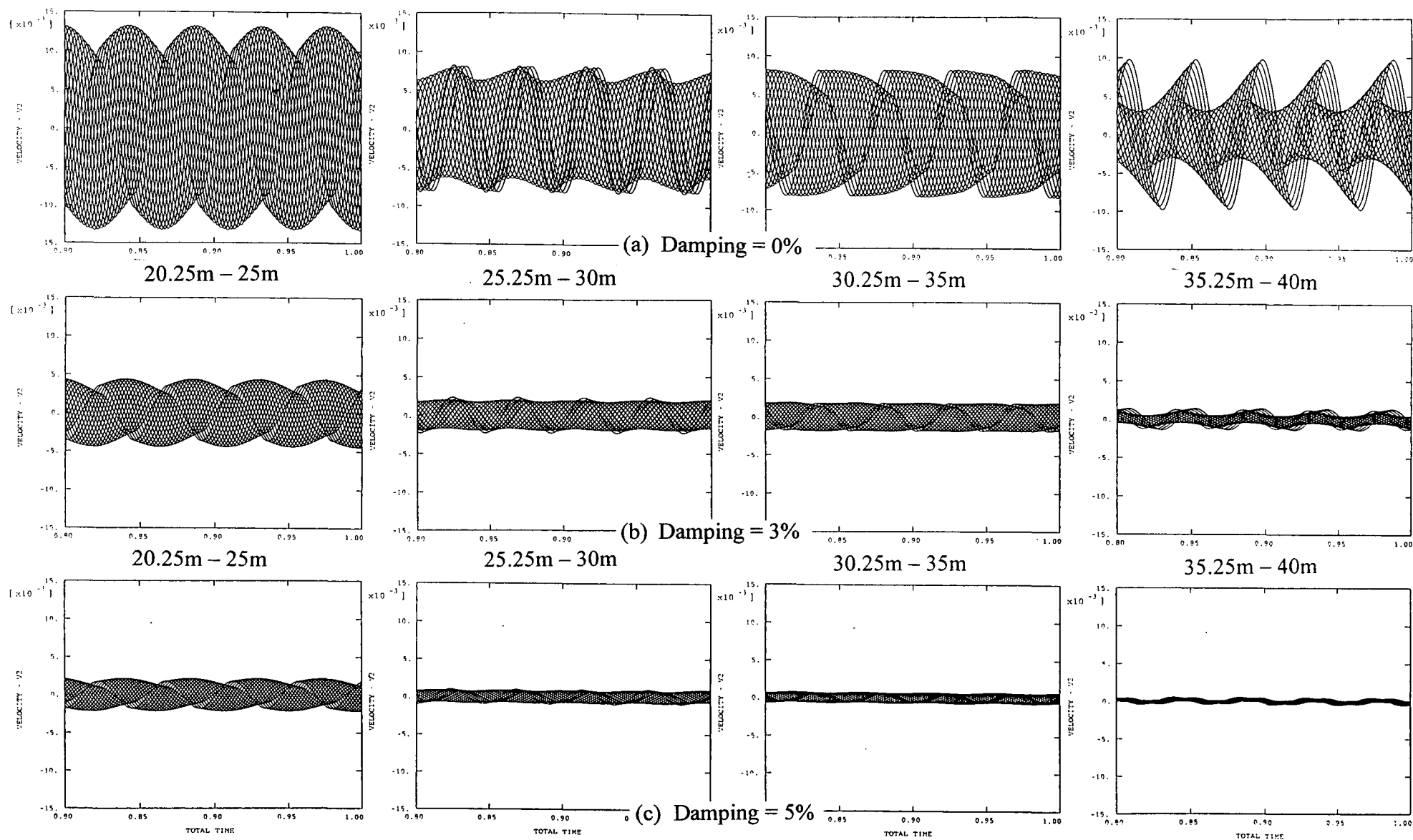
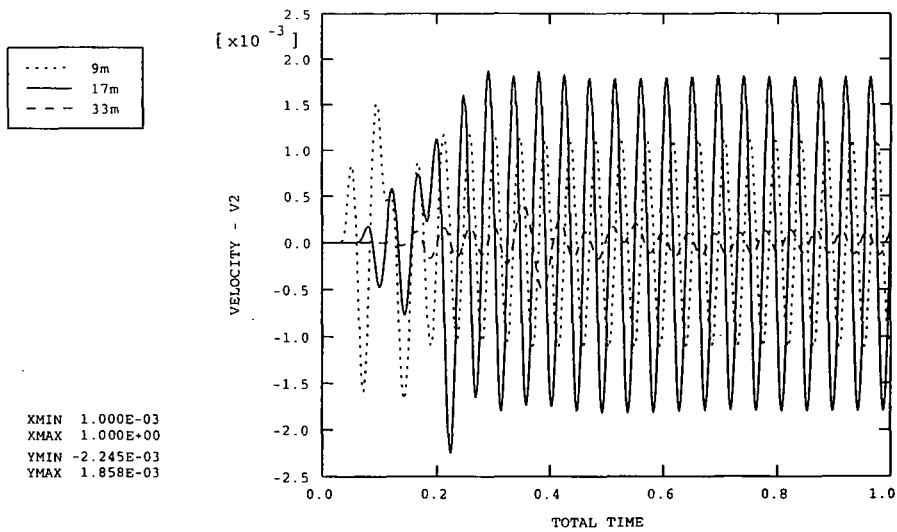
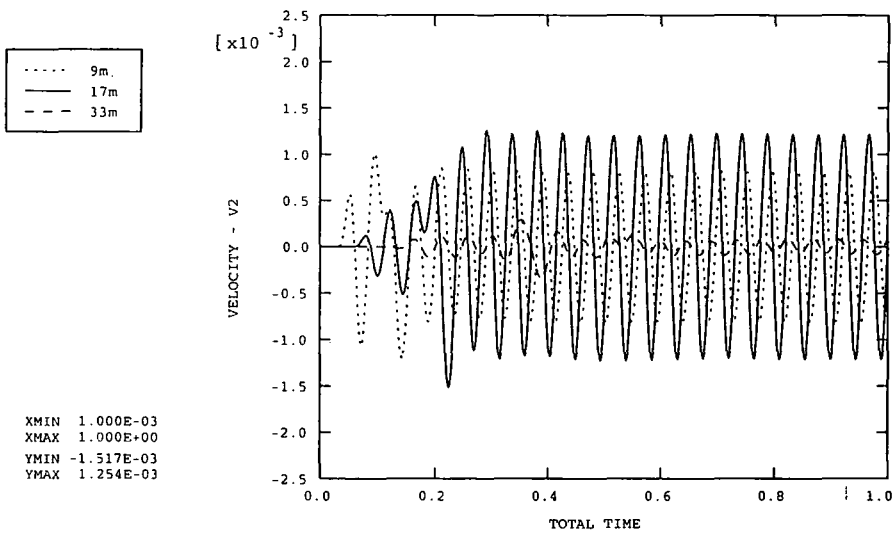


Figure 5.64

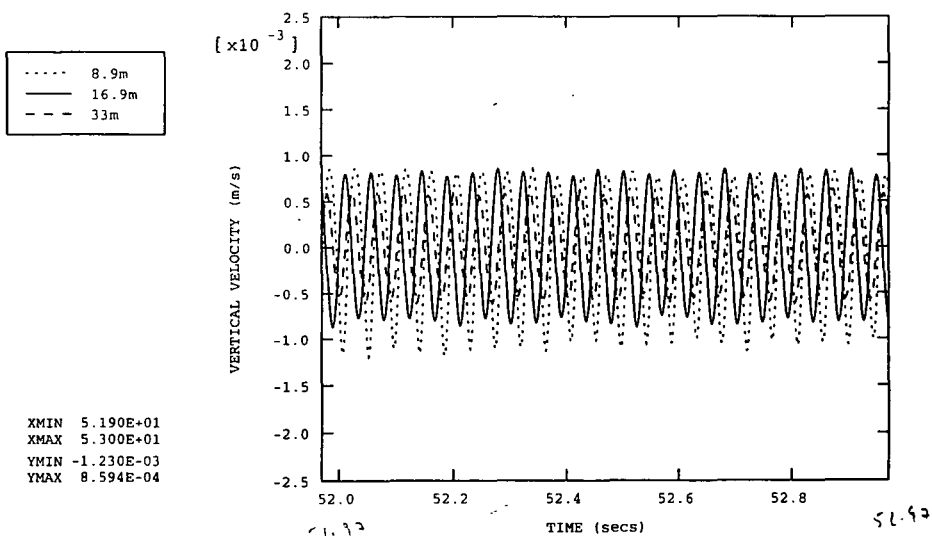
Comparison of predicted vertical velocity/time traces for material damping ratios of 0%, 3% and 5%. (All surface nodes between 20.25m and 40m) (SSC site)



(a) $\mu = 0.1$



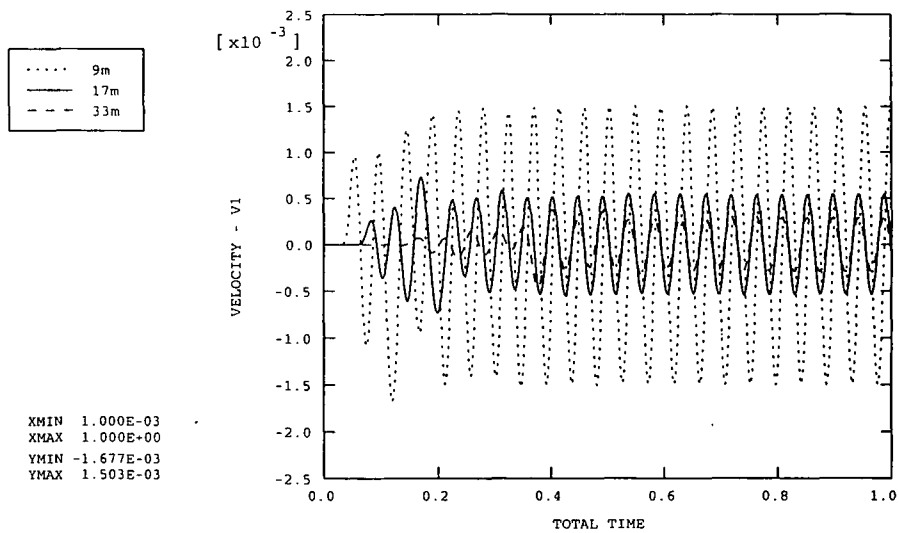
(b) $\mu = 0.15$



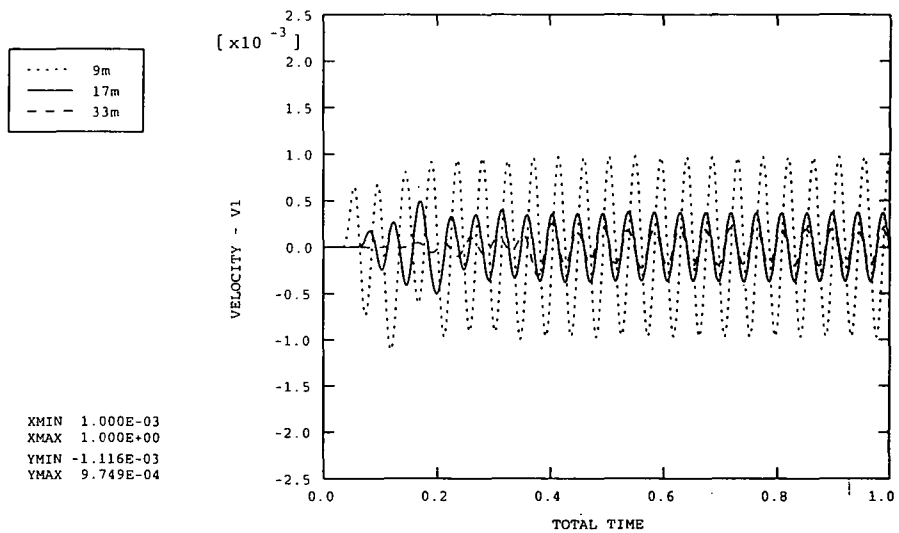
(c) Measured

Figure 5.65

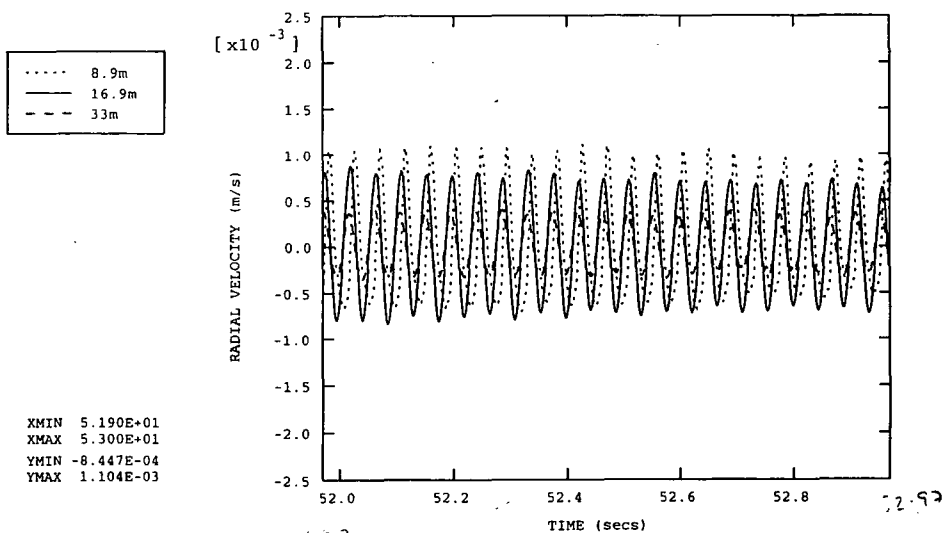
Comparison of predicted vertical velocity/time traces assuming overall coefficients of friction of 0.1 and 0.15 and the measured vertical velocity/time traces. Toe of casing at 11m below GL. (SSC site)



(a) $\mu = 0.1$



(b) $\mu = 0.15$



(c) Measured

Figure 5.66

Comparison of predicted radial velocity/time traces assuming overall coefficients of friction of 0.1 and 0.15 and the measured radial velocity/time traces. Toe of casing at 11m below GL. (SSC site)

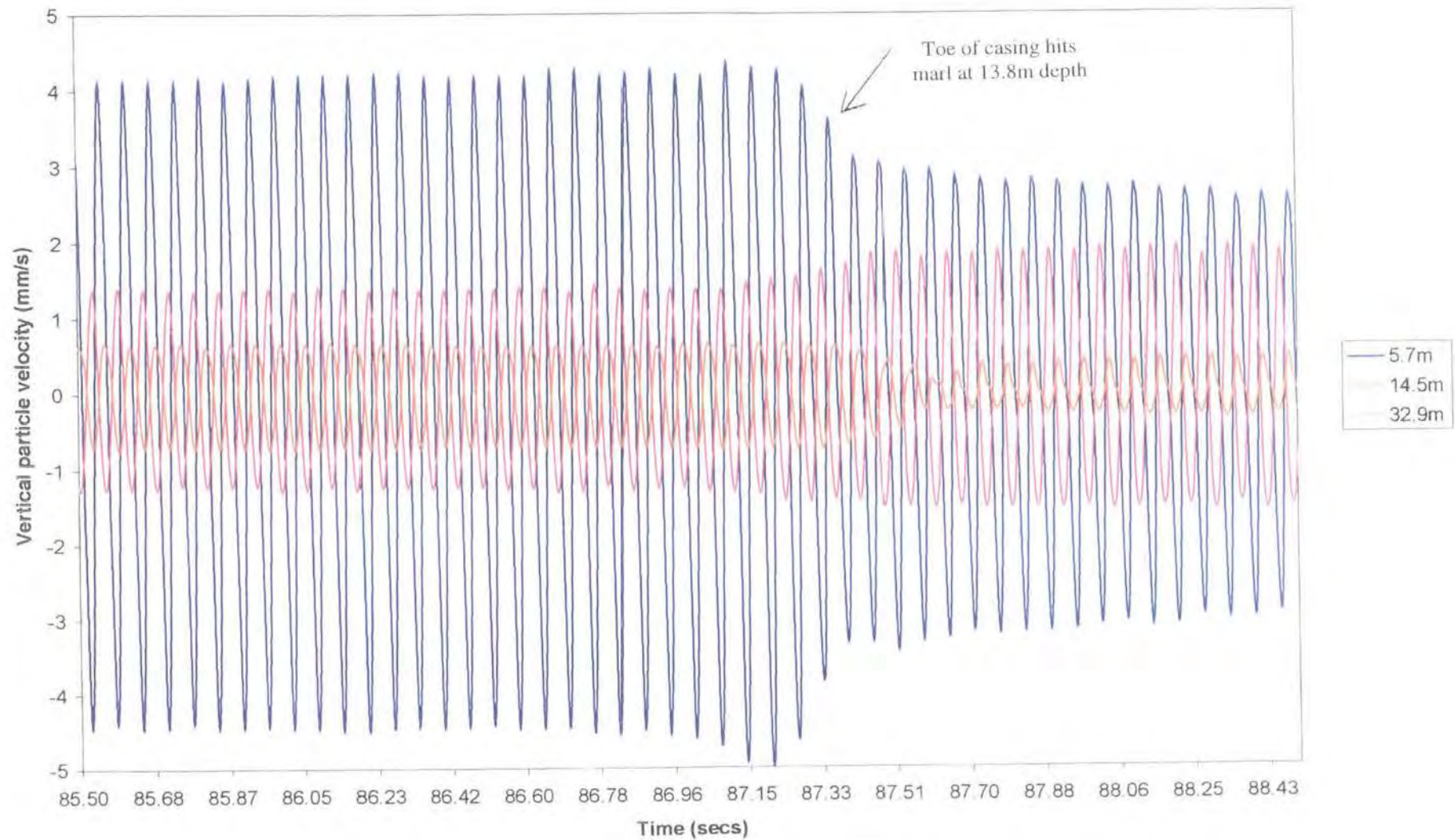
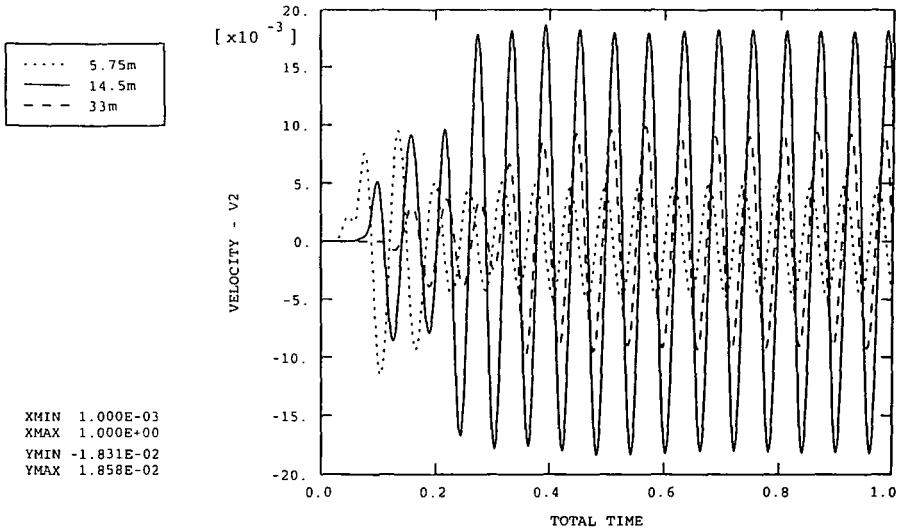
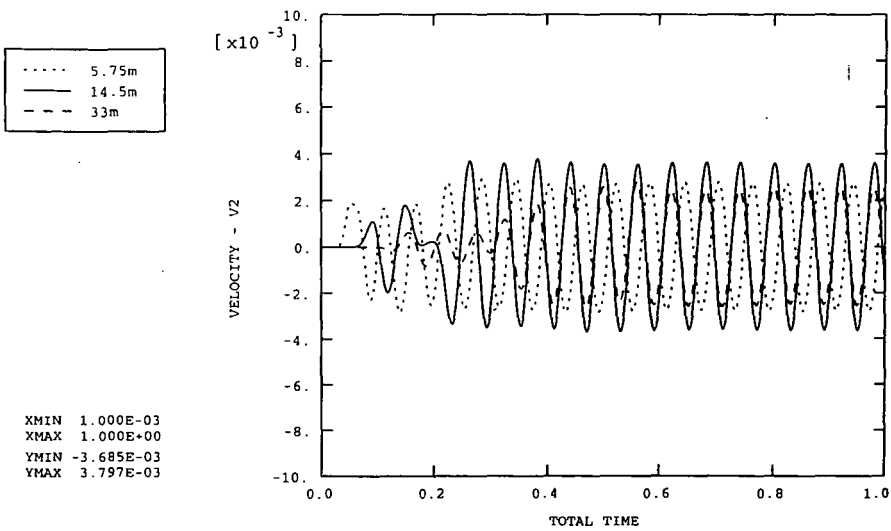


Figure 5.67 Vertical velocity/time traces recorded during installation of casing as the toe moves from alluvium into marl at 13.8m depth (SSC site)



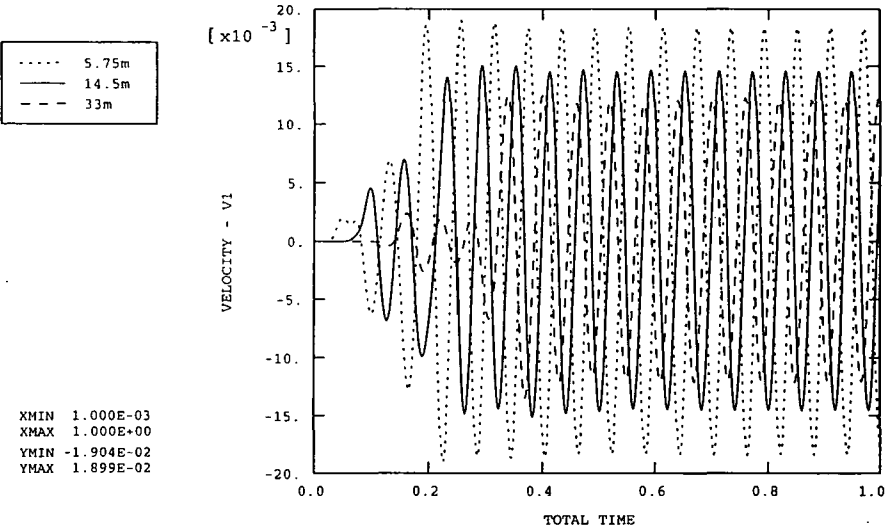
(a) $E_{toe} = 15\text{MPa}$



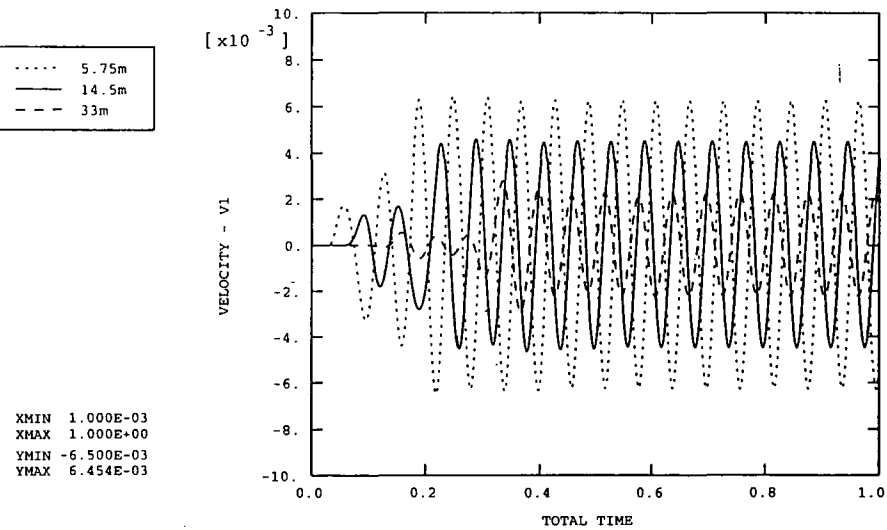
(b) $E_{toe} = 200\text{MPa}$

Figure 5.69

Comparison of predicted vertical velocity/time traces for $E_{toe} = 15\text{MPa}$ and $E_{toe} = 200\text{MPa}$. Overall coefficient of friction of 0.15 assumed in both cases. (SSC site)

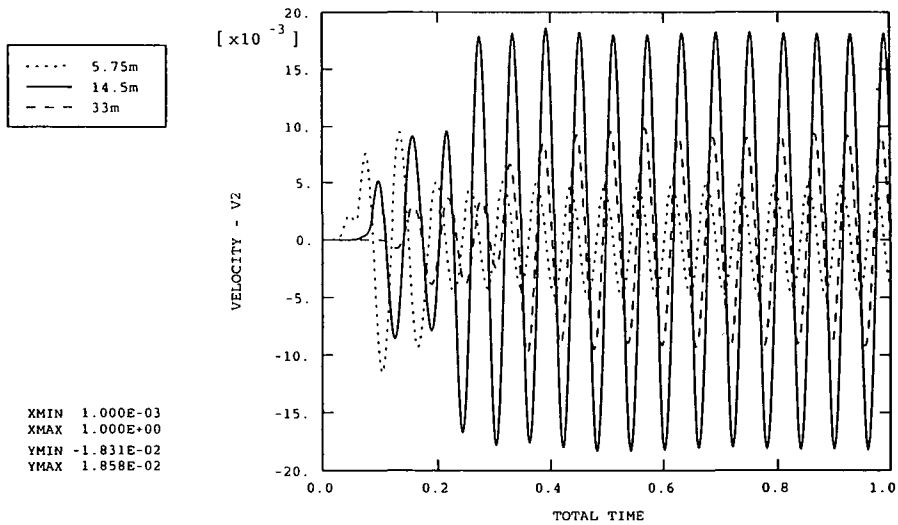


(a) $E_{toe} = 15\text{MPa}$

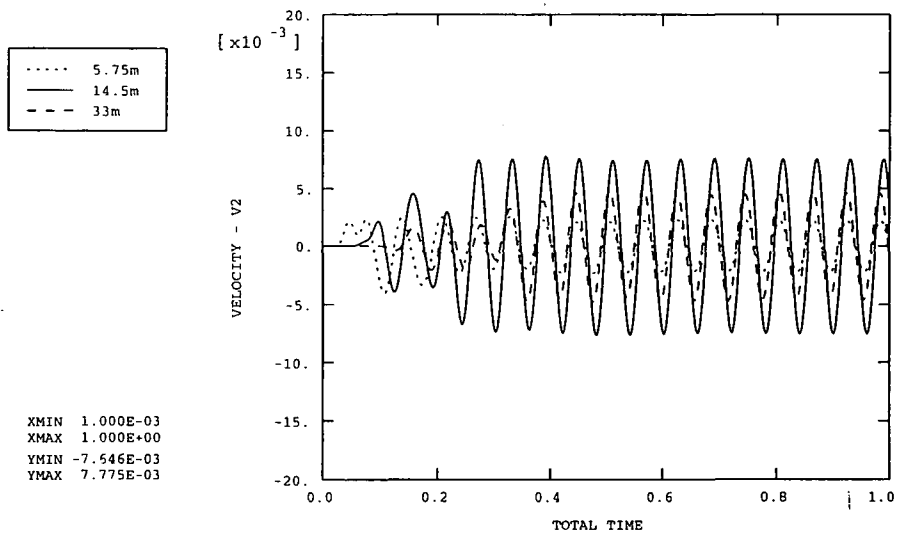


(b) $E_{toe} = 200\text{MPa}$

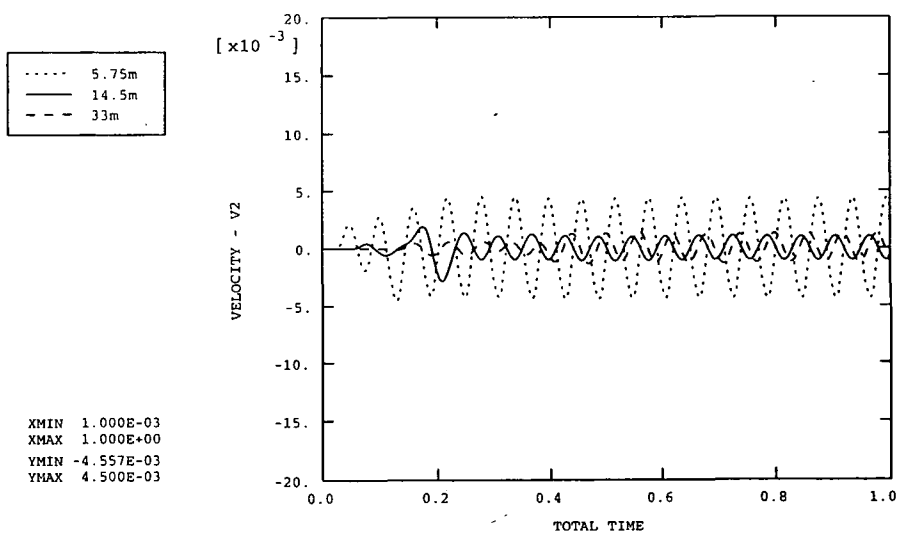
Figure 5.70 Comparison of predicted radial velocity/time traces for $E_{toe} = 15\text{MPa}$ and $E_{toe} = 200\text{MPa}$. Overall coefficient of friction of 0.15 assumed in both cases. (SSC site)



(a) 100% of the pile displacement



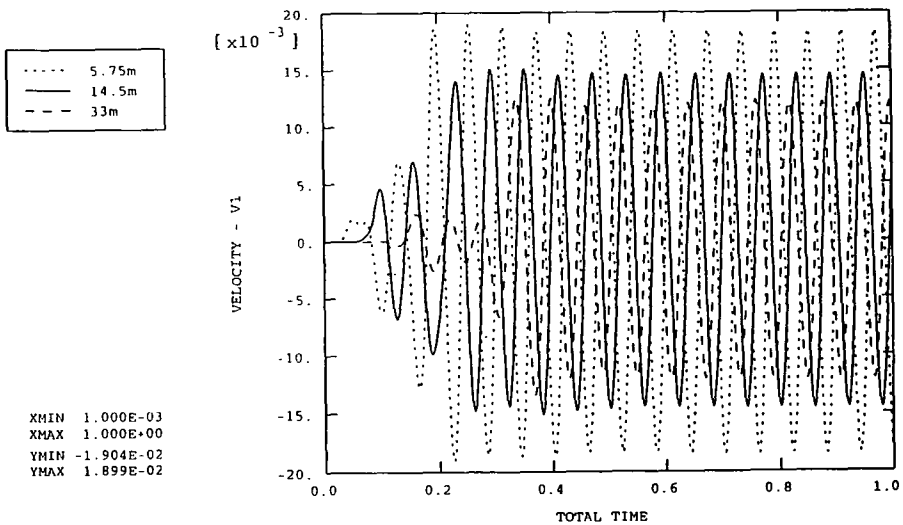
(b) 50% of the pile displacement



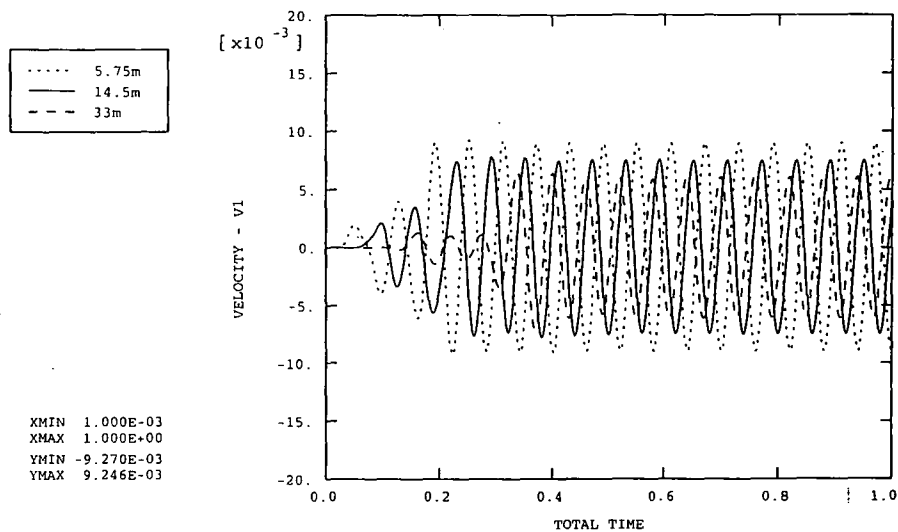
(c) 10% of the pile displacement

Figure 5.71

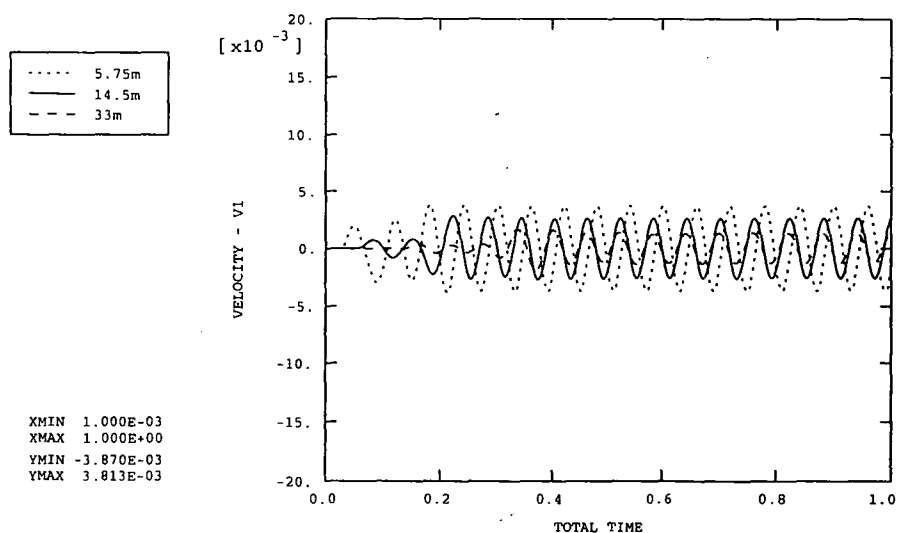
The effect of the magnitude of the soil displacement under the toe on the predicted vertical velocity/time traces. Toe in alluvium (assuming $E_{\text{toe}} = 15\text{MPa}$ and $\mu=0.15$). (SSC site)



(a) 100% of the pile displacement



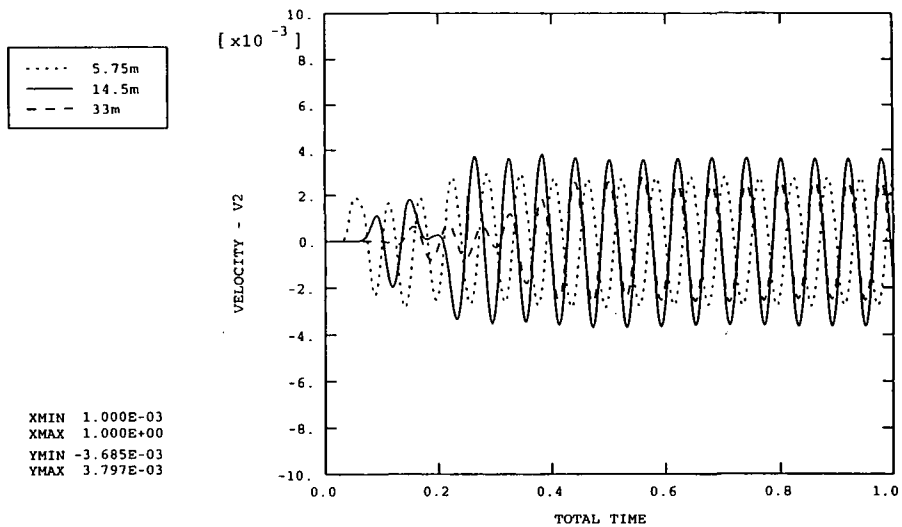
(b) 50% of the pile displacement



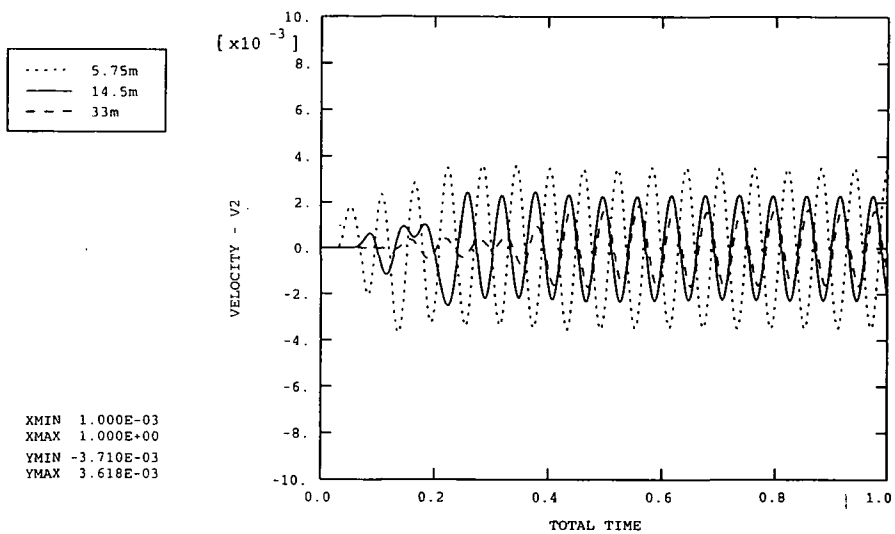
(c) 10% of the pile displacement

Figure 5.72

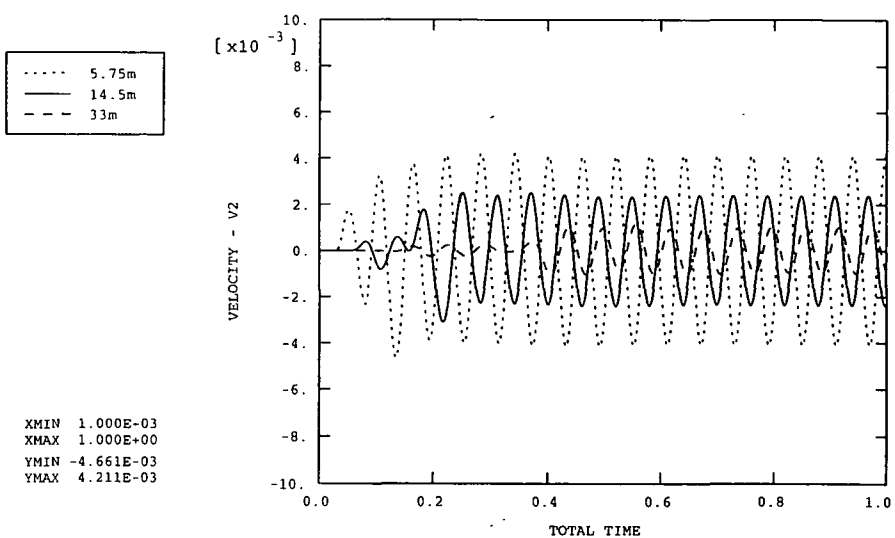
The effect of the magnitude of the soil displacement under the toe on the predicted radial velocity/time traces. Toe in alluvium (assuming $E_{\text{toe}} = 15\text{MPa}$ and $\mu = 0.15$). (SSC site)



(a) 100% of the pile displacement



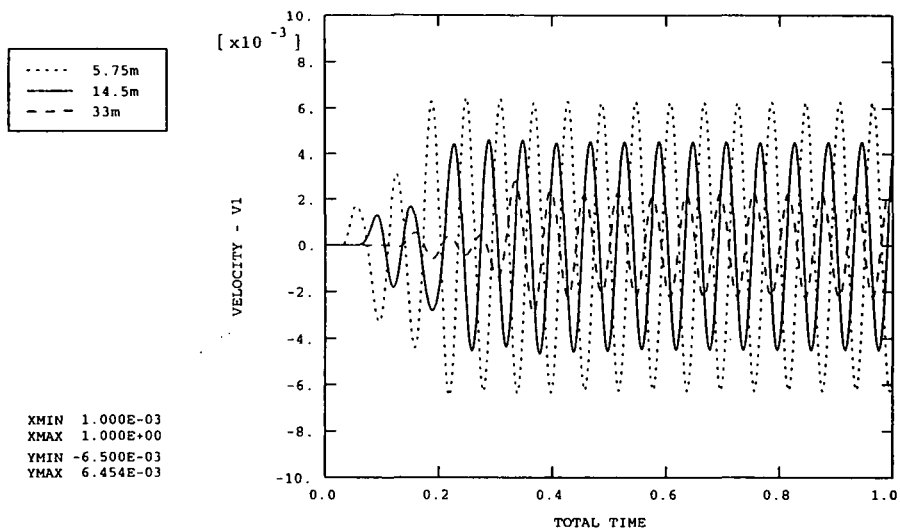
(b) 50% of the pile displacement



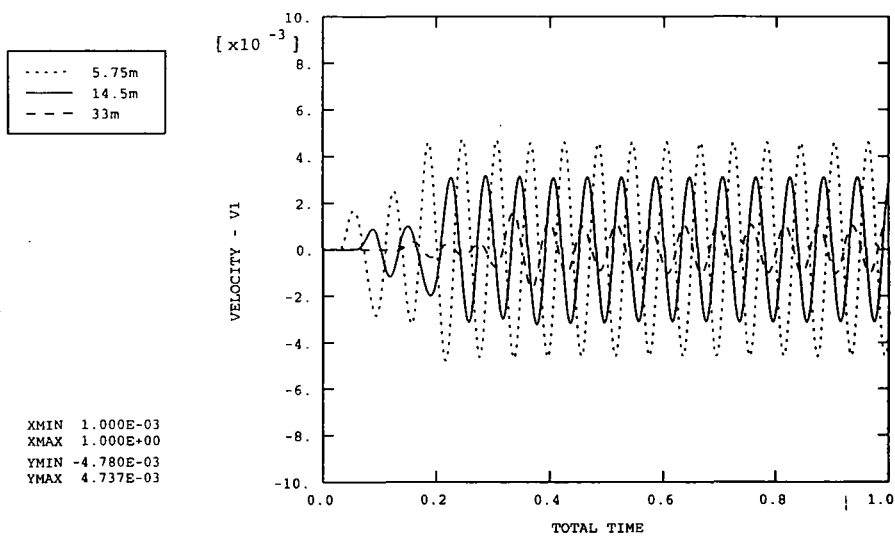
(c) 10% of the pile displacement

Figure 5.73

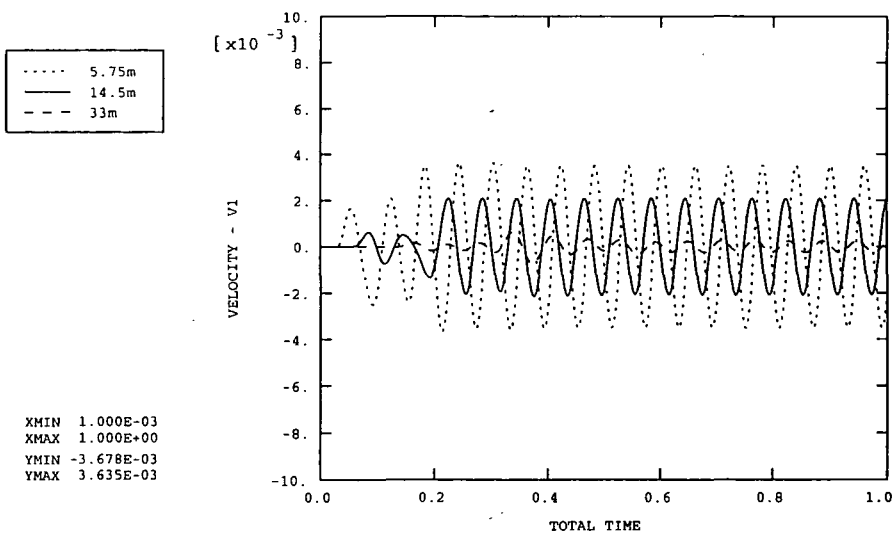
The effect of the magnitude of the soil displacement under the toe on the predicted vertical velocity/time traces. Toe in marl (assuming $E_{\text{toe}} = 200\text{MPa}$ and $\mu = 0.15$). (SSC site)



(a) 100% of the pile displacement



(b) 50% of the pile displacement

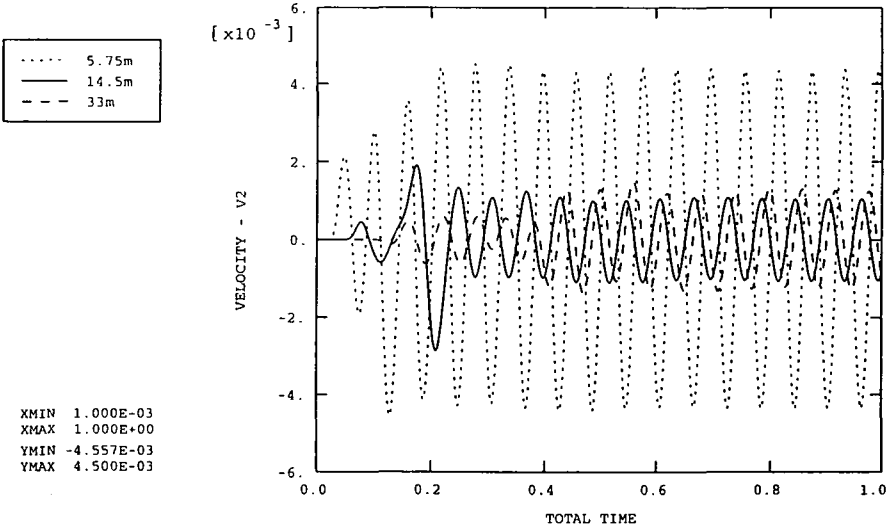


(c) 10% of the pile displacement

Figure 5.74

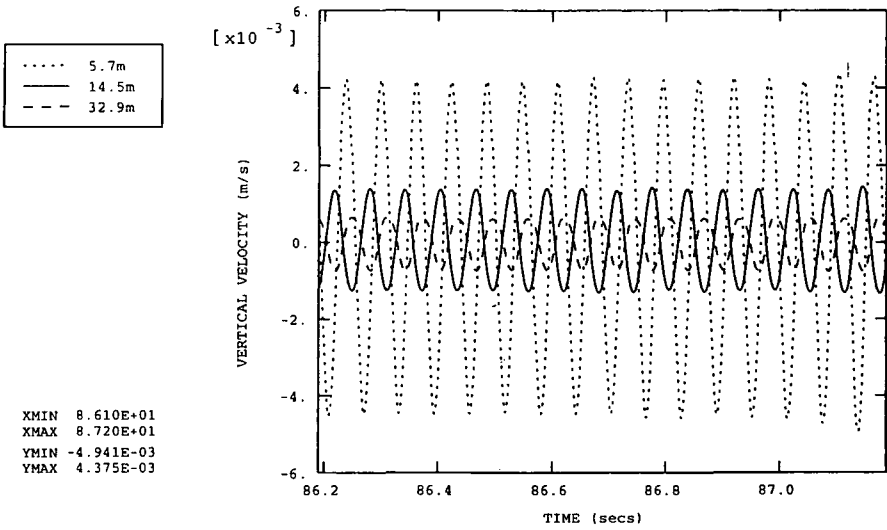
The effect of the magnitude of the soil displacement under the toe on the predicted radial velocity/time traces. Toe in marl (assuming $E_{\text{toe}} = 200\text{MPa}$ and $\mu=0.15$). (SSC site)

ABAQUS



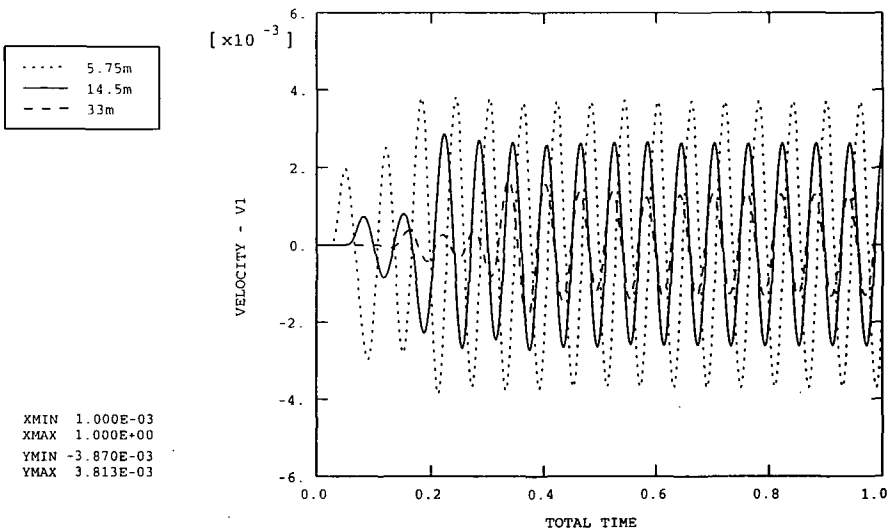
(a) Predicted (assuming $E_{\text{toe}} = 15\text{MPa}$, toe displacement = 10% of pile displacement and $\mu=0.15$).

ABAQUS

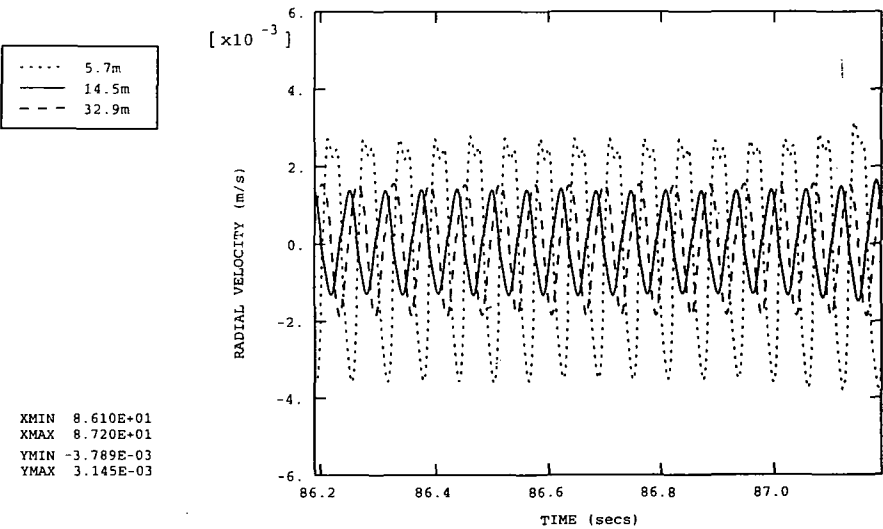


(b) Measured

Figure 5.75 Comparison of predicted and measured vertical velocity/time traces. Toe in alluvium. (SSC site)



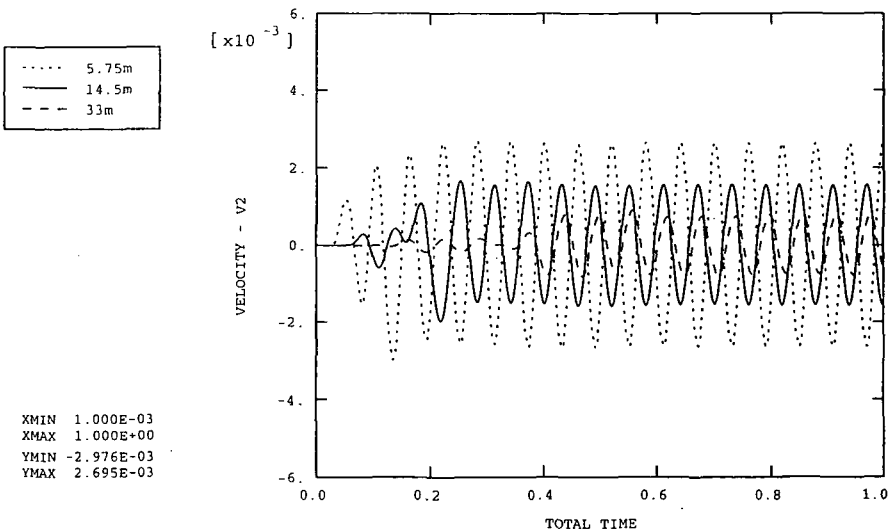
(a) Predicted (assuming $E_{\text{toe}} = 15\text{MPa}$, toe displacement = 10% of pile displacement and $\mu=0.15$).



(b) Measured

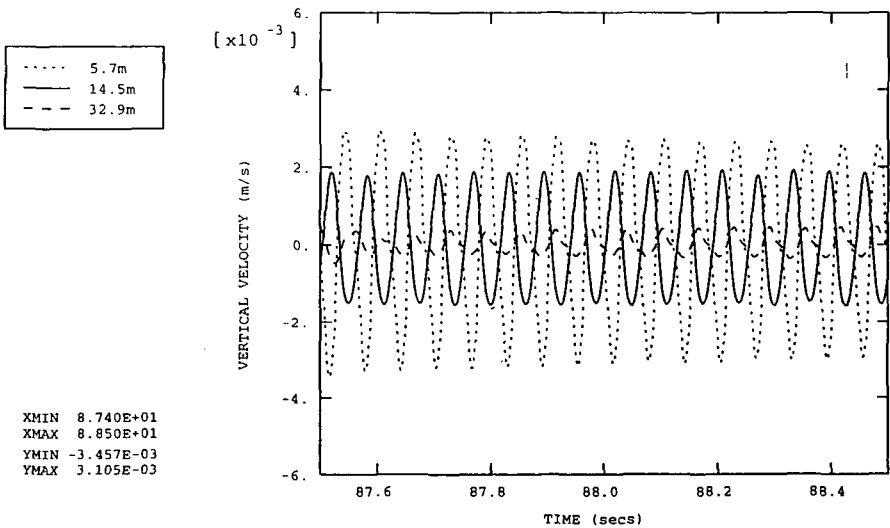
Figure 5.76 Comparison of predicted and measured radial velocity/time traces. Toe in alluvium. (SSC site)

ABAQUS



(a) Predicted (assuming $E_{\text{toe}} = 200\text{MPa}$, toe displacement = 10% of pile displacement and $\mu=0.1$).

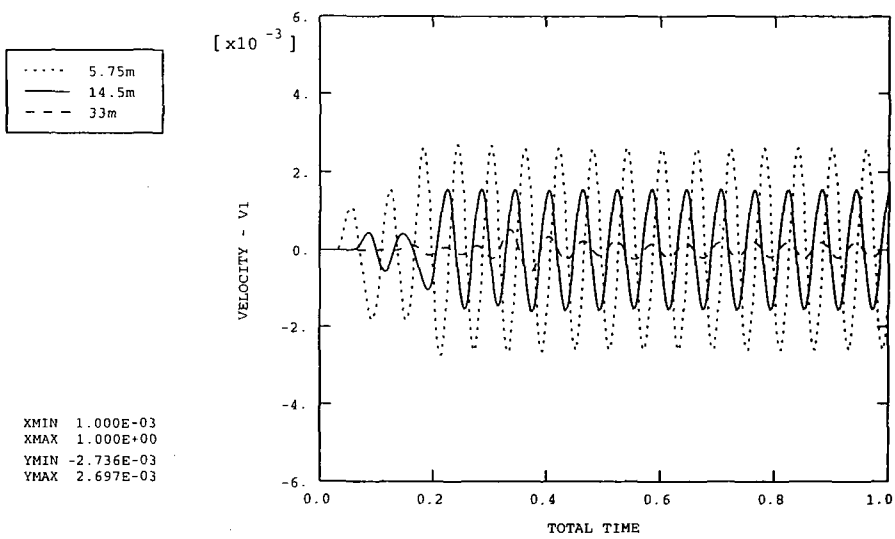
ABAQUS



(b) Measured

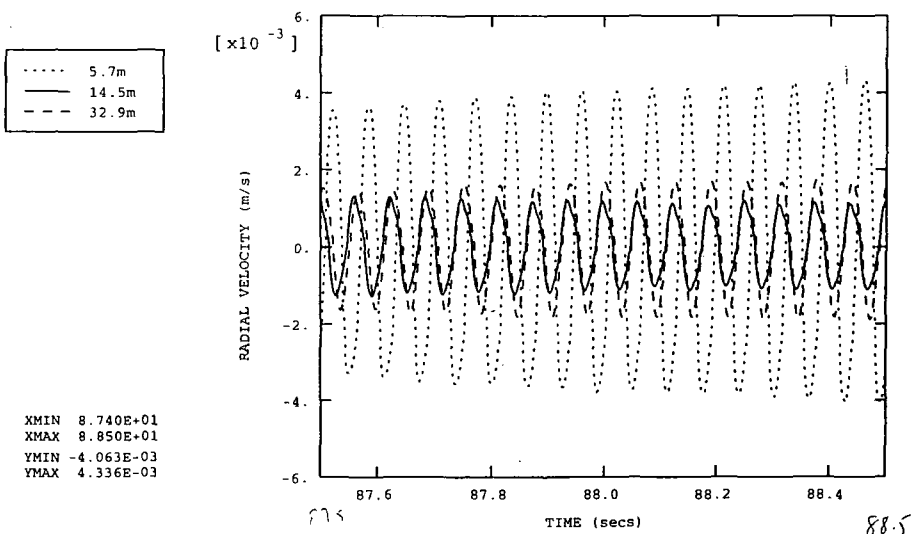
Figure 5.77 Comparison of predicted and measured vertical velocity/time traces. Toe in marl. (SSC site)

ABAQUS



(a) Predicted (assuming $E_{\text{toe}} = 200\text{MPa}$, toe displacement = 10% of pile displacement and $\mu=0.1$).

ABAQUS



(b) Measured

Figure 5.78

Comparison of predicted and measured radial velocity/time traces.
Toe in marl. (SSC site)

222

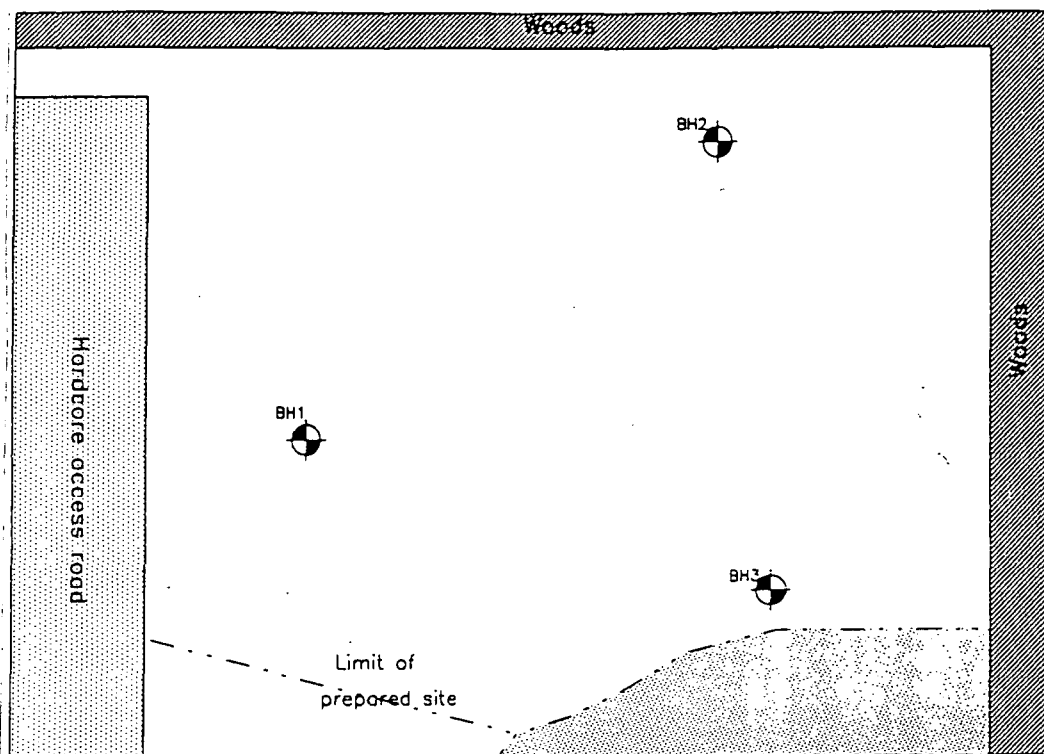


Figure 5.79

Plan of the site at Flitwick showing borehole locations

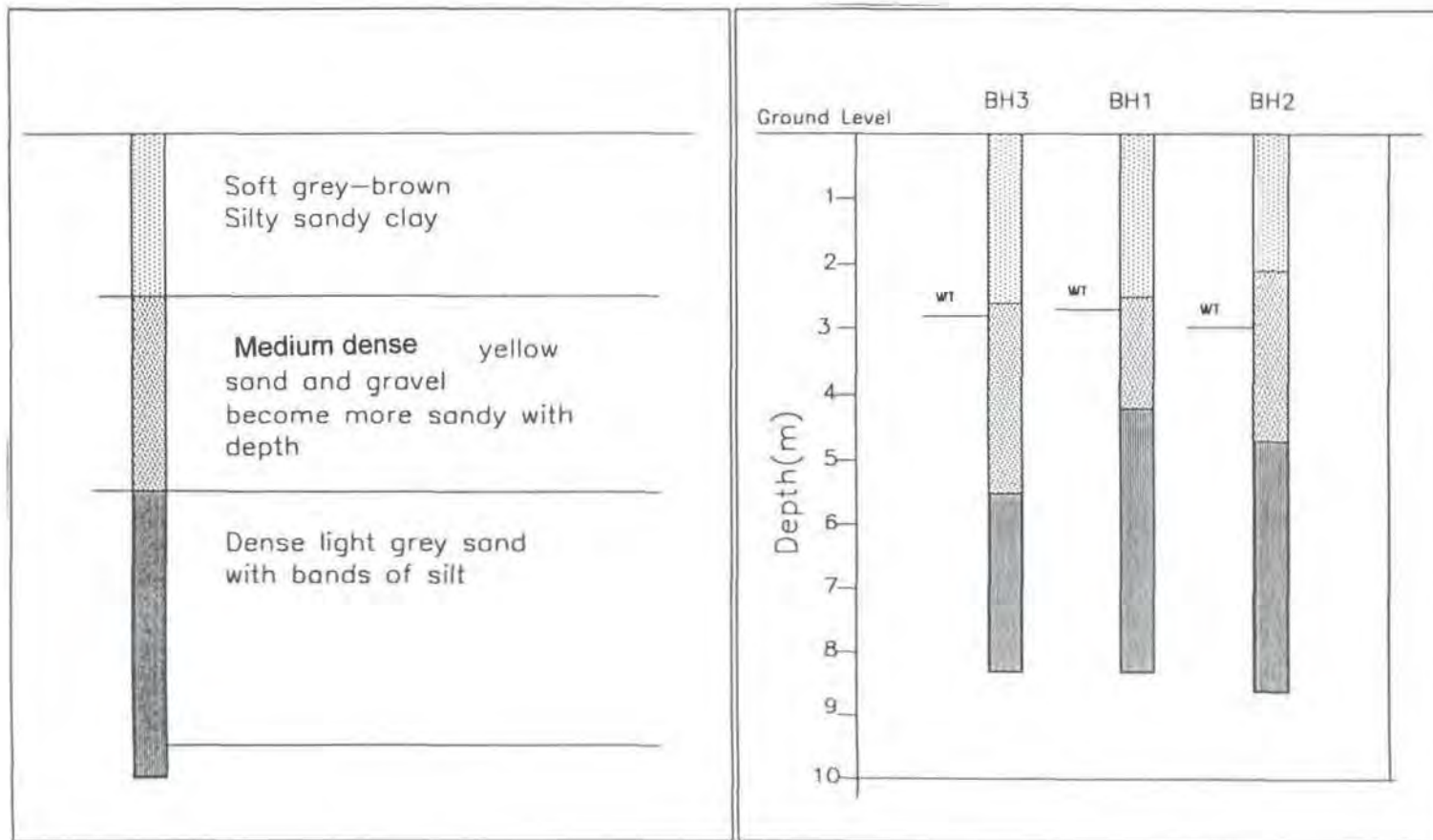


Figure 5.80 Ground conditions at Flitwick

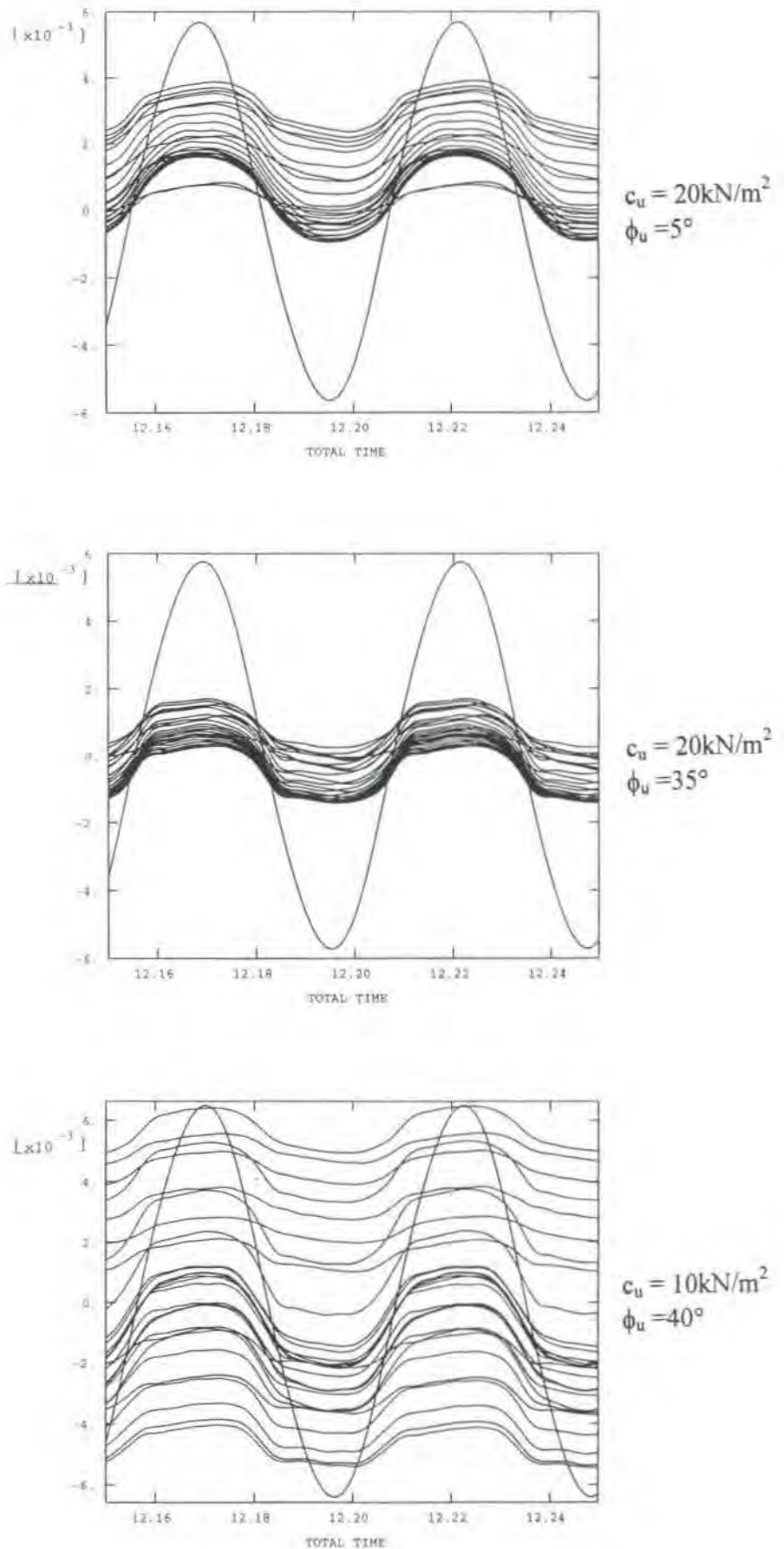


Figure 5.81

Sensitivity of pile/soil interaction model to Mohr Coulomb parameters: Vertical displacements of all soil nodes on pile/soil interface (Flitwick site)

ABAQUS

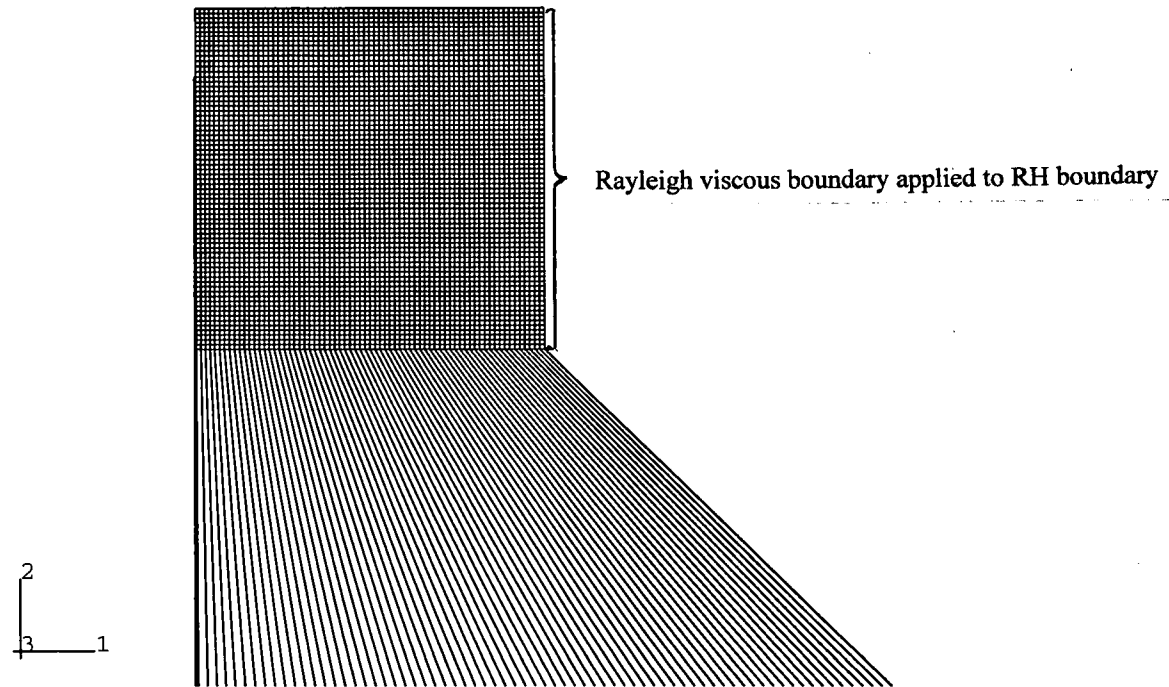
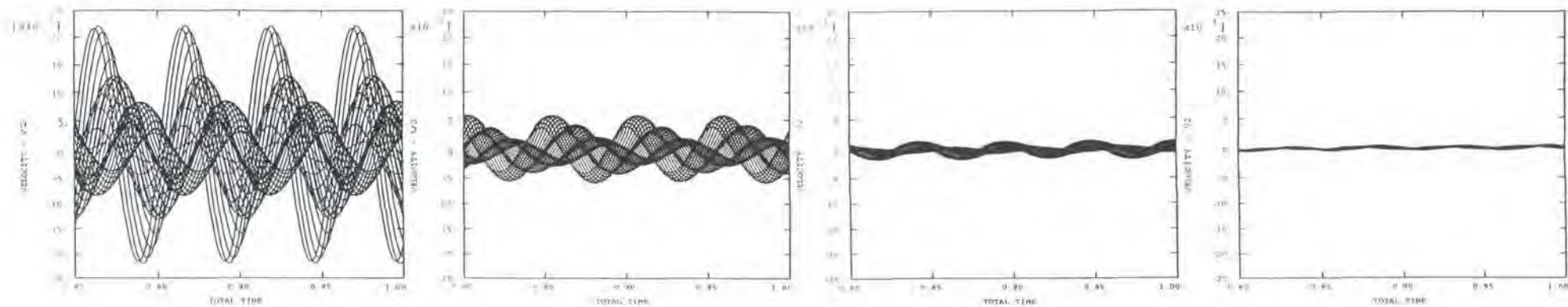
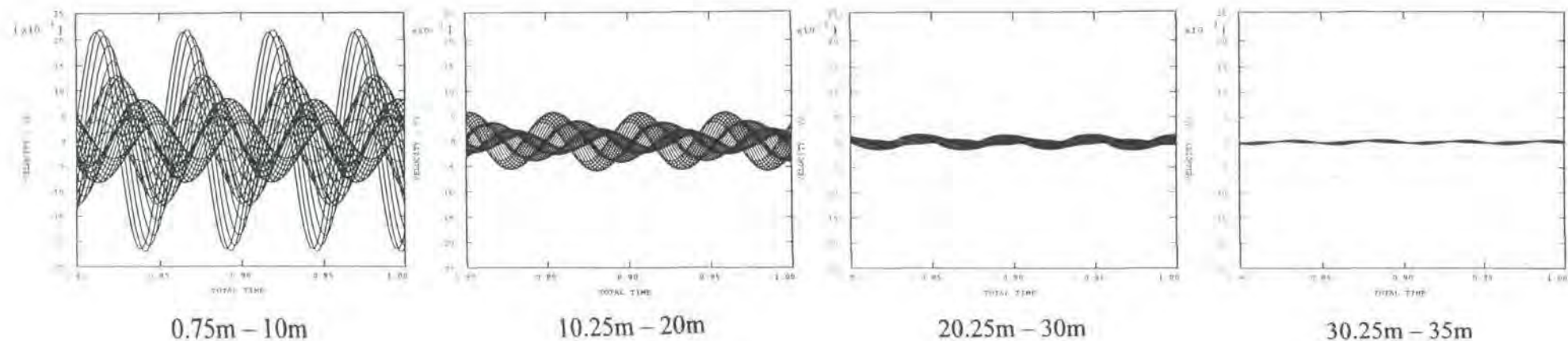


Figure 5.82

FE/IE mesh used for wave propagation analysis at Flitwick site



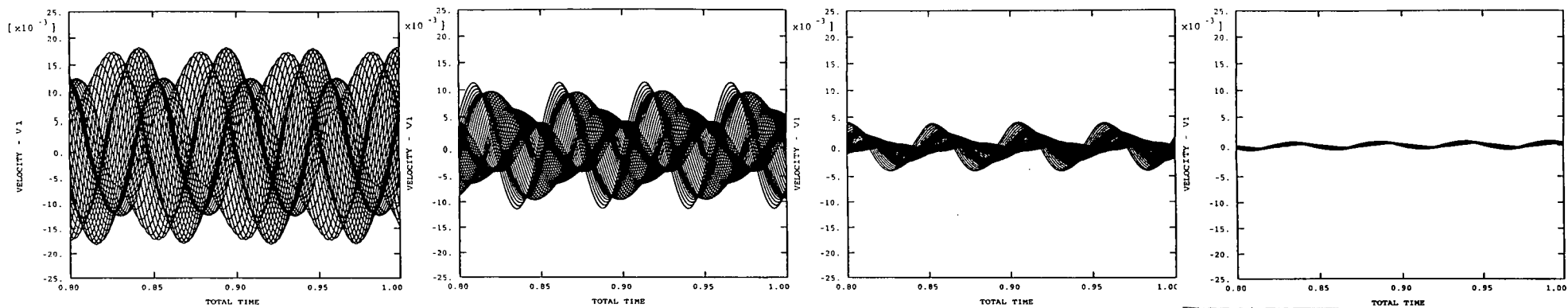
(a) 35m wide FE mesh with ABAQUS IE on RH boundary



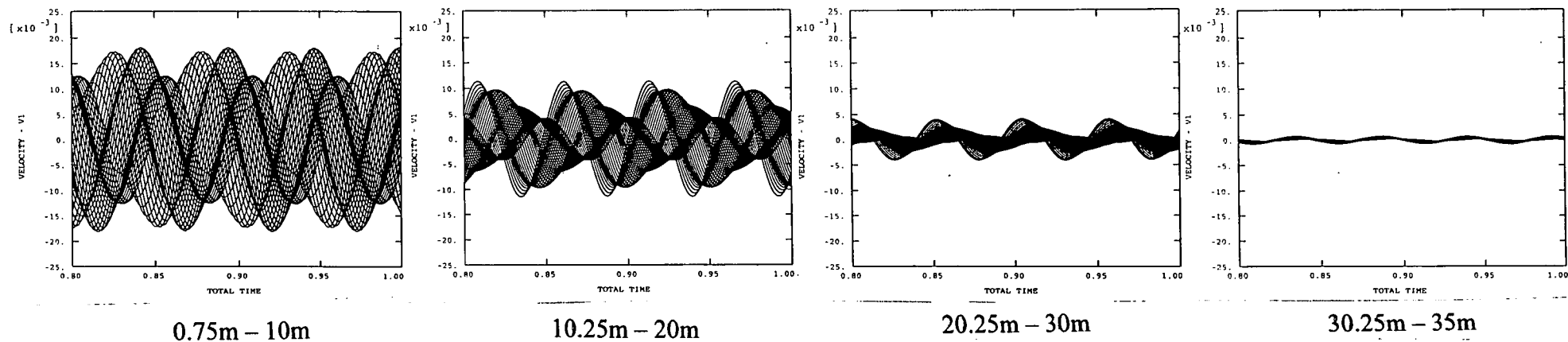
(b) 35m wide FE mesh with Rayleigh viscous boundary applied to RH boundary

Figure 5.83

Comparison of the predicted vertical velocity/time traces from a 35m wide FE mesh with ABAQUS IE and a 35m wide FE mesh with a Rayleigh viscous boundary (time period of 0.8-1.0 second). (Flitwick site).



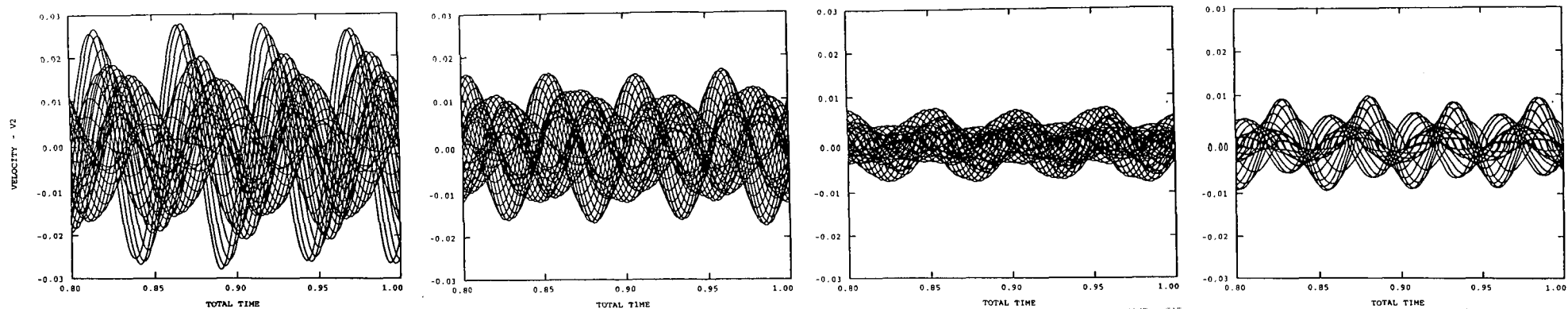
(a) 35m wide FE mesh with ABAQUS IE on RH boundary



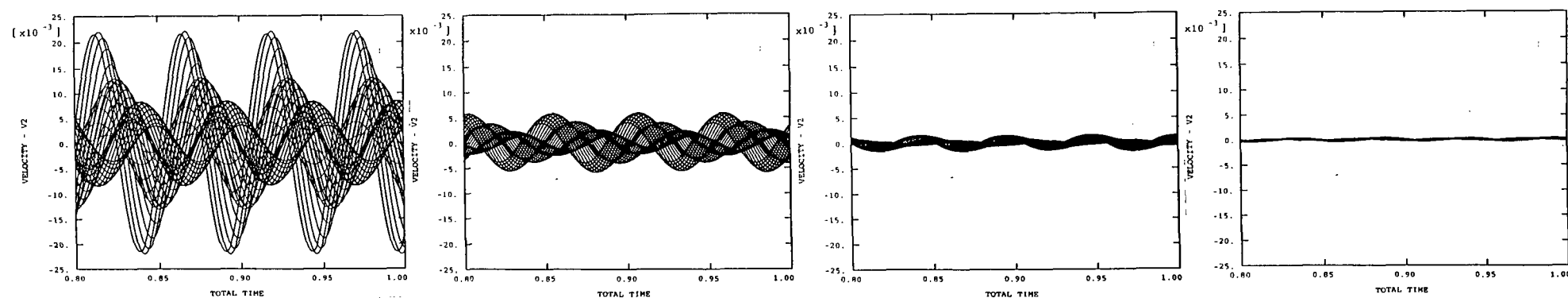
(b) 35m wide FE mesh with Rayleigh viscous boundary applied to RH boundary

Figure 5.84

Comparison of the predicted radial velocity/time traces from a 35m wide FE mesh with ABAQUS IE and a 35m wide FE mesh with a Rayleigh viscous boundary (time period of 0.8-1.0 second). (Flitwick site).



(a) No material damping



0.75m – 10m

10.25m – 20m

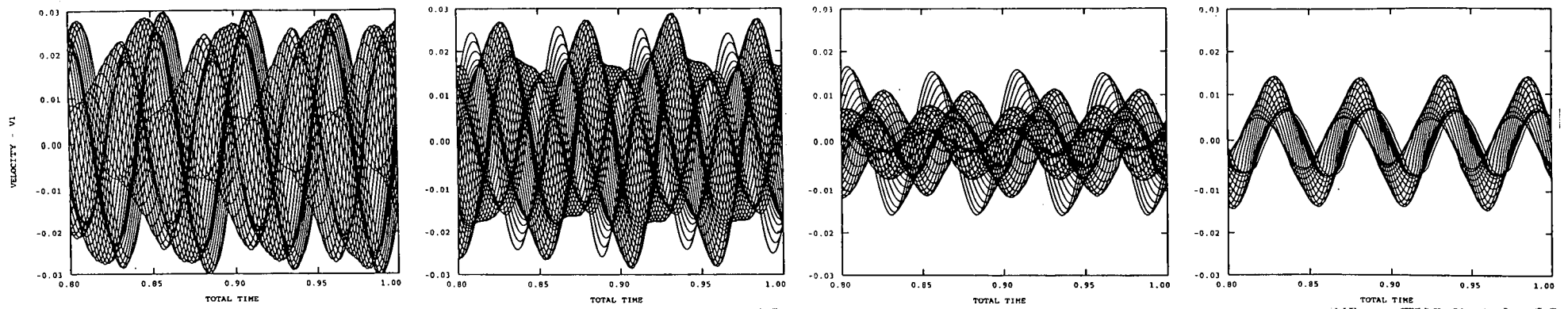
20.25m – 30m

30.25m – 35m

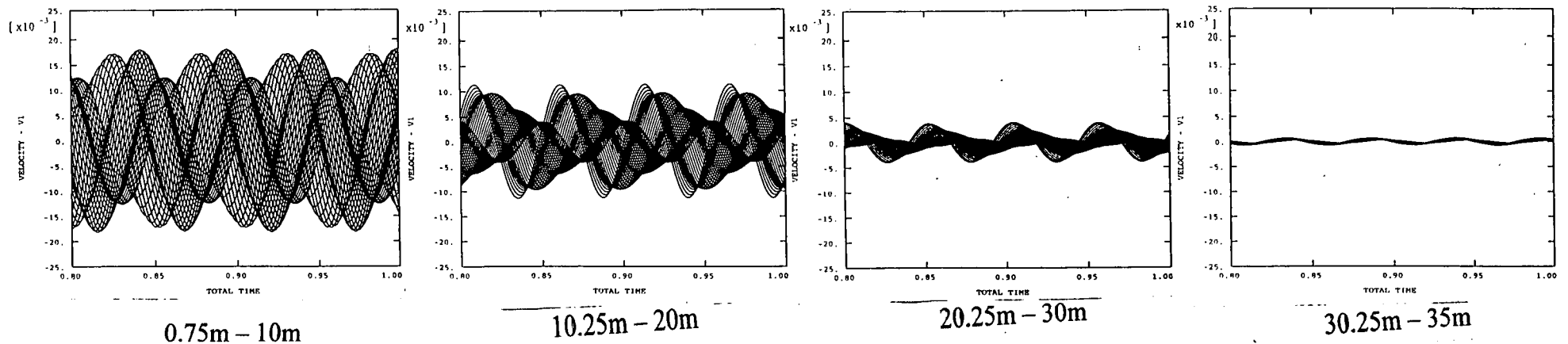
(b) Material damping = 5%

Figure 5.85

Comparison of the predicted vertical velocity/time traces assuming material damping ratios of 0% and 5% (time period of 0.8-1.0 second). (Flitwick site).

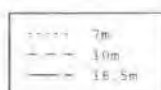


(a) No material damping

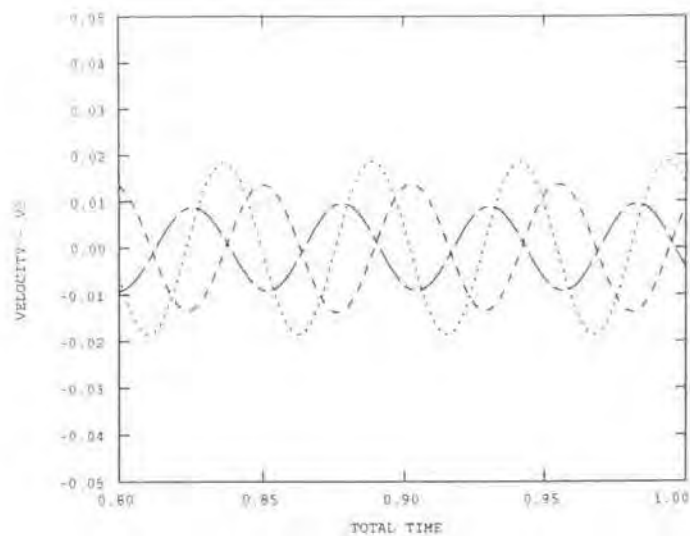


(b) Material damping = 5%

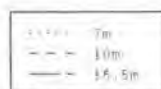
Figure 5.86 Comparison of the predicted radial velocity/time traces assuming material damping ratios of 0% and 5% (time period of 0.8-1.0 second). (Flitwick site).



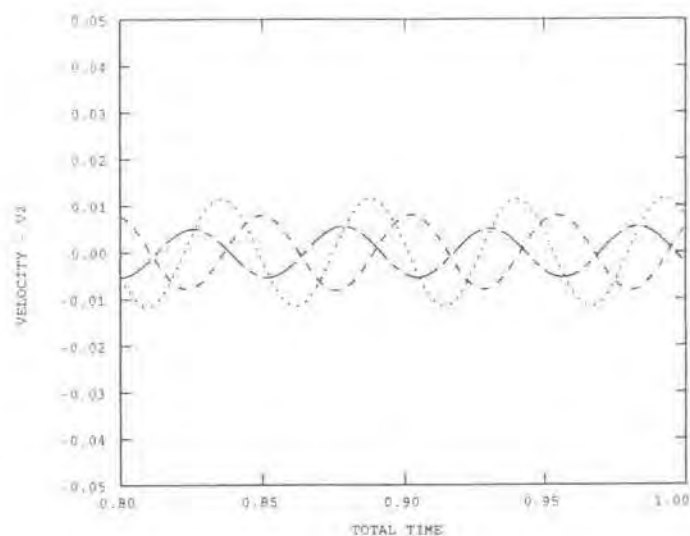
XMIN 1.000E-03
 XMAX 1.000E+00
 YMIN -2.002E-02
 YMAX 2.085E-02



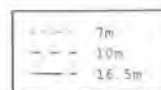
(a) 100% of the pile displacement



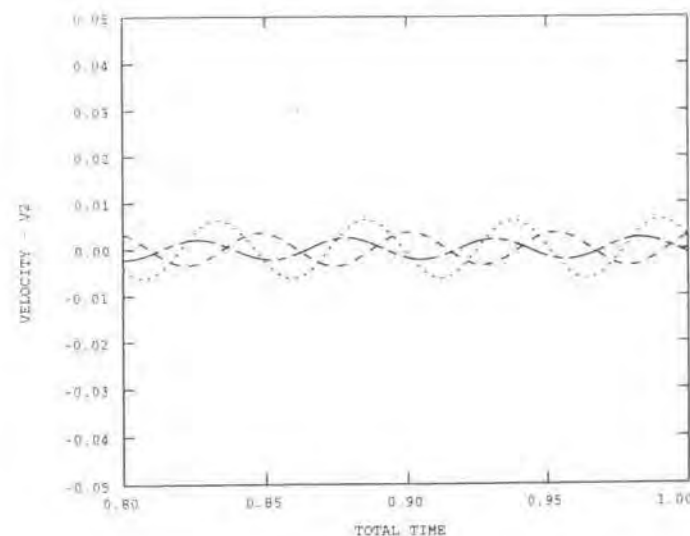
XMIN 1.000E-03
 XMAX 1.000E+00
 YMIN -1.263E-02
 YMAX 1.328E-02



(b) 50% of the pile displacement



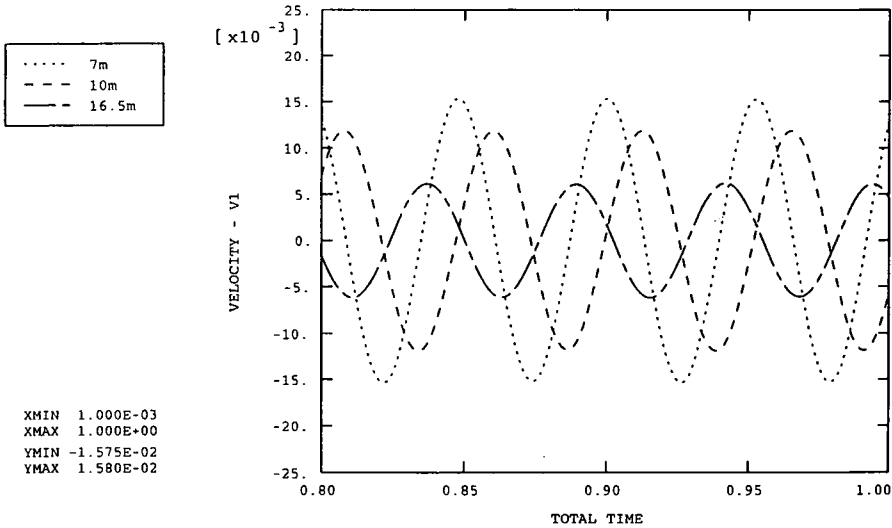
XMIN 1.000E-03
 XMAX 1.000E+00
 YMIN -6.717E-03
 YMAX 7.545E-03



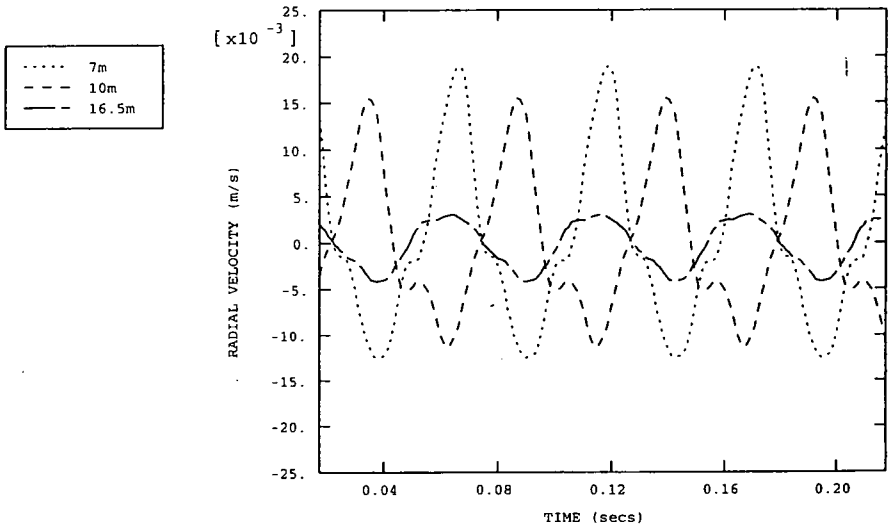
(c) 10% of the pile displacement

Figure 5.87

The effect of the magnitude of the soil displacement under the toe on the predicted vertical velocity/time traces. (Flitwick site)



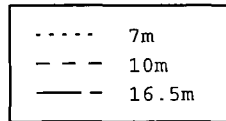
(a) Predicted



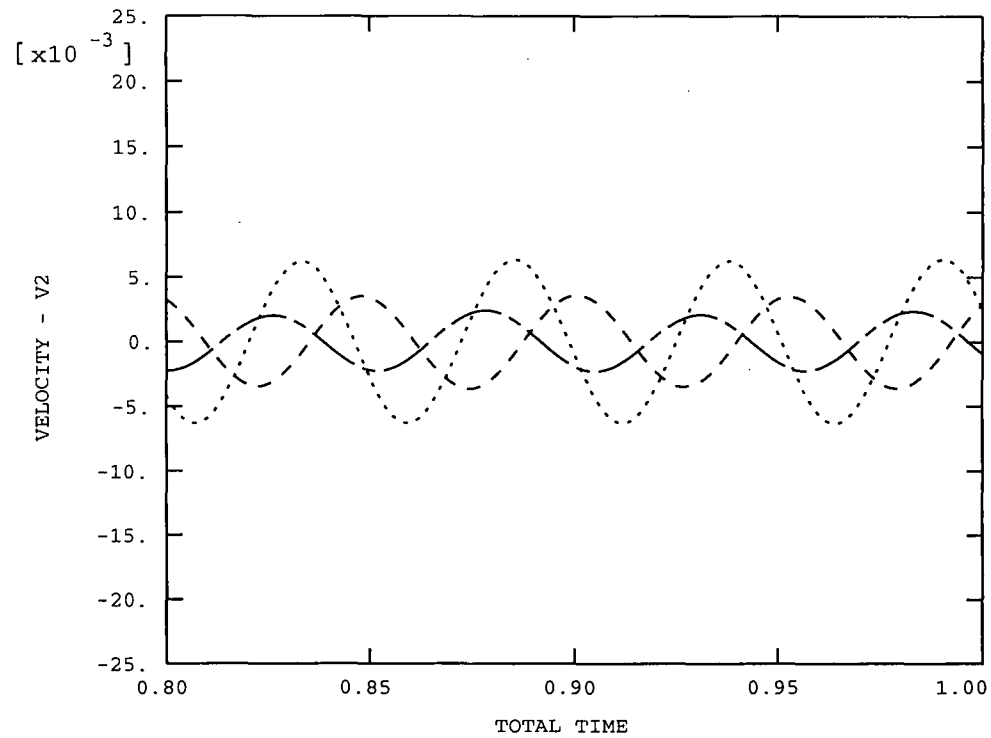
(b) Measured

Figure 5.89 Comparison of the predicted and measured radial velocity/time traces at geophone locations (Flitwick site)

ABAQUS



XMIN 1.000E-03
 XMAX 1.000E+00
 YMIN -6.717E-03
 YMAX 7.545E-03



Measured vertical ppv's	
7m	4.55mm/s
10m	3.81mm/s
16.5m	3.23mm/s

Figure 5.90

Predicted vertical velocity/time traces at geophone locations (Flitwick site)

CHAPTER 6

DEVELOPMENT OF A NUMERICAL MODEL FOR IMPACT PILING

6.1 GENERAL BACKGROUND

The form of surface vibrations generated by pile driving is well known from the large quantity of site data that has been collected over many years, and simple empirical equations (Chapter 2) have been proposed to describe their attenuation. However very little work has been done on modelling the ground waves generated by impact piling computationally. Such techniques potentially offer a means of understanding the complex processes of ground wave generated during piling.

An extensive literature search has revealed that the only attempt to model the ground waves generated by impact piling to date is the work by the TNO Building and Construction Research organisation in the Netherlands (van Staalduinen & Waarts, 1992). Waarts & Bielefeld (DFI, 1994) used the TNOWAVE stress wave program, based on one-dimensional stress wave theory and developed for pile drivability predictions, to calculate the force at the pile toe and shaft friction as a function of time. The parameters for soil response (yield stress, quake and damping) were based on cone penetration test results. The results of the stress wave analysis were then input into an axisymmetric finite element mesh to model wave propagation through the soil. Comparison of predicted and measured vibration levels indicated reasonably good agreement.

The only other published work on modelling ground waves generated by impact piling appears to be by Hanazato and Kishida (1992). They used the Smith model to calculate dynamic loads at soil-pile interfaces. The dynamic loads were then used as input exciting forces to an axisymmetric finite element technique with thin layered elements. One field test was modelled where measured dynamic strains in the pile and ground vibrations were recorded.

Although very little work has been undertaken on the computation of ground waves generated by piling, many workers have developed numerical and analytical models for the simulation of pile driving in the context of pile drivability. This was the obvious starting point for this research which develops the models in a pragmatic way and extends them into the far-field so that they can be used for vibration prediction.

The first empirical pile driving formulae were developed in the 1800's and were valid over a very limited range of soil and pile types. A method of analysis based on the wave equation was presented by Glanville et al (1938), but the simplifications required to permit manual solution did not allow satisfactory accuracy to be attained. Consequently, pile driving formulae remained in common use.

However, the advent of the digital computer permitted the solution of the wave equation. Smith (1960) published a numerical method for analysing pile driving problems using the wave equation. The pile and hammer are represented by a system of discrete springs and masses, and the surrounding soil is represented by dynamic reaction forces dependent on the pile displacement and velocity (Figure 6.1). The equations of motion are solved using the finite difference method.

Computer programs implementing the Smith model in both the original and modified forms are still used in engineering practice. The choice of quake and damping factors has been the subject of much research. Coyle et al (1977) reviewed some of this work and recommended slightly different parameter values to those proposed by Smith.

Although the Smith model has been used successfully for many years, it has some shortcomings. The empirical nature of the soil influence on the pile is a major problem. The relationships between the pile motion and the soil reactions are not based on rigorous analysis of dynamic soil behaviour. Consequently, the quake and damping parameters can not be associated with fundamental soil properties and can not be measured by standard geotechnical investigation techniques. Experience with the Smith model over many years has led to quake and damping parameters which can be used in normal pile driving situations with reasonable confidence. However, unusual situations can be encountered in which reliable Smith parameters are difficult to estimate prior to driving.

The damping parameter J was originally associated with soil viscosity. However, laboratory studies into the strain rate and penetration velocity dependency of soil viscosity consistently showed non-linear velocity dependence. Indeed, Randolph and Simons (1986) have examined the available data and found little evidence of velocity dependency once shaft velocity exceeds 0.1m/s.

Meynard and Corte (1984) conducted experimental work based on the analytical work of Novak (1977) and Novak et al (1978) which led them to conclude that most wave attenuation in piles can be explained by radiation damping along the pile shaft, rather than soil viscosity. They used the work of Novak et al (1978) to show that radiation damping could be modelled by a viscous dashpot, and that the dynamic shear stiffness of the soil could be modelled by a spring. The spring and damping parameters are dependent mainly on the shear modulus and density of the soil.

Deeks (1992) developed a new one-dimensional pile driving model, consisting of a one-dimensional pile with new base and shaft radiation models, which gave results which agreed very closely with those obtained by accurate FE analysis. He compared the new one-dimensional model with published examples of pile driving analysis and found that the new one-dimensional model was more accurate than previous FE analyses of pile driving by other workers.

This Chapter presents a new finite element model for the simulation of ground waves generated by impact piling. The main objective in the development of the pile driving simulation is to design a model that can use and be calibrated against the large amount of vibration data available (Uromehy, 1990 and Hiller & Crabb, 2000). Valuable comprehensive data sets will also become available when the extensive records from the SIPDIS programme (Chapter 2) are published.

This thesis therefore presents a pragmatic approach to the problem. The lack of excitation data in conjunction with vibration measurements necessitated the modelling of the entire pile driving process including the hammer impact. This is achieved by combining and adapting analytical models and finite element techniques developed by other workers and extending them to model the propagation of ground waves out into

the far field. Various assumptions and simplifications have been adopted in the absence of detailed information on soil parameters.

A three-part process was found to be required:

1. The hammer impact is modelled by a lumped ram and an anvil separated by a damped cushion represented by a spring and dashpot in parallel.
2. The propagation of the stress wave through the pile is modelled by applying the forcing function calculated by the hammer impact model to a finite element representation of the pile with soil response modelled by simple mass-spring-dashpot systems based on typical soil parameters.
3. The resulting pile response is then transferred to an axisymmetric finite element model of the ground in order to simulate the propagation of the ground waves generated by the pile driving process. Pile/soil interaction is simulated using the friction model available in ABAQUS. Propagation of the ground waves is simulated assuming that the soil is an elastic medium. Parametric studies based on the arrival times of ground waves at various distances from the vibration source are used to estimate values for the small strain stiffness of various soil types.

The resulting procedures are therefore not intended to be rigorous geotechnical analyses. The models are designed so that they can be calibrated against the large databases of vibration data that exist and then used to improve the current empirical and conservative guidelines. The simplicity of the models also means that they could be used as a preliminary design tool for the prediction of ground surface vibrations where site data are sparse.

Development of the impact model has been undertaken in a number of stages and these are reflected in the structure of the remainder of this chapter. The chronological development of the model, including the difficulties encountered and their resolution, is described in Section 6.2. The model itself is described in detail in Section 6.3. The model was then calibrated against data from a site on the M66 motorway near Manchester (Section 6.4). This section also demonstrates the sensitivity of the various parameters involved. The model is verified by applying it to another case history at Flitwick in Bedfordshire as described in Section 6.5. Conclusions and recommendations for further work are given in Section 6.6.

6.2 CHRONOLOGICAL DEVELOPMENT OF THE MODEL

The aim of this section of work is to develop a computational model which can be used to simulate the ground waves generated by impact piling using only desk study data and hence to give some indication of the levels and patterns of ground vibration. This model could be used not only as a vibration predictor but as a tool for understanding the behaviour of ground waves generated by impact piling in various ground conditions.

As stated above, although several substantial databases of site records of vibrations generated by impact piling exist, the databases do not contain detailed records of pile

excitation, such as pile head strain, acceleration and transient displacement and they do not contain information about plastic and dynamic soil behaviour.

It was decided that a pragmatic approach to the problem was required. The lack of excitation data concurrent with ground vibrations meant that the entire pile driving process would have to be modelled including hammer impact. In order to do this, some of the computational models developed by other workers for the simulation of pile drivability have been adapted and combined with the proposed model. The model has then been extended into the far-field in order to simulate the vibrations resulting from the ground waves generated by the impact piling.

The finite element modelling of the interaction between the hammer, pile and soil does in itself present a number of difficulties. The model was developed in stages as a series of smaller pilot runs to determine the most effective method of simulating each part of the piling process. This section describes the chronological development of the model and the thought processes behind the design of the model presented in Section 6.3.

The initial pilot runs modelled the hammer as a rigid body with an initial velocity equal to $\sqrt{2gh}$ impacting on a pile represented by deformable finite elements. The ground was represented by a large axisymmetric finite element mesh of uniform eight-noded quadrilateral elements with infinite elements around the boundaries to model the far-field and prevent reflection back into the finite element mesh. The finite element mesh would have to be very large in order to prevent waves, principally P waves, reflecting back into the mesh and interfering with the ground waves within the zone of interest. For example, for a soil stiffness of about 150MPa (the dynamic stiffness of soils at small strains can be several times higher than their static stiffness), the propagation velocity of a P wave is about 300m/s compared to that of an R wave of 160m/s. Therefore any P waves travel almost twice as far as the R waves generated by the pile in the same time interval. This means that the boundary of the FE mesh would have to extend about twice as far (and be twice the size) as the furthest point of interest (ie the furthest geophone from the pile) in order to prevent the P wave from reflecting back into the mesh and interfering with any R waves. A much smaller FE mesh can therefore be used if infinite elements are inserted around the boundaries of the mesh, thus reducing the size and duration of the dynamic analysis. ABAQUS infinite elements are considered to provide a sufficiently effective boundary as it has been shown (Chapter 3) that they are almost perfect absorbers of body waves. The reduced effectiveness of the ABAQUS infinite elements in absorbing R waves is not important in this case because the analysis can be terminated as soon as the R waves have reached the furthest point of interest (ie the furthest geophone) and before they reach the FE/IE boundary.

Several problems were encountered with this FE/IE model. Firstly it was difficult to simulate the horizontal stresses on the pile from the soil without causing rigid body motion (see Chapter 5). The shaft friction on piles in both non-cohesive and cohesive soils has been shown to be dependent on the effective overburden pressure (see Section 6.3). Several techniques were trialled in order to overcome this problem, one of which was to model the pile as a rigid body in the first step of the analysis, push it laterally into the soil (in a similar manner to the vibratory piling model described in Chapter 5) and then replace the rigid pile with deformable elements for the remaining of the analysis. Although a form of this model did work, it was cumbersome and the analyses were prone to convergence problems.

This model also produced some very high frequency output (Figure 6.2) and it was realised that this was caused by the method of modelling the hammer impact. This effect is described in detail by Deeks (1992) who demonstrated that a simple hammer/pile impact model results in a poor approximation of the actual stresses in the pile even when very fine meshes and various element types are used. He concluded that the problem was because the hammer/impact contained a discontinuity which can not be modelled accurately in a finite element mesh. His solution to the problem was to develop various models (Figure 6.3) to produce continuous hammer impact functions. The axial force distributions in the pile resulting from the hammer/pile, hammer/cushion/pile and hammer/cushion/anvil/pile models are shown in Deeks & Randolph (1992) which clearly demonstrate the superiority of Deeks' hammer/cushion/anvil/pile model. It was therefore decided to adopt the damped cushion model shown in Figure 6.3(d) to simulate the hammer impact function. This approach effectively separated the calculation of the force/time function at the pile head from the rest of the computational model. It was decided to name this sub-model the hammer impact model.

Deeks (1992) developed analytical solutions for the various hammer impact models in order to allow rapid parametric studies. The resulting graphs showing the effect of various parameters are reproduced in Deeks & Randolph (1993). Deeks suggested that the analytical solutions should be inserted into a spreadsheet in order to calculate the force/time functions for various combinations of parameters. Rather than use Deeks' analytical solutions directly, it was decided to reproduce the damped cushion model numerically in ABAQUS and use the graphs developed by Deeks to aid in the choice of parameters. The advantage of this approach was that the output (ie the force/time function) was in the correct form for insertion into the second stage of the model (the pile/soil model) and the graphical package available in ABAQUS could be used to compare and present data.

The separation of the hammer impact model from the rest of the computational model also simplified the procedure for the application of the horizontal soil stresses onto the pile. (There was no need to model the pile as a rigid body first and then replace it with deformable elements.) It was possible to use a similar technique to that developed for the vibratory piling model (Chapter 5) but this had to be adapted for use with deformable pile elements rather than a rigid pile (as in the vibratory model.) In the vibratory piling model, the horizontal stresses on the pile are simulated by applying an equivalent lateral force to effectively expand the rigid pile into the soil (Section 5.2.5). In order to achieve this with a pile model comprising deformable elements, it was necessary to apply a lateral displacement to each of the pile elements to effectively expand it into the soil and hence simulate the horizontal contact pressure between the pile and the soil. The magnitude of the displacements applied to the pile elements was determined by undertaking an additional analysis, similar to stage one of the vibratory piling model, with the pile modelled as a rigid body which is expanded laterally into the soil.

Work then continued on developing the rest of the model. A typical forcing function (Figure 6.4) was applied to the top of the pile in order to examine the stress waves in the pile and the resulting ground waves. However these analyses took an excessively long time to run (several days) because very small time steps were required to model the

stress waves in the pile accurately. This is because the propagation velocity of stress waves in a pile is an order of magnitude greater than in soil (approximately 4000m/s in concrete and 5200m/s in steel). Therefore, in order to satisfy the requirement of 10 nodes per wavelength for accurate FE modelling of the wave, the time steps have to be very small ($\Delta t \leq \Delta x/c$). To overcome this difficulty, it was decided to separate the stress-wave analysis of the pile from the wave propagation analysis so that the model was split into three sub-models as follows:

- Hammer impact model
- Pile/soil model
- Wave propagation model

It was decided to model the pile and the pile/soil interface in a similar manner to the Smith (1960) method which has been used successfully for many years in the context of pile drivability. A literature search revealed that many refinements have been made to this method over the years in order to make the method less empirical. In particular, the development of one-dimensional models for pile driving by Simons & Randolph (1985), Randolph & Simons (1986), Randolph (1991) and Deeks (1992) have been shown to give excellent agreement with measured data. Following a detailed review of Deeks' and Randolph's work, it was decided to adopt the new base model proposed by Deeks and Randolph (1995) and the new shaft/soil boundary model proposed by Deeks (1992).

A finite element model of the pile was then constructed incorporating the base model proposed by Deeks and Randolph (1995) and the shaft/soil boundary model proposed by Deeks (1992) and a typical forcing function was applied to the pile head (see Figure 6.4). The model appeared to simulate the stress waves in the pile very well (Figure 6.5 and 6.6) and was therefore adopted for this study.

The major component of the simulation was the computation of ground waves. This was undertaken using the FE/IE model developed for the vibratory piling model to represent the ground (Chapter 5). The problem was then how to transfer the pile response to the ground model. This required a model which would simulate the horizontal stresses on the pile shaft from the soil and also adequately model the frictional transfer of the pile response to the hammer impact (ie the stress wave) to the surrounding soil.

After some pilot runs, it was decided that this could be achieved by way of an unrestrained 'dummy' pile made up of axisymmetric finite elements, see Figure 6.7. The 'dummy' pile could be expanded laterally into the soil to generate the horizontal soil stresses on the pile in the first step of the analysis. The vertical displacement/time functions of the pile nodes computed in the pile-soil model were then applied to the nodes of the 'dummy' pile and the soil nodes immediately under the pile toe.

The contact between the 'dummy' pile and the FE/IE mesh was modelled using a surface-based contact simulation, with slip controlled by the ABAQUS friction model, as described in Section 6.3.3.

The transfer of the displacement/time functions computed by the pile-soil model to the nodes of the 'dummy' pile was not straight-forward due to the limitations of the

ABAQUS post-processing package. Firstly the displacement/time functions for all of the nodes on the pile shaft were extracted and saved in a file with an .xy extension. Unix commands were then used to separate and store the time and displacement data in separate files for each node. A short fortran program was then written to reformat the data so that it could be inserted into the ABAQUS input file. (A displacement/time function is defined in ABAQUS under the *AMPLITUDE command followed by data lines defining the function as pairs of time and displacement variables, with four pairs per line.)

As the nodal spacing of the pile models was generally about 0.25m, the number of pile shaft nodes, and hence the number of displacement/time functions to be manipulated in this way, was quite large in each case. Several analyses were therefore undertaken to investigate the sensitivity of the analysis to the number of nodal displacement/time functions modelled. It was concluded that the application of the displacement/time function to every fourth node of the 'dummy' pile resulted in an adequate representation of the pile response.

In summary, it was concluded that best method for modelling impact piling would be to break problem into three sub-models, comprising:

1. A hammer impact model to simulate the force imposed onto the pile head
2. A pile-soil model to simulate the propagation of the impact waves down the pile shaft with soil response modelled by spring and dashpots
3. A wave propagation model to simulate the outgoing ground waves into the surrounding ground

There are two advantages of breaking down the computations in this way. Firstly, each parameter or group of parameters can be isolated, and rapid parametric studies can be used to ascribe values. Secondly, more efficient computations are possible; a finite element (FE) model of the pile requires very small nodal spacings ($\Delta x = \lambda/10$) and very short time steps ($\Delta t = \Delta x/c$, c =wave velocity), which is essentially a one-dimensional system; an axisymmetric finite/infinite element (FE-IE) mesh of the surrounding soils can use larger elements and longer time increments (subject to equivalent constraints for soil properties).

6.3 A FINITE ELEMENT MODEL FOR IMPACT PILING

The final model for the simulation of ground waves generated by impact piling, comprising three sub-models for hammer impact, pile-soil interaction and wave propagation, will now be described in some detail.

6.3.1 Hammer Impact Model

The hammer impact model used here is that presented by Deeks & Randolph (1993). The conceptual model includes lumped ram and anvil masses separated by a damped cushion which is represented by a spring and dashpot in parallel. These rest on the pile which is modelled by a dashpot, see Figure 6.8.

In this stage it is sufficient to represent the pile by a dashpot of impedance equal to that of the pile, defined as

$$Z = \frac{E_p \cdot A_p}{c_p}, \quad (6.1)$$

where E_p is the elastic modulus of the pile, A_p is its cross sectional area, and c_p is the axial pile wave velocity.

Deeks & Randolph showed that the behaviour of the hammer impact model is governed by three dimensionless parameters: the cushion stiffness, k_c^* , the anvil mass, m_a^* , and the cushion damping, c_c^* , defined as follows:

$$k_c^* = \frac{k_c \cdot m_r}{Z^2} \quad (6.2)$$

$$m_a^* = \frac{m_a}{m_r} \quad (6.3)$$

$$c_c^* = \frac{c_c}{Z} \quad (6.4)$$

where k_c is the stiffness of the cushion spring, m_r is the mass of the hammer ram, m_a is the anvil mass and c_c is the damping in the cushion.

6.3.2 Pile/Soil Model

The second stage of the simulation is the propagation of compression waves down the shaft of the pile. This is done using a model, based upon that developed by Deeks (1992), shown in Figure 6.4. The pile is modelled by 8-noded axisymmetric finite elements, the toe response is modelled by a mass-spring-dashpot model proposed by Deeks & Randolph (1995), and the shaft/soil boundary is a spring-dashpot system similar to that developed by Deeks (1992), for transmitting shear waves independent of frequency.

The model for the toe resistance was developed by Deeks from that proposed by Wolf (1988). The complex stiffness of the Wolf model was matched to the results of FE

analyses for several values of Poisson's ratio, ν , taken across a large range of dimensionless frequencies.

The equations of motion for the toe model are

$$m_0\ddot{u}_1 + c_0\dot{u}_1 + c_1(\dot{u}_1 - \dot{u}_2) + ku_1 = f(t) \quad (6.5)$$

$$m_1\ddot{u}_2 + c_1(\dot{u}_2 - \dot{u}_1) = 0 \quad (6.6)$$

The parameters can be non-dimensionalised in the following way.

$$\alpha_0 = \frac{m_0}{k} \left(\frac{c_s}{R} \right)^2 = 0 \quad (6.7)$$

$$\alpha_1 = \frac{m_1}{k} \left(\frac{c_s}{R} \right)^2 \quad (6.8)$$

$$\beta_0 = \frac{c_0}{k} \left(\frac{c_s}{R} \right) = 0.8 \quad (6.9)$$

$$\beta_1 = \frac{c_1}{k} \left(\frac{c_s}{R} \right) \quad (6.10)$$

where

$$k = \frac{4GR}{1-\nu} \quad (6.11)$$

$$c_s = \sqrt{\frac{G}{\rho}} \quad (6.12)$$

and R = radius of the pile base (m).

Further, Deeks proposed the following expressions to accommodate variations in Poisson's ratio, ν , as:

$$\alpha_1 = 0.63 - 3.6\nu + 6\nu^2 \quad (6.13)$$

$$\beta_1 = 1.58 - 10.3\nu + 19\nu^2 \quad (6.14)$$

The response of the pile shaft to the impact wave is modelled using a new frequency independent transmitting boundary for axisymmetric shear waves derived by Deeks

(1992). This boundary is equivalent to viscous dashpots with a distributed damping constant, c_{sft} , (identical to a viscous boundary) and a distributed spring constant, k_{sft} , defined as follows:

$$c_{sft} = \rho c_s \quad (6.15)$$

$$k_{sft} = \frac{G}{2R} \quad (6.16)$$

where ρ is the density of the soil, c_s is the shear wave velocity in the soil, G is the shear stiffness of the soil and R is the pile radius.

The velocity/time function derived from the hammer impact model is then imposed onto the simplified pile model described above as a force on the pile head (after multiplication by the pile impedance). The output results are the displacement/time functions at the shaft interface nodes, and at the base.

6.3.3 Wave Propagation Model

The objective of the third and final stage of the procedure is to simulate the interaction between the pile and the surrounding soil and then to model the propagation of ground waves that are generated as a result of this interaction. The surrounding soils are represented by a large FE/IE axisymmetric mesh (Figure 6.9).

The response of the pile to the hammer impact, which depends upon the soil resistance on the shaft and at the toe, is computed by the pile/soil model. The soil in contact with the pile will experience large strains and therefore large strain stiffness parameters are used to derive the spring and dashpot constants which model the soil resistance and the resulting displacement of the pile.

The main purpose of the third stage of analysis, however, is to model the propagation of ground waves through the soil. It has been shown (Massarsch 1992) that at a short distance from the pile (about one pile radius) most of the energy from the driven pile is transmitted to the soil in the form of elastic waves. In this zone, the passage of the elastic waves through the ground induces small strains in the soil and thus small strain stiffness parameters should be used. It is believed that most soils behave elastically at very small strains (ie $<0.001\%$) giving rise to a constant and maximum value of shear stiffness. At small strains (0.001-0.1 %) the stiffness becomes sensitive to the magnitude of strain and significant reduction in stiffness has been observed with increasing strain. At intermediate and large strains ($>0.1\%$) plastic behaviour dominates and the stiffness becomes less sensitive to strain and approaches a minimum value as the material is brought to failure (Matthews *et al*, 1996). Parametric studies based on the arrival times of ground waves at various distances from the vibration source confirm that the dynamic soil stiffness is much greater than the values of stiffness commonly associated with soils which are based on static values.

The difficulty of transferring between the large strain plastic behaviour of the soil in the immediate vicinity of the pile and the small strain elastic behaviour of the soil in the propagation of ground waves is simplified by the separation of the model into three sub-models. The large strain behaviour of the soil is simulated in the pile/soil model which calculates the response of the pile to the hammer impact. Small strain elastic

parameters are then assumed for the soil in the wave propagation model. The pile-soil interface is modelled using a surface-based contact simulation, with slip controlled by a friction model with $\mu=0.1$ (Mabsout & Tassoulas, 1994). In order to simulate the horizontal stresses on the pile from the soil, a 'dummy' pile (Figure 6.7) is expanded laterally into the soil by a predetermined distance. (This avoids the problem of rigid body motion.)

The determination of the magnitude and distribution of the shaft friction on piles during driving is not straightforward. It depends on the ground conditions, the pile type and the method of installation. However the basic methods for determining the skin friction for piles in non-cohesive and cohesive soils generally assume that the shaft friction is dependent on the effective overburden pressure as described by Fleming et al (1992) and summarised below.

The starting point for calculating values of skin friction, τ_s , for piles in non-cohesive soils is the expression

$$\tau_s = \sigma'_n \tan \delta = K \sigma'_v \tan \delta \quad (6.17)$$

where σ'_n is the normal effective stress acting around the pile shaft after installation, and δ is the angle of friction between pile and soil. The normal stress may be taken as some ratio K of the vertical effective stress σ'_v , resulting in the second form of the expression. The appropriate values of K will depend on the in-situ earth pressure coefficient, K_0 , the method of installation of the pile and the initial density of the non-cohesive soil.

From pile test results (Vesic, 1977), the rate of increase of skin friction with depth gradually reduces and there is a tendency towards some limiting value. Fleming et al (1992) suggest that for full displacement, driven piles, K may be estimated from the bearing capacity factor, N_q , as

$$K \approx N_q / 50 \quad (6.18)$$

This expression will give values of K varying between about 1.5 at low stress levels, down to unity or even lower at greater depths, with an average value around 1.2.

For partial displacement piles, the normal effective stress acting on the pile shaft will be lower than for full displacement piles and the value of skin friction should be reduced by 20%. For driven cast-in-situ piles where the casing is removed, loosening of the surrounding soil may occur, followed by some increase in the stress level as the concrete is placed. The appropriate value of K in equation (6.17) will depend on the details of the construction method.

For driven cast-in situ piles, while the value of K may be 1.2 or higher outside the casing, some reduction in normal stress may occur during extraction of the casing. If wet concrete is placed, a value of K of 1.0 may be taken, while values up to 1.2 are appropriate where dry concrete is rammed into the pile shaft.

Historically, the skin friction around a pile shaft in a cohesive soil has been estimated in terms of the undrained shear strength of the soil, by means of an empirical factor, α , (Tomlinson, 1957) giving

$$\tau_s = \alpha \cdot c_u \quad (6.19)$$

The value of α deduced from pile load tests appears to reduce from unity or more for piles in clay of low strength, down to 0.5 or below for clay above about 100kN/m². However, plots of measured values of skin friction from driven piles against the shear strength of the soil demonstrate a large amount of scatter and this has prompted a more scientific approach.

In 1968, Chandler described an alternative approach, considering the bond between pile and soil as purely frictional in nature, with the resulting skin friction a function of the normal effective stress, σ'_n , and an interface friction angle, δ , in much the same way as for piles in free-draining soils. The normal stress was related to the effective overburden stress, σ'_v , by a factor, K , to give

$$\tau_s = \sigma'_n \tan \delta = K \sigma'_v \tan \delta = \beta \sigma'_v \quad (6.20)$$

where $\beta = K \tan \delta$. The value of K will vary depending on the type of pile (driven or bored) and the past stress history of the soil. For piles in soft, normally consolidated or lightly overconsolidated clay, Burland (1973) and Párry & Swain (1977) have suggested values of K lying between $(1 - \sin \phi')$ and $\cos^2 \phi' / (1 + \sin^2 \phi')$. Neither of these suggestions takes due account of the stress changes which occur during and after pile installation.

Meyerhof (1976) deduced, empirically, an expression for the ratio $\beta = \tau_s / \sigma'_v$, from the results of a number of pile tests in clay of varying overconsolidation ratio. Assuming that the full angle of internal friction, ϕ' , was mobilised on the shaft of the pile, he showed that the value of K consistent with the measured shaft capacities varied between 1 and 2 times the in-situ horizontal stress, with an average ratio of 1.5. Francescon (1982) conducted instrumented model pile tests, where the normal effective stress acting on the pile was measured directly, which showed that this stress was indeed close to 1.5 times the original horizontal effective stress in the soil.

Piles driven into cohesive soil generate high excess pore pressures close to the pile. The pore pressures arise partly as a results of a decrease in effective stress, as the soil is sheared and remoulded, and partly due to the increase in total stress, as the pile forces soil out of its path. Typically, the excess pore pressures may be as high as the effective overburden stress, and may extend out over a zone up to 10 times the diameter of the pile. With time after installation, dissipation of excess pore pressures generated during the driving process leads to an increase in effective stresses around the pile, and a resulting increase in the pile capacity. For piles driven into clay, this increase may be as much as factor of 5 to 6 (Vesic, 1977).

All of the values of K suggested above for non-cohesive and cohesive soils are for calculating the capacity of the pile shaft after installation. As the pile is installed or extracted, there are large stress changes around the pile. The actual value of K is very difficult to determine but is likely to vary between K_0 and K_p (the passive limit).

Once a suitable distribution of normal stress on the pile has been chosen, a static analysis is undertaken to determine the magnitude of lateral displacement to be applied to the deformable elements of the 'dummy' pile in order to generate the required normal stresses between the pile and soil elements. This analysis is similar to the stage one of the vibratory piling model, with the pile modelled as a rigid body which is expanded laterally into the soil. The resulting lateral displacements are then applied to the nodes of the deformable 'dummy' pile in a static analysis. Once the horizontal stresses have equilibrated, the vertical displacements computed from the pile model are applied to the pile shaft nodes of the 'dummy' pile and the soil nodes immediately under the pile toe in a dynamic analysis with time steps of 0.001secs.

A general transient dynamic analysis using implicit time integration of the entire model is performed to calculate the transient dynamic response of the system. The general direct-integration method provided in ABAQUS/Standard is called the Hilber-Hughes-Taylor operator and is an extension of the trapezoidal rule. The Hilber-Hughes-Taylor operator is implicit: the equations must be solved at each time increment. This solution is done iteratively using Newton's method. (The Jacobian of the system is defined exactly and quadratic convergence is obtained when the estimate of the solution is within the radius of convergence of the algorithm.)

An automatic incrementation scheme is provided for use with the general implicit dynamic integration method. The scheme uses a half-step residual control (Hibbitt & Karlsson, 1979) to ensure an accurate dynamic solution. Further details are contained in the ABAQUS manuals.

6.4 MODELLING IMPACT PILING AT GREENGATE RAILBRIDGE, M66, MANCHESTER

6.4.1 Site Conditions

A valuable example of site data which includes both pile head records and ground surface vibrations was obtained during dynamic testing of bored cast in situ piling forming the foundations for a new bridge over a railway line. The new bridge comprises part of the M66 extension in Manchester.

Ten of the 750mm diameter piles, installed to a depth of 21m, were tested using the SIMBAT system (Stain, 1992) which has been specifically developed for dynamic load testing of cast in situ piles. On such piles there is no convenient driving hammer to generate the input force and the pile tops are usually cast to ground level so there is no free-standing section of pile on which to mount the measuring instruments. The SIMBAT system uses a number of different size drop hammers complete with guide tube mechanisms to generate the input force. An instrumentation section is provided by building a concrete extension about three pile diameters in height. After a sufficient curing period, two strain gauges, two accelerometers and an electronic theodolite target are bonded to this extension, two pile diameters below the top (Stain and Davis, 1989).

The piles at the M66 were subjected to blows from a 2.2 tonne hammer falling through heights of between 0.2m and 1.2m. The strain, acceleration and displacement of the pile head were recorded for each blow. The measured penetration and dynamic soil reaction

calculated by the SIMBAT technique for each of the ten piles are presented in Tables 1-10 in Appendix I.

The resulting vertical, radial and transverse vibrations were monitored by geophones placed on the ground surface at distances of 5.5m, 10m, and 16.5m from each pile.

The ground conditions at the site comprised approximately 0.5m of made ground overlying 10m of firm becoming firm to stiff silty clay, overlying dense sand at a depth of about 10.5m below ground level. A typical borehole log and a summary of the laboratory test results for the soils are given in Appendix I.

6.4.2 Initial Parameters and Assumptions

The 21m long pile comprising a 750mm diameter steel casing filled with cast in situ concrete was modelled, for simplicity, in ABAQUS as a solid concrete pile with an equivalent impedance to the actual pile.

The impedance of a pile is calculated as follows:

$$Z = \rho c A = \frac{EA}{c}$$

where ρ is the density of the pile, c is the wave propagation velocity in the pile, A is the cross-sectional area of the pile and E is the Young's modulus.

The following parameters were assumed for the cast in situ piles in the SIMBAT calculations and are adopted for use in the computational model:

	CONCRETE	STEEL
Density, ρ	2400 kg/m ³	7800 kg/m ³
Velocity, c	4000 m/s	5200 m/s
Cross-sectional area, A	0.424 m ²	0.176 m ²
Impedance ($Z=\rho c A$)	4.07e ⁶ Ns/m	0.71e ⁶ Ns/m

Table 6.1: Calculation of pile impedance

$$\begin{aligned} \text{Total Pile Impedance} &= \text{Concrete Impedance} + \text{Steel Impedance} \\ &= 4.07e^6 + 0.71e^6 \\ &= 4.78e^6 \text{ Ns/m} \end{aligned}$$

The Young's modulus of the equivalent solid concrete pile modelled in ABAQUS was adjusted so that it had the same impedance as the actual pile as follows:

$$E = \frac{Zc}{A} = \frac{(4.78e^6)(4000)}{442e^{-3}} = 4.33e^{10} \text{ N/m}^2$$

The ground conditions were modelled by interpretation of the borehole logs and laboratory test results in Appendix I. Typical soil parameters based on the soil descriptions and laboratory test results were assumed as follows:

Depth (m)	Soil type	E (Pa)	v	ρ (kg/m ³)
0 – 10.5	Firm/stiff CLAY	13×10^6	0.35	1970
10.5>>	Dense SAND	50×10^6	0.30	2100

Table 6.2: Soil parameters at the M66 site

6.4.3 Parametric Study of Hammer Impact Model (for pile23)

Unfortunately only one set of pile head measurement data still exists for this site. This is for blow 5 (drop height of 1.0m) to pile 23 (resulting in a penetration of 0.3mm). Vibration data only exists for blow 6 (drop height of 1.2m) to pile18 (resulting in a penetration of 1.4mm).

It was therefore decided to model the hammer impact for pile 23, use the data to undertake a parametric study, and then adjust the parameters to model the larger impact on pile 18.

The parameters required for input into the hammer impact model (Figure 6.8) are as follows:

Initial velocity, $v_0 = \sqrt{2gh}$

Drop height, h

Mass of ram, $m_r = 2200\text{kg}$

Pile impedance, $Z = 4.7861\text{e}^6 \text{ Ns/m}$

Mass of anvil, $m_a = \text{mass of concrete pile cap extension (1.875m in height)}$
 $= \text{volume of pile cap extension} \times \text{density (2400 kg/m}^3\text{)}$
 $= ((\pi \times 0.75)^2/4) \times 1.875 \times 2400$
 $= 1988 \text{ kg}$

Cushion stiffness, k_c (unknown)

Cushion damping, c_c (unknown)

The hammer impact model was constructed in ABAQUS using these parameters and trial values were input for k_c and c_c using the guidance given by Deeks (1992). The resulting force/time functions at the pile head (velocity/time function multiplied by pile impedance, Z) for various combinations of k_c and c_c are compared to the measured force/time function for pile 23 in Figures 6.10(a)-(d). The optimum values appear to be a value of k_c of 1e^7 and a value of c_c of 0.15 as shown in Figure 6.11

6.4.4 Parametric Study of Pile/Soil Model (for Pile 23)

The force/time function computed from the hammer impact model was then imposed onto the pile head for the second stage of the computational procedure in order to determine the displacement/time functions on the pile shaft.

According to dynamic pile testing theory (Stain 1992 and Rausche *et al* 1972), if there were no soil restraints on the pile, the force at the pile head would be equal to the velocity at the pile head multiplied by the pile impedance. However, the effect of the soil restraints on the pile is to reduce the velocity and to increase the force at the pile head. (The hammer is trying to push the pile top down while the return wave is trying

to push it back up again. The downward and upward velocities therefore partially cancel each other out, but the total force increases as the upward and downward waves “collide”).

Inspection of the penetration data recorded for the ten piles at the M66 site (Appendix I) indicated that pile 23 achieved an unusually low penetration for a hammer drop of 1.0m. In fact, the penetration achieved by pile 23 was only about 35% of the average pile penetration recorded by the majority of the piles on the site. This was probably due to an inefficient hammer strike. A parametric study was undertaken to investigate the effect of altering the spring and dashpot constants. It was found that increasing the dashpot constants by a factor of 10 reduced the maximum displacements of the pile head by 35% (Figure 6.12). Doubling the stiffness of the sand from 24 MPa to 50 MPa did not have much effect on the pile head displacement, as shown in Figure 6.13. However, doubling the stiffness of the clay surrounding the upper pile shaft from 13MPa to 26 MPa reduced the pile head displacement by about 15%, as shown in Figure 6.13.

The computed displacements and forces at the pile head showed good agreement with the field data as shown in Figures 6.14 and 6.15. This model assumed a value of k_c of $1e^7$ N/m and a value of c_c^* of 0.15, values of Young's modulus of 13MPa and 50 MPa for the clay and sand respectively, and factored dashpot constants to represent the unusually low penetration of pile 23.

6.4.5 Derivation of input functions for Pile 18 and application to the wave propagation model

The larger impact on pile 18 (resulting from a drop height of 1.2m) was then simulated using the hammer impact model and a value of k_c of $1e^7$ N/m and a value of c_c^* of 0.15. The resulting force/time function (Figure 6.16) was then imposed onto the nodes representing the pile head in the second stage pile/soil model. This model assumed values of Young's modulus of 13MPa and 50 MPa for the clay and sand respectively. The calculated dashpot values were not factored for pile 18. The resulting displacements of the pile/soil interface nodes computed by the pile/soil model are shown on Figure 6.17. These displacement/time functions were then used as the input to the wave propagation model using the extraction technique described in Section 6.2.

6.4.6 Determination of Small Strain Stiffness Parameters from Measured Vibration Traces

The arrival times of the wavefronts at the various geophones at the M66 site were used to calculate the propagation velocities of the P, S and R waves. Assuming that soils behave elastically at very small strains, an upper bound value of stiffness G_{max} can be calculated for the soil.

The vertical and radial particle velocities recorded at the geophones are presented in Figures 6.19(a-c) and 6.20(a-c) respectively. Calculation of the arrival times of the wavefronts at the geophones required some interpretation to determine which peaks corresponded to each wavefront, such as the P wave from the shaft, the S wave from the shaft and the P wave from the toe.

This is not straightforward because each wave type travels at a different velocity and travels a different distance depending on whether it is generated on the pile shaft or at

the pile toe (Chapter 2). The arrival sequence of the wavefronts is therefore likely to differ depending on the particular configuration of pile depth, geophone position and soil properties. For example, at shallow depths, the P wave from the pile toe may arrive at a geophone before the S wave from the shaft, but this is likely to change as the pile is driven deeper. The P wave from the toe also tends to arrive before the S wave from the shaft at more distant geophones. The interpretation process is therefore quite complicated and involves a “trial-and-error” approach to ensure that not only are the arrival times of each wavefront at each geophone consistent with each other, but also that the stiffness parameters of each soil layer are consistent for each wave velocity.

The measured vibration records may also contain spurious vibrations from adjacent machinery, and a P wave may be generated from the shaft by flexing of the pile, non-verticality of the pile, whip, or ‘bulging’ of the pile as the impact wave travels down the pile. These effects are not simulated in the model.

A technique for interpreting measured vibration records has been developed in order to determine which peaks correspond to each wavefront. The arrival times of each wavefront can then be used to calculate approximate stiffness parameters for the soils. The technique is described below using the M66 data.

The first peak registered by all the geophones at the M66 appears to be due to the arrival of a P wave from the pile shaft (P waves have the highest propagation velocity and the distance between the pile shaft and the geophones is shorter than that between the pile toe and the geophones. The peaks interpreted as corresponding to the P wave from the shaft are labelled on the vertical and radial particle velocity traces for the M66 (Figures 6.19 and 6.20). The interpreted arrival times of the P wave from the shaft at each geophone are summarised in Table 6.3 below together with the calculated P wave velocity.

Horizontal distance between geophone & pile	Arrival time of P wave from shaft	Distance travelled by P wave from shaft	Velocity (=distance/time) of P wave from shaft
RADIAL TRACES			
5.5m	16.9ms	5.5m	325m/s
10m	30.8ms	10m	325m/s
16.5m	50.5ms	16.5m	327m/s
VERTICAL TRACES			
5.5m	16.9ms	5.5m	325m/s
10m	30.7ms	10m	326m/s
16.5m	50.6ms	16.5m	326m/s

TABLE 6.3: Arrival times of the P wave from the pile shaft

Table 6.3 indicates that the P wave from the shaft travels at about 325m/s through the surface soils. The stiffness of the fill can therefore be calculated by assuming values of ν of 0.35 and ρ of 1970kg/m³ for the fill (see Table 6.2), and using the equation

$$c_p = \sqrt{\frac{\lambda + 2G}{\rho}}$$

This gives an E value for the fill of about 130MPa.

The corresponding spacing of peaks at each geophone position are then examined. The second peak appears to be due to the arrival of an S wave from the shaft. The interpreted arrival times of the S wave from the shaft at each geophone are summarised in Table 6.4 below together with the calculated S wave velocity.

Horizontal distance between geophone & pile	Arrival time of S wave from shaft	Distance travelled by S wave from shaft	Velocity (=distance/time) of S wave from shaft
RADIAL TRACES			
5.5m	53.3ms	5.5m	103m/s
10m	100.1ms	10m	100m/s
16.5m	160ms	16.5m	103m/s
VERTICAL TRACES			
5.5m	59ms	5.5m	93m/s
10m	118ms	10m	85m/s
16.5m	164.8ms	16.5m	100m/s

TABLE 6.4: Arrival times of the S wave from the pile shaft

Table 6.4 indicates that the S wave from the shaft travels at about 100m/s through the upper soils. The combined stiffness of the fill and the clay can therefore be calculated by assuming values of ν of 0.35 and ρ of 1970kg/m³ (see Table 6.2), and using

$$c_s = \sqrt{\frac{G}{\rho}}$$

This gives a combined E value for the fill and the clay of about 55MPa.

The third peak on Figures 6.19 and 6.20 appears to be due to a P wave generated at the toe of the pile. This wave has much further to travel than those generated on the pile shaft. The interpreted arrival times of the P wave from the toe at each geophone are summarised in Table 6.5 below together with the calculated P wave velocity.

Horizontal distance between geophone & pile	Arrival time of P wave from toe	Distance travelled by P wave from toe (at 21m depth)	Velocity (=distance/time) of P wave from toe
RADIAL TRACES			
5.5m	92.6ms	21.7m	234m/s
10m	120.7ms	23.3m	193m/s
16.5m	144.1ms	26.7m	185m/s
VERTICAL TRACES			
5.5m	88ms	21.7m	247m/s
10m	106.8ms	23.3m	218m/s
16.5m	132.1ms	26.7m	202m/s

TABLE 6.5: Arrival times of the P wave from the pile toe

Table 6.5 indicates that the P wave from the toe travels at about 215m/s through the soils. The combined stiffness of the soils can therefore be calculated by assuming average overall values of v of 0.33 and ρ of 2035kg/m³ (see Table 6.2), and using

$$c_p = \sqrt{\frac{\lambda + 2G}{\rho}}$$

This gives a combined E value for the soil of about 63MPa. Assuming that the P waves from the pile toe travels through about 11-13m of dense sand and about 11-13m of the firm clay before they reach the geophones, it seems reasonable to assume that the dense sand has an E value of about 75MPa.

6.4.7 The ground response predicted by the wave propagation model

As discussed in section 6.3.3, the objective of the wave propagation model is to simulate the interaction between the pile and the surrounding soil and then to model the propagation of waves that are generated as a result of this interaction. The first task is therefore to determine a suitable distribution of normal stress on the pile.

The assumed total normal stress distribution on the pile from the soil was calculated using equation (6.20), assuming a value of K_0 of about 0.65 (using the formula $K_0 = 1 - \sin\phi'$ for normally consolidated soils proposed by Jaky, 1944) multiplied by a factor of 1.5 as suggested by Meyerhof (1976) and Francescon (1982) resulting in a value of K of about 1.0. The assumption of a value of K of unity does not take account of the stress changes which occur during pile installation. However as the actual value of the coefficient of friction, μ , down the pile shaft was unknown and the ABAQUS friction model defines the limiting shear stress between the two contacting surfaces as the product μp , where p is the contact pressure between the two surfaces, the actual value of K is academic. If the normal stresses on the pile are calculated assuming a value of K of 1.0 on total vertical stresses, it is relatively straightforward to manipulate the value of friction to take account of stress changes during pile installation by factoring the friction coefficient accordingly.

pile head. However, the model also reproduced this secondary event which appears to be caused by the simultaneous generation of a P and an S wave when the stress wave reaches the toe of the pile. This is the first time this effect has been identified.

6.5 VALIDATION OF IMPACT PILING MODEL (Flitwick)

6.5.1 General

Following the successful application of the model to actual data from the M66 site, it was necessary to validate the model by simulating impact piling at another site with different ground conditions and pile/hammer combination. A case study from a site at Flitwick in Bedfordshire was chosen because comprehensive vibration data and site conditions were well documented (Uromeihy, 1990).

6.5.2 Site Conditions

An example of a calibration of the procedure against site data is given for a site at Flitwick, Bedfordshire, UK where a 12m long steel H-pile (305 x 305 x 89kg/m) was installed to a depth of 7m by a 3200kg hammer falling through 1.0m.

The site near Flitwick in Bedfordshire was loaned to the University of Durham for pile testing by Dawson Construction Plant in July 1988. The site was chosen because of its fairly uniform ground conditions and the access to various types of pile driving equipment in the adjacent yard.

The topsoil over an area of approximately 24m by 20m was removed and the soft subsoil was trimmed level prior to the commencement of pile driving.

A site investigation was carried out in August 1988 which comprised three boreholes to a maximum depth of 9m. The locations of the boreholes are indicated in Figure 5.79. The borehole logs are included in Appendix H and are summarised in Figure 5.80.

A number of laboratory tests, including particle size distributions, undrained triaxial tests and consolidated shear box tests were undertaken on selected samples. The results of these tests are summarised in Tables H1-4 in Appendix H.

Monitoring of pile driving was undertaken in October 1988. A 12m long steel H pile (305 x 305 x 89kg/m) was driven to a depth of 7m by a 3200kg simple drop hammer falling through 1.0m.

The vibrations induced by pile driving were recorded by a portable digital recorder unit which stored and later processed the data. The ground vibrations were measured simultaneously by five sets of geophones which were placed at different horizontal stand-offs from the driven pile. Each set included three geophone units which were oriented orthogonally for measuring the three components of vibration along the radial, transverse and vertical axes.

6.5.3 Hammer Impact Model

The parameters required for input into the hammer impact model were as follows:

Drop height, $h = 1.0\text{m}$

Initial velocity, $v_0 = \sqrt{2gh} = 4.43\text{m/s}$

Mass of ram, $m_r = 3200\text{kg}$

The impedance of the pile is calculated as follows:

$$Z = \rho c A = \frac{EA}{c}$$

where ρ is the density of the pile, c is the wave propagation velocity in the pile, A is the cross-sectional area of the pile and E is the Young's modulus.

Typical values for a steel H pile (305 x 305 x 89kg/m) are as follows:

$$E = 2.0 \times 10^{11} \text{ N/m}^2$$

$$\rho = 7850 \text{ kg/m}^3$$

$$\nu = 0.27$$

$$c = 5000 \text{ m/s}$$

$$A = 11.3 \times 10^{-3} \text{ m}^2$$

Therefore,

$$Z = \frac{(2.0 \times 10^{11})(11.3 \times 10^{-3})}{5000} = 452 \times 10^3 \text{ N s/m}$$

Typical values were assumed for the mass of the anvil, m_a , the cushion stiffness, k_c and the cushion damping, c_c on the basis of typical ranges of values suggested by Deeks (1992) as follows:

Mass of anvil, $m_a = 320\text{kg}$ ($\equiv m_a^*$ of 0.1, normal range = 0.1-0.7)

Cushion stiffness, $k_c = 63.85 \times 10^6 \text{ N/m}$ ($\equiv k_c^*$ of 1.0, normal range = 1-1000)

Cushion damping, $c_c = 226 \times 10^3 \text{ N s/m}$ ($\equiv c_c^*$ of 0.5, normal range = 0.0-1.0)

The hammer impact model was constructed in ABAQUS using these parameters and the resulting force/time function at the pile head (velocity/time function multiplied by pile impedance, Z) is shown in Figure 6.25.

6.5.4 Pile/Soil Model

The force/time function computed from the hammer impact model was then imposed onto the pile head for the second stage of the model in order to determine the displacement/time functions at various intervals of depth down the pile shaft.

The 12m long steel H pile (305 x 305 x 89kg/m) had to be modelled as a solid circular section pile with an equivalent impedance to the actual pile in the axisymmetric finite element mesh. The density of the equivalent solid steel pile modelled in ABAQUS was adjusted as follows:

$$Density, \rho = \frac{Mass}{Volume} = \frac{89}{(\pi)(0.1525^2)} = 1218kg / m^3$$

The Young's modulus of the equivalent solid steel pile modelled in ABAQUS was adjusted as follows

$$\frac{E_{steel}}{\rho_{steel}} = \frac{2.0e^{11}}{7850} = \frac{E_{equivalent}}{1218}$$

Therefore

$$E_{equivalent} = 3.1e^{10} N / m^2$$

The ground conditions were modelled by interpretation of the borehole logs and laboratory test results in Appendix H. Typical soil parameters were assumed based on the soil descriptions and laboratory test results and are given in Table 6.6 below. The values for the spring and damping constants on the pile shaft (k_{sft} and c_{sft} respectively) were calculated using equations (6.15) and (6.16) and are given for each soil type in Table 6.6.

SOIL TYPE	E (MPa)	ν	ρ (kg/m ³)	k_{sft} (N/m)	c_{sft} (N/ms)
Soft Clay (0.0 – 2.4m)	5	0.45	1920	$5.7e^6$	$57.6e^3$
Medium dense Sand & Gravel (2.4 – 4.8m)	35	0.33	1750	$43.1e^6$	$151.7e^3$
Dense Sand (>4.8m)	50	0.25	2000	$65.6e^6$	$200.0e^3$

Table 6.6: Soil and shaft resistance parameters for impact piling at Flitwick

The mass, spring and dashpot parameters used in the pile toe model were calculated using equations (6.7) to (6.14) and have the following values in the Dense Sand:

m_0	0.0
k	$16.27e^6$ N/m
c_0	$19.85e^3$ N/ms
m_1	3.97 kg
c_1	$4.78e^3$ N/ms

Table 6.7: Pile toe parameters for impact piling at Flitwick

These parameters were inserted into the pile/soil model and the force/time function calculated by the hammer impact model was applied to the pile head nodes. The resulting vertical displacement/time functions for all nodes on the pile/soil interface are shown in Figure 6.26. These functions were extracted for all of the nodes on the pile shaft and pile toe and manipulated and formatted ready for input into the final stage of the model.

6.5.6 Determination of Small Strain Stiffness Parameters from Measured Vibration Traces

The radial particle velocity/time traces recorded by the geophones at 2m, 7m, 12m, 15m and 16.5m are presented in Figure 6.27. The vertical, radial and transverse velocity/time traces recorded by the geophone at a horizontal distance of 7m from the pile are shown in Figure 6.28.

Some interpretation of the measured vibrations is required to determine which peaks correspond to each wavefront, such as the P waves from the shaft, S waves from shaft, and the P waves from the toe.

Given that the pile toe is at a depth of 7m, and that shear waves generally travel at about 60% of the speed of a P wave, it is assumed that the first wavefront registered at each geophone represents the arrival of the P wave from the pile toe. Indeed this is the only valid explanation as it takes 50ms for the first wavefront to reach the 7m geophone but it only takes another 40ms for the first wavefront to travel another 9.5m to reach the 16.5 geophone. As it is physically impossible for waves to speed up with distance from their source of excitation, the only explanation is that the first wavefront originates at the pile toe and travels a radial distance of 9.9m to reach the 7m geophone and a radial distance of 17.9m to reach the 16.5m geophone.

The arrival times of the P wave from the pile toe are summarised in Table 6.8 below together with the calculated P wave velocity.

Horizontal distance between geophone & pile	Arrival time of P wave from toe	Distance travelled by P wave from toe (at 7m depth)	Velocity (=distance/time) of P wave from toe
RADIAL TRACES			
7m	50ms	9.9m	198m/s
16.5m	90ms	17.9m	199m/s
VERTICAL TRACES			
7m	50ms	9.9m	198m/s

Table 6.8: Arrival times of the P wave from the pile toe

Table 6.8 indicates that the P wave from the toe travels at about 199m/s through the soils. The combined stiffness of the soils can therefore be calculated by assuming overall values of ν of 0.25 and ρ of 1998kg/m³ and using

$$c_p = 199\text{m/s} = \sqrt{\frac{\lambda + 2G}{\rho}}$$

This gives a combined E value for the soil of about 66MPa.

6.5.6 Wave Propagation Model

An overall Young's Modulus of 66MPa was then used in the wave propagation model (Figure 6.29). The 'dummy' pile was pushed laterally into the soil in a static analysis and then the displacement/time functions calculated by the pile/soil model were applied to the nodes of the 'dummy' pile. The pile-soil interface was modelled using a surface-based contact simulation, with slip controlled by the friction model available in ABAQUS as described in Section 6.2. An overall value for the friction coefficient of 0.7 was used in the analyses. The resulting velocity/time traces at distances of 7m and 16.5m from the pile are shown in Figures 6.30 and 6.31 together with the measured velocity/time traces. The velocity/time traces predicted by the model are of smaller magnitude than those measured and only comprise one main event. The measured radial velocity/time trace however is much more complex and has a number of secondary peaks following the arrival of the first wavefront.

It seemed likely that these discrepancies were due to the assignation of one overall stiffness to the ground rather than layered properties to reflect the actual stratification of the soils. It was therefore decided to model the two main strata in the ground, namely the soft clay overlying the dense sand. A parametric study was undertaken using various consistent multiples (between 4 and 6) of the E values used for the clay and sand in the pile/soil model (Table 6.6) to model the small strain stiffness of the ground. The results are shown in Figures 6.32-6.34 together with the measured radial velocity/time traces for the 7m and 16.5m geophones.

The difference between the arrival times of the main event at the 7m and 16.5m geophones was too large in all of these peaks analyses. It was therefore decided to factor the stiffness of the clay and sand by different amounts. An analysis was run using an E value of 15MPa for the clay and an E value of 349MPa for the sand. Using these parameters and the diagram in Figure 6.35, the P wave from the toe should arrive at the 7m geophone in about 50ms and at the 16.5m geophone in about 90.5ms.

An extremely good match was achieved with the measured data using these E values as shown in Figures 6.36 and 6.37. The slight discrepancies between the measured and the predicted vibrations are likely to be caused by spurious vibrations from variability in ground conditions, and P wave generation on the shaft of the pile. These effects are not simulated in the model.

The effect of the value of the friction coefficient, μ , was investigated by inserting various values into one analysis. The results are shown in Figures 6.38, 6.39 and 6.40 for values of μ of 0.2, 0.4 and 0.7 (for E values of 20MPa and 200MPa for the clay and sand respectively). It can be seen that the magnitude of the resulting velocity/time

traces at various distances from the pile appear to be directly proportional to the magnitude of the friction coefficient. The use of an overall value of friction is an oversimplification of a very complicated mechanism. However, given the current lack of field data, further refinement of the simulation of pile/soil interaction and the choice of suitable parameters is not possible.

6.6 CONCLUSIONS AND RECOMMENDATIONS FOR FURTHER WORK

This Chapter presents a model for the prediction of ground waves generated by impact piling. The model is used to simulate impact piling at two very different sites, one where cast in situ piles were installed into estuarine soils to a depth of 21m, and the other where a steel H pile was installed into dense sands to a depth of 7m. The results are very encouraging and support the validity of the model as a suitable technique for the prediction of vibrations generated by impact piling.

The use of a computational model to simulate the ground waves generated by impact piling has been shown to have a great advantage over empirical formulae, in that it helps to identify and explain the patterns of ground waves generated by piling. An improved understanding of the mechanisms of vibration generation and propagation has many benefits, notably the identification of suitable techniques for vibration reduction such as cut-off trenches and barriers.

One of the main conclusions of this work has been that much more field testing with very comprehensive monitoring is required in order to construct viable computational models. The models in this Chapter have been constructed on the basis of many assumptions and simplifications but they have demonstrated that numerical modelling of this complex problem is a suitable technique and potentially very valuable. The work has shown that it is the lack of field data rather than computational capability which is preventing further progress.

It is envisaged that the results of the SIPDIS program will provide a very valuable data set when they become available and may allow further refinement of this model. Further validation of the model against actual data would allow the formulation of guidelines as to suitable parameters for various soil types and would also increase confidence in the validity of the model. The model could then be used not only as a preliminary design tool to predict vibration levels from various piling operations, but also to determine the optimum combination of pile and hammer to minimise vibrations at any particular site.

It should be noted, however, that there will always be spurious vibrations due to non-verticality of piles, non-homogeneous ground conditions and other uncontrollable site conditions which can not be simulated in the model. The model should therefore only be used to give an *indication* of likely levels of vibration.

The main drawback of the model is that it is time-consuming and labour-intensive to construct because it consists of three separate stages of analysis. In addition, the functions calculated by each stage have to be extracted manually, formatted and input into the following stage, but this is a particular requirement of the ABAQUS program which is very specific about the format of input data, and does not necessarily apply to all FE programs.

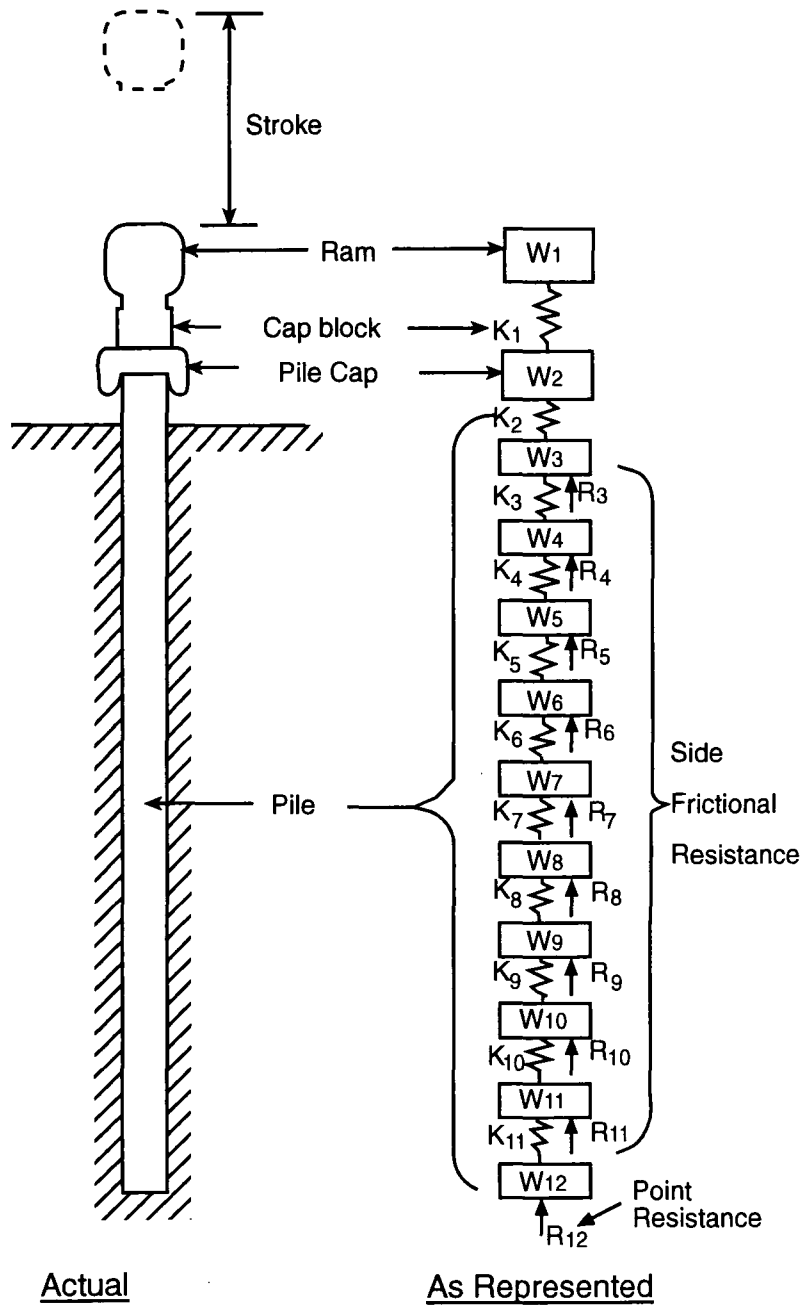


Figure 6.1

Modelling of pile by discrete springs and dashpots (after Smith, 1960)

ABAQUS

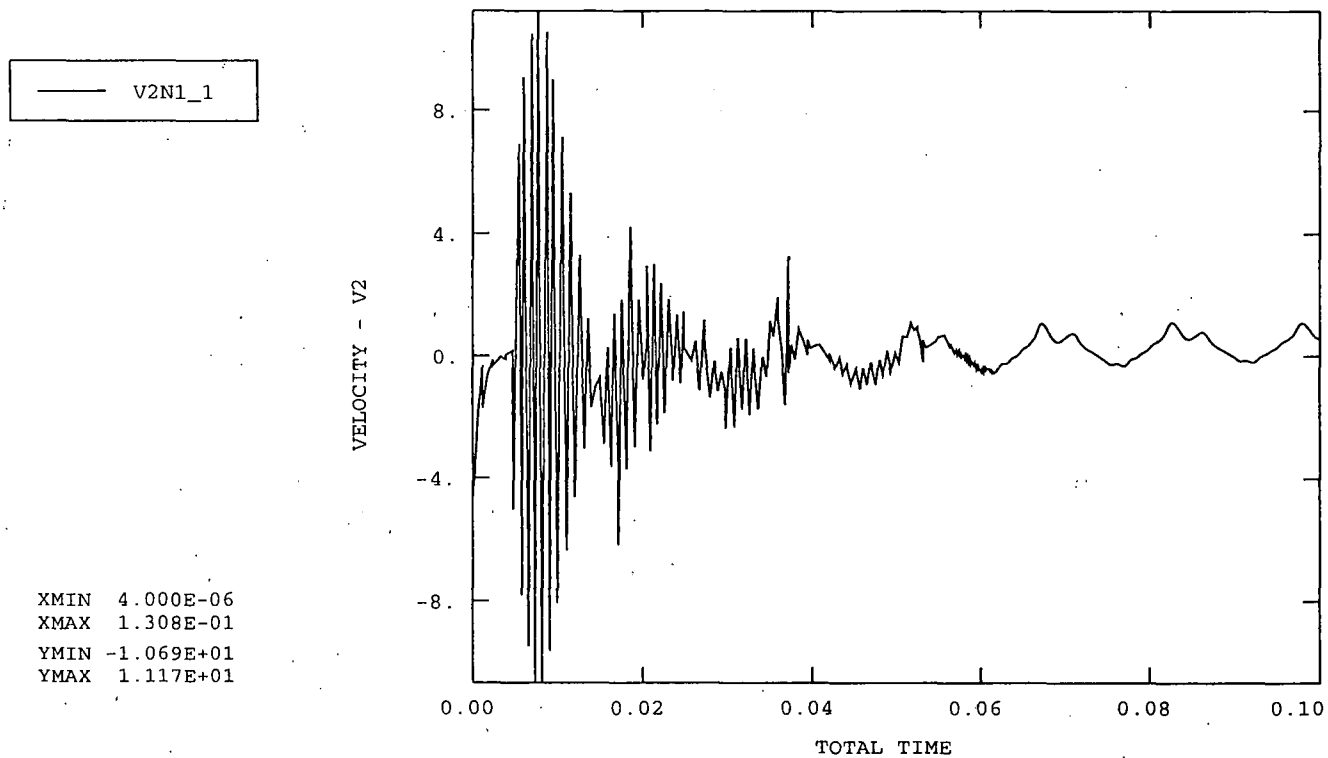


Figure 6.2

Vertical velocity of pile head: Simple hammer/pile model

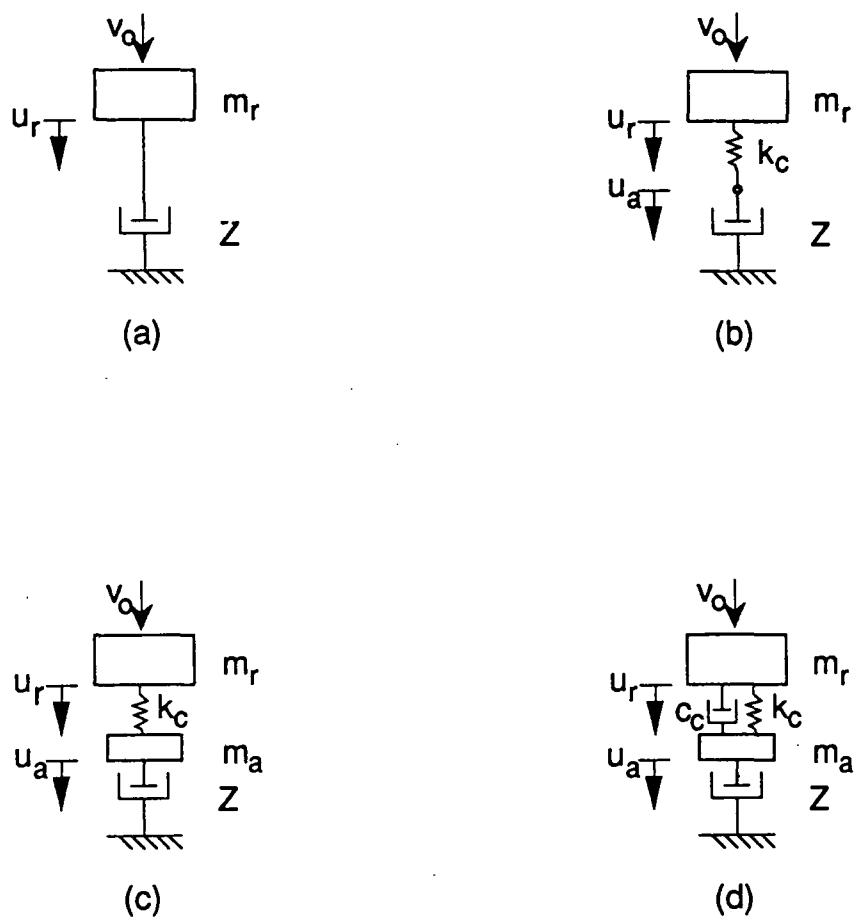


Figure 6.3 Analytical pile hammer models (after Deeks, 1992)

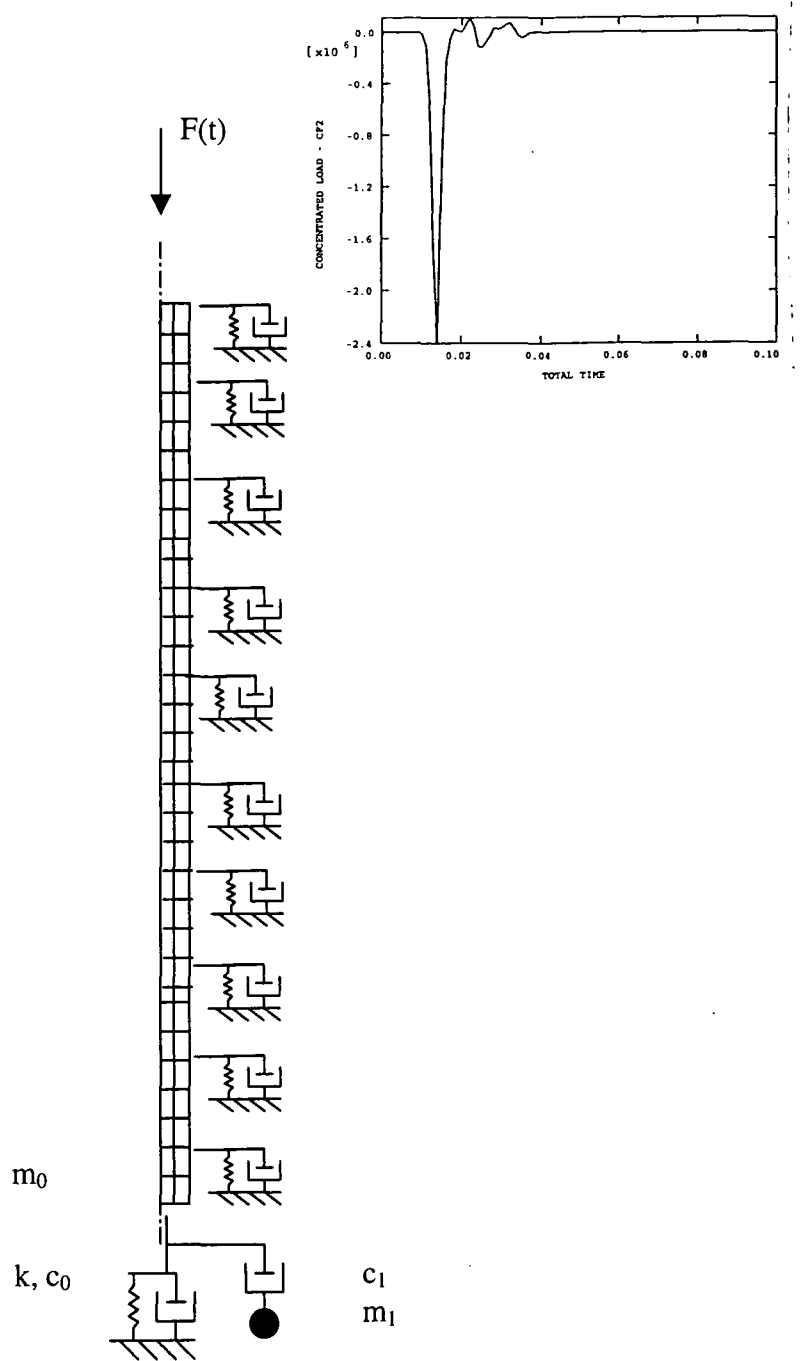


Figure 6.4

FE model of the pile with new base model and new shaft model.
Typical forcing function applied to pile head.

ABAQUS

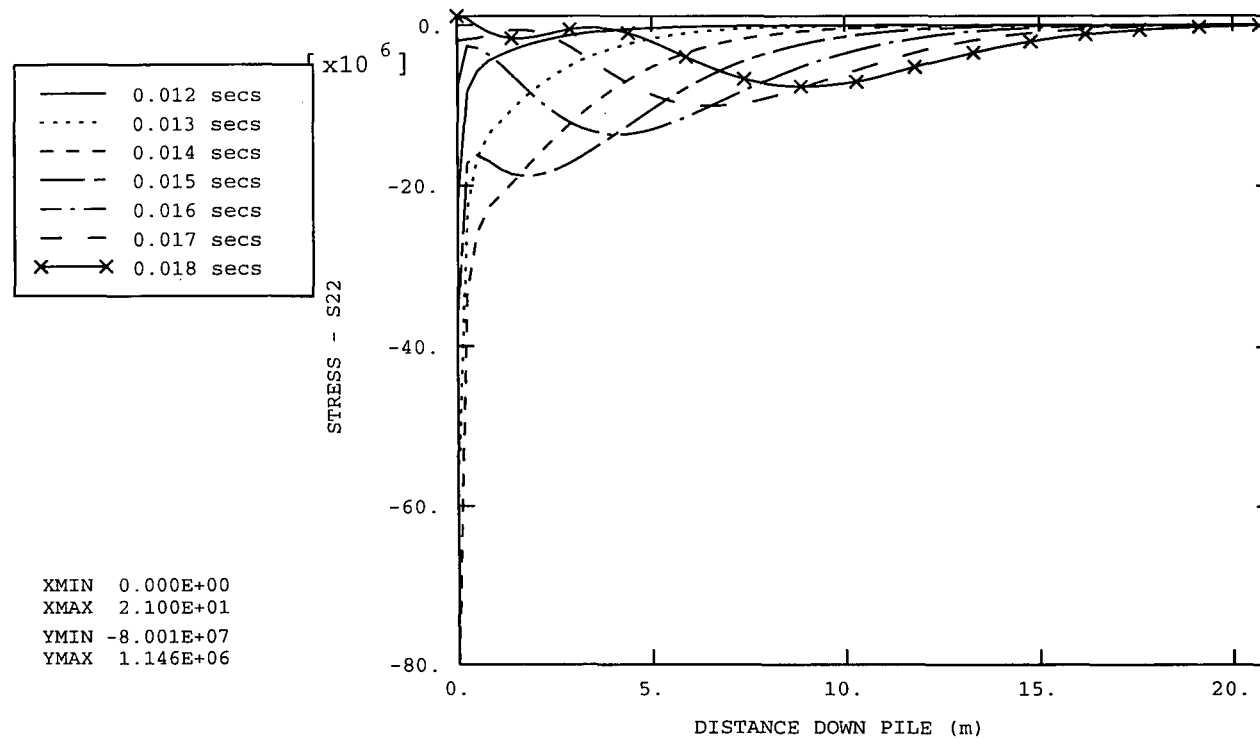


Figure 6.5

Vertical stresses in the pile at various intervals during the first 0.02 seconds.

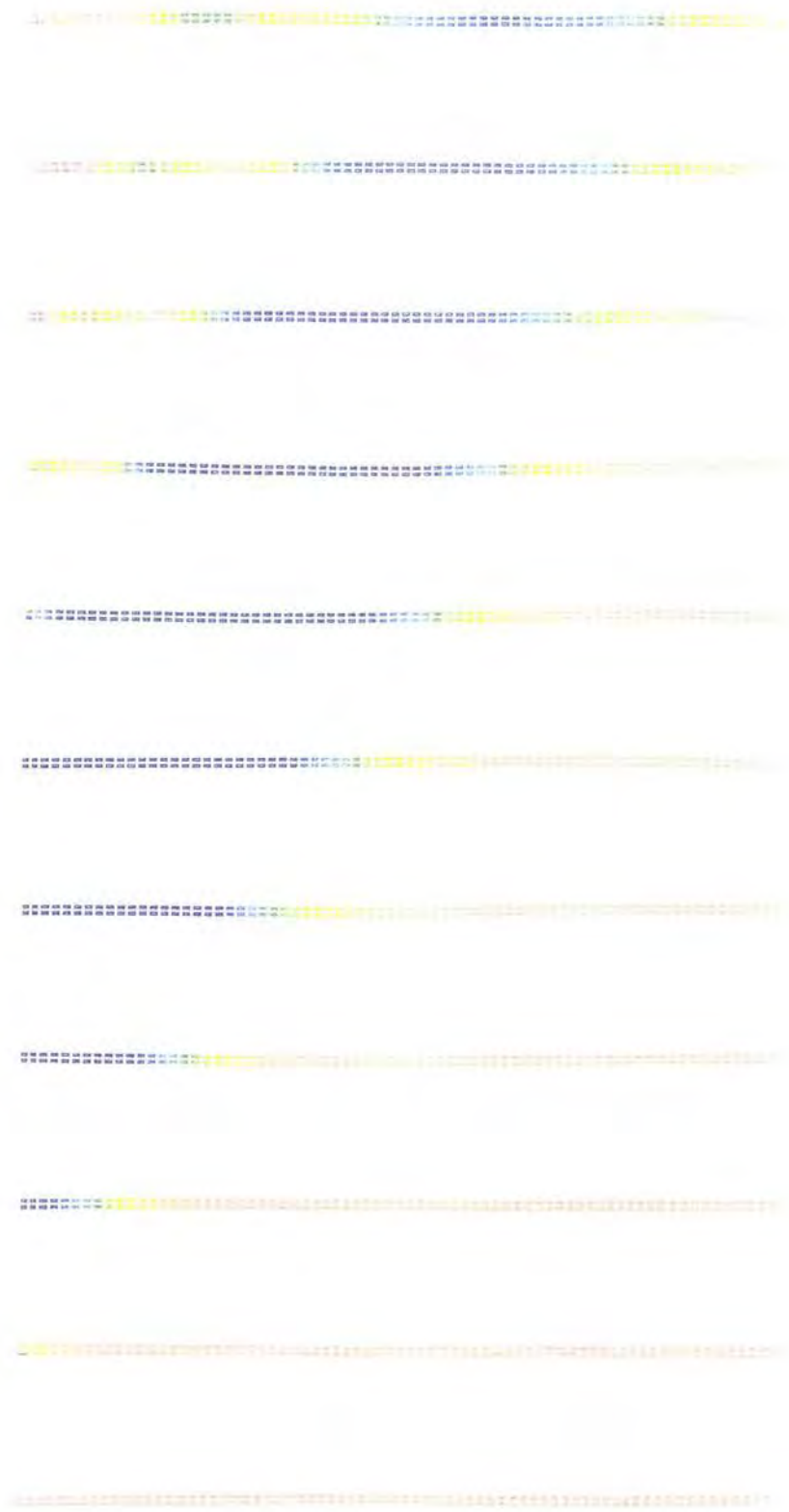
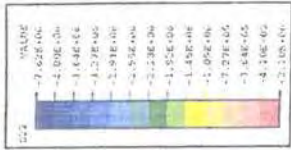


Figure 6.6 Contour plots of the vertical stresses in the pile at intervals of 0.001 seconds

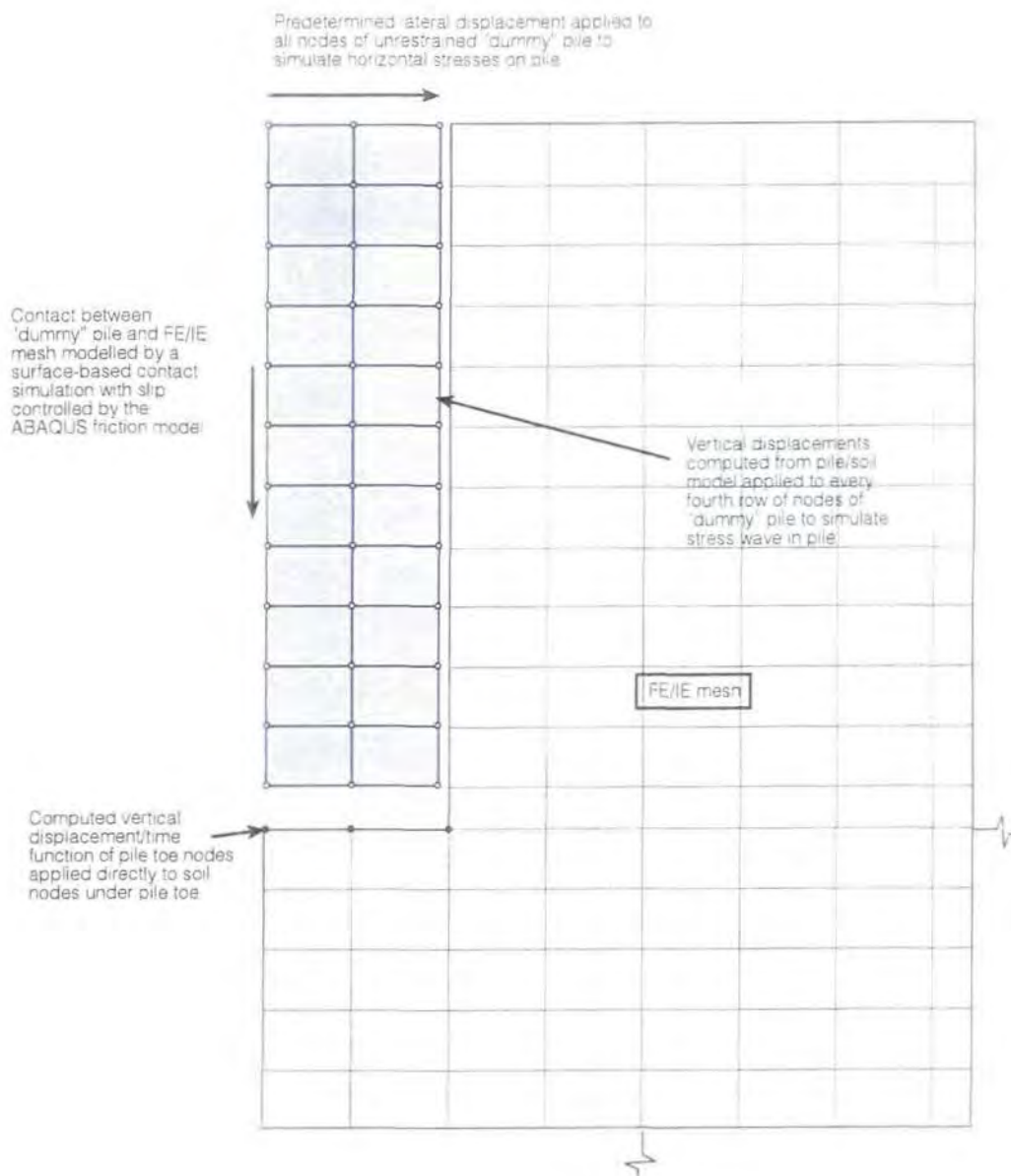


Figure 6.7 The 'dummy' pile

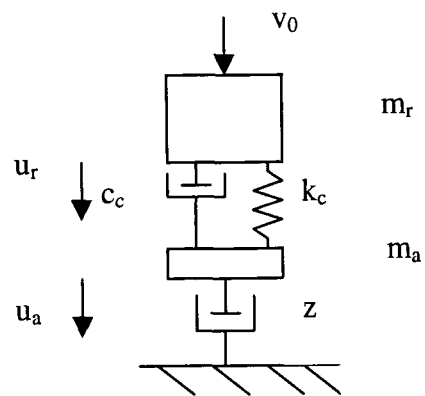


Figure 6.8 Hammer impact model

ABAQUS

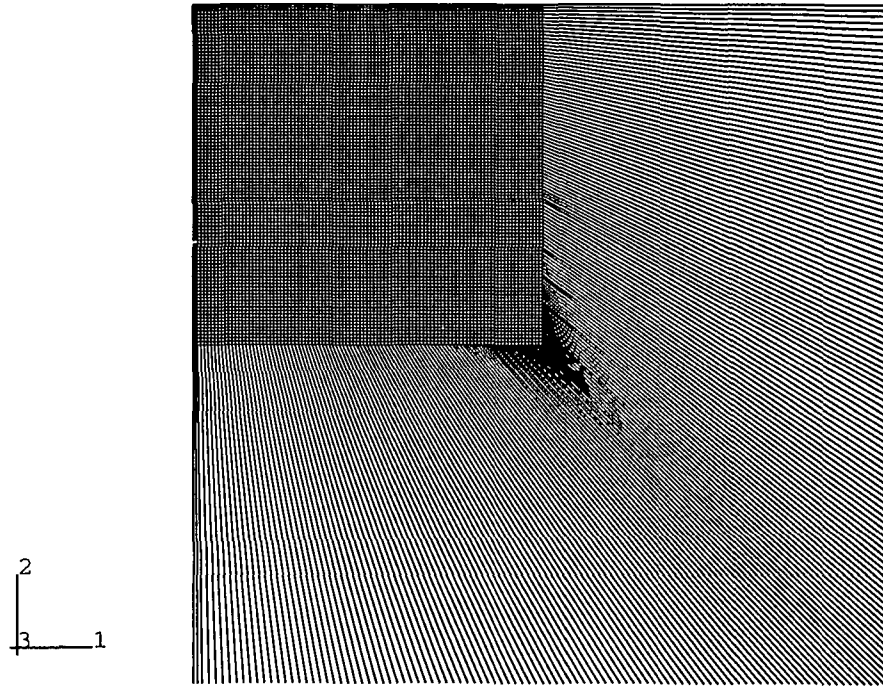


Figure 6.9

Large FE/IE mesh used for wave propagation analysis

ABAQUS

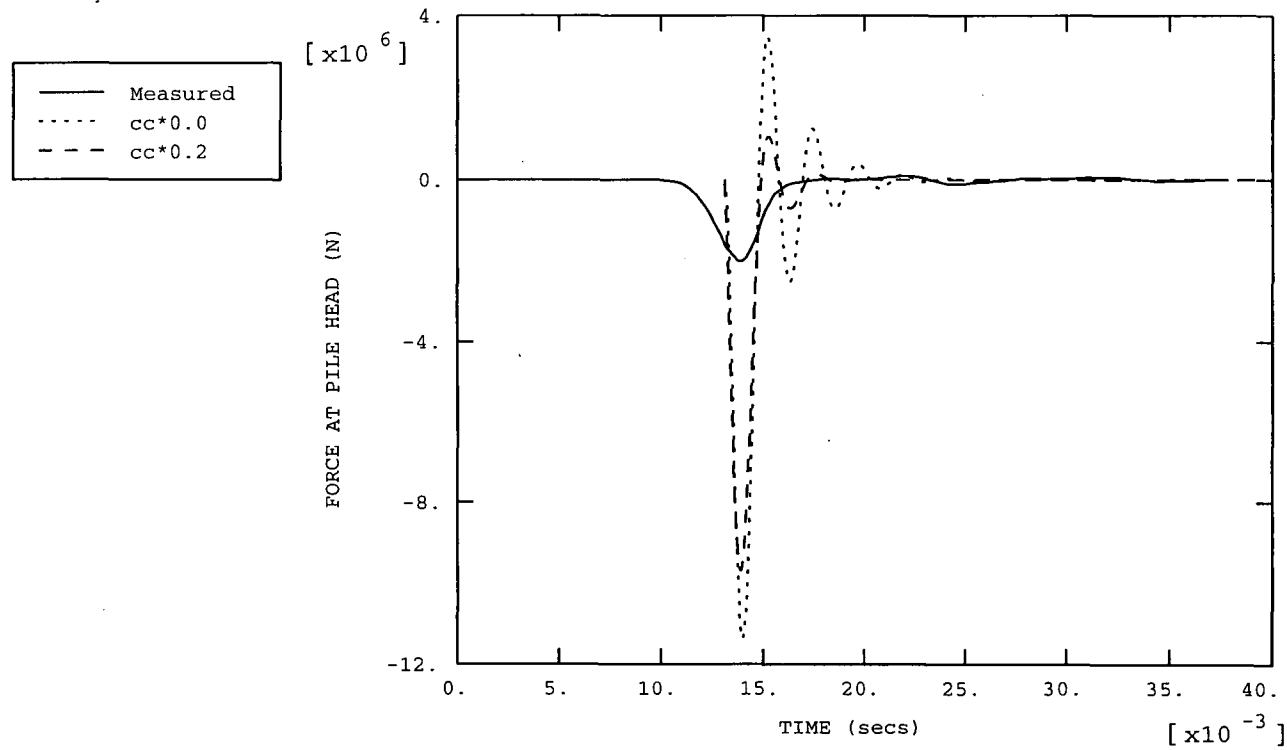


Figure 6.10a Force/time functions at the pile head (pile 23) for $k_c = 1e^{10}$ N/m and various values of c_c^*

ABAQUS

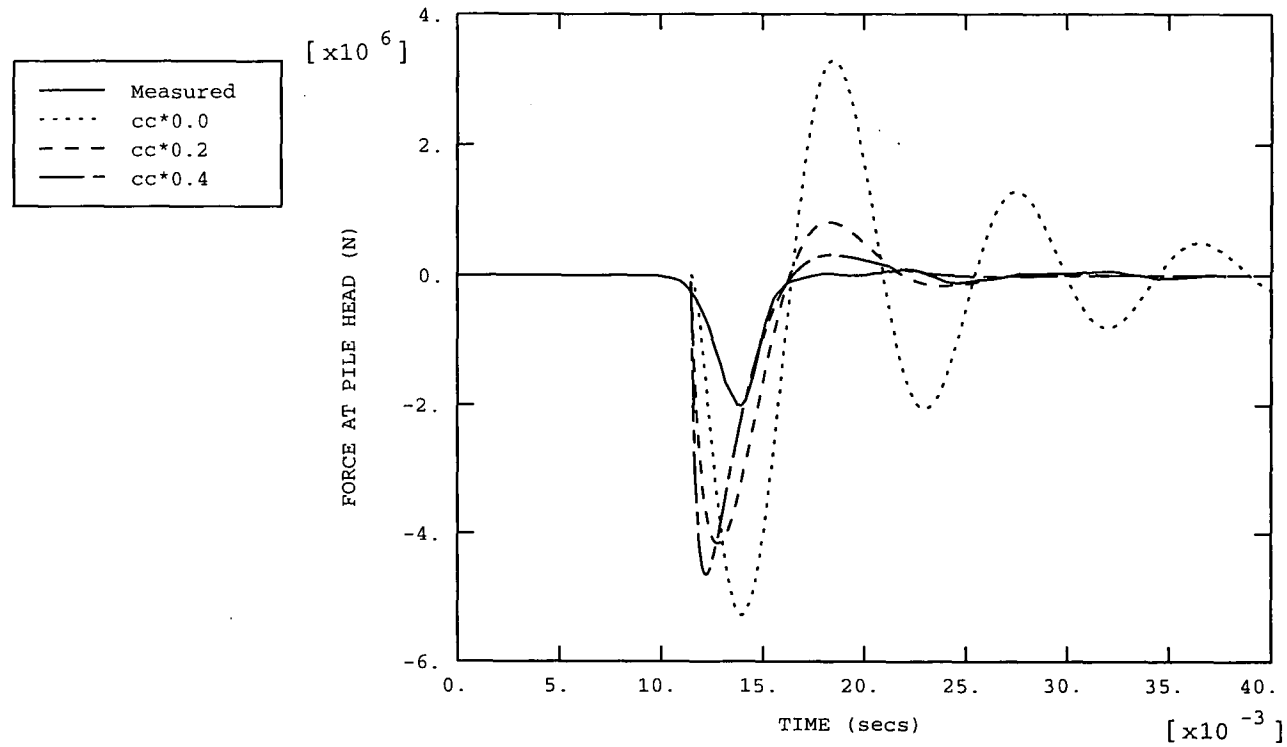


Figure 6.10b Force/time functions at the pile head (pile 23) for $k_c = 1e^9$ N/m and various values of c_c^*

ABAQUS

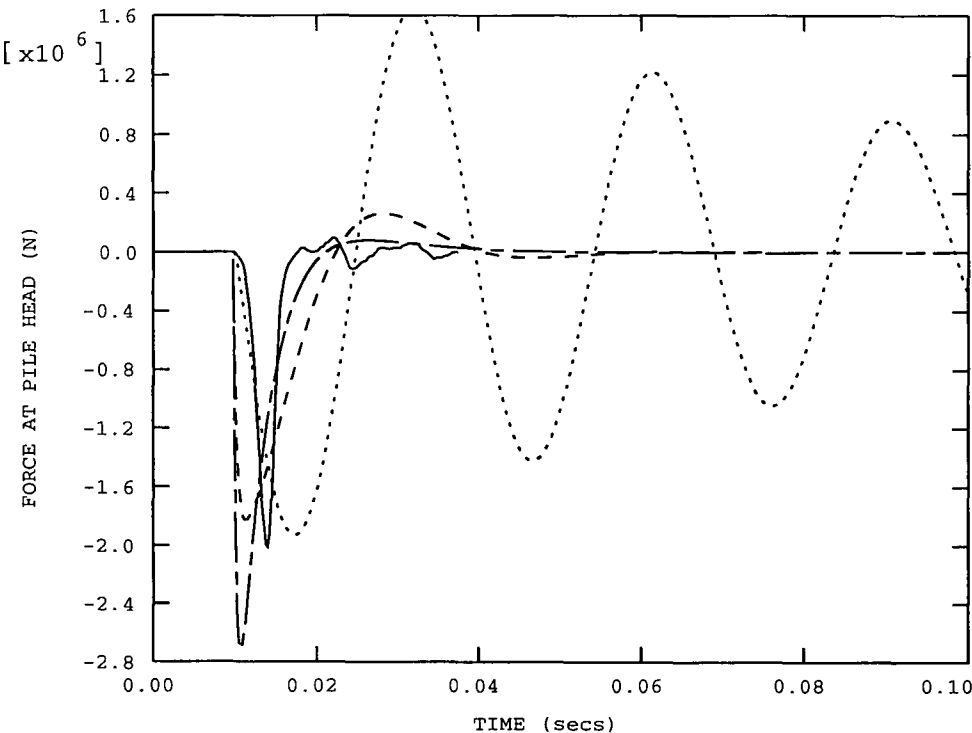
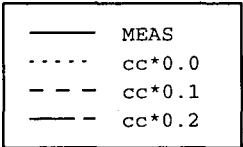


Figure 6.10c Force/time functions at the pile head (pile 23) for $k_c = 1e^8$ N/m and various values of c_c^*

ABAQUS

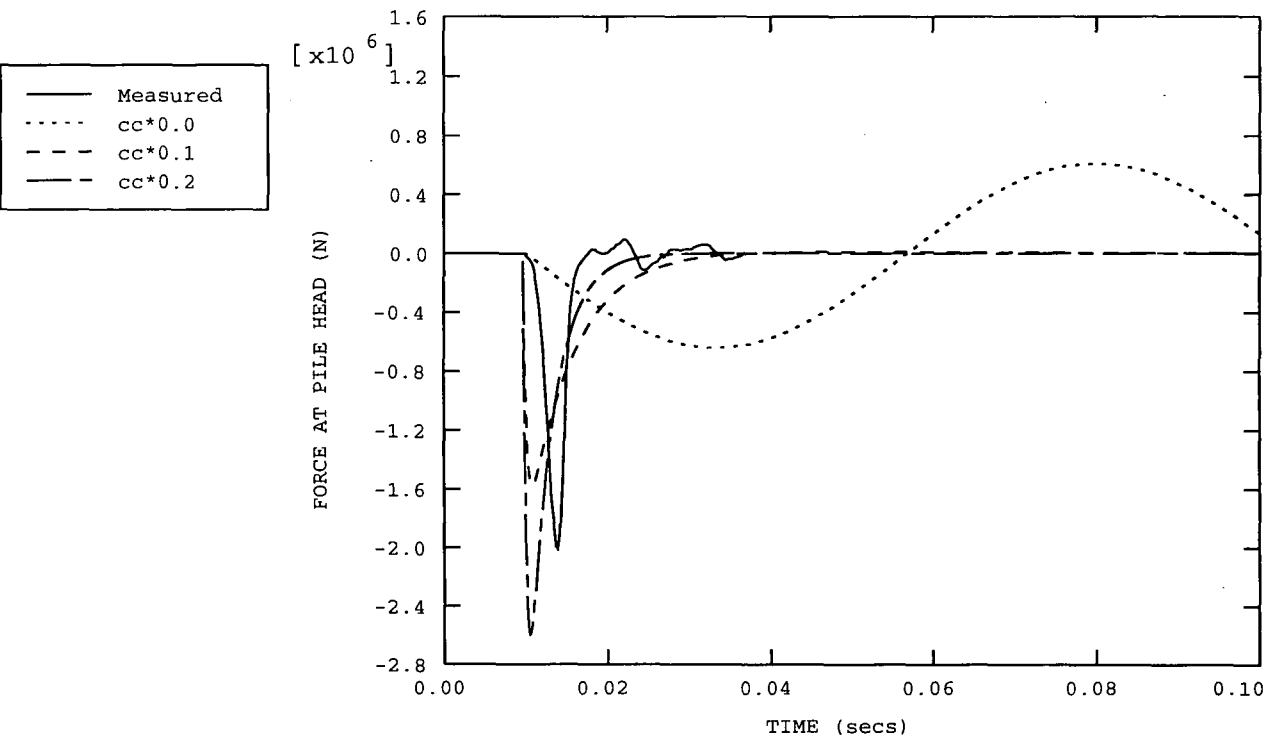


Figure 6.10d Force/time functions at the pile head (pile 23) for $k_c = 1e^7$ N/m and various values of c_c^*

ABAQUS

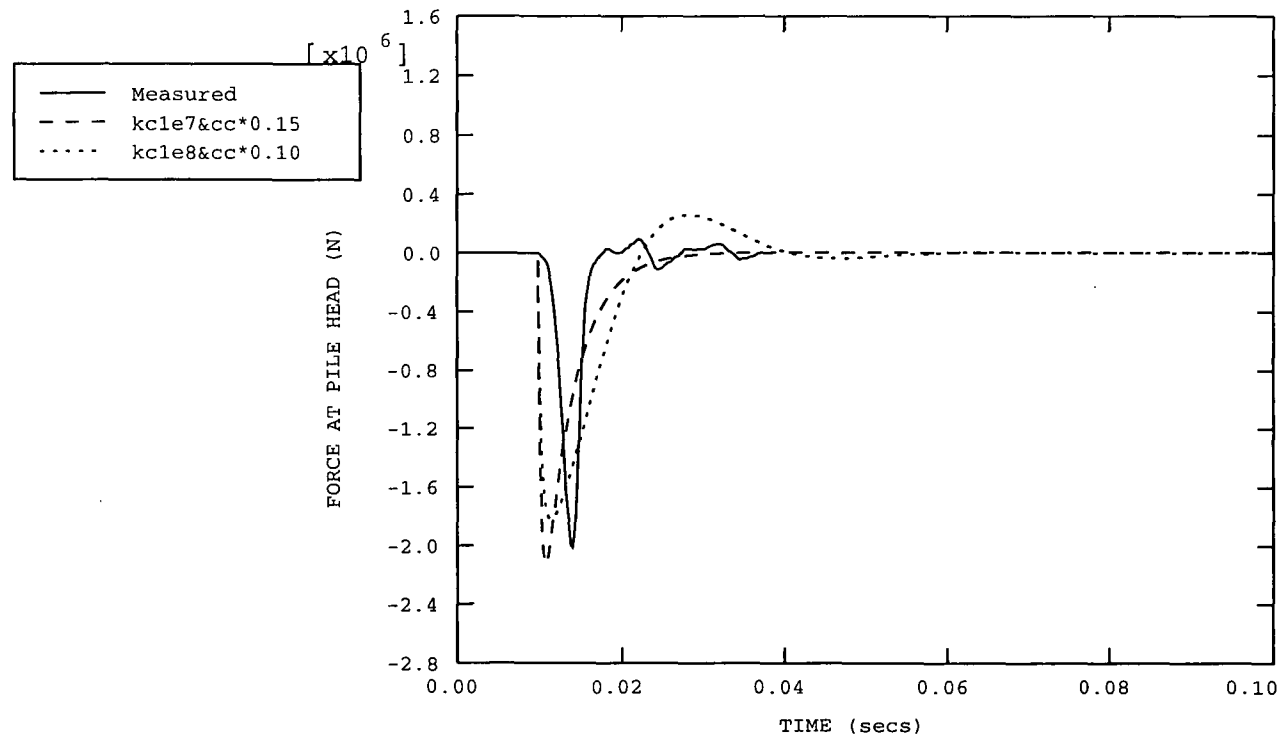


Figure 6.11 Comparison of measured and computed force/time functions at the pile head (pile 23) assuming $k_c = 1e^7$ N/m and $c_c^* = 0.15$

ABAQUS

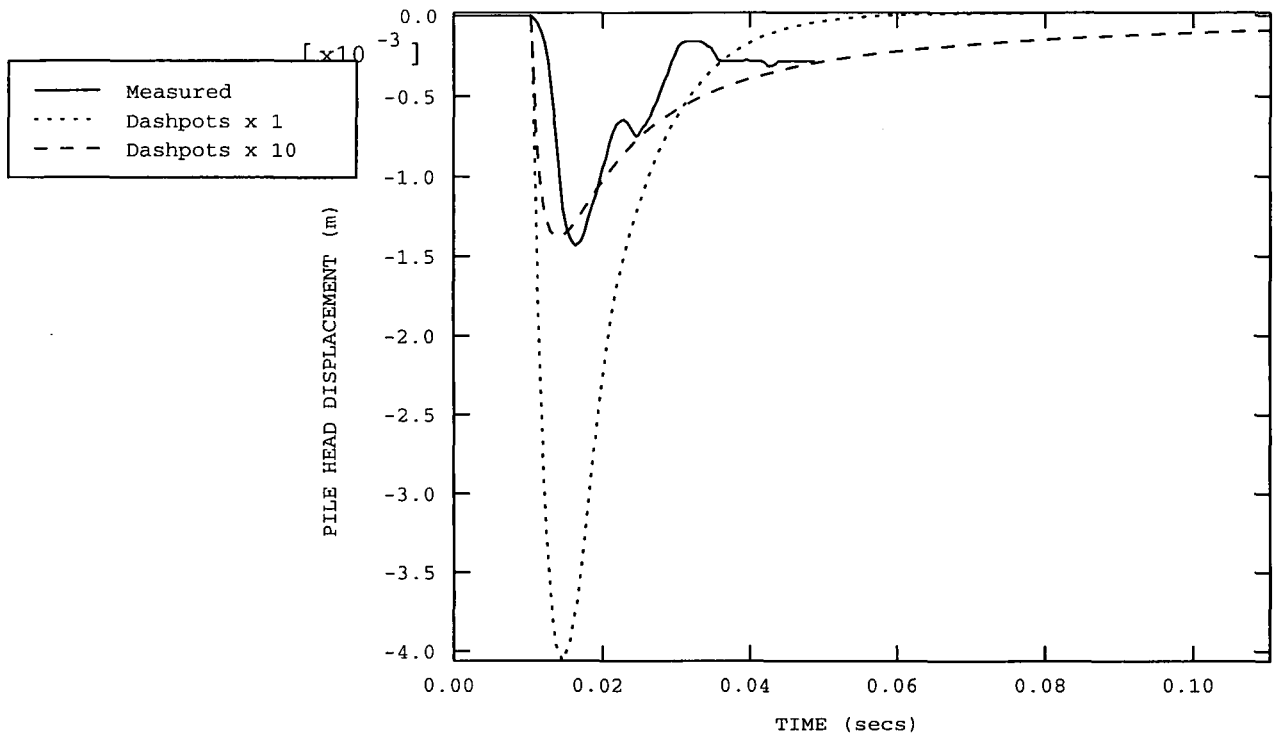


Figure 6.12 Effect of increasing dashpot constants on pile head displacement (pile 23)

ABAQUS

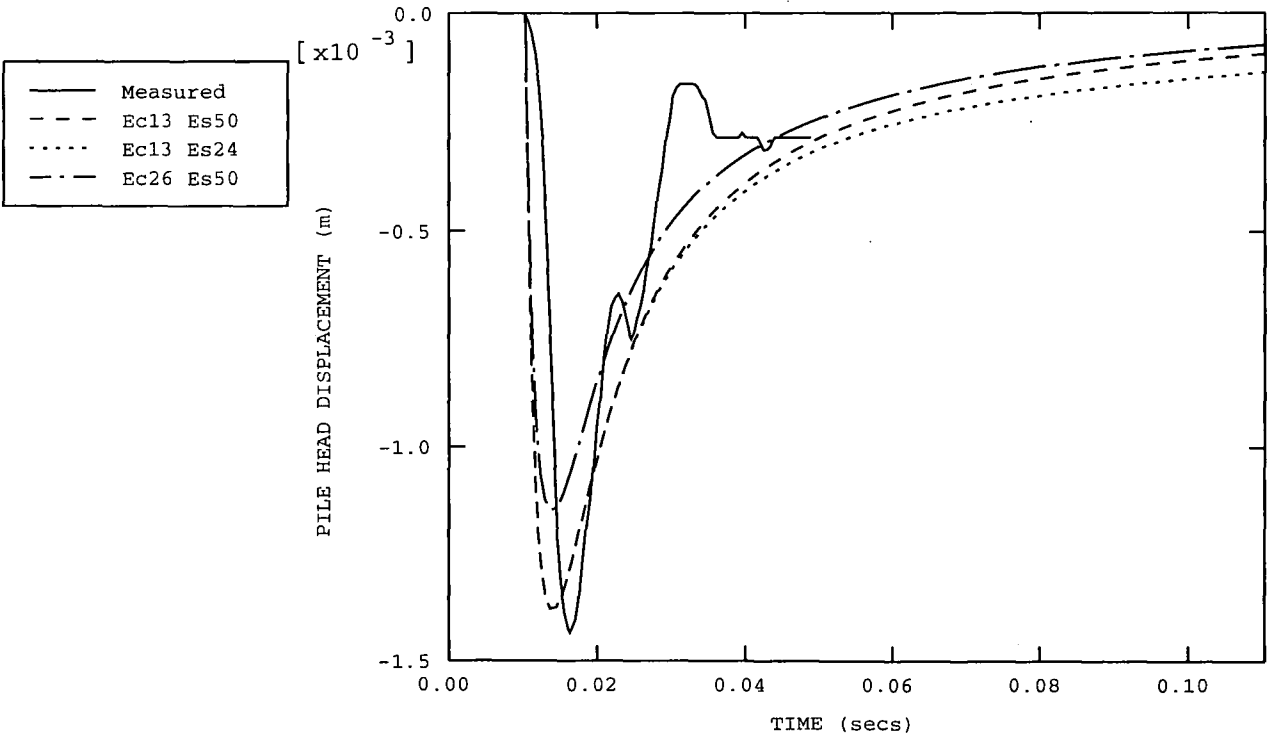


Figure 6.13 Effect of soil stiffness on pile head displacement (pile 23)

ABAQUS

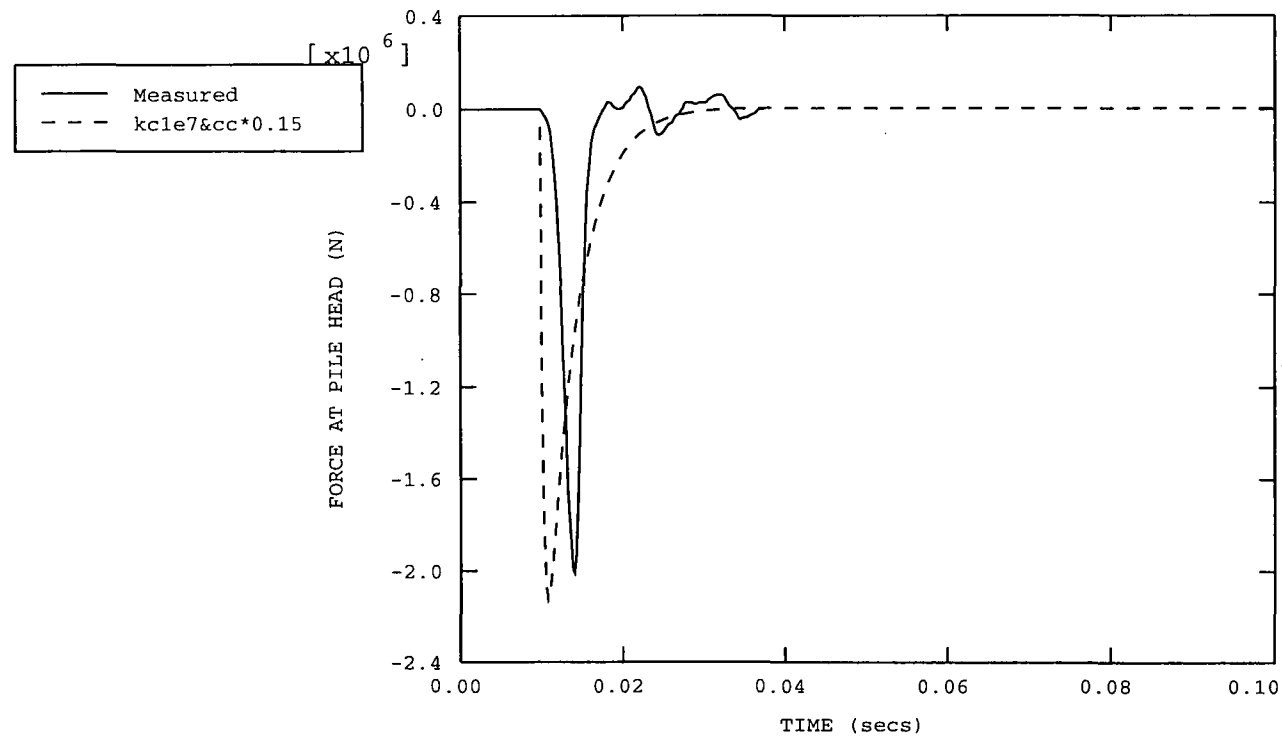


Figure 6.14

Comparison of the measured and computed force/time functions at the pile head (pile 23) assuming $k_c = 1e^7$ N/m and $c_c^* = 0.15$ ($E_{\text{clay}} = 13e^6$ MPa and $E_{\text{sand}} = 50e^6$ MPa)

ABAQUS

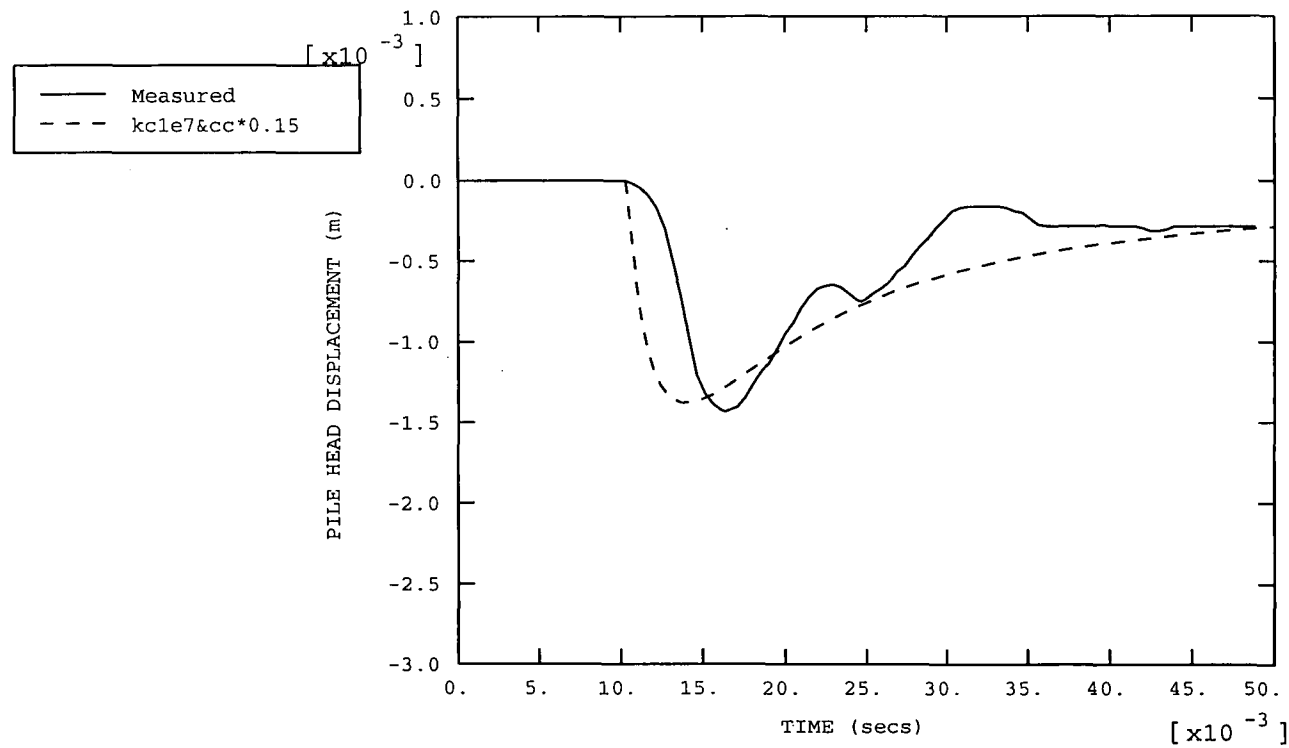


Figure 6.15

Comparison of the measured and computed pile head displacements (pile 23) assuming $k_c = 1e^7$ N/m and $c_c^* = 0.15$ ($E_{\text{clay}} = 13e^6$ MPa and $E_{\text{sand}} = 50e^6$ MPa)

ABAQUS

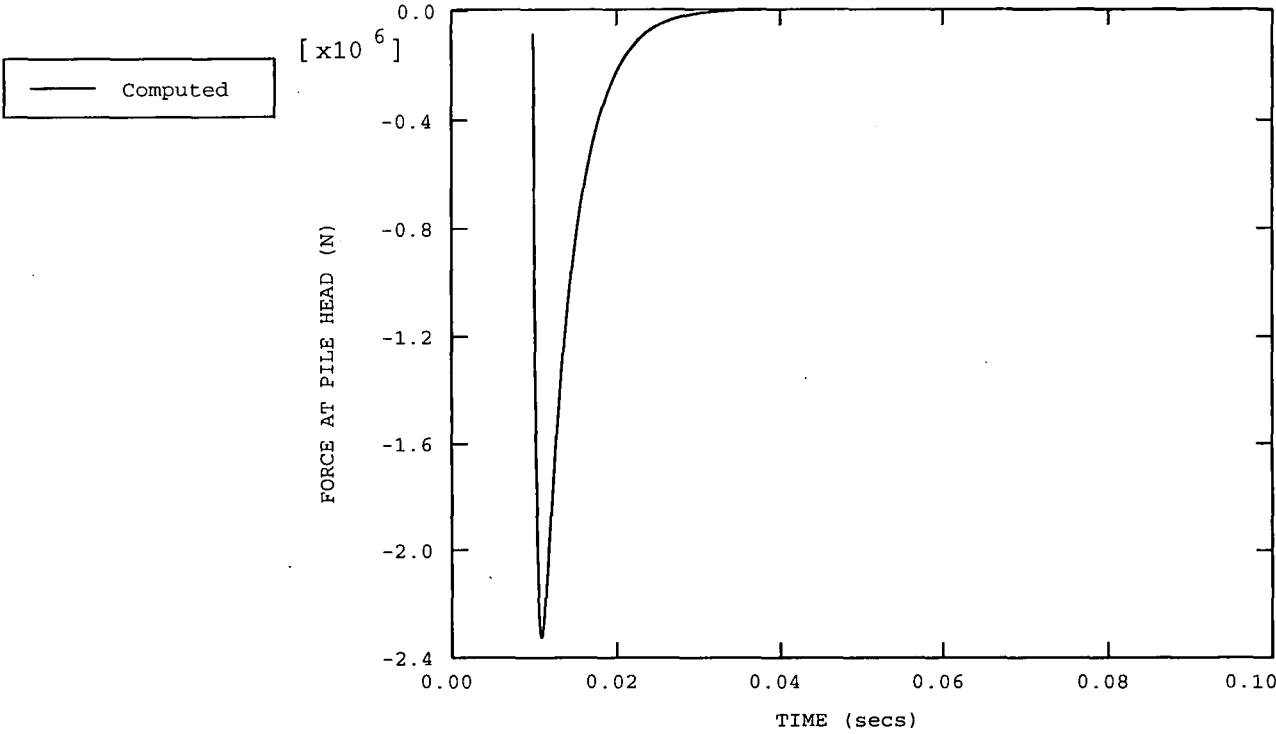


Figure 6.16 Computed force/time function for pile 18 assuming $k_c = 1e^7$ N/m and $c_c^* = 0.15$

ABAQUS

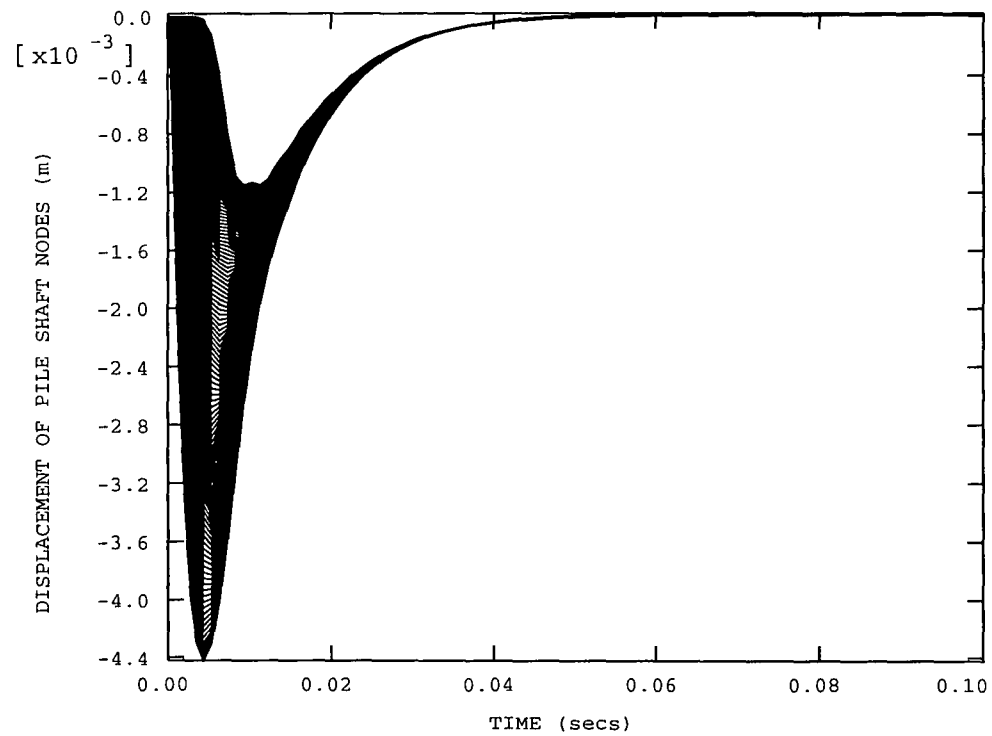


Figure 6.17b Computed vertical displacement of all pile interface nodes for pile 18

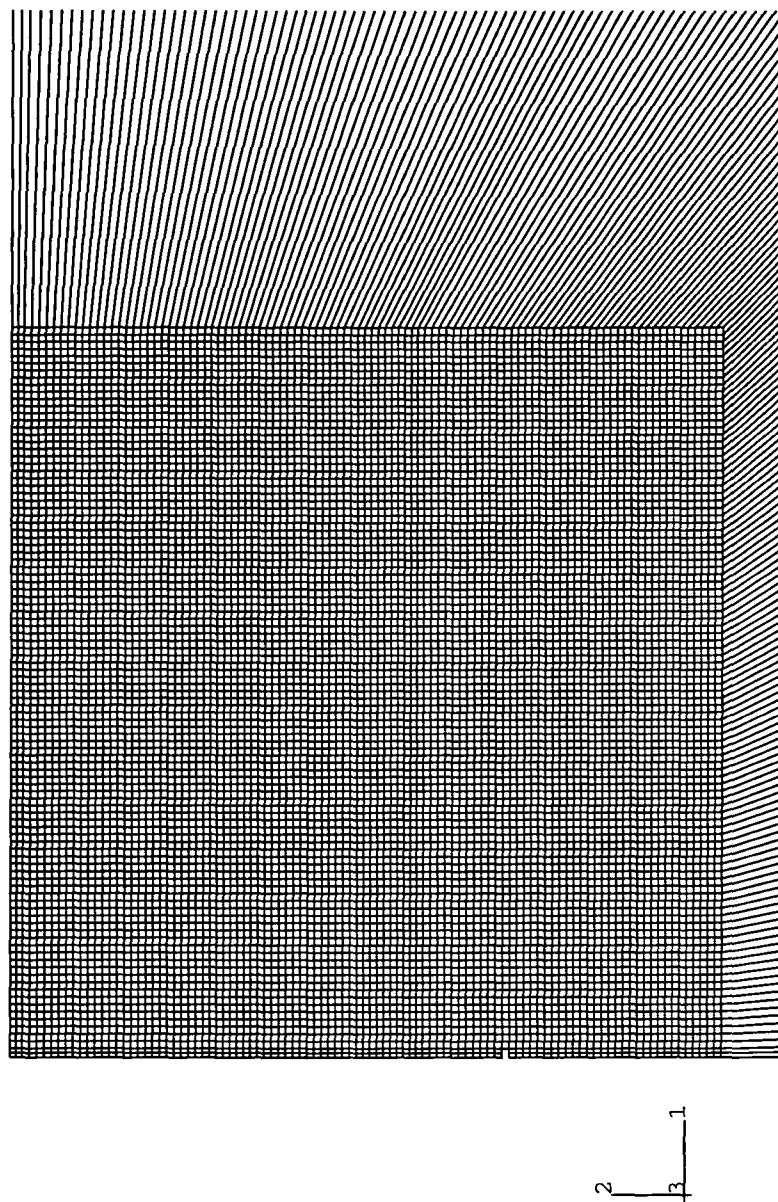
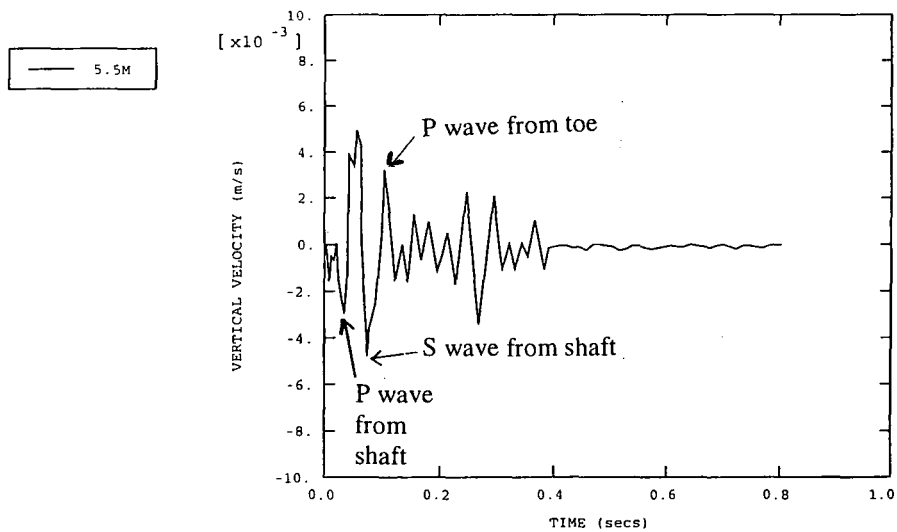
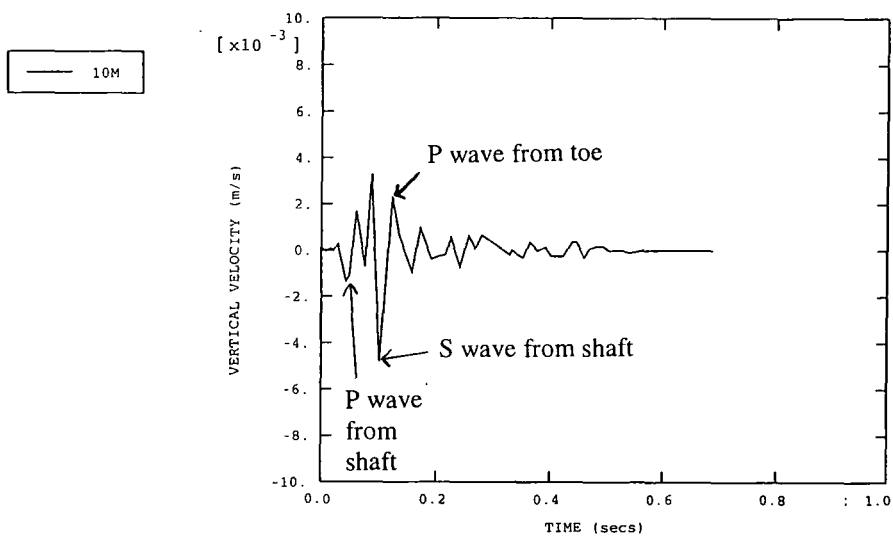


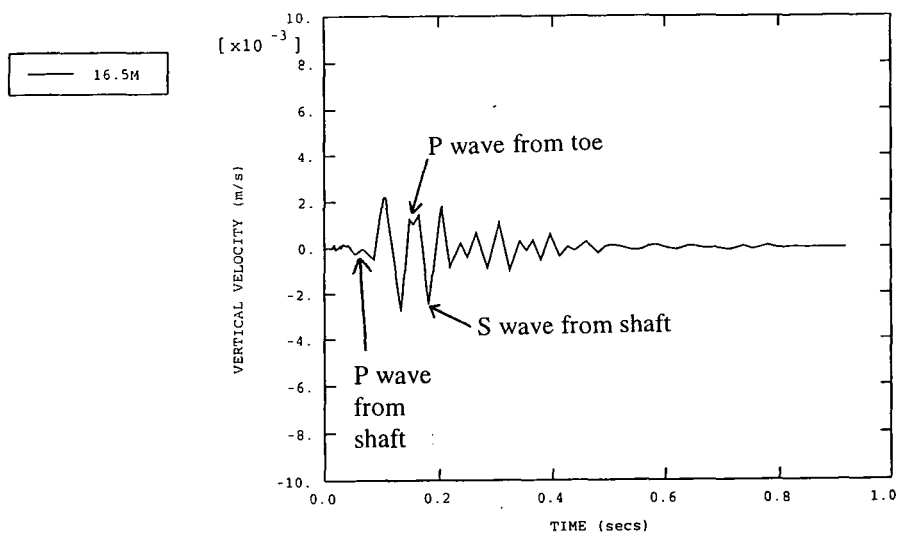
Figure 6.18 Wave propagation model for pile 18 (M66 site)



(a) 5.5m from pile



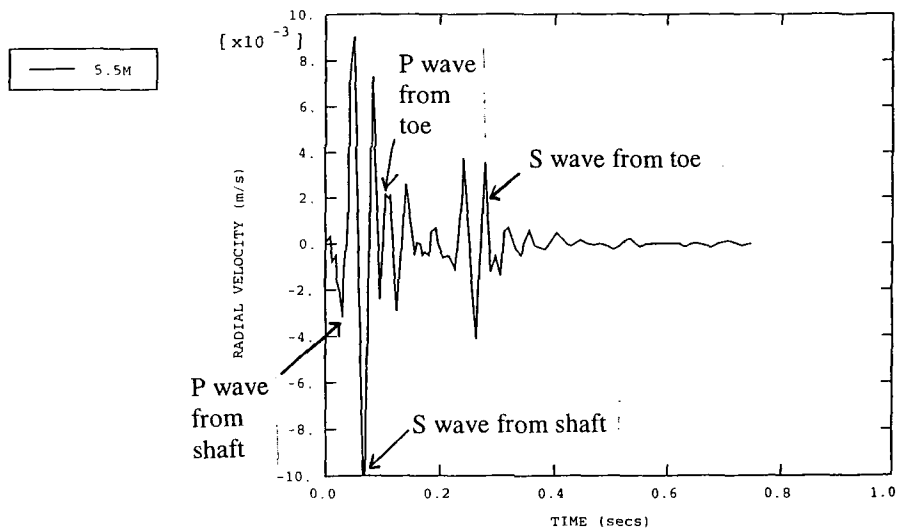
(b) 10m from pile



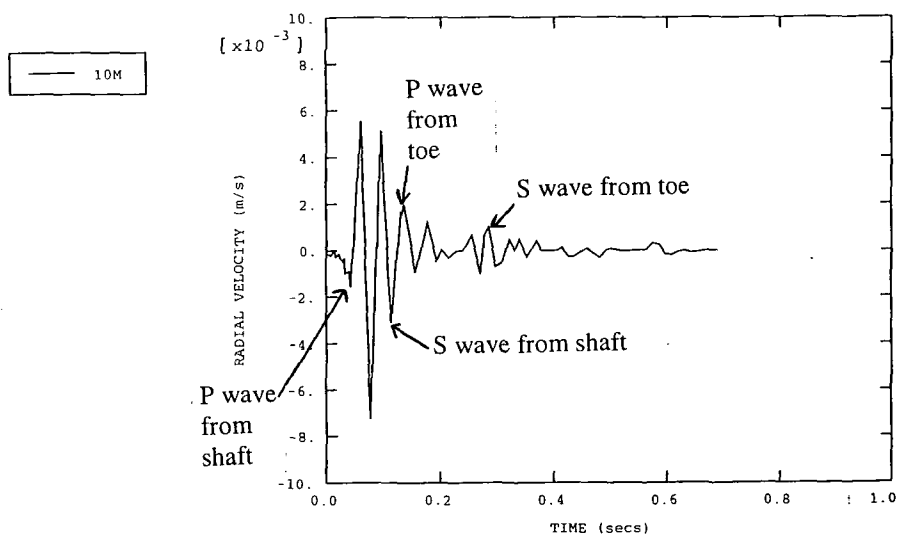
(c) 16.5m from pile

Figure 6.19

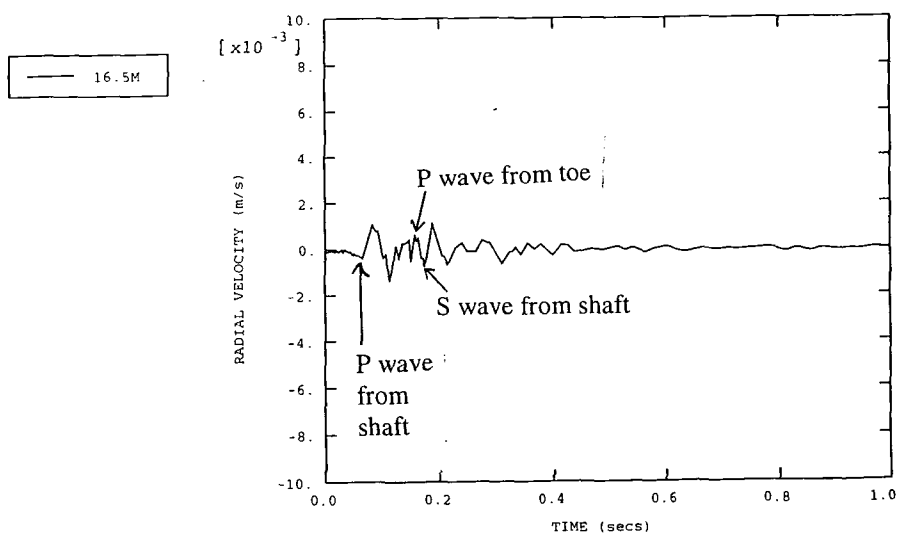
Vertical velocity/time traces recorded at the M66 site at horizontal distances of 5.5m, 10m and 16.5m from pile.



(a) 5.5m from pile



(b) 10m from pile

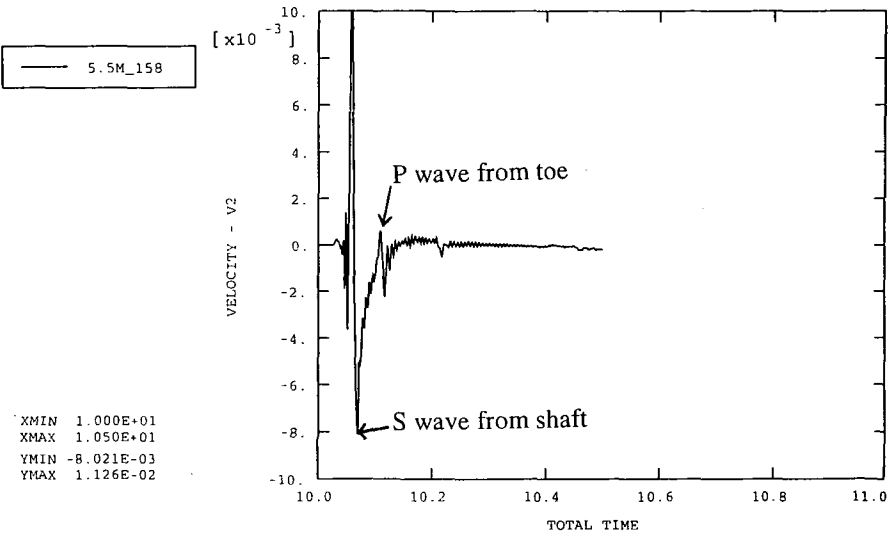


(c) 16.5m from pile

Figure 6.20

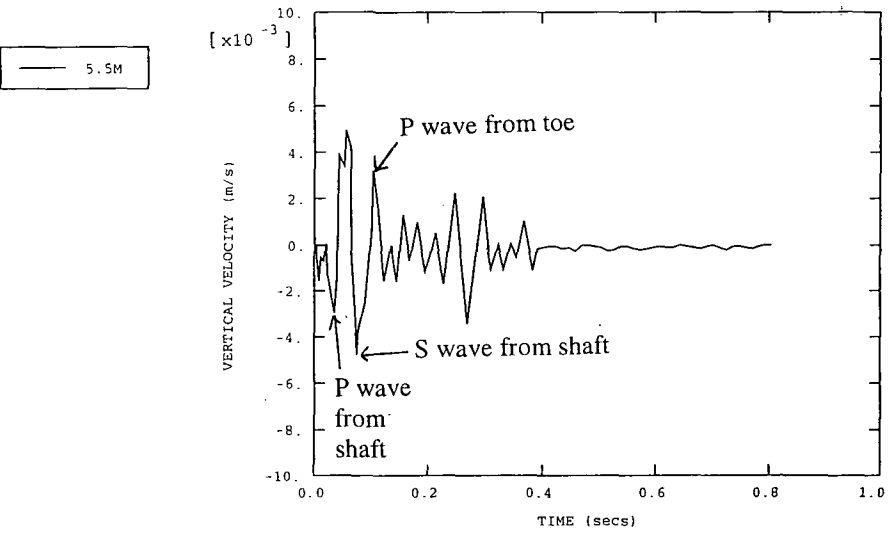
Radial velocity/time traces recorded at the M66 site at horizontal distances of 5.5m, 10m and 16.5m from pile.

ABAQUS



Predicted

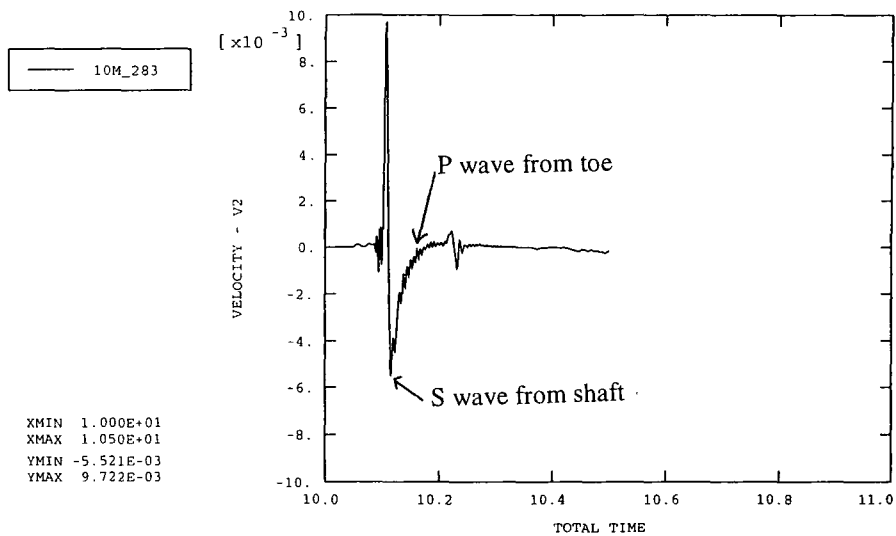
ABAQUS



Measured

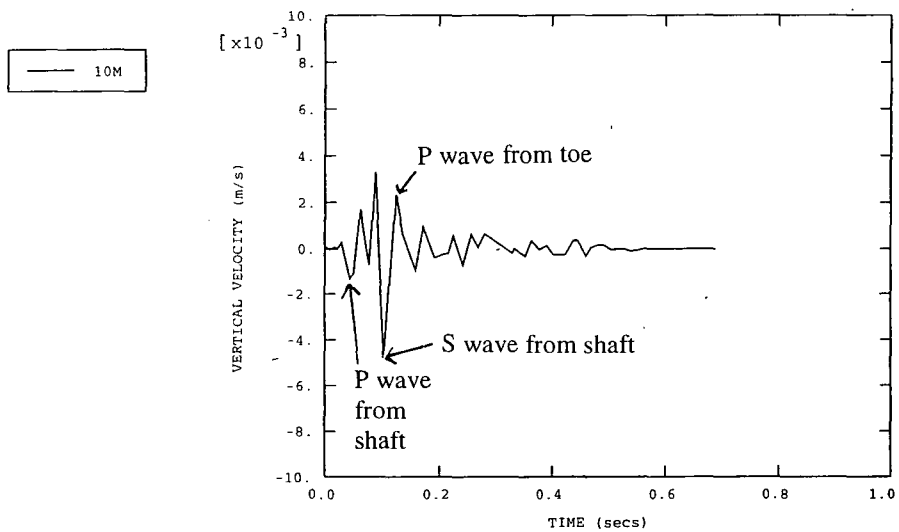
Figure 6.21(a) Comparison of predicted and measured vertical velocity/time traces for geophone at 5.5m (M66 site)

ABAQUS



Predicted

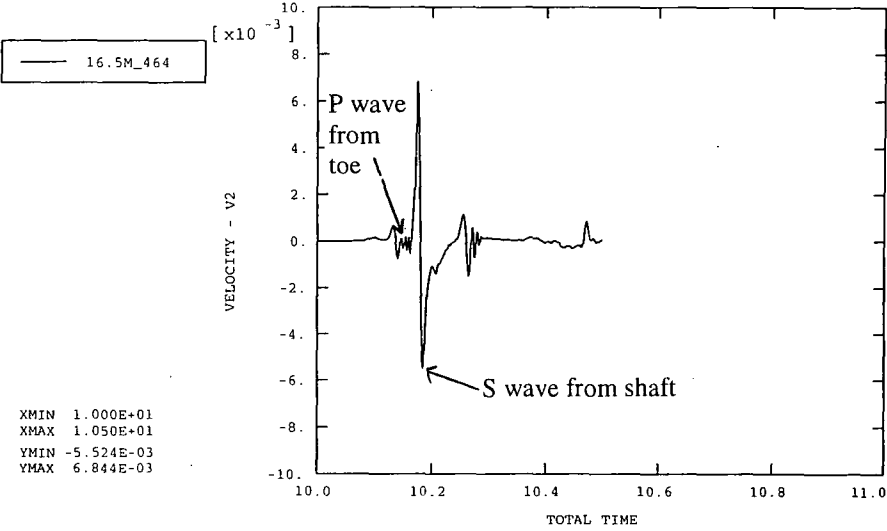
ABAQUS



Measured

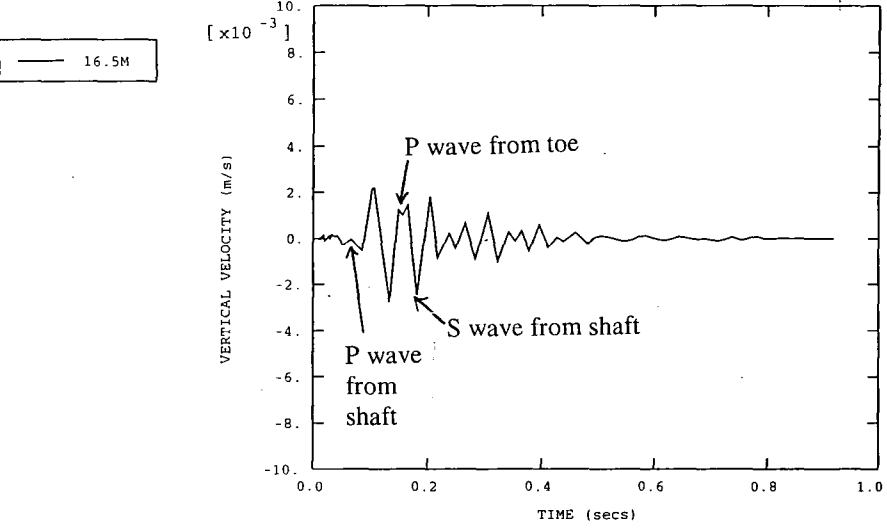
Figure 6.21(b) Comparison of predicted and measured vertical velocity/time traces for geophone at 10m (M66 site)

ABAQUS



Predicted

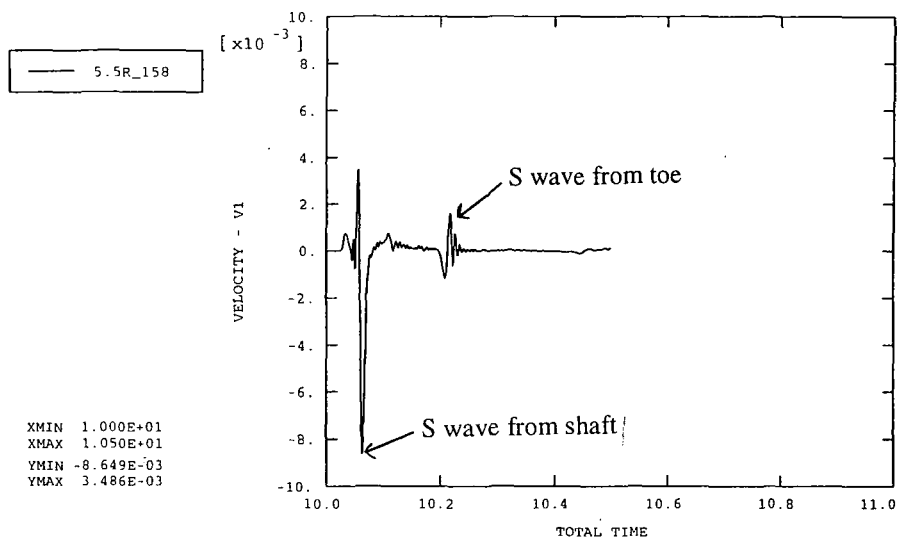
ABAQUS



Measured

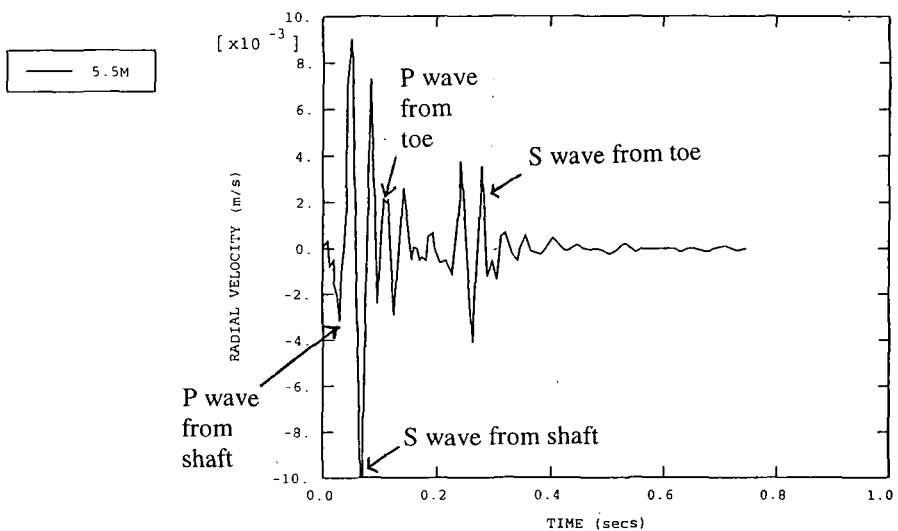
Figure 6.21(c) Comparison of predicted and measured vertical velocity/time traces for geophone at 16.5m (M66 site)

ABAQUS



Predicted

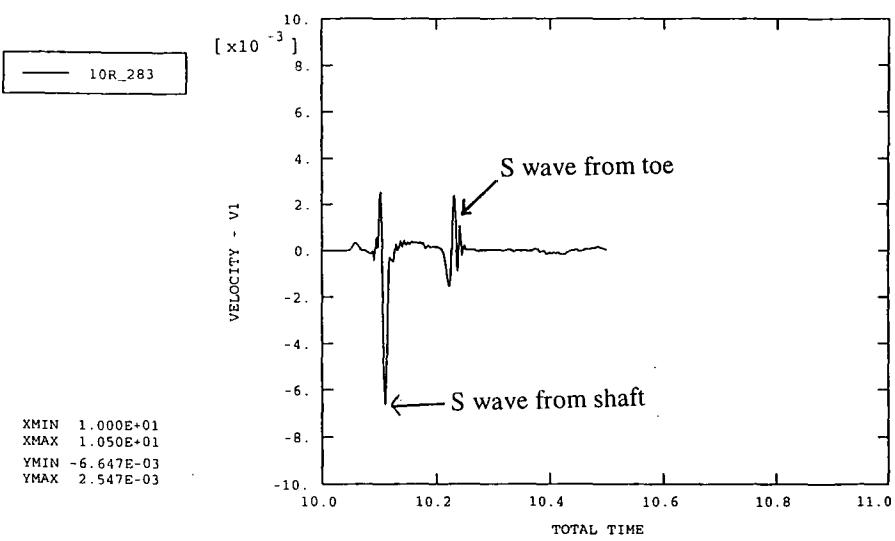
ABAQUS



Measured

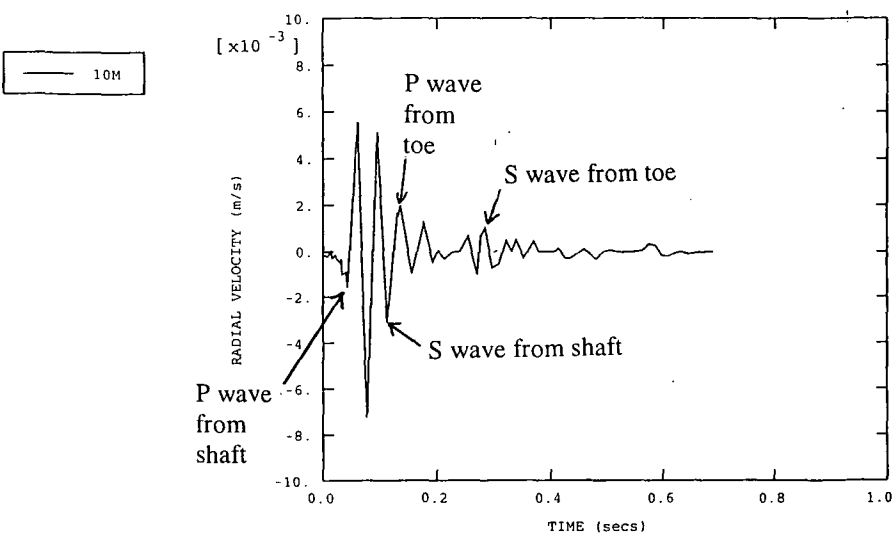
Figure 6.22(a) Comparison of predicted and measured radial velocity/time traces for geophone at 5.5m (M66 site)

ABAQUS



Predicted

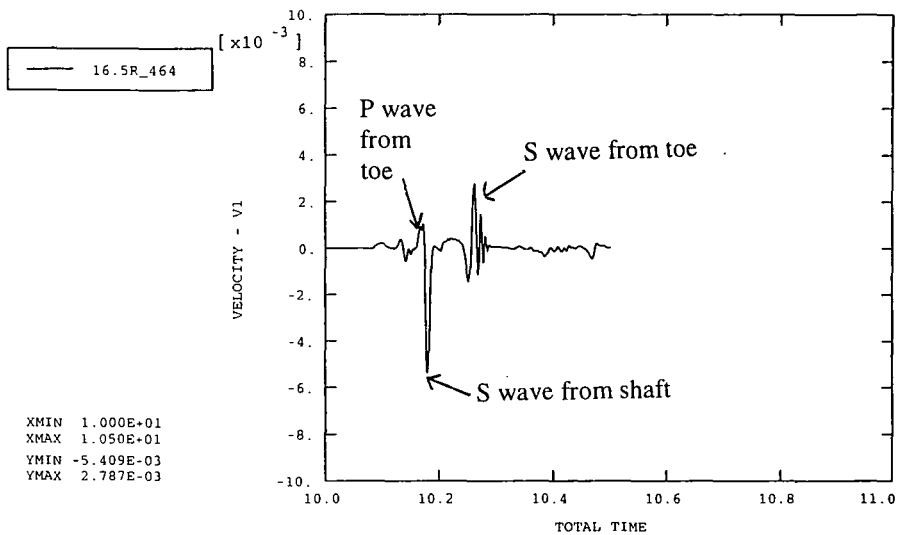
ABAQUS



Measured

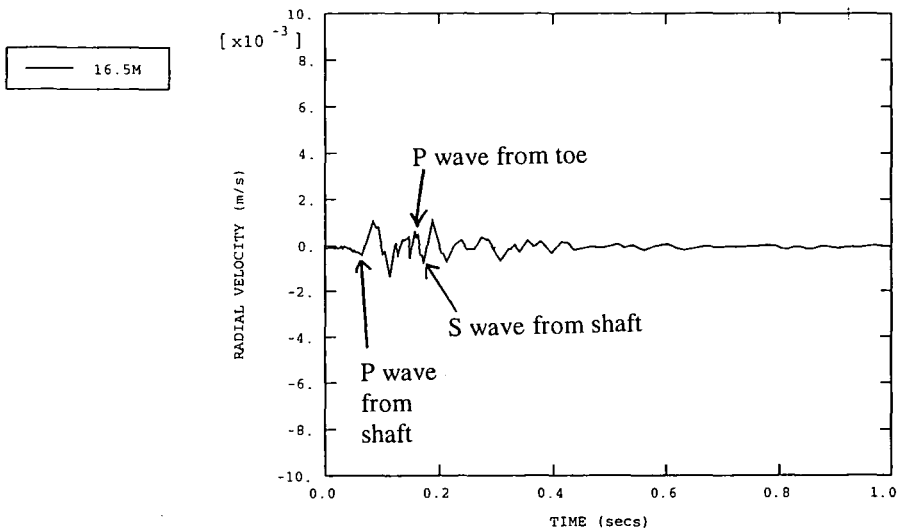
Figure 6.22(b) Comparison of predicted and measured radial velocity/time traces for geophone at 10m (M66 site)

ABAQUS



Predicted

ABAQUS



Measured

Figure 6.22(c) Comparison of predicted and measured radial velocity/time traces for geophone at 16.5m (M66 site)

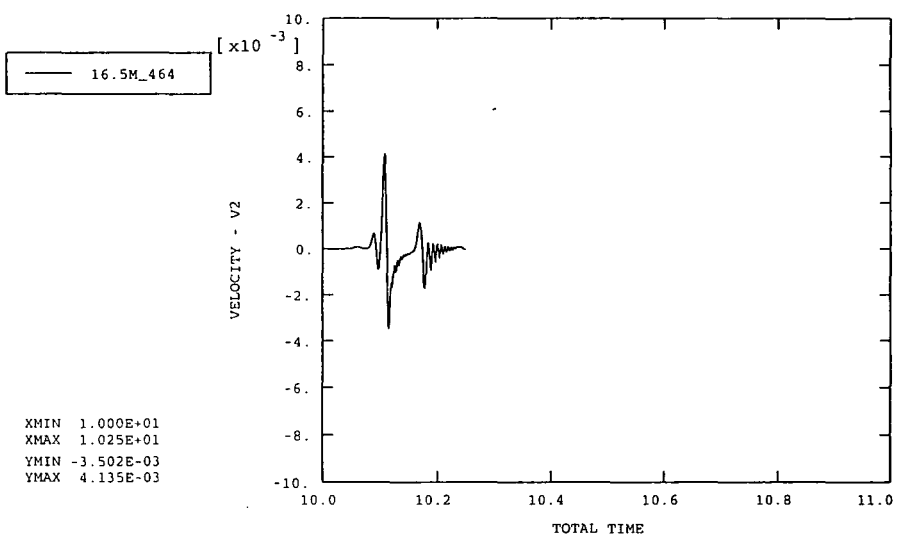
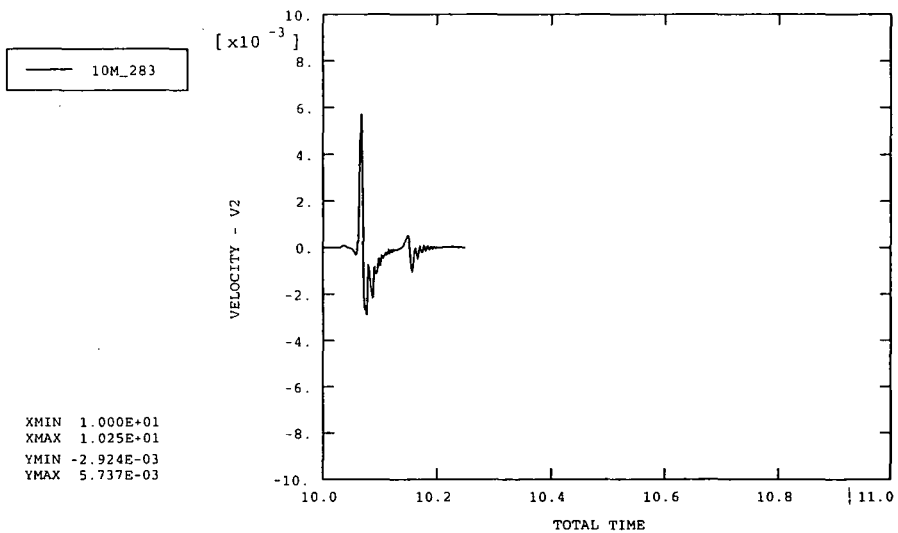
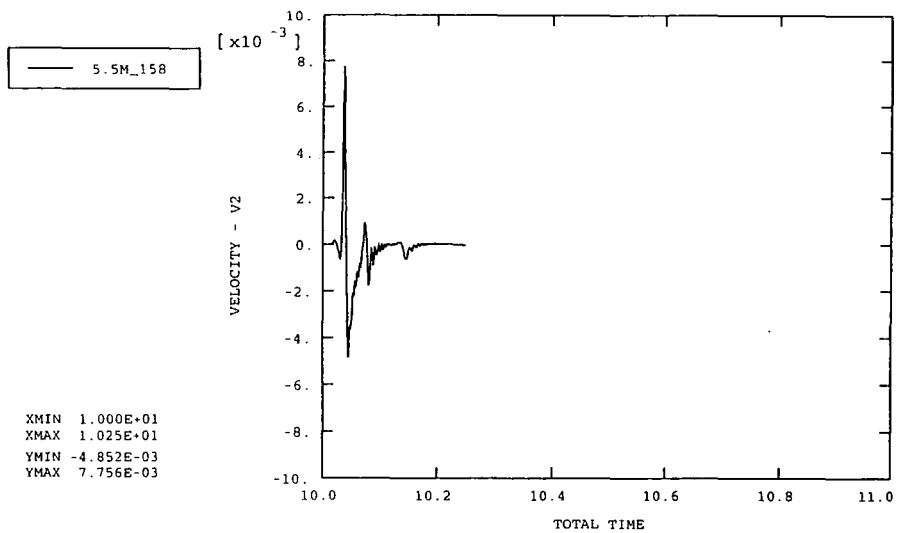


Figure 6.23(a) Computed vertical velocity/time traces for geophones at 5.5m, 10m and 16.5m assuming an overall stiffness for the soil of 150MPa. (M66 site)

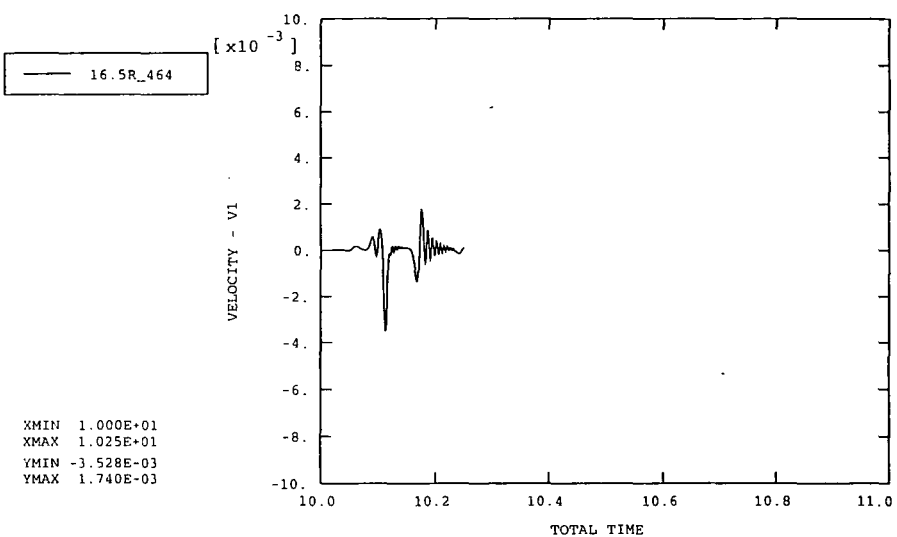
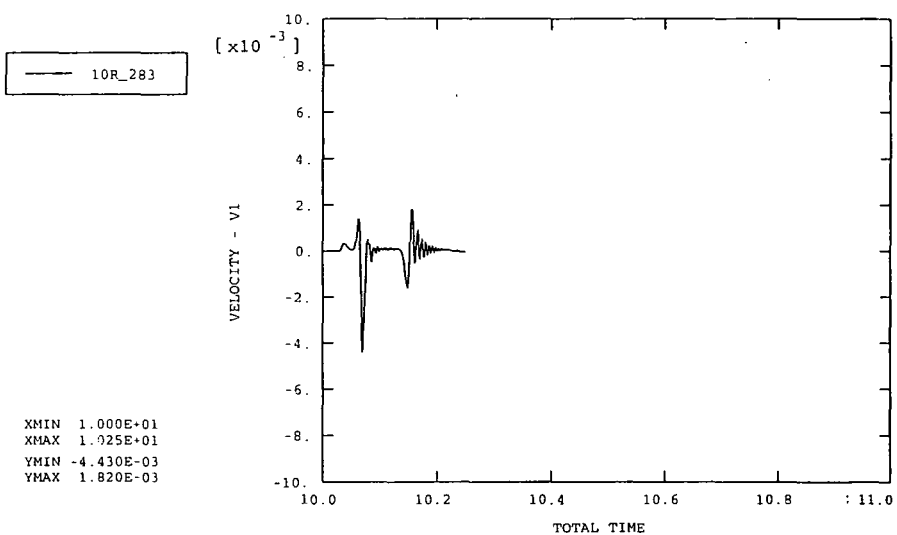
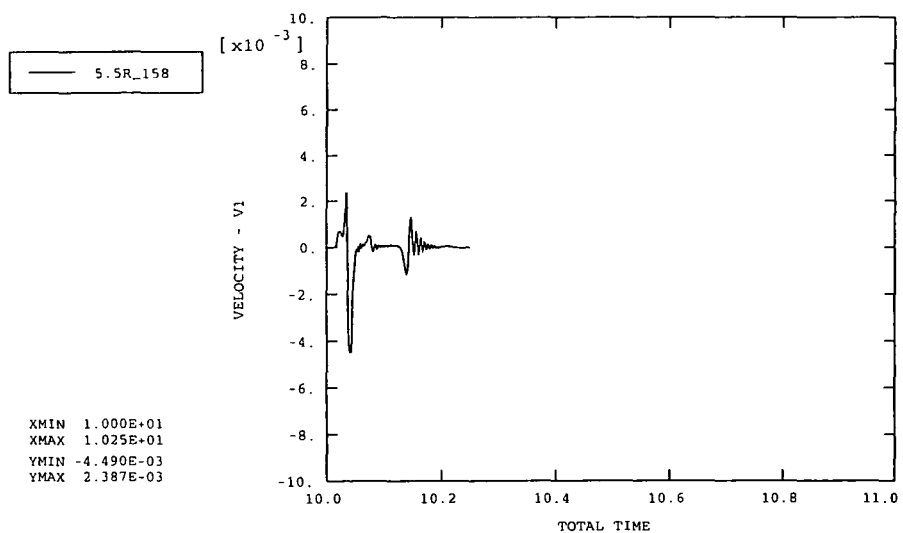


Figure 6.23(b)

Computed radial velocity/time traces for geophones at 5.5m, 10m and 16.5m assuming an overall stiffness for the soil of 150MPa. (M66 site)

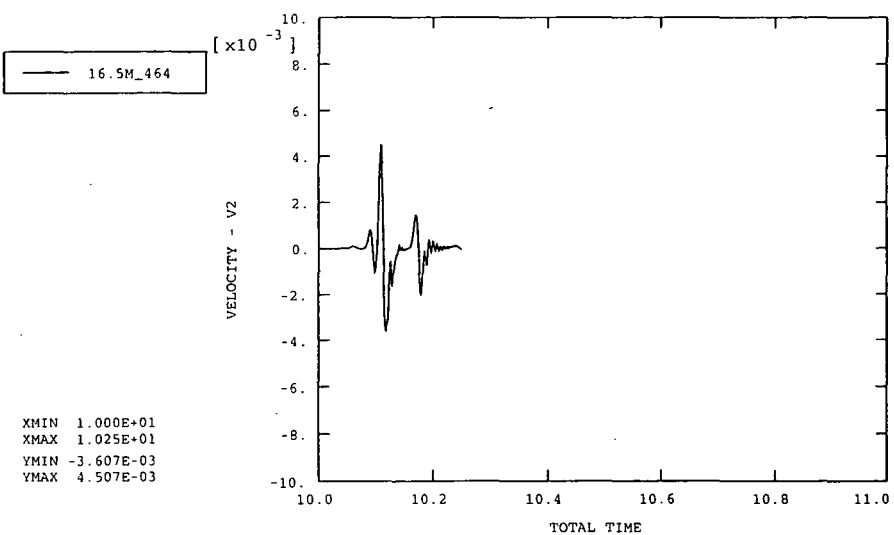
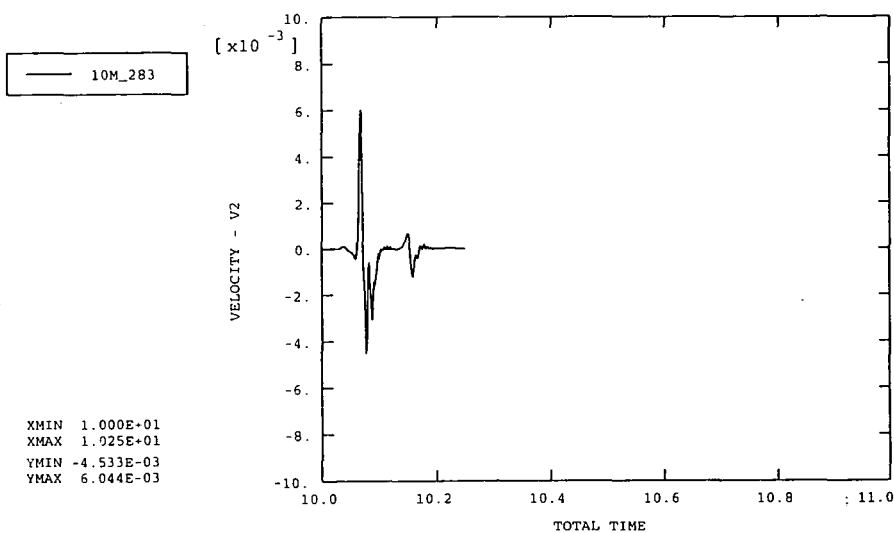
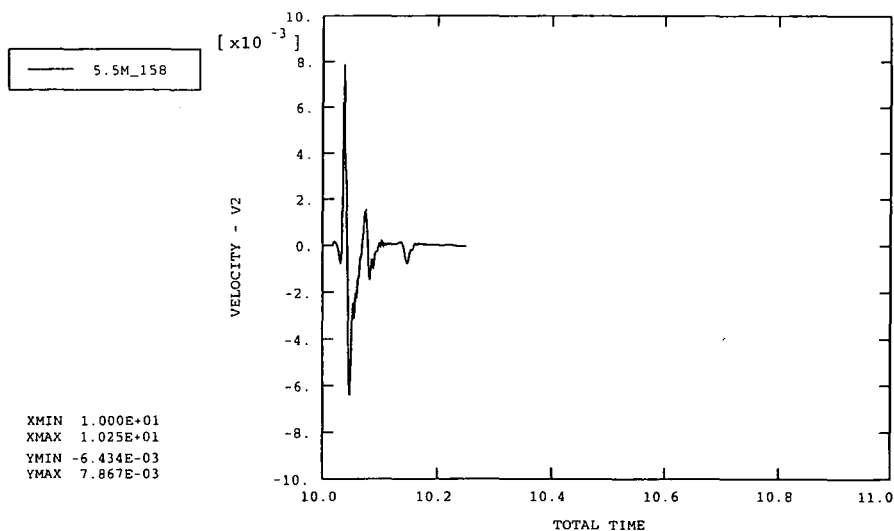


Figure 6.24(a) Computed vertical velocity/time traces for geophones at 5.5m, 10m and 16.5m assuming values of $k_c = 1e^8$ N/m and $c_c^* = 0.1$. (M66 site)

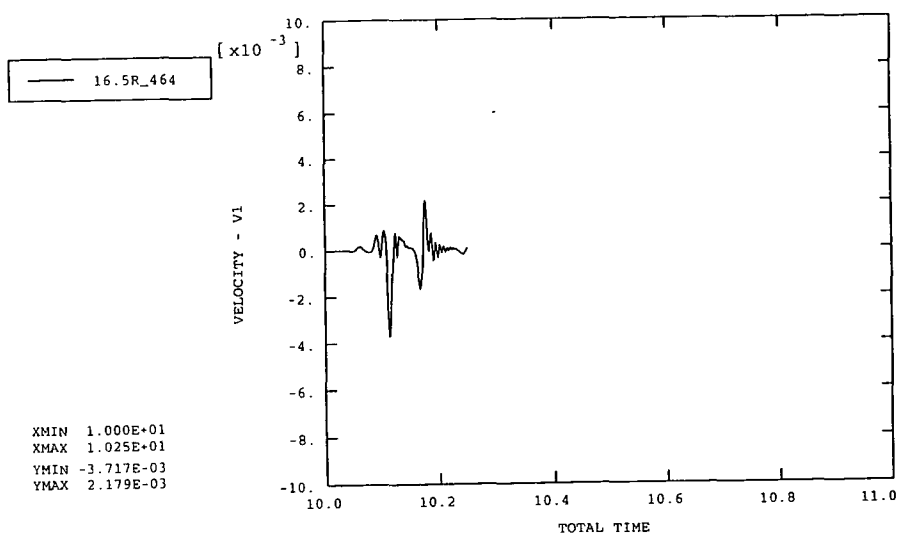
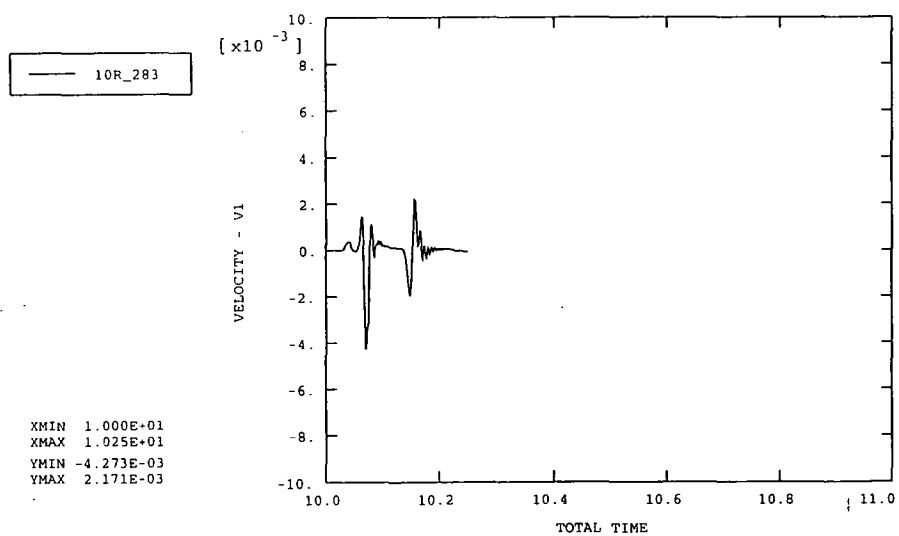
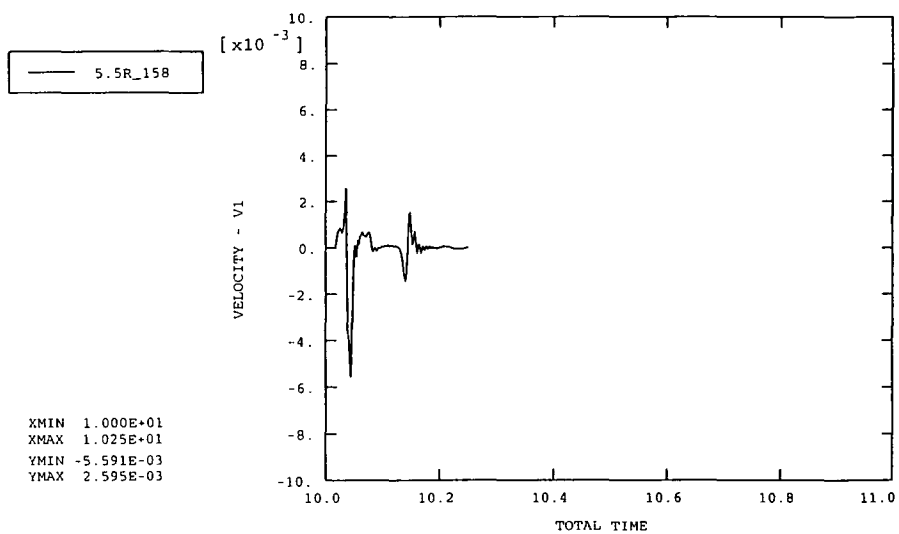


Figure 6.24(b) Computed radial velocity/time traces for geophones at 5.5m, 10m and 16.5m assuming values of $k_c = 1e^8$ N/m and $c_c^* = 0.1$. (M66 site)

ABAQUS

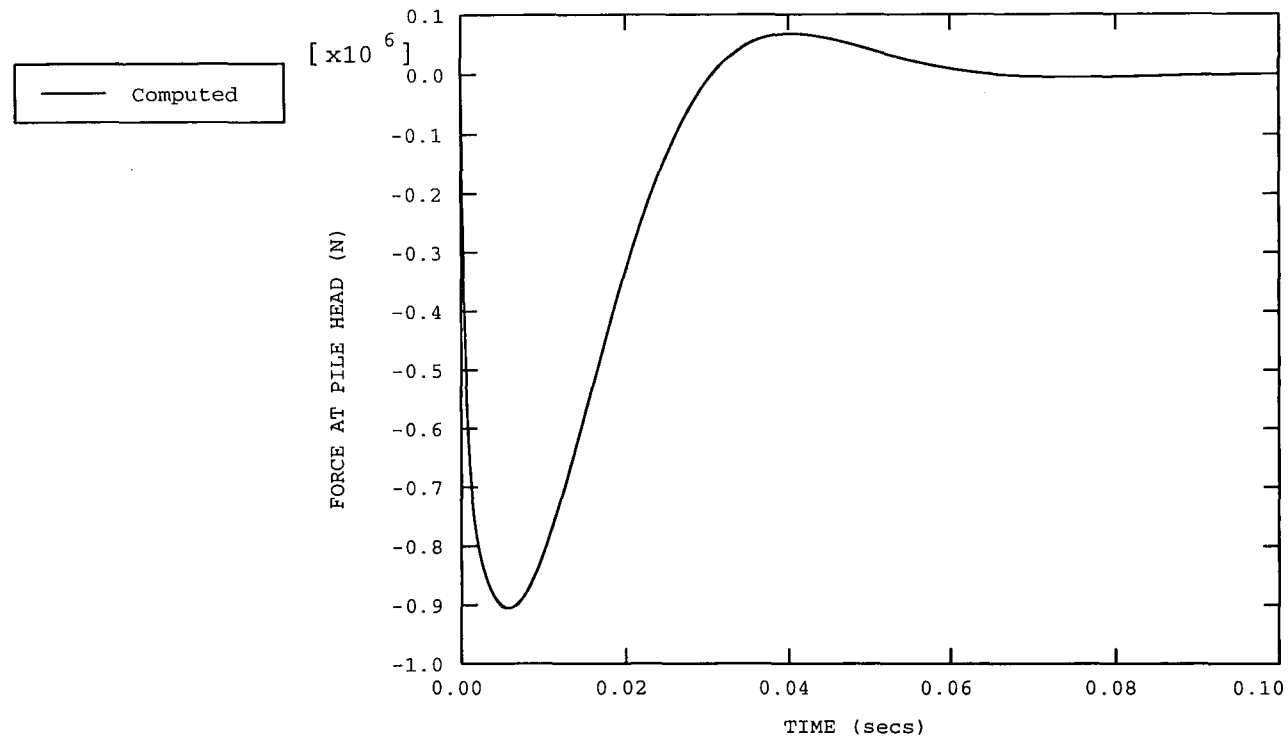


Figure 6.25 Computed force/time function at the pile head (Flitwick site)

ABAQUS

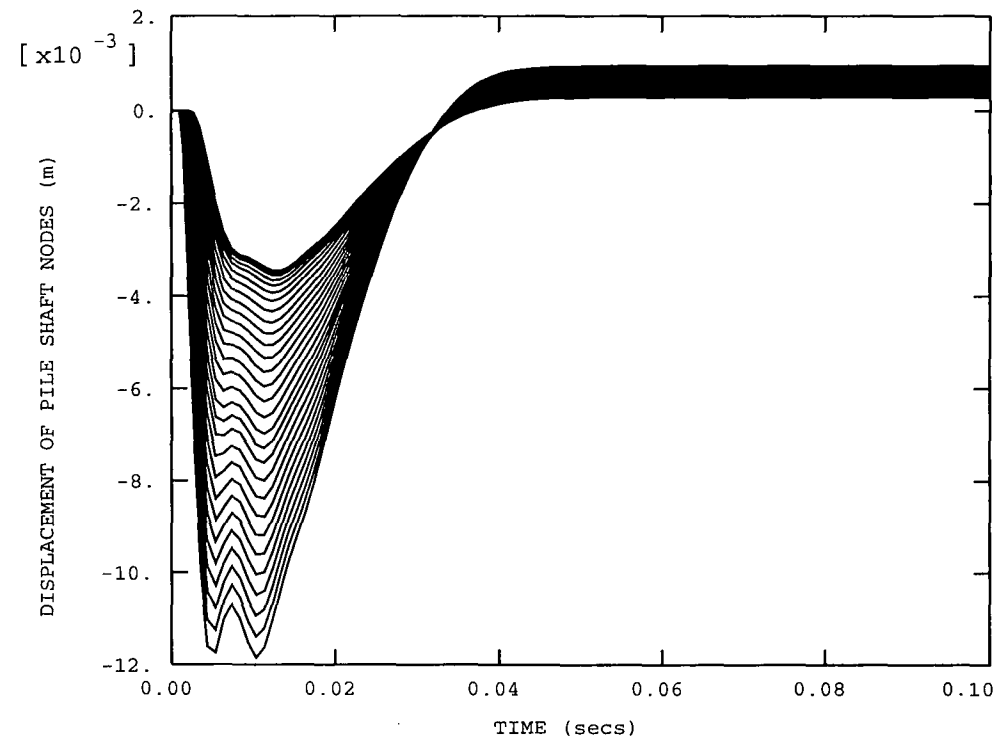


Figure 6.26 Computed vertical displacement/time functions for all of the nodes on the pile/soil interface (Flitwick site)

Ground Vibration Measurement
Drop-hammer, Weight=3200kg, Drop=1m
H-pile, Toe-depth=7m

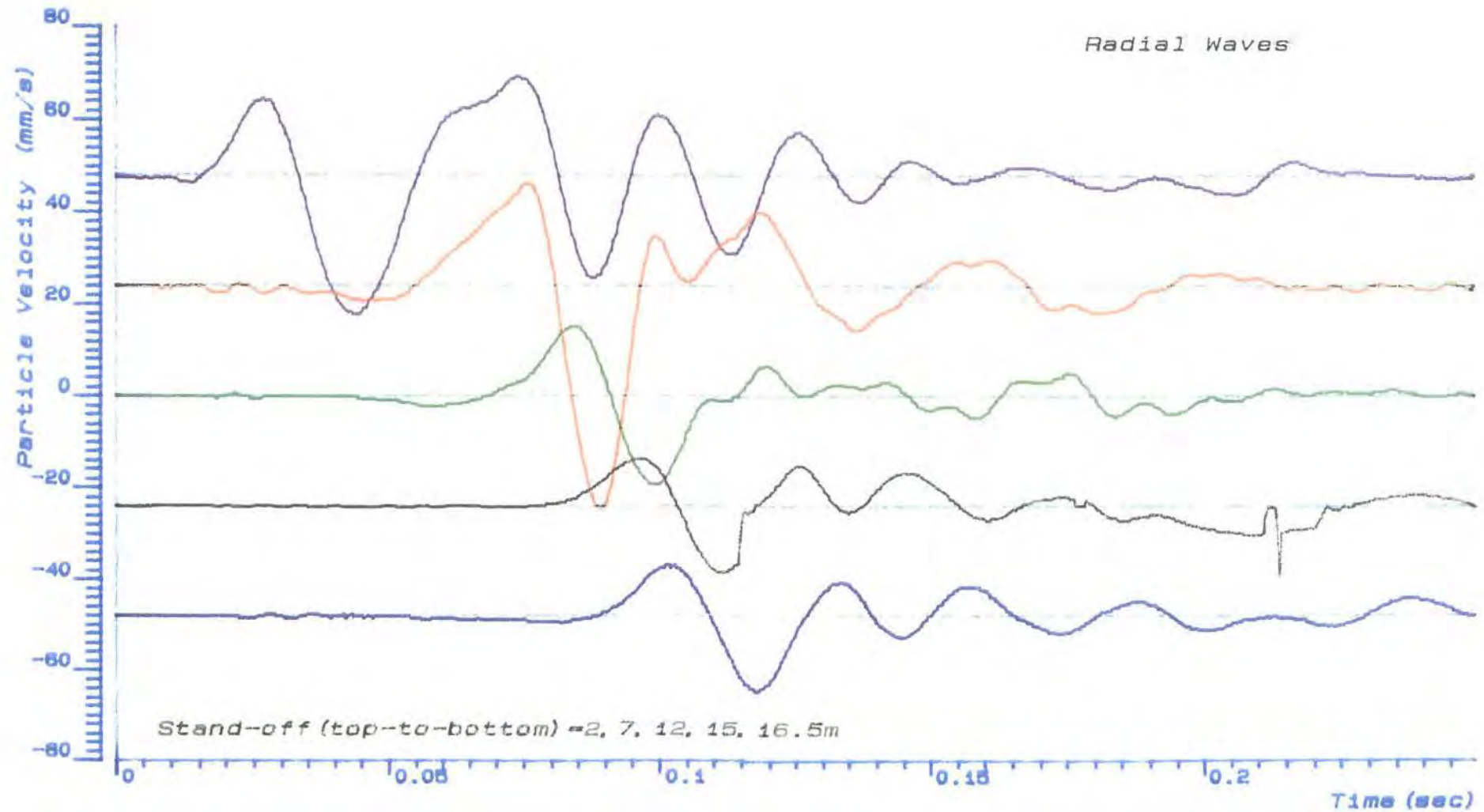


Figure 6.27 Radial velocity/time traces recorded by geophones at 2m, 7m, 12m, 15m, and 16.5m (Flitwick site)

Ground Vibration Measurement
Drop-hammer, Weight=3200kg, Drop=1m
H-pile, Toe-depth=7m

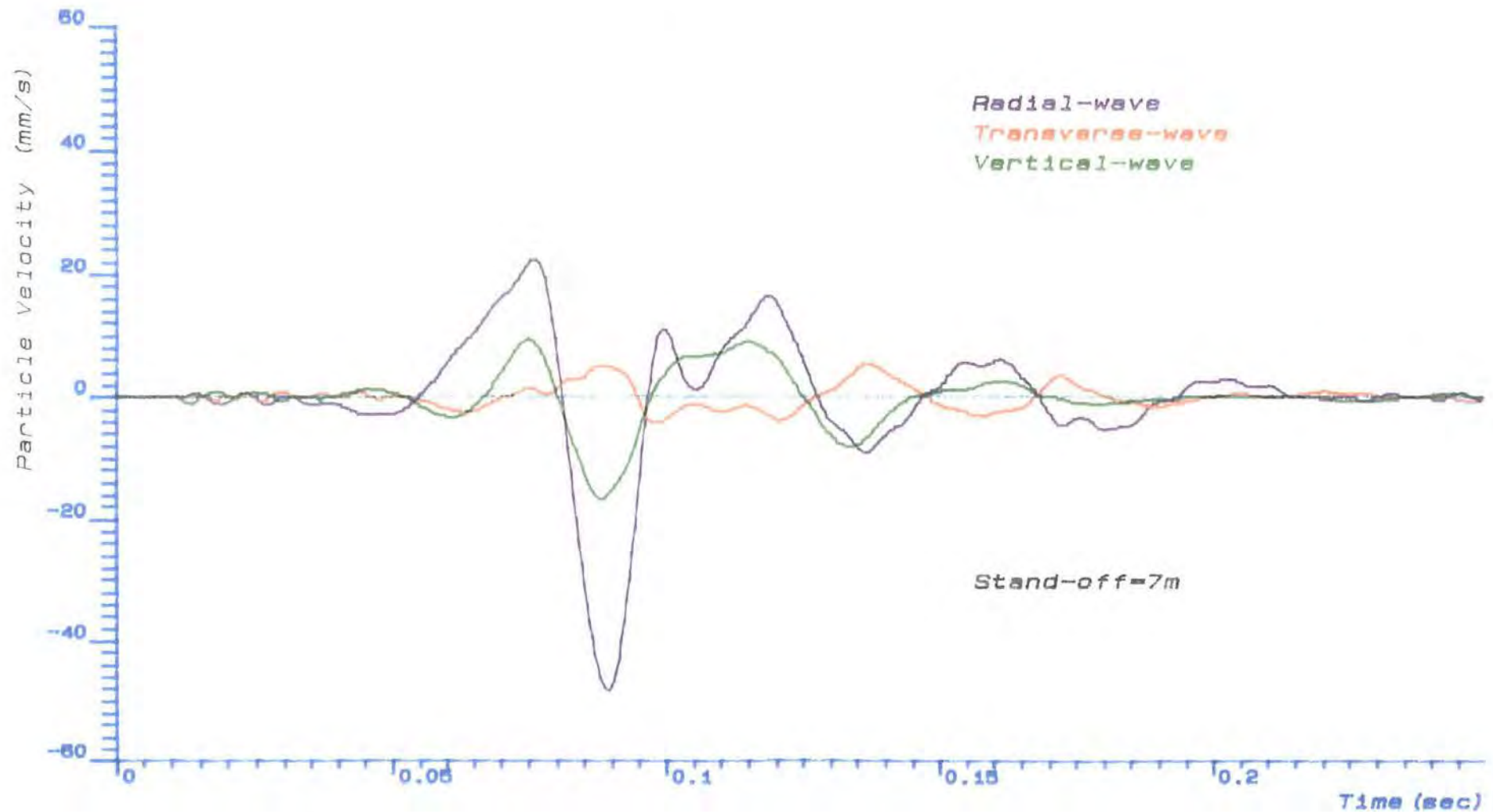


Figure 6.28

Vertical, radial and transverse velocity/time traces recorded by a geophone at 7m from the pile (Flitwick site)

ABAQUS

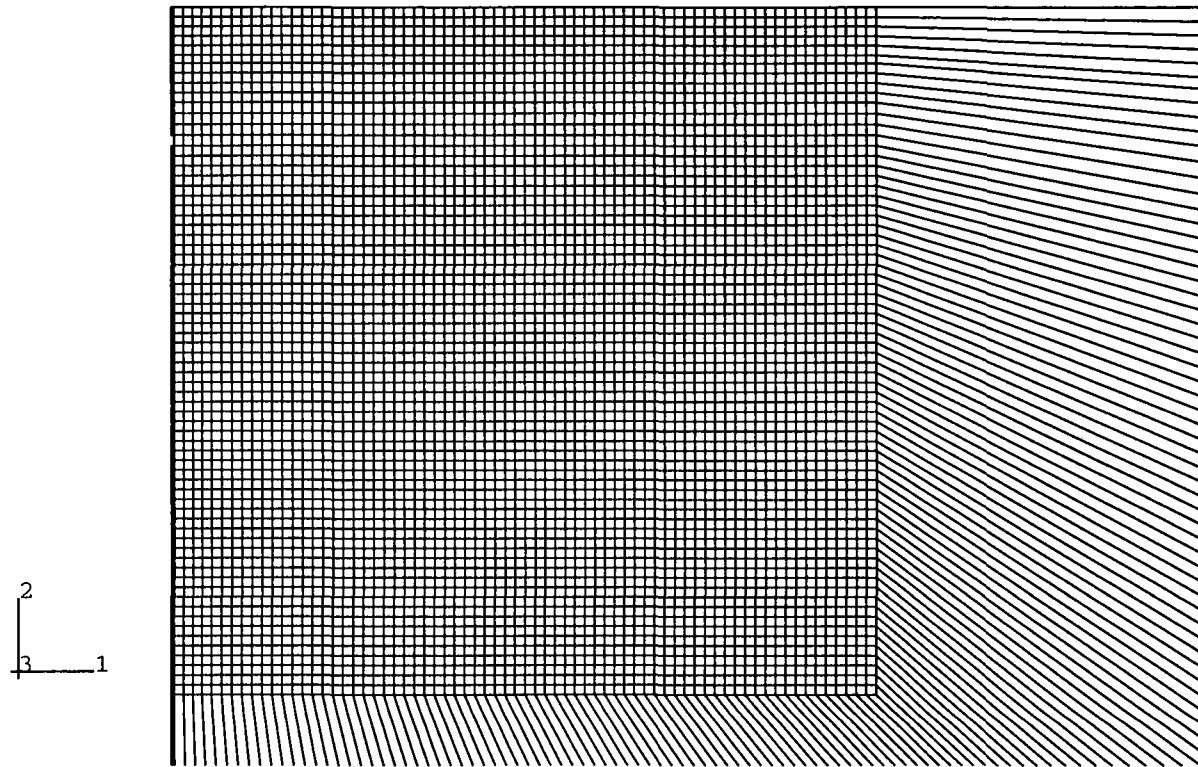
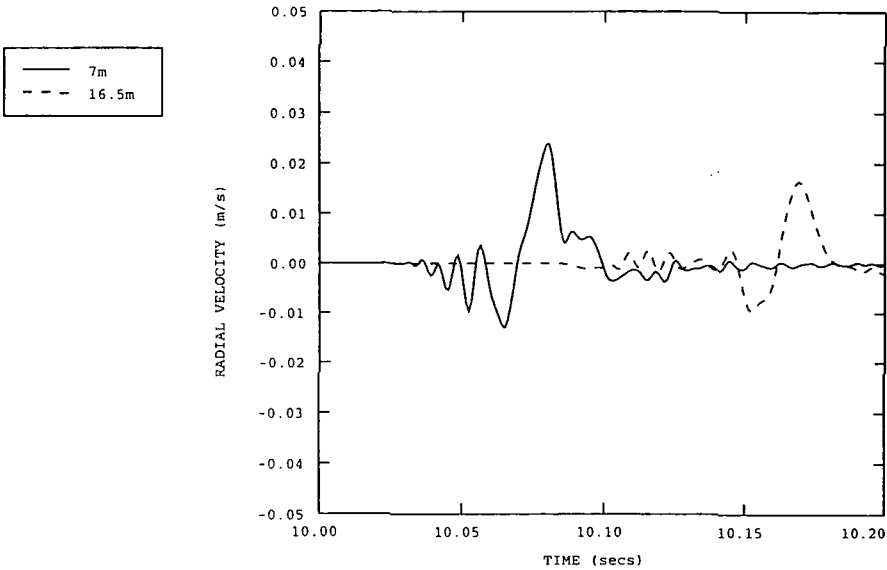


Figure 6.29

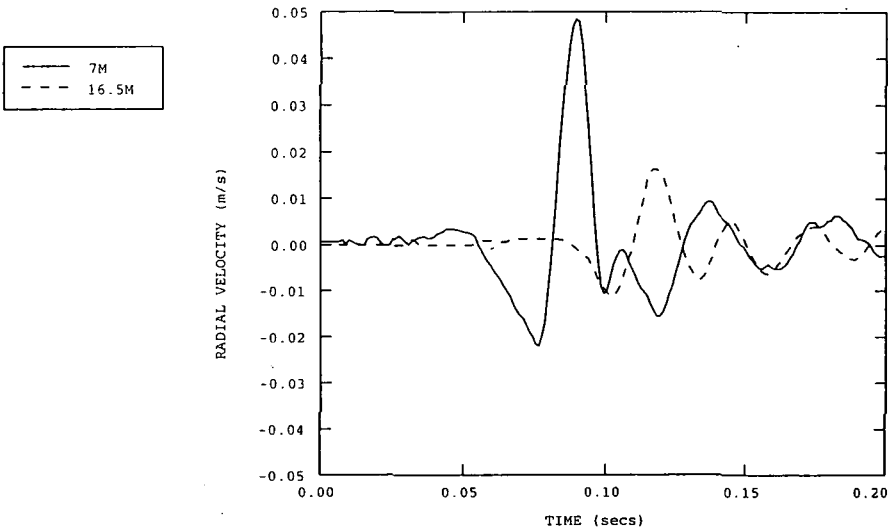
FE/IE mesh used for the wave propagation analysis (Flitwick site)

ABAQUS



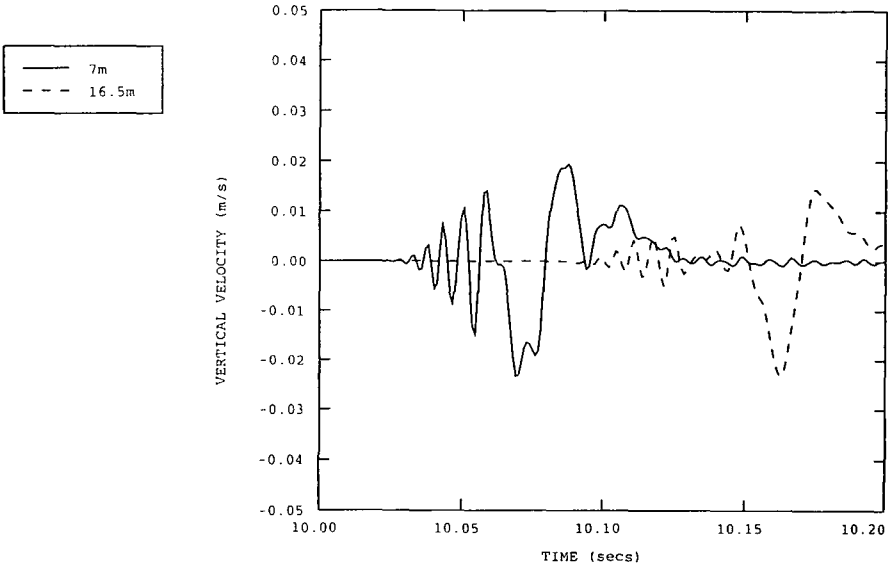
(a) Predicted

ABAQUS

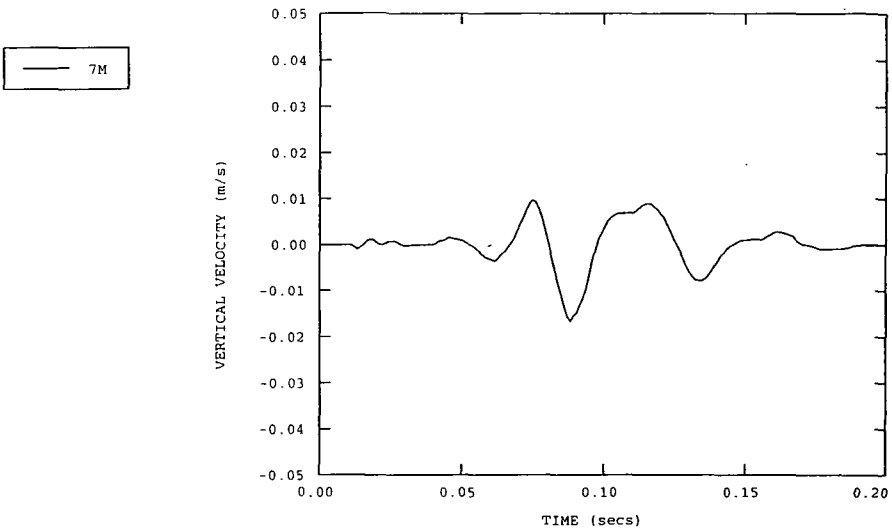


(b) Measured

Figure 6.30 Comparison of the predicted and measured radial velocity/time traces at 7m and 16.5m (Flitwick site) ($E_{\text{overall}} = 66\text{MPa}$)



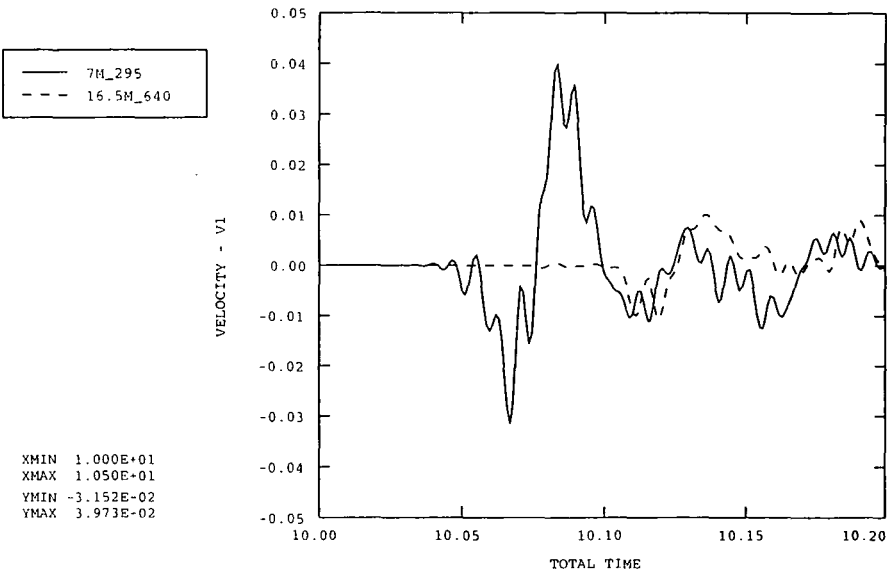
(a) Predicted



(b) Measured

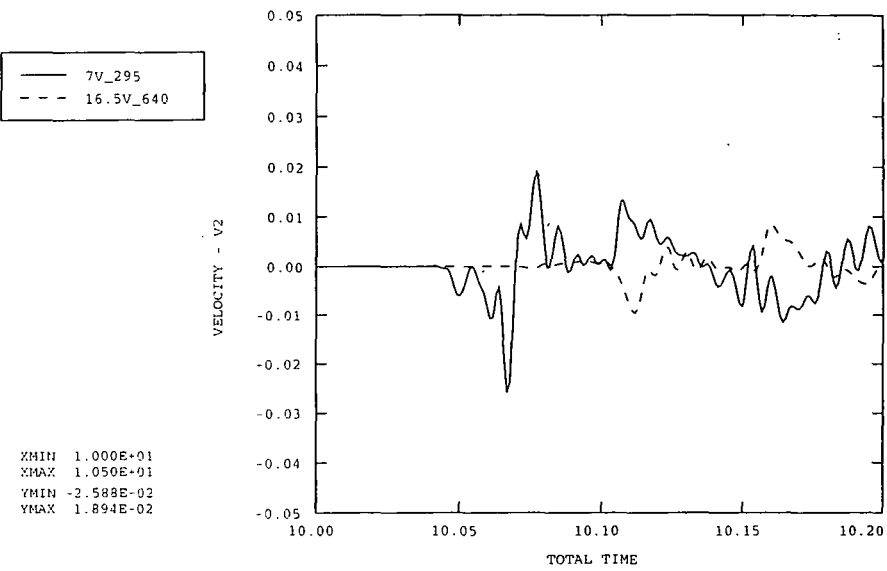
Figure 6.31 Comparison of the predicted and measured vertical velocity/time traces at 7m and 16.5m (Flitwick site) ($E_{\text{overall}} = 66\text{MPa}$)

ABAQUS



(a) Radial velocity/time traces

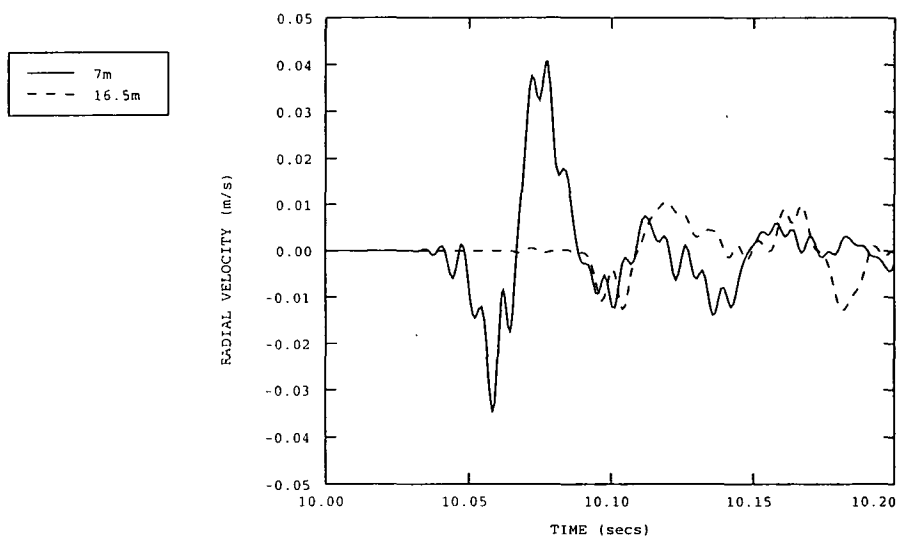
ABAQUS



(b) Vertical velocity/time traces

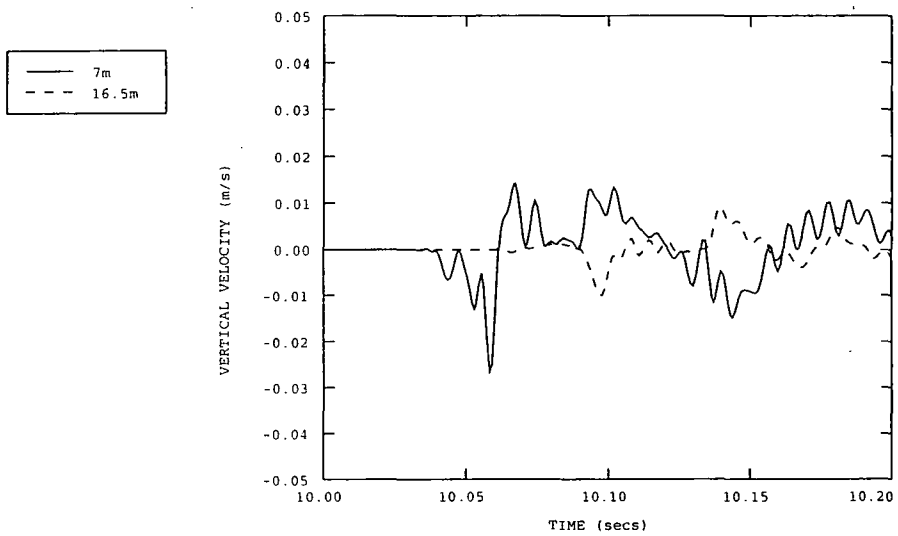
Figure 6.32 Computed velocity/time traces at 7m and 16.5m assuming $E_{\text{clay}} = 20\text{MPa}$ and $E_{\text{sand}} = 200\text{MPa}$ (Flitwick site)

ABAQUS



(a) Radial velocity/time traces

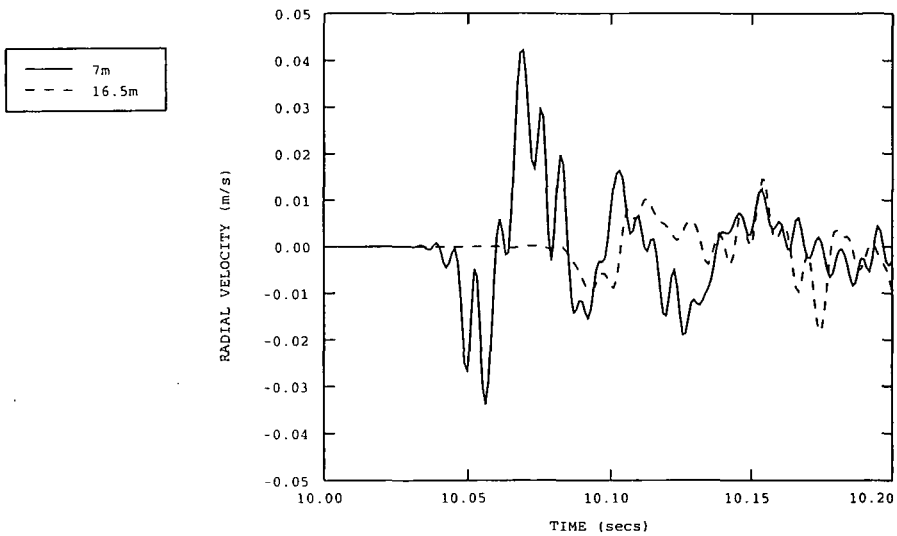
ABAQUS



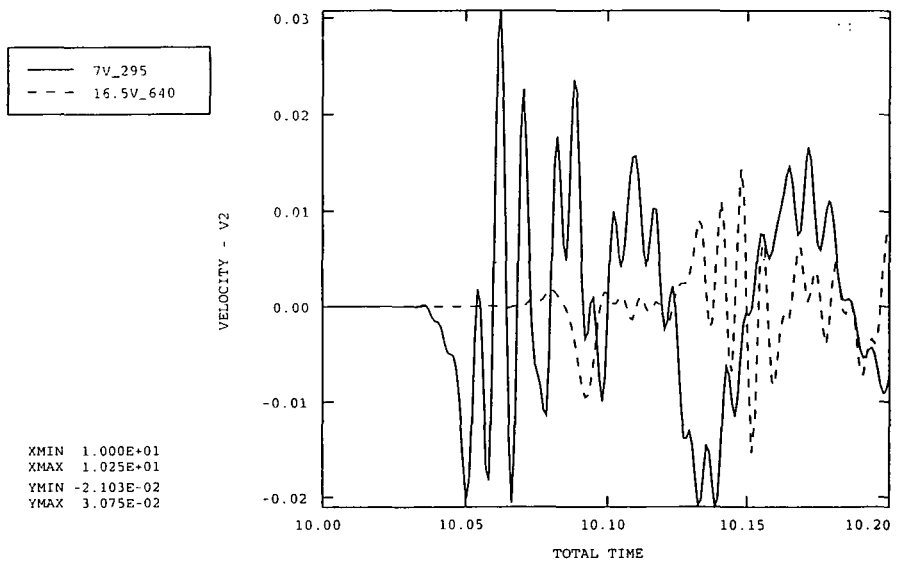
(b) Vertical velocity/time traces

Figure 6.33

Computed velocity/time traces at 7m and 16.5m assuming $E_{\text{clay}} = 27\text{MPa}$ and $E_{\text{sand}} = 267\text{MPa}$ (Flitwick site)



(a) Radial velocity/time traces



(b) Vertical velocity/time traces

Figure 6.34 Computed velocity/time traces at 7m and 16.5m assuming $E_{\text{clay}} = 30\text{MPa}$ and $E_{\text{sand}} = 300\text{MPa}$ (Flitwick site)

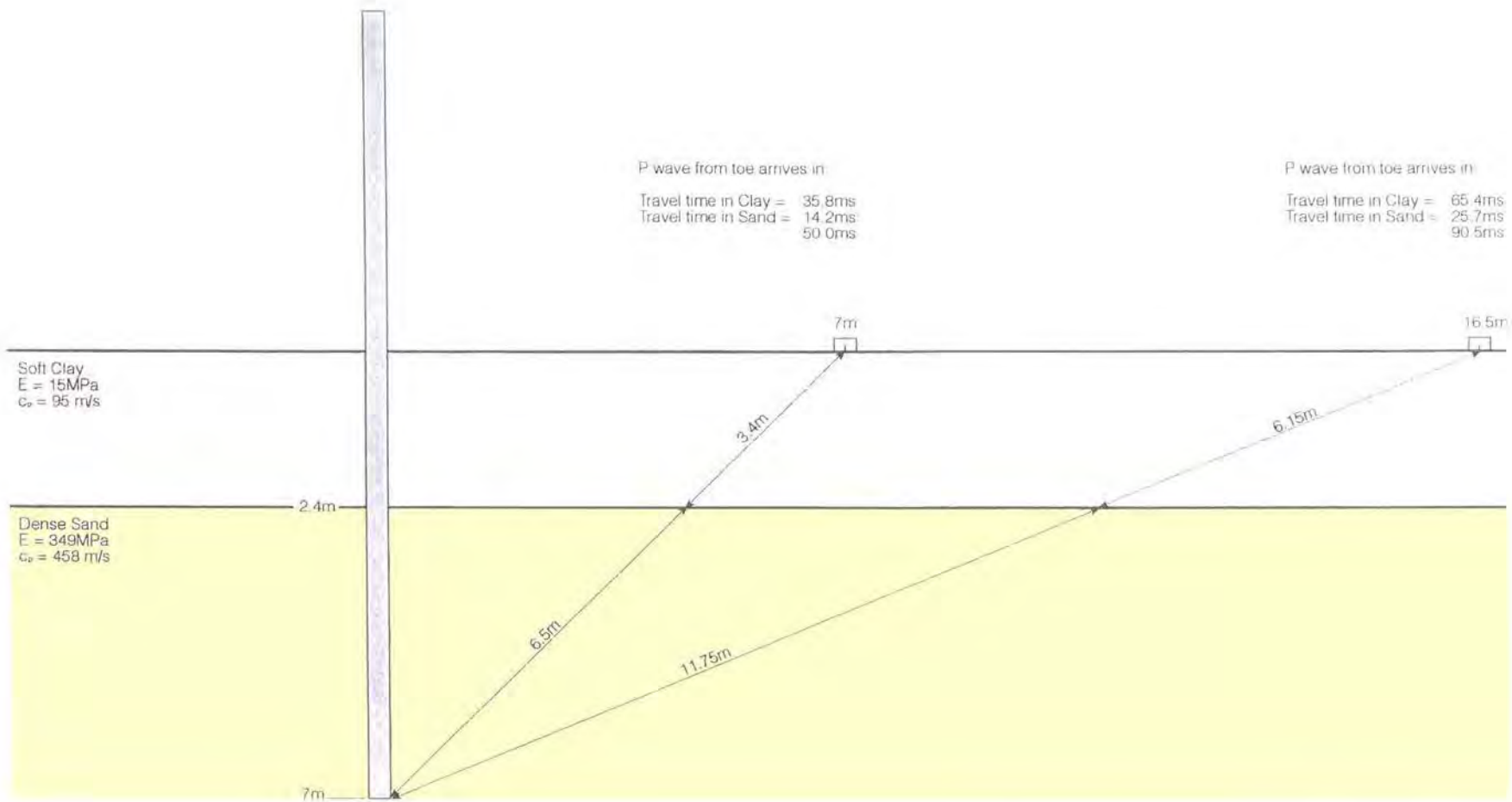
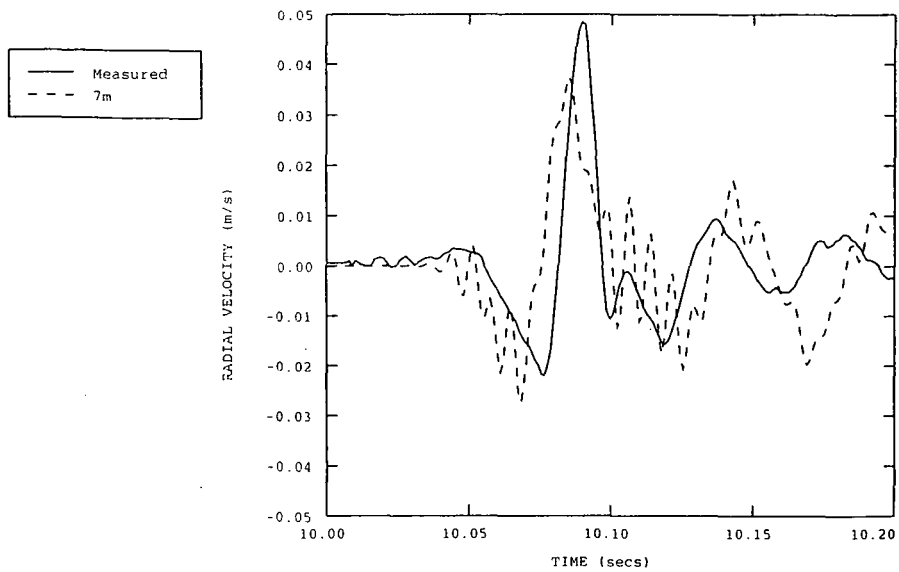


Figure 6.35 Cross-section showing computed travel times of P waves generated at pile toe (Flitwick site)

ABAQUS



ABAQUS

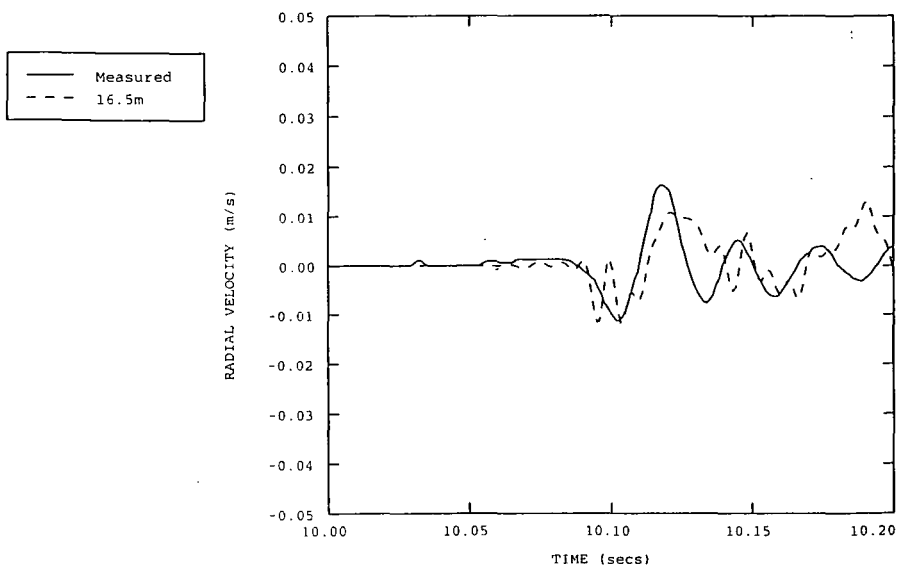
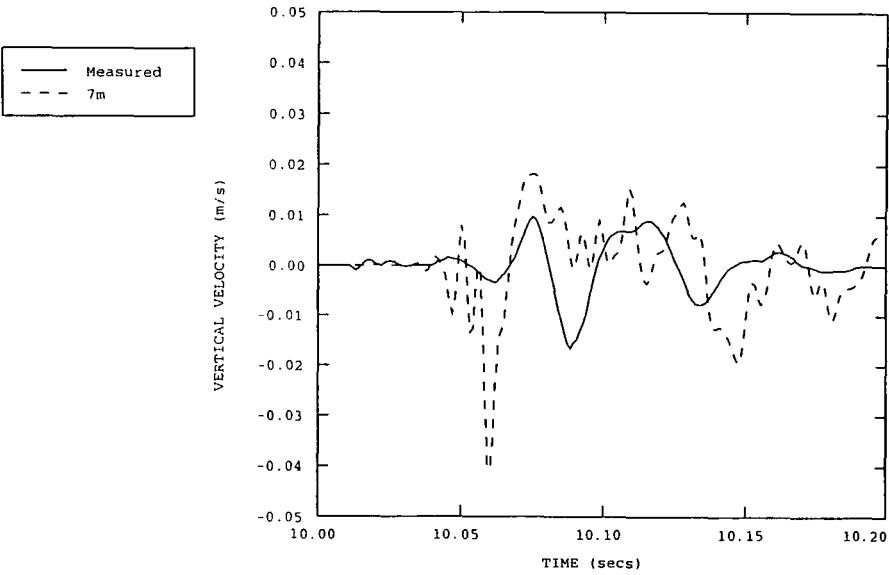


Figure 6.36 Comparison of the predicted and measured radial velocity/time traces for geophones at 7m and 16.5m assuming $E_{\text{clay}} = 15\text{MPa}$ and $E_{\text{sand}} = 349\text{MPa}$ (Flitwick site)

ABAQUS



ABAQUS

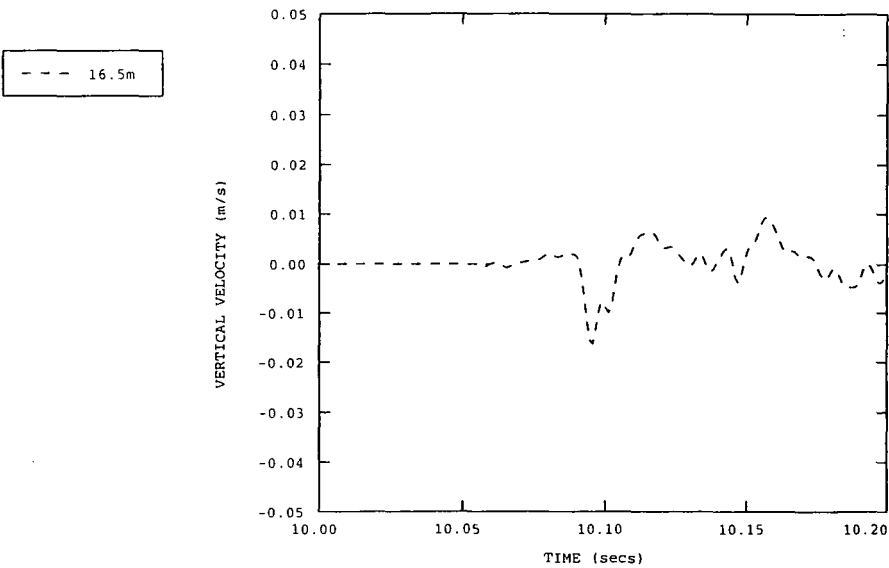
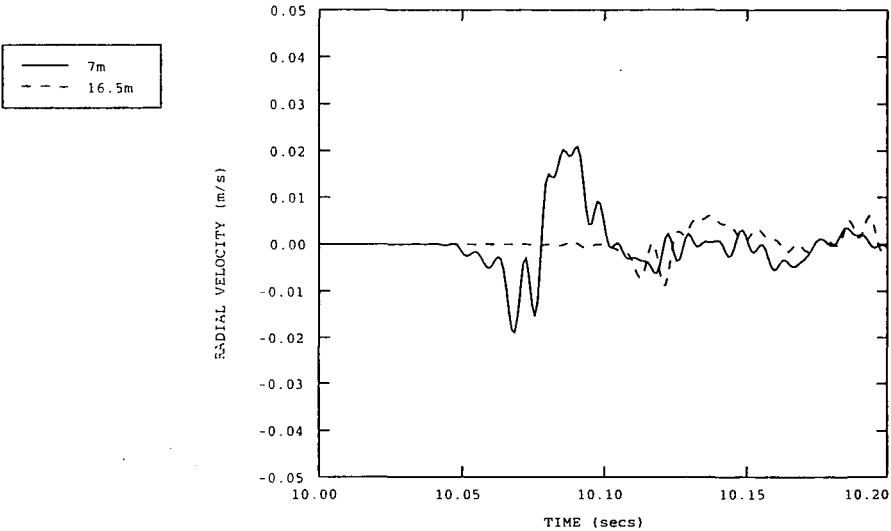
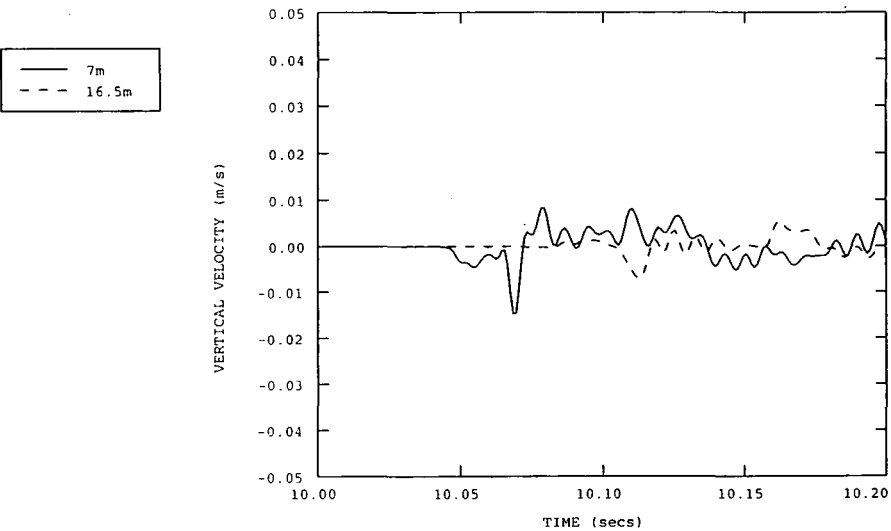


Figure 6.37 Comparison of the predicted and measured vertical velocity/time traces for geophones at 7m and 16.5m assuming $E_{\text{clay}} = 15\text{MPa}$ and $E_{\text{sand}} = 349\text{MPa}$ (Flitwick site)



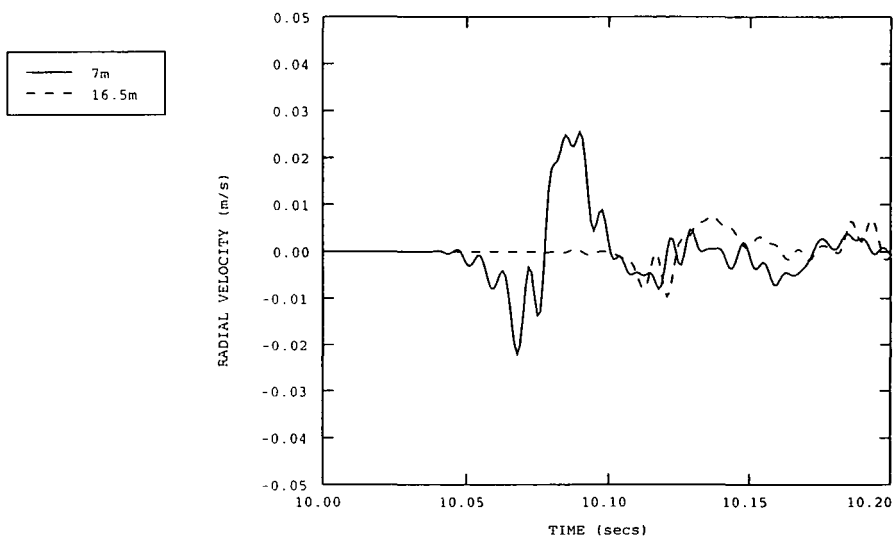
(a) Radial velocity/time traces



(b) Vertical velocity/time traces

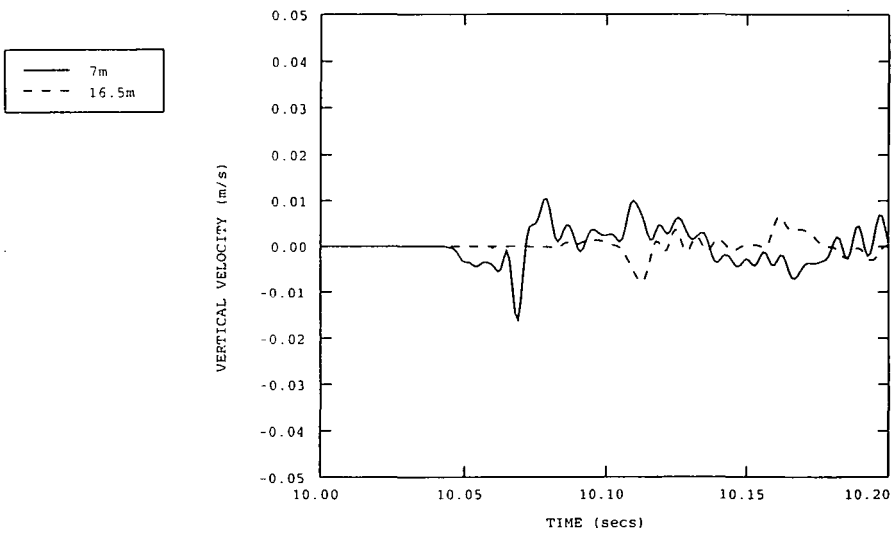
Figure 6.38 Computed velocity/time traces for geophones at 7m and 16.5m assuming an overall coefficient of friction of 0.2 ($E_{\text{clay}} = 20\text{MPa}$ and $E_{\text{sand}} = 200\text{MPa}$) (Flitwick site)

ABAQUS



(a) Radial velocity/time traces

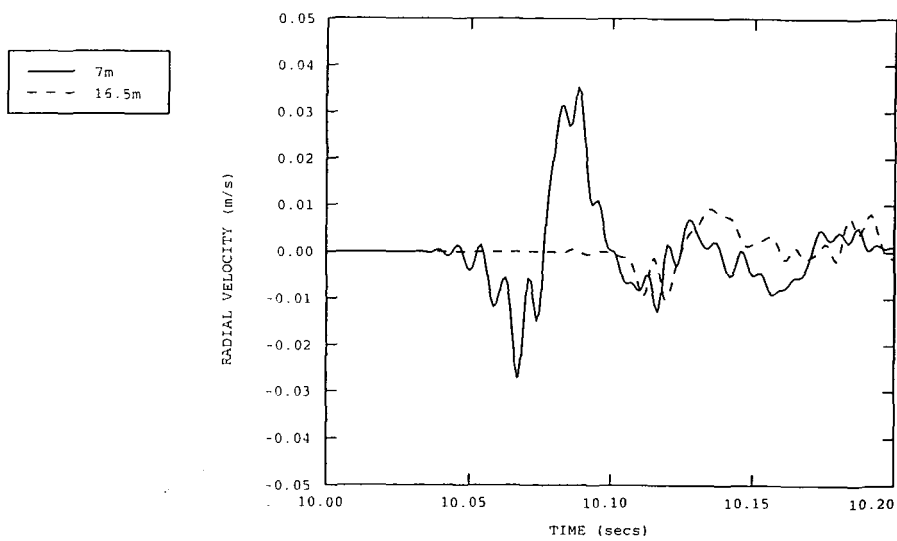
ABAQUS



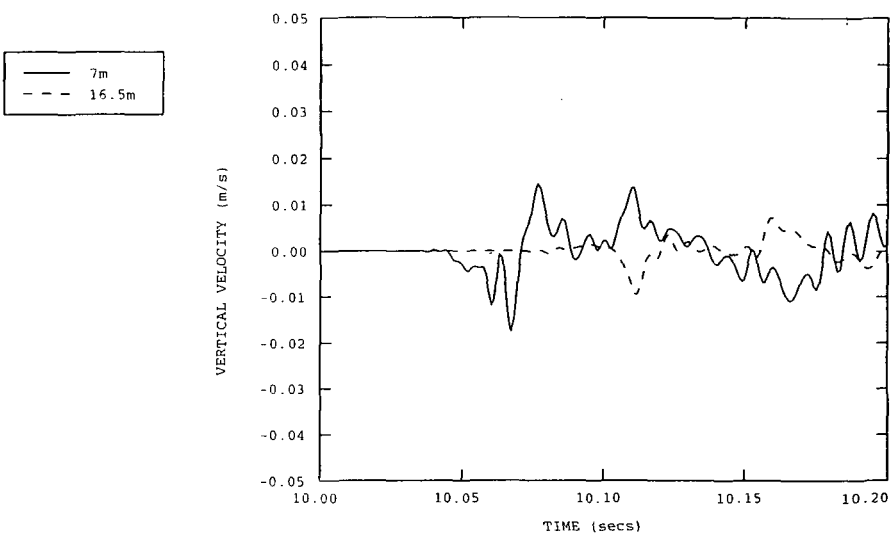
(b) Vertical velocity/time traces

Figure 6.39

Computed velocity/time traces for geophones at 7m and 16.5m assuming an overall coefficient of friction of 0.4 ($E_{\text{clay}} = 20\text{MPa}$ and $E_{\text{sand}} = 200\text{MPa}$) (Flitwick site)



(a) Radial velocity/time traces



(b) Vertical velocity/time traces

Figure 6.40 Computed velocity/time traces for geophones at 7m and 16.5m assuming an overall coefficient of friction of 0.7 ($E_{\text{clay}} = 20\text{MPa}$ and $E_{\text{sand}} = 200\text{MPa}$) (Flitwick site)

CHAPTER 7

INCORPORATION OF STRUCTURES INTO THE NUMERICAL MODELS FOR VIBRATORY AND IMPACT PILING

7.1 INTRODUCTION

The environmental consequences of the ground vibrations induced by pile driving operations can be grouped into three: disturbance to the occupiers of neighbouring properties; direct effects of the vibrations on adjacent structures and buried services; and compaction settlement of loose granular soils. In severe cases, buildings and buried services in the near vicinity of pile driving operations may be at risk of cosmetic or minor structural damage, Head & Jardine (1992), Wiss (1967) and Todd (1994). Two British standards, BS5228 Part 4 (1992), BS7385 Part 2 (1993) and Eurocode 3 (CEN, 1998) (and a number of standards from around the world), address the specific issue of threshold limits of vibration on nearby structures so as to provide an acceptably low risk of cosmetic and structural damage. These various national standards, and indeed the two British standards offer conflicting advice. This is perhaps not surprising, since the basis for the recommendations is primarily empirical, sometimes taking account of the condition of the building. There is general recognition that continuous vibration is more damaging than intermittent, and also that high frequency vibrations pose a smaller risk than low frequency vibrations. However, the global approach adopted by these standards considers neither the interactive effects of foundation and structure, nor detailed frequency and duration. There seems to have been a general move towards more restrictive threshold limits in recent years in the shape of the draft DIN 4150 (1990) and CEN (1998), although BS 7385 Part 2 is less conservative than the earlier BS 5228 Part 4.

Within this framework of empiricism, it would be of considerable reference value to the piling industry to clarify the risks of direct vibration damage, and to classify combinations of piling and structure systems which offer higher or lower risk of damage. Adaptation of the numerical models developed in Chapters 5 and 6 to incorporate various structural forms would allow the prediction of ground response resulting from various types of pile driving operations and the assessment of risk to adjacent structures prior to the commencement of site operations.

This chapter commences with a description of the chronological development of the soil-structure interaction model. It describes the difficulties that were encountered and how they were resolved, and the philosophy behind the model itself which is described in Section 7.3. The results of applying verified piling-induced ground excitations from vibratory and impact piling at a site in Flitwick, Bedfordshire to the soil-structure interaction model are described in Sections 7.4 and 7.5 respectively. Various structural forms typical of steel framed structures and domestic brick walls were modelled. Conclusions and recommendations for further work are given in Section 7.6.

7.2 CHRONOLOGICAL DEVELOPMENT OF THE MODEL

The models described in Chapters 5 and 6 for the computation of ground waves from pile driving are constructed of axisymmetric finite and infinite elements (Figure 7.1).

Although a semi-infinite axisymmetric FE/IE mesh is the optimum representation for the attenuation of ground waves from a central excitation source, the natural choice for a section through a frame structure, or for a wall element of a brick building, is a plane stress configuration. A full representation of a pile-soil-structure would require a full three-dimensional model.

Initial comparisons of the computation times required for axisymmetric and 3D analyses of simple wave propagation problems indicated that the 3D analyses took 16 to 17 times longer than the corresponding axisymmetric analyses. Given that the FE analyses undertaken during the development of the vibratory and impact models described in Chapters 5 and 6 generally took 6-10 hours to run, it became apparent that full 3D analyses of wave propagation problems would be prohibitively time-consuming. It was therefore necessary to consider alternative techniques for modelling the pile-soil-structure.

The original proposal for this research suggested that a plane strain model could be used to model the soil and structure with a de-rated energy input so as to match the wave energy of the axisymmetric computation at the required stand-off distance from the pile. However, this proposal was rejected following the discovery of the complex non-monotonical attenuation (the 'standing wave' phenomenon) of ground waves generated by vibratory piling as described in Chapter 5.

It was therefore decided that the optimum representation of the problem was to develop a simplified 3D model with the number of degrees of freedom kept to a minimum in order to reduce the duration of the FE analyses. This was achieved in two ways. Firstly, the full 3D model was reduced to a wedge-shaped "slice" of the axisymmetric system (Figure 7.2), two elements thick in the θ dimension, with appropriate restraints on the boundaries. Secondly, the elements used in the 3D model were reduced from 20-noded quadratic brick elements (corresponding to 8-node quadrilateral axisymmetric elements) to 8-noded linear brick elements. This effectively halved the number of nodes per wavelength and resulted in some loss of accuracy in modelling the waveforms. This is discussed in more detail later in this Chapter. The 3D infinite elements modelling the far-field were reduced to 8-noded linear one-way infinite elements and the elements representing the soil under the pile toe were reduced to 6-noded linear triangular prism elements.

A full 3D analysis of the pile-soil interaction was not considered to provide any additional benefit over the axisymmetric pile-soil interaction models described in Chapters 5 and 6. The verified vertical soil displacements on the pile-soil interface computed by the axisymmetric pile-soil interaction models were therefore applied to the corresponding soil nodes in the 3D model as shown in Figure 7.3.

The radial (r) and axial (z) dimensions of the elements in the axisymmetric FE meshes were transferred directly to the cylindrical coordinate system of the 3D model as radial (r) and axial (z) dimensions. The size of the elements in the third dimension (θ) of the cylindrical coordinate system was chosen to optimise the aspect ratio of the elements at the position of the structure. The aspect ratio for a 3D element is defined as the ratio of the maximum distance between any two faces of the element to the minimum distance between any two faces of the element. Ideally, the aspect ratio should be less than 5.0. As the size of the elements in the θ direction increases with distance from the symmetry

axis in an axisymmetrical model, the aspect ratio will increase accordingly. It was therefore decided to design the mesh to have a minimum aspect ratio at a radius of 17.5m and then centre the required structure about this radius. The θ dimension of the elements was chosen to be 12° which gave the optimum value of aspect ratio (3.7) at a radius of 17.5m for the particular mesh size and taking account of the restrictions imposed on the minimum size of the “slice” by ABAQUS. (The aspect ratios of the elements in this mesh varied from 15.6 at a radius of 0.1525m to 15.3 at a radius of 35m.)

It was considered unlikely that the increasing size of the 3D elements in the θ dimension would cause any significant reflection in the mesh because the simulated waves have no transverse component. It should be noted that field measurements of vibrations from pile driving usually contain a transverse component. Any attempt to simulate this effect would require a model with a uniform θ dimension in order to prevent spurious wave reflection within the FE mesh itself.

The performance of the 3D wedge-shaped mesh was then tested by comparison with the results of the axisymmetric wave propagation analyses. The same verified soil displacements were applied to the soil nodes on the pile/soil interface in both models and the resulting particle velocity/time traces were compared. The results are presented in Sections 7.4.2 and 7.5.2 below.

Once the 3D model was shown to be modelling the ground waves satisfactorily, various structural forms, typical of steel frame structures and of domestic brick walls were incorporated into the model. The 3D FE/IE model that has been developed for pile-soil-structure interaction is presented in the following section.

7.3 A FINITE ELEMENT MODEL FOR PILE-SOIL-STRUCTURE INTERACTION

7.3.1 General

The simulation of pile-soil-structure interaction has been developed as a two-stage procedure as follows.

In the first stage, the axisymmetric FE/IE models that have been developed for the computation of ground waves generated by pile driving (see Chapters 5 and 6) are used to compute the vertical soil displacements on the pile/soil interface.

In the second stage, the time-based displacement functions computed by the axisymmetric FE/IE model are applied to the corresponding soil nodes in a 3D wedge-shaped model of a “slice” of the axisymmetric system, see Figure 7.3. This allows connectivity with two-dimensional plane stress finite element representations of various structural forms.

7.3.2 Mesh design (Representation of the ground)

A three-dimensional wedge-shaped FE/IE mesh with axial symmetry is used to represent the ground. This is much less computationally expensive than a full three-dimensional analysis. Eight-noded (first order) linear brick elements are used to represent the soil although a more accurate solution would be achieved with 20-noded

(second order) quadratic brick elements if the analyses could be performed within a reasonable time period. The latter is likely to become possible as the power and speed of computers increase. The soil under the pile toe is represented by 6-noded linear triangular prism elements although again a more accurate solution would be achieved with 15-noded quadratic triangular prism elements.

Since the mesh will be used in dynamic analyses, it is designed to be as uniform as possible in order to prevent spurious reflection within the finite element mesh. This is easily achieved in the radial and axial dimensions but the size of elements in the θ direction increases with distance from the symmetry axis in an axisymmetrical wedge-shaped model. The θ dimension of the model should therefore be chosen to optimise the aspect ratios of the elements in the particular area of interest (see Section 7.2).

The 3D wedge shaped model is two elements thick in the θ dimension, with appropriate radial and symmetry boundary conditions as shown in Figure 7.4. In order to model axial symmetry, the nodes on the axial symmetry axis ($r=0$) are restrained in the radial direction. The nodes on the pile/soil interface are also restrained in the radial direction to simulate the horizontal restraint provided by the pile. The nodes on the two “faces” of the wedge at $\theta = 0^\circ$ and 12° are restrained in the θ direction in order to model axial symmetry about the z axis.

The infinite elements provided within the ABAQUS program (simple tuned dampers) are placed around the boundaries of the FE mesh to model the far-field and minimise the reflection of outgoing waves back into the FE mesh. Eight-noded linear, one-way infinite elements are used for compatibility with the linear finite elements used in the mesh.

7.3.3 Application of the computed piling induced ground excitation to the three-dimensional model

The first stage of analysis comprises computation of the piling induced ground excitation using one of the axisymmetric FE/IE models developed in Chapters 5 and 6. Both the vibratory piling and the impact piling models require computation and output of the vertical soil displacements on the shaft and the toe of the pile/soil interface. As it has been shown that the ground response is very sensitive to the magnitude and distribution of soil movements around the pile, a good match with measured vibration traces can be assumed to indicate that the computed soil excitation is approximately correct.

The verified vertical soil displacements on the pile/soil interface computed by the axisymmetric models are then used as input to the three-dimensional FE/IE model. The displacement/time functions computed for each of the nodes representing the soil around the pile shaft and toe are directly applied to the corresponding nodes in the 3D model as shown in Figure 7.3.

7.3.4 Representation of a steel portal frame

In order to investigate the effects of the propagating ground waves on an in-plane slender frame structure, it was decided to add an FE representation of a steel portal frame structure constructed of typical Universal Beams and Columns to the free surface of the 3D wedge shaped FE/IE model.

As the computed ground waves do not contain a transverse component, it is only necessary to model a single cross-section through the structure because restraint in the third dimension will not affect the radial and vertical displacements of the structure.

A variety of beam element types can be inserted into an ABAQUS finite element analysis. These include open thin walled sections such as I-sections and L-sections. The parameters required to define an I-section in ABAQUS are shown in Figure 7.5. The orientation of the beam cross-section can be defined by the user or ABAQUS will calculate a default orientation. The orientation is defined in terms of a local, right-handed axis system.

The appropriate nodes of the beam elements are joined to the nodes of the 3D brick elements as a simple pinned connection representative of pad footings. It is possible to create varying degrees of fixity to this connection in ABAQUS by applying linear or non-linear constraints between nodes.

7.3.5 Representation of a brick wall

In order to investigate the response of a very stiff structure to the ground waves induced by piling, it was decided to add an FE representation of an in-plane brickwork wall, typical of those used in domestic housing.

Two-dimensional four-noded bilinear plane stress elements are used to represent the brickwork wall. The wall elements are joined to the appropriate nodes of the 3D brick elements as a simple pinned connection representative of a shallow strip foundation.

7.4 VIBRATORY WAVES ON SOIL AND STRUCTURE

7.4.1 General

The performance of the three-dimensional FE/IE wedge-shaped soil-structure model was investigated by inputting the verified excitation data from vibratory piling at Flitwick, Bedfordshire (Section 5.8 in Chapter 5). Firstly, the ground response computed by the 3D model was compared to that computed by the axisymmetric model for the same excitation data to check the accuracy of the 3D model. Typical structural forms representative of steel portal frames and domestic brick walls were then added to the free surface of the 3D model.

The ground conditions and vibratory piling data for the Flitwick case history are described in full in Chapter 5 (section 5.8), but in summary comprised the vibratory installation of a 12m long steel H pile into dense sands to a depth of 7m. The axisymmetric FE/IE model developed for vibratory piling computed a very similar ground response to that measured.

The 3D model was constructed using exactly the same parameters as the axisymmetric model.

7.4.2 Comparison of ground response predicted by axisymmetric mesh and 3D mesh

The radial and vertical particle velocities computed by the axisymmetric and 3D models at horizontal distances of 2m, 7m, 10m and 16.5m (the positions of the geophones) are compared in Figures 7.6 and 7.7 respectively. These figures demonstrate that both

models predict a very similar ground response and that there is an almost negligible loss of accuracy in using the 3D wedge-shaped model with bilinear brick elements as opposed to the axisymmetric model with quadratic elements.

It was therefore concluded that the 3D wedge-shaped FE/IE model with bilinear brick elements modelled the propagation of vibratory ground waves with sufficient accuracy.

7.4.3 Effect on a portal frame structure

A typical single bay rectangular steel portal frame on pad footings was chosen for addition to the soil surface. The portal frame was assumed to be 3m high with a 12.5m span and comprised 203 x 203 x 60 Universal Columns and 610 x 229 x 125 Universal Beams. The dimensions of the corresponding beam elements representing these sections are given in Table 7.1 below.

Dimensions required in ABAQUS (refer to Figure 7.5)	203 x 203 x 60 Universal Column (Typical dimensions taken from Steel Designer's Manual)	610 x 229 x 125 Universal Beam (Typical dimensions taken from Steel Designer's Manual)
l (=h/2)	104.8e ⁻³ m	305.95e ⁻³ m
h	209.6e ⁻³ m	611.9e ⁻³ m
b1	205.2e ⁻³ m	229.0e ⁻³ m
b2	205.2e ⁻³ m	229.0e ⁻³ m
t1	14.2e ⁻³ m	19.6e ⁻³ m
t2	14.2e ⁻³ m	19.6e ⁻³ m
t3	9.3e ⁻³ m	11.9e ⁻³ m

Table 7.1: Dimensions of the ABAQUS beam elements representing the Universal Columns and Beams in the portal frame

The beam elements were assumed to be linear elastic with the following material properties:

Young's Modulus, $E = 2.0e^{11} \text{N/m}^2$

Poisson's ratio, $\nu = 0.27$

Density, $\rho = 7.7e^3 \text{kg/m}^3$

The steel portal frame was placed on the free surface of the 3D mesh with one footing at a radius of 10m and the other footing at a radius of 22.5m as shown in Figure 7.8.

Typical deformations of the ground and the portal frame as the vibratory waves passed through are shown in Figure 7.9. The response is a function of ground wave length with peak distress in the frame when the feet of the columns are in anti-phase. In this particular case, examination of the vertical velocity/time traces for the surface nodes indicated that the nodes were in anti-phase every 4.17m. A span of 12.5m was therefore chosen so that the feet of the columns would be in anti-phase.

For the chosen combination of vibrodriver frequency and frame dimensions, there was no resonance in evidence. Nor was there evidence of dynamic magnification of the vibrations of a long span floor beam.

For comparison, the vibratory displacements of the free ground surface with no structure are compared to those with the portal in place, see Figure 7.10. This shows that the portal caused hardly any modification to the ground surface waves. In such cases, it would therefore be acceptable, and time-saving, to impose the ground wave displacements directly onto the structure alone.

7.4.4. Effects on an in-plane wall

A typical brickwork wall, 6m high, 10m long and 0.2m thick was superimposed on to the 3D wedge-shaped model of the soil. The wall was placed in the radial plane on the free surface of the 3D FE/IE mesh with one end at a radius of 10m and the other at a radius of 20m, as shown in Figure 7.11.

The wall was represented by 0.5m square two-dimensional 4-noded bilinear plane stress elements. The brick elements were assumed to be linear elastic with the following material properties:

Young's Modulus, $E=30.0\text{e}^9\text{N/m}^2$

Poisson's ratio, $\nu = 0.2$

Density, $\rho = 2000\text{kg/m}^3$

The in-plane response of the wall is typical of a very stiff structure, in that it shows rigid-body movements of lift and pitch, but only very small deformations, see Figure 7.12. Contour plots of the stresses in the wall (Figure 7.13) indicate that the vertical and horizontal stresses are of similar magnitude, with the maximum horizontal stress of about 49kPa at the base of the wall and a maximum vertical stress of about 44kPa.

Comparison of the vibratory displacements of the free ground surface with no structure to those with the brick wall in place (Figure 7.14) demonstrate that the presence of the wall substantially reduces the ground movements. It is therefore concluded that it is inadmissible to impose the free ground displacements onto a very stiff structure and so the whole three-dimensional analysis is necessary.

7.5 IMPACT WAVES ON SOIL AND STRUCTURE

7.5.1 General

The ability of the 3D soil-structure interaction model to simulate impact waves was then investigated by inputting the verified excitation data from impact piling at Flitwick, Bedfordshire. Firstly, the ground response computed by the 3D model was compared to that computed by the axisymmetric model to check its accuracy. The same portal frame and brickwork structures were then added to the 3D model.

The ground conditions and impact piling data for the Flitwick case history are described in full in Chapter 6 (section 6.5). To summarise, the impact piling at Flitwick comprised the installation of a 12m long steel H pile was installed into dense sands to a depth of 7m by a 3200kg hammer falling through 1.0m. The axisymmetric FE/IE model

developed for impact piling computed a very similar ground response to that measured by geophones on site.

The 3D model was constructed using exactly the same parameters as the axisymmetric model.

7.5.2 Comparison of ground response predicted by axisymmetric mesh and 3D mesh

The radial and vertical particle velocities computed by the axisymmetric and 3D models at horizontal distances of 7m and 16.5m (the positions of the geophones) are compared in Figures 7.15 and 7.16 respectively. These figures demonstrate that there is a substantial loss of accuracy when the 3D model is used to simulate the propagation of ground waves generated by impact piling. This is likely to be due to the use of 8-noded bilinear brick elements, with a uniform node spacing of 0.5m, rather than 20-noded quadrilateral brick elements, with a uniform node spacing of 0.25m. As impact waves generally have a much shorter wavelength than waves generated by vibratory piling, closer node spacings are required to remain within the general rule for accurate FE simulation of 10 nodes per wavelength. Unfortunately the increased computing time required for analysis of a 3D mesh comprising 20-noded brick elements did not allow further checks.

Although the ground response computed by the 3D model was fairly inaccurate, it was generally of a similar form and magnitude to the measured vibrations generated by impact piling. It was therefore decided to add the structures to the 3D model anyway in order to gain some understanding of the general behaviour of structures subjected to vibrations from impact piling. However, the actual data resulting from these analyses should be treated with caution and it is recommended that a 3D mesh with much closer node spacings is used to simulate the propagation of impact waves.

7.5.3 Effect on a portal frame structure

The portal frame structure described in section 7.4.3 was applied to the free surface of the 3D mesh with one footing at a radius of 10m and the other at a radius of 22.5m as shown in Figure 7.8.

Typical deformations of the ground and the portal frame as the impact waves passed through are shown in Figure 7.17. The response is a function of ground wave length with peak distress in the frame when the feet of the columns are in anti-phase.

For comparison, the transient displacements of the free ground surface with no structure are compared to those with the portal in place, see Figure 7.18. This shows that the portal caused hardly any modification to the ground surface waves. In such cases, it would therefore be acceptable, and time-saving, to impose the ground wave displacements directly onto the structure alone.

7.5.4 Effects on an in-plane wall

The brickwork wall described in Section 7.4.4 was superimposed onto the 3D model with one end at a radius of 10m and the other at a radius of 20m, as shown in Figure 7.11.

Typical deformations of the ground and the wall as the transient waves passed through are shown in Figure 7.19. The in-plane response of the wall is typical of a very stiff structure, in that it shows rigid-body movements of lift and pitch, but only very small deformations. Contour plots of the stresses in the wall (Figure 7.20) indicated that the dominant effect was due to the horizontal ground displacements, peaking at about 19kPa at the base of the wall. The maximum vertical stresses were of the order of 9kPa.

Comparison of the transient displacements of the free ground surface with no structure to those with the brick wall in place demonstrated that the presence of the wall substantially reduced the ground movements. It is therefore concluded that it is inadmissible to impose the free ground displacements onto a very stiff structure and so a full three-dimensional analysis is necessary.

7.6 CONCLUSIONS AND RECOMMENDATIONS FOR FURTHER WORK

A computationally efficient technique has been developed to model the effects of ground waves generated by either vibratory or impact piling on various structural forms. The displacements around the pile/soil interface generated by the motion of the pile are computed using the two-dimensional axisymmetric FE/IE models developed in Chapters 5 and 6. The computed piling-induced ground excitation is verified by comparison of the predicted ground response with the ground surface velocities measured by geophones. The verified displacements are then used as input to a three-dimensional FE/IE wedge-shaped model of a “slice” of the axisymmetric system. The use of symmetry in this respect reduces the number of degrees of freedom in the FE analysis and hence the computing time required. Once the 3D model has been verified against site-measured vibrations, it is possible to incorporate various structural forms. This approach gives a full soil-structure analysis of the system, allowing appreciation of the effects of different wave types and structural forms. It is potentially a very useful and economic tool for the prediction of the effects of vibrations generated by pile driving on various structural forms. The entire model can be created with a minimum of site data and can therefore be used as a preliminary design tool to assess the potential effects of various types of pile driving on adjacent structures.

It has been demonstrated that the 3D wedge-shaped model accurately simulates the ground waves generated by vibratory pile driving. However, a much finer 3D mesh is required for accurate representation of impact waves. Further work is required to identify an adequate, refined, mesh.

The insertion of computed ground excitations to the soil-structure model, verified against site-measured data from both vibratory and impact piling, has demonstrated that the model can be used to identify dynamic displacements and stresses in simple structures. When the structure comprises a slender frame, then imposition of free-ground deformations gives a close representation of the coupled behaviour. However, stiff structures such as in-plane walls show substantial reduction of the free ground movements and so a full three-dimensional analysis is necessary. The soil-structure model has also demonstrated the importance of considering both the vertical and the horizontal wave components when examining the stresses induced in a structure by a passing wave.

Development of this soil-structure interaction model has only reached a very preliminary stage. It would be desirable to verify the model against site-measured data. However, once this has been done, the model could be extended to investigate and predict the effects of piling-induced vibrations on a wide range of structural forms.

ABAQUS

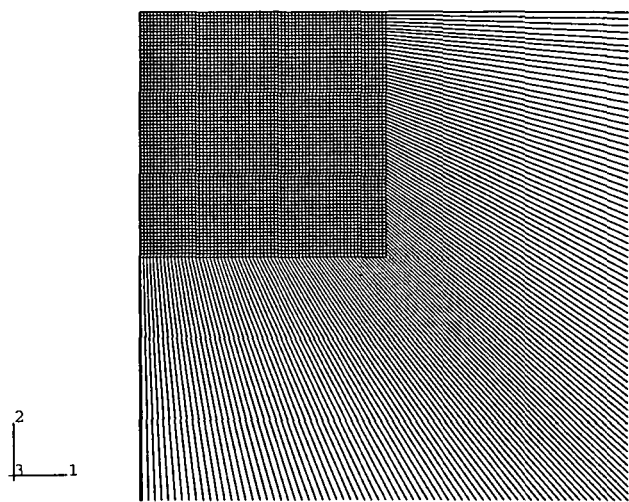


Figure 7.1 FE/IE mesh used in axisymmetric analysis

ABAQUS

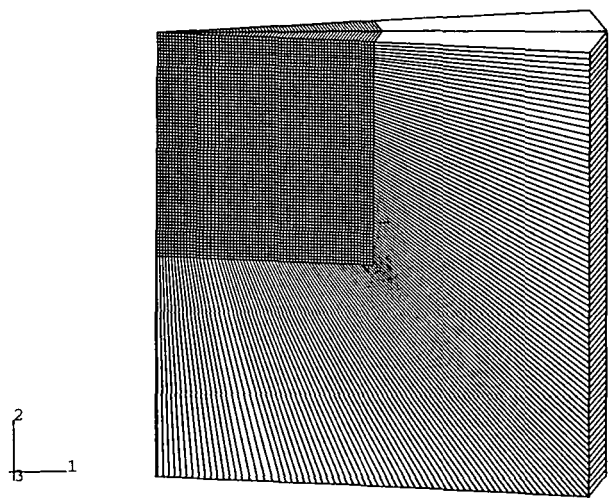


Figure 7.2 FE/IE mesh used in 3D analysis

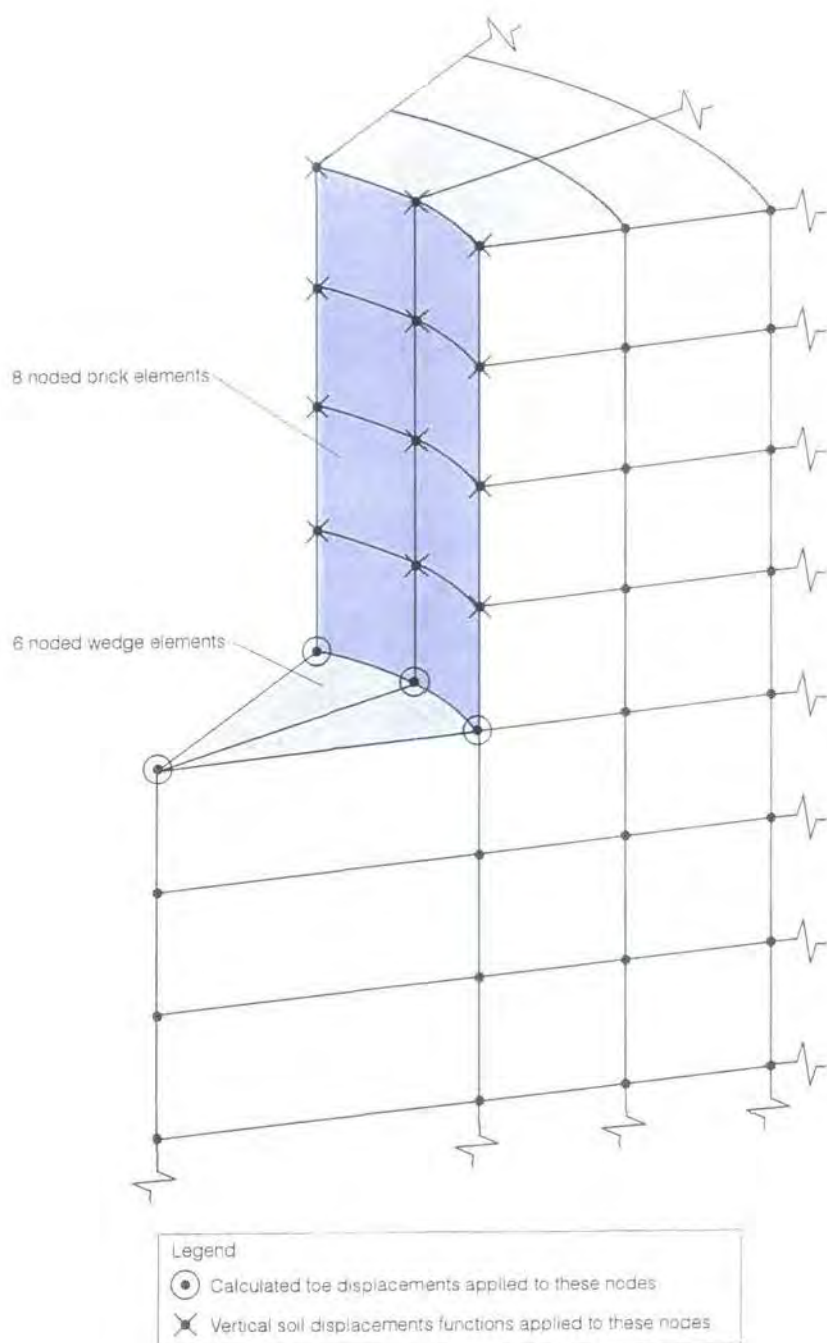


Figure 7.3 Simplified view of 3D model of ground around the pile

ABAQUS



Figure 7.4 Boundary conditions applied to 3D FE/IE mesh

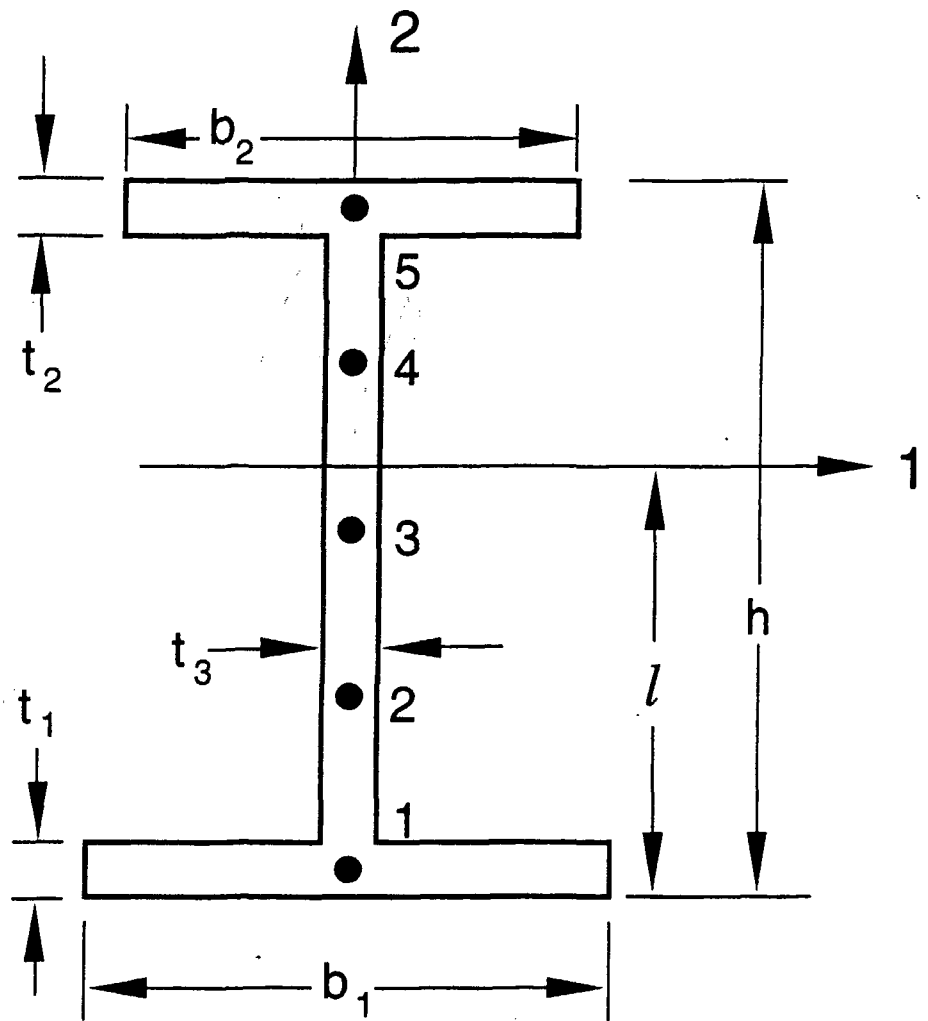
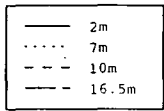
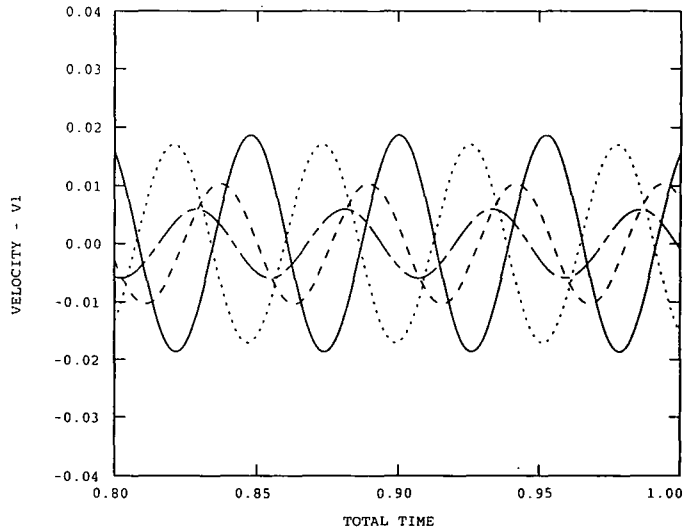


Figure 7.5 Definition of a beam in ABAQUS

ABAQUS

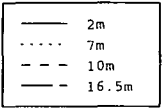


XMIN 1.000E-03
XMAX 1.000E+00
YMIN -1.906E-02
YMAX 1.909E-02

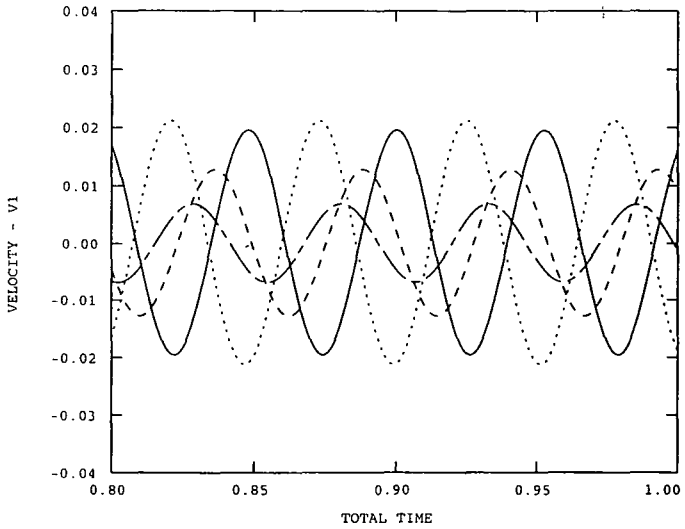


(a) Axisymmetric model

ABAQUS

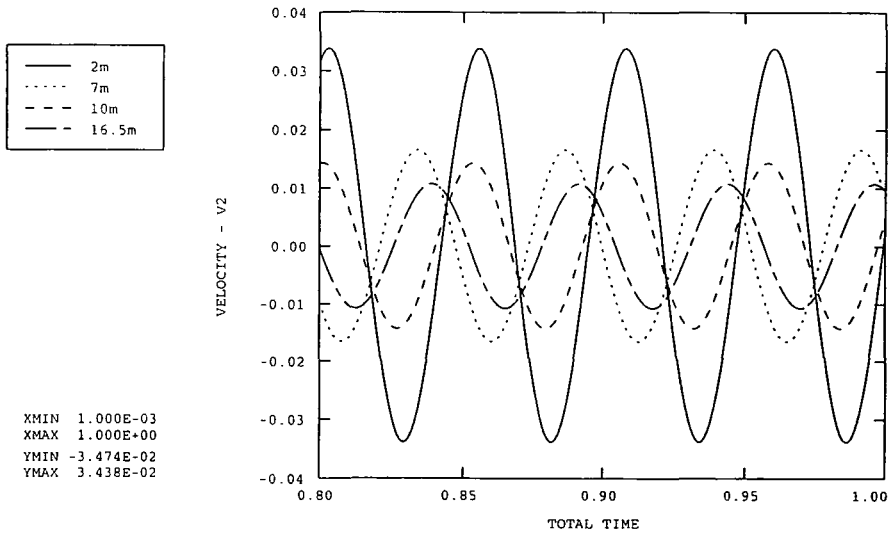


XMIN 1.000E-03
XMAX 1.000E+00
YMIN -2.143E-02
YMAX 2.145E-02

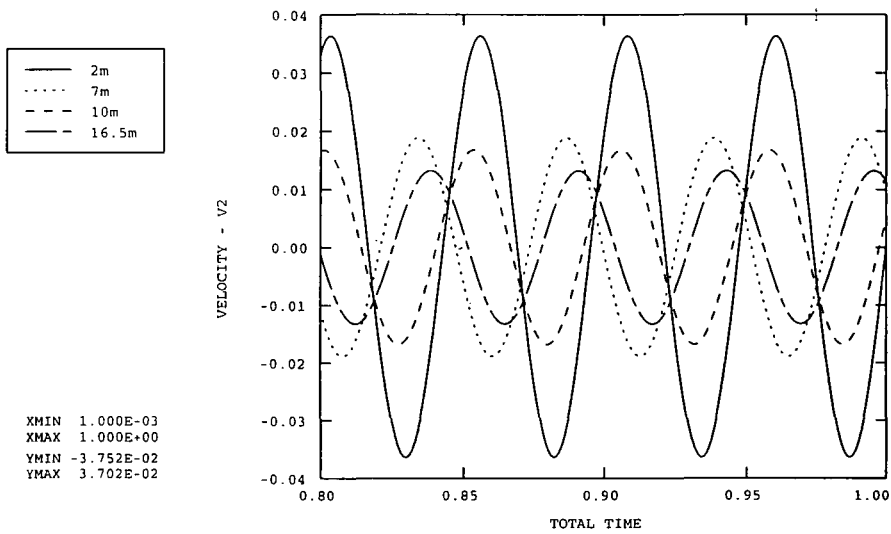


(b) 3D model

Figure 7.6 Radial velocity/time traces predicted by the axisymmetric and 3D models at horizontal distances of 2m, 7m, 10m and 16.5m



(a) Axisymmetric model



(b) 3D model

Figure 7.7 Vertical velocity/time traces predicted by the axisymmetric and 3D models at horizontal distances of 2m, 7m, 10m and 16.5m

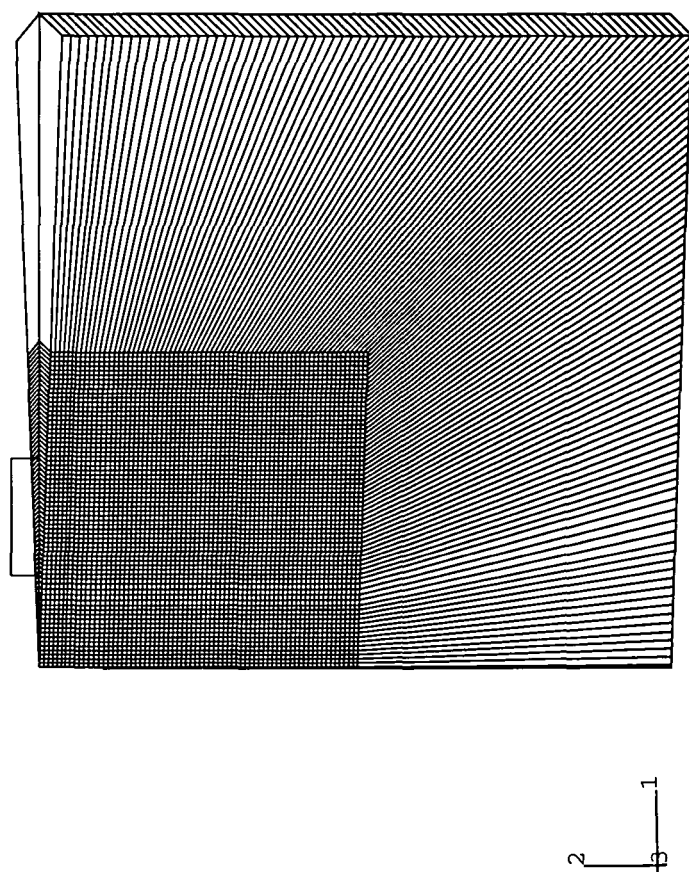


Figure 7.8 Steel portal frame on 3D mesh

ABAQUS

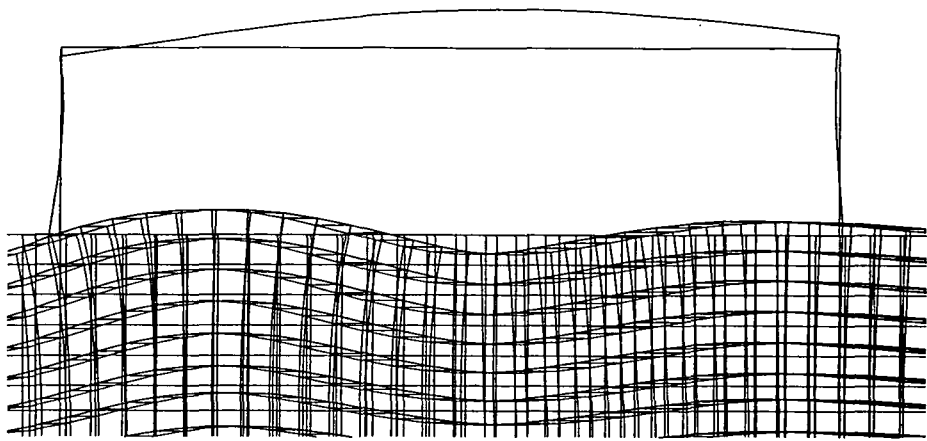


Figure 7.9(a) Typical deformation of the ground and the portal frame as the vibratory waves pass through. Time = 0.15 seconds.
(Magnification x 3000)

ABAQUS

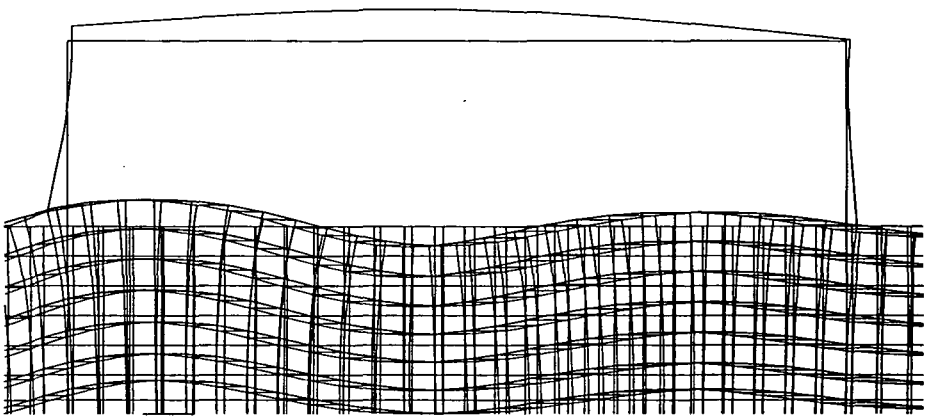


Figure 7.9(b) Typical deformation of the ground and the portal frame as the vibratory waves pass through. Time = 0.3 seconds.
(Magnification x 3000)

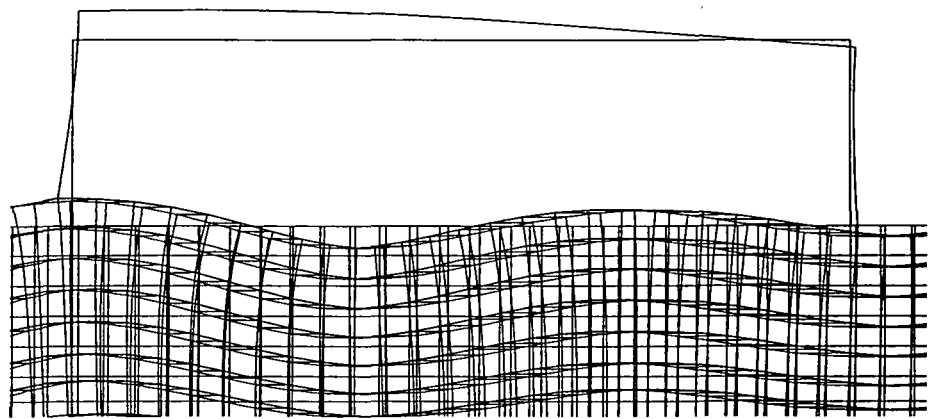


Figure 7.9(c) Typical deformation of the ground and the portal frame as the vibratory waves pass through. Time = 0.45 seconds.
(Magnification x 3000)

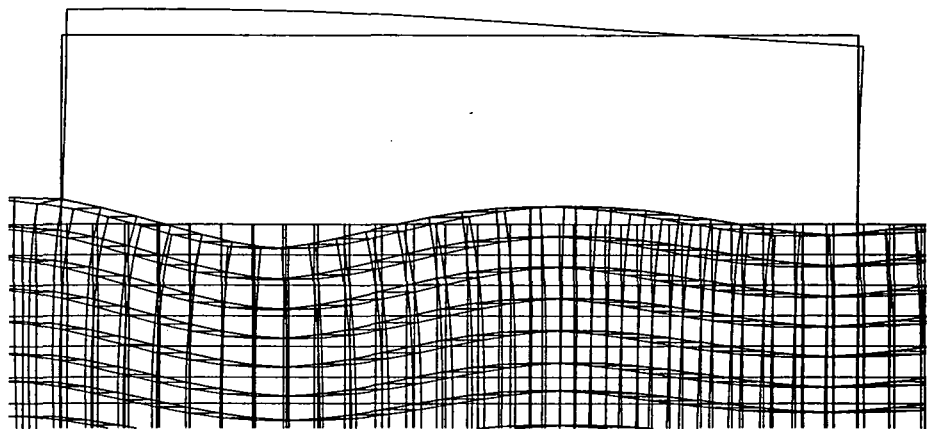


Figure 7.9(d) Typical deformation of the ground and the portal frame as the vibratory waves pass through. Time = 0.6 seconds.
(Magnification x 3000)

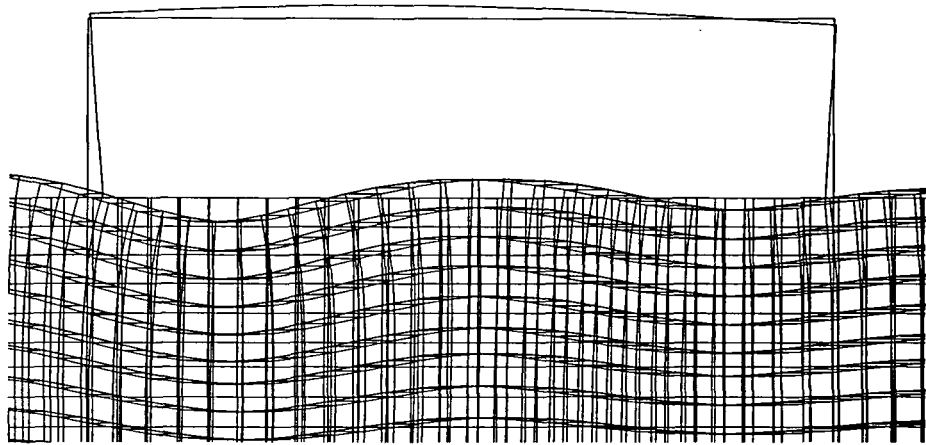


Figure 7.9(e) Typical deformation of the ground and the portal frame as the vibratory waves pass through. Time = 0.75 seconds.
(Magnification x 3000)

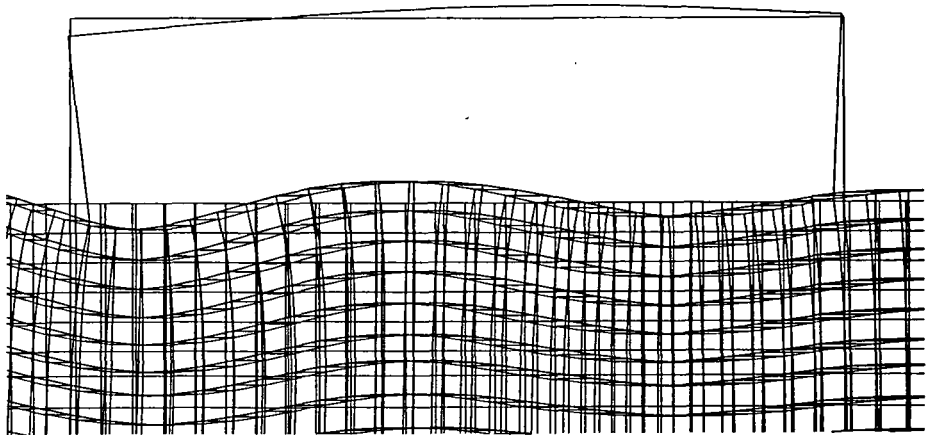


Figure 7.9(f) Typical deformation of the ground and the portal frame as the vibratory waves pass through. Time = 0.9 seconds.
(Magnification x 3000)

ABAQUS

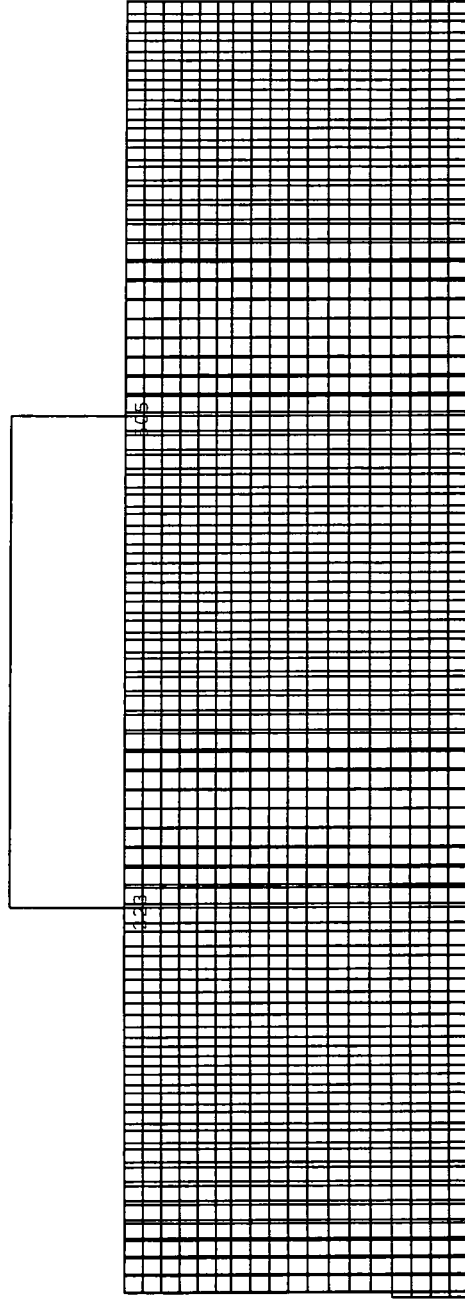
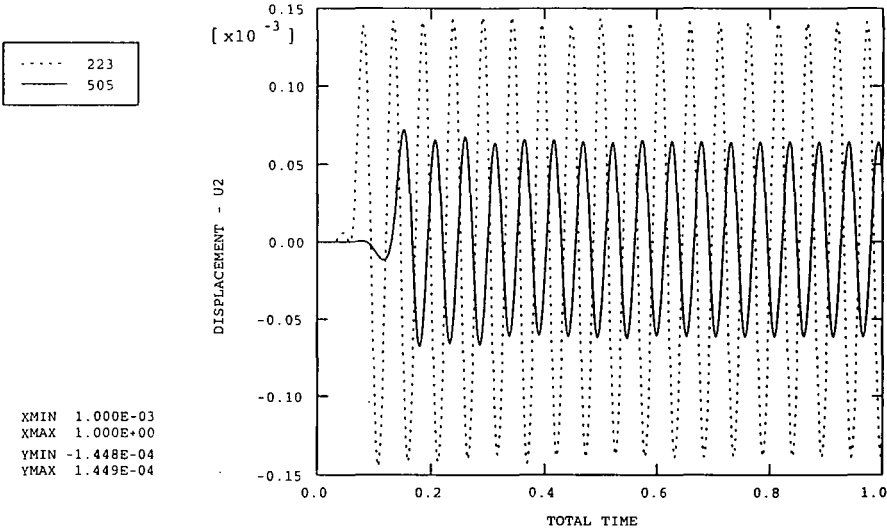


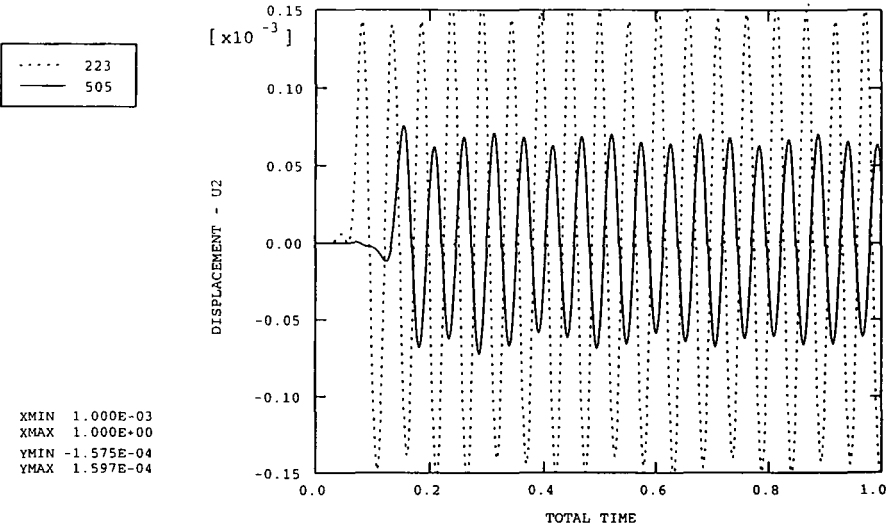
Figure 7.10(a) Locations of nodes 223 and 505 (Vibratory piling model)

ABAQUS



No structure

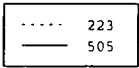
ABAQUS



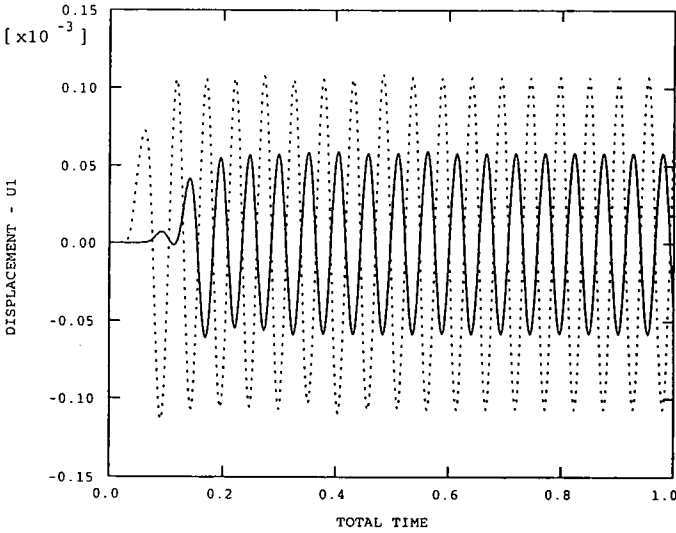
With portal frame

Figure 7.10(b) Comparison of the vibratory displacements of the free ground surface with no structure against those with the portal frame in place:
vertical displacements

ABAQUS

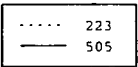


XMIN 1.000E-03
XMAX 1.000E+00
YMIN -1.138E-04
YMAX 1.090E-04

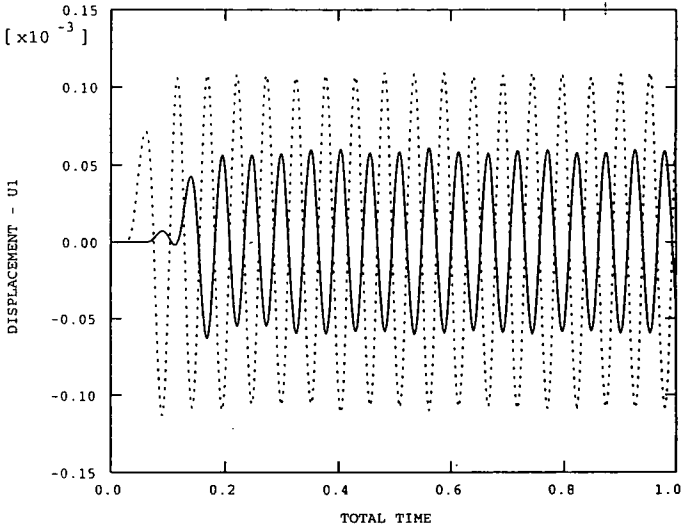


No structure

ABAQUS



XMIN 1.000E-03
XMAX 1.000E+00
YMIN -1.131E-04
YMAX 1.095E-04



With portal frame

Figure 7.10(c) Comparison of the vibratory displacements of the free ground surface with no structure against those with the portal frame in place: horizontal displacements

ABAQUS

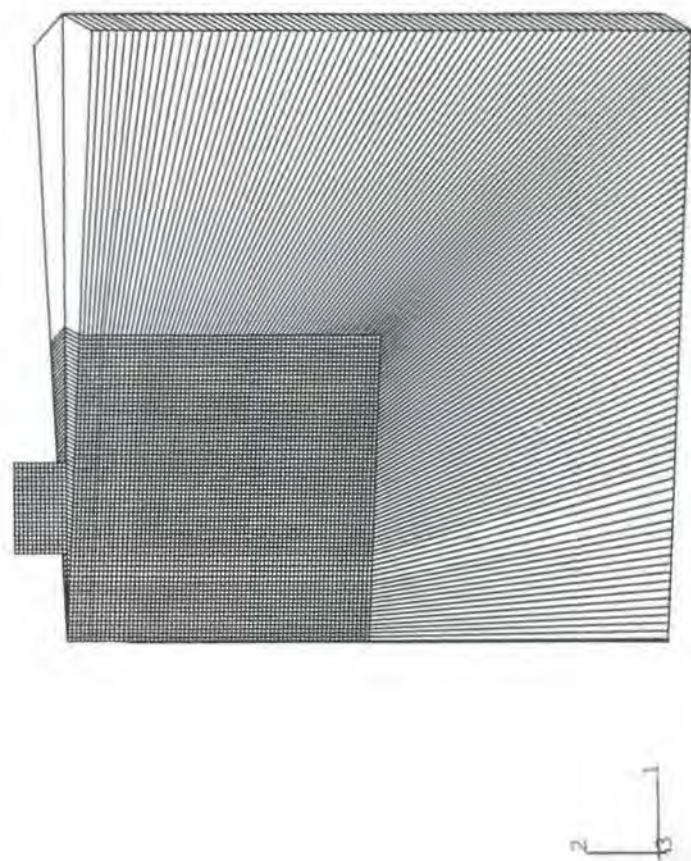


Figure 7.11 In-plane wall on 3D mesh

ABAQUS

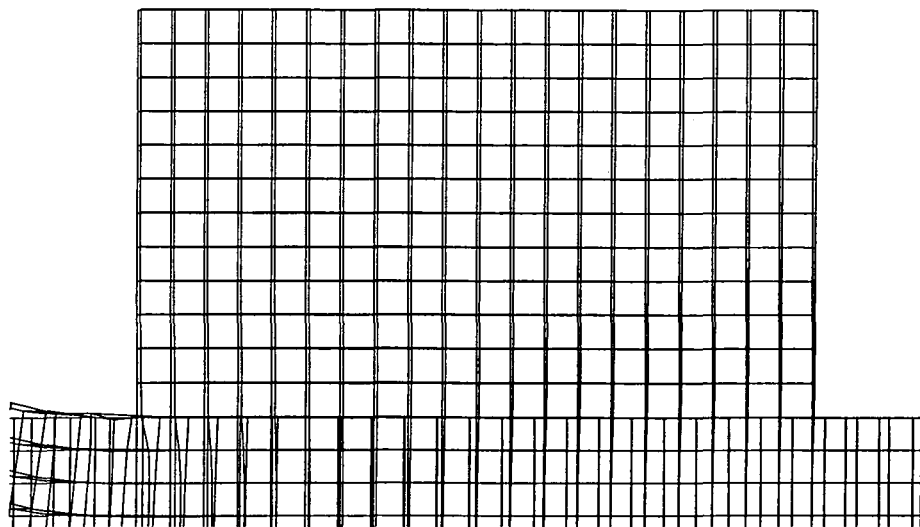


Figure 7.12(a) Typical deformation of the ground and the wall as the vibratory waves pass through. Time = 0.05 seconds.
(Magnification x 5000)

ABAQUS

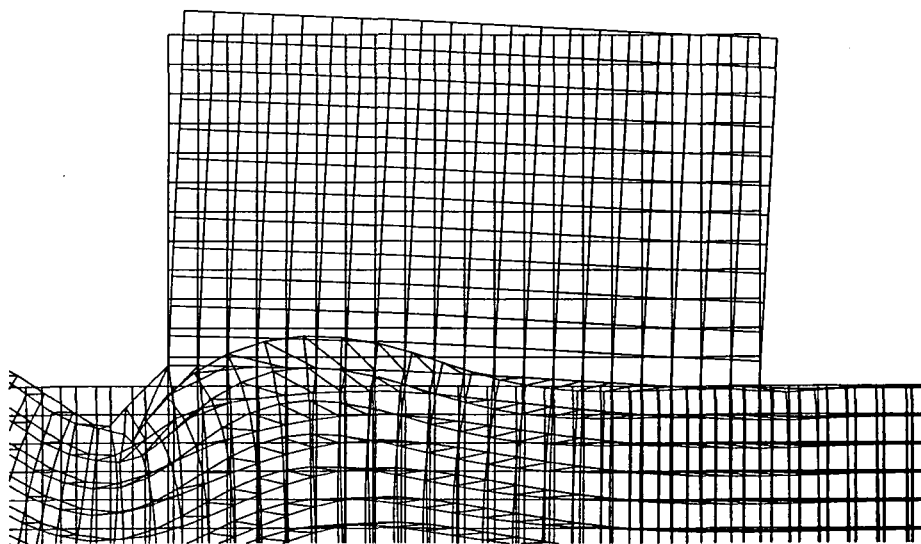


Figure 7.12(b) Typical deformation of the ground and the wall as the vibratory waves pass through. Time = 0.10 seconds.
(Magnification x 5000)

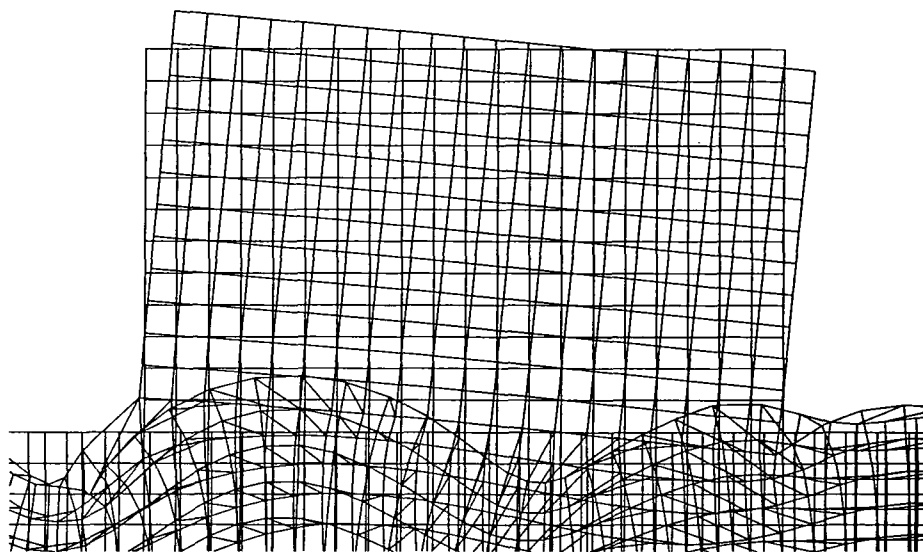


Figure 7.12(c) Typical deformation of the ground and the wall as the vibratory waves pass through. Time = 0.15 seconds.
(Magnification x 5000)

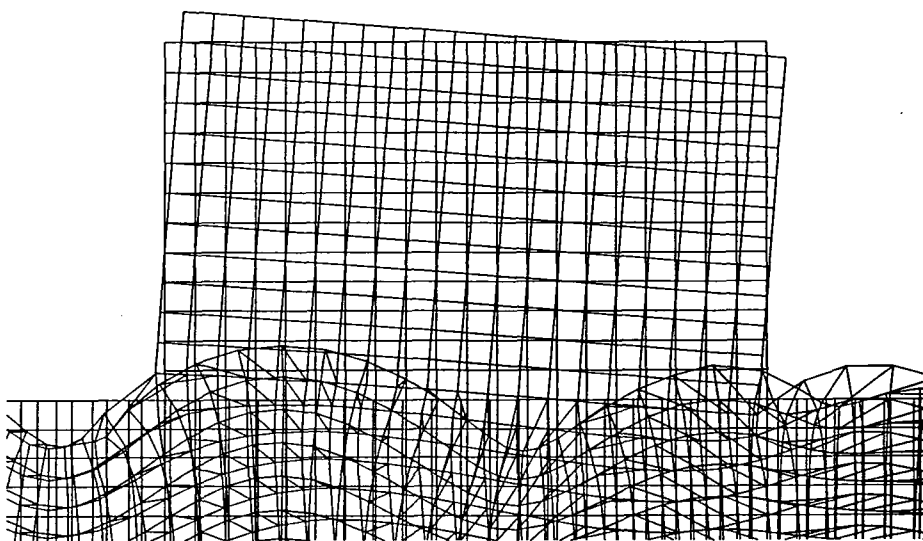


Figure 7.12(d) Typical deformation of the ground and the wall as the vibratory waves pass through. Time = 0.20 seconds.
(Magnification x 5000)

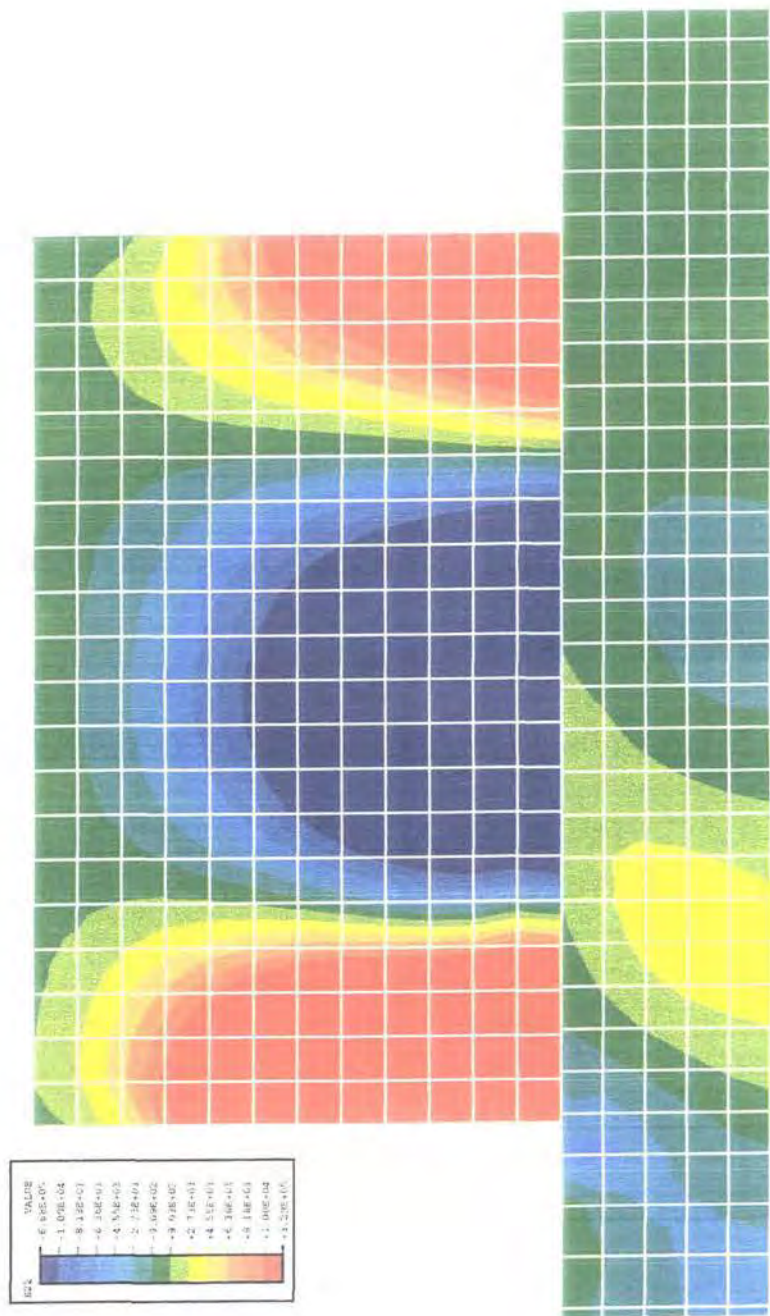


Figure 7.13(a) Contour plot of the vertical stresses in the wall during vibratory piling

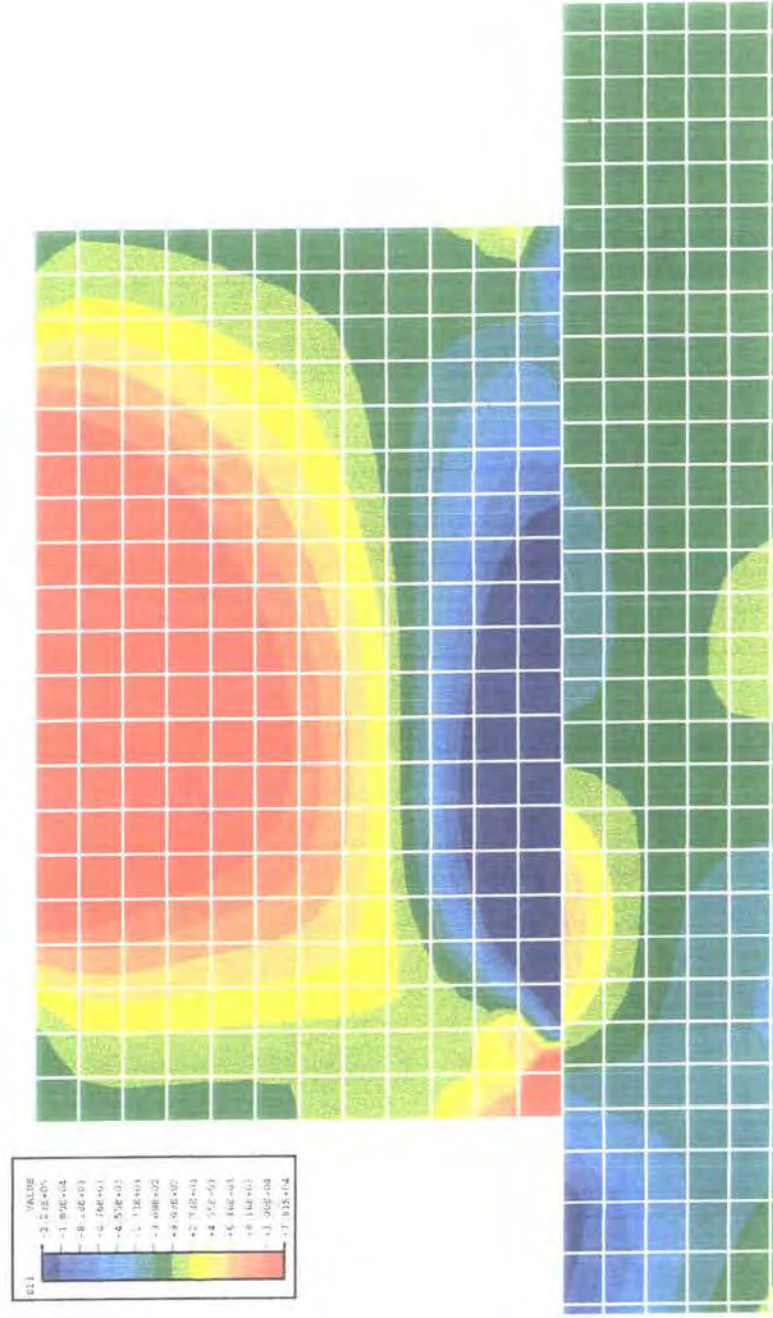


Figure 7.13(b) Contour plot of the horizontal stresses in the wall during vibratory piling

ABAQUS

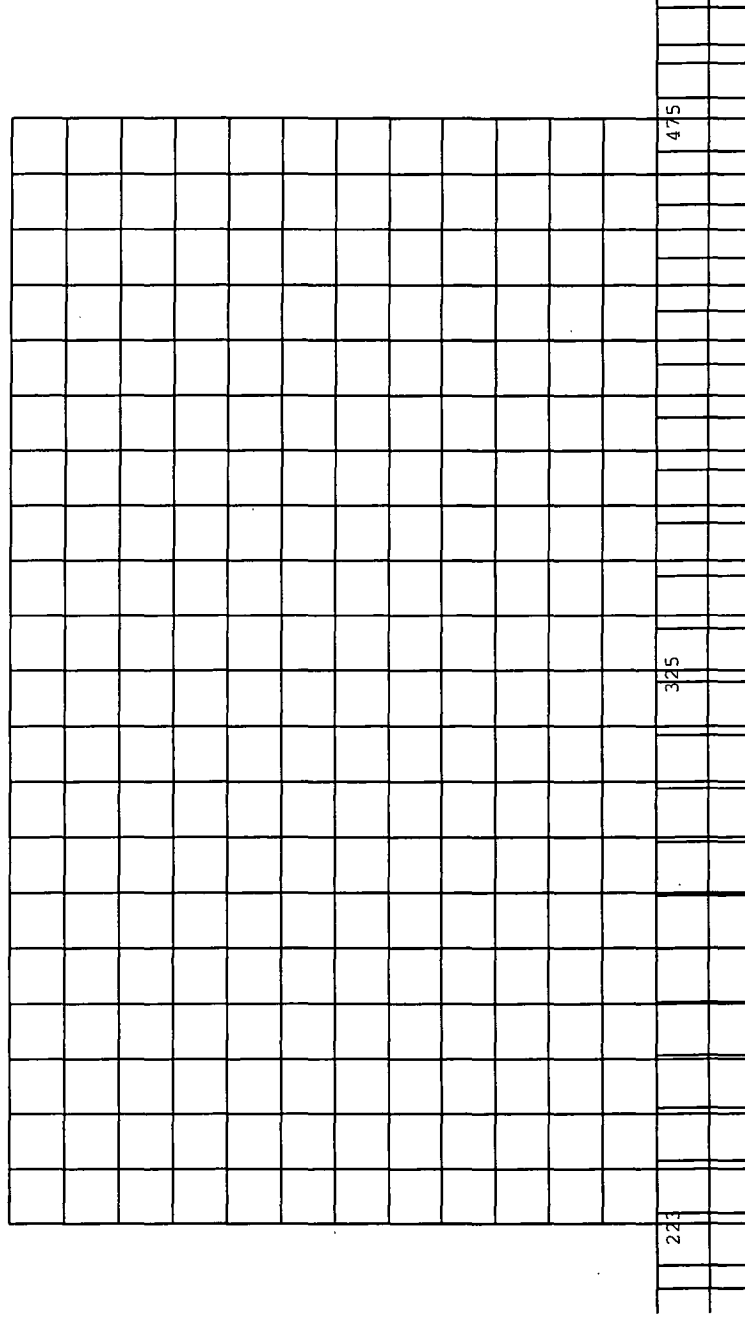
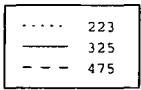
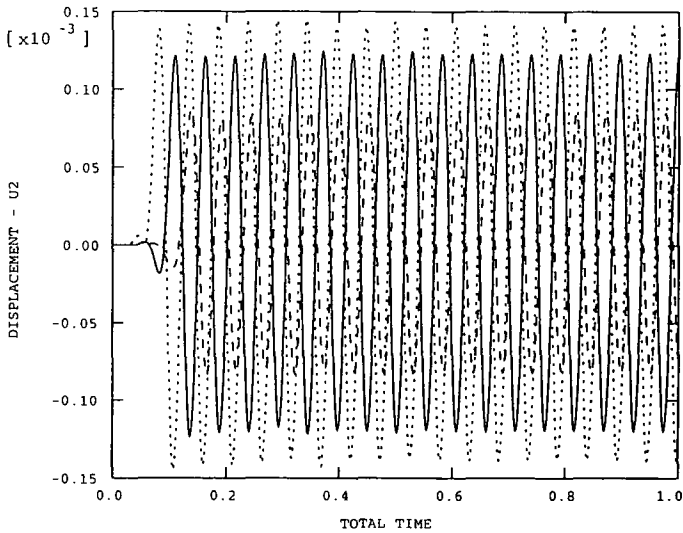


Figure 7.14(a) Location of nodes 223, 325 and 475

ABAQUS

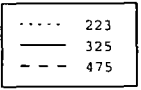


XMIN 1.000E-03
XMAX 1.000E+00
YMIN -1.448E-04
YMAX 1.449E-04

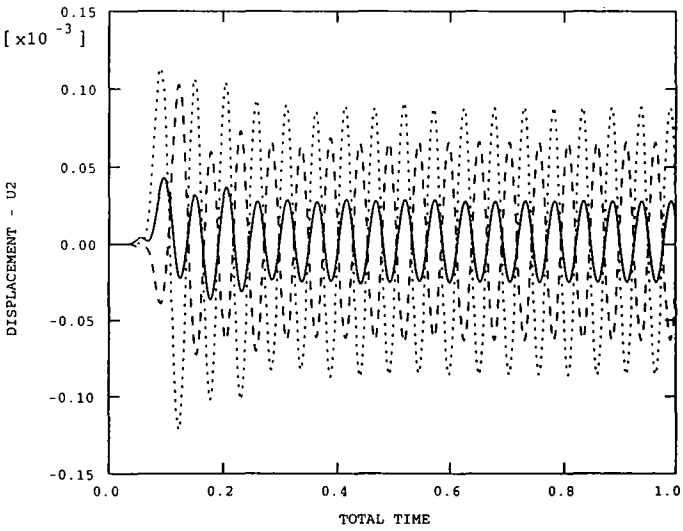


No structure

ABAQUS



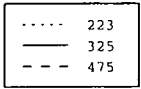
XMIN 1.000E-03
XMAX 1.000E+00
YMIN -1.217E-04
YMAX 1.134E-04



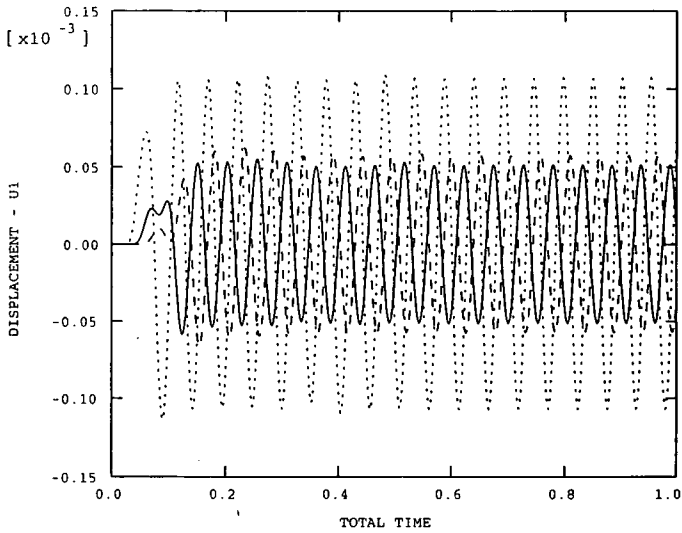
With brick wall

Figure 7.14(b) Comparison of the vibratory displacements of the free ground surface with no structure against those with the brick wall in place: vertical displacements

ABAQUS

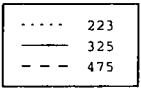


XMIN 1.000E-03
XMAX 1.000E+00
YMIN -1.138E-04
YMAX 1.090E-04

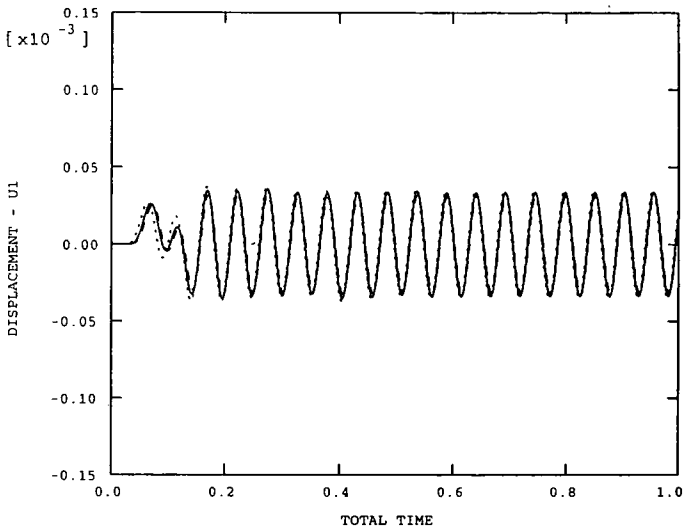


No structure

ABAQUS



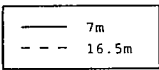
XMIN 1.000E-03
XMAX 1.000E+00
YMIN -3.715E-05
YMAX 3.709E-05



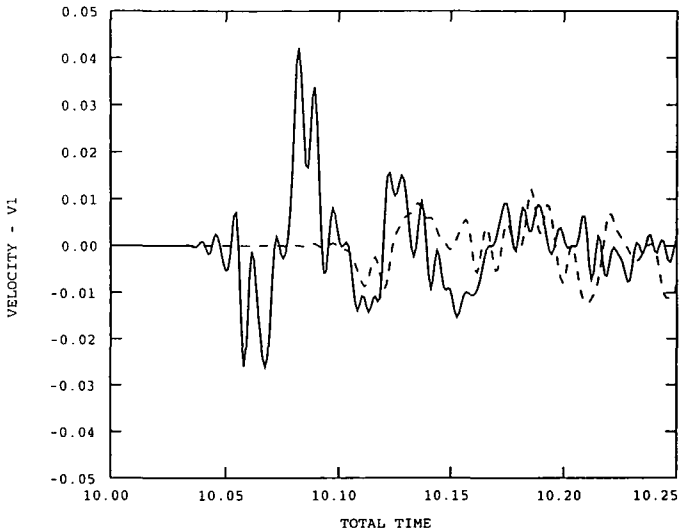
With brick wall

Figure 7.14(c) Comparison of the vibratory displacements of the free ground surface with no structure against those with the brick wall in place: horizontal displacements

ABAQUS

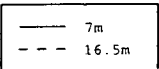


XMIN 1.000E+01
XMAX 1.025E+01
YMIN -2.617E-02
YMAX 4.214E-02

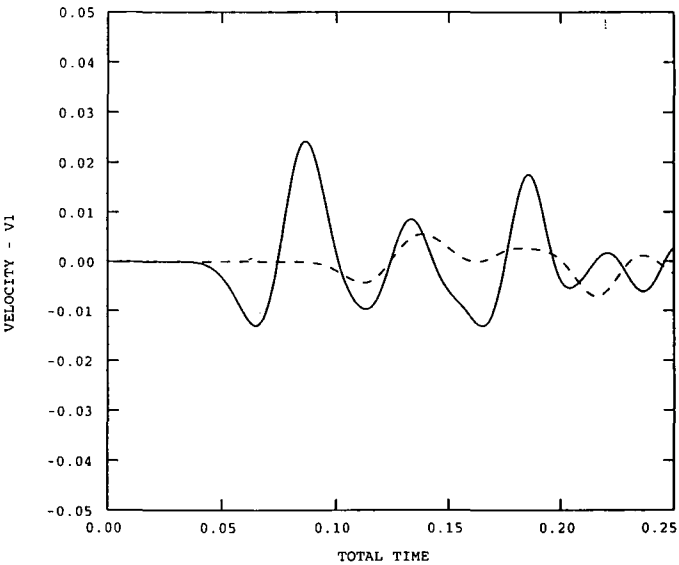


(a) Axisymmetric mesh

ABAQUS



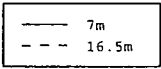
XMIN 1.000E-03
XMAX 1.000E+00
YMIN -1.313E-02
YMAX 2.419E-02



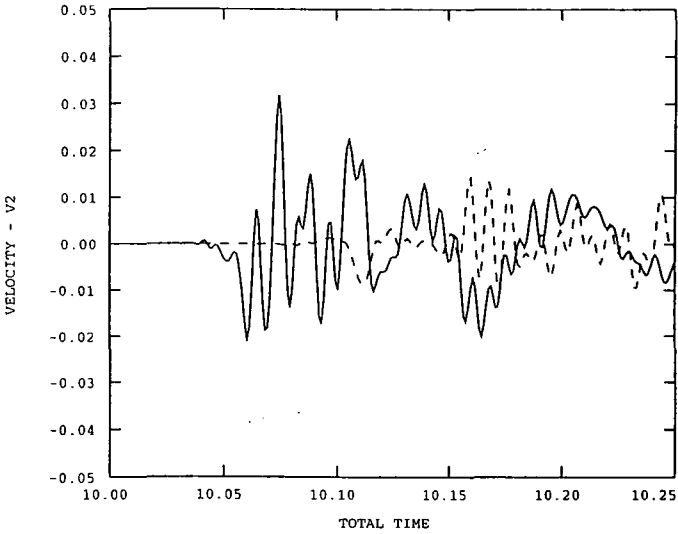
(b) 3D mesh

Figure 7.15 Comparison of the radial velocity/time traces computed by the axisymmetric and 3D models at horizontal distances of 7m and 16.5m

ABAQUS

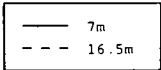


XMIN 1.000E+01
XMAX 1.025E+01
YMIN -2.080E-02
YMAX 3.176E-02

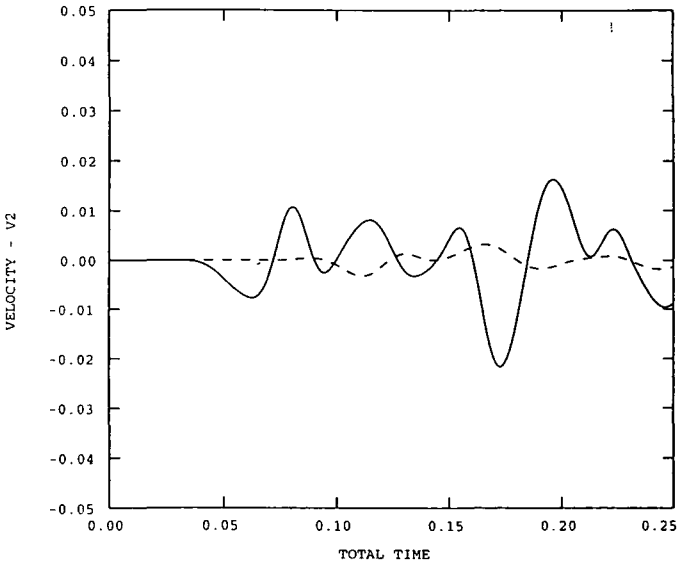


(a) Axisymmetric mesh

ABAQUS



XMIN 1.000E-03
XMAX 1.000E+00
YMIN -2.161E-02
YMAX 1.630E-02



(b) 3D mesh

Figure 7.16 Comparison of the vertical velocity/time traces computed by the axisymmetric and 3D models at horizontal distances of 7m and 16.5m

ABAQUS

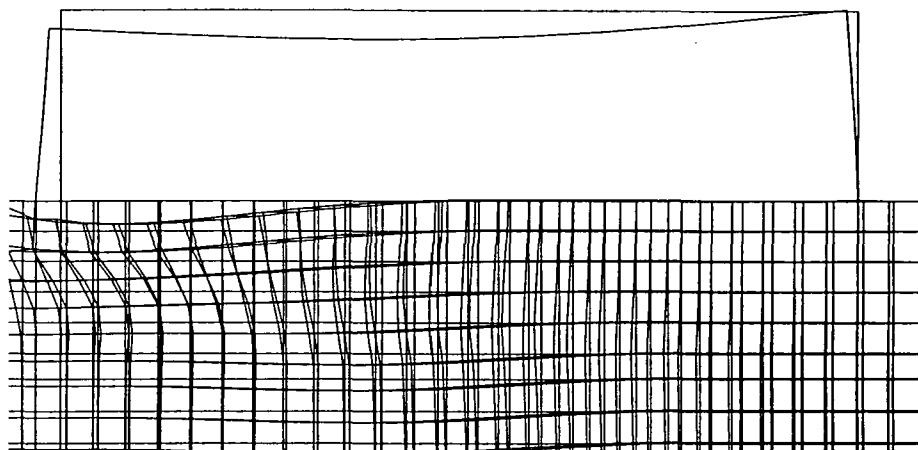


Figure 7.17(a) Typical deformation of the ground and the portal frame as the impact waves pass through. Time = 0.10 seconds.
(Magnification x 5000)

ABAQUS

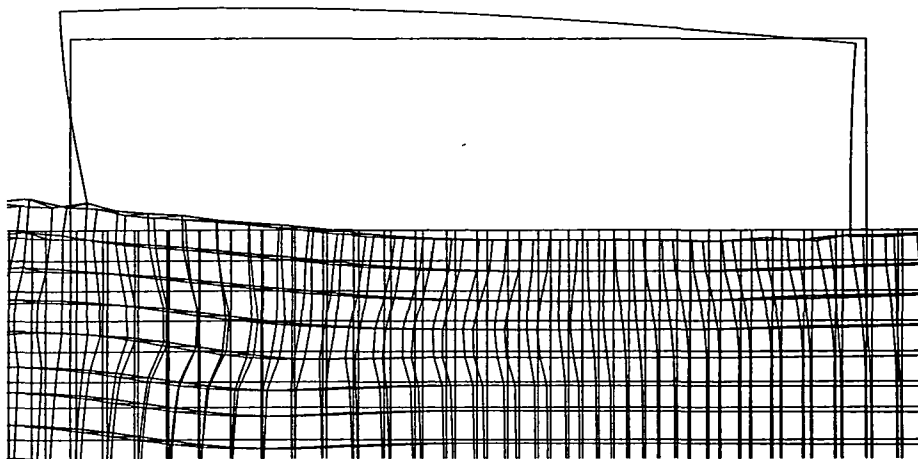


Figure 7.17(b) Typical deformation of the ground and the portal frame as the impact waves pass through. Time = 0.15 seconds.
(Magnification x 5000)

ABAQUS

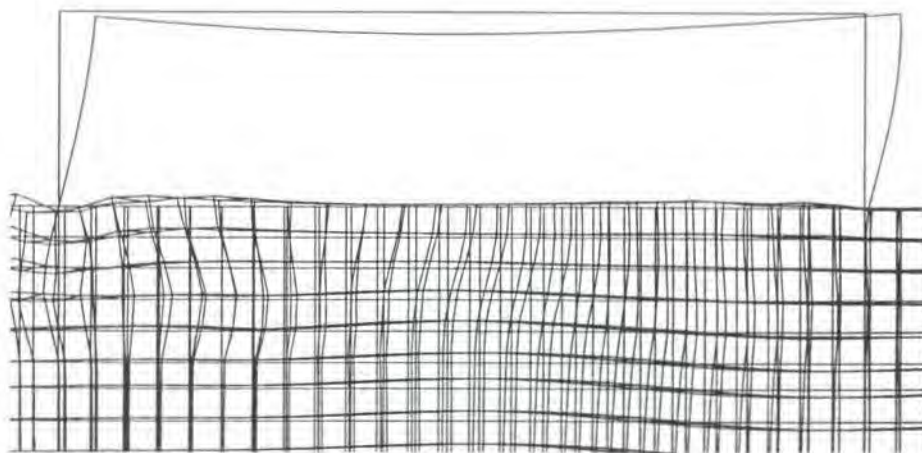


Figure 7.17(c) Typical deformation of the ground and the portal frame as the impact waves pass through. Time = 0.20 seconds.
(Magnification x 5000)

ABAQUS

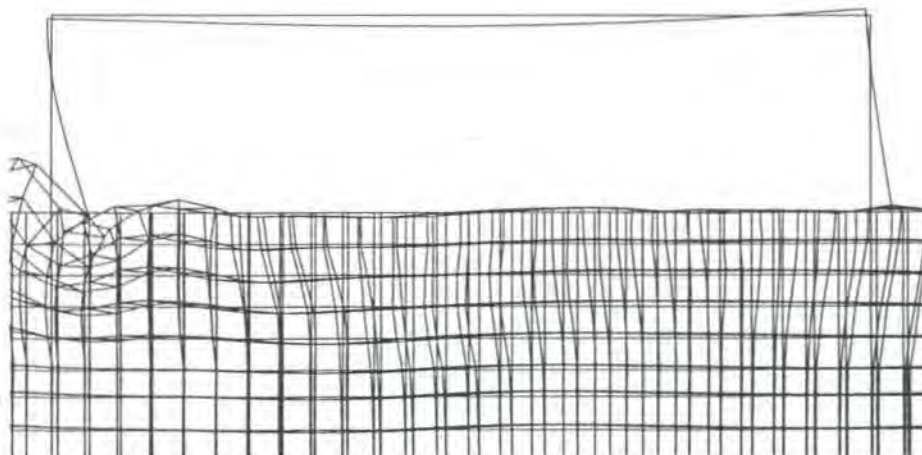


Figure 7.17(d) Typical deformation of the ground and the portal frame as the impact waves pass through. Time = 0.25 seconds.
(Magnification x 5000)

ABAQUS

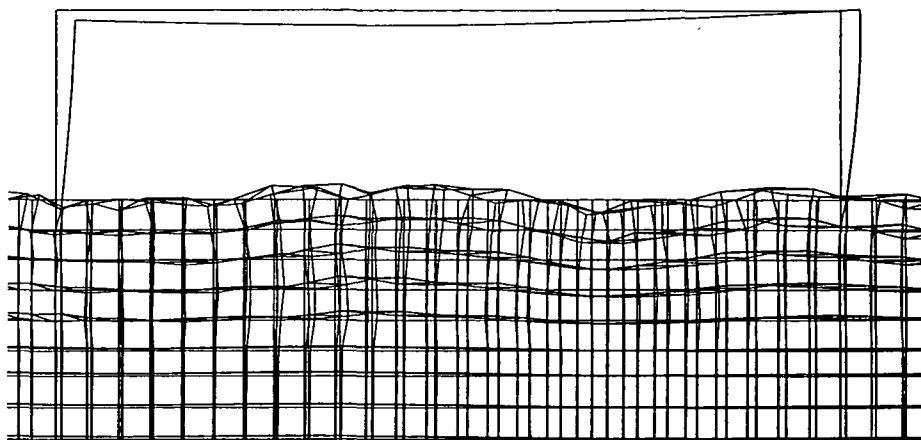


Figure 7.17(g) Typical deformation of the ground and the portal frame as the impact waves pass through. Time = 0.60 seconds.
(Magnification x 5000)

ABAQUS

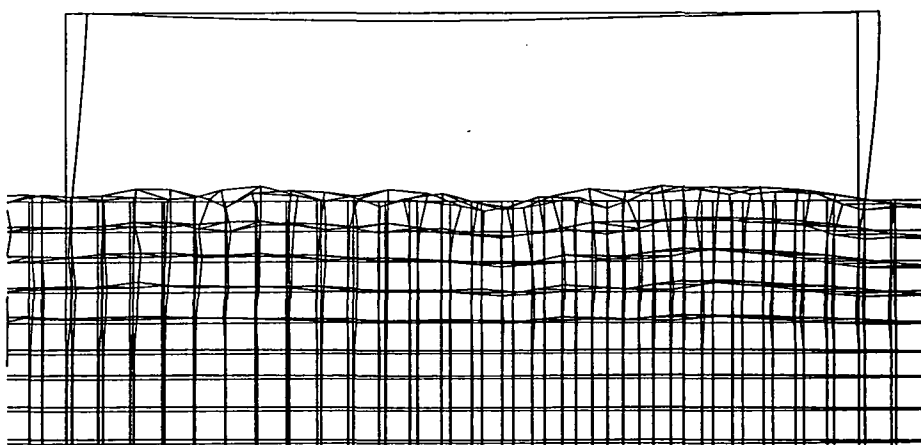


Figure 7.17(h) Typical deformation of the ground and the portal frame as the impact waves pass through. Time = 0.75 seconds.
(Magnification x 5000)

ABAQUS

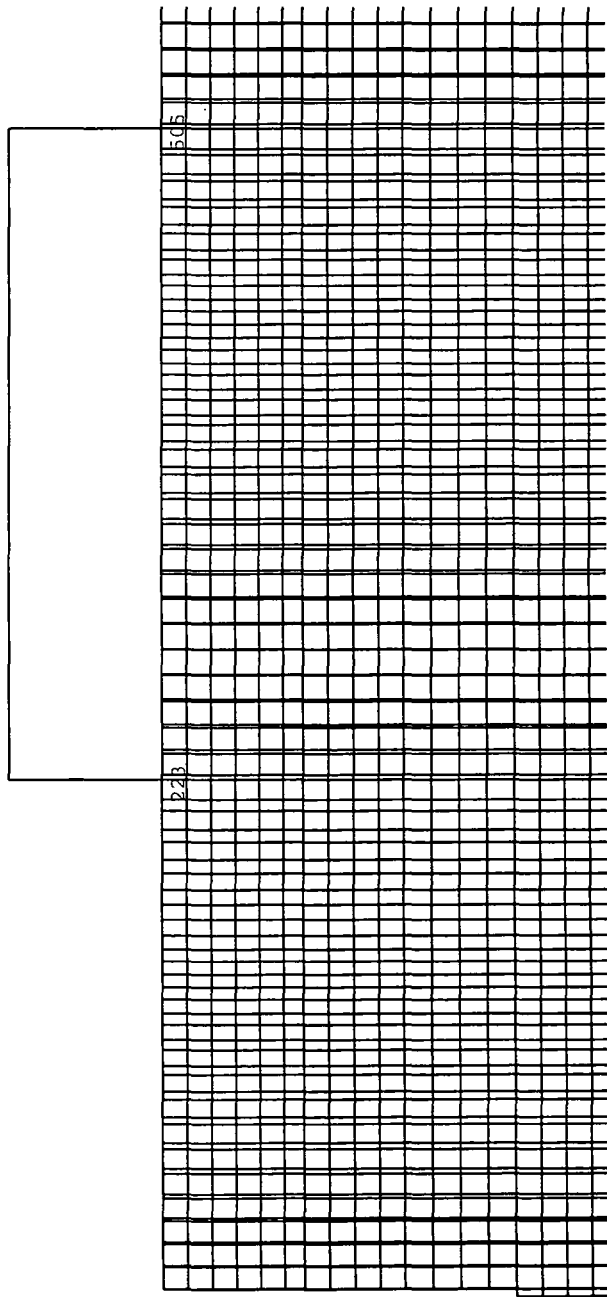
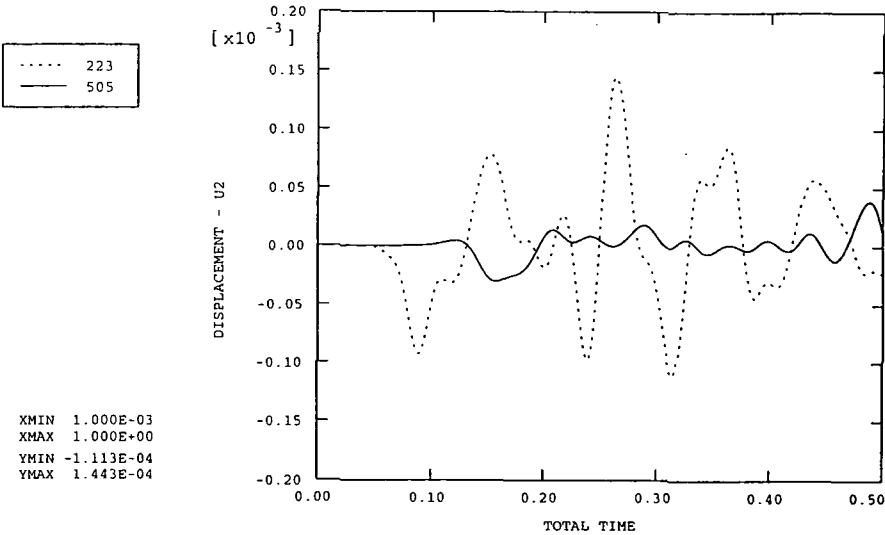


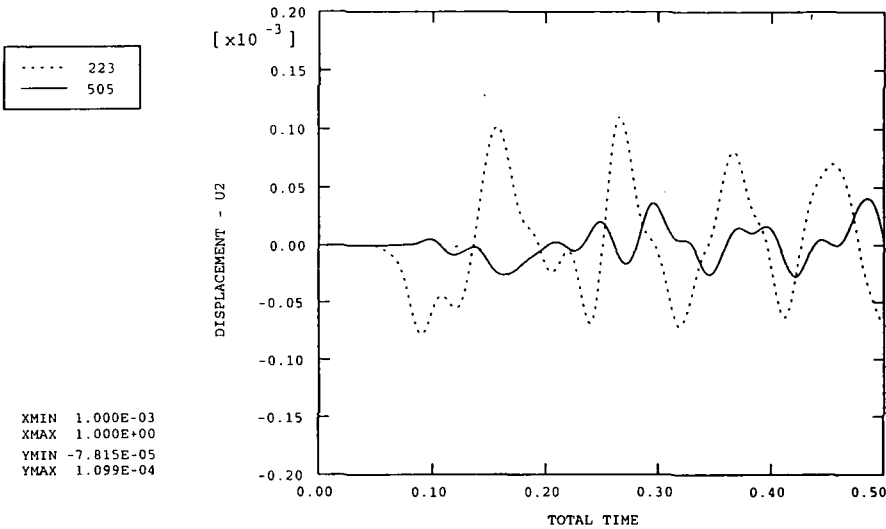
Figure 7.18(a) Locations of nodes 223 and 505 (Impact piling model)

ABAQUS



No structure

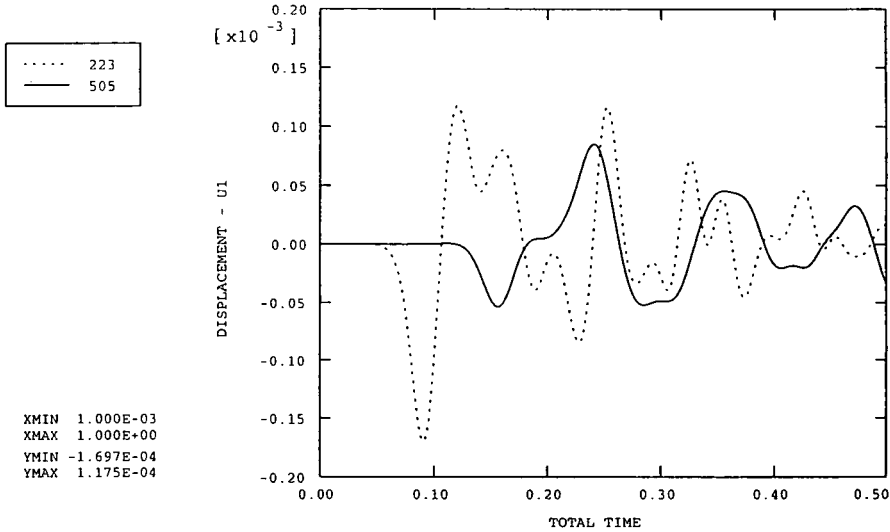
ABAQUS



With portal frame

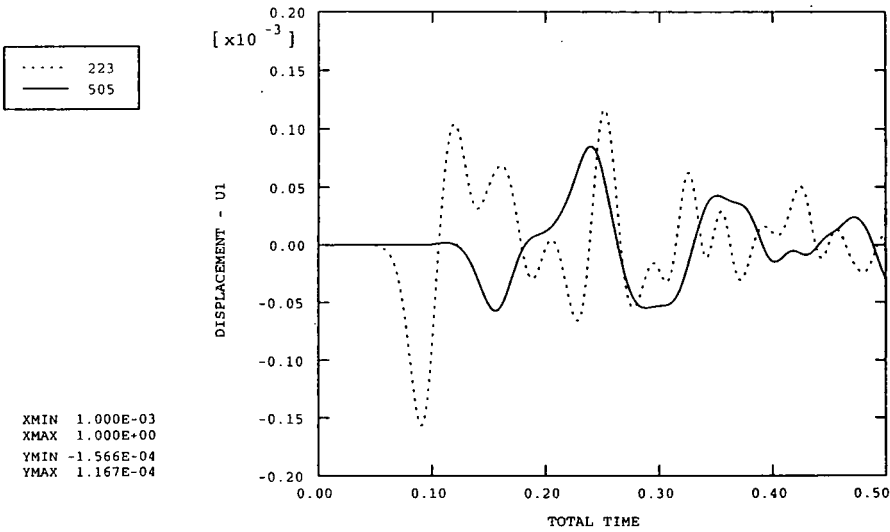
Figure 7.18(b) Comparison of the transient displacements of the free ground surface with no structure against those with the portal frame in place: vertical displacements

ABAQUS



No structure

ABAQUS



With portal frame

Figure 7.18(c) Comparison of the transient displacements of the free ground surface with no structure against those with the portal frame in place:
horizontal displacements

ABAQUS

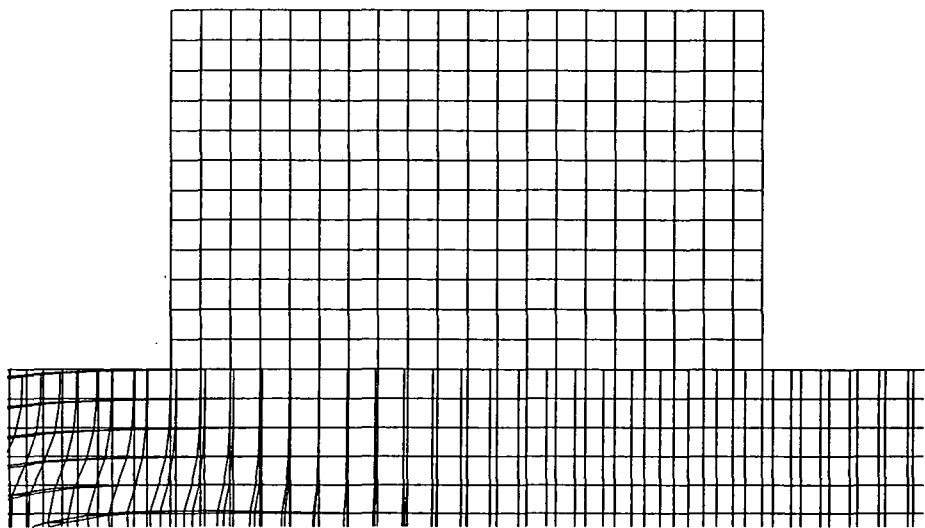


Figure 7.19(a) Typical deformation of the ground and the wall as the impact waves pass through. Time = 0.05 seconds.
(Magnification x 10000)

ABAQUS

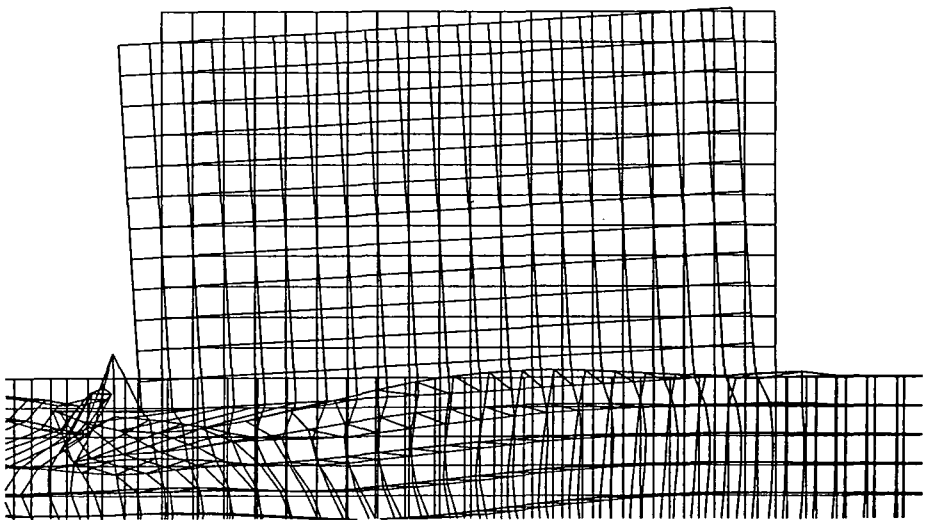


Figure 7.19(b) Typical deformation of the ground and the wall as the impact waves pass through. Time = 0.10 seconds.
(Magnification x 10000)

ABAQUS

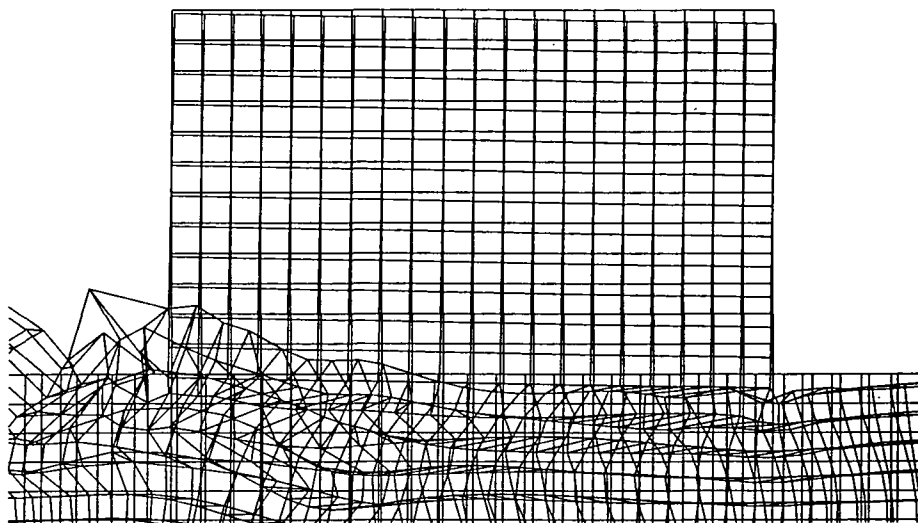


Figure 7.19(c) Typical deformation of the ground and the wall as the impact waves pass through. Time = 0.15 seconds.
(Magnification x 10000)

ABAQUS

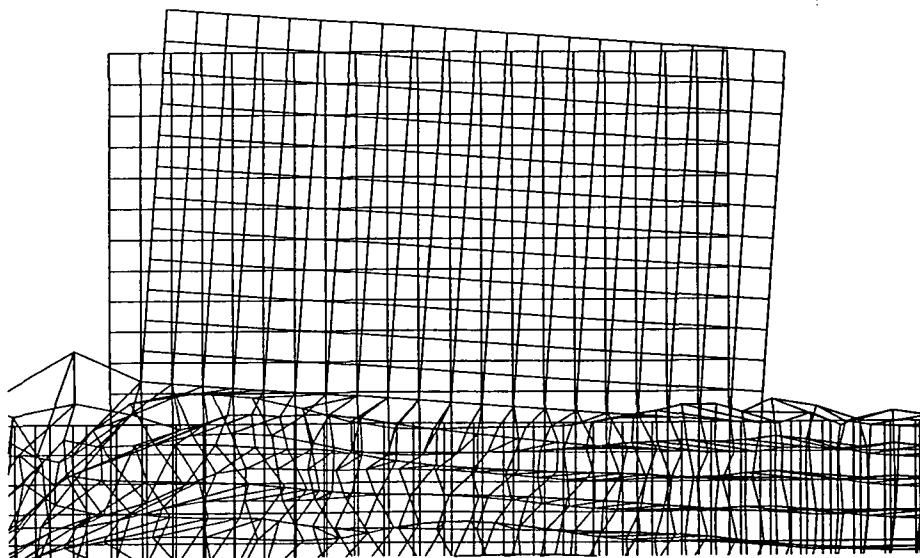


Figure 7.19(d) Typical deformation of the ground and the wall as the impact waves pass through. Time = 0.20 seconds.
(Magnification x 10000)

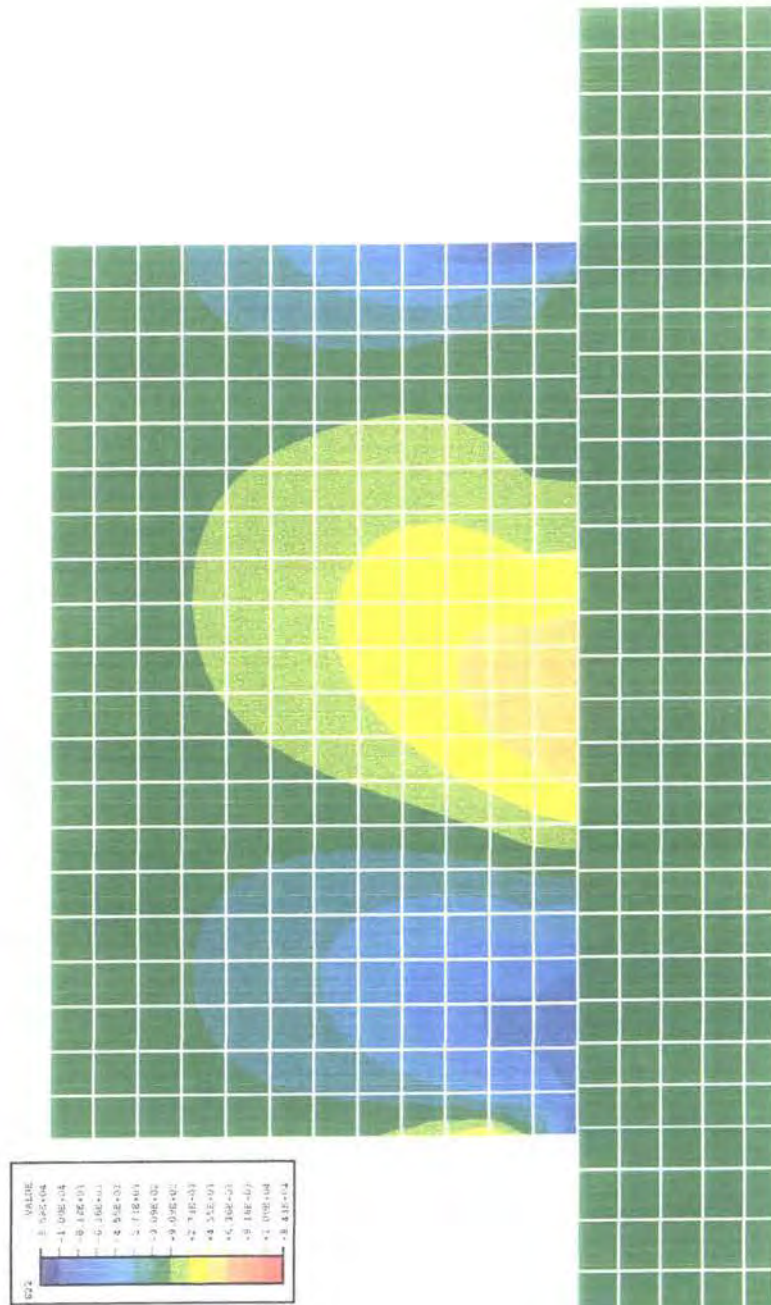


Figure 7.20(a) Contour plot of the vertical stresses in the wall during impact piling

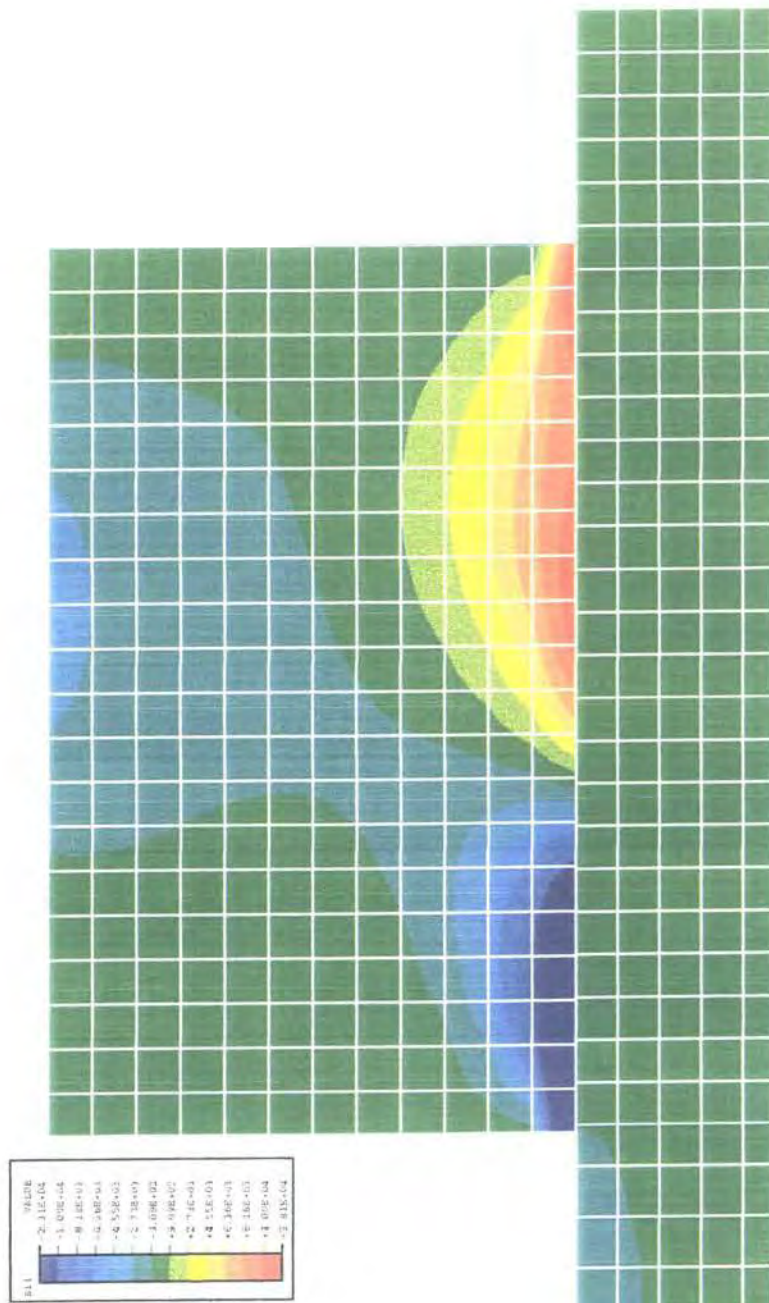


Figure 7.20(b) Contour plots of the horizontal stresses in the wall during impact piling

CHAPTER 8

CONCLUSIONS

8.1 Introduction

The main aim of the work described in this thesis has been the development of computational models for the simulation of ground waves generated by piling. Although several workers have developed finite element and analytical models for the simulation of pile driving in the context of pile drivability, the ground waves generated by pile driving have not been modelled computationally.

Finite element procedures including infinite element and quite boundary formulations have been developed to model the ground waves generated by both vibratory and impact piling. The procedures do not require a detailed knowledge of site conditions and are therefore particularly useful as a preliminary design tool and for modelling the large amount of data that currently exists in order to assist in the development of more rational guidance. The work has brought together research from several areas of study to produce computational procedures for modelling vibrations from pile driving. Detailed comparisons have been made with measured vibrations on pile installation sites. Good correlations have been achieved.

The models have been extended to incorporate a range of common building forms. The techniques could be usefully extended to model the effects of pile driving on various geotechnical structures and pipelines and also other forms of excitation, such as vibrocompaction.

The work in this thesis has concentrated on four main areas. The main findings are summarised below together with recommendations for further work.

8.2 Quiet boundaries for the effective absorption of ground waves from pile driving

One of the limitations of a finite element analysis is the reflection of outgoing waves from the boundaries of the mesh. This effect can be greatly reduced by the use of infinite elements around the boundaries of the finite element mesh. ABAQUS currently provides first- and second-order infinite elements which can be used for dynamic response in the form of a simple tuned damper giving 'quiet boundary' behaviour. The performance of the FE/IE model has been verified in Chapter 3 by applying pure P, S and R waves in turn along a channelled wave guide of finite elements with infinite elements at the far end. The model reproduced the analytical wave patterns very closely within the finite element zone and the ABAQUS infinite elements were shown to absorb the P and S waves almost exactly. However inaccuracies were observed for the more complex Rayleigh waveform where some reflection from the boundary was evident.

It is particularly important to address these inaccuracies as the model needs to be calibrated against measurements of vertical and horizontal particle velocities from geophones on the ground surface and R waves tend to be the dominant waveform at distance from the source.

In order to address these inaccuracies, the Rayleigh viscous boundary proposed by Lysmer & Kuhlemeyer (1969) was programmed into ABAQUS as a 'user-defined'

element. This demonstrated a marked improvement over the ABAQUS infinite elements in the absorption of pure R waves.

The Rayleigh viscous boundary was then applied to the boundary of the axisymmetric finite element mesh used in the wave propagation model for vibratory piling (Chapter 5). The waves generated by pile driving are much more complex than those generated by a single excitation source, and neither classical solutions nor experimental data are available for comparison. The effectiveness of the quiet boundary was therefore determined by comparing the response of the FE/IE mesh with that of a very large finite element mesh, of sufficient size to prevent any boundary reflection into the area (time period) of interest.

Application of the Rayleigh viscous boundary to the vibratory piling model demonstrated its superiority over the ABAQUS infinite elements in absorbing ground waves from vibratory piling. Some S wave reflection was still evident and further work may demonstrate that, theoretically, the optimum boundary for the vibratory piling model is a combined Rayleigh/standard viscous boundary. However it is considered unlikely that this will demonstrate any significant improvement over the very effective Rayleigh viscous boundary.

8.3 A numerical model for vibratory piling

A new two-part finite element model including infinite element and quiet boundary formulations has been developed for the computation of ground waves generated by vibratory piling. The model has been validated by comparisons with vibration measurements taken during vibratory extraction and installation of different pile types at two sites with very different ground conditions. The performance of the model in simulating the ground response at each site is very encouraging. It suggests that further testing of the model by simulating a range of case history data or very comprehensive sets, such as that which will be provided when the 'SIPDIS' results are published, could lead to the development of a very useful predictive tool.

One of the main benefits of the model is that it offers a means of understanding the complex processes of vibration generation during piling. The parametric studies that have been undertaken give some indication of the sensitivity of the ground response to various parameters. The results of these investigations, in conjunction with the interpretation of measured vibration records, give some indication as to the nature of pile/soil interaction, the mechanisms whereby ground waves are formed and the interaction between the various wavefronts.

One of the main findings of this work has been the identification of a 'standing wave' on the ground surface which may be generated by the vibratory motion at certain frequencies and ground conditions. This phenomenon appears to explain the non-monotonical decay of ground surface vibrations with distance from the vibratory piling which has been recorded on many sites. It is suggested that the shape of the 'standing wave' is primarily influenced by the nature of soil displacement around the pile shaft and so the depth of pile penetration has a major influence. However, it should be noted that the resistance of the soil to vibratory motion is dependent upon many factors, not least the frequency of the motion.

Further field monitoring at various sites is required to confirm the occurrence of a 'standing wave' at certain frequencies and ground conditions. If field tests substantiate the existence of this phenomenon, there are likely to be several important implications for the monitoring and modelling of ground waves generated by vibratory piling

Application of 'user-defined' quiet boundary formulations to the model proved to be effective in absorbing the ground waves generated by vibratory piling and demonstrated a marked improvement over the ABAQUS infinite elements. Due to limitations in ABAQUS, the insertion of 'user-defined' elements dictated the use of a general dynamic analysis in the time domain, rather than the frequency domain. However, following the use of the model to simulate some case history data, it was discovered that the use of large FE meshes in conjunction with ABAQUS infinite elements gave satisfactory results, particularly in the cases where material damping greatly reduced the magnitude of the ground waves reaching the boundaries. In these cases, it would be possible and desirable to undertake a direct harmonic response analysis and thus allow the identification of the natural frequencies of the soils and the likelihood of resonance and amplification of ground vibrations at certain operating frequencies.

Full-scale vibratory driving tests with extensive and comprehensive field monitoring are required to provide sufficient data for full refinement and validation of the computational model. High quality measurements of all of the parameters required for full validation of the model does not presently exist and various assumptions and simplifications have been necessary. During vibration monitoring, it is particularly important to ensure that the depth of the pile and the amplitude of pile displacement are recorded against time. The recording and reporting vibration in three orthogonal directions has been shown to be critical in validation of the vibratory model. It would also be particularly useful to gain data from closely spaced geophones in order to establish whether the 'standing wave' is generated.

Soil mechanics research is required in the area of large cyclic deformation to better understand and assess the effects of degradation and liquefaction under the extreme conditions that are generated by vibratory piling. Work is required to investigate the transmission of vibration to the soil under the pile for various end conditions and soil types. The model has been designed to allow future refinements to be incorporated relatively easily.

The new and successful procedures developed for the computation of ground waves from vibratory piling now need to be applied to a large number of varied sites in order to develop site specific guidance. It is envisaged that this guidance could be in the form of design charts or simple formulae for incorporation into the relevant British Standards and Eurocodes.

8.4 A numerical model for impact piling

A new finite element model has been developed for the computation of ground waves from impact piling. A three-part computation was found to be the most effective. The model has been designed to allow incorporation of infinite elements around its boundaries so that the size of the FE mesh, and hence the size of the analyses, can be minimised. The model has been validated by comparisons with measurements of vibrations during impact piling at two sites with very different ground conditions. The performance of the model in simulating the ground response at each site is very

encouraging, especially for the Flitwick site where the correlation with the field data was extremely good.

The model now needs to be tested further by simulating a wider range of case history data, especially those with very comprehensive data sets. Refinement of the model and the development of guidance for the choice of suitable parameters for a range of ground conditions could lead to the development of a very useful predictive tool.

Further soil mechanics research is required to understand the behaviour of the soil adjacent to the pile when it is subjected to an impact. The work that has been done to define soil resistance to piling in the context of pile drivability should be extended to consider the consequent transmission of vibration to the far-field.

8.5 The incorporation of structures into the wave propagation models

A method has been developed to overcome the difficulty of coupling a plane stress configuration (a section through a frame structure) with an axisymmetric FE/IE representation of ground waves from a central excitation source. A full representation of a pile-soil-structure would require a full three-dimensional, computationally expensive model.

The verified ground disturbances adjacent to the pile, computed by the axisymmetric FE/IE models developed in Chapters 5 and 6, were used as input to a three-dimensional wedge-shaped model of a 'slice' of the axisymmetric system. The 3D model accurately simulated the ground waves generated by vibratory pile driving. However, a much finer 3D mesh is required for accurate representation of impact waves. Further work is required to identify suitable models.

The insertion of computed ground excitations to the soil-structure model, verified against site-measured data from both vibratory and impact piling, has demonstrated that the model can be used to identify dynamic displacements and stresses in simple structures. When the structure comprises a slender frame, then imposition of free-ground deformations gives a close representation of the coupled behaviour. However, stiff structures such as in-plane walls show substantial reduction of the free ground movements and so a full three-dimensional analysis is necessary. The soil-structure model has also demonstrated the importance of considering both the vertical and the horizontal wave components when examining the stresses induced in a structure by a passing wave.

Application of this working soil-structure interaction model has only reached a very preliminary stage. Further work is required to verify the model against site-measured data. However, once this has been done, the model could be extended to investigate and predict the effects of piling-induced vibrations on a wide range of structural forms, including geotechnical structures and pipelines. The techniques could be usefully extended to model other forms of excitation, such as vibrocompaction.

REFERENCES

- Anderson, J C (1972). Seismic response effects on embedded structures, *Bull. Seismological Soc. of Amer.*, Vol 62, pp177-194
- Astley, R J (1995). A transient infinite element for multi-dimensional acoustic radiation, submitted to *ASME 15th Biennial Conf. on Mechanical Vibration and Noise*.
- Attewell P B and Farmer I (1973). Attenuation of ground vibration from pile driving. *Ground Engineering*, June, No 4, pp 26-29.
- Attewell, P B, Selby, A R and Uromeihy, A (1991). Non-monotonical decay of ground surface vibrations caused by pile driving', *Earthquake, Blast and Impact*, SECED, Elsevier, pp463-481
- Attewell P B (1995). *Tunnelling contracts and site investigation*. Chapman and Hall, London.
- Attewell, P B, Selby, A R and O'Donnell, L (1992a). Estimation of ground vibration from driven piling based on statistical analyses of recorded data, *Geotechnical and Geological Eng*, Vol 10, No 1, Chapman Hall, pp 41-59.
- Attewell, P B, Selby, A R and O'Donnell, L (1992b). Tables and graphs for the estimation of ground vibration from driven piling operations. *Geotechnical and Geological Eng*, Vol 10, No 1, Chapman Hall, pp 61-87.
- Bamberger, A, Chalindar, B, Joly, P, Roberts, J E, and Teron J L (1988). Absorbing boundary conditions for Rayleigh waves, *SIAM J Sci Stat Comp*, Vol 9, pp 1016-1049.
- Barkan D D (1962). *Dynamics of bases and foundations*. McGraw-Hill, New York.
- Beer, G, and Meek, L (1981). Infinite domain elements, *Int J Num Meth Engng*, Vol 17, pp 43-52.
- Bettess, P and Zienkiewicz, O C, (1977). Diffraction and refraction of surface waves using finite and infinite elements, *Int J Num Meth Eng*, Vol 11, pp 1271-1290.
- Bettess, P (1980). More on infinite elements, *Int J Num Meth Engng*, Vol 15, pp 1613-1626.
- Bettess, P and Zienkiewicz, O C (1977). Diffraction and refraction of surface waves using finite and infinite elements, *Int J Num Meth Engng*, Vol 11, pp 1271-1290.
- Bettess, P (1992). *Infinite Elements*, Penshaw Press.
- Bettess, P (1977). Infinite elements, *Int J Num Meth Engng*, Vol 11, pp 53-64.

Bielefeld M W (1994). Prediction of installation of sheet piles using vibratory hammers. *Fifth International Conference and Exhibition on Piling and Deep Foundations*, DFI 94, Bruges, Belgium.

Bornitz G (1931). *Über die Ausbreitung der von Großkolbenmaschinen erzeugten Bodenschwingungen in die Tiefe*. (On the propagation of groundborne vibration from large steam engines). J Springer, Berlin. [In German]

British Standards Institution (1981). BS5930. *Code of practice for site investigations*. BSI, London.

British Standards Institution (1986). BS8004. *Code of practice for foundations*. BSI, London.

British Standards Institution (1992a) BS 6472 : 1992. *Evaluation of human exposure to vibration in buildings (1Hz to 80Hz)*. BSI, London.

British Standards Institution (1992b). BS5228 : Part 4 : 1992. *Noise control on construction and open sites. Part 4. Code of practice for noise and vibration control applicable to piling operations*. BSI, London.

British Standards Institution (1993). BS7385 :Part 2 : 1993. *Evaluation and measurement for vibration in buildings. Part 2. Guide to damage levels from groundborne vibration*. BSI, London.

Burland J B (1973). Shaft friction of piles in clay – a simple fundamental approach. *Ground Engineering*, Vol 6, No 3, pp 30-42.

CEN 1998. *Adopted European Prestandard ENV 1993-5 : 1998, Eurocode 3: Design of steel structures – Part 5: Piling*. European Committee for Standardisation, Brussels.

Chandler R J (1968). The shaft friction of piles in cohesive soils in terms of effective stresses. *Civ Eng Public Wks Rev* 63, 48-51.

Chow, Y K, and Smith, I M (1981). Static and periodic infinite solid elements, *Int J Num Meth Engng*, Vol 17, No 4, pp 503-526.

Claerbout, J F (1976). *Fundamentals of Geophysical Data Processing*, McGraw-Hill, New York, 1976.

Clayton, J, and Engquist, B (1977). Absorbing boundary conditions for acoustic and elastic wave equations, *Bull. Seismological Soc of Amer*, Vol 67, pp 1529-1541.

Clough G W and Chameau J-L (1980). Measured effects of vibratory sheetpile driving. *Journal of Geotechnical Engineering, Proc ASCE*, Vol 106, No GT10, pp 1081-1099.

Cohen, M and Jennings, P C (1983). Silent boundary methods for transient analysis (in 'Computational Methods for Transient Analysis') Ed T Belytschko and T R J Hughes, Elsevier.

Coyle H M, Lowery L L Jr and Hirsch T J (1977). Wave equation analysis of piling behaviour. *Numerical Methods in Geotechnical Engineering*, Desai C S and Christian J T (eds), McGraw Hill.

Cundall, P A (1978). Solution of infinite dynamic problems by finite modelling in time domain, *Proc 2nd Int Conf Appl Math Modelling*, Madrid.

Crabb G I, New B M and Hiller D M (1991). Ground vibrations caused by the construction and operation of transport systems. *Proc 3rd Symposium on Field Measurements in Geomechanics*, pp 443-454. Balkema, Rotterdam.

D'Appolonia D J (1971). Effects of foundation construction on nearby structures. *Proc 4th Pan-American Conference on Soil Mechanics and Foundation Engineering*, Vol 1, pp 189-236. ASCE, New York.

Das B M (1983). *Fundamentals of soil dynamics*. Elsevier, Amsterdam, 399pp.

Day, S M (1977): 'Finite element analysis of seismic scattering problems', PhD thesis, University of California, San Diego

Deeks A J (1992). *Numerical analysis of pile driving dynamics*, PhD Thesis, The University of Western Australia.

Deeks A J and Randolph M F (1993). Analytical modelling of hammer impact for pile driving. *Int J Numerical Analysis and Methods in Geomechanics*, Vol 17, pp 279-302.

Deeks A J and Randolph M F (1995). A simple model for inelastic footing response to transient loading. *International Journal for Numerical and Analytical Methods in Geomechanics*, Vol 19, pp 307-329, John Wiley & Sons

DIN 4150 *Draft* (1990): 'Vibrations in structures', Berlin

Doring, H (1997): 'Verformungseigenschaften von bindigen Boden bei kleinen Deformationen', Kungl Tekniska Hogskolan, Stockholm

Ewing, W M, Jardetzky, W S and Press, F (1957): 'Elastic waves in layered media', McGraw-Hill, New York

Fleming W G K, Weltman A J, Randolph, M F and Elson W K (1992). *Piling Engineering*. 2nd Edition. E & F N Spon.

Francescon M (1983). *Model pile tests in clay: stresses and displacements due to installation and axial loading*. PhD Thesis, University of Cambridge.

Gajo, A, Saetta, A and Vitaliani, R (1996): 'Silent boundary conditions for wave propagation in saturated porous media', *Internat. J. Numerical Methods in Eng.*, Vol 20, pp253-273

Glanville W H, Grime G, Fox E N and Davies W W (1938). An investigation of the stresses in reinforced concrete piles during driving. British Building Research Board, Technical Paper 20.

Griffin M J (1998). Fundamentals of human responses to vibration. In *Fundamentals of Noise and Vibration*, ed F Fahy and J Walker. pp179-224. E and F N Spon, London.

Gutowski T G and Dym C L (1976). Propagation of ground vibration: A review. *Journal of Sound and Vibration*, Vol 49, No 2 pp 179-193.

Häggblad, B and Nordgren, G (1987): 'Modelling nonlinear soil-structure interaction using interface elements, elastic-plastic soil elements and absorbing infinite elements', *Computers and Structures*, Vol 26, No 1/2, pp307-324

Hanazato T and Kishida H (1992). Analysis of ground vibrations generated by pile driving – Application of pile driving analysis to environmental problem. *Application of Stress-Wave Theory to Piles*, F B J Barends (ed), Balkema, Rotterdam.

Harris F (1983). *Ground Engineering Equipment and Methods*. Granada.

Haupt, W A (1977): 'Surface-waves in nonhomogeneous half-space', *Dynamical Methods in Soil and Rock Mechanics Proceedings*, Karlsruhe, Germany, 5-16 Sept 1977.

Haupt W (1986). *Bodendynamik, Grundlagen und Anwendungen*. Hrsg. Haupt, W. Friedr. Vieweg & Sohn, Braunschweig/Wiesbaden, pp 53-105.

Head J M and Jardine F M (1992). Ground-borne vibrations arising from piling. *CIRIA Technical Note 142*. Construction Industry Research and Information Association, London. 83pp.

Heckman W S and Hagerty D J (1978). Vibrations associated with pile driving. *Journal of the Construction Division, Proc ASCE*, Vol 104, No CO4, pp 385-394.

Hibbitt H D and Karlsson B I (1979). Analysis of Pipe Whip, EPRI, Report NP-1208, 1979.

Hibbitt, Karlsson & Sorenson, Inc (1998) ABAQUS Manuals, version 5.8

Higdon, R L (1986): 'Initial-boundary value problems for linear hyperbolic systems', *SIAM Rev.*, Vol 28, pp177-217

Higdon, R L (1990): 'Radiation boundary conditions for elastic wave propagation', *SIAM J. Numer. Anal.*, Vol 27, pp831-870

Higdon, R L (1992): 'Absorbing boundary conditions for acoustic and elastic waves in stratified media', *J. Comput. Phys.*, Vol 101, pp386-418

Hilber, H M, Hughes, T J R and Taylor, R L (1977): 'Improved numerical dissipation for time integration algorithms in structural dynamics', *Earthquake Eng. and Structural Dynamics*, Vol 6, pp283-292

Hiller D M and Bowers K H (1997). Groundborne vibration from mechanised construction works. *Proc Tunnelling '97*, pp 721-735. Institution of Mining and Metallurgy, London.

Hiller, D M (1999): 'The prediction of groundborne vibration caused by mechanised construction works', PhD Thesis, University of Surrey.

Hiller D M and Crabb G I (2000). Groundborne vibration caused by mechanised construction works. *Transport Research Laboratory Project Report 429*, Transport Research Laboratory, Crowthorne.

Holeyman A, Legrand C and Van Rompaey D (1996). A Method to predict the driveability of vibratory driven piles. Proceedings of the 3rd International Conference on the Application of Stress-Wave Theory to Piles, pp 1101-1112, Orlando, USA, 1996

Holeyman A E (2000). Keynote lecture: Vibratory driving analysis. *Application of Stress-Wave Theory to Piles*, Niyama & Beim (eds), Balkema, Rotterdam, pp479-494. ISBN 90 5809 150 3

Hughes, T J R (1978): 'A simple scheme for developing "upwind" finite elements', *Internat. J. Numerical Methods in Eng.*, Vol 12, pp1359-1369

Isenberg, J, Vaughan, D K and Sandler, I (1978): 'Non-linear soil-structure interaction', report prepared by Weidlinger Associated for the Electric Power Research Institute, Dec. 1978

Ishihara, K (1986): 'Evaluation of soil properties for use in earthquake response analysis', *Geomechanical modelling in Engineering practice*, Balkema, Rotterdam, pp241-275

Jaky J (1944). The coefficient of earth pressure at rest. *Jour Soc Hungarian Architects and Engineers* 78(22).

Jongmans D (1996). Prediction of ground vibrations caused by pile driving: a new methodology. *Engineering Geology*, Vol 42, pp 25-36.

Laghrouche, O (1996): 'Simulation numerique de propagations d'ondes dans les sols - application a l'isolation vibratoire', PhD thesis, University of Nantes, France, April 1996

Liao, Z P and Wong, H L (1984): 'A transmitting boundary for the numerical simulation of elastic wave propagation', *Soil Dyn. Earthquake Eng.*, Vol 3, pp133-144

Liao, Z P, and Liu, J B (1992): 'Numerical instabilities of a local transmitting boundary', *Earthquake Eng. Struct. Dyn.*, Vol 21, pp65-77

- Luco, J E, Hadjian, A H and Bos, H D (1975): 'The dynamic modelling of the half-plane by finite elements', *Nuclear Eng. and Design*, Vol 31, pp184-194
- Lysmer J and Richart F E (1966). Dynamic response of footings to vertical loading. *Journal of the Soil Mechanics and Foundations Division*, Vol 92, pp 65-91.
- Lysmer, J and Kuhlemeyer, R L (1969): 'Finite dynamic model for infinite media', *J Eng Mech Div ASCE*, pp859-877, August 1969
- Lysmer, J (1970): 'Lumped mass method for Rayleigh waves', *Bull. Seismological Soc. of Amer.*, Vol 60, p89-104
- Lysmer, J, and Waas, G (1972): 'Shear waves in plane infinite structures', *J. Eng. Mechanics Div. ASCE*, pp85-105, Feb. 1972
- Lysmer, J and Drake, L A (1972): 'A finite element method for seismology', in *Methods of Computational Physics*, Vol 11, Chapter 6, Academic Press, New York
- Mabsout M E and Tassoulas J L (1994). A finite element model for the simulation of pile driving. *International Journal for Numerical Methods in Engineering*, Vol 37, pp 257-278, John Wiley & Sons.
- Mabsout M E, Reese L C and Tassoulas J L (1995). Study of Pile Driving by Finite-Element Method. *Journal of Geotechnical Engineering, Proc ASCE*, Vol 121, No 7, pp 535-543.
- Maguire J R and Wyatt T A (1999). *Dynamics, an introduction for civil and structural engineers*. ICE design and practice guide. Thomas Telford Limited, London.
- Makris N and Gazetas G (1993). Displacement phase differences in a harmonically oscillating pile. *Geotechnique*, Vol 43, No 1, pp 135-150.
- Malam D (1993): Assessing the effect of environmental vibration in buildings. BS 7385 Part 2. *Proceedings of Institute of Acoustics*, Vol 15, Part 4, pp23-51. Institute of Acoustics, St Albans
- Mallard D J and Bastow P (1979). Some observations on the vibrations caused by pile driving. *Proc ICE Conference on Recent developments in the design and construction of piles*, pp 261-284. Institution of Civil Engineers, London.
- Martin D J (1980). Ground vibrations from impact pile driving during road construction. *Transport and Road Research Laboratory Research Report 544*, Transport Research Laboratory, Crowthorne.
- Massarsch K R and Broms B B (1991). Damage Criteria for Small Amplitude Ground Vibrations, *Second International Conference on Recent Advances in Geotechnical Earthquake Engineering and Soil Dynamics*, St Louis, Missouri, March 11-15, 1991, pp1451-1459.

Massarsch K R (1992). Keynote lecture: Static and dynamic soil displacements caused by pile driving. *Proc 4th International Conference on the Application of Stress-Wave Theory to Piles*, pp 15-25. Balkema, Rotterdam.

Matthews M C, Hope V S and Clayton C R I (1996). The use of surface waves in the determination of ground stiffness profiles. *Proc Institution of Civil Engineers, Geotechnical Engineering*, Vol 119, April, pp 84-95

Medina, F (1981): 'An axisymmetric infinite element', *Int. J. Num. Meth. Engng.*, Vol 17, pp1177-1185

Medina, F and Penzian, J (1982): 'Infinite elements for elastodynamics', *Earthquake Eng and Structural Dynamics*, Vol 10(5), pp699-709

Medina, F and Taylor, R L (1983): 'Finite element techniques for problems of unbounded domains', *Int. J. Num. Meth. Engng.*, Vol 19, pp1209-1226

Meyerhof G G (1976). Bearing capacity and settlement of pile foundations. *J Geot Engng Div, ASCE*, 102(GT3), pp 197-228.

Meynard A and Corte J-F (1984). Experimental study of lateral resistance during driving. *Second Int Conf on the Application of Stress-Wave Theory to Piles*, Stockholm.

Miller, G F and Pursey, H (1955): 'On the partition of energy between elastic waves in a semi-infinite solid', *Proc. of the Royal Society of London, Series A: Mathematical and Physical Sciences*, Vol 233, No 1192, pp55-69

Mintrop L (1911). Über die Ausbreitung der von den Massendrukken einer Großgassmaschine erzeugten Bodenschwingungen. (On the propagation of groundborne vibration from heavy gas powered printing press.) Dissertation, Gottingen. [In German]

New B M (1982). Vibration caused by underground construction. *Proc Tunnelling '82*, pp 217-229. Institution of Mining and Metallurgy, London.

New B M (1986). Ground vibration caused by civil engineering works. *Transport and Road Research Laboratory Research Report 53*, Transport Research Laboratory, Crowthorne.

Noorzaei, J, Viladkar, M N and Godbole, P N (1994): 'Non-linear soil-structure interaction in plane frames', *Engineering Comp*, Vol 11

Novak M (1977). Vertical vibration of floating piles. *J Eng Mech Div, ASCE*, Vol 103, pp 153-168.

Novak M, Nogami T and Aboul-Ella F (1978). Dynamic soil reactions for plane strain case. *J Eng Mech Div, ASCE*, Vol 104, pp 953-959.

O'Neill D B (1971). Vibration and dynamic settlement from pile driving. *Proceedings of Conference on Behaviour of Piles*, pp135-140. ICE, London.

Parry R H G and Swain C W (1977). Effective stress methods of calculating skin friction of driven piles in soft clay. *Ground Engineering*, Vol 10, No 3, pp 24-26.

Parry R H G and Swain C W (1977). A study of skin friction on piles in stiff clay. *Ground Engineering*, Vol 10, No 8, pp 33-37.

Peng, C and Toksoz, M N (1994): 'An optimal absorbing boundary condition for finite difference modelling of acoustic and elastic wave propagation', *J. Acoust. Soc. Am.*, Vol 95, p733-745

Ramshaw C L, Selby A R and Bettess P (1998a). Computation of the transmission of waves from pile driving. In *Ground Dynamics and Man-made processes*, ed B O Skipp, pp 115-128. Thomas Telford, London.

Ramshaw C L, Selby A R and Bettess P (1998b). Computed ground waves due to piling. *Geotech Sp Pub No 75* ed Dakoulas P, Yegian M & Holtz R D. Geo Inst of ASCE. Proc Conf Geotechnical Earthquake Eng & Soil Dynamics. Vol 2, Seattle

Ramshaw C L, Selby A R and Bettess P (2000). Computation of ground waves due to piling. *Application of Stress-Wave Theory to Piles*, Niyama & Beim (eds), Balkema, Rotterdam, pp 495-502, Proc of the 6th International Conf on the Application of Stress-Wave Theory to Piles, Sao Paulo, Brazil, 2000.

Ramshaw C L, Selby A R and Bettess P (2001). Ground waves generated by pile driving, and structural interaction. Fourth International Conference on Recent Advances in Geotechnical Earthquake Engineering and Soil Dynamics, ASCE, San Diego, March 2001

Randolph M F and Simons H A (1986). An improved soil model for one-dimensional pile driving analysis. *Third Int Conf on Numerical Methods in Offshore Piling*, Nantes, pp 3-15.

Randolph M F (1991). Analysis of the dynamics of pile driving. In *Developments in Soil Mechanics IV: Advanced Geotechnical Analyses*, (eds P K Banerjee and R Butterfield), Elsevier Applied Science, also *University of Western Australia Research Report No G1001*.

Rausche F, Moses F and Goble G G (1972). Soil Resistance Predictions from Pile Dynamics. *Journal of the Soil Mechanics and Foundations Division*, ASCE, Vol 98 No SM9 Proc Paper 9220, Sept 1972.

Rempe D M and Davisson M T (1977). Performance of diesel pile hammers. *Proc 9th International Conference on Soil Mechanics and Foundation Engineering*, Vol 2, pp 347-354. Japanese Society of Soil Mechanics and Foundation Engineering.

Richart F E, Hall J R and Woods R D (1970). *Vibrations of soils and foundations*. Prentice-Hall, New Jersey.

Robinson, A R (1976): 'The transmitting boundary - again', *Structural and Geotechnical Mechanics*, Ed W J Hall, Prentice-Hall, New Jersey.

- Uromeihy, A (1990): 'Ground vibration measurements with special reference to pile driving', PhD Thesis, University of Durham, June 1990
- Van Staaldunin P C and Waarts P H (1992). Prediction of vibrations due to pile driving. *Proc 4th International Conference on the Application of Stress-Wave Theory to Piles*, pp 159-166. Balkema, Rotterdam.
- Vesic A S (1977). Design of Pile Foundations, National Co-operative Highway Research Program, Synthesis of Highway Practice No 42, Transportation Research Board, National Research Council, Washington D C.
- Waarts P H and Bielefeld M W (1994). Prediction and control of vibrations due to piled riving and sheet pile vibration. Fifth International Conference and Exhibition on Piling and Deep Foundations, DFI 94, Bruges, Belgium.
- Whyley P J and Sarsby R W (1992). Groundborne vibration from piling. *Ground Engineering*, May 1992, pp 32-27.
- White, W, Valliappan, S and Lee, I K (1977): 'Unified Boundary for Finite Dynamic Models', *J. Eng. Mechanics Div. ASCE*, pp949-964, Oct 1977.
- Wiss J F (1967). Damage effects of pile driving vibration. *Highway Research Record No 155*, pp 14-20. Highways Research Board, Washington DC.
- Wolf J P (1988). *Soil-Structure-Interaction Analysis in Time Domain*. Prentice-Hall, New Jersey.
- Wong D, O'Neill M W and Vipulanandan C (1992). Modelling of vibratory pile driving in sand. *International Journal for Numerical and Analytical Methods in Geomechanics*, Vol 16, pp189-210, John Wiley & Sons.
- Woods, R D and Jedeled, L P (1985): 'Energy-attenuation relationships from construction vibrations', *Vibration problems in geotechnical engineering*, ASCE, Spec Tech Pub, pp229-246
- Woods R D and Jedeled L P (1985). Energy-attenuation relationships from construction vibrations. "*Vibration problems in geotechnical engineering*" *Proc symposium sponsored by Geotechnical Engineering Division, ASCE*, ed. G Gazetas and E T Selig, pp 229-246. ASCE, New York.
- Yang, S C and Yun, C B (1992): 'Axisymmetric infinite elements for soil-structure interaction analysis', *Eng. Struct.*, Vol 14, No 6, pp361-370
- Yang, Y B, Kuo, S R and Hung, H H (1996): 'Frequency-independent infinite elements for analysing semi-infinite problems', *Int. J. Num. Meth. Engng.*, Vol 39, pp3553-3569
- Zhao, C and Valliappan, S (1993): 'A dynamic infinite element for three-dimensional infinite-domain wave problems', *Int. J. Num. Meth. Engng.*, Vol 36, pp2567-2580

Zienkiewicz, O C and Bettess, P (1975): 'Infinite elements in the study of fluid structure interaction problems', Proc 2nd Int Symp on Comp Methods Appl Sci, Versailles

Zienkiewicz, O C, Bettess, P, Chiam, T C and Emson, E (1981): 'Numerical methods for unbounded field problems and a new infinite element formulation', in *Computational Methods for Infinite Domain Media Structure Interaction*, A J Kalinowski, ed., ASME, AMD Vol 46, pp115-148, New York

Zienkiewicz, O C, Emson, C and Bettess, P (1983): 'A novel boundary infinite element', *International Journal for Numerical Methods in Engineering*, Vol 19, pp393-404

APPENDIX A

Publications resulting from this research

Publications resulting from this research

Ramshaw C L, Selby A R and Bettess P (1998a). Computation of the transmission of waves from pile driving. In *Ground Dynamics and Man-made processes*, ed B O Skipp, pp 115-128. Thomas Telford, London.

Ramshaw C L, Selby A R and Bettess P (1998b). Computed ground waves due to piling. *Geotech Sp Pub No 75* ed Dakoulas P, Yegian M & Holtz R D. Geo Inst of ASCE. Proc Conf Geotechnical Earthquake Eng & Soil Dynamics. Vol 2, Seattle

Ramshaw C L (1998). Computation of ground waves from pile driving. Extended abstract and presentation for the Fifth BGS Young Geotechnical Engineers' Conference, university of Newcastle, March 1998

Ramshaw C L, Selby A R and Bettess P (2000). Computation of ground waves due to piling. *Application of Stress-Wave Theory to Piles*, Niyama & Beim (eds), Balkema, Rotterdam, pp 495-502, Proc of the 6th International Conf on the Application of Stress-Wave Theory to Piles, Sao Paulo, Brazil, 2000.

Ramshaw C L (2000). The use of ABAQUS to model vibrations generated by pile driving. Fourteenth UK ABAQUS User Group Conference, Warrington, September 2000

Ramshaw C L, Selby A R and Bettess P (2001). Ground waves generated by pile driving, and structural interaction. Fourth International Conference on Recent Advances in Geotechnical Earthquake Engineering and Soil Dynamics, ASCE, San Diego, March 2001

APPENDIX B

Calculation of Fourier Constants for P, S and R waves

CALCULATION OF FOURIER CONSTANTS FOR A P WAVE

1. Choose

$$E = 0.2e^9 \text{ N/m}^2$$

$$\nu = 0.2$$

$$\rho = 1998 \text{ kg/m}^3$$

2. Calculate G and λ

$$G = \frac{E}{2(1+\nu)} = 83.3e^6$$

$$\lambda = \frac{E\nu}{(1+\nu)(1-2\nu)} = 55e^6$$

3. Choose $T = 1.0$ second

$$\varpi = \frac{2\pi}{T} \quad \therefore \varpi = 2\pi$$

4. Calculate the propagation velocity

$$c_p = \sqrt{\frac{\lambda + 2G}{\rho}} = 333.5 \text{ m/s}$$

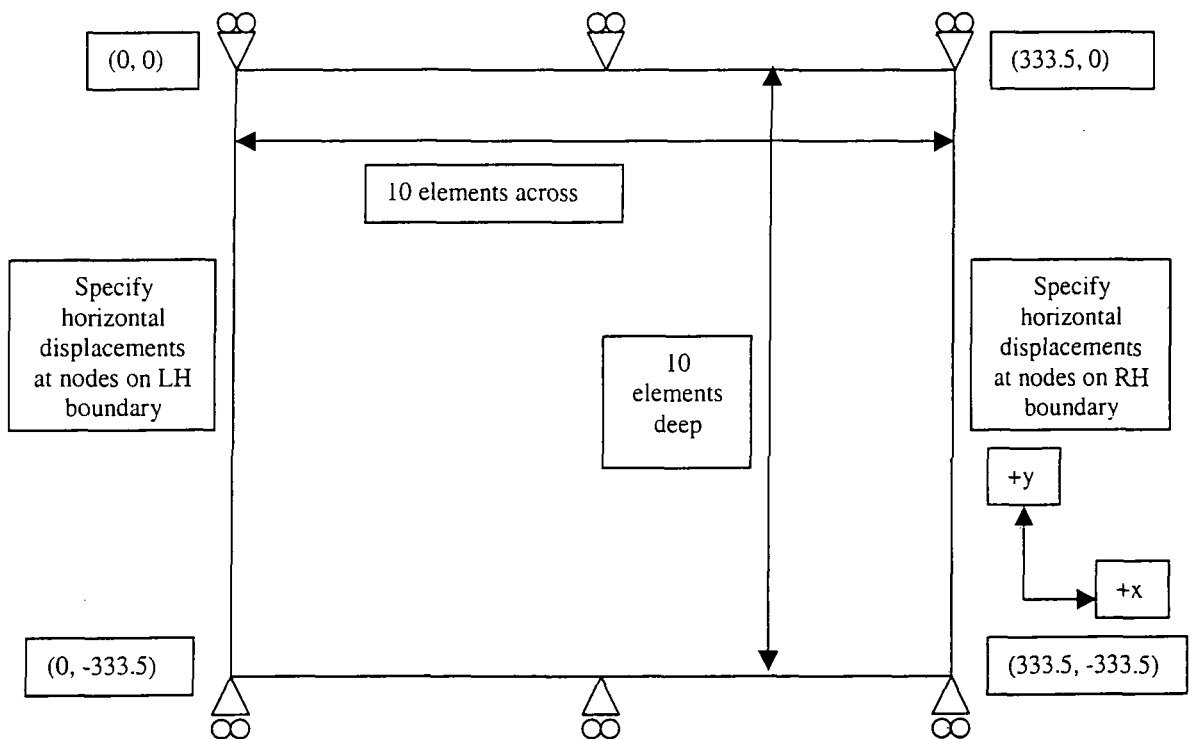
5. Calculate the wave number

$$k = \frac{\varpi}{c_p} = \frac{2\pi}{333.5} = 0.0188$$

6. Calculate the wavelength

$$\Lambda = \frac{2\pi}{k} = 333.5 \text{ m}$$

7. Create a mesh with 10 nodes per wavelength. Fix the nodes on the top and bottom boundaries in the vertical direction



8. Use $u_x = -k\sin(kx - \omega t)$ to specify horizontal displacements on LH and RH boundaries as a function of time.

9. In ABAQUS, the periodic displacement of nodes is specified as a Fourier series as follows:

$$a = A_0 + \sum_{n=1}^N [A_n \cos n\omega(t - t_0) + B_n \sin n\omega(t - t_0)] \quad \text{for } t \geq t_0$$

$$a = A_0 \quad \text{for } t < 0$$

where

a = amplitude of displacement ($= u_x$)

and

$t_0, \omega, A_0, A_n, B_n, n = 1, 2, \dots, N$ are constants defined on the datalines as follows:

* AMPLITUDE, DEFINITION = PERIODIC

N, ω, t_0, A_0

$A_1, B_1, A_2, B_2, \dots, A_n, B_n$

10. Calculation of Fourier constant for LH boundary

On LH boundary, $x = 0$

$$\therefore u_x = -k \sin(-\omega t)$$

$$= \frac{-2\pi}{333.5} \sin(-2\pi)$$

$$= A_0 + \sum_{n=1}^N [A_n \cos n\omega(t - t_0) + B_n \sin n\omega(t - t_0)]$$

$$\therefore N = 1$$

$$\omega = -2\pi$$

$$t_0 = 0$$

$$A_0 = 0$$

$$A_1 = 0$$

$$B_1 = \frac{-2\pi}{333.5}$$

\therefore ABAQUS command is:

*AMPLITUDE, DEFINITION = PERIODIC

1, -2 π , 0, 0

0, $\frac{-2\pi}{333.5}$

11. Calculation of Fourier constant for RH boundary

On RH boundary, $x = 333.5$

$$\begin{aligned}\therefore u_x &= -k \sin(333.5k - \omega t) \\ &= \frac{-2\pi}{333.5} \sin(2\pi - 2\pi t) \\ &= \frac{-2\pi}{333.5} \sin -2\pi(t - 1) \\ &= A_0 + \sum_{n=1}^N [A_n \cos n\omega(t - t_0) + B_n \sin n\omega(t - t_0)]\end{aligned}$$

$$\begin{aligned}\therefore N &= 1 \\ \omega &= -2\pi \\ t_0 &= 1 \\ A_0 &= 0 \\ A_1 &= 0 \\ B_1 &= \frac{-2\pi}{333.5}\end{aligned}$$

\therefore ABAQUS command is:

*AMPLITUDE, DEFINITION = PERIODIC

1, -2 π , 1, 0

0, $\frac{-2\pi}{333.5}$

CALCULATION OF FOURIER CONSTANTS FOR AN S WAVE

1. Choose

$$E = 0.2e^9 \text{ N/m}^2$$

$$\nu = 0.2$$

$$\rho = 1998 \text{ kg/m}^3$$

2. Calculate G and λ

$$G = \frac{E}{2(1+\nu)} = 83.3e^6$$

$$\lambda = \frac{E\nu}{(1+\nu)(1-2\nu)} = 55e^6$$

3. Choose $T = 1.0$ second

$$\varpi = \frac{2\pi}{T} \quad \therefore \varpi = 2\pi$$

4. Calculate the propagation velocity

$$c_s = \sqrt{\frac{G}{\rho}} = 204.23 \text{ m/s}$$

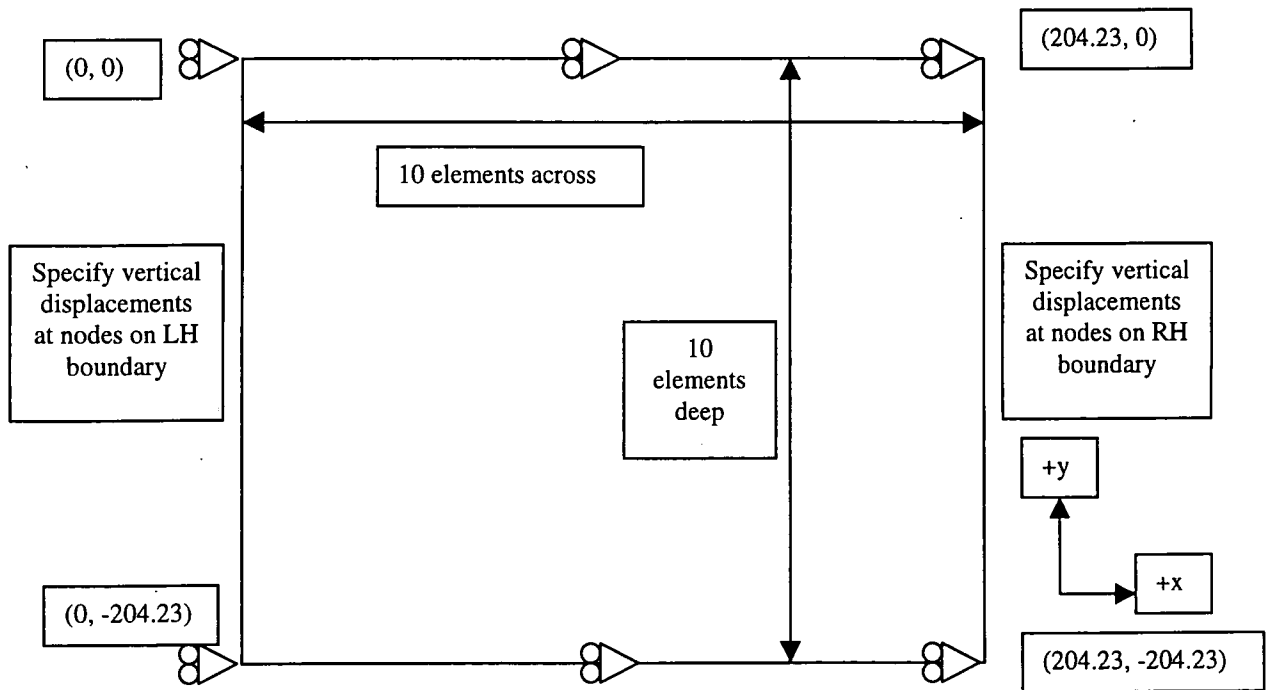
5. Calculate the wave number

$$k = \frac{\varpi}{c_s} = \frac{2\pi}{204.23} = 0.031$$

6. Calculate the wavelength

$$\Lambda = \frac{2\pi}{k} = 204.23 \text{ m}$$

7. Create a mesh with 10 nodes per wavelength. Fix the nodes on the top and bottom boundaries in the horizontal direction



8. Use $u_y = -k\sin(kx - \omega t)$ to specify vertical displacements on LH and RH boundaries as a function of time.

9. In ABAQUS, the periodic displacement of nodes is specified as a Fourier series as follows:

$$a = A_0 + \sum_{n=1}^N [A_n \cos n\omega(t - t_0) + B_n \sin n\omega(t - t_0)] \quad \text{for } t \geq t_0$$

$$a = A_0 \quad \text{for } t < 0$$

where

a = amplitude of displacement (= u_y)

and

$t_0, \omega, A_0, A_n, B_n, n = 1, 2, \dots, N$ are constants defined on the datalines as follows:

* AMPLITUDE, DEFINITION = PERIODIC

N, ω, t_0, A_0

$A_1, B_1, A_2, B_2, \dots, A_n, B_n$

10. Calculation of Fourier constant for LH boundary

On LH boundary, $x = 0$

$$\therefore u_y = -k \sin(-\omega t)$$

$$= \frac{-2\pi}{204.23} \sin(-2\pi)$$

$$= A_0 + \sum_{n=1}^N [A_n \cos n\omega(t - t_0) + B_n \sin n\omega(t - t_0)]$$

$$\therefore N = 1$$

$$\omega = -2\pi$$

$$t_0 = 0$$

$$A_0 = 0$$

$$A_1 = 0$$

$$B_1 = \frac{-2\pi}{204.23}$$

\therefore ABAQUS command is:

*AMPLITUDE, DEFINITION = PERIODIC

1, -2 π , 0, 0

0, $\frac{-2\pi}{204.23}$

REFERENCES

- Anderson, J C (1972). Seismic response effects on embedded structures, *Bull. Seismological Soc. of Amer.*, Vol 62, pp177-194
- Astley, R J (1995). A transient infinite element for multi-dimensional acoustic radiation, submitted to *ASME 15th Biennial Conf. on Mechanical Vibration and Noise*.
- Attewell P B and Farmer I (1973). Attenuation of ground vibration from pile driving. *Ground Engineering*, June, No 4, pp 26-29.
- Attewell, P B, Selby, A R and Uromeihy, A (1991). Non-monotonical decay of ground surface vibrations caused by pile driving', *Earthquake, Blast and Impact*, SECED, Elsevier, pp463-481
- Attewell P B (1995). *Tunnelling contracts and site investigation*. Chapman and Hall, London.
- Attewell, P B, Selby, A R and O'Donnell, L (1992a). Estimation of ground vibration from driven piling based on statistical analyses of recorded data, *Geotechnical and Geological Eng*, Vol 10, No 1, Chapman Hall, pp 41-59.
- Attewell, P B, Selby, A R and O'Donnell, L (1992b). Tables and graphs for the estimation of ground vibration from driven piling operations. *Geotechnical and Geological Eng*, Vol 10, No 1, Chapman Hall, pp 61-87.
- Bamberger, A, Chalindar, B, Joly, P, Roberts, J E, and Teron J L (1988). Absorbing boundary conditions for Rayleigh waves, *SIAM J Sci Stat Comp*, Vol 9, pp 1016-1049.
- Barkan D D (1962). *Dynamics of bases and foundations*. McGraw-Hill, New York.
- Beer, G, and Meek, L (1981). Infinite domain elements, *Int J Num Meth Engng*, Vol 17, pp 43-52.
- Bettess, P and Zienkiewicz, O C, (1977). Diffraction and refraction of surface waves using finite and infinite elements, *Int J Num Meth Eng*, Vol 11, pp 1271-1290.
- Bettess, P (1980). More on infinite elements, *Int J Num Meth Engng*, Vol 15, pp 1613-1626.
- Bettess, P and Zienkiewicz, O C (1977). Diffraction and refraction of surface waves using finite and infinite elements, *Int J Num Meth Engng*, Vol 11, pp 1271-1290.
- Bettess, P (1992). *Infinite Elements*, Penshaw Press.
- Bettess, P (1977). Infinite elements, *Int J Num Meth Engng*, Vol 11, pp 53-64.

Bielefeld M W (1994). Prediction of installation of sheet piles using vibratory hammers. *Fifth International Conference and Exhibition on Piling and Deep Foundations*, DFI 94, Bruges, Belgium.

Bornitz G (1931). *Über die Ausbreitung der von Großkolbenmaschinen erzeugten Bodenschwingungen in die Tiefe*. (On the propagation of groundborne vibration from large steam engines). J Springer, Berlin. [In German]

British Standards Institution (1981). BS5930. *Code of practice for site investigations*. BSI, London.

British Standards Institution (1986). BS8004. *Code of practice for foundations*. BSI, London.

British Standards Institution (1992a) BS 6472 : 1992. *Evaluation of human exposure to vibration in buildings (1Hz to 80Hz)*. BSI, London.

British Standards Institution (1992b). BS5228 : Part 4 : 1992. *Noise control on construction and open sites. Part 4. Code of practice for noise and vibration control applicable to piling operations*. BSI, London.

British Standards Institution (1993). BS7385 :Part 2 : 1993. *Evaluation and measurement for vibration in buildings. Part 2. Guide to damage levels from groundborne vibration*. BSI, London.

Burland J B (1973). Shaft friction of piles in clay – a simple fundamental approach. *Ground Engineering*, Vol 6, No 3, pp 30-42.

CEN 1998. *Adopted European Prestandard ENV 1993-5 : 1998, Eurocode 3: Design of steel structures – Part 5: Piling*. European Committee for Standardisation, Brussels.

Chandler R J (1968). The shaft friction of piles in cohesive soils in terms of effective stresses. *Civ Eng Public Wks Rev* 63, 48-51.

Chow, Y K, and Smith, I M (1981). Static and periodic infinite solid elements, *Int J Num Meth Engng*, Vol 17, No 4, pp 503-526.

Claerbout, J F (1976). *Fundamentals of Geophysical Data Processing*, McGraw-Hill, New York, 1976.

Clayton, J, and Engquist, B (1977). Absorbing boundary conditions for acoustic and elastic wave equations, *Bull. Seismological Soc of Amer*, Vol 67, pp 1529-1541.

Clough G W and Chameau J-L (1980). Measured effects of vibratory sheetpile driving. *Journal of Geotechnical Engineering, Proc ASCE*, Vol 106, No GT10, pp 1081-1099.

Cohen, M and Jennings, P C (1983). Silent boundary methods for transient analysis (in 'Computational Methods for Transient Analysis') Ed T Belytschko and T R J Hughes, Elsevier.

Coyle H M, Lowery L L Jr and Hirsch T J (1977). Wave equation analysis of piling behaviour. *Numerical Methods in Geotechnical Engineering*, Desai C S and Christian J T (eds), McGraw Hill.

Cundall, P A (1978). Solution of infinite dynamic problems by finite modelling in time domain, *Proc 2nd Int Conf Appl Math Modelling*, Madrid.

Crabb G I, New B M and Hiller D M (1991). Ground vibrations caused by the construction and operation of transport systems. *Proc 3rd Symposium on Field Measurements in Geomechanics*, pp 443-454. Balkema, Rotterdam.

D'Appolonia D J (1971). Effects of foundation construction on nearby structures. *Proc 4th Pan-American Conference on Soil Mechanics and Foundation Engineering*, Vol 1, pp 189-236. ASCE, New York.

Das B M (1983). *Fundamentals of soil dynamics*. Elsevier, Amsterdam, 399pp.

Day, S M (1977): 'Finite element analysis of seismic scattering problems', PhD thesis, University of California, San Diego

Deeks A J (1992). *Numerical analysis of pile driving dynamics*, PhD Thesis, The University of Western Australia.

Deeks A J and Randolph M F (1993). Analytical modelling of hammer impact for pile driving. *Int J Numerical Analysis and Methods in Geomechanics*, Vol 17, pp 279-302.

Deeks A J and Randolph M F (1995). A simple model for inelastic footing response to transient loading. *International Journal for Numerical and Analytical Methods in Geomechanics*, Vol 19, pp 307-329, John Wiley & Sons

DIN 4150 *Draft* (1990): 'Vibrations in structures', Berlin

Doring, H (1997): 'Verformungseigenschaften von bindigen Boden bei kleinen Deformationen', Kungl Tekniska Hogskolan, Stockholm

Ewing, W M, Jardetzky, W S and Press, F (1957): 'Elastic waves in layered media', McGraw-Hill, New York

Fleming W G K, Weltman A J, Randolph, M F and Elson W K (1992). *Piling Engineering*. 2nd Edition. E & F N Spon.

Francescon M (1983). *Model pile tests in clay: stresses and displacements due to installation and axial loading*. PhD Thesis, University of Cambridge.

Gajo, A, Saetta, A and Vitaliani, R (1996): 'Silent boundary conditions for wave propagation in saturated porous media', *Internat. J. Numerical Methods in Eng.*, Vol 20, pp253-273

Glanville W H, Grime G, Fox E N and Davies W W (1938). An investigation of the stresses in reinforced concrete piles during driving. British Building Research Board, Technical Paper 20.

Griffin M J (1998). Fundamentals of human responses to vibration. In *Fundamentals of Noise and Vibration*, ed F Fahy and J Walker. pp179-224. E and F N Spon, London.

Gutowski T G and Dym C L (1976). Propagation of ground vibration: A review. *Journal of Sound and Vibration*, Vol 49, No 2 pp 179-193.

Häggblad, B and Nordgren, G (1987): 'Modelling nonlinear soil-structure interaction using interface elements, elastic-plastic soil elements and absorbing infinite elements', *Computers and Structures*, Vol 26, No 1/2, pp307-324

Hanazato T and Kishida H (1992). Analysis of ground vibrations generated by pile driving – Application of pile driving analysis to environmental problem. *Application of Stress-Wave Theory to Piles*, F B J Barends (ed), Balkema, Rotterdam.

Harris F (1983). *Ground Engineering Equipment and Methods*. Granada.

Haupt, W A (1977): 'Surface-waves in nonhomogeneous half-space', *Dynamical Methods in Soil and Rock Mechanics Proceedings*, Karlsruhe, Germany, 5-16 Sept 1977.

Haupt W (1986). *Bodendynamik, Grundlagen und Anwendungen*. Hrsg. Haupt, W. Friedr. Vieweg & Sohn, Braunschweig/Wiesbaden, pp 53-105.

Head J M and Jardine F M (1992). Ground-borne vibrations arising from piling. *CIRIA Technical Note 142*. Construction Industry Research and Information Association, London. 83pp.

Heckman W S and Hagerty D J (1978). Vibrations associated with pile driving. *Journal of the Construction Division, Proc ASCE*, Vol 104, No CO4, pp 385-394.

Hibbitt H D and Karlsson B I (1979). Analysis of Pipe Whip, EPRI, Report NP-1208, 1979.

Hibbitt, Karlsson & Sorenson, Inc (1998) ABAQUS Manuals, version 5.8

Higdon, R L (1986): 'Initial-boundary value problems for linear hyperbolic systems', *SIAM Rev.*, Vol 28, pp177-217

Higdon, R L (1990): 'Radiation boundary conditions for elastic wave propagation', *SIAM J. Numer. Anal.*, Vol 27, pp831-870

Higdon, R L (1992): 'Absorbing boundary conditions for acoustic and elastic waves in stratified media', *J. Comput. Phys.*, Vol 101, pp386-418

Hilber, H M, Hughes, T J R and Taylor, R L (1977): 'Improved numerical dissipation for time integration algorithms in structural dynamics', *Earthquake Eng. and Structural Dynamics*, Vol 6, pp283-292

Hiller D M and Bowers K H (1997). Groundborne vibration from mechanised construction works. *Proc Tunnelling '97*, pp 721-735. Institution of Mining and Metallurgy, London.

Hiller, D M (1999): 'The prediction of groundborne vibration caused by mechanised construction works', PhD Thesis, University of Surrey.

Hiller D M and Crabb G I (2000). Groundborne vibration caused by mechanised construction works. *Transport Research Laboratory Project Report 429*, Transport Research Laboratory, Crowthorne.

Holeyman A, Legrand C and Van Rompaey D (1996). A Method to predict the driveability of vibratory driven piles. Proceedings of the 3rd International Conference on the Application of Stress-Wave Theory to Piles, pp 1101-1112, Orlando, USA, 1996

Holeyman A E (2000). Keynote lecture: Vibratory driving analysis. *Application of Stress-Wave Theory to Piles*, Niyama & Beim (eds), Balkema, Rotterdam, pp479-494. ISBN 90 5809 150 3

Hughes, T J R (1978): 'A simple scheme for developing "upwind" finite elements', *Internat. J. Numerical Methods in Eng.*, Vol 12, pp1359-1369

Isenberg, J, Vaughan, D K and Sandler, I (1978): 'Non-linear soil-structure interaction', report prepared by Weidlinger Associated for the Electric Power Research Institute, Dec. 1978

Ishihara, K (1986): 'Evaluation of soil properties for use in earthquake response analysis', *Geomechanical modelling in Engineering practice*, Balkema, Rotterdam, pp241-275

Jaky J (1944). The coefficient of earth pressure at rest. *Jour Soc Hungarian Architects and Engineers* 78(22).

Jongmans D (1996). Prediction of ground vibrations caused by pile driving: a new methodology. *Engineering Geology*, Vol 42, pp 25-36.

Laghrouche, O (1996): 'Simulation numerique de propagations d'ondes dans les sols - application a l'isolation vibratoire', PhD thesis, University of Nantes, France, April 1996

Liao, Z P and Wong, H L (1984): 'A transmitting boundary for the numerical simulation of elastic wave propagation', *Soil Dyn. Earthquake Eng.*, Vol 3, pp133-144

Liao, Z P, and Liu, J B (1992): 'Numerical instabilities of a local transmitting boundary', *Earthquake Eng. Struct. Dyn.*, Vol 21, pp65-77

- Luco, J E, Hadjian, A H and Bos, H D (1975): 'The dynamic modelling of the half-plane by finite elements', *Nuclear Eng. and Design*, Vol 31, pp184-194
- Lysmer J and Richart F E (1966). Dynamic response of footings to vertical loading. *Journal of the Soil Mechanics and Foundations Division*, Vol 92, pp 65-91.
- Lysmer, J and Kuhlemeyer, R L (1969): 'Finite dynamic model for infinite media', *J Eng Mech Div ASCE*, pp859-877, August 1969
- Lysmer, J (1970): 'Lumped mass method for Rayleigh waves', *Bull. Seismological Soc. of Amer.*, Vol 60, p89-104
- Lysmer, J, and Waas, G (1972): 'Shear waves in plane infinite structures', *J. Eng. Mechanics Div. ASCE*, pp85-105, Feb. 1972
- Lysmer, J and Drake, L A (1972): 'A finite element method for seismology', in *Methods of Computational Physics*, Vol 11, Chapter 6, Academic Press, New York
- Mabsout M E and Tassoulas J L (1994). A finite element model for the simulation of pile driving. *International Journal for Numerical Methods in Engineering*, Vol 37, pp 257-278, John Wiley & Sons.
- Mabsout M E, Reese L C and Tassoulas J L (1995). Study of Pile Driving by Finite-Element Method. *Journal of Geotechnical Engineering, Proc ASCE*, Vol 121, No 7, pp 535-543.
- Maguire J R and Wyatt T A (1999). *Dynamics, an introduction for civil and structural engineers*. ICE design and practice guide. Thomas Telford Limited, London.
- Makris N and Gazetas G (1993). Displacement phase differences in a harmonically oscillating pile. *Geotechnique*, Vol 43, No 1, pp 135-150.
- Malam D (1993): Assessing the effect of environmental vibration in buildings. BS 7385 Part 2. *Proceedings of Institute of Acoustics*, Vol 15, Part 4, pp23-51. Institute of Acoustics, St Albans
- Mallard D J and Bastow P (1979). Some observations on the vibrations caused by pile driving. *Proc ICE Conference on Recent developments in the design and construction of piles*, pp 261-284. Institution of Civil Engineers, London.
- Martin D J (1980). Ground vibrations from impact pile driving during road construction. *Transport and Road Research Laboratory Research Report 544*, Transport Research Laboratory, Crowthorne.
- Massarsch K R and Broms B B (1991). Damage Criteria for Small Amplitude Ground Vibrations, *Second International Conference on Recent Advances in Geotechnical Earthquake Engineering and Soil Dynamics*, St Louis, Missouri, March 11-15, 1991, pp1451-1459.

Massarsch K R (1992). Keynote lecture: Static and dynamic soil displacements caused by pile driving. *Proc 4th International Conference on the Application of Stress-Wave Theory to Piles*, pp 15-25. Balkema, Rotterdam.

Matthews M C, Hope V S and Clayton C R I (1996). The use of surface waves in the determination of ground stiffness profiles. *Proc Institution of Civil Engineers, Geotechnical Engineering*, Vol 119, April, pp 84-95

Medina, F (1981): 'An axisymmetric infinite element', *Int. J. Num. Meth. Engng.*, Vol 17, pp1177-1185

Medina, F and Penzian, J (1982): 'Infinite elements for elastodynamics', *Earthquake Eng and Structural Dynamics*, Vol 10(5), pp699-709

Medina, F and Taylor, R L (1983): 'Finite element techniques for problems of unbounded domains', *Int. J. Num. Meth. Engng.*, Vol 19, pp1209-1226

Meyerhof G G (1976). Bearing capacity and settlement of pile foundations. *J Geot Engng Div, ASCE*, 102(GT3), pp 197-228.

Meynard A and Corte J-F (1984). Experimental study of lateral resistance during driving. *Second Int Conf on the Application of Stress-Wave Theory to Piles*, Stockholm.

Miller, G F and Pursey, H (1955): 'On the partition of energy between elastic waves in a semi-infinite solid', *Proc. of the Royal Society of London, Series A: Mathematical and Physical Sciences*, Vol 233, No 1192, pp55-69

Mintrop L (1911). Über die Ausbreitung der von den Massendrukken einer Großgassmaschine erzeugten Bodenschwingungen. (On the propagation of groundborne vibration from heavy gas powered printing press.) Dissertation, Gottingen. [In German]

New B M (1982). Vibration caused by underground construction. *Proc Tunnelling '82*, pp 217-229. Institution of Mining and Metallurgy, London.

New B M (1986). Ground vibration caused by civil engineering works. *Transport and Road Research Laboratory Research Report 53*, Transport Research Laboratory, Crowthorne.

Noorzaei, J, Viladkar, M N and Godbole, P N (1994): 'Non-linear soil-structure interaction in plane frames', *Engineering Comp*, Vol 11

Novak M (1977). Vertical vibration of floating piles. *J Eng Mech Div, ASCE*, Vol 103, pp 153-168.

Novak M, Nogami T and Aboul-Ella F (1978). Dynamic soil reactions for plane strain case. *J Eng Mech Div, ASCE*, Vol 104, pp 953-959.

O'Neill D B (1971). Vibration and dynamic settlement from pile driving. *Proceedings of Conference on Behaviour of Piles*, pp135-140. ICE, London.

Parry R H G and Swain C W (1977). Effective stress methods of calculating skin friction of driven piles in soft clay. *Ground Engineering*, Vol 10, No 3, pp 24-26.

Parry R H G and Swain C W (1977). A study of skin friction on piles in stiff clay. *Ground Engineering*, Vol 10, No 8, pp 33-37.

Peng, C and Toksoz, M N (1994): 'An optimal absorbing boundary condition for finite difference modelling of acoustic and elastic wave propagation', *J. Acoust. Soc. Am.*, Vol 95, p733-745

Ramshaw C L, Selby A R and Bettess P (1998a). Computation of the transmission of waves from pile driving. In *Ground Dynamics and Man-made processes*, ed B O Skipp, pp 115-128. Thomas Telford, London.

Ramshaw C L, Selby A R and Bettess P (1998b). Computed ground waves due to piling. *Geotech Sp Pub No 75* ed Dakoulas P, Yegian M & Holtz R D. Geo Inst of ASCE. Proc Conf Geotechnical Earthquake Eng & Soil Dynamics. Vol 2, Seattle

Ramshaw C L, Selby A R and Bettess P (2000). Computation of ground waves due to piling. *Application of Stress-Wave Theory to Piles*, Niyama & Beim (eds), Balkema, Rotterdam, pp 495-502, Proc of the 6th International Conf on the Application of Stress-Wave Theory to Piles, Sao Paulo, Brazil, 2000.

Ramshaw C L, Selby A R and Bettess P (2001). Ground waves generated by pile driving, and structural interaction. Fourth International Conference on Recent Advances in Geotechnical Earthquake Engineering and Soil Dynamics, ASCE, San Diego, March 2001

Randolph M F and Simons H A (1986). An improved soil model for one-dimensional pile driving analysis. *Third Int Conf on Numerical Methods in Offshore Piling*, Nantes, pp 3-15.

Randolph M F (1991). Analysis of the dynamics of pile driving. In *Developments in Soil Mechanics IV: Advanced Geotechnical Analyses*, (eds P K Banerjee and R Butterfield), Elsevier Applied Science, also *University of Western Australia Research Report No G1001*.

Rausche F, Moses F and Goble G G (1972). Soil Resistance Predictions from Pile Dynamics. *Journal of the Soil Mechanics and Foundations Division*, ASCE, Vol 98 No SM9 Proc Paper 9220, Sept 1972.

Rempe D M and Davisson M T (1977). Performance of diesel pile hammers. *Proc 9th International Conference on Soil Mechanics and Foundation Engineering*, Vol 2, pp 347-354. Japanese Society of Soil Mechanics and Foundation Engineering.

Richart F E, Hall J R and Woods R D (1970). *Vibrations of soils and foundations*. Prentice-Hall, New Jersey.

Robinson, A R (1976): 'The transmitting boundary - again', *Structural and Geotechnical Mechanics*, Ed W J Hall, Prentice-Hall, New Jersey.

- Selby A R (1991). Ground vibrations caused by pile installation. *4th International DFI Conference*, pp 497-502. Balkema, Rotterdam.
- Selby A R (1989). Acquisition by microcomputer of some ground vibration data during pile driving. *Computer and Physical Modelling in Geotechnical Engineering*, ed A S Balasubramaniam et al, pp 133-147. Balkema, Rotterdam.
- Simons H A and Randolph M F (1985). A new approach to one-dimensional pile driving analysis. *Proc Fifth Int Conf on Numerical Methods in Geomechanics*, Nagoya, Vol 3, pp 1457-1464.
- Siskind D E, Stagg M S, Kopp J W and Dowding C H (1980). Structure response and damage produced by ground vibration from surface mine blasting. *United States Bureau of Mines Report of Investigations 8507*. United States Bureau of Mines, Twin Cities, Minnesota.
- Smith E A L (1960). Pile driving analysis by the wave equation. *J Soil Mech and Found*, ASCE, Vol 86, pp 35-61
- Smith, W D (1974): 'A non-reflecting plane boundary for wave propagation problems', *J. Comput. Phys.*, Vol 15, pp492-503
- Stain R T (1992). SIMBAT – a dynamic load test for bored piles. *Piling: European practice and worldwide trends*, pp 198-205, Thomas Telford, London.
- Stain R T and Davis A G (1989). An improved method for the prediction of pile bearing capacity from dynamic testing. *Proc International Conference on Piling and Deep Foundations*, London, May 1989, pp 429-433
- Svinkin M R (1992). Pile driving induced vibrations as a source of industrial seismology. *Proc 4th International Conference on the Application of Stress-Wave Theory to Piles*, pp 167-174. Balkema, Rotterdam.
- Timoshenko, S P and Goodier, J N (1970): 'Theory of Elasticity', McGraw-Hill, New York
- Todd A (1994). Berwick river walls – an unique scheme to safeguard an historic part of Berwick upon Tweed. *ICE papers competition*. London.
- Tomlinson M J (1957). *The adhesion of piles driven in clay soils*. Proc 4th Int Conf on Soil Mech and Found Eng, Vol 2, pp66-71
- Tomlinson M J (1994). *Pile design and construction practice*, 4th edition. E and F N Spon, London.
- Ungless, R L (1973): 'An infinite element method', MASC Thesis, University of British Columbia

11. Calculation of Fourier constant for RH boundary

On RH boundary, $x = 204.23$

$$\begin{aligned}
 \therefore u_y &= -k \sin(204.23k - \omega t) \\
 &= \frac{-2\pi}{204.23} \sin(2\pi - 2\pi t) \\
 &= \frac{-2\pi}{204.23} \sin -2\pi(t - 1) \\
 &= A_0 + \sum_{n=1}^N [A_n \cos n\omega(t - t_0) + B_n \sin n\omega(t - t_0)]
 \end{aligned}$$

$$\begin{aligned}
 \therefore N &= 1 \\
 \omega &= -2\pi \\
 t_0 &= 1 \\
 A_0 &= 0 \\
 A_1 &= 0 \\
 B_1 &= \frac{-2\pi}{204.23}
 \end{aligned}$$

\therefore ABAQUS command is:

*AMPLITUDE, DEFINITION = PERIODIC

1, -2 π , 1, 0

0, $\frac{-2\pi}{204.23}$

CALCULATION OF FOURIER CONSTANTS FOR AN R WAVE

1. Choose

$$\begin{aligned}E &= 0.2e^9 \text{ N/m}^2 \\ \nu &= 0.25 \\ \rho &= 1998 \text{ kg/m}^3\end{aligned}$$

2. Calculate G and λ

$$G = \frac{E}{2(1+\nu)} = 80e^6$$

$$\lambda = \frac{E\nu}{(1+\nu)(1-2\nu)} = 80e^6$$

3. Choose $T = 1.0$ second

$$\varpi = \frac{2\pi}{T} \quad \therefore \varpi = 2\pi$$

4. Calculate the propagation velocity

For $\nu = 0.25$,

$$c_R = 0.9194 \sqrt{\frac{G}{\rho}} = 183.972 \text{ m/s}$$

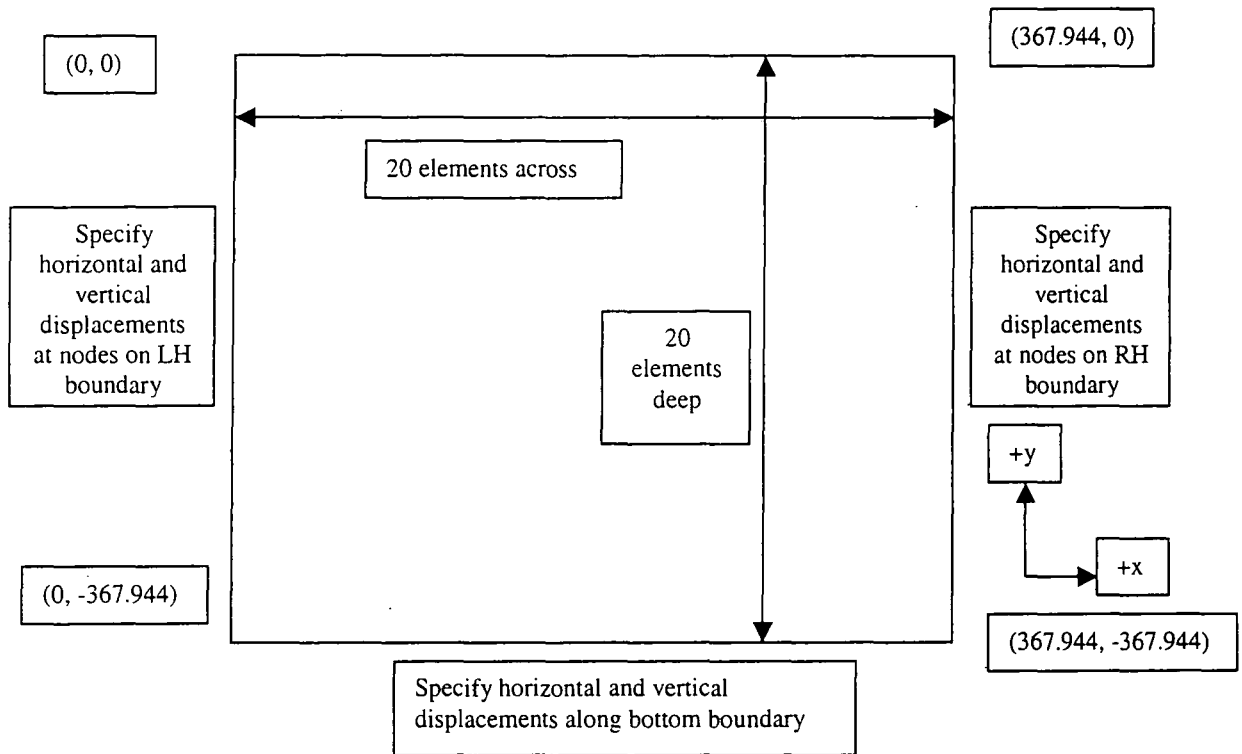
5. Calculate the wave number

$$k = \frac{\varpi}{c_R} = \frac{2\pi}{183.972} = 0.0342$$

6. Calculate the wavelength

$$\Lambda = \frac{2\pi}{k} = 183.972 \text{ m}$$

7. Create a mesh with 10 nodes per wavelength, at least 2 wavelengths wide and 2 wavelengths deep. Leave the top boundary free.



8. Use

$$u_x = D[e^{0.8475ky} - 0.5773e^{0.3933ky}] \sin(kx - \omega t)$$

and

$$u_y = D[-0.8475e^{0.8475ky} + 1.4679e^{0.3933ky}] \cos(kx - \omega t)$$

to specify the horizontal and vertical displacements on the LH, RH and bottom boundaries as a function of time.

9. In ABAQUS, the periodic displacement of nodes is specified as a Fourier series as follows:

$$a = A_0 + \sum_{n=1}^N [A_n \cos n\omega(t - t_0) + B_n \sin n\omega(t - t_0)] \quad \text{for } t \geq t_0$$

$$a = A_0 \quad \text{for } t < 0$$

where

a = amplitude of displacement

and

$t_0, \omega, A_0, A_n, B_n, n = 1, 2, \dots, N$ are constants defined on the datalines as follows:

* AMPLITUDE, DEFINITION = PERIODIC

N, ω, t_0, A_0

$A_1, B_1, A_2, B_2, \dots, A_n, B_n$

10. Calculation of Fourier constant for LH boundary

On LH boundary, $x = 0$ and y varies

$$\therefore u_x = D[e^{0.8475ky} - 0.5773e^{0.3933ky}] \sin(0 - \omega t)$$

Take $D = 1$

\therefore Fourier constants are:

$$N = 1$$

$$\omega = -2\pi$$

$$t_0 = 0$$

$$A_0 = 0$$

$$A_1 = 0$$

$$B_1 = e^{0.8475ky} - 0.5773e^{0.3933ky}$$

\therefore ABAQUS command is:

*AMPLITUDE, DEFINITION = PERIODIC

1, -2 π , 0, 0

0, B_1

$$\text{and } u_y = D[-0.8475e^{0.8475ky} + 1.4679e^{0.3933ky}] \cos(0 - \omega t)$$

Take $D = 1$

∴ Fourier constants are:

$$N = 1$$

$$\omega = -2\pi$$

$$t_0 = 0$$

$$A_0 = 0$$

$$A_1 = -0.8475e^{0.8475ky} + 1.4679e^{0.3933ky}$$

$$B_1 = 0$$

∴ ABAQUS command is:

*AMPLITUDE, DEFINITION = PERIODIC

1, -2π, 0, 0

A₁, 0

11. Calculation of Fourier constant for RH boundary

On RH boundary, x = 367.944, y varies

$$\therefore u_x = D[e^{0.8475ky} - 0.5773e^{0.3933ky}] \sin - \omega \left(t - \frac{kx}{\omega} \right)$$

Take D = 1

∴ Fourier constants are:

$$N = 1$$

$$\omega = -2\pi$$

$$t_0 = \frac{367.944k}{\omega} = 2.0$$

$$A_0 = 0$$

$$A_1 = 0$$

$$B_1 = e^{0.8475ky} - 0.5773e^{0.3933ky}$$

∴ ABAQUS command is:

*AMPLITUDE, DEFINITION = PERIODIC

1, -2π, 2.0, 0

0, B₁

$$\text{and } u_y = D[-0.8475e^{0.8475ky} + 1.4679e^{0.3933ky}] \cos - \omega \left(t - \frac{kx}{\omega} \right)$$

Take D = 1

∴ Fourier constants are:

$$N = 1$$

$$\omega = -2\pi$$

$$t_0 = \frac{367.944k}{\omega} = 2.0$$

$$A_0 = 0$$

$$A_1 = -0.8475e^{0.8475ky} + 1.4679e^{0.3933ky}$$

$$B_1 = 0$$

∴ ABAQUS command is:

*AMPLITUDE, DEFINITION = PERIODIC

1, -2π, 2.0, 0

A₁, 0

12. Calculation of Fourier constant for bottom boundary

On bottom boundary, $y = 367.944$, x varies

$$\therefore u_x = D \left[e^{0.8475ky} - 0.5773e^{0.3933ky} \right] \sin - \omega \left(t - \frac{kx}{\omega} \right)$$

Take $D = 1$

∴ Fourier constants are:

$$N = 1$$

$$\omega = -2\pi$$

$$t_0 = \frac{kx}{2\pi}$$

$$A_0 = 0$$

$$A_1 = 0$$

$$B_1 = 4.0969e^{-3}$$

∴ ABAQUS command is:

*AMPLITUDE, DEFINITION = PERIODIC

1, -2π, $\frac{kx}{2\pi}$, 0

0, 4.0969e⁻³

and $u_y = D \left[-0.8475e^{0.8475ky} + 1.4679e^{0.3933ky} \right] \cos - \omega \left(t - \frac{kx}{\omega} \right)$

Take $D = 1$

\therefore Fourier constants are:

$$N = 1$$

$$\omega = -2\pi$$

$$t_0 = \frac{kx}{2\pi}$$

$$A_0 = 0$$

$$A_1 = 10.4574e^{-3}$$

$$B_1 = 0$$

\therefore ABAQUS command is:

*AMPLITUDE, DEFINITION = PERIODIC

$$1, -2\pi, \frac{kx}{2\pi}, 0$$

A_1, B_1


```

*HEADING
CHECK FOR DILATATION WAVES
WITH USER INFINITE ELEMENTS
*NODE, INPUT=pwave82-node.inp
*ELEMENT, TYPE=CPE8, INPUT=pwave82-elem-fe.inp, ELSET=FE
*USER ELEMENT, NODES=3, TYPE=U4, PROPERTIES=4, COORDINATES=3, VARIABLES=6
1, 2, 3
*USER SUBROUTINE, INPUT=uelsub3nier.for
*ELEMENT, TYPE=U4, ELSET=IE
101, 321, 322, 323
102, 323, 324, 325
103, 325, 326, 327
104, 327, 328, 329
105, 329, 330, 331
106, 331, 332, 333
107, 333, 334, 335
108, 335, 336, 337
109, 337, 338, 339
110, 339, 340, 341
*UEL PROPERTY, ELSET=IE
1.0, 0.2e9, 0.2, 1998.
*NSET, NSET=LHS, GENERATE
1, 21
*NSET, NSET=RHS, GENERATE
321, 341
*NSET, NSET=TOP, GENERATE
1, 321, 32
22, 310, 32
*NSET, NSET=BOT, GENERATE
21, 341, 32
32, 320, 32
*NSET, NSET=FILEN, GENERATE
7, 327, 32
25, 313, 32
*SOLID SECTION, ELSET=FE, MATERIAL=ONE
*MATERIAL, NAME=ONE
*ELASTIC
0.2E9, 0.2
*DENSITY
1998.
*BOUNDARY
TOP, 2
BOT, 2
*AMPLITUDE, NAME=SINELHS, DEFINITION=PERIODIC, TIME=TOTAL
1, -6.283, 0.0, 0.0
0.0, -18.84e-3
*AMPLITUDE, NAME=SINERHS, DEFINITION=PERIODIC, TIME=TOTAL
1, -6.283, 1., 0.
0., -18.84e-3
*RESTART, WRITE, FREQUENCY=1
*PREPRINT, ECHO=NO, MODEL=NO
*STEP, INC=200
*DYNAMIC, NOHAF
0.01, 2.0
*BOUNDARY, AMPLITUDE=SINELHS
LHS, 1, 1.
*EL PRINT, FREQUENCY=0
*NODE PRINT, NSET=FILEN
U
*NODE PRINT, NSET=RHS
U, V
*NODE FILE, NSET=FILEN
U, V, A
*END STEP

```

```

SUBROUTINE UEL(RHS,AMATRX,SVARS,ENERGY,NDOFEL,NRHS,NSVARS,PROPS,
1 NPROPS,COORDS,MCRD,NNODE,U,DU,V,A,JTYPE,TIME,DTIME,KSTEP,KINC,
2 JELEM,PARAMS,NDLOAD,JDLTYP,ADLMAG,PREDEF,NPREDF,LFLAGS,
3 MLVARX,DDLMAG,MDLOAD,PNEWDT,JPROPS,NJPROP,PERIOD)
C
C   INCLUDE 'ABA_PARAM.INC'
C
C   DOUBLE PRECISION CONST1,CONST2,CP,DP,CS,DS,ALEN,HFALEN,
1 STRESS,ENDALEN,ALENMID
C
C   DIMENSION RHS(MLVARX,*),AMATRX(NDOFEL,NDOFEL),SVARS(NSVARS),
1 ENERGY(8),PROPS(*),COORDS(MCRD,NNODE),
2 U(NDOFEL),DU(MLVARX,*),V(NDOFEL),A(NDOFEL),TIME(2),
3 PARAMS(3),JDLTYP(MDLOAD,*),ADLMAG(MDLOAD,*),
4 DDLMAG(MDLOAD,*),PREDEF(2,NPREDF,NNODE),LFLAGS(*),JPROPS(*)
C   DIMENSION SRESID(9)
C   DIMENSION STRESS(9)
C
C   SRESID - stores the static residual at time t+dt
C   SVARS - In 1-6, contains the static residual at time t upon
C           entering the routine. SRESID is copied to SVARS(1-6)
C           after the dynamic residual has been calculated.
C           - For half-step residual calculations: In 7-12, contains
C           the static residual at the beginning of the previous
C           increment. SVARS(1-6) are copied into SVARS(7-12) after
C           the dynamic residual has been calculated.
C
C   PRINT *, 'Entering UEL'
C   PRINT *, 'JELEM =',JELEM
C   AREA= PROPS(1)
C   E = PROPS(2)
C   ANU = PROPS(3)
C   RHO = PROPS(4)
C   PRINT *, 'AREA = ',AREA
C   PRINT *, 'E = ',E
C   PRINT *, 'ANU = ',ANU
C   PRINT *, 'RHO = ',RHO
C   PRINT *, 'NDOFEL = ',NDOFEL
C
C   Calculate wave speed of P-wave
C
C   CONST1 = (E*ANU)/((1.0+ANU)*(1.0-(ANU+ANU)))
C   CONST2 = E/((1.0+ANU)+(1.0+ANU))
C   CP = ((CONST1+(CONST2+CONST2))/RHO)**0.5
C   DP = RHO*CP
C   PRINT *, 'CONST1 =',CONST1
C   PRINT *, 'CONST2 =',CONST2
C   PRINT *, 'CP =',CP
C   PRINT *, 'DP =',DP
C
C   Calculate wave speed of S-wave
C
C   CS = (CONST2/RHO)**0.5
C   DS = RHO*CS
C   PRINT *, 'CS =',CS
C   PRINT *, 'DS =',DS
C
C   ALEN = COORDS(2,1) - COORDS(2,3)
C
C   DO 6 K1=1,NDOFEL
C   SRESID(K1) = 0.0D0
C   DO 2 KRHS=1,NRHS
C   RHS(K1,KRHS) = 0.0D0
2 CONTINUE
C   DO 4 K2=1,NDOFEL
C   AMATRX(K2,K1)=0.0D0

```

```

4 CONTINUE
6 CONTINUE

C
DO 8 K1=1,NDOFEL
STRESS(K1) = 0.0D0
8 CONTINUE
*****
IF (LFLAGS(3).EQ.1) THEN
C
Normal incrementation
PRINT *, 'Entering 1st IF Statement(LFLAGS3=1)'
IF (LFLAGS(1).EQ.11 .OR. LFLAGS(1).EQ.12) THEN
PRINT *, 'Entering 2nd IF statement(LFLAGS1=11or12
1 *DYNAMIC ANALYSIS)'
C
*DYNAMIC
ALPHA = PARAMS(1)
BETA = PARAMS(2)
GAMMA = PARAMS(3)
PRINT *, 'ALPHA =',ALPHA
PRINT *, 'BETA =',BETA
PRINT *, 'GAMMA =',GAMMA
PRINT *, 'MLVARX =',MLVARX
PRINT *, 'DTIME =',DTIME

C
C
PRINT *, 'Velocity matrix = '
WRITE (6,890) (V(K1),K1=1,9)
890 FORMAT (1X,1E10.3)
C
C Calculate stresses by multiplying V(1),V(4),V(7) by DP
C and V(2),V(5) and V(8) by DS
C
DO 10 K1 = 1,7,3
STRESS(K1) = V(K1) * DP
10 CONTINUE
C
DO 15 K1 = 2,8,3
STRESS(K1) = V(K1) * DS
15 CONTINUE
C
PRINT *, 'Stress matrix = '
WRITE (6,895) (STRESS(K1),K1=1,9)
895 FORMAT (1X,1E20.5)
C
C Calculate forces at nodes by multiplying {STRESS}
C by L/6 for end nodes and 2L/3 for midside node
C
ENDALEN = ALEN/6.0
ALENMID = (ALEN+ALEN)/3.0
PRINT *, 'ENDALEN =',ENDALEN
PRINT *, 'ALENMID =',ALENMID

C
C Multiply end node terms in {STRESS} by -ENDALEN
C
DO 20 K1 = 1,3,1
RHS(K1,1) = -STRESS(K1) * ENDALEN
20 CONTINUE
DO 30 K1 = 7,9,1
RHS(K1,1) = -STRESS(K1) * ENDALEN
30 CONTINUE
C
C Multiply midside node terms in {STRESS} by -ALENMID
C
DO 40 K1 = 4,6,1
RHS(K1,1) = -STRESS(K1) * ALENMID
40 CONTINUE
C

```

```
      PRINT *, 'RHS ='
      WRITE (6,897) ((RHS(I,J),J=1,13),I=1,13)
897  FORMAT (1X,13E10.3)
C
      END IF
*****
      END IF
      RETURN
      END
```

```

*HEADING
***Axisymmetric elements***
CHECK FOR DILATATION WAVES
WITH USER INFINITE ELEMENTS
*NODE, INPUT=pwave82ax-node.inp
*ELEMENT, TYPE=CAX8, INPUT=pwave82ax-elem-fe.inp, ELSET=FE
*USER ELEMENT, NODES=3, TYPE=U4, PROPERTIES=4, COORDINATES=3, VARIABLES=6
1,2,3
*USER SUBROUTINE, INPUT=uelsub3nierax.for
*ELEMENT, TYPE=U4, ELSET=IE
101,321,322,323
102,323,324,325
103,325,326,327
104,327,328,329
105,329,330,331
106,331,332,333
107,333,334,335
108,335,336,337
109,337,338,339
110,339,340,341
*UEL PROPERTY, ELSET=IE
4190.8846,0.2e9,0.2,1998.
*NSET, NSET=LHS, GENERATE
1,21
*NSET, NSET=RHS, GENERATE
321,341
*NSET, NSET=TOP, GENERATE
1,321,32
22,310,32
*NSET, NSET=BOT, GENERATE
21,341,32
32,320,32
*NSET, NSET=FILEN, GENERATE
7,327,32
25,313,32
*SOLID SECTION, ELSET=FE, MATERIAL=ONE
*MATERIAL, NAME=ONE
*ELASTIC
0.2E9,0.2
*DENSITY
1998.
*BOUNDARY
TOP,2
BOT,2
*AMPLITUDE, NAME=SINELHS, DEFINITION=PERIODIC, TIME=TOTAL
1,-6.283,0.0,0.0
0.0,-18.84e-3
*AMPLITUDE, NAME=SINERHS, DEFINITION=PERIODIC, TIME=TOTAL
1,-6.283,1.,0.
0.,-18.84e-3
*RESTART, WRITE, FREQUENCY=1
*PREPRINT, ECHO=NO, MODEL=NO
*STEP, INC=200
*DYNAMIC, NOHAF
0.01,2.0
*BOUNDARY, AMPLITUDE=SINELHS
LHS,1,,1.
*EL PRINT, FREQUENCY=0
*NODE PRINT, NSET=FILEN
U
*NODE PRINT, NSET=RHS
U,V
*NODE FILE, NSET=FILEN
U,V,A
*END STEP

```

```

C      Subroutine for Pwave in axisymmetric mesh
C
      SUBROUTINE UEL(RHS,AMATRX,SVARS,ENERGY,NDOFEL,NRHS,NSVARS,PROPS,
1 NPROPS,COORDS,MCRD,NNODE,U,DU,V,A,JTYPE,TIME,DTIME,KSTEP,KINC,
2 JELEM,PARAMS,NDLOAD,JDLTYP,ADLMAG,PREFDEF,NPREFD,LFLAGS,
3 MLVARX,DDL MAG,MDLOAD,PNEWDT,JPROPS,NJPROP,PERIOD)
C
      INCLUDE 'ABA_PARAM.INC'
C
      DOUBLE PRECISION CONST1,CONST2,CP,DP,CS,DS,ALEN,HFALEN,
1 STRESS,ENDALEN,ALENMID
C
      DIMENSION RHS(MLVARX,*),AMATRX(NDOFEL,NDOFEL),SVARS(NSVARS),
1 ENERGY(8),PROPS(*),COORDS(MCRD,NNODE),
2 U(NDOFEL),DU(MLVARX,*),V(NDOFEL),A(NDOFEL),TIME(2),
3 PARAMS(3),JDLTYP(MDLOAD,*),ADLMAG(MDLOAD,*),
4 DDL MAG(MDLOAD,*),PREFDEF(2,NPREFD,NNODE),LFLAGS(*),JPROPS(*)
      DIMENSION SRESID(9)
      DIMENSION STRESS(9)
C
C      SRESID - stores the static residual at time t+dt
C      SVARS - In 1-6, contains the static residual at time t upon
C              entering the routine. SRESID is copied to SVARS(1-6)
C              after the dynamic residual has been calculated.
C              - For half-step residual calculations: In 7-12, contains
C                the static residual at the beginning of the previous
C                increment. SVARS(1-6) are copied into SVARS(7-12) after
C                the dynamic residual has been calculated.
C
      PRINT *, 'Entering UEL'
      PRINT *, 'JELEM =',JELEM
      AREA= PROPS(1)
      E = PROPS(2)
      ANU = PROPS(3)
      RHO = PROPS(4)
      PRINT *, 'AREA = ',AREA
      PRINT *, 'E = ',E
      PRINT *, 'ANU = ',ANU
      PRINT *, 'RHO = ',RHO
      PRINT *, 'NDOFEL = ',NDOFEL
C
C      Calculate wave speed of P-wave
C
      CONST1 = (E*ANU)/((1.0+ANU)*(1.0-(ANU+ANU)))
      CONST2 = E/((1.0+ANU)+(1.0+ANU))
      CP = ((CONST1+(CONST2+CONST2))/RHO)**0.5
      DP = RHO*CP
      PRINT *, 'CONST1 =',CONST1
      PRINT *, 'CONST2 =',CONST2
      PRINT *, 'CP =',CP
      PRINT *, 'DP =',DP
C
C      Calculate wave speed of S-wave
C
      CS = (CONST2/RHO)**0.5
      DS = RHO*CS
      PRINT *, 'CS =',CS
      PRINT *, 'DS =',DS
C
      ALEN = COORDS(2,1) - COORDS(2,3)
C
      DO 6 K1=1,NDOFEL
      SRESID(K1) = 0.0D0
      DO 2 KRHS=1,NRHS
      RHS(K1,KRHS) = 0.0D0
2 CONTINUE

```

```

        DO 4 K2=1,NDOFEL
          AMATRX(K2,K1)=0.0D0
        4 CONTINUE
        6 CONTINUE
C
        DO 8 K1=1,NDOFEL
          STRESS(K1) = 0.0D0
        8 CONTINUE
*****
        IF (LFLAGS(3).EQ.1) THEN
C          Normal incrementation
          PRINT *, 'Entering 1st IF Statement(LFLAGS3=1)'
          IF (LFLAGS(1).EQ.11 .OR. LFLAGS(1).EQ.12) THEN
            PRINT *, 'Entering 2nd IF statement(LFLAGS1=11or12
1          *DYNAMIC ANALYSIS)'
C            *DYNAMIC
            ALPHA = PARAMS(1)
            BETA  = PARAMS(2)
            GAMMA = PARAMS(3)
            PRINT *, 'ALPHA =',ALPHA
            PRINT *, 'BETA =',BETA
            PRINT *, 'GAMMA =',GAMMA
            PRINT *, 'MLVARX =',MLVARX
            PRINT *, 'DTIME =',DTIME
C
C
          PRINT *, 'Velocity matrix = '
          WRITE (6,890) (V(K1),K1=1,9)
890  FORMAT (1X,1E10.3)
C
C          Calculate stresses by multiplying V(1),V(4),V(7) by DP
C          and V(2),V(5) and V(8) by DS
C
          DO 10 K1 = 1,7,3
            STRESS(K1) = V(K1) * DP
          10 CONTINUE
C
          DO 15 K1 = 2,8,3
            STRESS(K1) = V(K1) * DS
          15 CONTINUE
C
          PRINT *, 'Stress matrix = '
          WRITE (6,895) (STRESS(K1),K1=1,9)
895  FORMAT (1X,1E20.5)
C
C          Calculate forces at nodes by multiplying {STRESS}
C          by L/6xAREA for end nodes and 2L/3xAREA for midside node
C
          ENDALEN = AREA*(ALEN/6.0)
          ALENMID = AREA*((ALEN+ALEN)/3.0)
          PRINT *, 'ENDALEN =',ENDALEN
          PRINT *, 'ALENMID =',ALENMID
C
C          Multiply end node terms in {STRESS} by -ENDALEN
C
          DO 20 K1 = 1,3,1
            RHS(K1,1) = -STRESS(K1) * ENDALEN
          20 CONTINUE
          DO 30 K1 = 7,9,1
            RHS(K1,1) = -STRESS(K1) * ENDALEN
          30 CONTINUE
C
C          Multiply midside node terms in {STRESS} by -ALENMID
C
          DO 40 K1 = 4,6,1
            RHS(K1,1) = -STRESS(K1) * ALENMID

```

40 CONTINUE

C

PRINT *, 'RHS ='

WRITE (6,897) ((RHS(I,J),J=1,13),I=1,13)

897 FORMAT (1X,13E10.3)

C

END IF

END IF

RETURN

END

APPENDIX D

Listings of ABAQUS input files and *UEL subroutines for user-defined Rayleigh viscous boundaries in plane strain and axisymmetric conditions

```

*HEADING
CHECK FOR RAYLEIGH WAVES - 8 NODDED ELEMENTS - REVISION 2 (BULLEN)
WITH USER INFINITE ELEMENTS
21 x 21 ELEMENT MESH
*NODE, INPUT=rw21-node.inp
*ELEMENT, TYPE=CPE8, INPUT=rw21-elem-fe.inp, ELSET=FE
*USER ELEMENT, NODES=3, TYPE=U4, PROPERTIES=4, COORDINATES=3, VARIABLES=6
1,2,3
*USER SUBROUTINE, INPUT=usub3nielk2np.for
*ELEMENT, TYPE=U4, ELSET=IE
701,1366,1367,1368
702,1368,1369,1370
703,1370,1371,1372
704,1372,1373,1374
705,1374,1375,1376
706,1376,1377,1378
707,1378,1379,1380
708,1380,1381,1382
709,1382,1383,1384
710,1384,1385,1386
711,1386,1387,1388
712,1388,1389,1390
713,1390,1391,1392
714,1392,1393,1394
715,1394,1395,1396
716,1396,1397,1398
717,1398,1399,1400
718,1400,1401,1402
719,1402,1403,1404
720,1404,1405,1406
721,1406,1407,1408
*UEL PROPERTY, ELSET=IE
1.0,0.2e9,0.25,1998.
*NSET, NSET=LHS, GENERATE
1,43,1
*NSET, NSET=RHS, GENERATE
1366,1408,1
*NSET, NSET=TOP, GENERATE
1,1366,65
44,1344,65
*NSET, NSET=BOT, GENERATE
43,1408,65
65,1365,65
*NSET, NSET=FILEN, GENERATE
15,1380,65
51,1351,65
*SOLID SECTION, ELSET=FE, MATERIAL=ONE
*MATERIAL, NAME=ONE
*ELASTIC
0.2E9,0.25
*DENSITY
1998.
***
*** LHS U ***
***
*AMPLITUDE, NAME=LHSU0, DEFINITION=PERIODIC, TIME=TOTAL
1,-6.283,0.0,0.0
0.0,0.422700E+00
*AMPLITUDE, NAME=LHSU0A, DEFINITION=PERIODIC, TIME=TOTAL
1,-6.283,0.0,0.0
0.0,0.261369E+00
*AMPLITUDE, NAME=LHSU1, DEFINITION=PERIODIC, TIME=TOTAL
1,-6.283,0.0,0.0
0.0,0.143884E+00
*AMPLITUDE, NAME=LHSU1A, DEFINITION=PERIODIC, TIME=TOTAL
1,-6.283,0.0,0.0

```

0.0,0.595056E-01
 *AMPLITUDE, NAME=LHSU2, DEFINITION=PERIODIC, TIME=TOTAL
 1, -6.283, 0.0, 0.0
 0.0,0.155568E-04
 *AMPLITUDE, NAME=LHSU2A, DEFINITION=PERIODIC, TIME=TOTAL
 1, -6.283, 0.0, 0.0
 0.0, -.408643E-01
 *AMPLITUDE, NAME=LHSU3, DEFINITION=PERIODIC, TIME=TOTAL
 1, -6.283, 0.0, 0.0
 0.0, -.679196E-01
 *AMPLITUDE, NAME=LHSU3A, DEFINITION=PERIODIC, TIME=TOTAL
 1, -6.283, 0.0, 0.0
 0.0, -.847895E-01
 *AMPLITUDE, NAME=LHSU4, DEFINITION=PERIODIC, TIME=TOTAL
 1, -6.283, 0.0, 0.0
 0.0, -.942327E-01
 *AMPLITUDE, NAME=LHSU4A, DEFINITION=PERIODIC, TIME=TOTAL
 1, -6.283, 0.0, 0.0
 0.0, -.983333E-01
 *AMPLITUDE, NAME=LHSU5, DEFINITION=PERIODIC, TIME=TOTAL
 1, -6.283, 0.0, 0.0
 0.0, -.986586E-01
 *AMPLITUDE, NAME=LHSU5A, DEFINITION=PERIODIC, TIME=TOTAL
 1, -6.283, 0.0, 0.0
 0.0, -.963815E-01
 *AMPLITUDE, NAME=LHSU6, DEFINITION=PERIODIC, TIME=TOTAL
 1, -6.283, 0.0, 0.0
 0.0, -.923738E-01
 *AMPLITUDE, NAME=LHSU6A, DEFINITION=PERIODIC, TIME=TOTAL
 1, -6.283, 0.0, 0.0
 0.0, -.872785E-01
 *AMPLITUDE, NAME=LHSU7, DEFINITION=PERIODIC, TIME=TOTAL
 1, -6.283, 0.0, 0.0
 0.0, -.815649E-01
 *AMPLITUDE, NAME=LHSU7A, DEFINITION=PERIODIC, TIME=TOTAL
 1, -6.283, 0.0, 0.0
 0.0, -.755714E-01
 *AMPLITUDE, NAME=LHSU8, DEFINITION=PERIODIC, TIME=TOTAL
 1, -6.283, 0.0, 0.0
 0.0, -.695374E-01
 *AMPLITUDE, NAME=LHSU8A, DEFINITION=PERIODIC, TIME=TOTAL
 1, -6.283, 0.0, 0.0
 0.0, -.636285E-01
 *AMPLITUDE, NAME=LHSU9, DEFINITION=PERIODIC, TIME=TOTAL
 1, -6.283, 0.0, 0.0
 0.0, -.579554E-01
 *AMPLITUDE, NAME=LHSU9A, DEFINITION=PERIODIC, TIME=TOTAL
 1, -6.283, 0.0, 0.0
 0.0, -.525880E-01
 *AMPLITUDE, NAME=LHSU10, DEFINITION=PERIODIC, TIME=TOTAL
 1, -6.283, 0.0, 0.0
 0.0, -.475668E-01
 *AMPLITUDE, NAME=LHSU10A, DEFINITION=PERIODIC, TIME=TOTAL
 1, -6.283, 0.0, 0.0
 0.0, -.429108E-01
 *AMPLITUDE, NAME=LHSU11, DEFINITION=PERIODIC, TIME=TOTAL
 1, -6.283, 0.0, 0.0
 0.0, -.386237E-01
 *AMPLITUDE, NAME=LHSU11A, DEFINITION=PERIODIC, TIME=TOTAL
 1, -6.283, 0.0, 0.0
 0.0, -.346988E-01
 *AMPLITUDE, NAME=LHSU12, DEFINITION=PERIODIC, TIME=TOTAL
 1, -6.283, 0.0, 0.0
 0.0, -.311222E-01
 *AMPLITUDE, NAME=LHSU12A, DEFINITION=PERIODIC, TIME=TOTAL
 1, -6.283, 0.0, 0.0

```

0.0, -.278757E-01
*AMPLITUDE, NAME=LHSU13, DEFINITION=PERIODIC, TIME=TOTAL
1, -6.283, 0.0, 0.0
0.0, -.249382E-01
*AMPLITUDE, NAME=LHSU13A, DEFINITION=PERIODIC, TIME=TOTAL
1, -6.283, 0.0, 0.0
0.0, -.222876E-01
*AMPLITUDE, NAME=LHSU14, DEFINITION=PERIODIC, TIME=TOTAL
1, -6.283, 0.0, 0.0
0.0, -.199013E-01
*AMPLITUDE, NAME=LHSU14A, DEFINITION=PERIODIC, TIME=TOTAL
1, -6.283, 0.0, 0.0
0.0, -.177571E-01
*AMPLITUDE, NAME=LHSU15, DEFINITION=PERIODIC, TIME=TOTAL
1, -6.283, 0.0, 0.0
0.0, -.158336E-01
*AMPLITUDE, NAME=LHSU15A, DEFINITION=PERIODIC, TIME=TOTAL
1, -6.283, 0.0, 0.0
0.0, -.141105E-01
*AMPLITUDE, NAME=LHSU16, DEFINITION=PERIODIC, TIME=TOTAL
1, -6.283, 0.0, 0.0
0.0, -.125688E-01
*AMPLITUDE, NAME=LHSU16A, DEFINITION=PERIODIC, TIME=TOTAL
1, -6.283, 0.0, 0.0
0.0, -.111908E-01
*AMPLITUDE, NAME=LHSU17, DEFINITION=PERIODIC, TIME=TOTAL
1, -6.283, 0.0, 0.0
0.0, -.996026E-02
*AMPLITUDE, NAME=LHSU17A, DEFINITION=PERIODIC, TIME=TOTAL
1, -6.283, 0.0, 0.0
0.0, -.886222E-02
*AMPLITUDE, NAME=LHSU18, DEFINITION=PERIODIC, TIME=TOTAL
1, -6.283, 0.0, 0.0
0.0, -.788305E-02
*AMPLITUDE, NAME=LHSU18A, DEFINITION=PERIODIC, TIME=TOTAL
1, -6.283, 0.0, 0.0
0.0, -.701040E-02
*AMPLITUDE, NAME=LHSU19, DEFINITION=PERIODIC, TIME=TOTAL
1, -6.283, 0.0, 0.0
0.0, -.623305E-02
*AMPLITUDE, NAME=LHSU19A, DEFINITION=PERIODIC, TIME=TOTAL
1, -6.283, 0.0, 0.0
0.0, -.554090E-02
*AMPLITUDE, NAME=LHSU20, DEFINITION=PERIODIC, TIME=TOTAL
1, -6.283, 0.0, 0.0
0.0, -.492484E-02
*AMPLITUDE, NAME=LHSU20A, DEFINITION=PERIODIC, TIME=TOTAL
1, -6.283, 0.0, 0.0
0.0, -.437667E-02
*AMPLITUDE, NAME=LHSU21, DEFINITION=PERIODIC, TIME=TOTAL
1, -6.283, 0.0, 0.0
0.0, -.388906E-02
***
*** LHS V ***
***
*AMPLITUDE, NAME=LHSV0, DEFINITION=PERIODIC, TIME=TOTAL
1, -6.283, 0.0, 0.0
0.620400E+00, 0.0
*AMPLITUDE, NAME=LHSV0A, DEFINITION=PERIODIC, TIME=TOTAL
1, -6.283, 0.0, 0.0
0.647399E+00, 0.0
*AMPLITUDE, NAME=LHSV1, DEFINITION=PERIODIC, TIME=TOTAL
1, -6.283, 0.0, 0.0
0.649542E+00, 0.0
*AMPLITUDE, NAME=LHSV1A, DEFINITION=PERIODIC, TIME=TOTAL
1, -6.283, 0.0, 0.0

```

0.634551E+00,0.0
 *AMPLITUDE, NAME=LHSV2, DEFINITION=PERIODIC, TIME=TOTAL
 1, -6.283, 0.0, 0.0
 0.608166E+00,0.0
 *AMPLITUDE, NAME=LHSV2A, DEFINITION=PERIODIC, TIME=TOTAL
 1, -6.283, 0.0, 0.0
 0.574620E+00,0.0
 *AMPLITUDE, NAME=LHSV3, DEFINITION=PERIODIC, TIME=TOTAL
 1, -6.283, 0.0, 0.0
 0.537004E+00,0.0
 *AMPLITUDE, NAME=LHSV3A, DEFINITION=PERIODIC, TIME=TOTAL
 1, -6.283, 0.0, 0.0
 0.497545E+00,0.0
 *AMPLITUDE, NAME=LHSV4, DEFINITION=PERIODIC, TIME=TOTAL
 1, -6.283, 0.0, 0.0
 0.457818E+00,0.0
 *AMPLITUDE, NAME=LHSV4A, DEFINITION=PERIODIC, TIME=TOTAL
 1, -6.283, 0.0, 0.0
 0.418916E+00,0.0
 *AMPLITUDE, NAME=LHSV5, DEFINITION=PERIODIC, TIME=TOTAL
 1, -6.283, 0.0, 0.0
 0.381565E+00,0.0
 *AMPLITUDE, NAME=LHSV5A, DEFINITION=PERIODIC, TIME=TOTAL
 1, -6.283, 0.0, 0.0
 0.346228E+00,0.0
 *AMPLITUDE, NAME=LHSV6, DEFINITION=PERIODIC, TIME=TOTAL
 1, -6.283, 0.0, 0.0
 0.313169E+00,0.0
 *AMPLITUDE, NAME=LHSV6A, DEFINITION=PERIODIC, TIME=TOTAL
 1, -6.283, 0.0, 0.0
 0.282515E+00,0.0
 *AMPLITUDE, NAME=LHSV7, DEFINITION=PERIODIC, TIME=TOTAL
 1, -6.283, 0.0, 0.0
 0.254290E+00,0.0
 *AMPLITUDE, NAME=LHSV7A, DEFINITION=PERIODIC, TIME=TOTAL
 1, -6.283, 0.0, 0.0
 0.228449E+00,0.0
 *AMPLITUDE, NAME=LHSV8, DEFINITION=PERIODIC, TIME=TOTAL
 1, -6.283, 0.0, 0.0
 0.204902E+00,0.0
 *AMPLITUDE, NAME=LHSV8A, DEFINITION=PERIODIC, TIME=TOTAL
 1, -6.283, 0.0, 0.0
 0.183528E+00,0.0
 *AMPLITUDE, NAME=LHSV9, DEFINITION=PERIODIC, TIME=TOTAL
 1, -6.283, 0.0, 0.0
 0.164188E+00,0.0
 *AMPLITUDE, NAME=LHSV9A, DEFINITION=PERIODIC, TIME=TOTAL
 1, -6.283, 0.0, 0.0
 0.146737E+00,0.0
 *AMPLITUDE, NAME=LHSV10, DEFINITION=PERIODIC, TIME=TOTAL
 1, -6.283, 0.0, 0.0
 0.131026E+00,0.0
 *AMPLITUDE, NAME=LHSV10A, DEFINITION=PERIODIC, TIME=TOTAL
 1, -6.283, 0.0, 0.0
 0.116909E+00,0.0
 *AMPLITUDE, NAME=LHSV11, DEFINITION=PERIODIC, TIME=TOTAL
 1, -6.283, 0.0, 0.0
 0.104245E+00,0.0
 *AMPLITUDE, NAME=LHSV11A, DEFINITION=PERIODIC, TIME=TOTAL
 1, -6.283, 0.0, 0.0
 0.929004E-01,0.0
 *AMPLITUDE, NAME=LHSV12, DEFINITION=PERIODIC, TIME=TOTAL
 1, -6.283, 0.0, 0.0
 0.827502E-01,0.0
 *AMPLITUDE, NAME=LHSV12A, DEFINITION=PERIODIC, TIME=TOTAL
 1, -6.283, 0.0, 0.0

```

0.736779E-01,0.0
*AMPLITUDE,NAME=LHSV13,DEFINITION=PERIODIC,TIME=TOTAL
1,-6.283,0.0,0.0
0.655762E-01,0.0
*AMPLITUDE,NAME=LHSV13A,DEFINITION=PERIODIC,TIME=TOTAL
1,-6.283,0.0,0.0
0.583469E-01,0.0
*AMPLITUDE,NAME=LHSV14,DEFINITION=PERIODIC,TIME=TOTAL
1,-6.283,0.0,0.0
0.519003E-01,0.0
*AMPLITUDE,NAME=LHSV14A,DEFINITION=PERIODIC,TIME=TOTAL
1,-6.283,0.0,0.0
0.461550E-01,0.0
*AMPLITUDE,NAME=LHSV15,DEFINITION=PERIODIC,TIME=TOTAL
1,-6.283,0.0,0.0
0.410371E-01,0.0
*AMPLITUDE,NAME=LHSV15A,DEFINITION=PERIODIC,TIME=TOTAL
1,-6.283,0.0,0.0
0.364801E-01,0.0
*AMPLITUDE,NAME=LHSV16,DEFINITION=PERIODIC,TIME=TOTAL
1,-6.283,0.0,0.0
0.324241E-01,0.0
*AMPLITUDE,NAME=LHSV16A,DEFINITION=PERIODIC,TIME=TOTAL
1,-6.283,0.0,0.0
0.288151E-01,0.0
*AMPLITUDE,NAME=LHSV17,DEFINITION=PERIODIC,TIME=TOTAL
1,-6.283,0.0,0.0
0.256047E-01,0.0
*AMPLITUDE,NAME=LHSV17A,DEFINITION=PERIODIC,TIME=TOTAL
1,-6.283,0.0,0.0
0.227497E-01,0.0
*AMPLITUDE,NAME=LHSV18,DEFINITION=PERIODIC,TIME=TOTAL
1,-6.283,0.0,0.0
0.202112E-01,0.0
*AMPLITUDE,NAME=LHSV18A,DEFINITION=PERIODIC,TIME=TOTAL
1,-6.283,0.0,0.0
0.179546E-01,0.0
*AMPLITUDE,NAME=LHSV19,DEFINITION=PERIODIC,TIME=TOTAL
1,-6.283,0.0,0.0
0.159488E-01,0.0
*AMPLITUDE,NAME=LHSV19A,DEFINITION=PERIODIC,TIME=TOTAL
1,-6.283,0.0,0.0
0.141663E-01,0.0
*AMPLITUDE,NAME=LHSV20,DEFINITION=PERIODIC,TIME=TOTAL
1,-6.283,0.0,0.0
0.125823E-01,0.0
*AMPLITUDE,NAME=LHSV20A,DEFINITION=PERIODIC,TIME=TOTAL
1,-6.283,0.0,0.0
0.111749E-01,0.0
*AMPLITUDE,NAME=LHSV21,DEFINITION=PERIODIC,TIME=TOTAL
1,-6.283,0.0,0.0
0.992459E-02,0.0
*****
*RESTART,WRITE,FREQUENCY=840
*PREPRINT,ECHO=NO,MODEL=NO
*STEP,INC=33600
*DYNAMIC,NOHAF
0.0025,16.8
*****
***
*** LHS U ***
***
*BOUNDARY,AMPLITUDE=LHSU0
1,1,,1.
*BOUNDARY,AMPLITUDE=LHSU0A
2,1,,1.

```

*BOUNDARY,AMPLITUDE=LHSU1
3,1,,1.
*BOUNDARY,AMPLITUDE=LHSU1A
4,1,,1.
*BOUNDARY,AMPLITUDE=LHSU2
5,1,,1.
*BOUNDARY,AMPLITUDE=LHSU2A
6,1,,1.
*BOUNDARY,AMPLITUDE=LHSU3
7,1,,1.
*BOUNDARY,AMPLITUDE=LHSU3A
8,1,,1.
*BOUNDARY,AMPLITUDE=LHSU4
9,1,,1.
*BOUNDARY,AMPLITUDE=LHSU4A
10,1,,1.
*BOUNDARY,AMPLITUDE=LHSU5
11,1,,1.
*BOUNDARY,AMPLITUDE=LHSU5A
12,1,,1.
*BOUNDARY,AMPLITUDE=LHSU6
13,1,,1.
*BOUNDARY,AMPLITUDE=LHSU6A
14,1,,1.
*BOUNDARY,AMPLITUDE=LHSU7
15,1,,1.
*BOUNDARY,AMPLITUDE=LHSU7A
16,1,,1.
*BOUNDARY,AMPLITUDE=LHSU8
17,1,,1.
*BOUNDARY,AMPLITUDE=LHSU8A
18,1,,1.
*BOUNDARY,AMPLITUDE=LHSU9
19,1,,1.
*BOUNDARY,AMPLITUDE=LHSU9A
20,1,,1.
*BOUNDARY,AMPLITUDE=LHSU10
21,1,,1.
*BOUNDARY,AMPLITUDE=LHSU10A
22,1,,1.
*BOUNDARY,AMPLITUDE=LHSU11
23,1,,1.
*BOUNDARY,AMPLITUDE=LHSU11A
24,1,,1.
*BOUNDARY,AMPLITUDE=LHSU12
25,1,,1.
*BOUNDARY,AMPLITUDE=LHSU12A
26,1,,1.
*BOUNDARY,AMPLITUDE=LHSU13
27,1,,1.
*BOUNDARY,AMPLITUDE=LHSU13A
28,1,,1.
*BOUNDARY,AMPLITUDE=LHSU14
29,1,,1.
*BOUNDARY,AMPLITUDE=LHSU14A
30,1,,1.
*BOUNDARY,AMPLITUDE=LHSU15
31,1,,1.
*BOUNDARY,AMPLITUDE=LHSU15A
32,1,,1.
*BOUNDARY,AMPLITUDE=LHSU16
33,1,,1.
*BOUNDARY,AMPLITUDE=LHSU16A
34,1,,1.
*BOUNDARY,AMPLITUDE=LHSU17
35,1,,1.

*BOUNDARY,AMPLITUDE=LHSU17A
36,1,,1.
*BOUNDARY,AMPLITUDE=LHSU18
37,1,,1.
*BOUNDARY,AMPLITUDE=LHSU18A
38,1,,1.
*BOUNDARY,AMPLITUDE=LHSU19
39,1,,1.
*BOUNDARY,AMPLITUDE=LHSU19A
40,1,,1.
*BOUNDARY,AMPLITUDE=LHSU20
41,1,,1.
*BOUNDARY,AMPLITUDE=LHSU20A
42,1,,1.

*** LHS V ***

*BOUNDARY,AMPLITUDE=LHSV0
1,2,,1.
*BOUNDARY,AMPLITUDE=LHSV0A
2,2,,1.
*BOUNDARY,AMPLITUDE=LHSV1
3,2,,1.
*BOUNDARY,AMPLITUDE=LHSV1A
4,2,,1.
*BOUNDARY,AMPLITUDE=LHSV2
5,2,,1.
*BOUNDARY,AMPLITUDE=LHSV2A
6,2,,1.
*BOUNDARY,AMPLITUDE=LHSV3
7,2,,1.
*BOUNDARY,AMPLITUDE=LHSV3A
8,2,,1.
*BOUNDARY,AMPLITUDE=LHSV4
9,2,,1.
*BOUNDARY,AMPLITUDE=LHSV4A
10,2,,1.
*BOUNDARY,AMPLITUDE=LHSV5
11,2,,1.
*BOUNDARY,AMPLITUDE=LHSV5A
12,2,,1.
*BOUNDARY,AMPLITUDE=LHSV6
13,2,,1.
*BOUNDARY,AMPLITUDE=LHSV6A
14,2,,1.
*BOUNDARY,AMPLITUDE=LHSV7
15,2,,1.
*BOUNDARY,AMPLITUDE=LHSV7A
16,2,,1.
*BOUNDARY,AMPLITUDE=LHSV8
17,2,,1.
*BOUNDARY,AMPLITUDE=LHSV8A
18,2,,1.
*BOUNDARY,AMPLITUDE=LHSV9
19,2,,1.
*BOUNDARY,AMPLITUDE=LHSV9A
20,2,,1.
*BOUNDARY,AMPLITUDE=LHSV10
21,2,,1.
*BOUNDARY,AMPLITUDE=LHSV10A
22,2,,1.
*BOUNDARY,AMPLITUDE=LHSV11
23,2,,1.
*BOUNDARY,AMPLITUDE=LHSV11A
24,2,,1.
*BOUNDARY,AMPLITUDE=LHSV12


```

25,2,,1.
*BOUNDARY,AMPLITUDE=LHSV12A
26,2,,1.
*BOUNDARY,AMPLITUDE=LHSV13
27,2,,1.
*BOUNDARY,AMPLITUDE=LHSV13A
28,2,,1.
*BOUNDARY,AMPLITUDE=LHSV14
29,2,,1.
*BOUNDARY,AMPLITUDE=LHSV14A
30,2,,1.
*BOUNDARY,AMPLITUDE=LHSV15
31,2,,1.
*BOUNDARY,AMPLITUDE=LHSV15A
32,2,,1.
*BOUNDARY,AMPLITUDE=LHSV16
33,2,,1.
*BOUNDARY,AMPLITUDE=LHSV16A
34,2,,1.
*BOUNDARY,AMPLITUDE=LHSV17
35,2,,1.
*BOUNDARY,AMPLITUDE=LHSV17A
36,2,,1.
*BOUNDARY,AMPLITUDE=LHSV18
37,2,,1.
*BOUNDARY,AMPLITUDE=LHSV18A
38,2,,1.
*BOUNDARY,AMPLITUDE=LHSV19
39,2,,1.
*BOUNDARY,AMPLITUDE=LHSV19A
40,2,,1.
*BOUNDARY,AMPLITUDE=LHSV20
41,2,,1.
*BOUNDARY,AMPLITUDE=LHSV20A
42,2,,1.
***
*** BOT ***
***
*BOUNDARY
BOT,1
BOT,2
*****
*EL PRINT,FREQUENCY=0
*ENERGY PRINT,FREQ=0
*NODE PRINT,FREQ=0
*NODE PRINT,NSET=RHS,FREQ=840
U,V
*END STEP

```

```

SUBROUTINE UEL(RHS,AMATRX,SVARS,ENERGY,NDOFEL,NRHS,NSVARS,PROPS,
1 NPROPS,COORDS,MCRD,NNODE,U,DU,V,A,JTYPE,TIME,DTIME,KSTEP,KINC,
2 JELEM,PARAMS,NDLOAD,JDLTYP,ADLMAG,PREDEF,NPREDF,LFLAGS,
3 MLVARX,DDLMAG,MDLOAD,PNEWDT,JPROPS,NJPROP,PERIOD)
C
C   INCLUDE 'ABA_PARAM.INC'
C
C   DOUBLE PRECISION CONST1,CONST2,CP,DP,CS,DS,ALEN,HFALEN,
1 STRESS,ENDALEN,ALENMID,CONSTN,S,DG,F,AKY,BKY,DF,G
C
C   DIMENSION RHS(MLVARX,*),AMATRX(NDOFEL,NDOFEL),SVARS(NSVARS),
1 ENERGY(8),PROPS(*),COORDS(MCRD,NNODE),
2 U(NDOFEL),DU(MLVARX,*),V(NDOFEL),A(NDOFEL),TIME(2),
3 PARAMS(3),JDLTYP(MDLOAD,*),ADLMAG(MDLOAD,*),
4 DDLMAG(MDLOAD,*),PREDEF(2,NPREDF,NNODE),LFLAGS(*),JPROPS(*)
C   DIMENSION SRESID(9)
C   DIMENSION STRESS(9)
C   DIMENSION DG(3)
C   DIMENSION F(3)
C   DIMENSION AKY(3)
C   DIMENSION DF(3)
C   DIMENSION G(3)
C   DIMENSION BKY(3)
C
C   SRESID - stores the static residual at time t+dt
C   SVARS - In 1-6, contains the static residual at time t upon
C           entering the routine. SRESID is copied to SVARS(1-6)
C           after the dynamic residual has been calculated.
C           - For half-step residual calculations: In 7-12, contains
C             the static residual at the beginning of the previous
C             increment. SVARS(1-6) are copied into SVARS(7-12) after
C             the dynamic residual has been calculated.
C
C   AREA= PROPS(1)
C   E = PROPS(2)
C   ANU = PROPS(3)
C   RHO = PROPS(4)
C
C   Calculate wave speed of P-wave
C
C   CONST1 = (E*ANU)/((1.0+ANU)*(1.0-(ANU+ANU)))
C   CONST2 = E/((1.0+ANU)+(1.0+ANU))
C   CP = ((CONST1+(CONST2+CONST2))/RHO)**0.5
C   DP = RHO*CP
C
C   Calculate wave speed of S-wave
C
C   CS = (CONST2/RHO)**0.5
C   DS = RHO*CS
C
C   ALEN = COORDS(2,1) - COORDS(2,3)
C
C   Calculate A(KY)
C
C   CONSTN = 1.08766D0
C   S = SQRT((1-(ANU+ANU))/((1.0-ANU)+(1.0-ANU)))
C
C   DO 11 K1=1,3
C       DG(K1) = (-0.718256D0*EXP(0.8475D0*0.034153D0
1         *COORDS(2,K1)))+(0.577325D0*EXP(0.3933D0*0.034153D0
2         *COORDS(2,K1)))
11 CONTINUE
C
C   DO 12 K1=1,3
C       F(K1) = (EXP(0.8475D0*0.0341563D0*COORDS(2,K1)))
1       - (0.5773D0*EXP(0.3933D0*0.034153D0*COORDS(2,K1)))

```

```

12 CONTINUE
C
DO 13 K1=1,3
    AKY(K1) = (CONSTN/S)*(1.0 + ((1.0 - ((S*S)+(S*S)))
1        *(DG(K1)/F(K1))))
13 CONTINUE
C
C    IF (AKY(1) .GE. 3.0 .OR. AKY(1) .LE. -1.0) THEN
C        U(1) = 0.0D0
C    ELSE
C        CONTINUE
C    ENDIF
C
C    IF (AKY(2) .GE. 3.0 .OR. AKY(2) .LE. -1.0) THEN
C        U(4) = 0.0D0
C    ELSE
C        CONTINUE
C    ENDIF
C
C    IF (AKY(3) .GE. 3.0 .OR. AKY(3) .LE. -1.0) THEN
C        U(7) = 0.0D0
C    ELSE
C        CONTINUE
C    ENDIF
C
*****
C
C
C    Calculate B(KY)
C
DO 21 K1=1,3
    DF(K1) = (0.8475D0*EXP(0.8475D0*0.034153D0
1        *COORDS(2,K1))) - (0.227052D0*EXP(0.3933D0*0.034153D0
2        *COORDS(2,K1)))
21 CONTINUE
C
DO 22 K1=1,3
    G(K1) = (-0.8475D0*EXP(0.8475D0*0.034153D0
1        *COORDS(2,K1))) + (1.4679D0*EXP(0.3933D0*0.034153D0
2        *COORDS(2,K1)))
22 CONTINUE
C
DO 23 K1=1,3
    BKY(K1) = CONSTN * (1.0 - (DF(K1)/G(K1)))
23 CONTINUE
C
C
DO 6 K1=1,NDOFEL
    SRESID(K1) = 0.0D0
DO 2 KRHS=1,NRHS
    RHS(K1,KRHS) = 0.0D0
2 CONTINUE
DO 4 K2=1,NDOFEL
    AMATRX(K2,K1)=0.0D0
4 CONTINUE
6 CONTINUE
C
DO 8 K1=1,NDOFEL
    STRESS(K1) = 0.0D0
8 CONTINUE
*****
IF (LFLAGS(3).EQ.1) THEN
C    Normal incrementation
    IF (LFLAGS(1).EQ.11 .OR. LFLAGS(1).EQ.12) THEN
C        *DYNAMIC
        ALPHA = PARAMS(1)

```

```

      BETA = PARAMS(2)
      GAMMA = PARAMS(3)

C
C
C   Calculate stresses by multiplying V(1),V(4),V(7) by DP and AKY
C   and V(2),V(5) and V(8) by DS
C
C
C
      IF (AKY(1) .GE. 3.0 .OR. AKY(1) .LE. -1.0) THEN
        U(1) = 0.0D0
        STRESS(1) = V(1) * DP
      ELSE
        STRESS(1) = V(1) * DP * AKY(1)
      ENDIF

C
      IF (AKY(2) .GE. 3.0 .OR. AKY(2) .LE. -1.0) THEN
        U(4) = 0.0D0
        STRESS(4) = V(4) * DP
      ELSE
        STRESS(4) = V(4) * DP * AKY(2)
      ENDIF

C
      IF (AKY(3) .GE. 3.0 .OR. AKY(3) .LE. -1.0) THEN
        U(7) = 0.0D0
        STRESS(7) = V(7) * DP
      ELSE
        STRESS(7) = V(7) * DP * AKY(3)
      ENDIF

C
C
      DO 15 K1 = 2,8,3
        STRESS(K1) = V(K1) * DS
15 CONTINUE

C
      STRESS(2) = STRESS(2) * BKY(1)
      STRESS(5) = STRESS(5) * BKY(2)
      STRESS(8) = STRESS(8) * BKY(3)

C
C
C   Calculate forces at nodes by multiplying {STRESS}
C   by L/6 for end nodes and 2L/3 for midside node
C
      ENDALEN = ALLEN/6.0
      ALENMID = (ALLEN+ALLEN)/3.0

C
C   Multiply end node terms in {STRESS} by -ENDALEN
C
      DO 20 K1 = 1,3,1
        RHS(K1,1) = -STRESS(K1) * ENDALEN
20 CONTINUE
      DO 30 K1 = 7,9,1
        RHS(K1,1) = -STRESS(K1) * ENDALEN
30 CONTINUE

C
C   Multiply midside node terms in {STRESS} by -ALENMID
C
      DO 40 K1 = 4,6,1
        RHS(K1,1) = -STRESS(K1) * ALENMID
40 CONTINUE

C
C
      END IF
*****
      END IF
      RETURN

```

END

```

*HEADING
**Revised mesh - central axis at 371.8**
***Axisymmetric elements***
CHECK FOR RAYLEIGH WAVES - 8 NODED ELEMENTS - REVISION 2 (BULLEN)
WITH USER INFINITE ELEMENTS
21 x 21 ELEMENT MESH
*NODE, INPUT=rw21r-node.inp
*ELEMENT, TYPE=CAX8, INPUT=rw21-elem-fe.inp, ELSET=FE
*USER ELEMENT, NODES=3, TYPE=U4, PROPERTIES=4, COORDINATES=3, VARIABLES=6
1, 2, 3
*USER SUBROUTINE, INPUT=usub3nielk2npax.for
*ELEMENT, TYPE=U4, ELSET=IE
701, 1366, 1367, 1368
702, 1368, 1369, 1370
703, 1370, 1371, 1372
704, 1372, 1373, 1374
705, 1374, 1375, 1376
706, 1376, 1377, 1378
707, 1378, 1379, 1380
708, 1380, 1381, 1382
709, 1382, 1383, 1384
710, 1384, 1385, 1386
711, 1386, 1387, 1388
712, 1388, 1389, 1390
713, 1390, 1391, 1392
714, 1392, 1393, 1394
715, 1394, 1395, 1396
716, 1396, 1397, 1398
717, 1398, 1399, 1400
718, 1400, 1401, 1402
719, 1402, 1403, 1404
720, 1404, 1405, 1406
721, 1406, 1407, 1408
*UEL PROPERTY, ELSET=IE
4672.746636, 0.2e9, 0.25, 1998.
*NSET, NSET=LHS, GENERATE
1, 43, 1
*NSET, NSET=RHS, GENERATE
1366, 1408, 1
*NSET, NSET=TOP, GENERATE
1, 1366, 65
44, 1344, 65
*NSET, NSET=BOT, GENERATE
43, 1408, 65
65, 1365, 65
*NSET, NSET=FILEN, GENERATE
15, 1380, 65
51, 1351, 65
*SOLID SECTION, ELSET=FE, MATERIAL=ONE
*MATERIAL, NAME=ONE
*ELASTIC
0.2E9, 0.25
*DENSITY
1998.
***
*** LHS U ***
***
*AMPLITUDE, NAME=LHSU0, DEFINITION=PERIODIC, TIME=TOTAL
1, -6.283, 0.0, 0.0
0.0, 0.422700E+00
*AMPLITUDE, NAME=LHSU0A, DEFINITION=PERIODIC, TIME=TOTAL
1, -6.283, 0.0, 0.0
0.0, 0.261369E+00
*AMPLITUDE, NAME=LHSU1, DEFINITION=PERIODIC, TIME=TOTAL
1, -6.283, 0.0, 0.0
0.0, 0.143884E+00

```

```

*AMPLITUDE, NAME=LHSU1A, DEFINITION=PERIODIC, TIME=TOTAL
1, -6.283, 0.0, 0.0
0.0, 0.595056E-01
*AMPLITUDE, NAME=LHSU2, DEFINITION=PERIODIC, TIME=TOTAL
1, -6.283, 0.0, 0.0
0.0, 0.155568E-04
*AMPLITUDE, NAME=LHSU2A, DEFINITION=PERIODIC, TIME=TOTAL
1, -6.283, 0.0, 0.0
0.0, -.408643E-01
*AMPLITUDE, NAME=LHSU3, DEFINITION=PERIODIC, TIME=TOTAL
1, -6.283, 0.0, 0.0
0.0, -.679196E-01
*AMPLITUDE, NAME=LHSU3A, DEFINITION=PERIODIC, TIME=TOTAL
1, -6.283, 0.0, 0.0
0.0, -.847895E-01
*AMPLITUDE, NAME=LHSU4, DEFINITION=PERIODIC, TIME=TOTAL
1, -6.283, 0.0, 0.0
0.0, -.942327E-01
*AMPLITUDE, NAME=LHSU4A, DEFINITION=PERIODIC, TIME=TOTAL
1, -6.283, 0.0, 0.0
0.0, -.983333E-01
*AMPLITUDE, NAME=LHSU5, DEFINITION=PERIODIC, TIME=TOTAL
1, -6.283, 0.0, 0.0
0.0, -.986586E-01
*AMPLITUDE, NAME=LHSU5A, DEFINITION=PERIODIC, TIME=TOTAL
1, -6.283, 0.0, 0.0
0.0, -.963815E-01
*AMPLITUDE, NAME=LHSU6, DEFINITION=PERIODIC, TIME=TOTAL
1, -6.283, 0.0, 0.0
0.0, -.923738E-01
*AMPLITUDE, NAME=LHSU6A, DEFINITION=PERIODIC, TIME=TOTAL
1, -6.283, 0.0, 0.0
0.0, -.872785E-01
*AMPLITUDE, NAME=LHSU7, DEFINITION=PERIODIC, TIME=TOTAL
1, -6.283, 0.0, 0.0
0.0, -.815649E-01
*AMPLITUDE, NAME=LHSU7A, DEFINITION=PERIODIC, TIME=TOTAL
1, -6.283, 0.0, 0.0
0.0, -.755714E-01
*AMPLITUDE, NAME=LHSU8, DEFINITION=PERIODIC, TIME=TOTAL
1, -6.283, 0.0, 0.0
0.0, -.695374E-01
*AMPLITUDE, NAME=LHSU8A, DEFINITION=PERIODIC, TIME=TOTAL
1, -6.283, 0.0, 0.0
0.0, -.636285E-01
*AMPLITUDE, NAME=LHSU9, DEFINITION=PERIODIC, TIME=TOTAL
1, -6.283, 0.0, 0.0
0.0, -.579554E-01
*AMPLITUDE, NAME=LHSU9A, DEFINITION=PERIODIC, TIME=TOTAL
1, -6.283, 0.0, 0.0
0.0, -.525880E-01
*AMPLITUDE, NAME=LHSU10, DEFINITION=PERIODIC, TIME=TOTAL
1, -6.283, 0.0, 0.0
0.0, -.475668E-01
*AMPLITUDE, NAME=LHSU10A, DEFINITION=PERIODIC, TIME=TOTAL
1, -6.283, 0.0, 0.0
0.0, -.429108E-01
*AMPLITUDE, NAME=LHSU11, DEFINITION=PERIODIC, TIME=TOTAL
1, -6.283, 0.0, 0.0
0.0, -.386237E-01
*AMPLITUDE, NAME=LHSU11A, DEFINITION=PERIODIC, TIME=TOTAL
1, -6.283, 0.0, 0.0
0.0, -.346988E-01
*AMPLITUDE, NAME=LHSU12, DEFINITION=PERIODIC, TIME=TOTAL
1, -6.283, 0.0, 0.0
0.0, -.311222E-01

```

```

*AMPLITUDE, NAME=LHSU12A, DEFINITION=PERIODIC, TIME=TOTAL
1, -6.283, 0.0, 0.0
0.0, -.278757E-01
*AMPLITUDE, NAME=LHSU13, DEFINITION=PERIODIC, TIME=TOTAL
1, -6.283, 0.0, 0.0
0.0, -.249382E-01
*AMPLITUDE, NAME=LHSU13A, DEFINITION=PERIODIC, TIME=TOTAL
1, -6.283, 0.0, 0.0
0.0, -.222876E-01
*AMPLITUDE, NAME=LHSU14, DEFINITION=PERIODIC, TIME=TOTAL
1, -6.283, 0.0, 0.0
0.0, -.199013E-01
*AMPLITUDE, NAME=LHSU14A, DEFINITION=PERIODIC, TIME=TOTAL
1, -6.283, 0.0, 0.0
0.0, -.177571E-01
*AMPLITUDE, NAME=LHSU15, DEFINITION=PERIODIC, TIME=TOTAL
1, -6.283, 0.0, 0.0
0.0, -.158336E-01
*AMPLITUDE, NAME=LHSU15A, DEFINITION=PERIODIC, TIME=TOTAL
1, -6.283, 0.0, 0.0
0.0, -.141105E-01
*AMPLITUDE, NAME=LHSU16, DEFINITION=PERIODIC, TIME=TOTAL
1, -6.283, 0.0, 0.0
0.0, -.125688E-01
*AMPLITUDE, NAME=LHSU16A, DEFINITION=PERIODIC, TIME=TOTAL
1, -6.283, 0.0, 0.0
0.0, -.111908E-01
*AMPLITUDE, NAME=LHSU17, DEFINITION=PERIODIC, TIME=TOTAL
1, -6.283, 0.0, 0.0
0.0, -.996026E-02
*AMPLITUDE, NAME=LHSU17A, DEFINITION=PERIODIC, TIME=TOTAL
1, -6.283, 0.0, 0.0
0.0, -.886222E-02
*AMPLITUDE, NAME=LHSU18, DEFINITION=PERIODIC, TIME=TOTAL
1, -6.283, 0.0, 0.0
0.0, -.788305E-02
*AMPLITUDE, NAME=LHSU18A, DEFINITION=PERIODIC, TIME=TOTAL
1, -6.283, 0.0, 0.0
0.0, -.701040E-02
*AMPLITUDE, NAME=LHSU19, DEFINITION=PERIODIC, TIME=TOTAL
1, -6.283, 0.0, 0.0
0.0, -.623305E-02
*AMPLITUDE, NAME=LHSU19A, DEFINITION=PERIODIC, TIME=TOTAL
1, -6.283, 0.0, 0.0
0.0, -.554090E-02
*AMPLITUDE, NAME=LHSU20, DEFINITION=PERIODIC, TIME=TOTAL
1, -6.283, 0.0, 0.0
0.0, -.492484E-02
*AMPLITUDE, NAME=LHSU20A, DEFINITION=PERIODIC, TIME=TOTAL
1, -6.283, 0.0, 0.0
0.0, -.437667E-02
*AMPLITUDE, NAME=LHSU21, DEFINITION=PERIODIC, TIME=TOTAL
1, -6.283, 0.0, 0.0
0.0, -.388906E-02
***
*** LHS V ***
***
*AMPLITUDE, NAME=LHSV0, DEFINITION=PERIODIC, TIME=TOTAL
1, -6.283, 0.0, 0.0
0.620400E+00, 0.0
*AMPLITUDE, NAME=LHSV0A, DEFINITION=PERIODIC, TIME=TOTAL
1, -6.283, 0.0, 0.0
0.647399E+00, 0.0
*AMPLITUDE, NAME=LHSV1, DEFINITION=PERIODIC, TIME=TOTAL
1, -6.283, 0.0, 0.0
0.649542E+00, 0.0

```



```

*AMPLITUDE, NAME=LHSV1A, DEFINITION=PERIODIC, TIME=TOTAL
1, -6.283, 0.0, 0.0
0.634551E+00, 0.0
*AMPLITUDE, NAME=LHSV2, DEFINITION=PERIODIC, TIME=TOTAL
1, -6.283, 0.0, 0.0
0.608166E+00, 0.0
*AMPLITUDE, NAME=LHSV2A, DEFINITION=PERIODIC, TIME=TOTAL
1, -6.283, 0.0, 0.0
0.574620E+00, 0.0
*AMPLITUDE, NAME=LHSV3, DEFINITION=PERIODIC, TIME=TOTAL
1, -6.283, 0.0, 0.0
0.537004E+00, 0.0
*AMPLITUDE, NAME=LHSV3A, DEFINITION=PERIODIC, TIME=TOTAL
1, -6.283, 0.0, 0.0
0.497545E+00, 0.0
*AMPLITUDE, NAME=LHSV4, DEFINITION=PERIODIC, TIME=TOTAL
1, -6.283, 0.0, 0.0
0.457818E+00, 0.0
*AMPLITUDE, NAME=LHSV4A, DEFINITION=PERIODIC, TIME=TOTAL
1, -6.283, 0.0, 0.0
0.418916E+00, 0.0
*AMPLITUDE, NAME=LHSV5, DEFINITION=PERIODIC, TIME=TOTAL
1, -6.283, 0.0, 0.0
0.381565E+00, 0.0
*AMPLITUDE, NAME=LHSV5A, DEFINITION=PERIODIC, TIME=TOTAL
1, -6.283, 0.0, 0.0
0.346228E+00, 0.0
*AMPLITUDE, NAME=LHSV6, DEFINITION=PERIODIC, TIME=TOTAL
1, -6.283, 0.0, 0.0
0.313169E+00, 0.0
*AMPLITUDE, NAME=LHSV6A, DEFINITION=PERIODIC, TIME=TOTAL
1, -6.283, 0.0, 0.0
0.282515E+00, 0.0
*AMPLITUDE, NAME=LHSV7, DEFINITION=PERIODIC, TIME=TOTAL
1, -6.283, 0.0, 0.0
0.254290E+00, 0.0
*AMPLITUDE, NAME=LHSV7A, DEFINITION=PERIODIC, TIME=TOTAL
1, -6.283, 0.0, 0.0
0.228449E+00, 0.0
*AMPLITUDE, NAME=LHSV8, DEFINITION=PERIODIC, TIME=TOTAL
1, -6.283, 0.0, 0.0
0.204902E+00, 0.0
*AMPLITUDE, NAME=LHSV8A, DEFINITION=PERIODIC, TIME=TOTAL
1, -6.283, 0.0, 0.0
0.183528E+00, 0.0
*AMPLITUDE, NAME=LHSV9, DEFINITION=PERIODIC, TIME=TOTAL
1, -6.283, 0.0, 0.0
0.164188E+00, 0.0
*AMPLITUDE, NAME=LHSV9A, DEFINITION=PERIODIC, TIME=TOTAL
1, -6.283, 0.0, 0.0
0.146737E+00, 0.0
*AMPLITUDE, NAME=LHSV10, DEFINITION=PERIODIC, TIME=TOTAL
1, -6.283, 0.0, 0.0
0.131026E+00, 0.0
*AMPLITUDE, NAME=LHSV10A, DEFINITION=PERIODIC, TIME=TOTAL
1, -6.283, 0.0, 0.0
0.116909E+00, 0.0
*AMPLITUDE, NAME=LHSV11, DEFINITION=PERIODIC, TIME=TOTAL
1, -6.283, 0.0, 0.0
0.104245E+00, 0.0
*AMPLITUDE, NAME=LHSV11A, DEFINITION=PERIODIC, TIME=TOTAL
1, -6.283, 0.0, 0.0
0.929004E-01, 0.0
*AMPLITUDE, NAME=LHSV12, DEFINITION=PERIODIC, TIME=TOTAL
1, -6.283, 0.0, 0.0
0.827502E-01, 0.0

```

```

*AMPLITUDE, NAME=LHSV12A, DEFINITION=PERIODIC, TIME=TOTAL
1, -6.283, 0.0, 0.0
0.736779E-01, 0.0
*AMPLITUDE, NAME=LHSV13, DEFINITION=PERIODIC, TIME=TOTAL
1, -6.283, 0.0, 0.0
0.655762E-01, 0.0
*AMPLITUDE, NAME=LHSV13A, DEFINITION=PERIODIC, TIME=TOTAL
1, -6.283, 0.0, 0.0
0.583469E-01, 0.0
*AMPLITUDE, NAME=LHSV14, DEFINITION=PERIODIC, TIME=TOTAL
1, -6.283, 0.0, 0.0
0.519003E-01, 0.0
*AMPLITUDE, NAME=LHSV14A, DEFINITION=PERIODIC, TIME=TOTAL
1, -6.283, 0.0, 0.0
0.461550E-01, 0.0
*AMPLITUDE, NAME=LHSV15, DEFINITION=PERIODIC, TIME=TOTAL
1, -6.283, 0.0, 0.0
0.410371E-01, 0.0
*AMPLITUDE, NAME=LHSV15A, DEFINITION=PERIODIC, TIME=TOTAL
1, -6.283, 0.0, 0.0
0.364801E-01, 0.0
*AMPLITUDE, NAME=LHSV16, DEFINITION=PERIODIC, TIME=TOTAL
1, -6.283, 0.0, 0.0
0.324241E-01, 0.0
*AMPLITUDE, NAME=LHSV16A, DEFINITION=PERIODIC, TIME=TOTAL
1, -6.283, 0.0, 0.0
0.288151E-01, 0.0
*AMPLITUDE, NAME=LHSV17, DEFINITION=PERIODIC, TIME=TOTAL
1, -6.283, 0.0, 0.0
0.256047E-01, 0.0
*AMPLITUDE, NAME=LHSV17A, DEFINITION=PERIODIC, TIME=TOTAL
1, -6.283, 0.0, 0.0
0.227497E-01, 0.0
*AMPLITUDE, NAME=LHSV18, DEFINITION=PERIODIC, TIME=TOTAL
1, -6.283, 0.0, 0.0
0.202112E-01, 0.0
*AMPLITUDE, NAME=LHSV18A, DEFINITION=PERIODIC, TIME=TOTAL
1, -6.283, 0.0, 0.0
0.179546E-01, 0.0
*AMPLITUDE, NAME=LHSV19, DEFINITION=PERIODIC, TIME=TOTAL
1, -6.283, 0.0, 0.0
0.159488E-01, 0.0
*AMPLITUDE, NAME=LHSV19A, DEFINITION=PERIODIC, TIME=TOTAL
1, -6.283, 0.0, 0.0
0.141663E-01, 0.0
*AMPLITUDE, NAME=LHSV20, DEFINITION=PERIODIC, TIME=TOTAL
1, -6.283, 0.0, 0.0
0.125823E-01, 0.0
*AMPLITUDE, NAME=LHSV20A, DEFINITION=PERIODIC, TIME=TOTAL
1, -6.283, 0.0, 0.0
0.111749E-01, 0.0
*AMPLITUDE, NAME=LHSV21, DEFINITION=PERIODIC, TIME=TOTAL
1, -6.283, 0.0, 0.0
0.992459E-02, 0.0
*****
*RESTART, WRITE, FREQUENCY=840
*PREPRINT, ECHO=NO, MODEL=NO
*STEP, INC=33600
*DYNAMIC, NOHAF
0.0025, 16.8
*****
***
*** LHS U ***
***
*BOUNDARY, AMPLITUDE=LHSU0
1, 1, , 1.

```

*BOUNDARY,AMPLITUDE=LHSU0A
2,1,,1.
*BOUNDARY,AMPLITUDE=LHSU1
3,1,,1.
*BOUNDARY,AMPLITUDE=LHSU1A
4,1,,1.
*BOUNDARY,AMPLITUDE=LHSU2
5,1,,1.
*BOUNDARY,AMPLITUDE=LHSU2A
6,1,,1.
*BOUNDARY,AMPLITUDE=LHSU3
7,1,,1.
*BOUNDARY,AMPLITUDE=LHSU3A
8,1,,1.
*BOUNDARY,AMPLITUDE=LHSU4
9,1,,1.
*BOUNDARY,AMPLITUDE=LHSU4A
10,1,,1.
*BOUNDARY,AMPLITUDE=LHSU5
11,1,,1.
*BOUNDARY,AMPLITUDE=LHSU5A
12,1,,1.
*BOUNDARY,AMPLITUDE=LHSU6
13,1,,1.
*BOUNDARY,AMPLITUDE=LHSU6A
14,1,,1.
*BOUNDARY,AMPLITUDE=LHSU7
15,1,,1.
*BOUNDARY,AMPLITUDE=LHSU7A
16,1,,1.
*BOUNDARY,AMPLITUDE=LHSU8
17,1,,1.
*BOUNDARY,AMPLITUDE=LHSU8A
18,1,,1.
*BOUNDARY,AMPLITUDE=LHSU9
19,1,,1.
*BOUNDARY,AMPLITUDE=LHSU9A
20,1,,1.
*BOUNDARY,AMPLITUDE=LHSU10
21,1,,1.
*BOUNDARY,AMPLITUDE=LHSU10A
22,1,,1.
*BOUNDARY,AMPLITUDE=LHSU11
23,1,,1.
*BOUNDARY,AMPLITUDE=LHSU11A
24,1,,1.
*BOUNDARY,AMPLITUDE=LHSU12
25,1,,1.
*BOUNDARY,AMPLITUDE=LHSU12A
26,1,,1.
*BOUNDARY,AMPLITUDE=LHSU13
27,1,,1.
*BOUNDARY,AMPLITUDE=LHSU13A
28,1,,1.
*BOUNDARY,AMPLITUDE=LHSU14
29,1,,1.
*BOUNDARY,AMPLITUDE=LHSU14A
30,1,,1.
*BOUNDARY,AMPLITUDE=LHSU15
31,1,,1.
*BOUNDARY,AMPLITUDE=LHSU15A
32,1,,1.
*BOUNDARY,AMPLITUDE=LHSU16
33,1,,1.
*BOUNDARY,AMPLITUDE=LHSU16A
34,1,,1.

*BOUNDARY,AMPLITUDE=LHSU17
35,1,,1.
*BOUNDARY,AMPLITUDE=LHSU17A
36,1,,1.
*BOUNDARY,AMPLITUDE=LHSU18
37,1,,1.
*BOUNDARY,AMPLITUDE=LHSU18A
38,1,,1.
*BOUNDARY,AMPLITUDE=LHSU19
39,1,,1.
*BOUNDARY,AMPLITUDE=LHSU19A
40,1,,1.
*BOUNDARY,AMPLITUDE=LHSU20
41,1,,1.
*BOUNDARY,AMPLITUDE=LHSU20A
42,1,,1.

*** LHS V ***

*BOUNDARY,AMPLITUDE=LHSV0
1,2,,1.
*BOUNDARY,AMPLITUDE=LHSV0A
2,2,,1.
*BOUNDARY,AMPLITUDE=LHSV1
3,2,,1.
*BOUNDARY,AMPLITUDE=LHSV1A
4,2,,1.
*BOUNDARY,AMPLITUDE=LHSV2
5,2,,1.
*BOUNDARY,AMPLITUDE=LHSV2A
6,2,,1.
*BOUNDARY,AMPLITUDE=LHSV3
7,2,,1.
*BOUNDARY,AMPLITUDE=LHSV3A
8,2,,1.
*BOUNDARY,AMPLITUDE=LHSV4
9,2,,1.
*BOUNDARY,AMPLITUDE=LHSV4A
10,2,,1.
*BOUNDARY,AMPLITUDE=LHSV5
11,2,,1.
*BOUNDARY,AMPLITUDE=LHSV5A
12,2,,1.
*BOUNDARY,AMPLITUDE=LHSV6
13,2,,1.
*BOUNDARY,AMPLITUDE=LHSV6A
14,2,,1.
*BOUNDARY,AMPLITUDE=LHSV7
15,2,,1.
*BOUNDARY,AMPLITUDE=LHSV7A
16,2,,1.
*BOUNDARY,AMPLITUDE=LHSV8
17,2,,1.
*BOUNDARY,AMPLITUDE=LHSV8A
18,2,,1.
*BOUNDARY,AMPLITUDE=LHSV9
19,2,,1.
*BOUNDARY,AMPLITUDE=LHSV9A
20,2,,1.
*BOUNDARY,AMPLITUDE=LHSV10
21,2,,1.
*BOUNDARY,AMPLITUDE=LHSV10A
22,2,,1.
*BOUNDARY,AMPLITUDE=LHSV11
23,2,,1.
*BOUNDARY,AMPLITUDE=LHSV11A

```

24,2,,1.
*BOUNDARY,AMPLITUDE=LHSV12
25,2,,1.
*BOUNDARY,AMPLITUDE=LHSV12A
26,2,,1.
*BOUNDARY,AMPLITUDE=LHSV13
27,2,,1.
*BOUNDARY,AMPLITUDE=LHSV13A
28,2,,1.
*BOUNDARY,AMPLITUDE=LHSV14
29,2,,1.
*BOUNDARY,AMPLITUDE=LHSV14A
30,2,,1.
*BOUNDARY,AMPLITUDE=LHSV15
31,2,,1.
*BOUNDARY,AMPLITUDE=LHSV15A
32,2,,1.
*BOUNDARY,AMPLITUDE=LHSV16
33,2,,1.
*BOUNDARY,AMPLITUDE=LHSV16A
34,2,,1.
*BOUNDARY,AMPLITUDE=LHSV17
35,2,,1.
*BOUNDARY,AMPLITUDE=LHSV17A
36,2,,1.
*BOUNDARY,AMPLITUDE=LHSV18
37,2,,1.
*BOUNDARY,AMPLITUDE=LHSV18A
38,2,,1.
*BOUNDARY,AMPLITUDE=LHSV19
39,2,,1.
*BOUNDARY,AMPLITUDE=LHSV19A
40,2,,1.
*BOUNDARY,AMPLITUDE=LHSV20
41,2,,1.
*BOUNDARY,AMPLITUDE=LHSV20A
42,2,,1.
***
*** BOT ***
***
*BOUNDARY
BOT,1
BOT,2
*****
*EL PRINT,FREQUENCY=0
*ENERGY PRINT,FREQ=0
*NODE PRINT,FREQ=0
*NODE PRINT,NSET=RHS,FREQ=840
U,V
*END STEP

```

```

SUBROUTINE UEL(RHS,AMATRX,SVARS,ENERGY,NDOFEL,NRHS,NSVARS,PROPS,
1 NPROPS,COORDS,MCRD,NNODE,U,DU,V,A,JTYPE,TIME,DTIME,KSTEP,KINC,
2 JELEM,PARAMS,NDLOAD,JDLTYP,ADLMAG,PREFDEF,NPREDF,LFLAGS,
3 MLVARX,DDL MAG,MDLOAD,PNEWDT,JPROPS,NJPROP,PERIOD)

```

```

C
INCLUDE 'ABA_PARAM.INC'

```

```

C
DOUBLE PRECISION CONST1,CONST2,CP,DP,CS,DS,ALEN,HFALEN,
1 STRESS,ENDALEN,ALENMID,CONSTN,S,DG,F,AKY,BKY,DF,G

```

```

C
DIMENSION RHS(MLVARX,*),AMATRX(NDOFEL,NDOFEL),SVARS(NSVARS),
1 ENERGY(8),PROPS(*),COORDS(MCRD,NNODE),
2 U(NDOFEL),DU(MLVARX,*),V(NDOFEL),A(NDOFEL),TIME(2),
3 PARAMS(3),JDLTYP(MDLOAD,*),ADLMAG(MDLOAD,*),
4 DDL MAG(MDLOAD,*),PREFDEF(2,NPREDF,NNODE),LFLAGS(*),JPROPS(*)
DIMENSION SRESID(9)
DIMENSION STRESS(9)
DIMENSION DG(3)
DIMENSION F(3)
DIMENSION AKY(3)
DIMENSION DF(3)
DIMENSION G(3)
DIMENSION BKY(3)

```

```

C
C SRESID - stores the static residual at time t+dt
C SVARS - In 1-6, contains the static residual at time t upon
C entering the routine. SRESID is copied to SVARS(1-6)
C after the dynamic residual has been calculated.
C - For half-step residual calculations: In 7-12, contains
C the static residual at the beginning of the previous
C increment. SVARS(1-6) are copied into SVARS(7-12) after
C the dynamic residual has been calculated.
C

```

```

C
AREA= PROPS(1)
E = PROPS(2)
ANU = PROPS(3)
RHO = PROPS(4)

```

```

C
C Calculate wave speed of P-wave
C

```

```

CONST1 = (E*ANU)/((1.0+ANU)*(1.0-(ANU+ANU)))
CONST2 = E/((1.0+ANU)+(1.0+ANU))
CP = ((CONST1+(CONST2+CONST2))/RHO)**0.5
DP = RHO*CP

```

```

C
C Calculate wave speed of S-wave
C

```

```

CS = (CONST2/RHO)**0.5
DS = RHO*CS

```

```

C
ALEN = COORDS(2,1) - COORDS(2,3)

```

```

C
C Calculate A(KY)
C

```

```

CONSTN = 1.08766D0
S = SQRT((1-(ANU+ANU))/((1.0-ANU)+(1.0-ANU)))

```

```

C
DO 11 K1=1,3
      DG(K1) = (-0.718256D0*EXP(0.8475D0*0.034153D0
1      *COORDS(2,K1)))+(0.577325D0*EXP(0.3933D0*0.034153D0
2      *COORDS(2,K1)))
11 CONTINUE

```

```

C
DO 12 K1=1,3
      F(K1) = (EXP(0.8475D0*0.0341563D0*COORDS(2,K1)))
1      - (0.5773D0*EXP(0.3933D0*0.034153D0*COORDS(2,K1)))

```

```

12 CONTINUE
C
DO 13 K1=1,3
    AKY(K1) = (CONSTN/S)*(1.0 + ((1.0 - ((S*S)+(S*S)))
1        *(DG(K1)/F(K1))))
13 CONTINUE
C
C    IF (AKY(1) .GE. 3.0 .OR. AKY(1) .LE. -1.0) THEN
C        U(1) = 0.0D0
C    ELSE
C        CONTINUE
C    ENDIF
C
C    IF (AKY(2) .GE. 3.0 .OR. AKY(2) .LE. -1.0) THEN
C        U(4) = 0.0D0
C    ELSE
C        CONTINUE
C    ENDIF
C
C    IF (AKY(3) .GE. 3.0 .OR. AKY(3) .LE. -1.0) THEN
C        U(7) = 0.0D0
C    ELSE
C        CONTINUE
C    ENDIF
C
*****
C
C
C    Calculate B(KY)
C
DO 21 K1=1,3
    DF(K1) = (0.8475D0*EXP(0.8475D0*0.034153D0
1        *COORDS(2,K1))) - (0.227052D0*EXP(0.3933D0*0.034153D0
2        *COORDS(2,K1)))
21 CONTINUE
C
DO 22 K1=1,3
    G(K1) = (-0.8475D0*EXP(0.8475D0*0.034153D0
1        *COORDS(2,K1))) + (1.4679D0*EXP(0.3933D0*0.034153D0
2        *COORDS(2,K1)))
22 CONTINUE
C
DO 23 K1=1,3
    BKY(K1) = CONSTN * (1.0 - (DF(K1)/G(K1)))
23 CONTINUE
C
C
DO 6 K1=1,NDOFEL
    SRESID(K1) = 0.0D0
DO 2 KRHS=1,NRHS
    RHS(K1,KRHS) = 0.0D0
2 CONTINUE
DO 4 K2=1,NDOFEL
    AMATRX(K2,K1)=0.0D0
4 CONTINUE
6 CONTINUE
C
DO 8 K1=1,NDOFEL
    STRESS(K1) = 0.0D0
8 CONTINUE
*****
IF (LFLAGS(3).EQ.1) THEN
C    Normal incrementation
    IF (LFLAGS(1).EQ.11 .OR. LFLAGS(1).EQ.12) THEN
C        *DYNAMIC
        ALPHA = PARAMS(1)

```

```

      BETA = PARAMS(2)
      GAMMA = PARAMS(3)

C
C
C   Calculate stresses by multiplying V(1),V(4),V(7) by DP and AKY
C   and V(2),V(5) and V(8) by DS
C
C
C
      IF (AKY(1) .GE. 3.0 .OR. AKY(1) .LE. -1.0) THEN
        U(1) = 0.0D0
        STRESS(1) = V(1) * DP
      ELSE
        STRESS(1) = V(1) * DP * AKY(1)
      ENDIF

C
      IF (AKY(2) .GE. 3.0 .OR. AKY(2) .LE. -1.0) THEN
        U(4) = 0.0D0
        STRESS(4) = V(4) * DP
      ELSE
        STRESS(4) = V(4) * DP * AKY(2)
      ENDIF

C
      IF (AKY(3) .GE. 3.0 .OR. AKY(3) .LE. -1.0) THEN
        U(7) = 0.0D0
        STRESS(7) = V(7) * DP
      ELSE
        STRESS(7) = V(7) * DP * AKY(3)
      ENDIF

C
C
      DO 15 K1 = 2,8,3
        STRESS(K1) = V(K1) * DS
15 CONTINUE

C
      STRESS(2) = STRESS(2) * BKY(1)
      STRESS(5) = STRESS(5) * BKY(2)
      STRESS(8) = STRESS(8) * BKY(3)

C
C
C   Calculate forces at nodes by multiplying {STRESS}
C   by L/6*AREA for end nodes and 2L/3*AREA for midside node
C
      ENDALEN = AREA*(ALEN/6.0)
      ALENMID = AREA*((ALEN+ALEN)/3.0)

C
C   Multiply end node terms in {STRESS} by -ENDALEN
C
      DO 20 K1 = 1,3,1
        RHS(K1,1) = -STRESS(K1) * ENDALEN
20 CONTINUE
      DO 30 K1 = 7,9,1
        RHS(K1,1) = -STRESS(K1) * ENDALEN
30 CONTINUE

C
C   Multiply midside node terms in {STRESS} by -ALENMID
C
      DO 40 K1 = 4,6,1
        RHS(K1,1) = -STRESS(K1) * ALENMID
40 CONTINUE

C
C
      END IF
      *****
      END IF
      RETURN

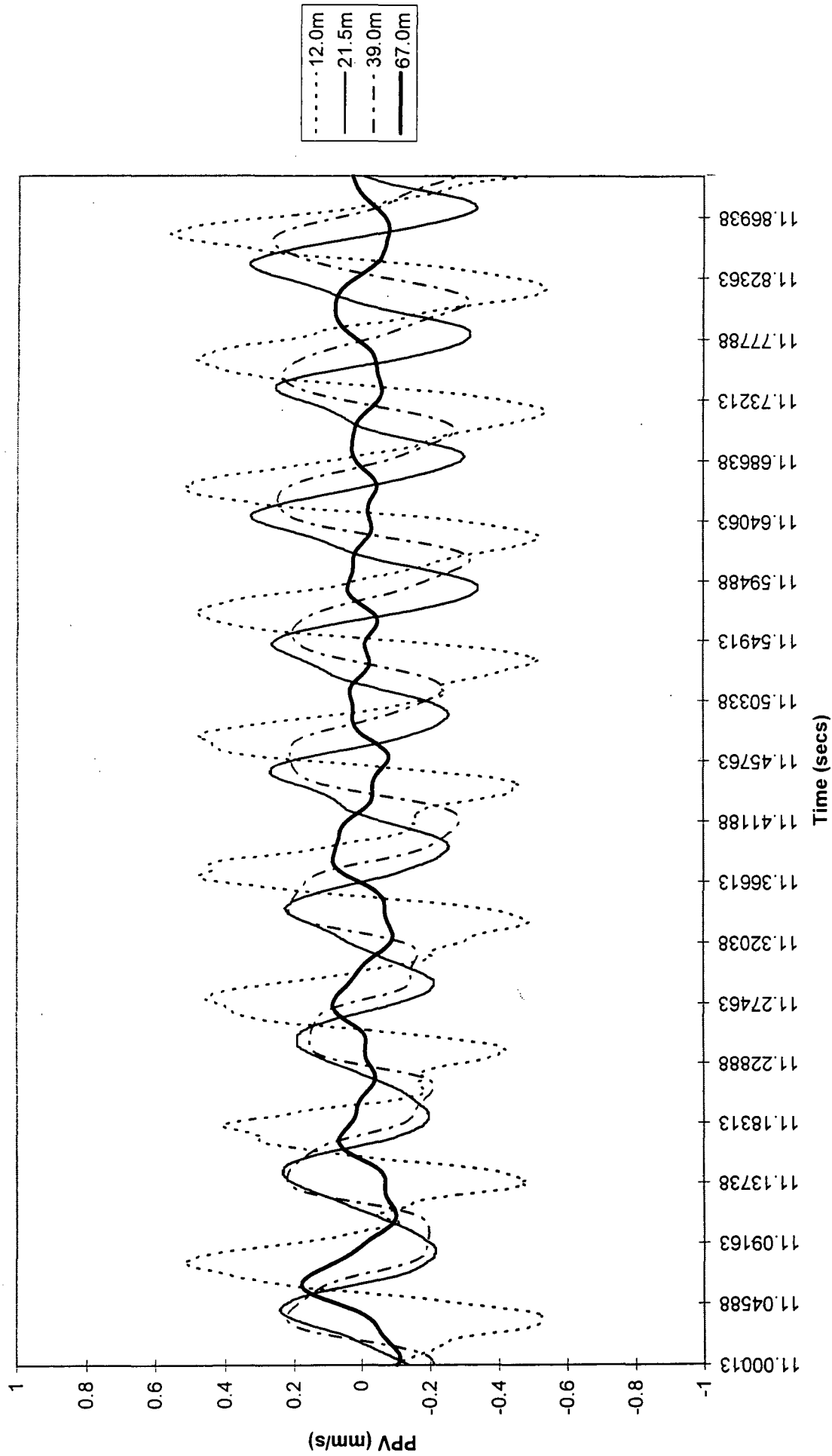
```


END

APPENDIX E

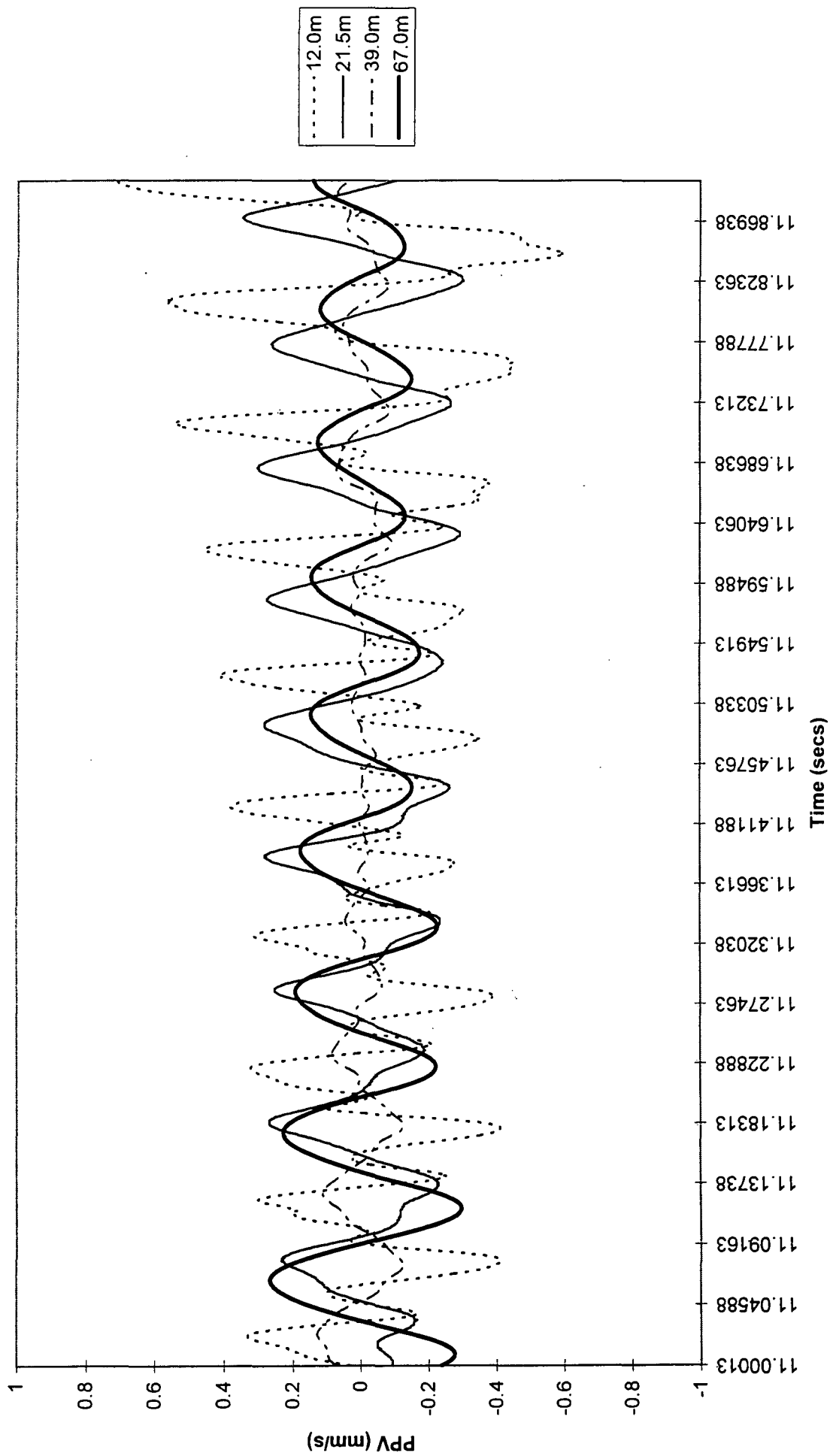
Velocity/time traces recorded during vibratory piling

SSCA8a
Vertical PPV's



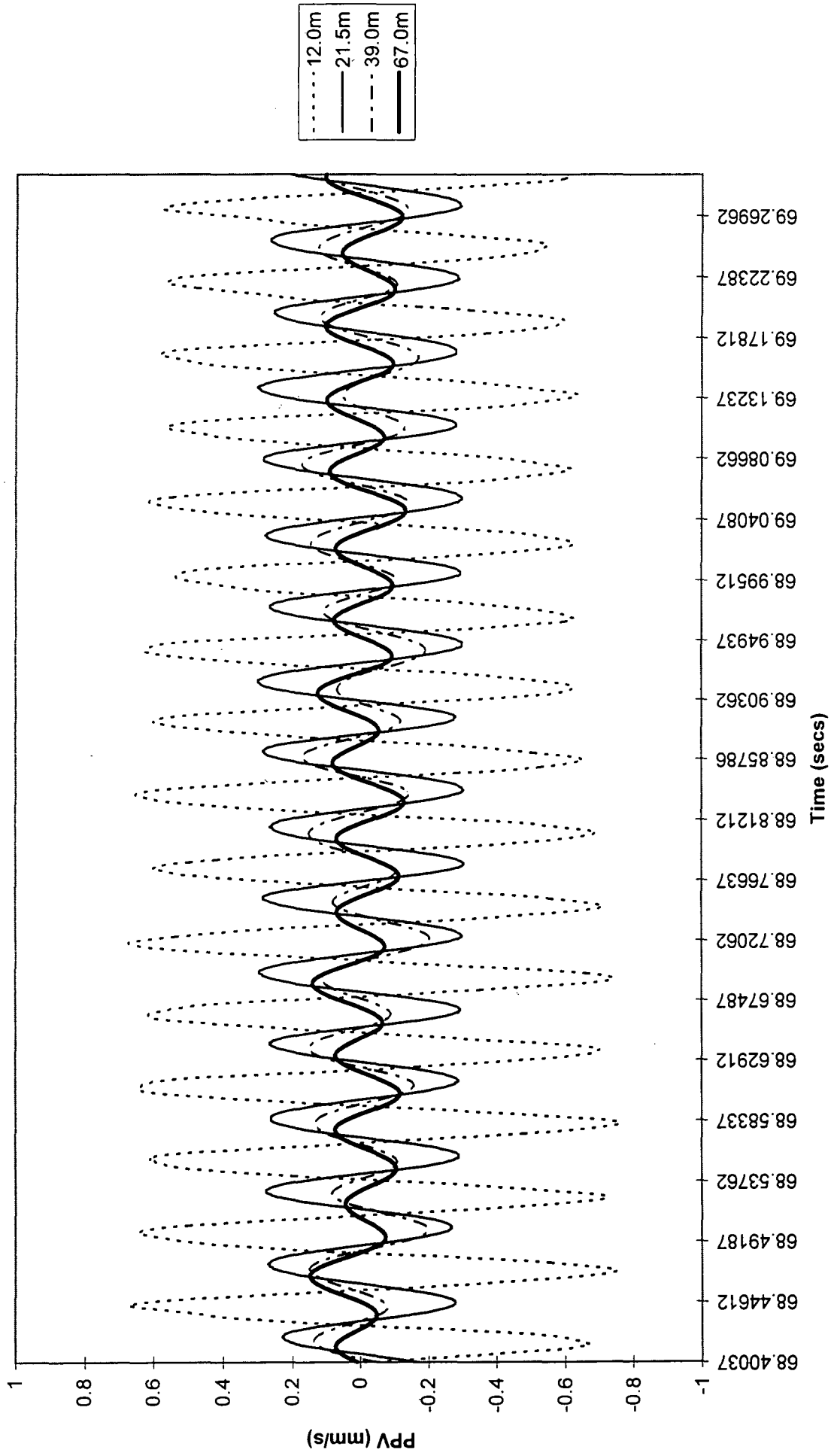
Extraction of a casing (toe at 15m). Vertical velocity/time traces. (SSC site)

SSCA8a
Radial PPV's



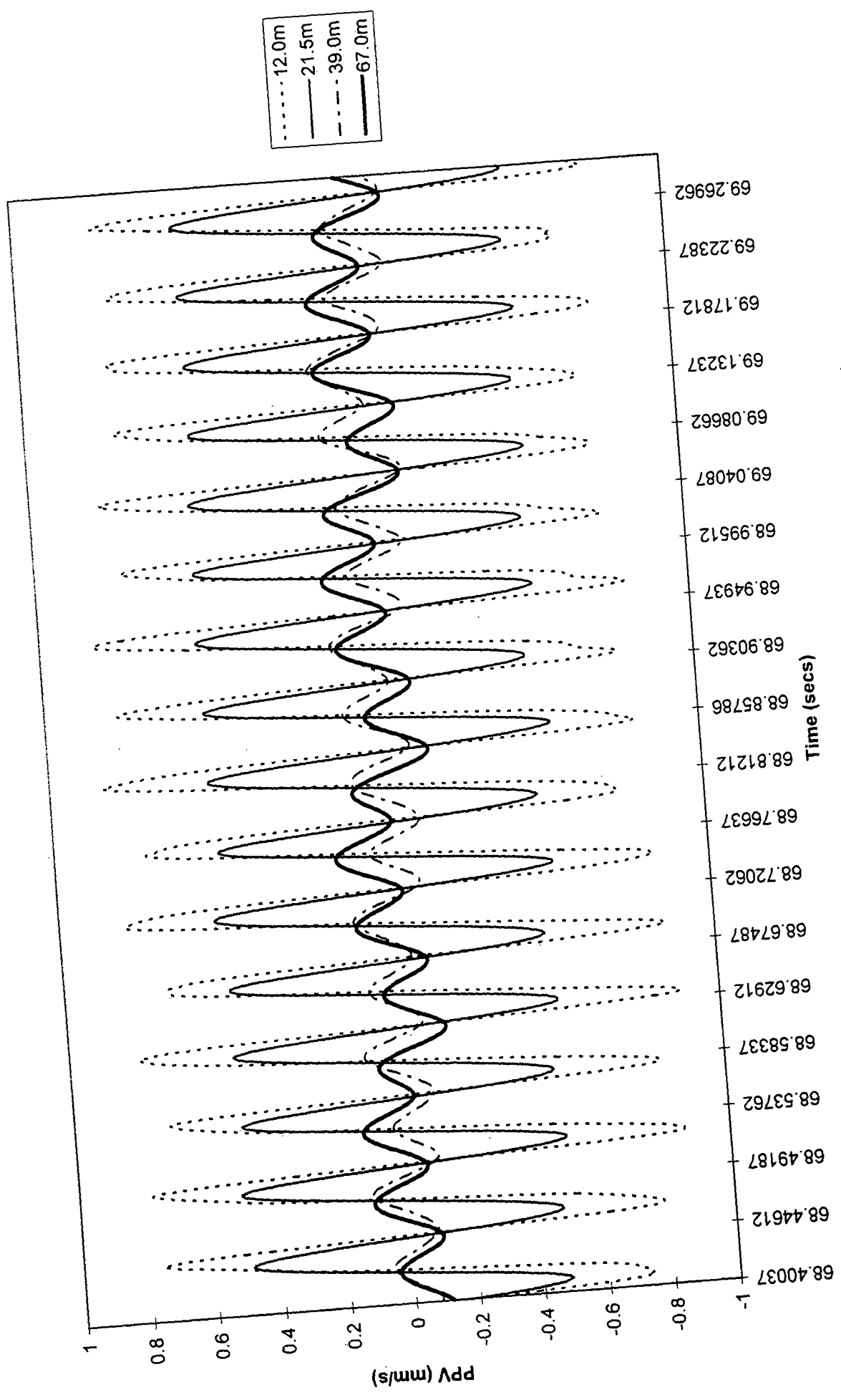
Extraction of a casing (toe at 15m). Radial velocity/time traces. (SSC site)

SSCA8i
Vertical PPV's



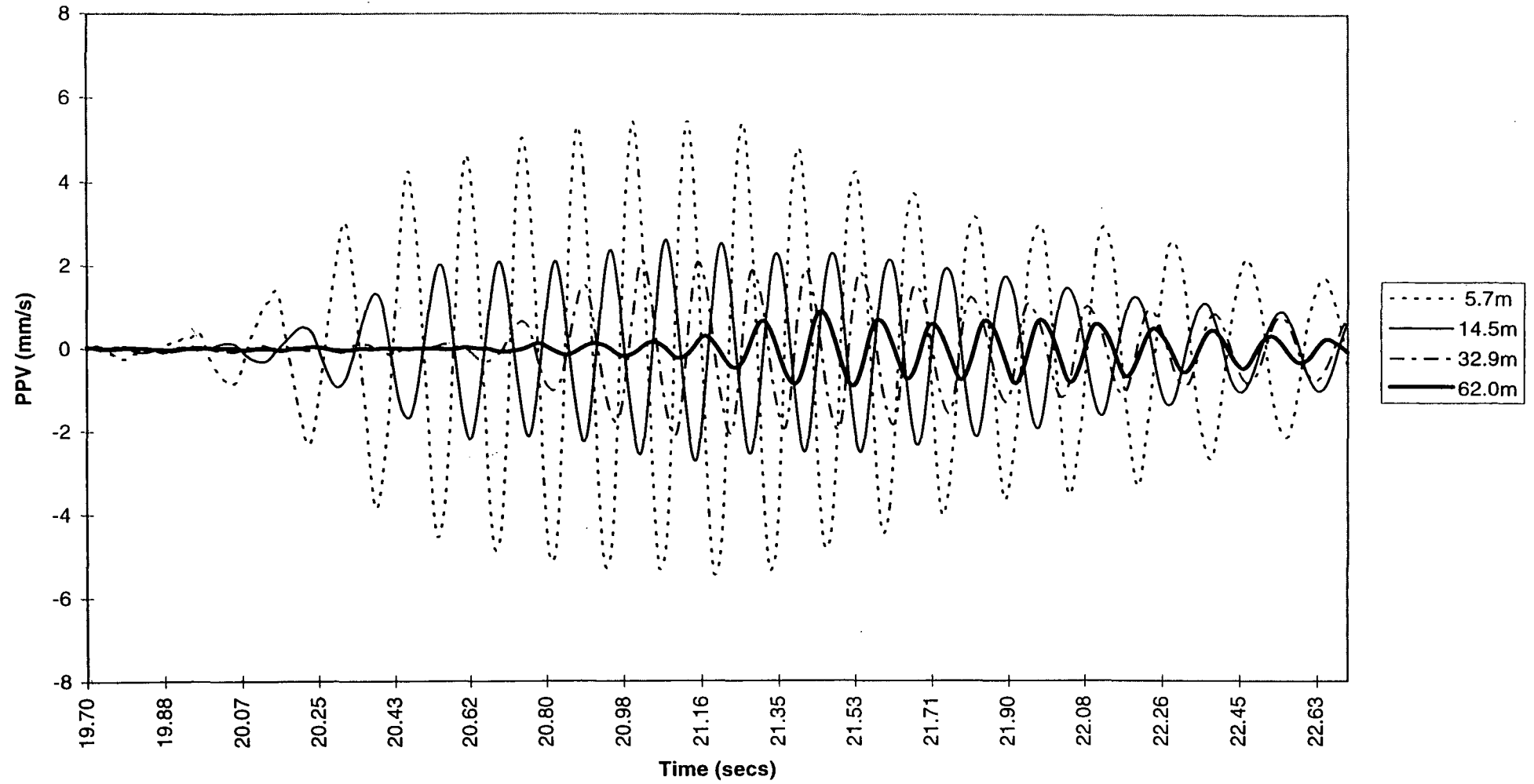
Extraction of a casing (toe at 6.2m). Vertical velocity/time traces. (SSC site)

SSCA8i
Radial PPV's

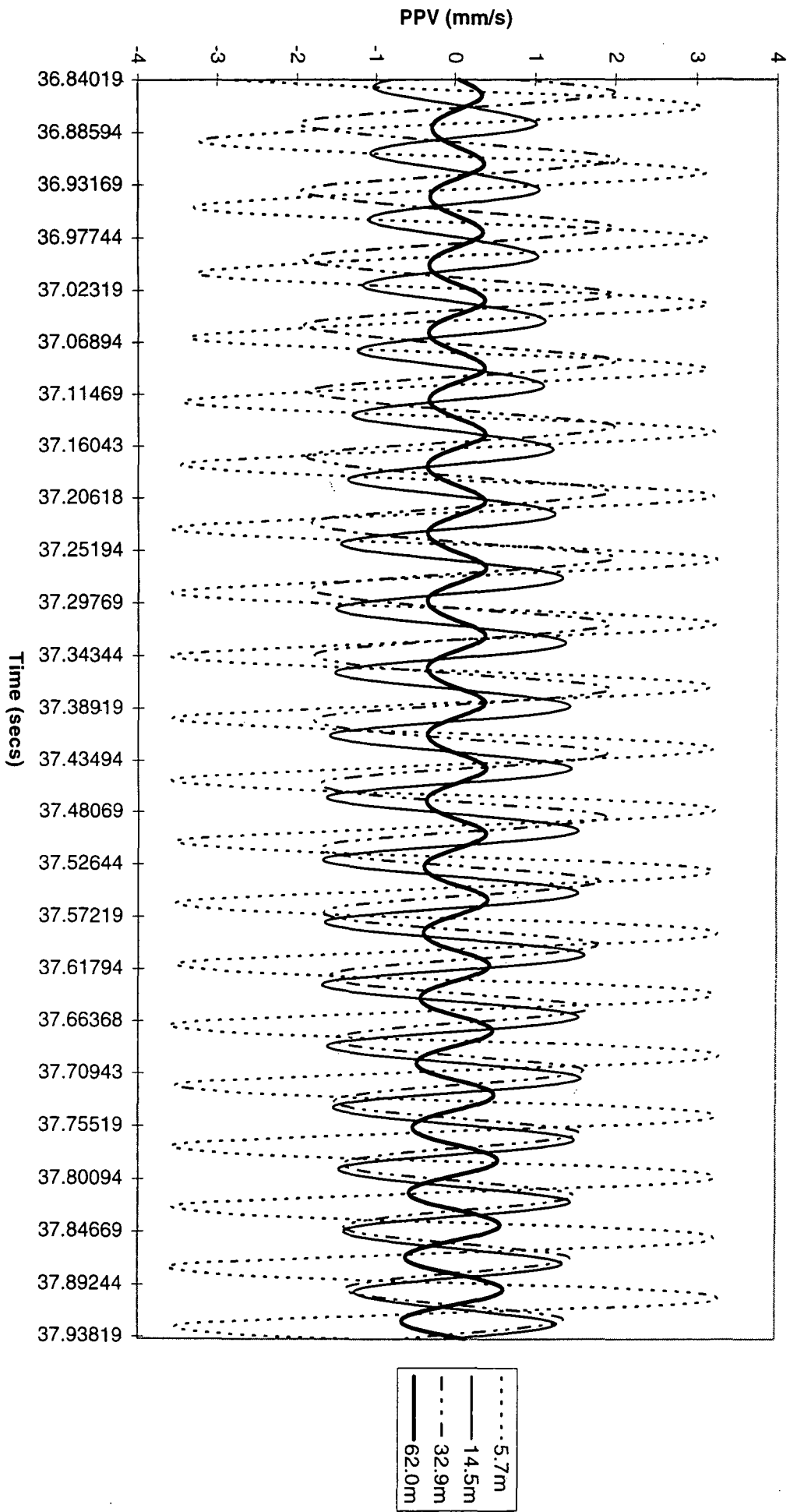


Extraction of a casing (toe at 6.2m). Radial velocity/time traces. (SSC site)

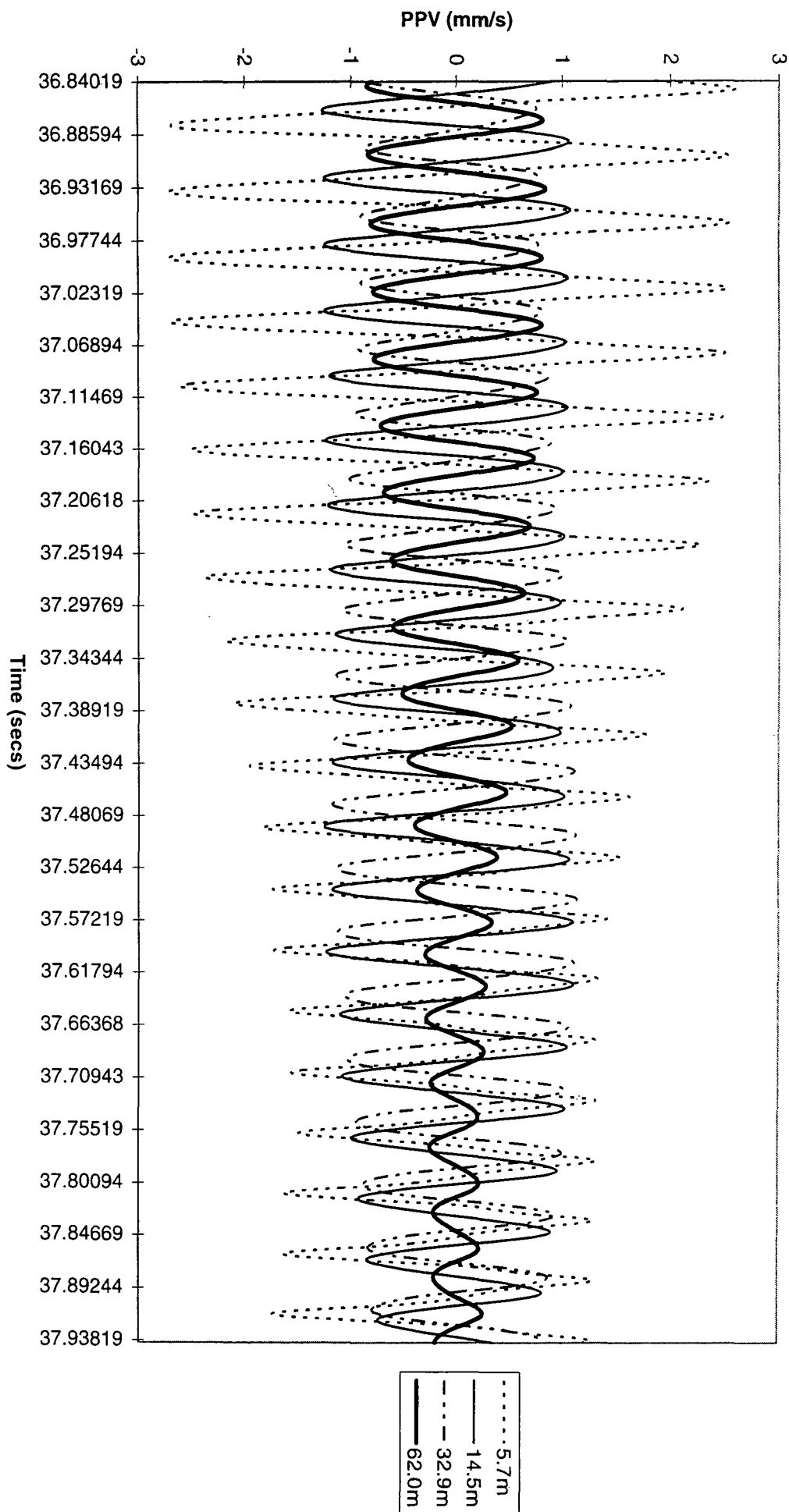
SSC A9a
Vertical PPV's



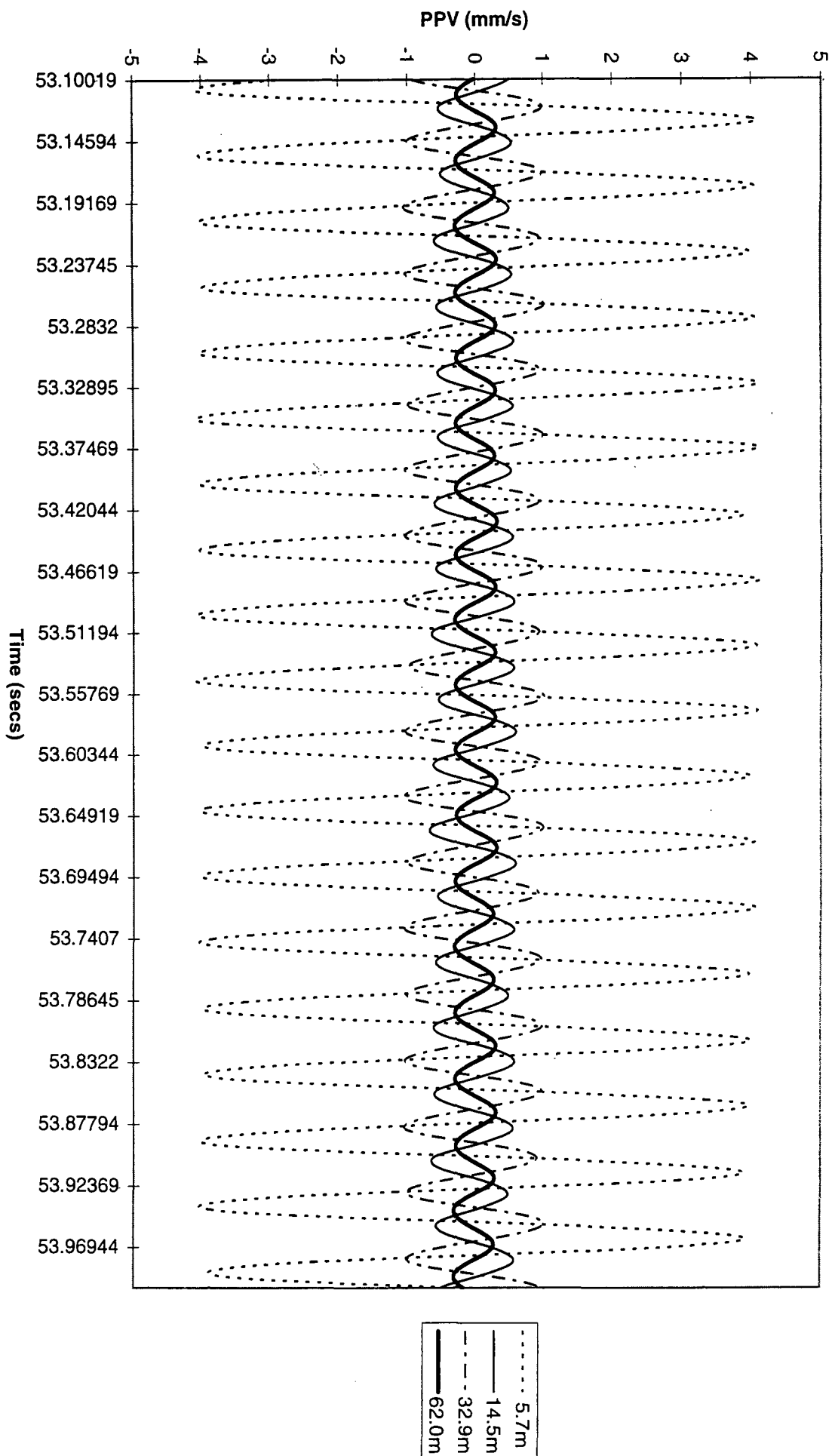
Installation of a casing (toe at 6m). Vertical velocity/time traces. (SSC site)



Installation of a casing (toe at 8m). Vertical velocity/time traces. (SSC site)

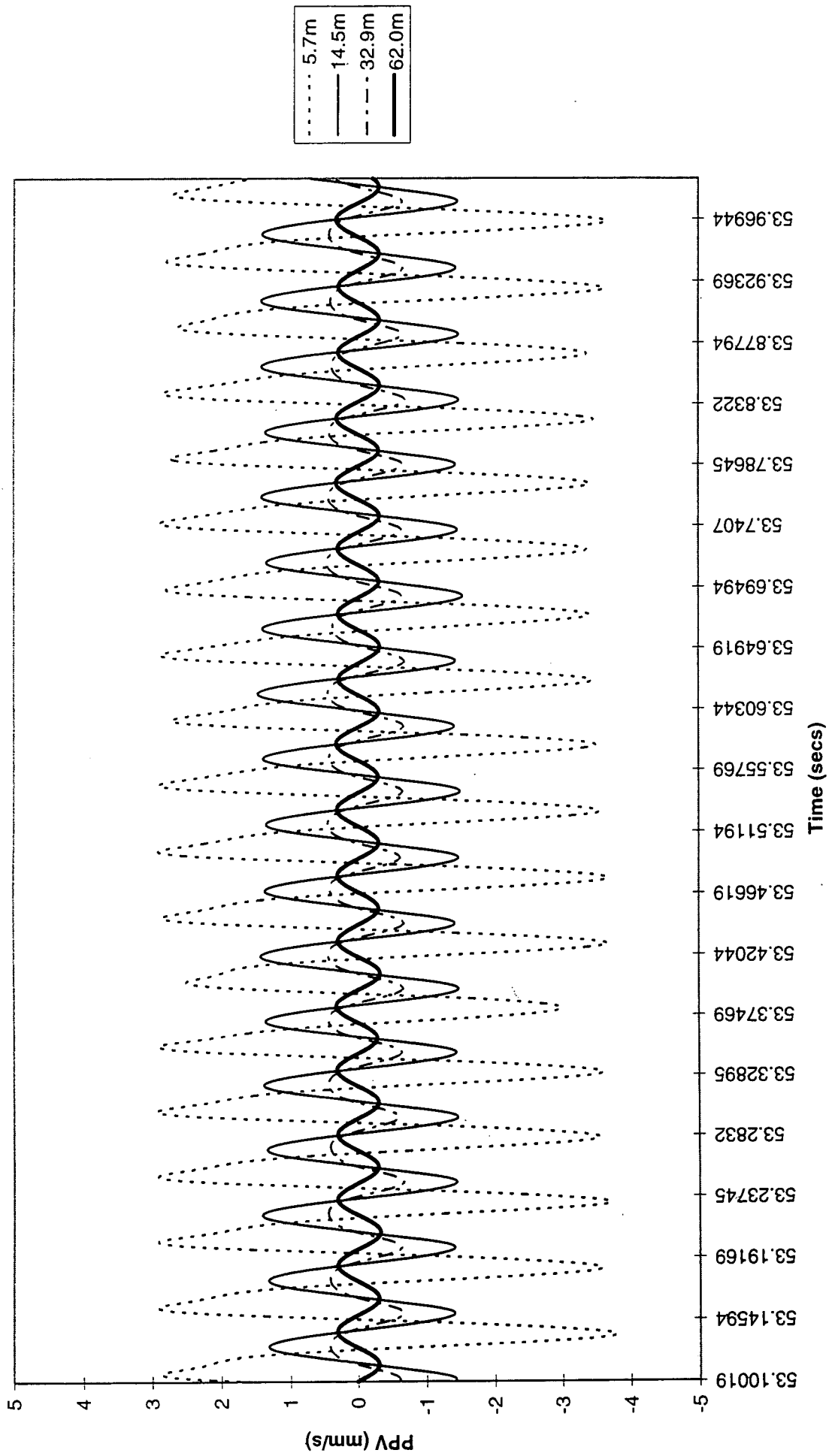


Installation of a casing (toe at 8m). Radial velocity/time traces. (SSC site)

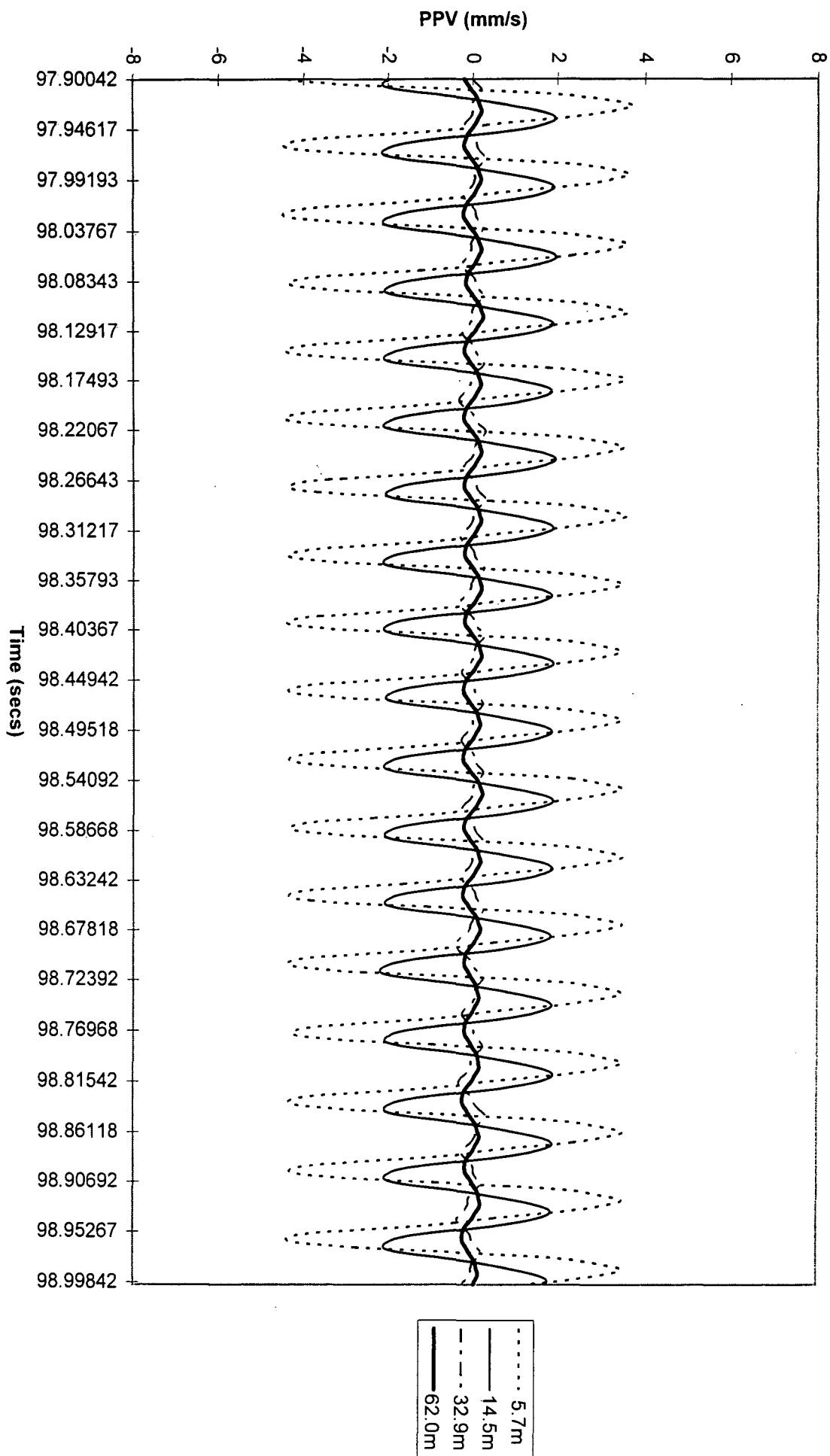


Installation of a casing (toe at 9.8m). Vertical velocity/time traces. (SSC site)

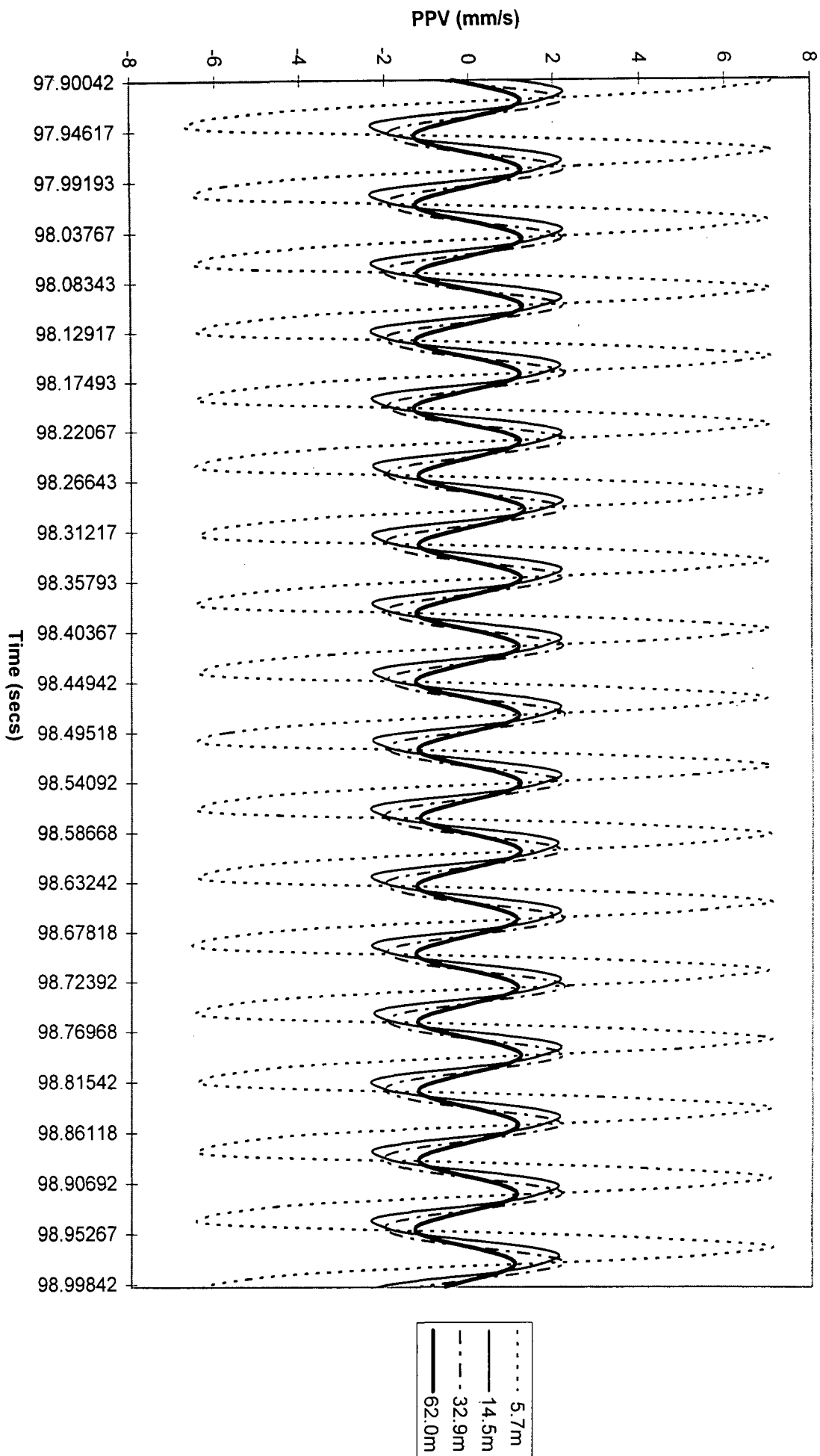
SSCA9e
Radial PPV's



Installation of a casing (toe at 9.8m). Radial velocity/time traces. (SSC site)



Installation of a casing (toe at 14.8m). Vertical velocity/time traces. (SSC site)



Installation of a casing (toe at 14.8m). Radial velocity/time traces. (SSC site)

```

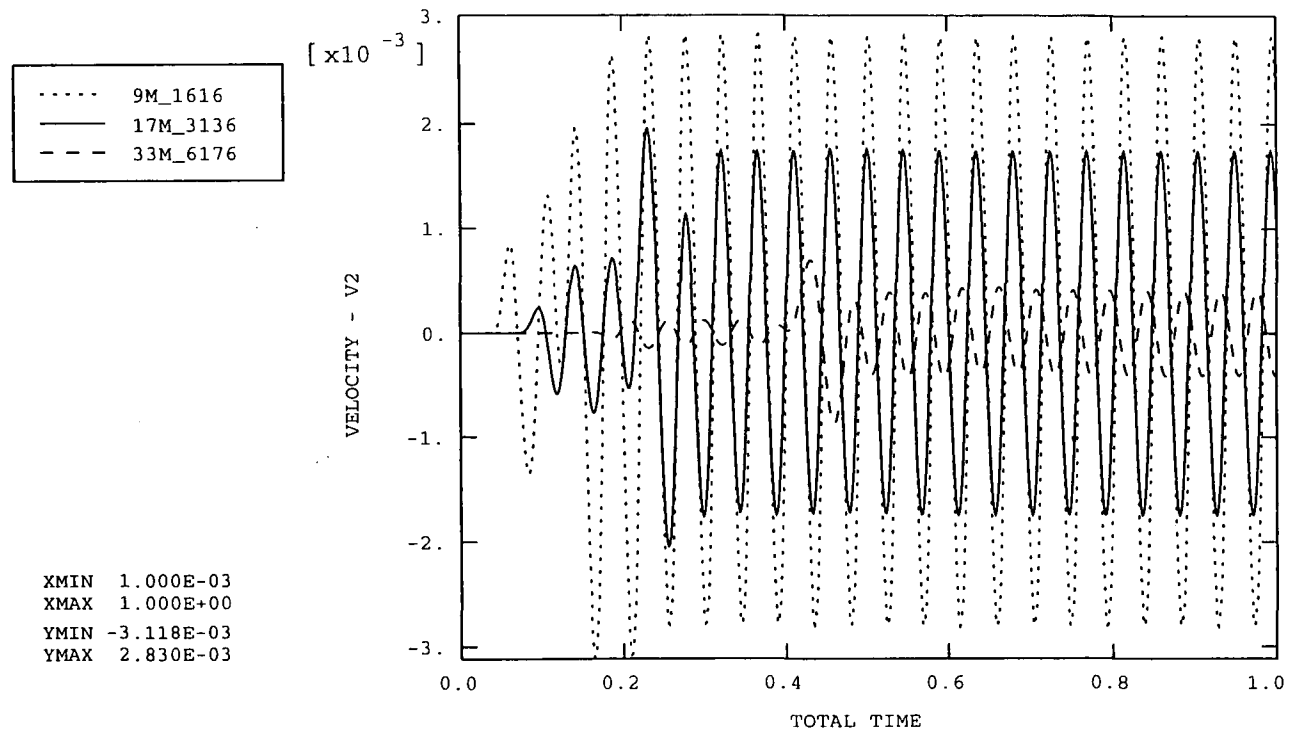
PROGRAM DISP2VIB
*
*   Program to calculate data lines for vibro analysis
*   from vertical displacements on soil-pile interface
*
REAL MAX(100),MIN(100),A0(100),
1  AMP(100),T0(100),TMAX(100),TREF
INTEGER NUM
*
OPEN (UNIT=4, FILE='max.dat')
OPEN (UNIT=5, FILE='min.dat')
OPEN (UNIT=6, FILE='a0.r')
OPEN (UNIT=7, FILE='amp.r')
OPEN (UNIT=8, FILE='tmax.dat')
*
* Insert number of nodes on pile-soil interface (NUM)
NUM = 33
* Insert value of tmax for ref node (99001)
TREF=11.289
*
*
DO 20 I=1,NUM
READ (4,10) MAX(I)
10  FORMAT (E12.4)
READ (5,25) MIN(I)
25  FORMAT (E12.4)
READ (8,30) TMAX(I)
30  FORMAT (F6.3)
A0(I) = 0.0
A0(I) = (MAX(I) + MIN(I))/2.0
T0(I) = TMAX(I) - TREF
* Writes out Fourier constants n,w,t0,a0 *
* (w=2*PI*f)
WRITE (6,35),
1  '1,120.01,',T0(I),',',A0(I)
35  FORMAT (/A,F6.3,A,E12.4/)
AMP(I) = 0.0
AMP(I) = (MAX(I) - MIN(I))/2.0
WRITE (7,45),',2,',AMP(I)
45  FORMAT (/A,E12.4)
20  CONTINUE
*
STOP
END

```

APPENDIX G

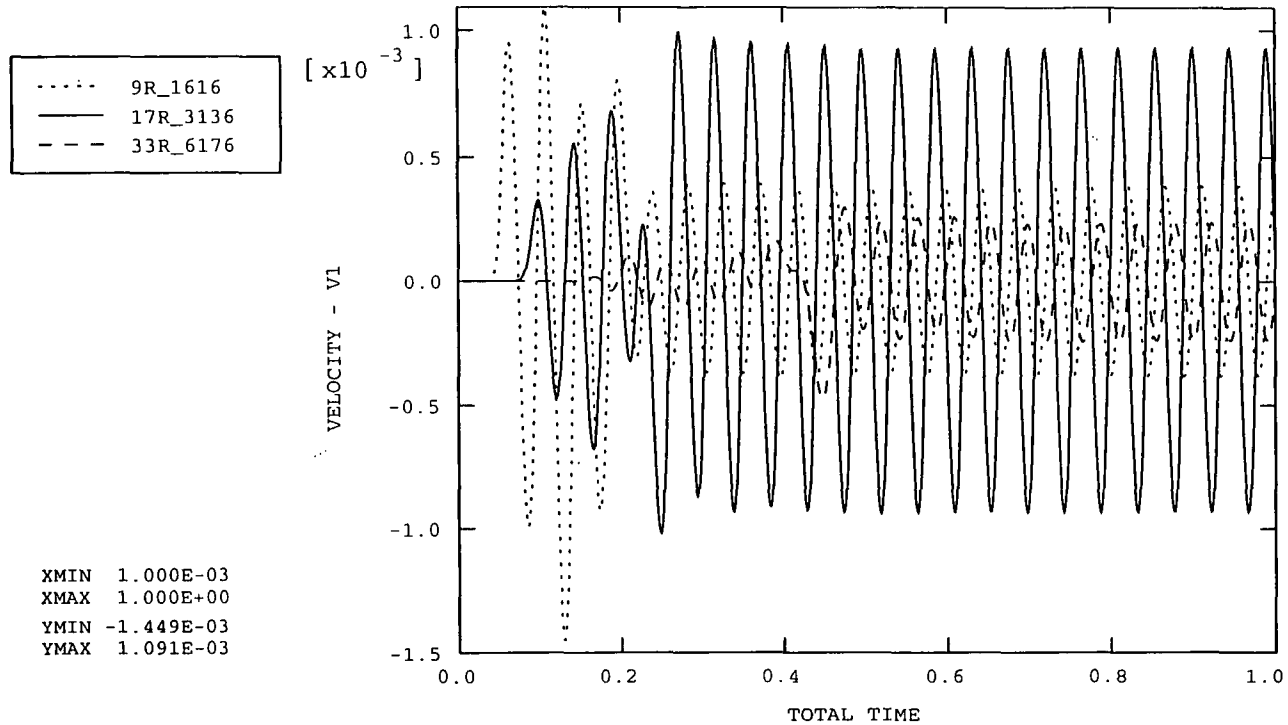
**Parametric study of the effect of soil stiffness parameters on the ground response
resulting from extraction of a casing from 13.8m depth at the Second Severn
Crossing site**

ABAQUS



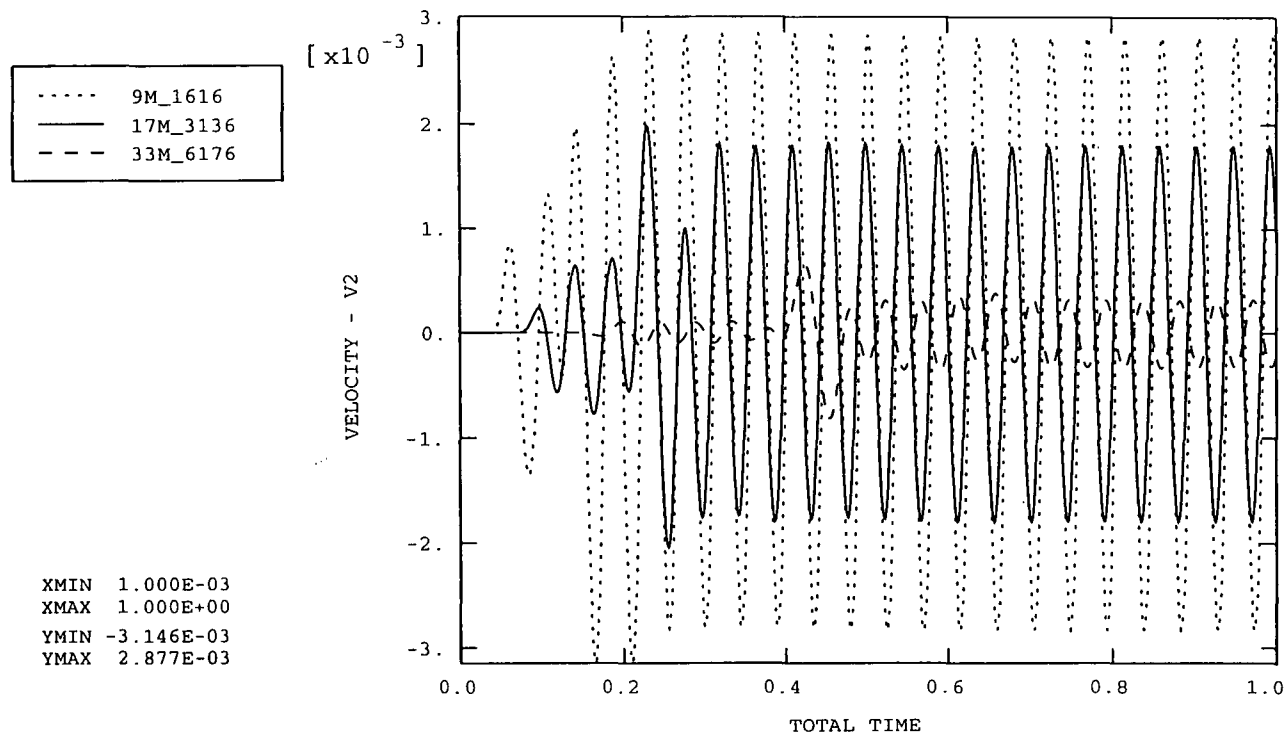
Vertical velocity/time traces assuming $E_{\text{alluvium}} = 30\text{MPa}$ and $E_{\text{marl}} = 50\text{MPa}$

ABAQUS



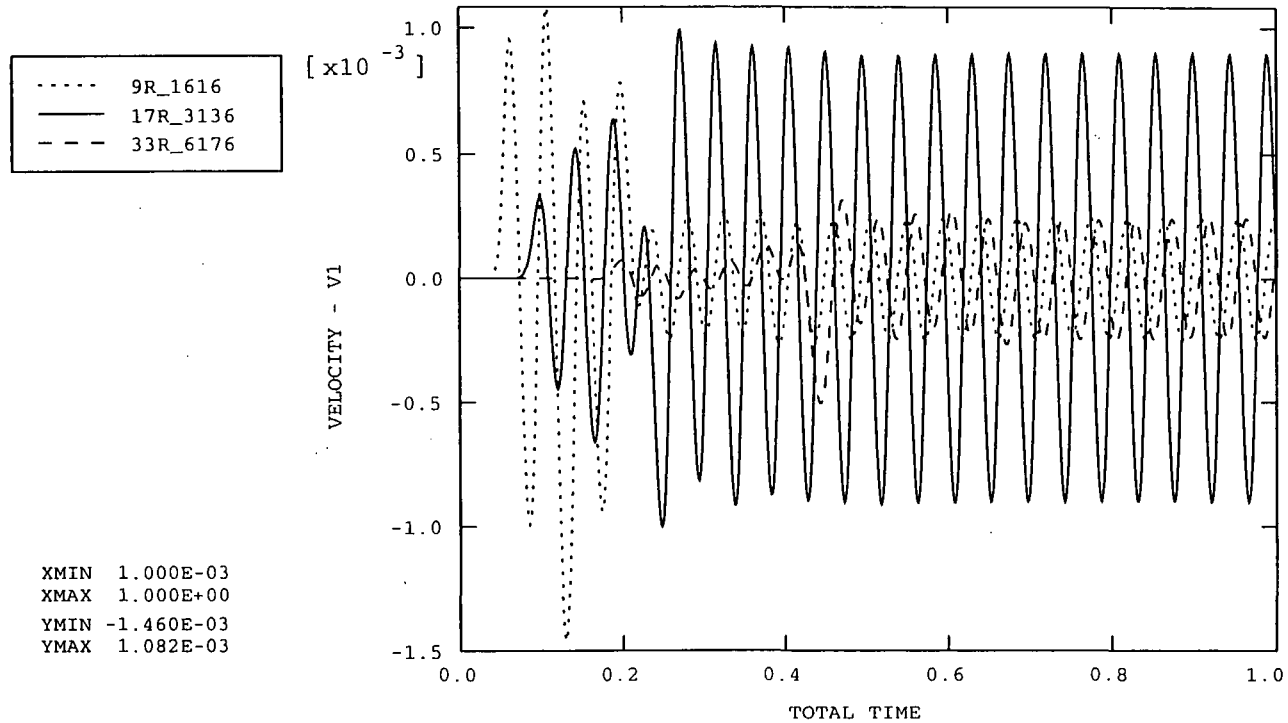
Radial velocity/time traces assuming $E_{\text{alluvium}} = 30\text{MPa}$ and $E_{\text{marl}} = 50\text{MPa}$

ABAQUS



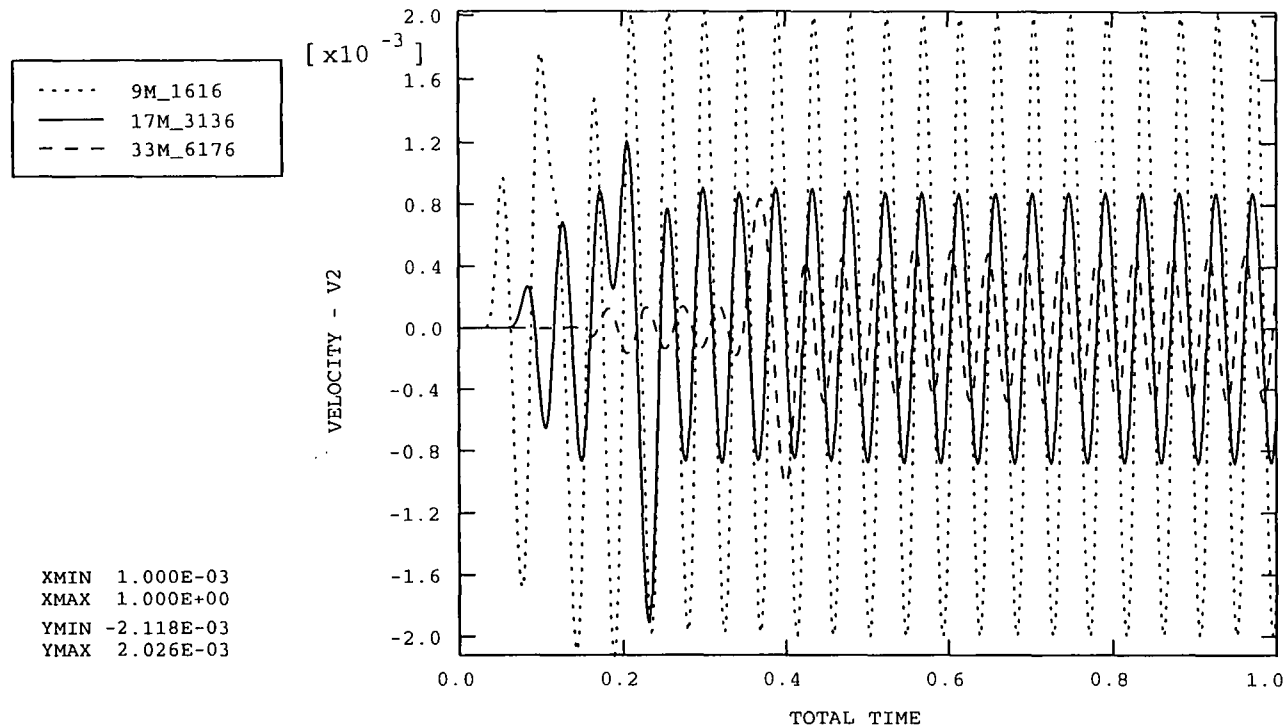
Vertical velocity/time traces assuming $E_{\text{alluvium}} = 30\text{MPa}$ and $E_{\text{marl}} = 70\text{MPa}$

ABAQUS



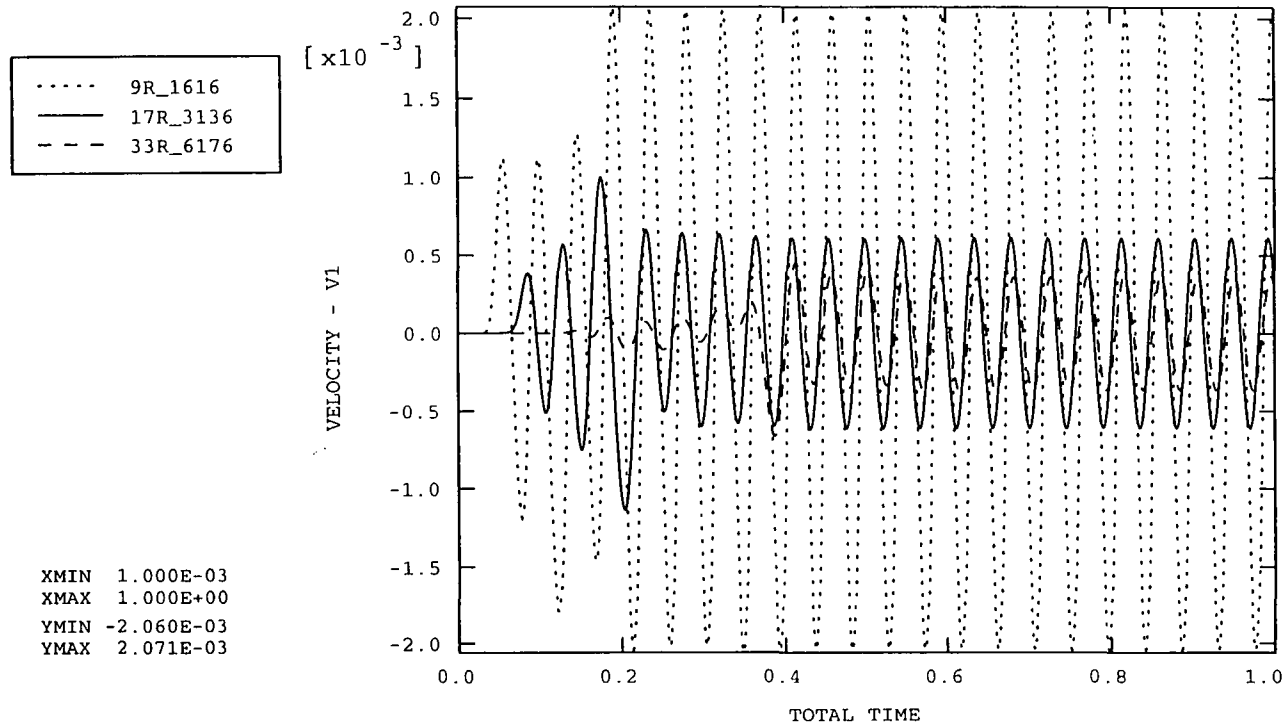
Radial velocity/time traces assuming $E_{\text{alluvium}} = 30\text{MPa}$ and $E_{\text{marl}} = 70\text{MPa}$

ABAQUS



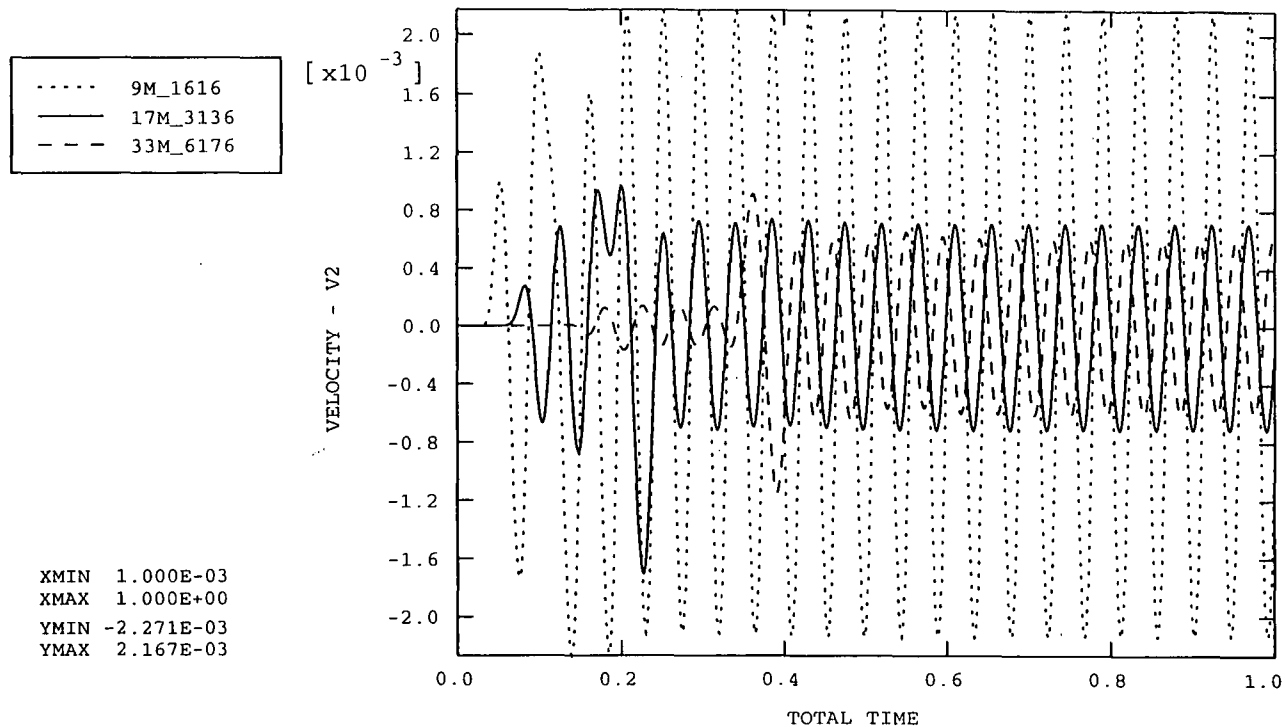
Vertical velocity/time traces assuming $E_{\text{alluvium}} = 40\text{MPa}$ and $E_{\text{marl}} = 70\text{MPa}$

ABAQUS



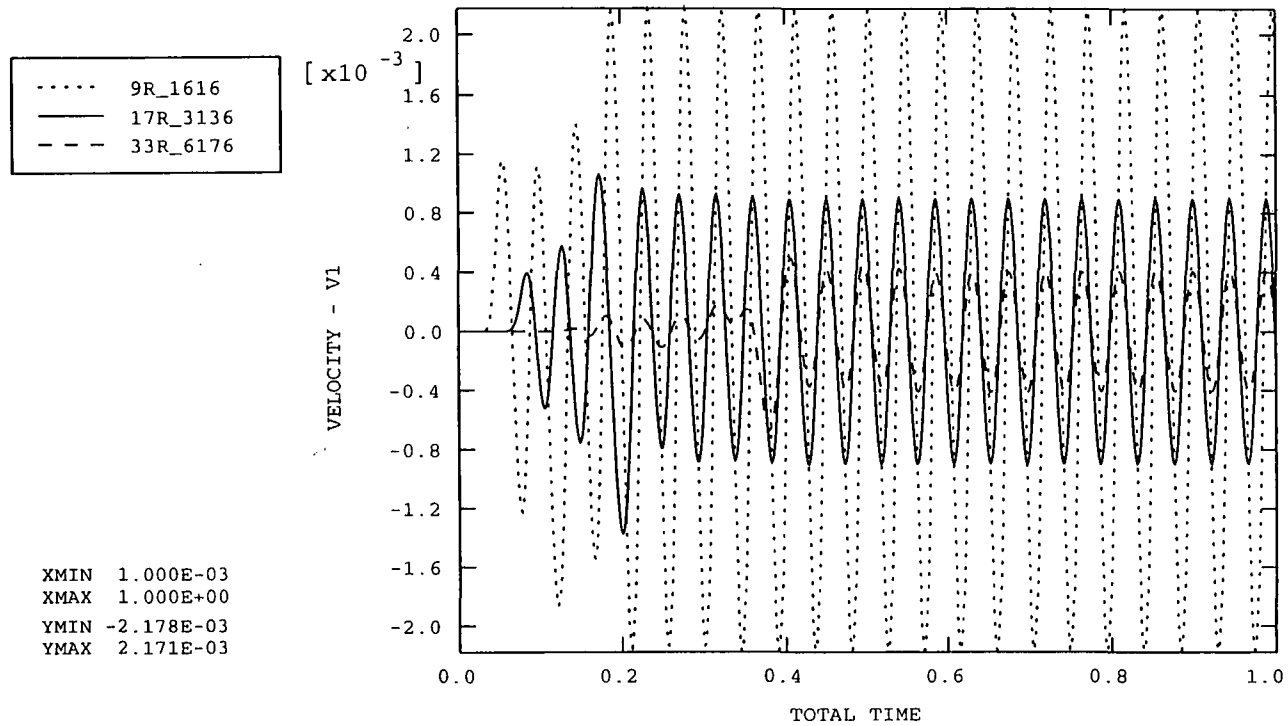
Radial velocity/time traces assuming $E_{\text{alluvium}} = 40\text{MPa}$ and $E_{\text{marl}} = 70\text{MPa}$

ABAQUS



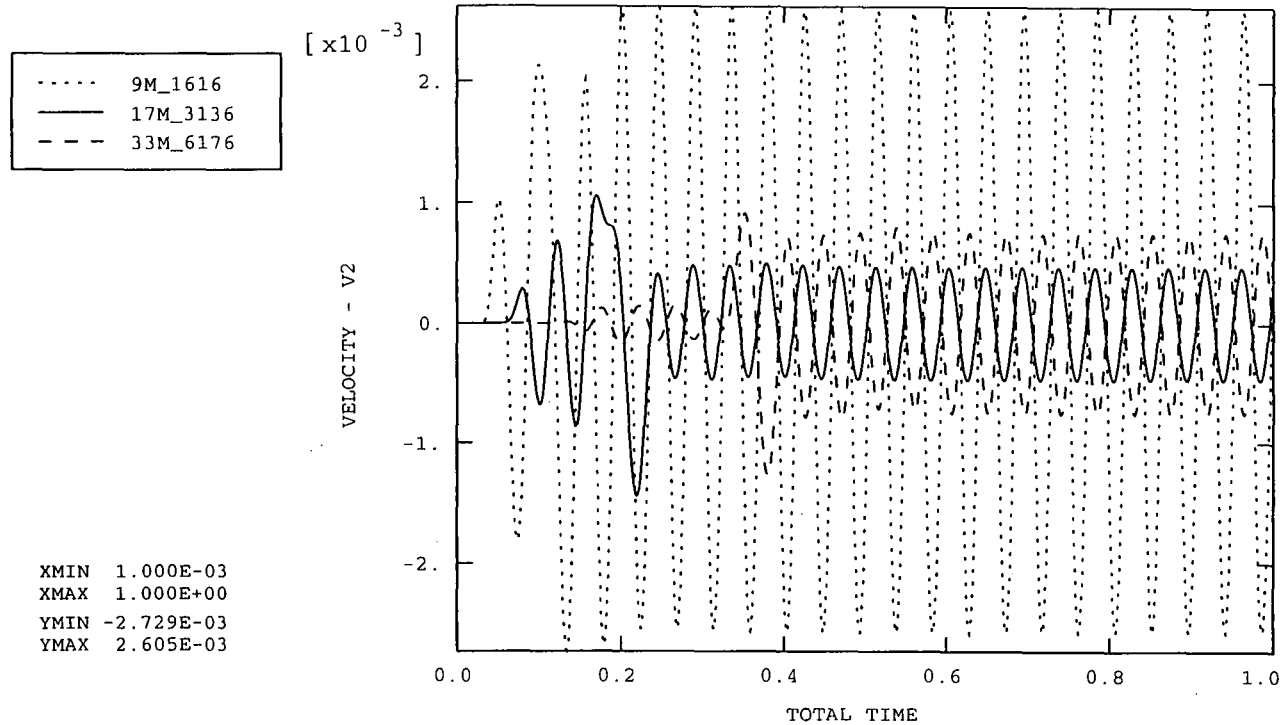
Vertical velocity/time traces assuming $E_{\text{alluvium}} = 42\text{MPa}$ and $E_{\text{marl}} = 70\text{MPa}$

ABAQUS



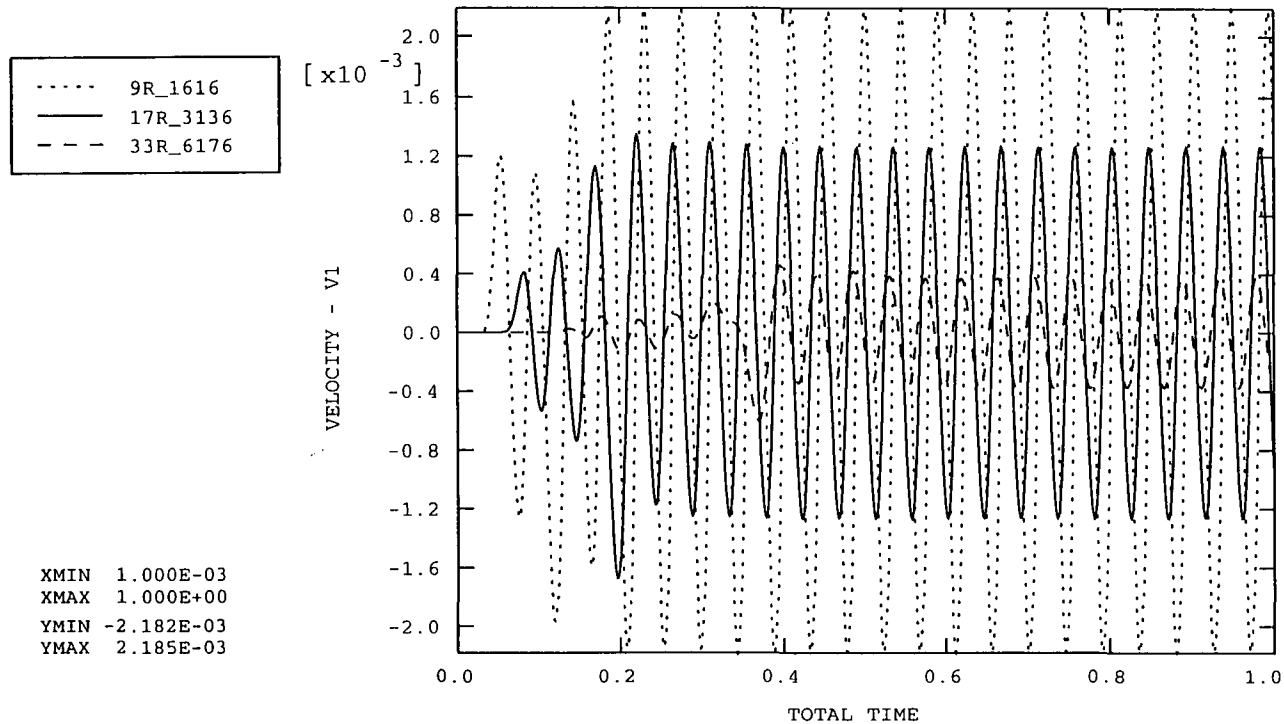
Radial velocity/time traces assuming $E_{\text{alluvium}} = 42\text{MPa}$ and $E_{\text{marl}} = 70\text{MPa}$

ABAQUS



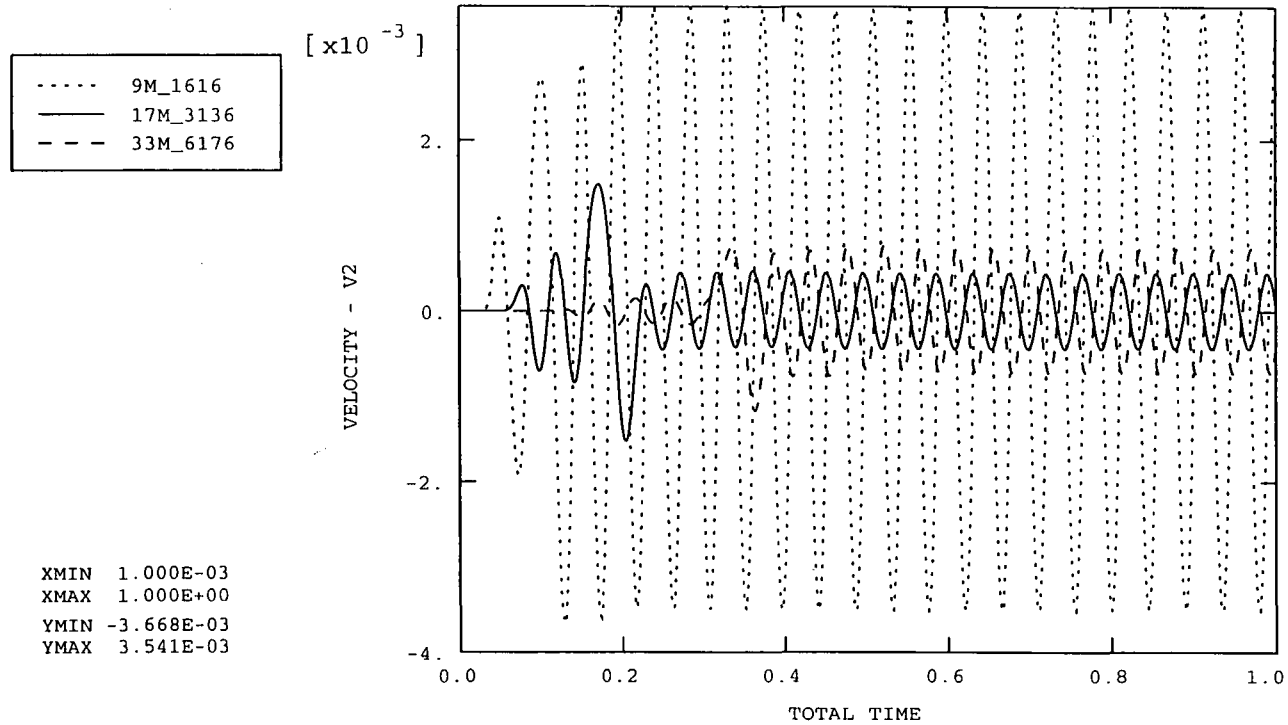
Vertical velocity/time traces assuming $E_{\text{alluvium}} = 45\text{MPa}$ and $E_{\text{marl}} = 70\text{MPa}$

ABAQUS



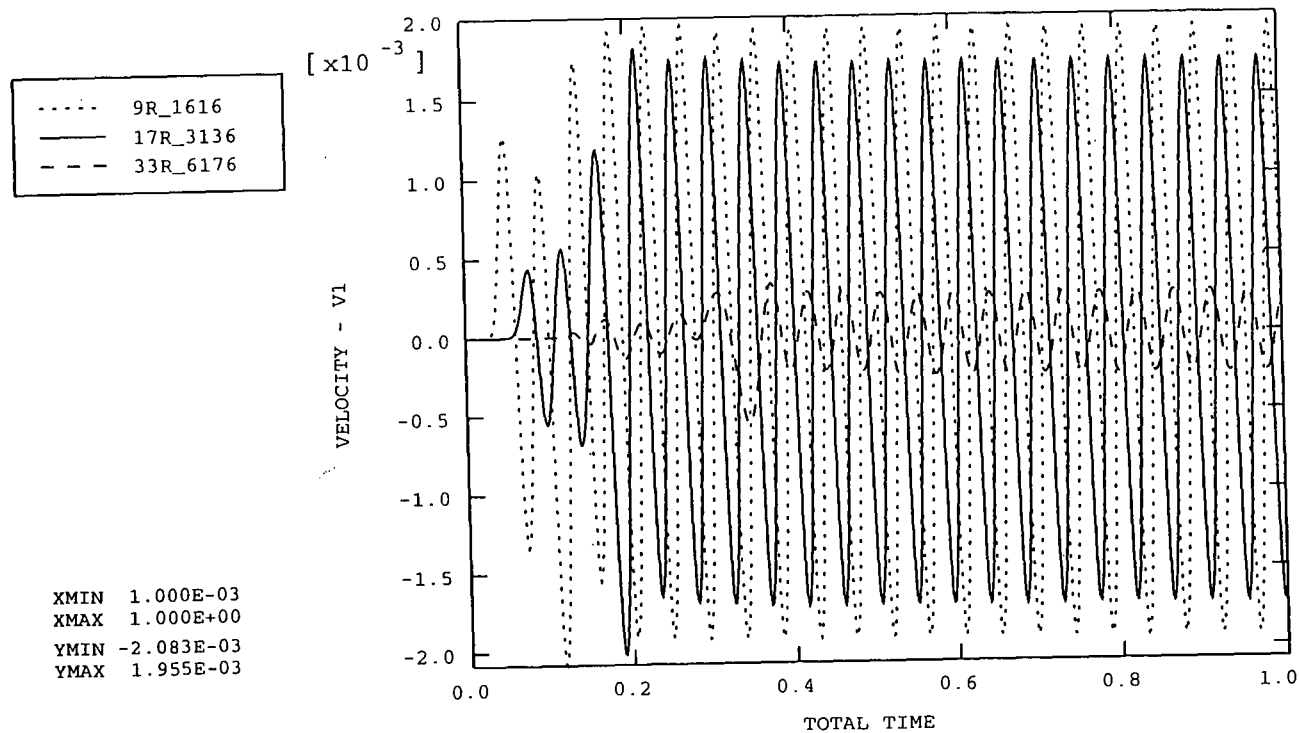
Radial velocity/time traces assuming $E_{\text{alluvium}} = 45\text{MPa}$ and $E_{\text{marl}} = 70\text{MPa}$

ABAQUS



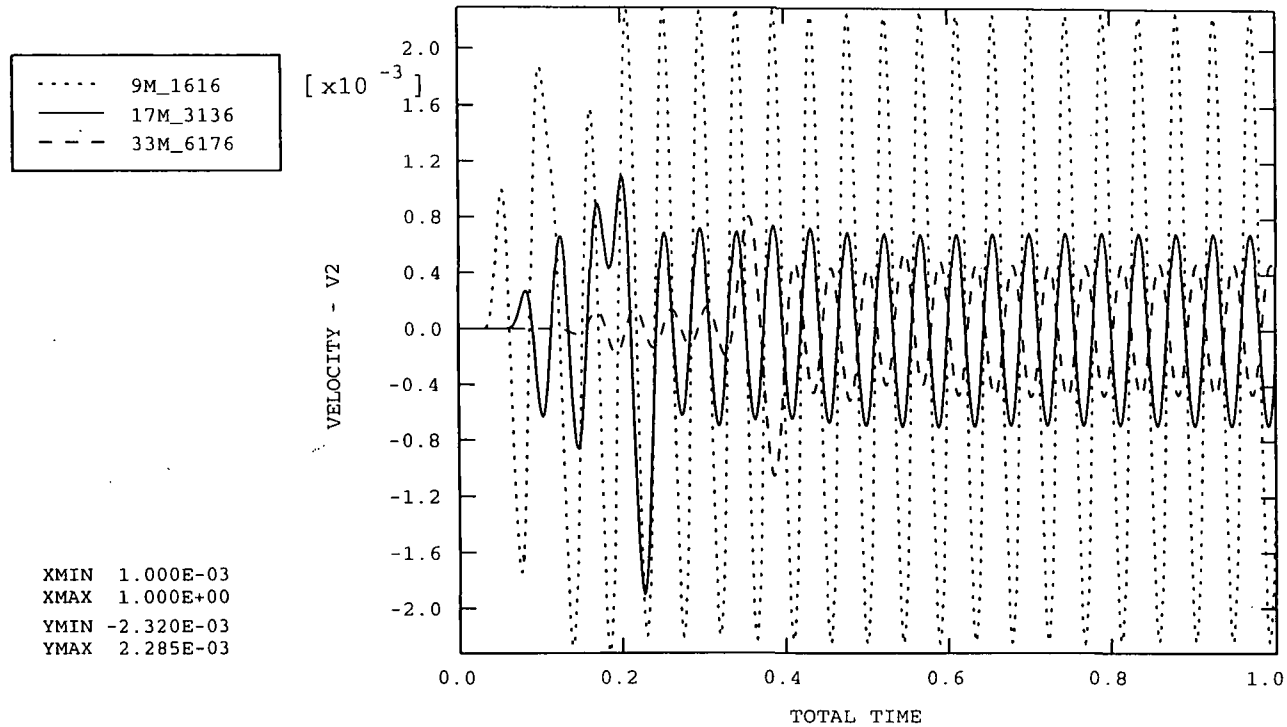
Vertical velocity/time traces assuming $E_{\text{alluvium}} = 50\text{MPa}$ and $E_{\text{marl}} = 70\text{MPa}$

ABAQUS



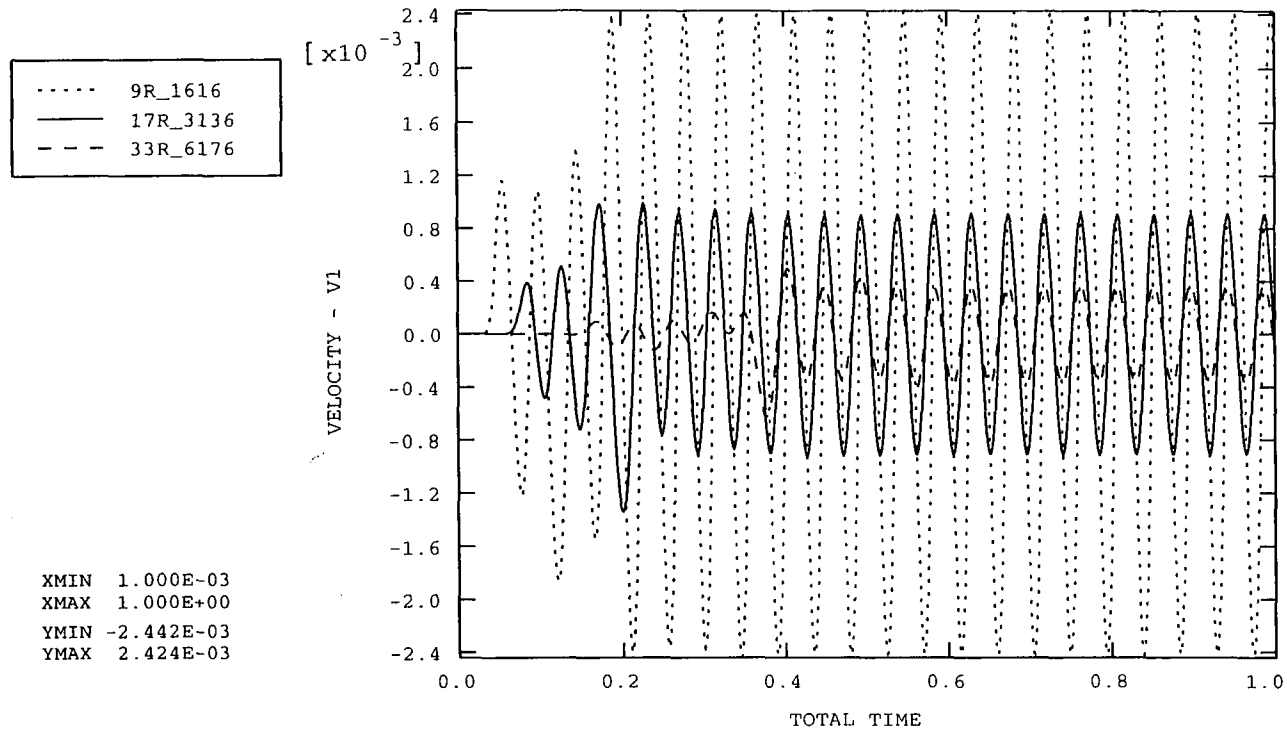
Radial velocity/time traces assuming $E_{\text{alluvium}} = 50\text{MPa}$ and $E_{\text{marl}} = 70\text{MPa}$

ABAQUS



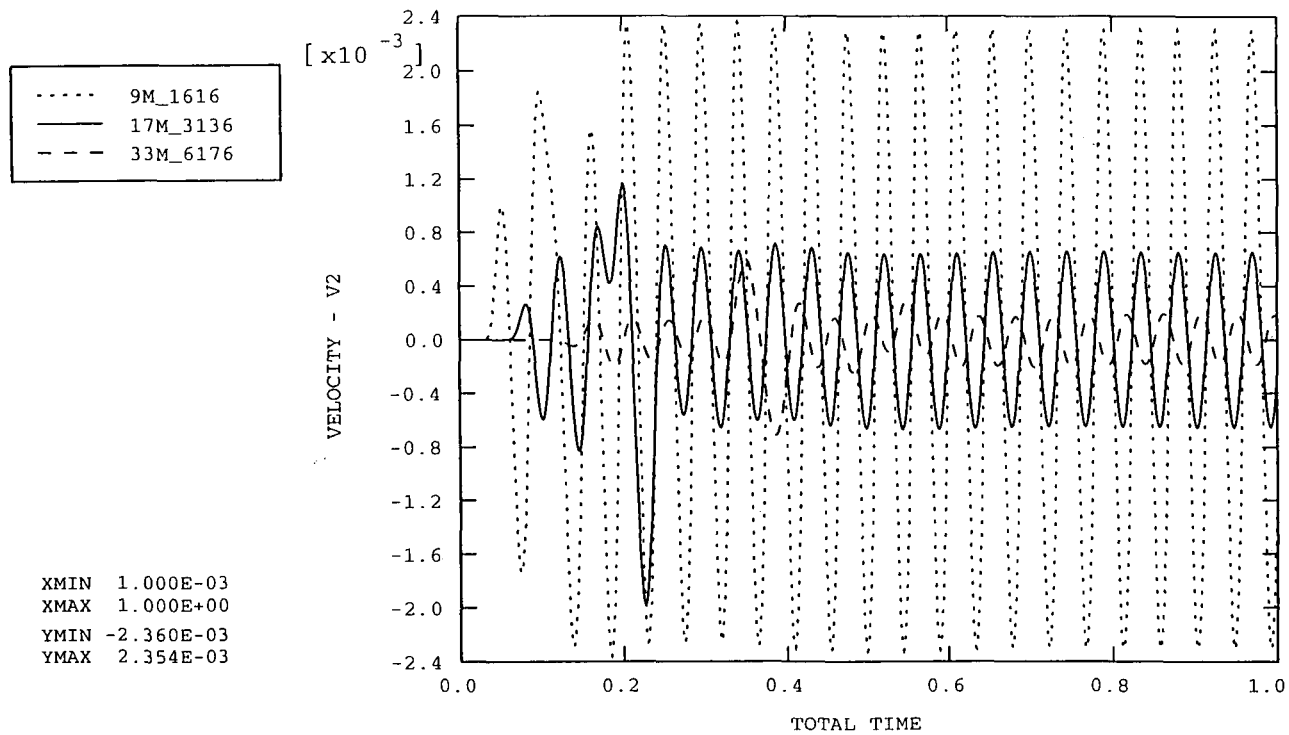
Vertical velocity/time traces assuming $E_{\text{alluvium}} = 42\text{MPa}$ and $E_{\text{marl}} = 100\text{MPa}$

ABAQUS



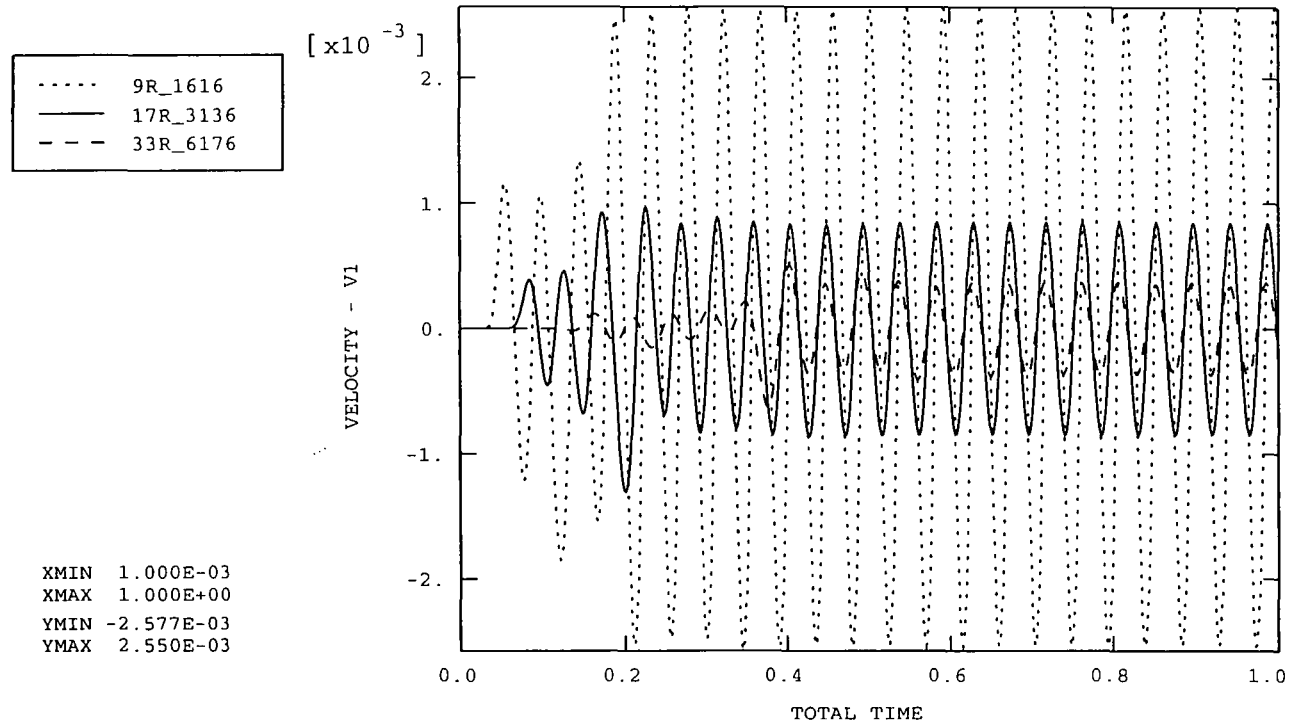
Radial velocity/time traces assuming $E_{\text{alluvium}} = 42\text{MPa}$ and $E_{\text{marl}} = 100\text{MPa}$

ABAQUS



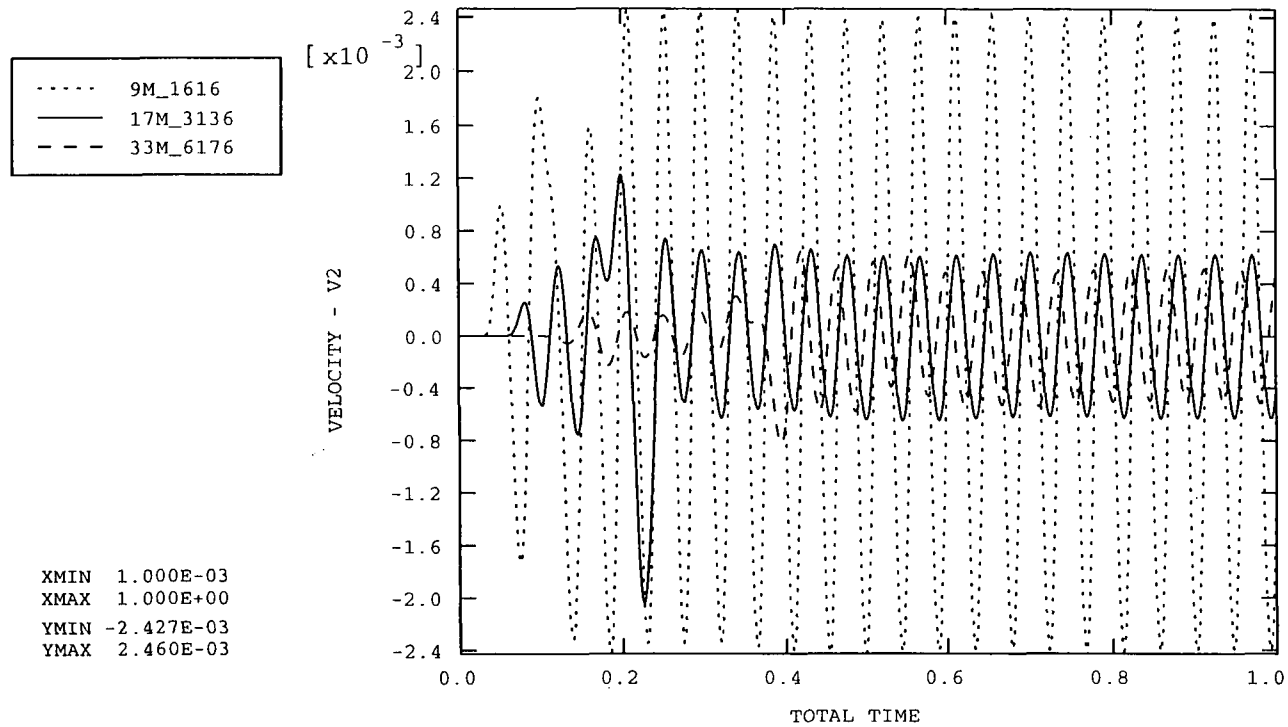
Vertical velocity/time traces assuming $E_{\text{alluvium}} = 42\text{MPa}$ and $E_{\text{marl}} = 120\text{MPa}$

ABAQUS



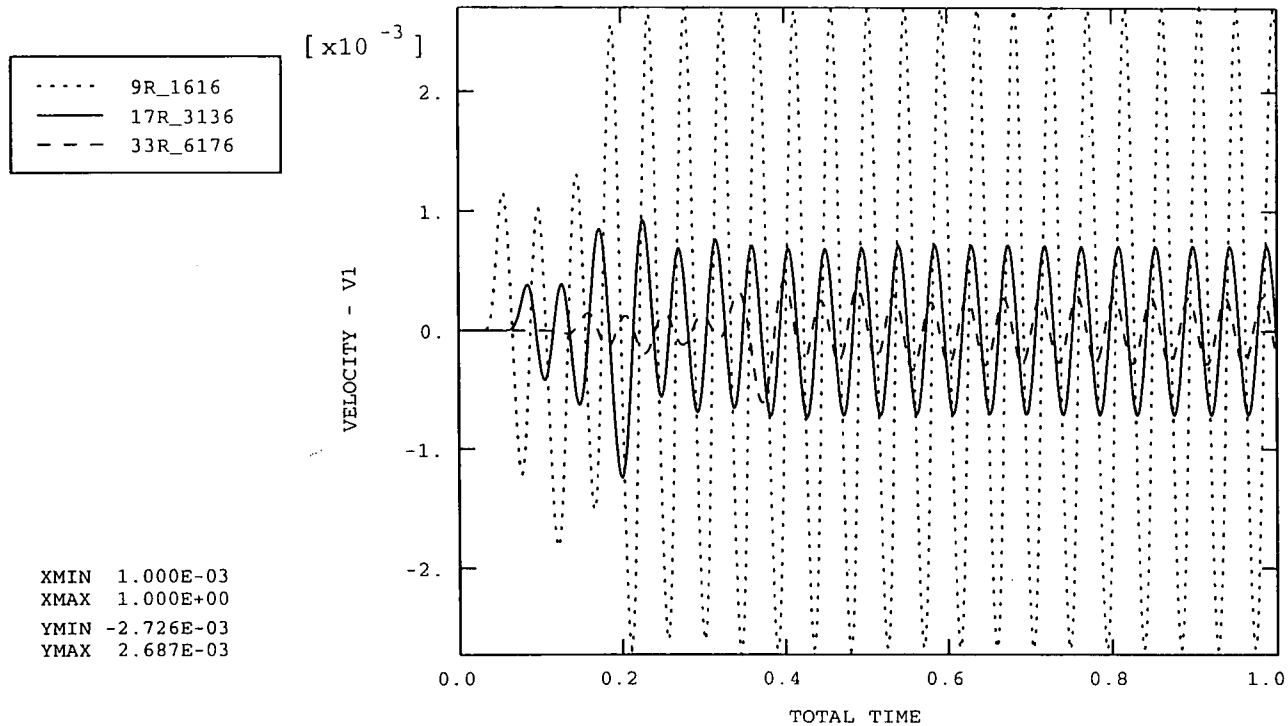
Radial velocity/time traces assuming $E_{\text{alluvium}} = 42\text{MPa}$ and $E_{\text{marl}} = 120\text{MPa}$

ABAQUS



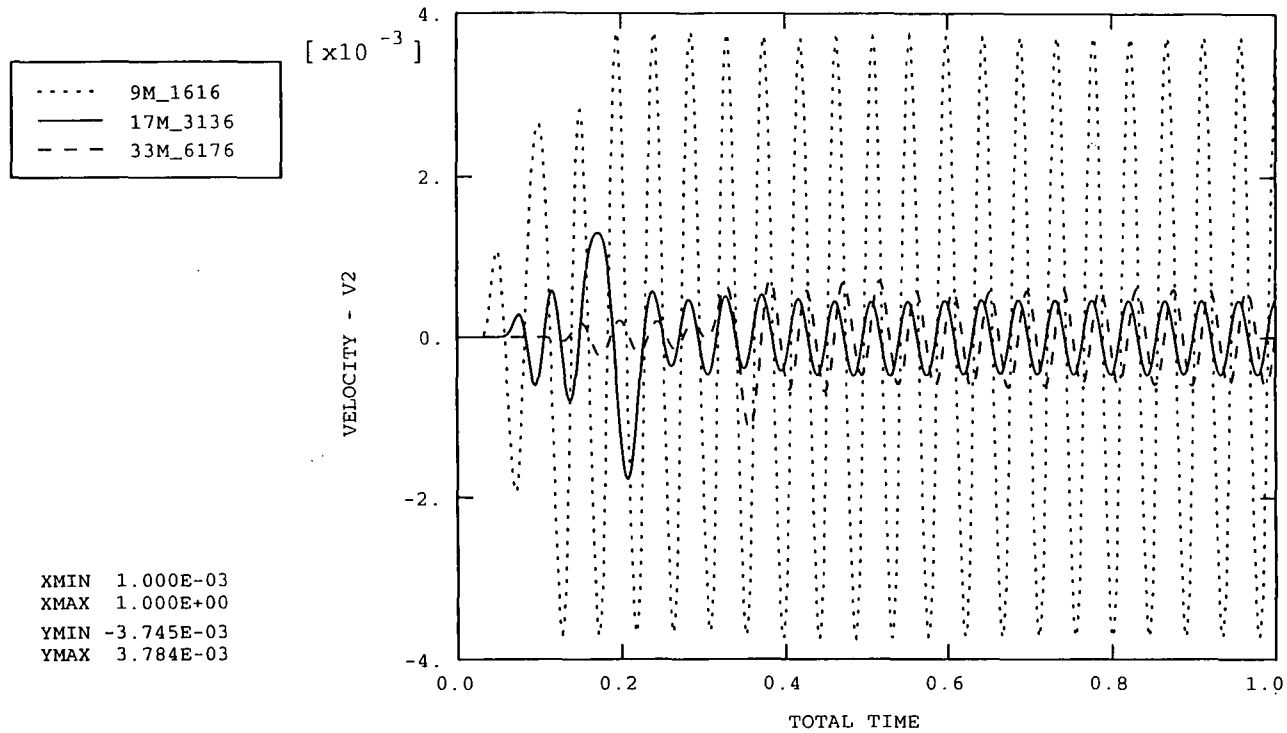
Vertical velocity/time traces assuming $E_{\text{alluvium}} = 42\text{MPa}$ and $E_{\text{marl}} = 150\text{MPa}$

ABAQUS



Radial velocity/time traces assuming $E_{\text{alluvium}} = 42\text{MPa}$ and $E_{\text{marl}} = 150\text{MPa}$

ABAQUS

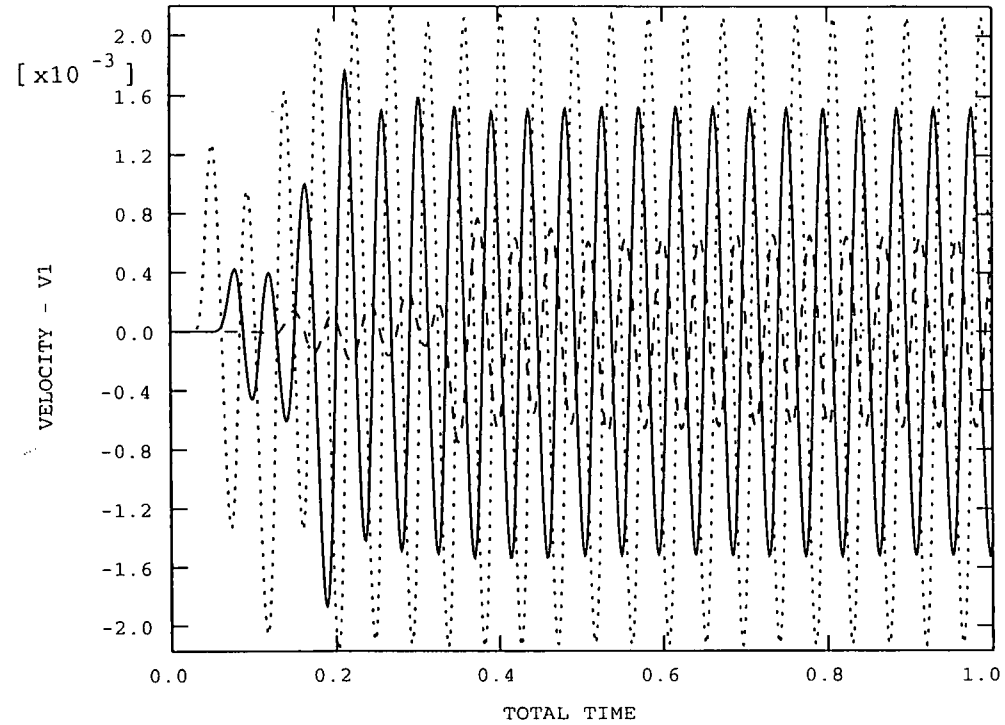


Vertical velocity/time traces assuming $E_{\text{alluvium}} = 50\text{MPa}$ and $E_{\text{marl}} = 150\text{MPa}$

ABAQUS

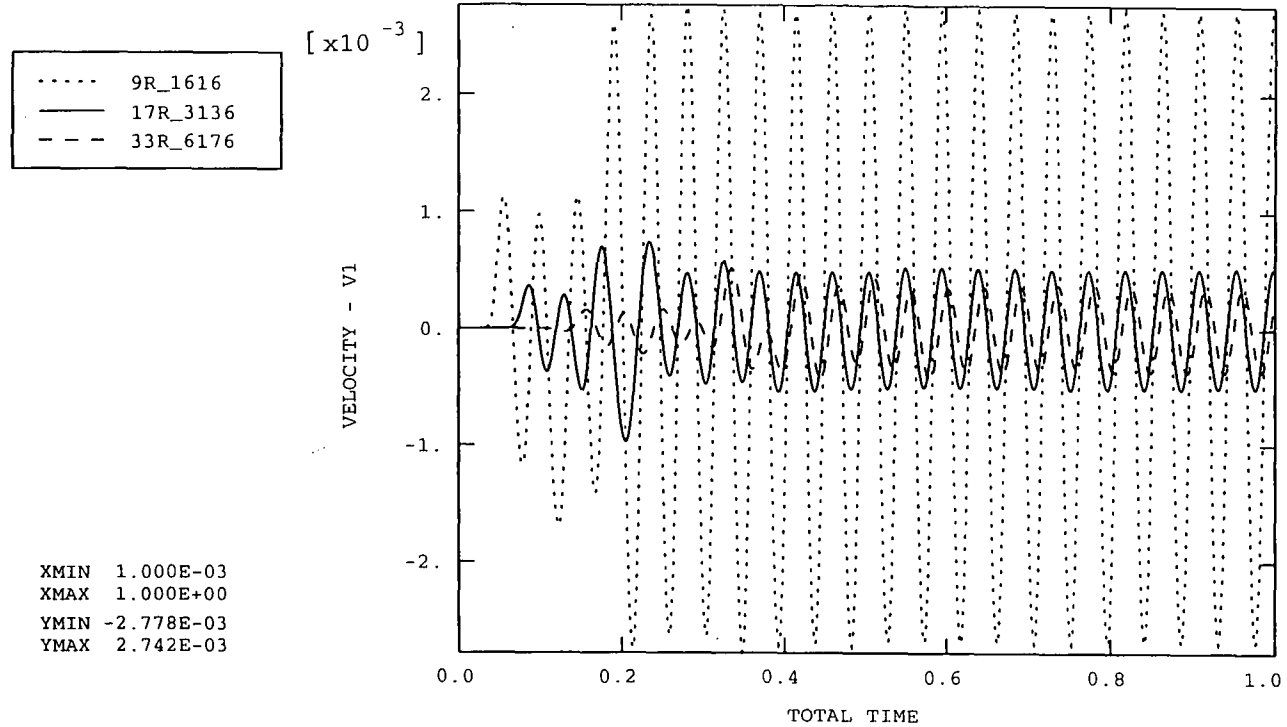
..... 9R_1616
—— 17R_3136
--- 33R_6176

XMIN 1.000E-03
XMAX 1.000E+00
YMIN -2.168E-03
YMAX 2.194E-03



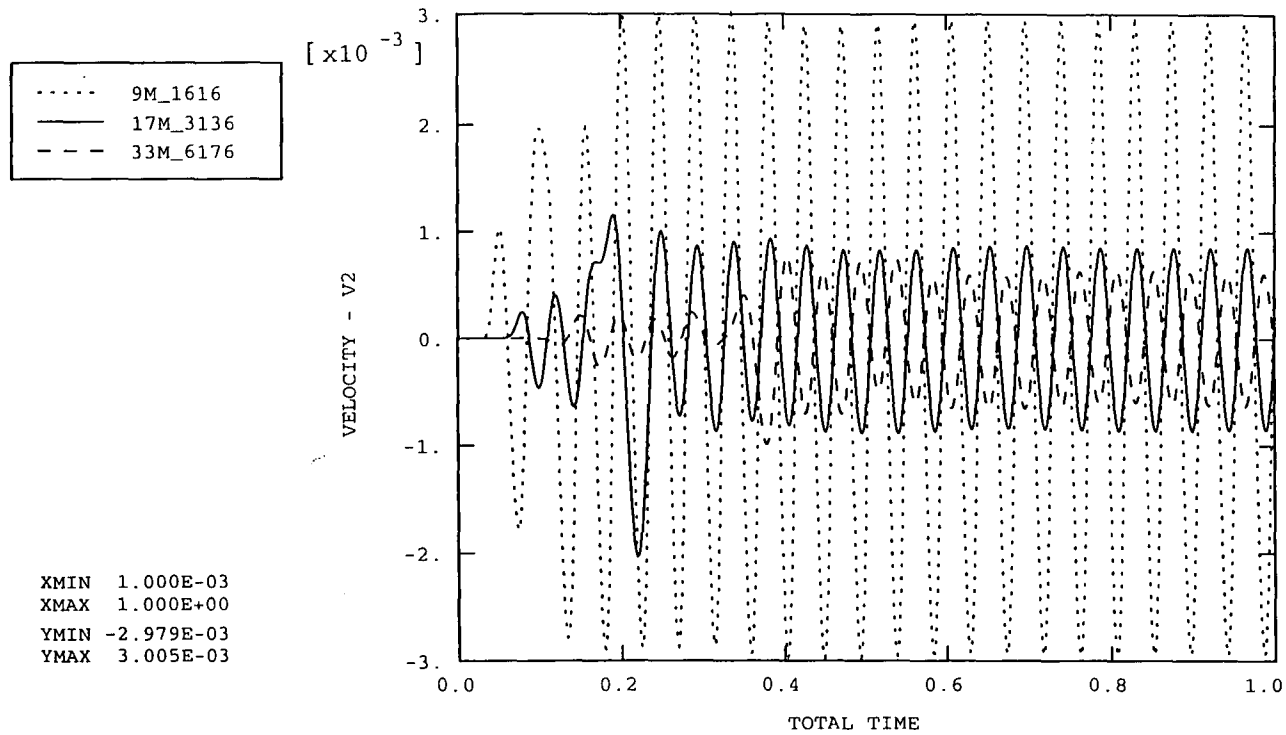
Radial velocity/time traces assuming $E_{\text{alluvium}} = 50\text{MPa}$ and $E_{\text{marl}} = 150\text{MPa}$

ABAQUS



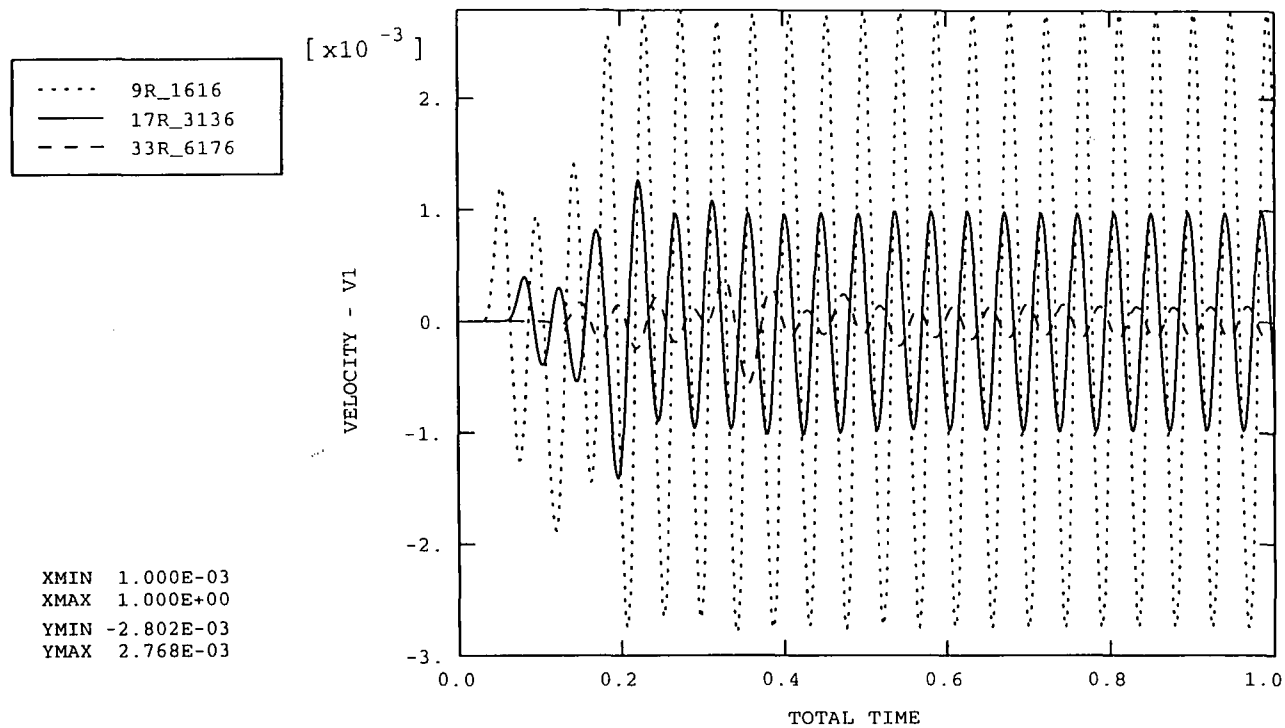
Radial velocity/time traces assuming $E_{\text{alluvium}} = 40\text{MPa}$ and $E_{\text{marl}} = 200\text{MPa}$

ABAQUS



Vertical velocity/time traces assuming $E_{\text{alluvium}} = 45\text{MPa}$ and $E_{\text{marl}} = 200\text{MPa}$

ABAQUS







Radial velocity/time traces assuming $E_{\text{alluvium}} = 45\text{MPa}$ and $E_{\text{marl}} = 200\text{MPa}$

APPENDIX H

Borehole records and laboratory test data for the Flitwick site

Location Flitwick
 Carried out for Durham University
 Borehole No. one


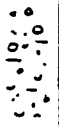



Ground Level 10.0 nom.
 Diameter 150mm
 Date 06.08.1988

DESCRIPTION	REDUCED LEVEL	LITHO	SAMPLE	DEPTH	THICKNESS	
Soft grey-brown silty sandy <u>clay</u>	7.50		B U4 J	0.5 1.0-1.45 1.5	2.50	
Medium dense yellow sandy <u>gravel</u> with flints and cobbles	6.30		B CPT	3.0 3.0-3.45	1.20	CPT 57 blows
Yellow <u>sand</u>	5.80		B	4.0	0.50	
Dense light grey <u>sand</u> with silty bands			SPT B SPT	6.10-6.55 7.0 7.90-8.35	 4.10	SPT 113 blows/270 mm SPT 28 blows - base of b.h. liquefied
End of b.h.	1.60					
Water strike 2.70 m depth, rising to 1.70 m						

Borehole log information, BH-1

Location Flitwick
 Carried out for Durham University
 Borehole No. two

Ground Level 10.0 nom.
 Diameter 150mm
 Date 06.08.1988

DESCRIPTION	REDUCED LEVEL	LEGEND	SAMPLE	DEPTH	THICKNESS	
Soft grey brown silty sandy <u>clay</u> with some peat	7.90		B U4 J	0.5 1.0-1.4 1.5	2.10	
Loose yellow clayey <u>sand</u> and <u>gravel</u>	7.00		B CPT	2.5 3.0-3.45	0.90	CPT 32 blows
Loose yellow <u>sand</u> gravel and flints	6.20		B	3.4	0.80	
Loose yellow <u>sand</u>	5.10		B	4.3	1.10	
Dense light grey <u>sand</u> with silty bands			SPT B SPT	5.0-6.45 7.0 8.2-8.65	3.70	SPT 80 blows SPT 90 blows
End of b.h.	1.35					
Water strike at 3.00 m depth, rising to 1.40 m						

Location Flitwick
 Carried out for Durham University
 Borehole No. three

Ground Level 10.0 nom.
 Diameter 150mm
 Date 06.08.1988

DESCRIPTION	REDUCED LEVEL	LEGEND	SAMPLE	DEPTH	THICKNESS	
Soft grey brown silty sandy <u>clay</u> with peat	7.40		B U4 J	0.6 1.0-1.45 1.5		
Loose to medium yellow <u>sand</u> <u>gravel</u> and flints	5.60		B CPT B	2.8 3.0-3.45 3.7		CPT 39 blows
Loose light grey <u>sand</u>	4.50					
Dense light grey <u>sand</u> with silty bands			SPT B SPT	6.0-6.45 6.7 7.90-8.35		SPT 77 blows SPT 47 blows (some liquefaction)
End of b.h.	1.65					
Water strike at 2.80 m depth, rising to 1.30 m						

Results of the Moisture Content Tests

Borehole no.	Sample no.	Depth (m)	U100 or Bag	Moisture Content (%)
1	2	1.0-1.45	U100	22.7
	4	2.5-3.7	Bag	7.1
	4	2.8-3.7	Bag	10.2
	5	3.7-4.7	Bag	22.0
	7	4.2-7.9	Bag	27.6
2	2	1.0-1.45	U100	18.3
	4	2.0-3.0	Bag	14.3
	5	3.0-3.8	Bag	8.9
	6	3.8-4.9	Bag	17.8
	7	4.9-6.0	Bag	22.1
	9	6.0-8.2	Bag	23.3
3	2	1.0-1.45	U100	33.0
	4	2.6-3.0	Bag	11.9
	5	3.0-4.4	Bag	10.2
	6	4.4-5.5	Bag	23.6
	8	5.5-7.9	Bag	21.8

Results of the Particle Size Distributions

Borehole no.	Sample no.	Depth (m)	< 60 μ m %	60 μ m – 2mm %	2mm – 60mm %	60mm > %
1	4	2.5-3.7	2	38	60	0
	4	2.8-3.7	3	51	46	0
	5	3.7-4.7	6	91	3	0
	7	4.2-7.9	5	94	1	0
2	4	2.0-3.0	9	49	42	0
	5	3.0-3.8	2	54	44	0
	6	3.8-4.9	1	98	1	0
	7	4.9-6.0	5	91	4	0
	9	6.0-8.2	6	92	2	0
3	2	1.0-1.45	26	64	10	0
	4	2.6-3.0	11	45	44	0
	5	3.0-4.4	5	39	56	0
	6	4.4-5.5	2	95	3	0
	8	5.5-7.9	5	94	1	0

Results of the Shear Box Tests

Borehole No.	Sample No.	Depth (m)	c (kN/m ²)	ϕ degrees	% passing 2mm
1	4	2.5-3.7	0	44°	40
	4	2.8-3.7	—	—	—
	5	3.7-4.2	0	37°	97
	7	4.2-7.9	0	38°	99
2	4	2.0-3.0	0	41°	58
	5	3.0-3.8	0	42°	56
	6	3.8-4.9	0	37°	99
	7	4.9-6.0	0	38°	96
	9	6.0-8.2	0	39.5°	98
3	4	2.6-3.0	—	—	—
	5	3.0-4.4	0	36°	44
	6	4.4-5.5	0	40°	97
	8	5.5-7.9	0	35°	99

Titles	Borehole [1]				Borehole [2]			Borehole [3]			
	sample 2, depth 1.0-1.45m				sample 2, depth 1.0-1.45m			sample 2, depth 1.0-1.45m			
Normal Pressure (kN.m^{-2})	70	115	140	210	70	140	210	70	115	140	210
Moisture Content (%)	22.7				18.3			33.0			
Bulk Desity (kg.m^{-3})	2139	1954	2015	1994	2132	2222	2158	1930	1712	1947	1612
Stress at Failure (kN.m^{-2})	44	38	38	36	60	70	68	27	17	31	19
Strain at Failure	7	20	20	20	20	20	20	20	20	18	20
Final M.C. (%)	19.7	26.8	24.4	25.8	17.3	15.0	16.3	19.8	45.6	27.1	44.7
Cohesion (c) (kN.m^{-2})	34.0				19.0			15.0			
Friction (ϕ°)	0°				0°			0°			

Quick Undrained Triaxial Tests

APPENDIX I

**Penetration Records for 10 piles subjected to dynamic load testing by the SIMBAT
Method at the M66 site in Manchester**

Borehole records and laboratory test results for the M66 site.

TABLE OF RESULTS (1)

SITE:

M66 Manchester

File No.

7

Working Load:

1425 KN

Theodolite Distance:

4.0 m

Date : 22 June 1995

Diameter: 750 mm

Test Load: 2138 KN

Distance from Pile Head to Gauges: 700 mm

Total Length: 21.0 m

Blow Number	File Name	Drop (m)	PEN (mm)	RDY (KN)	REMARKS
1	M667-1.DAT	0.2	0.02	581	
2	M667-2.DAT	0.4	0.14	946	
3	M667-3.DAT	0.6	0.16	1042	
4	M667-4.DAT	0.8	0.35	1674	
5	M667-5.DAT	1.0	0.67	2187	
6	M667-6.DAT	1.2	0.79	2460	

TABLE OF RESULTS (2)

SITE:

M66 Manchester

File No.

8

Working Load:

1425 KN

Theodolite Distance:

4.0 m

Date : 22 June 1995

Diameter: 750 mm

Test Load: 2138 KN

Distance from Pile Head to Gauges: 700 mm

Total Length: 21.0 m

Blow Number	File Name	Drop (m)	PEN (mm)	RDY (KN)	REMARKS
1	M668-1.DAT	0.2	0.18	667	
2	M668-2.DAT	0.4	0.32	991	
3	M668-3.DAT	0.6	0.56	1342	
4	M668-4.DAT	0.8	0.81	1651	
5	M668-5.DAT	1.0	1.00	2049	
6	M668-6.DAT	1.2	1.39	2432	

TABLE OF RESULTS (3)

SITE: M66 Manchester

File No. 12

Working Load: 1425 KN

Theodolite Distance: 4.0 m

Date : 21 June 1995

Diameter: 750 mm

Test Load: 2138 KN

Distance from Pile Head to Gauges: 600 mm

Total Length: 21.0 m

Blow Number	File Name	Drop (m)	PEN (mm)	RDY (KN)	REMARKS
1	M6612-1.DAT	0.2	0.02	491	
2	M6612-2.DAT	0.4	0.09	861	
3	M6612-3.DAT	0.6	0.35	1041	
4	M6612-4.DAT	0.8	0.60	1303	
5	M6612-5.DAT	1.0	0.76	1839	
6	M6612-6.DAT	1.2	1.02	2376	

TABLE OF RESULTS (4)

SITE: M66 Manchester

File No. 14

Working Load: 1425 KN

Theodolite Distance: 4.0 m

Date : 21 June 1995

Diameter: 750 mm

Test Load: 2138 KN

Distance from Pile Head to Gauges: 800 mm

Total Length: 21.0 m

Blow Number	File Name	Drop (m)	PEN (mm)	RDY (KN)	REMARKS
1	M6614-1.DAT	0.2	0.35	467	
2	M6614-2.DAT	0.4	0.46	907	
3	M6614-3.DAT	0.6	0.53	1352	
4	M6614-4.DAT	0.8	0.83	1787	
5	M6614-5.DAT	1.0	1.37	2341	

TABLE OF RESULTS (5)

SITE:

M66 Manchester

Date :

22 June 1995

Pile No.

17

Diameter:

750 mm

Total Length:

21.0 m

Working Load:

1425 KN

Test Load:

2138 KN

Theodolite Distance:

4.0 m

Distance from Pile Head to Gauges:

700 mm

Blow Number	File Name	Drop (m)	PEN (mm)	RDY (KN)	REMARKS
1	M6617-1.DAT	0.2	-	-	Poor Data
2	M6617-2.DAT	0.4	0.23	842	
3	M6617-3.DAT	0.6	0.28	1093	
4	M6617-4.DAT	0.8	0.19	1693	
5	M6617-5.DAT	1.0	0.74	2225	
6	M6617-6.DAT	1.2	0.67	2583	

TABLE OF RESULTS (6)

SITE:

M66 Manchester

Date :

21 June 1995

Pile No.

18

Diameter:

750 mm

Total Length:

21.0 m

Working Load:

1425 KN

Test Load:

2138 KN

Theodolite Distance:

4.0 m

Distance from Pile Head to Gauges:

700 mm

Blow Number	File Name	Drop (m)	PEN (mm)	RDY (KN)	REMARKS
1	M6618-1.DAT	0.2	-	-	Poor Data
2	M6618-2.DAT	0.4	0.23	685	
3	M6618-3.DAT	0.6	0.65	1050	
4	M6618-4.DAT	0.8	0.70	1275	
5	M6618-5.DAT	1.0	1.07	1918	
6	M6618-6.DAT	1.2	1.40	2175	

TABLE OF RESULTS (7)

SITE: M66 Manchester **Date :** 22 June 1995
Pile No. 19 **Diameter:** 750 mm **Total Length:** 21.0 m
Working Load: 1425 KN **Test Load:** 2138 KN
Theodolite Distance: 4.0 m **Distance from Pile Head to Gauges:** 700 mm

Blow Number	File Name	Drop (m)	PEN (mm)	RDY (KN)	REMARKS
1	M6619-1.DAT	0.2	0.02	581	
2	M6619-2.DAT	0.4	0.0	921	
3	M6619-3.DAT	0.6	0.16	1141	
4	M6619-4.DAT	0.8	0.09	1467	
5	M6619-5.DAT	1.0	0.19	1964	
6	M6619-6.DAT	1.2	0.35	2336	

TABLE OF RESULTS (8)

SITE: M66 Manchester **Date :** 21 June 1995
Pile No. 22 **Diameter:** 750 mm **Total Length:** 21.0 m
Working Load: 1425 KN **Test Load:** 2138 KN
Theodolite Distance: ---- m **Distance from Pile Head to Gauges:** 600 mm

Blow Number	File Name	Drop (m)	PEN (mm)	RDY (KN)	REMARKS
1	M6622-1.DAT	0.2	0.1	490	
2	M6622-2.DAT	0.4	0.2	872	
3	M6622-3.DAT	0.6	0.2	1167	
4	M6622-4.DAT	0.8	0.35	1542	
5	M6622-5.DAT	1.0	0.45	2174	

TABLE OF RESULTS (9)

SITE: M66 Manchester

Date : 22 June 1995

Pile No. 23

Diameter: 750 mm

Total Length: 21.0 m

Working Load: 1425 KN

Test Load: 2138 KN

Theodolite Distance: 4.0 m

Distance from Pile Head to Gauges: 600 mm

Blow Number	File Name	Drop (m)	PEN (mm)	RDY (KN)	REMARKS
1	M6623-1.DAT	0.2	-	-	No Trigger
2	M6623-2.DAT	0.4	0.15	867	
3	M6623-3.DAT	0.6	0.29	1186	
4	M6623-4.DAT	0.8	0.21	1385	
5	M6623-5.DAT	1.0	0.30	1581	
6	M6623-6.DAT	1.2	0.53	2155	

TABLE OF RESULTS (10)

SITE: M66 Manchester

Date : 21 June 1995

Pile No. 77

Diameter: 750 mm

Total Length: 21.0 m

Working Load: 1425 KN

Test Load: 2138 KN

Theodolite Distance: 4.0 m

Distance from Pile Head to Gauges: 600 mm

Blow Number	File Name	Drop (m)	PEN (mm)	RDY (KN)	REMARKS
1	M6677-1.DAT	0.2	0.11	445	
2	M6677-2.DAT	0.4	0.11	879	
3	M6677-3.DAT	0.6	0.30	1158	
4	M6677-4.DAT	0.8	0.51	1639	
5	M6677-5.DAT	1.0	0.52	1904	
6	M6677-6.DAT	1.2	0.52	2211	

SEPARATION OF FORCES PLOT PILE NUMBER: 23 BLOW NUMBER: 5

x E 0

M6623-5.DAT

27.5

4786.0

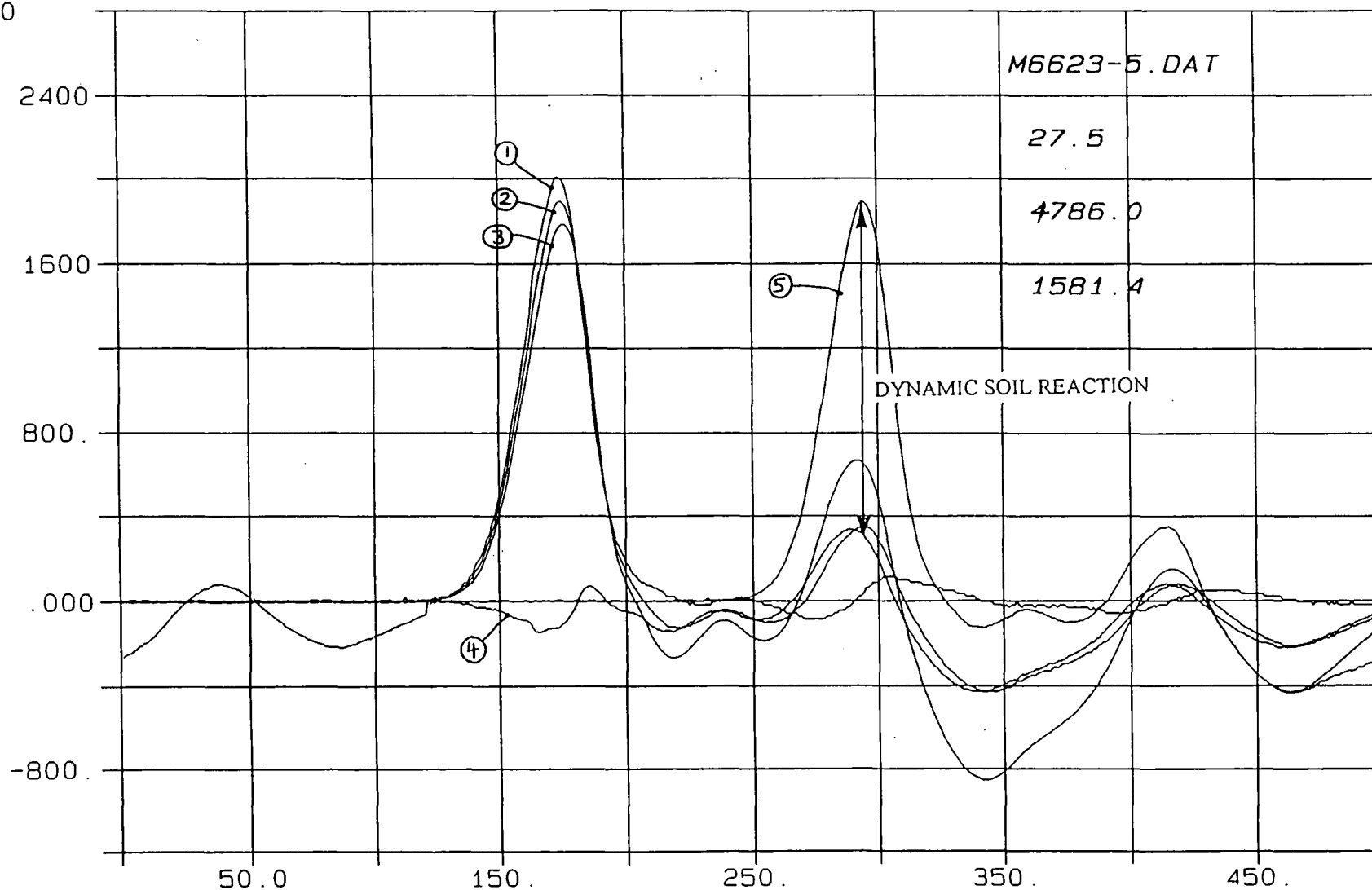
1581.4

DYNAMIC SOIL REACTION

DYNAMIC REACTION (KN)

x E 0

TIMESCALE (X 80 micro secs)

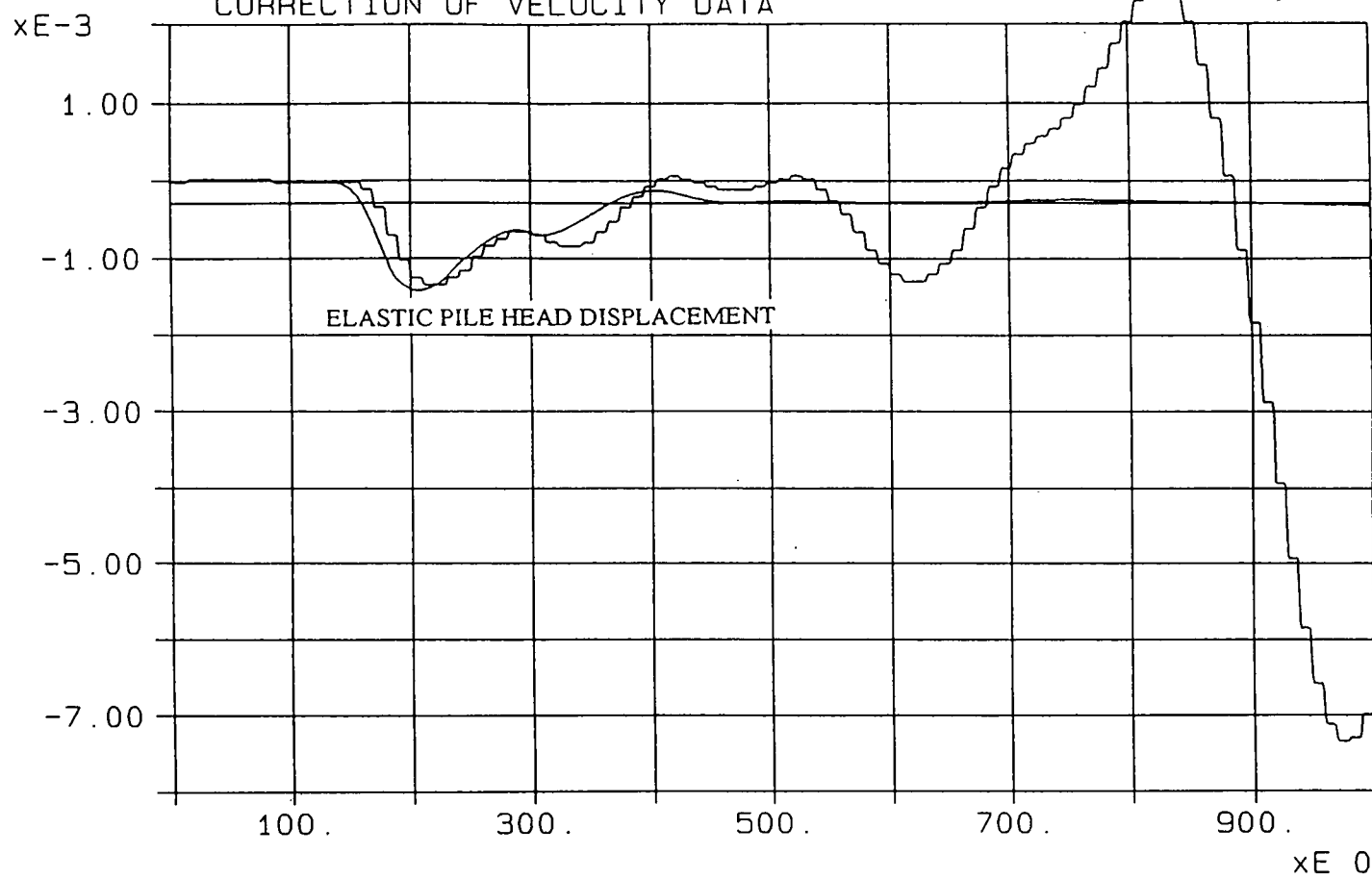


SITE:

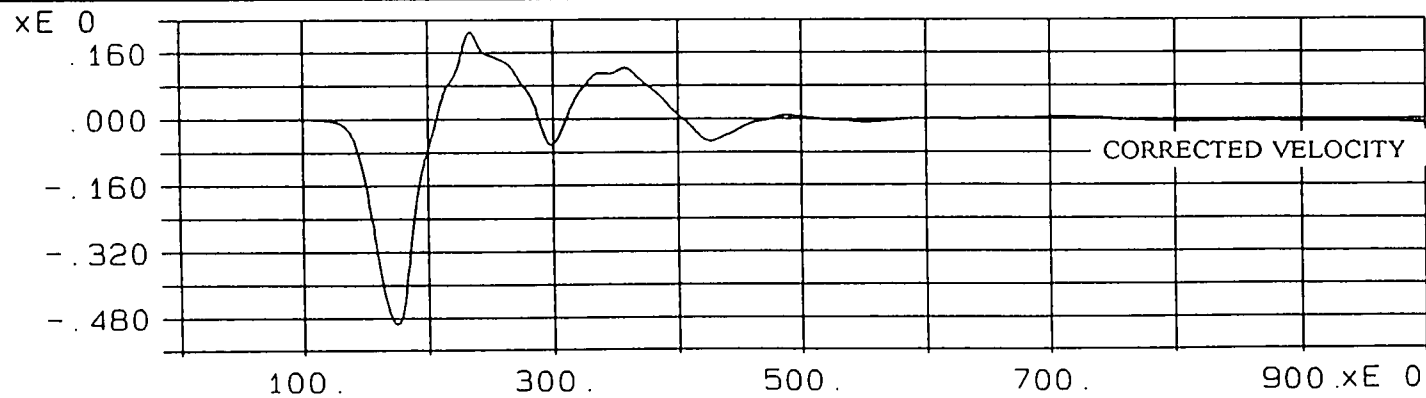
M66 EXTENSION


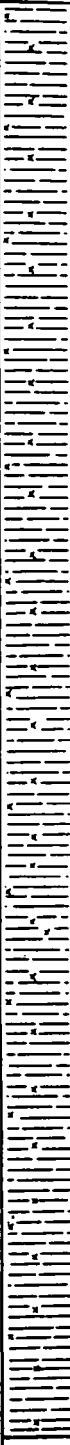
M6617-3.DAT

THEODOLITE DATA



VELOCITY



Sampling		Properties			Strata			
Depth	Type	Strength kN m ²	w %	SPT N	Description	Depth	Level mm	Legend
0.0	D	50	30		MADE GROUND:- Ash, stone and clay.	G.L.	100.73	
0.5-1.0	U(34)					0.48	100.2	
1.0	D		30		Firm becoming firm to stiff dark brown poorly laminated silty CLAY with occasional rock fragments			
1.25	D		31					
1.5-2.0	U(35)		25					
2.0	D							
2.25	D							
2.5-3.0	U(34)	50	25					
3.0	D		26					
3.25	D		26					
3.5-4.0	U(35)		23					
4.0	D							
4.25	D							
4.5-5.0	U(36)							
5.0	D							
5.5	D							
6.0-6.5	U(35)	65	23					
6.5	D		24					
7.0	D		24					
7.5-8.0	U(37)							
8.0	D							
8.5	D							
9.0-9.5	U(45)	90	23					
9.5	D		23					
					Continued over from 10.0m.	10.0	90.7	

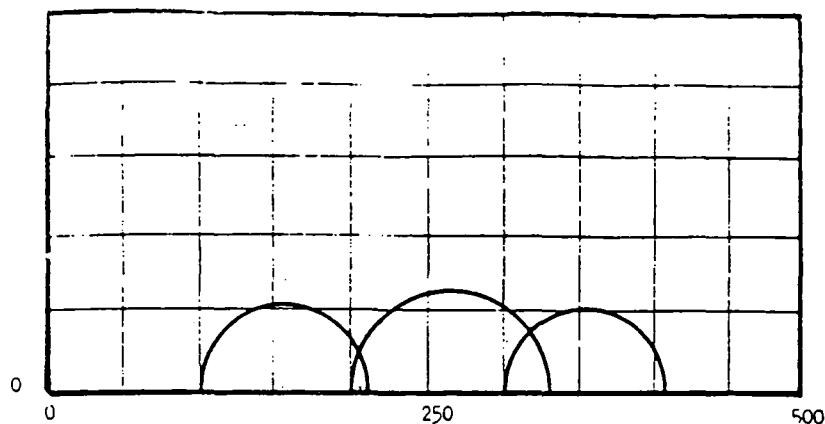
Drilling					Ground Water						
Type	From	To	Size	Fluid	Struck	Behaviour	Sealed	Date	Hole	Cased	Water
Shell and Auger	G.L.	10.0	0.15	-	14.4	Slow flow, rise to 14.5 in 20 mins		25.8.81	Nil	Nil	Nil
							15.2	25.8.81	13.0	12.0	Nil
						(casing at 13.5m).		26.8.81	12.5	12.0	Nil

Remarks											
Borehole Record					Project North Western Road Construction Unit,					Contract S2904	
exploration associates					L. G. Mouchel & Partners, M66 Manchester Outer Ring Road, Supplementary Site Investigation Section 3					Borehole 379 Sheet 1 of 3	

Sampling		Properties			Strata						
Depth	Type	Strength kN m ²	w %	SPT N	Description	Depth	Level	Legend			
10.0	B				As above.	10.0	90.7				
10.5-11.5 10.65-10.95	B DS			36		10.3	90.4				
					Dense brown silty fine to medium SAND.						
12.0-13.0 12.15-12.45	B DS			38							
						12.5	88.2				
13.5-14.5 13.65-13.95	B DS			38	Dense brown silty fine to medium SAND with bands of clayey SILT/silty CLAY.						
14.4	W										
15.0-16.0 15.15-15.45	B OC			23							
						16.2	84.5				
16.4-17.3 16.55-16.85	B OC			44	Dense brown fine to medium subrounded/subangular GRAVEL with silty fine to medium sand.						
						17.3	83.4				
17.5-18.5 17.65-17.95	B DS			30	Dense brown medium to coarse SAND with occasional subround-d fine gravel.						
19.5-20.0 19.65-19.95	B DS			43	Continued over from 20.0m.	20.0	80.7				
Drilling					Ground Water						
Type	From	To	Size	Fluid	Struck	Behaviour	Sealed	Date	Hole	Cased	Water
Shell and Auger	10.0	20.0	0.15	-	21.8	Slow flow, but increasing with		26.8.81	25.5	25.0	21.3
						depth. Rose to 21.4m in 20 mins	-				
						(casing at 21.0m).					
Remarks											
Borehole Record					Project North Western Road Construction Unit, L. G. Mouchel & Partners, M66 Manchester Outer Ring Road, Supplementary Site Investigation Section 3					Contract S2904	
exploration associates										Borehole 379 Sheet 2 of 3	

Remarks * Untestable due to insufficient sample. + Parts per 100,000.		
Laboratory Results - Summary	Project M66 Manchester Outer Ring Road, Supplementary Site Investigation Section 3.	Contract S2904 Figure 379/1
exploration associates		

Shear Stress kN/m^2

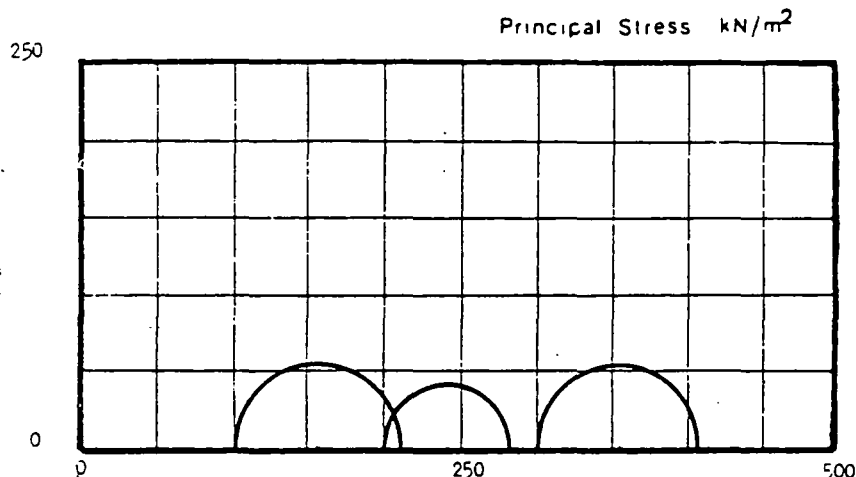


Borehole 379
Depth 0.5-1.0

C_u 60 kN/m^2
 ϕ_u - Degrees

Failure mode Plastic

Shear Stress kN/m^2

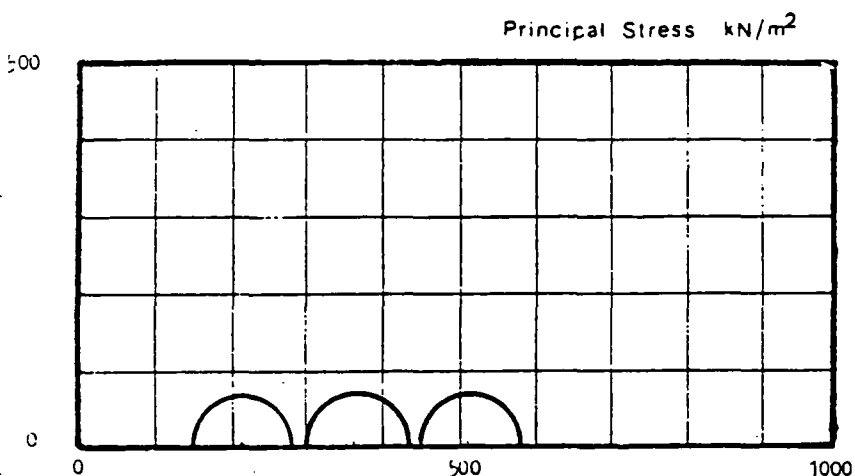


Borehole 379
Depth 2.5-3.0

C_u 50 kN/m^2
 ϕ_u - Degrees

Failure mode Plastic

Shear Stress kN/m^2

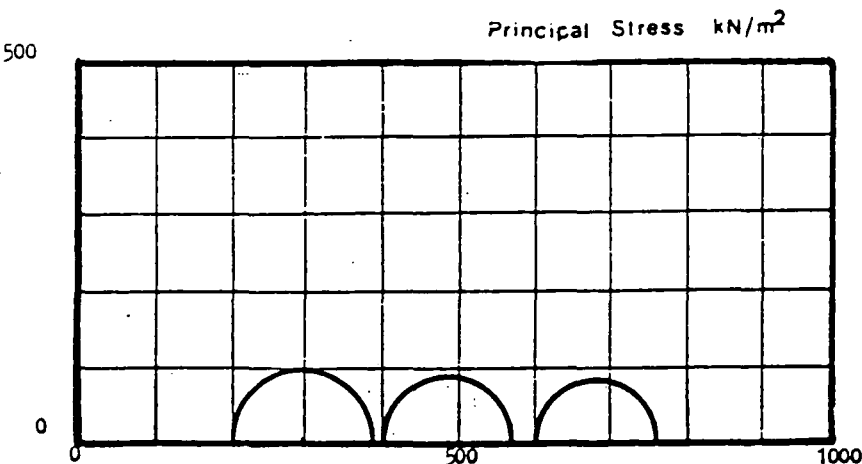


Borehole 379
Depth 6.0-6.5

C_u 65 kN/m^2
 ϕ_u - Degrees

Failure mode Plastic

Shear Stress kN/m^2



Borehole 379
Depth 9.0-9.5

C_u 90 kN/m^2
 ϕ_u - Degrees

Failure mode A Plastic
B Brittle
C Plastic

Laboratory-Mohr's Circles

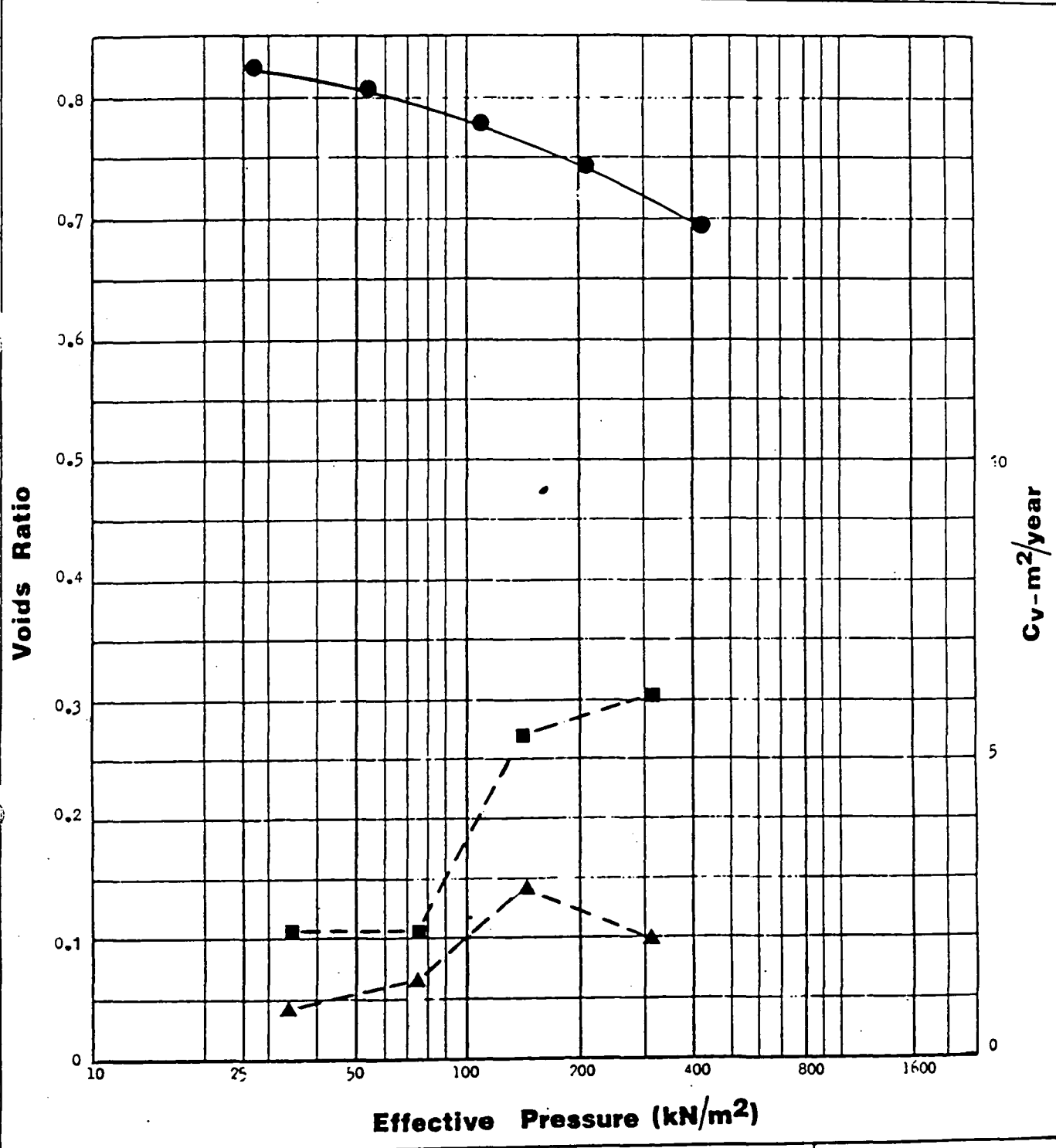
Project North Western Road Construction Unit,
L. G. Mouchel & Partners,
M66 Manchester Outer Ring Road,
Supplementary Site Investigation Section 3

Contract S2904

exploration associates

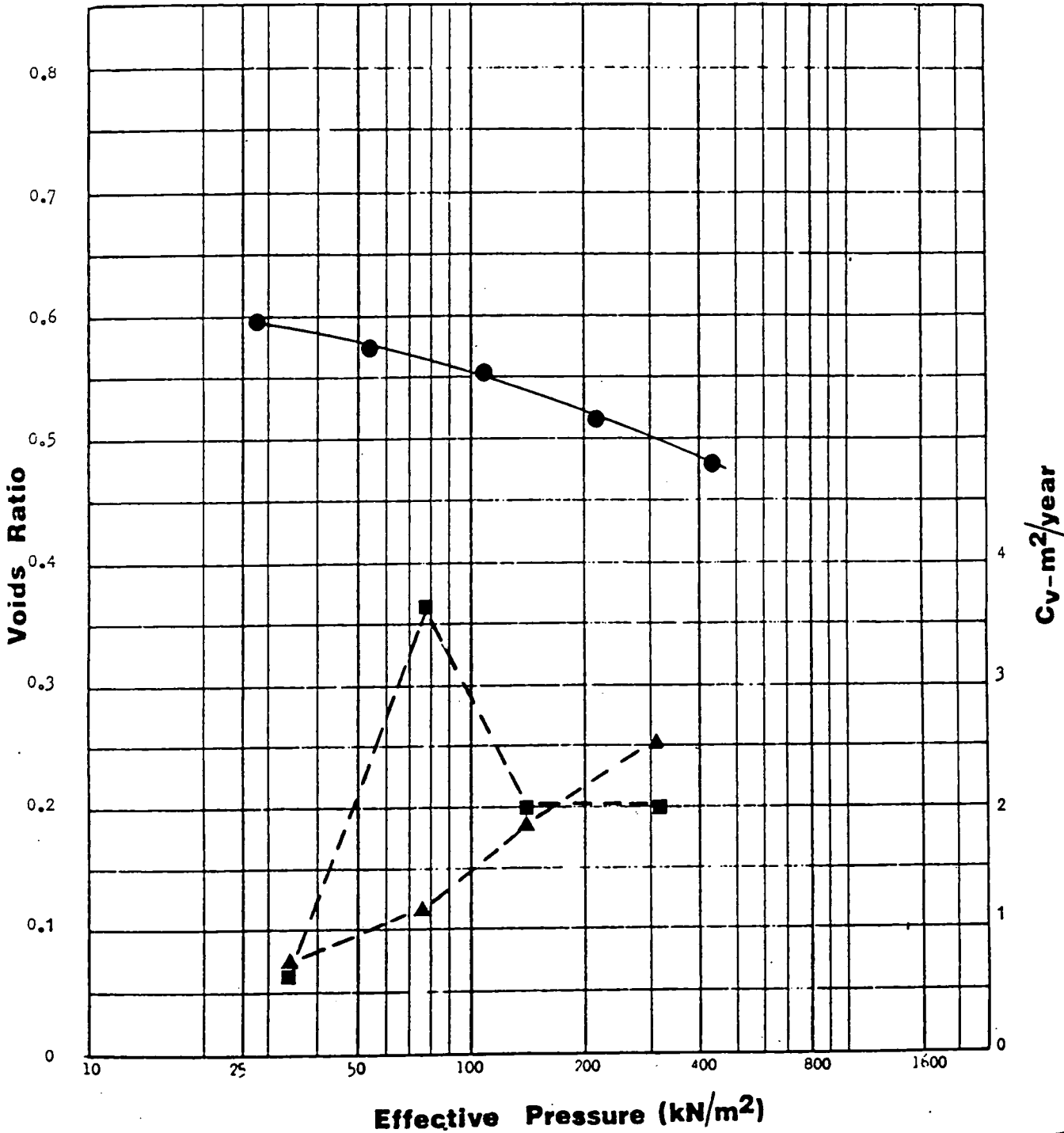
Figure 379/2

Rate										Compression					Sample	
C = m / (1 + e) × 10 ⁻³										m = m / kN × 10 ⁻³					Type	
	10 25	25 50	50 110	110 210	210 430	430 850	850 1700			Fitting Method	Po+ 50	Po+ 100	Po+ 300		Hole 379	Depth 0.5-1.0
		0.9	1.3	2.9	2.0					log time t ₅₀ ▲	3.90	2.72	1.50			
		2.1	2.1	5.5	6.1					root time t ₉₀ ■						



Description	Brown very silty clay.	Voids Ratio Initial	0.855	Initial	w%	31
		Voids Ratio Final	0.699	Final	w%	26
		Specific Gravity	2.67 (Assumed)	γ_b	Mg/m ³	1.88
Laboratory – Consolidation		Project North Western Road Construction Unit, L. G. Mouchal & Partners, M66 Manchester Outer Ring Road, Supplementary Site Investigation Section?			Contract	S2904
exploration associates					Figure	379/3

Rate										Compression					Sample	
C _v = 10 ⁻⁴ year = 0.000104 year										C _v = 10 ⁻⁴ year = 0.000104 year					Type	
	10	25	50	100	200	400	800			Fitting Method	Po + 50	Po + 100	Po + 300			moie
	25	50	100	200	400	800	1600									379
		0.2	1.2	1.9	2.5					log time t ₅₀ ▲	3.07	2.56	1.45			Depth 2.5-3.0
		0.7	3.7	2.0	2.0					root time t ₉₀ ■						



Description Brown very silty clay.	Voids Ratio Initial	0.638	Initial w%	26
	Voids Ratio Final	0.479	Final w%	23
	Specific Gravity	2.67 (Assumed)	γ_b Mg/m ³	2.06
Laboratory – Consolidation	Project North Western Road Construction Unit, L. G. Mouchel & Partners, M66 Manchester Outer Ring Road, Supplementary Site Investigation Section			Contract S2904
exploration associates				Figure 379/4

